Energy CONSERVATION

DOE/CE/40936--T3
(DE97050772)

BLACK LIQUOR COMBUSTION VALIDATED RECOVERY BOILER MODELING FIVE-YEAR REPORT

By
T. M. Grace
W. J. Frederick
M. Salcudean
R. A. Wessel

August 1996

Work Performed Under Contract No. FG07-90CE40936

For
U.S. Department of Energy
Office of Industrial Technologies
Washington, DC

By
The Institute of Paper Science and Technology
Atlanta, Georgia

and

Oregon State University
Corvallis, Oregon

and

University of British Columbia
Vancouver, BC, Canada

and

Babcock & Wilcox Company
Alliance, Ohio

DISCLAIMER

DOE/CE/40936--T3
(DE97050772)
Distribution Category UC-1400

BLACK LIQUOR COMBUSTION VALIDATED RECOVERY BOILER MODELING FIVE YEAR REPORT

by

T.M. Grace, W.J. Frederick, M. Salcudean, and R.A. Wessel

August 1996

A Summary Report
for the First Five Years
of the Project

Work Performed Under Contract DE-FG07-90CE40936

Prepared for

The U.S. Department of Energy
Office of Industrial Technologies
Washington, D.C.

Prepared by

The Institute of Paper Science and Technology
Atlanta, GA

Oregon State University
Corvallis, OR

University of British Columbia
Vancouver, BC, Canada

Babcock & Wilcox Company
Alliance, OH

Table of Contents

EXECUTIVE SUMMARY

This project was initiated in October 1990 and extended for three additional years in October 1994. During 1995 the extended project was restructured so as to bring it to closure in a manner that would maximize the value of the entire project to the pulp and paper industry. The restructured project was initiated at the end of October 1995 and is scheduled to be completed in January 1997. This report covers the project from the beginning up to the start of the restructured project.

PROJECT OBJECTIVES

The objective of this project was to develop a new computer model of a recovery boiler furnace using a computational fluid dynamics (CFD) code specifically tailored to the requirements for solving recovery boiler flows, and using improved submodels for black liquor combustion based on continued laboratory fundamental studies. The project originated in October 1990 and was scheduled to run for four years. At that time, there was considerable emphasis on developing accurate predictions of the physical carryover of macroscopic particles of partially burnt black liquor and smelt droplets out of the furnace, since this was seen as the main cause of boiler plugging. This placed a major emphasis on gas flow patterns within the furnace and on the mass loss rates and swelling and shrinking rates of burning black liquor drops.

As work proceeded on developing the recovery boiler furnace model, it became apparent that some recovery boilers encounter serious plugging problems even when physical carryover was minimal. After the original four-year period was completed, the project was extended to address this issue. The objective of the extended project was to improve the utility of the models by including the black liquor chemistry relevant to air emissions predictions and aerosol formation, and by developing the knowledge base and computational tools to relate furnace model outputs to fouling and plugging of the convective sections of the boilers.

ACCOMPLISHMENTS

The work done to date includes CFD model development and validation, acquisition of information on black liquor combustion fundamentals and development of improved burning models, char bed model development, and model application and simplification.

CFD Model Development and Validation

UBC has developed computer codes for a CFD-based model of the recovery furnace. These codes have been tailored to meet the special requirements of recovery boiler flows. The UBC codes employ multigrid methods and segmentation techniques to provide a good resolution of the complex flows near the air ports and greatly improve the convergence characteristics of the numerical procedure. Specifically, a non-linear multigrid method with a symmetrically coupled Gauss-Seidel method is used to improve convergence. The segmentation technique allows non-matching grids to coexist in adjacent parts of the flow field. This allows modeling air ports at their correct location without unnecessary grid refinement.

Isothermal flow predictions made with the UBC code have been validated against measured flows made in water models of two recovery boilers and with cold air flow measurements made on a recovery boiler. The results indicate that the computational model is capable of yielding velocity distributions that are representative of actual flow fields. The up flow and down flow regions were correctly predicted as were the contours of zero upward velocity. Peak values of upflow and downflow velocities were reasonably well predicted in most cases. Additional validation tests are planned with different combustion air supply distributions.

Additional insight into recovery boiler flows has been obtained from flow measurements on two 1:28 scale water models of recovery boilers at UBC. The first is a model of a recovery boiler at Weyerhaeuser's Plymouth, NC mill and the second is a model of a recovery boiler at Weyerhaeuser's Kamloops, BC mill. Flow fields were measured using laser-Doppler velocimetry and particle-image velocimetry. Tests showed that these flows were frequently subject to low-frequency unsteadiness.

A hot flow version of the UBC code has been developed. This incorporates variable gas density, black liquor combustion with associated source/sink terms, simplified treatment of the bed and of black liquor striking the walls, and heat transfer (including radiation) to the walls. The hot flow model is still under intense development, but it has been used for simulations that give apparently reasonable results.

It now takes 1-3 days to run a hot flow case including black liquor combustion with the UBC model. The actual CPU time to run a case is about one 24-hr day. Time is also required for setting up a case and for adjustments of boundary conditions, etc. This is a significant reduction in solution time.

IPST has developed a simplified recovery boiler model, called In-Flight, using the commercially available FLUENT CFD code. This model uses a preestablished, fixed gas field (usually a calculated isothermal flow field with uniform temperature and gas concentrations) and looks at the burning behavior of black liquor drops sprayed into the furnace. The black liquor chemistry used in this model needs updating.

Commercially available CFD codes have undergone significant improvement since this project was initiated, and could provide a viable basis for recovery boiler models. Several boiler manufacturers are currently using such CFD codes as platforms for recovery boiler models.

There has been very little comparison of how well different CFD codes predict recovery boiler flows, even under isothermal conditions. No attempts have been made to compare hot flow predictions. Benchmarking of recovery boiler model codes against one another should be an essential element of model validation programs.

Considering all available information, current recovery boiler models appear to adequately handle flow predictions. At the very least, flow prediction is not the area of greatest uncertainty. This is particularly true with respect to the information most needed to improve recovery boiler performance, which is very dependent on detailed black liquor chemistry, aerosol formation and radiant heat transfer.

Black Liquor Combustion Fundamentals

The black liquor combustion models that were available at the start of this project were based on fundamental studies carried out at IPST and Åbo Akademi, in Finland, in the late 1980s. These studies were focused primarily on the mass changes and diameter changes that accompanied black liquor burning, since these factors had a major influence on the trajectories followed by the liquor particles in the furnace and thus on the amount of carryover. Drying and volatiles formation were treated as separate heat transfer controlled processes and char burning was treated as an oxygen mass transfer controlled process.

It was recognized that these black liquor burning models were highly oversimplified and additional fundamental studies were carried out at OSU and Åbo Akademi to provide better models for black liquor burning. These studies showed that in typical furnace atmospheres, gasification of carbon by reaction with CO_2 and H_2O was much more important than direct oxidation during the char burning step. Kinetic rate equations for these gasification reactions were developed and combined with external and internal mass transfer correlations to provide an overall rate equation for the char burning step. It was recognized that evaporation of water and pyrolysis of black liquor organics occurred simultaneously because of the strong internal temperature gradients in burning droplets and a method of treating this was developed. Algorithms have also been developed for determining the extent of volatile formation during pyrolysis and for apportioning the volatiles to specific species for further reaction in the gas phase. Most of the work on this second generation drop burning model is now complete. However, the current model still contains empirical parameters that are correlated in terms of variables that have meaning in the laboratory systems in which the burning data were obtained, but which do not have

obvious counterparts in the recovery furnace, where drops are moving through a variable temperature and gas concentration field. This issue remains to be resolved.

The second generation black liquor burning model is adequate for determining the source/sink terms needed to compute the velocity, temperature, and gas concentration fields in a full, hot flow simulation. However, it does not contain the necessary information on sulfur release and recapture and on sodium, potassium, and chloride volatilization needed to predict air emissions or deal adequately with boiler fouling and plugging. Ongoing work at OSU has shown that sulfur release is strongly dependent on the nature of the sulfur compounds in the black liquor and that the paths by which sulfide is formed in the furnace is complicated. Initial rate equations for sodium and potassium release during char burning have been developed, but there remains uncertainty about the extent of alkali release during pyrolysis. The work at OSU planned for the remaining phase on this project should resolve these uncertainties and result in reliable rate equations for incorporation into furnace models.

Considerable new information on aerosol formation during black liquor combustion is being developed at several laboratories. Much of this was presented at the International Chemical Recovery Conference in April 1995. This work needs to be interpreted and the implications to modeling determined. A proper treatment of aerosol formation is believed to be critical to developing models with the capability to predict the effects of firing conditions on boiler fouling and plugging.

Bed Models

Much of the chemistry involved in bed burning is essentially the same as that during the char burning stage of a liquor drop and rate equations for treating these processes are now available. These have been implemented in bed models with a highly simplified geometry. Proper treatment of devolatilization from incompletely pyrolyzed liquor solids reaching the bed is more uncertain and requires further work. The rate of bed burning can be coupled with the rate at which combustible material reaches the bed to determine an inventory imbalance and thus an indication of bed growth or decay rates. An alternative approach is to force a steady state by assuming the bed burning rate is equal to the rate at which combustible material reaches the bed. However, this latter approach begs the question of whether or not such burning rates are actually attainable for the firing conditions being simulated. Further work is required on the role played by the char bed in fume formation and smelt reduction.

It is recognized that bed shape can affect flow patterns, especially in the lower furnace. However, no bed models currently have the capability of predicting bed size and shape. The current practice is either to ignore the bed or to arbitrarily impose a bed shape as part of the set up conditions. In addition, none of the current models incorporate the effects of gas flow over the bed transporting char particles toward the center or of entraining char particles off the bed.

IPST has done some work on a bed model, using a FLUENT code with body-fitted coordinates, in which the size of the computational cells making up the bed were adjustable and coupled with bed material balances. This had the potential for adjusting bed shape in response to inventory changes. This line of attack has currently been abandoned as it is incompatible with the formulation of the UBC model. It remains to be determined if it represents a viable approach to bed modeling.

Model Application and Simplification

Experience in applying models to actual recovery boilers has underscored the need to find methods for simplifying the calculation effort. The models provide an enormous amount of information on details of the furnace flows, temperatures, etc., most of which is not directly needed in application. Most of the critical model outputs needed in a particular application are on the boundaries.

Another problem with CFD-based recovery boiler models is that a completely new solution must be generated (which may take days to set up and compute) when any variable (such as firing rate) is changed. It is not evident that starting with the fields from one solution provides any significant reduction in solution time for a second case which is a modification of the first. This severely limits the number of cases that can be examined.

IPST has developed a fixed-field approach, called In-Flight, in which the gas fields are preselected and held constant. Usually, the flow field is calculated as a CFD isothermal flow solution and the gas temperature and gas concentration fields are arbitrarily supplied. Alternatively, the gas fields from one complete hot flow solution can be used. Then the behavior of the black liquor being sprayed into the furnace can be determined with a fair degree of detail in a non-iterative manner. This greatly shortens the computational effort. This has proved to be a useful way of looking at the effects of spray variables. The validity of the approach is strongly dependent on the degree that isothermal flow fields approximate hot flow fields, and this remains to be determined.

Code Status and Availability

UBC is continuing to develop the hot flow code that incorporates variable gas density, black liquor combustion with associated source/sink terms, highly oversimplified treatment of the bed and of black liquor striking the walls, and heat transfer (including radiation) to the walls. Early versions of the UBC isothermal flow code have been transferred to IPST according to a prearranged schedule, and this is continuing. A working version of the current UBC hot flow code has been transferred to IPST. An updated code will be transferred at the end of the project.

IPST is not currently developing codes for black liquor recovery boiler models. IPST continues to use the In-Flight model and will use the UBC model for hot flow simulations for model validation.

Several boiler manufacturers have developed recovery boiler models based either on in-house CFD codes or commercially available CFD platforms. They have expressed interest in black liquor combustion submodels, either as algebraic equations and algorithms, or as documented code, for incorporation in their own models.

WORK REMAINING

A critical review of recovery boiler modeling was carried out as part of this project. This review concluded that the most important information needed (and thus the critical model outputs) was the following:

- amount, size and composition of aerosols leaving the furnace
- amount of physical carryover out of furnace
- furnace exit gas temperature distribution
- furnace exit gas velocity distribution
- wall heat flux distribution
- concentrations of air emission gases leaving the furnace
- bed size, shape, surface temperature distribution, and burning rate distribution
- some measure of bed stability and "goodness"
- overall reduction efficiency.

In addition, sufficient understanding of fouling and plugging processes needs to be acquired to permit interpretation of model outputs in terms of plugging/fouling rates

This recovery boiler modeling project is now entering its final phase. The overall objective is to bring closure to the project in an effective manner that maximizes the usefulness of the total effort to the kraft pulp industry. The key remaining tasks to accomplish this are as follows.

1. Complete the development of enhanced furnace models that have the capability to accurately predict the outputs listed above.

2. Validate these enhanced furnace models so that users will have confidence in the predicted results.

3. Obtain fundamental information on aerosol formation, deposition, and hardening so as to develop the knowledge base needed to relate furnace model outputs to plugging and fouling in the convective sections of the boiler.

4. Facilitate the transfer of codes, black liquor submodels, and fundamental knowledge to the US kraft pulp industry.

The final phase is scheduled to take fifteen months and should be completed in January 1997.

INTRODUCTION

BACKGROUND ON RECOVERY BOILER MODELS

General Background Information

During the 1980s, the kraft pulp industry undertook a major activity of retrofitting recovery boilers to improve performance and increase capacity. Many of the retrofits took the form of changes in the way air was supplied to the furnace and the way liquor was sprayed into the furnace. Considerable attention was paid to gas flow patterns within the furnace and on gas temperature distributions leaving the furnace cavity (which were believed to be coupled to the flow pattern). The objective was to try to minimize channeling of gases and smooth out gas velocity and temperature distributions. A number of paper companies and boiler manufacturers carried out air flow tests on scaled down mockups of recovery boilers to gain insight into how air supply variables influenced flow patterns within the furnace. While these scaled flow tests were difficult to quantify and interpret, they did provide considerable guidance to the evolution of recovery boiler designs, particularly with regard to means for supplying air to the furnace.

At the same time, during the 1980s, continued increase in the capabilities of computers along with developments in the theory of computational fluid dynamics (CFD), made it possible to calculate numerical solutions to increasingly more complex flow problems. Thus the possibility of supplementing or replacing the scaled flow tests with calculated flows from CFD models became a realistic alternative.

Combustion researchers in academia, in government laboratories, and at boiler manufacturers began to develop methodologies for coupling combustion information into CFD codes for a number of different fossil fuels. This resulted in increasingly sophisticated methods for calculating hot gas flow fields in different types of furnaces. The work carried out by the Advanced Combustion Engineering Research Center (ACERC) at Brigham Young University and the University of Utah is typical of what was developed. ACERC developed codes for 2-dimensional and then 3-dimensional furnace flows and considered such computer models as the ultimate technology transfer mechanism for the fundamental combustion information they were acquiring.

Computer modeling of recovery boilers began with some rather simple zonal equilibrium models in the 1970s. Toward the end of the decade, a fairly detailed model with some capability of predicting physical carryover of liquor and smelt drops was developed by Arthur D. Little, Inc. under sponsorship of the American Paper Institute (now AF&PA) Recovery Boiler Committee. However, the state of knowledge of black liquor combustion behavior and real flows in recovery boilers at that time was totally inadequate to provide a scientific basis for such a model, and it was not very successful. However, this early

model effort did serve to define the critical information needs and provided a road map for much of the research on black liquor combustion that was carried out during the 1980s.

Background of Current Program

The current recovery boiler modeling program is the culmination of work on black liquor combustion and recovery boiler modeling that began at the Institute of Paper Science & Technology in the mid 1980s. The early work showed the potential of using CFD-based models for understanding the effects of liquor spray conditions and air supply conditions on recovery boiler performance. However, there were a number of limitations to these early recovery boiler models. The solutions required long times (weeks) to converge and would not converge without active intervention by the person running the simulation. There were also concerns about computational artifacts and the compromises necessary to match the geometry of recovery boiler air ports to workable computational grids. Thus, in the 1989-1990 period, CFD issues, especially as they applied to the particular conditions relevant to recovery boilers, were a dominant concern.

This recovery boiler project started in October 1990 and was originally scheduled to run for four years. The objective of the project was to develop a computer model of a recovery boiler furnace using a CFD code specifically tailored to the requirements for solving recovery boiler flows and using improved submodels for black liquor combustion based on continued laboratory fundamental studies. There was considerable emphasis on developing accurate predictions of the physical carryover of macroscopic particles of partially burnt black liquor and smelt out of the furnace, since this was seen as the main cause of boiler plugging. This placed strong emphasis on gas flow patterns within the furnace and on mass loss rates and swelling and shrinking rates of burning black liquor drops.

The original project involved three institutions, the Institute of Paper Science & Technology (IPST), the University of British Columbia (UBC), and Oregon State University (OSU). IPST was responsible for overall project leadership, bed modeling, model simplification and application, and overall model validation. UBC was responsible for CFD code development and flow modeling and validation. OSU was responsible for fundamental data on black liquor combustion and formulation of improved black liquor burning models. In addition, T. M. Grace Company, Inc. was involved to provide technical coordination and interpretation.

When the original four year period was completed, the project was extended for an additional three years. The extension started in September 1994. By this time it had become apparent that many recovery boilers encountered serious plugging problems even when physical carryover was minimal. The objective of the extended project was to improve the utility of the models by including the black liquor chemistry relevant to air emissions predictions and aerosol formation, and by developing the knowledge base and

computational tools to relate furnace model outputs to fouling and plugging of the convective sections of the boilers.

Two new members were added to the project team in the extended project. Babcock & Wilcox (B&W) became involved to provide experimentally based information on radiation heat transfer. Tran Industrial Research (TIR) was brought in to provide guidance and information relevant to boiler plugging. In January 1995, as a result of staff changes at IPST, Thomas M. Grace became a part-time employee of IPST in order to serve as principal investigator on the project. As a consequence, T. M. Grace Company, Inc. was no longer involved as as subcontractor.

Early in 1995, a critical review of recovery boiler modeling was carried out. As a result of this review and other factors, the extended project was restructured so as to bring it to closure in a manner that would maximize the value of the entire project to the pulp and paper industry. The restructured project was initiated at the end of October 1995 and is scheduled to be completed in January 1997.

This report covers the project from the beginning up to the time of the restructuring. A final report will be prepared at the end of the project.

Elements of Recovery Boiler Models

Recovery boilers are rather unique in that the fuel and combustion air are introduced into the furnace completely separately and the flow patterns and general turbulence in the furnace are relied upon to achieve adequate mixing and combustion. Air is introduced through a large number of jets, arranged in complicated patterns along each wall. The convergence and interaction of these jets results in a very complex flow field in the furnace. Black liquor fuel is introduced through a number of relatively coarse sprays located on the walls. The gas flow patterns have a large effect on the locations for heat release in the furnace and the physical carryover of particles of partially burned liquor drops and smelt.

It is helpful to think of the overall recovery boiler model as consisting of a number of distinct parts or elements. In recovery boiler models, the liquor and gas are treated as two separate phases. The gas phase is treated as a continuum, while the liquor is treated as distinct drops which dry and burn as they move through the gas.

The CFD part of the model deals with the gas phase. The differential equations describing mass, heat, and momentum balances for the gas phase are converted to difference equations and solved numerically. The furnace volume is broken up into cells or nodes using an appropriate grid structure. Numerical solution of the equations requires specification of boundary conditions and also of sources and/or sinks of mass, energy, and momentum resulting from liquor burning. The coupling with the black liquor phase takes place through these source/sink terms.

The black liquor burning model consists of two distinct parts, a drop burning model and a trajectory model. The drop burning model describes how the liquor drop interacts with the surrounding gas with respect to mass and energy. It includes an appropriate chemical description of the burning drop and means for tracking state changes (composition and temperature) in the drop, and rate equations that describe the exchange of mass and energy between the liquor and the gas. The drop burning model also provides means for handling the swelling and deswelling that occurs when black liquor burns. The rate equations that describe mass and energy exchange between the liquor and the gas are the basis for the gas-phase source/sink terms needed by the CFD part of the model.

The trajectory equations come from a force balance on the burning drop as it moves through the furnace. Forces acting on the drop include gravity and drag by the gas through which it is moving. The drag force depends on the vector velocity difference between the drop and the gas and is oriented in this direction. The initial condition for the drop trajectory as it enters the furnace comes from a model for the liquor spray. Typically, this sets the initial drop size and vector velocity. The drops continue on their trajectories until they reach the bed, strike a furnace wall, or are carried up out of the furnace.

The source/sink terms apply to the gas phase. These include the masses of each of the specific chemical species entering/leaving the gas phase, the energy transferred in both directions by chemical species transfer and by heat transfer, and the momentum transfer to the gas by fluid drag from the particles. These must be specifically written for the black liquor burning process, as they are not part of the CFD codes themselves. Means of handling the source/sink terms are a part of CFD codes, but not the specific source/sink equations.

Models are also required to describe what happens to the liquor drops that reach the walls or land on the bed. These are referred to as wall models and bed models. The bed models usually incorporate some way of handling bed burning by interacting with the gas phase in the region directly above the bed.

Other elements of recovery boiler models include means for setting up the grid structure, means for setting appropriate boundary conditions, solution algorithms, and means for displaying model outputs.

The output of a CFD-based recovery boiler model includes a quantitative description of the gas flow, temperature and concentration fields, the trajectories of the liquor drops and the ultimate fate of all of the liquor drops, heat fluxes to the bounding surfaces, and possibly information on bed burning rates, temperatures, etc. The gas field information includes data on the three velocity components, temperature and the concentration of each of the designated gas chemical species at each of the grid points or volume elements (cells). If the grid is divided into 100,000 elements, the output will be well over one million pieces of data not including the information needed to describe drop trajectories.

Graphical displays or other methods of compressing the data are required to make this amount of information manageable.

CFD platforms

There are a large number of CFD codes that can provide a platform for a recovery boiler model. Some, such as FLUENT and PHOENICS are commercially available. Others have been developed within universities or within companies. The advantage of commercial codes is that they allow a CFD-based furnace model to be developed without an extensive effort or expertise in fluid dynamics. The disadvantage is that the codes are general and not necessarily efficient for a particular type of problem.

The original recovery furnace model developed at IPST used a FLUENT platform. A similar recovery furnace model developed at Tampere Technical University used PHOENICS as a CFD platform. The In-Flight furnace model at IPST is still based on a FLUENT platform.

In this current program, UBC has developed computer codes for a CFD-based model of the recovery furnace. These codes have been tailored to meet the special requirements of recovery boiler flows. The UBC codes employ multigrid methods and segmentation techniques to provide a good resolution of the complex flows near the air ports and greatly improve the convergence characteristics of the numerical procedure. Specifically, a non-linear multigrid method with a symmetrically coupled Gauss-Seidel method is used to improve convergence. The segmentation technique allows non-matching grids to coexist in adjacent parts of the flow field. This allows modeling air ports at their correct location without unnecessary grid refinement.

A hot flow version of the UBC code has been developed. This incorporates variable gas density, black liquor combustion with associated source/sink terms, highly oversimplified treatment of the bed and of black liquor striking the walls, and heat transfer (including radiation) to the walls. The hot flow model is still under intense development, but it has been used to for initial simulations that give apparently reasonable results.

It now takes 1-3 days to run a hot flow case including black liquor combustion with the UBC model for a reasonably coarse grid. The actual CPU time to run a case is about one 24-hr day. Time is also required for setting up a case and for adjustments of boundary conditions, etc. This is a significant reduction in solution time from the past.

IPST extended the old recovery boiler models that were based on the commercially available FLUENT CFD code, to produce a model known as "In-flight". This model uses a preestablished, fixed gas field (usually a calculated isothermal flow field with uniform temperature and gas concentrations) and looks at the burning behavior of black liquor drops sprayed into the furnace. The black liquor chemistry currently used in this model is

somewhat outdated, but it is a useful and quicker way of exploring the effects of liquor sprays on combustion behavior.

Commercially available CFD codes have undergone significant improvement since this project was initiated, and could now provide a viable basis for recovery boiler models. Several boiler manufacturers are currently using such CFD codes as platforms for recovery boiler models.

Black liquor combustion models

Black liquor combustion models that were available at the start of this project were based on fundamental studies carried out at IPST and Åbo Akademi, in Finland, in the late 1980s. These models were focused primarily on the mass changes and diameter changes that accompanied black liquor burning, since these factors had a major influence on the trajectories followed by the liquor particles in the furnace and thus on the amount of carryover. In these first generation models, drying and volatiles formation were treated as separate heat transfer controlled processes and char burning was treated as an oxygen mass transfer controlled process.

It was recognized that the first generation black liquor burning models were highly oversimplified and additional fundamental studies were carried out at OSU and Åbo Akademi to provide better models for black liquor burning. These studies showed that in typical furnace atmospheres, gasification of carbon by reaction with CO_2 and H_2O was much more important than direct oxidation during the char burning step. Kinetic rate equations for these gasification reactions were developed and combined with external and internal mass transfer correlations to provide an overall rate equation for the char burning step. It was recognized that evaporation of water and pyrolysis of black liquor organics occurred simultaneously because of the strong internal temperature gradients in burning droplets and a method of treating this was developed. Algorithms have also been developed for determining the extent of volatile formation during pyrolysis and for apportioning the volatiles to specific species for further reaction in the gas phase. Most of the work on this second generation drop burning model is now complete. However, the current model still contains empirical parameters that are correlated in terms of variables that have meaning in the laboratory systems in which the burning data were obtained, but which do not have obvious counterparts in the recovery furnace, where drops are moving through a variable temperature and gas concentration field. This remains to be resolved.

The second generation black liquor burning model is adequate for determining the source/sink terms needed to compute the velocity, temperature, and gas concentration fields in a full, hot flow simulation. However, it does not contain the necessary information on sulfur release and recapture and on sodium, potassium, and chloride volatilization needed to predict air emissions or deal adequately with boiler fouling and plugging. This additional information is being developed at OSU.

Ongoing work at OSU has shown that sulfur release is strongly dependent on the nature of the sulfur compounds in the black liquor and that the paths by which sulfide is formed in the furnace are complicated. Complete rate equations for sulfur release and recapture are not yet available. Initial rate equations for sodium and potassium release during char burning have been developed but need elaboration and verification. The work at OSU planned for the remaining phase on this project should resolve these uncertainties and result in reliable rate equations for incorporation into furnace models.

Considerable new information on aerosol formation during black liquor combustion is being developed at several laboratories. Much of this was presented at the International Chemical Recovery Conference in April 1995. This work needs to be interpreted and the implications to modeling determined. A proper treatment of aerosol formation is believed to be critical to developing models with the capability to predict the effects of firing conditions on boiler fouling and plugging.

The third generation black liquor burning model which will come from the continuing work will describe the transfer of all of the important elements in black liquor to the gas phase and include all of the key chemical species needed to describe aerosol formation and emissions-related reactions.

Bed models

The char bed causes considerable complications in developing a CFD-based recovery furnace model. The CFD portion of the model is based on the gas phase and the bed acts as a boundary condition for the gas. However, it is a boundary that is able to exchange mass (chemical species), energy, and possibly momentum with the gas phase. Moreover, the bed is able to act as a fuel reservoir and for any given set of furnace operating conditions, fuel may be accumulating or depleting in the bed. This can have a pronounced effect on overall energy balances. Finally, the bed occupies space in the lower furnace that is not available for gas flow, and thus can have a pronounced effect on the gas flow patterns in the lower furnace.

Up to now, bed burning has been treated as if the chemistry involved is essentially the same as that during the char burning stage of a liquor drop. The same rate equations used for describing char burning in a drop can be applied to bed burning with an allowance for the difference in geometry. These rate equations have been implemented in bed models with a highly simplified geometry. There are some problems with this approach. The reaction rates depend strongly on temperature and a heat balance over a bed surface layer to predict temperature can be very sensitive to arbitrary assumptions. It is known that endothermic reactions occur below the surface of the bed and result in strong temperature gradients within the bed. No allowance is made for this in current bed models. Another problem in modeling bed burning is how to handle the water and combustible volatiles that reach the bed with incompletely dried and pyrolyzed black liquor. In the drop burning models, the drying and devolatilization processes are modeled as going to

completion before char burning is initiated. The bed is an assemblage of many different liquor particles in various states of fuel depletion, and all of the burning processes need to be considered as going on in parallel. This is handled in a very arbitrary manner in current bed models.

It is also necessary to deal with the inventory question. The rate of bed burning can be coupled with the rate at which combustible material reaches the bed to determine an inventory imbalance and thus an indication of bed growth or decay rates. An alternative approach is to force a steady state by assuming the bed burning rate is equal to the rate at which combustible material reaches the bed. However, this latter approach begs the question of whether or not such burning rates are actually attainable for the firing conditions being simulated.

The experimental data base for char bed burning rates is very limited. Most of the current bed models are either based on the experimental work carried out with the char bed reactor at IPC (now IPST) in 1988 [1] or on single particle char burning rate data.

While it is recognized that bed shape can affect flow patterns, especially in the lower furnace, no bed models currently have the capability of predicting bed size and shape. The current practice is either to ignore the bed or to arbitrarily impose a bed shape as part of the set up conditions. In addition, none of the current models incorporate the effects of gas flow over the bed transporting char particles toward the center or of entraining char particles off the bed.

IPST did some initial studies toward development of a bed model using a FLUENT code with body-fitted coordinates. The size of the computational cells making up the bed were adjusted and coupled to the bed inventory, thus providing the potential for handling inventory changes and adjusting bed shape in response to inventory changes. However, such a bed model would not interface with the UBC model or other codes being used, and this approach has been abandoned.

Setup, input and output

A considerable part of a CFD-based recovery boiler model simulation is involved with setting up the problem. The geometry of the furnace must be known including the shape of the nose arch (bullnose). The furnace volume must be divided up into a large number of computational cells for the CFD difference equations. A suitable grid structure to define the location of all of these cells must be set up. In order to provide for air and liquor entry into the furnace, the grid structure needs to be aligned with the air port openings and the liquor gun openings. Air entry through burner ports and other furnace openings may also need to be allowed for.

Considerable compromises usually need to be made in setting up a problem. There is a direct relation between the number of cells or grid points used and the calculation

requirements. Thus requirements for computer memory and solution time have a major influence on the number of cells that can be used. Current models typically use something on the order of 100,000 cells for a simulation. This effectively prevents using enough cells to completely define the jets coming in from each individual air port. Primary air is normally modeled as a slot jet in order to accomodate the need to keep the number of cells down. Secondary air and tertiary air ports are usually modeled as individual ports. However, even for these ports, compromises may be necessary in locating the ports in the computational geometry. Ports may be arbitrarily located directly above other ports in order to be aligned with the chosen grid. Thus the computational geometry may differ from the real furnace geometry. Symmetry assumptions are often made so that only one-half or one-fourth of the furnace is actually modeled. This allows a finer mesh size on the computational grid but it also forces the flows to be symmetrical. All of this can affect the validity of the predicted flows. There is no doubt that the compromises forced on the modeler by the limitations on number of cells can influence the results to a significant extent.

Problem setup also requires specification of the boundary conditions, in particular, the conditions at which air and liquor enter the unit. The simplest approach is to assume that the air at a given level entering the furnace is evenly distributed to all of the ports. This may introduce biases into the predicted flows that do not reflect reality. Pressure drops through windboxes and across dampers, etc. can result in considerable unevenness in the distribution of air between different air ports. Liquor spray specification usually involves assuming the liquor enters the furnace as discrete drops with a defined drop size distribution and vector velocity distribution. The relation between actual liquor firing variables and the specification of the sprays is often arbitrary and/or obscure.

The consequence of all of these factors is that the results of a furnace simulation can be greatly influenced by the setup of the case. Case setup remains very much an art at the present time.

The output of a CFD-based recovery boiler model includes;

- a quantitative description of the gas flow, temperature and concentration fields,
- the trajectories of the liquor drops and the ultimate fate of all of the liquor drops,
- heat fluxes to the bounding surfaces, and
- possibly information on bed burning rates, temperatures, etc.

The gas field information includes data on all three velocity components, temperature and the concentration of each of the designated gas chemical species at each of the grid points or volume elements (cells). If the grid is divided into 100,000 elements, the output will be well over one million pieces of data to describe the gas fields alone. Even more data is required to describe heat fluxes, drop trajectories and fates, and bed burning rates and temperatures. Graphical displays or other methods of compressing the data are required to make this large amount of information manageable. Commercial CFD codes come with built-in graphic routines for displaying the data. UBC has also developed special

graphical data display routines for their code. Care must be taken that the averaging processes used in displaying field information do no themselves generate artifacts.

NEED FOR RECOVERY BOILER MODELING PROGRAM

CFD-based recovery boiler models have the potential for being a powerful tool in optimizing recovery boiler process design and operation. They are capable of dealing with the complex flow patterns that exist in recovery boilers as well as the black liquor combustion process. Thus they can provide a means for relating firing practices and furnace design directly to furnace performance.

During the course of this program, recovery boiler models have been developed at a number of different organizations. A summary of the models currently known to be in existence is given below.

1. Models (codes) developed in this study

UBC	"UBC model"
IPST	FLUENT-based In-Flight model

2. Boiler Manufacturers

B&W	full in-house model	own CFD base
ABBCE	full in house model	based on FLUENT
Tampella	full in-house model	based on PHOENICS
Ahlstrom	in-house model	based on FLUENT
Kvaerner	simple in-house model	based on FLUENT
Jansen	simple in-house model	own base (also have KIVA)

3. Other Recovery Furnace Model Codes

Tampere Technical University	based on PHOENICS
STFI/Royal Institute of Technology	own CFD base

4. Various straight CFD codes for flow problems

It is useful to look at the recovery boiler model development work in this program in the context of the availability of various CFD-based models. This look will focus on how the models would be used and how they could provide the greatest benefit to the pulp and paper industry.

Users Wants and Needs

A computer model of a recovery boiler has no value in and by itself. If there is to be value in developing a computer model of a recovery furnace, there must be a user for the model

who would obtain value from carrying out simulations with the model. The potential users of recovery boiler models include;

- boiler manufacturers,
- kraft pulp manufacturers,
- engineering firms and consultants,
- academic institutions, and
- R&D institutions.

Boiler manufacturers are the source of most recovery boiler technology developments. They are looking to improve recovery boiler designs to gain a competitive edge through providing greater capability per dollar spent by the customer. Boiler manufacturers derive their main economic benefit from the sale of recovery boilers and in upgrading older units. They do not gain directly from improved operations. They usually need to meet guarantees. Boiler manufacturer service engineers may be involved in troubleshooting recovery boiler operating problems. There are currently not many new recovery boilers being sold and manufacturers are struggling to keep technical capability in place. As a result, they may have limited resources to devote to developing their own recovery boiler models.

The main needs of boiler manufacturers are process insight to guide design changes, increased credibility with customers to aid sales of recovery boilers, guidance in troubleshooting recovery boiler operating problems, confidence in making guarantees, and means for gaining a competitive advantage over other boiler manufacturers.

Recovery boiler manufacturers can be divided into two groups; those that have in-house recovery boiler models and those that do not. This will significantly affect how they would use the results of this project. Those with in-house models could;

- obtain necessary information on black liquor combustion and related behavior which can then be incorporated into their in-house models,
- obtain specific submodels (eg. a bed model) for incorporation in their own codes,
- keep in touch with the state-of-the-art in boiler modelling,
- evaluate methods for simplifying models,
- increase confidence in their own models through model project validation efforts,
- cross-check predictions of in-house models against other models, and
- obtain general information on boiler performance from simulations done with other models.

It should be noted that recovery boiler manufacturers with in-house models do not need the availability of one or more external recovery boiler models and could perceive the existence of accessible external models as a threat to competitive advantages.

Boiler manufacturers without an in-house model could;

- use available model(s) to run simulations on a contract basis as needed,
- license external models to obtain codes for use in-house,
- benefit from fundamental data on black liquor combustion and related behavior, and
- benefit from general information on boiler performance from model simulations.

The second group of potential model users are kraft pulp manufacturers. They derive direct economic benefit from more effective utilization of recovery boilers such as improved efficiency, increased uptime, or higher throughput and have by far the most to gain from improvements in recovery boiler technology. With a few exceptions, pulp manufacturers would not be directly responsible for improving recovery boiler technology and would not devote major corporate technical effort to it. Pulp manufacturers gain economic benefit from improved utilization of existing recovery boilers and from reducing the capital cost of new recovery boilers. Productivity gains tend to have the biggest payoff. Individual pulp mills generally seek outside help in troubleshooting recovery boiler operating problems. This outside help could be from internal corporate resources, OEMs, or consultants.

The main needs of pulp manufacturers are:

- more confidence that boiler manufacturers understand black liquor combustion and can provide equipment and operating guidance that will meet specifications,
- process insights that can guide evolutionary changes to improve recovery boiler productivity,
- specific knowledge of changes in operating procedures and/or hardware modifications that would provide incremental gains in liquor burning capacity in existing units,
- assistance in troubleshooting operating problems,
- means for increasing operator acceptance of changes in operating procedures, and
- confidence that changes in boiler design or operating procedures will not adversely affect boiler integrity.

In considering potential model use by pulp manufacturers, it is necessary to distinguish between use at individual pulp mills and at the corporate level. At the current state of development, there is little need nor desire to have a CFD recovery boiler model available at individual pulp mills. The mills do not have the computer/manpower resources to devote to model use, and operating problems requiring this level of capability are relatively infrequent. Individual mills would look to outside sources for help. They might be interested in a highly-simplified, very user-friendly model for on-site use if one was available. At the corporate level, some (larger) companies might have the computer and manpower resources and the expertise to have codes available in-house for their own utilization. Other companies (probably the majority) would simply need to have access to the model(s), and would provide their own interpretation of model results. Both individual mills and corporate could utilize general knowledge and process insight that has been obtained as a result of model development and model simulations

The next group of potential users are engineering firms and consultants.They derive economic benefits from providing services to pulp manufacturers in troubleshooting operating problems, and seek to get a competitive advantage through "knowhow". This group is normally not a source of recovery boiler technology developments. They may be involved in the selection of OEM's and/or evaluating proposals from different vendors. With one exception, they would likely have little interest in developing in-house expertise in recovery boiler models and their interpretation.

The main needs of this group are:

- the ability to evaluate proposed offerings from boiler manufacturers,
- the capability to evaluate the effectiveness of equipment modifications or changes in operating procedures, and
- process insights that can help in troubleshooting operating problems.

This group could be interested in accessing modeling capability on a contract basis and would provide their own problem definition and interpretation of results. If it were cost-effective, some engineering firms or consultants may wish to have in-house modeling capability through licensing of boiler model(s) developed elsewhere.

The academic world and some R&D organizations would see the development of the models themselves as the major interest. In general, they would not have sufficient knowledge and expertise to make direct use of the models in applications. They could provide a service function by setting up cases and running simulations for others.

Another way recovery boiler models could be used is through generic modelling and simulations to produce general results that could be interpreted and delivered as technical papers and reports. When this project was first conceived, this latter approach was considered to be one of the main ways for getting results to pulp manufacturers. As the project proceeded, the feedback from users was that the focus should be on developing a good model and validating it. The users themselves would take care of the applications.

Usefulness of a General Furnace Model

Recovery furnace models are aimed at optimizing design and operation of kraft recovery boilers. In order to judge the effectiveness of furnace models, one needs to know what kind of information is important to improving recovery boiler design and operation. The information needs can be summarized as follows.

1. The effect of operating practices and liquor quality on fouling and plugging rates in the convective sections.

2. The effect of operating practices and liquor quality on corrosion and other boiler integrity issues.

3. The relationship between air emissions and furnace operating practices and liquor quality.

4. The effect of operating practices and liquor quality on steam production.

5. The effect of operating practices and liquor quality on combustion stability and bed control.

6. The effect of operating practices and liquor quality on reduction efficiency and dissolving tank operation

7. Definition of optimum operating strategies including means for maximizing firing rates

A general furnace model could provide considerable help in dealing with boiler fouling and plugging issues if good descriptions of aerosol formation and characteristics were part of the model. The effects of variables such as gas temperature and composition and convective section geometry on deposits also needs to be understood to make maximum use of furnace model predictions. A global furnace model could also provide considerable help in understanding emissions behavior, combustion stability and bed control, and in developing operating strategies for maximizing firing rates.

Current recovery furnace models do not have the capability of predicting corrosion rates and this is not likely to be a capability in the near future. Steam production is determined by firing rates and heat balance considerations, and a CFD-based furnace model is not needed to determine this. Reduction and dissolving tank behaviour would be dependent on a very sophisticated bed model and these are currently not in hand.

Usefulness of Simplified Submodels

Because of the requirements for problem set up and interpretation of results and the need for substantial machine time to obtain converged solutions, CFD-based recovery boiler models are not a very cost effective way for gaining information. Although there is very limited data available, the cost of using a CFD-based furnace model to do a small number of cases (2 to 4) is probably on the order of about $50,000. One boiler manufacturer has specifically stated that recovery boiler modeling needs to become more "cost-effective".

If the results of model calculations were completely reliable, and if decisions on design or operation could be made by comparing a very small number of cases (say 2 to 4), then the cost of model simulations could be easily covered through the returns from improved

operation. This is not normally the case at present, where the model provides some, basically qualitative, information and the number of possible variables is very high.

The following items are considered to be the keys to cost-effective modeling:
1. simplified methods for getting results must be developed,
2. key problems must be solved once and the results then applied to many boilers,
3. models must complement other knowledge - not used as a brute force means of overcoming a lack of understanding.

Impediments to Model Use and Means for Overcoming Them

There are a number of impediments to more effective use of recovery furnace models. These include the following:

1. the high computational intensity of calculations,
2. the high degree of skill needed to set up problems and guide convergence,
3. the limited correspondence between the type of information needed to solve recovery boiler problems and the type of information a furnace model can produce,
4. the immense amount of information developed by the models that must be distilled and condensed and presented in a manner that the user can understand it,
5. the inefficiency in re-solving the entire recovery boiler furnace field to see the effects of changing a single parameter,
6. the lack of knowledge about recovery boiler design and operation on the part of the some of the institutions that have developed and are running the CFD models,
7. the need for boiler manufacturers to preserve proprietary information obtained with their own models, and
8. ownership and license issues that inhibit getting the codes directly into the hands of users

Some ways to overcome impediments include:

1. developing the understanding of flows in the convective section along with fundamental information on ash deposition and removal processes so that the relation between furnace output variables and boiler plugging can be determined,
2. developing means for running recovery furnace models on superfast parallel computers to allow greatly shortened run times,
3. developing techniques such as the fixed-field method for solving only certain critical aspects of a problem and which allow efficient systematic studies of the effects of specific parameters,
4. developing algorithms for summarizing model output in a way that addresses directly the needs for improving boiler operation,
5. facilitating transfer of models to organizations that can effectively utilize them, and
6. generic modeling and publication of results.

Role of This DOE Supported Program

This particular DOE supported program plays a three-fold role in advancing the capability of CFD-based recovery furnace models for improving recovery boiler design and operation.

1. It will develop a validated CFD-based recovery furnace model specifically tailored to deal with the particular geometries and flow effects characteristic of recovery boilers and incorporating the most reliable information of the relevant burning behavior of black liquor in a recovery boiler environment.

2. It will obtain substantial fundamental information on the combustion of black liquor and on processes relevant to air emissions and aerosol formation, deposition, and removal in recovery boilers and make that information available not only for incorporation into the codes being specifically developed as part of the project but also to other developers of recovery furnace models.

3. It will advance the confidence in using recovery furnace models by validating simulation predictions against actual data and disseminating the results.

SUMMARY OF UBC RECOVERY BOILER MODEL

The CFD-based recovery boiler model which is being developed as a specific objective of this project is the one at the University of British Columbia and is referred to herein as the UBC model. Other recovery boiler models have been, or are being, developed by parties who are part of this project or by others, but these other models are incidental to this project. This section provides a brief summary of the UBC model. The model is described in much greater detail in Appendix 1.

NATURE OF MODEL

The model involves mathematical representation of the physical and chemical processes occurring in the boiler and obtaining a solution to the resulting conservation equations for mass momentum, energy and gas species concentration. The turbulent flow inside the boiler is modeled using the k-ε turbulence model. The black liquor spray is simulated by computing the trajectories followed by individual drops from the time of injection until it lands on the bed or is carried over, and accounting for mass and energy exchange with the gas phase. This drop - gas phase exchange is handled with source/sink terms in the conservation equations. Gas combustion rates are computed using the Magnussen model [2]. The gas radiation heat transfer is calculated using the discrete-ordinates method.

UBC has developed computer codes tailored to meet the special requirements of recovery boiler flows. These codes employ multigrid methods and segmentation techniques to provide a good resolution of the complex flows near the air ports and greatly improve the convergence characteristics of the numerical procedure. The segmentation technique allows non-matching grids to coexist in adjacent parts of the flow field. This allows modeling air ports at their correct location without unnecessary grid refinement.

The hot flow version incorporates variable gas density, black liquor combustion with associated source/sink terms, simplified treatment of the bed and of black liquor striking the walls, and heat transfer (including radiation) to the walls. The hot flow model is still under intense development, but it has been used for simulations that give apparently reasonable results.

Additional insight into recovery boiler flows has been obtained from flow measurements on two 1:28 scale water models of recovery boilers at UBC. The first is a model of a recovery boiler at Weyerhaeuser's Plymouth, NC mill and the second is a model of a recovery boiler at Weyerhaeuser's Kamloops, BC mill. Flow fields were measured using laser-Doppler velocimetry and particle-image velocimetry. Tests showed that these flows were frequently subject to low-frequency unsteadiness. The flow data obtained with water models has been used for purposes of validating the flow predictions of the computer model.

The model consists of a number of coordinated programs that fulfill specific functions. These include:

geo.f — a pre-processing program for generating geometric information of the grid, dimensions of arrays, and sequences of boundary data,

trans.f — a CFD program for solving the Navier-Stokes equations plus the enthalpy equation using the finite volume method on a staggered grid,

prnt.f — a post-processing program for writing results in a format that is useable by the graphic software "Tecplot",

spray.f — a program for computing the in-flight and combustion processes of black liquor drops (particles) as they move through the gas phase in the simulated furnace, and

rad.f — a program that carries out radiation heat transfer calculations using the discrete-ordinates method.

The model can be used at different levels, depending on the specific purpose intended. For example, it can be used for isothermal flow calculations, both for steady-state cases and for time-dependent solutions. Hot flow calculations can be done for prescribed boundary conditions and prescribed source/sink terms. Alternatively, the full hot flow model with black liquor combustion can be used for full recovery boiler simulations.

TECHNICAL STATUS

It now takes 1-3 days to run a hot flow case including black liquor combustion with the UBC model. The actual CPU time to run a case is about one 24-hr day. Time is also required for setting up a case and for adjustments of boundary conditions, etc. This is a significant reduction in solution time.

CFD Code

Mathematical modeling of flows in recovery boilers is not an easy task. The flow is three-dimensional and generally unsymmetric, often grossly unsteady, and turbulent.. The equations in mathematical models of recovery boilers may not have steady-state solutions under these circumstances. Recovery boilers are characterized by large differences in scales and the grid used in the numerical method has to be non-uniform with cells having large aspect ratios. This can affect the convergence of the numerical procedure. Use of fine grid structures over the entire boiler domain is not practical because of the very large number of nodes that would be needed. The functioning of the recovery boiler is critically

dependent on the flow patterns, so it is required to be able to compute the flow with sufficient detail and correctly represent the air port geometries.

The UBC code is designed to address two critical issues in modeling recovery boiler flows; the need for high local resolution at air port levels, and slow convergence rates for large domains. This is achieved through multigridding and segmentation. In multigridding, the relaxation techniques are applied on a hierarchy of grids to remove errors corresponding to a wide range of frequencies.The segmentation technique allows setting up the grid at certain segments of the boiler independently of the grid at other segments. This allows more effective use of nodes in those locations where high resolution is necessary.

The CFD model has been a prime focus of this effort and is described in much greater detail in Appendix 1. Although it continues to be improved, it is capable of modeling recovery boiler flows.

The flow predictions from this code have been compared with flow data from water models of recovery boilers and with cold flow data taken on full-scale recovery boilers. The comparisons have been quite reasonable. [3]

Drop Combustion

The elemental analysis and HHV of the black liquor are used to set up the liquor phase material and energy balances. The liquor is assumed to consist of liquid water, volatiles, smelt and char carbon. The volatiles are CO, CH_4, H_2, and CO_2. The smelt is assumed to contain Na_2CO_3, Na_2S, Na_2SO_4, K_2CO_3, and NaCl. Algorithms are used to determine the amounts of each of the volatiles and smelt compounds in the liquor solids from the elemental balances. The HHV of the black liquor solids is used along with the heats of formation of all of the volatiles and smelt compounds to determine a heat for the pyrolysis reaction (the volatiles releasing reaction). In this manner the energy balance over the burning process is closed.

A statistical method is used to model the black liquor spray. Each computational particle (drop) is assumed to represent a number of real particles that have the same location, velocity, chemical composition and properties. A distribution function is assumed for the drop diameters. The number of computational drops is selected as an optimum between the available computer resources and the required simulation accuracy. In a typical case, 10,000 drops are used to model the spray. The diameter range is divided into intervals and for each interval a mean interval drop diameter is computed. Once this is done, the mass and number of real drops represented by a computational drop is determined. This does not have to be an integer. The spray is defined by the horizontal and vertical spread angles for each nozzle. A random method is used to distribute the drops among the nozzles and ranges of injection directions. Once the nozzle location and initial drop velocity magnitude and direction are known, the initial velocity components, u, v, and w,

are computed. The selected number of drops are injected at the same time and their positions, mass changes, and chemical composition are tracked and recorded until each drop/particle leaves the computational domain. The forces acting on the drop are gravity and fluid drag. As the drops move on their trajectories, they are subject to drag from a gas-drop relative velocity that includes a turbulent gas velocity component. This is determined statistically and is related to the local turbulent intensity. As a result of this, identical drops, starting with identical initial conditions do not follow the same trajectories.

After the black liquor drops are injected into the furnace, liquor combustion begins. This consists of evaporation of water (drying), volatiles release by pyrolysis, and reactions between char carbon and surrounding gases.

Drying is assumed to be heat transfer controlled. Each drop is assumed to heat up to 150°C and then evaporate. The heat transfer rate is the sum of a convective and radiative heat transfer term. The convective heat transfer rate is the product of a heat transfer coefficient, the drop surface area, and the difference between the drop temperature and that of the surrounding gas. The heat transfer coefficient is calculated from a standard Nusselt number calculation. The radiative heat transfer is calculated as the sum of the radiative heat transfer from the gas, walls, and bed, using a constant, assigned gas emissivity and a bed view factor. Swelling during drying is assumed to occur instantly and then to stay constant during the rest of the drying phase. The typical diameter swelling factor used is 1.6. Ignition may be allowed to occur before drying is complete by specifying a solids at ignition value. In this case the remaining drying is assumed to occur during pyrolysis.

Devolatilization is also modeled as a heat transfer controlled process. The total heat required to complete pyrolysis (devolatilization) is computed as the sum of the sensible heat needed to heat the drop solids up to the final temperature (an arbitrary T_{max}), the heat to evaporate the remaining water, and the heat of any pyrolysis reaction. The mass loss that occurs in any time step is determined as the ratio of the heat transfer that occurs in that time step to the total heat required to complete pyrolysis. The heat transfer rate is calculated in the same manner as during the drying phase. Swelling during pyrolysis is treated by assuming a linear increase in drop diameter from that at the end of drying to a value of D_{max} (user supplied) at the end of pyrolysis.

Char burning (removal of char carbon) is assumed to occur by reaction with O_2, CO_2, and H_2O. The mass transfer rates of O_2, CO_2 and H_2O from the gas to the particle are calculated using mass transfer coefficients computed from a Sherwood number correlation. The gasification reactions with CO_2 and H_2O are taken to be combined mass transfer and kinetically controlled. Oxygen is assumed to be consumed in the boundary layer by CO and H_2 coming from the particle and only the excess O_2 transfer, if any, is able to react with carbon in the char. Shrinkage of the particle during char burning is handled by assuming a linear change in particle density with carbon removal.

Inorganic reactions have been ignored in the existing model.

The net volatile combustibles that are given off (CO, CH_4, and H_2) are assumed to react with O_2 in the gas phase. These are assumed to react at a rate controlled by mixing. The Magnussen model [2] is used for this purpose. The rates are assumed to be proportional to ε/k from the k-ε turbulence model.

Bed Modeling

The bed shape is approximated by a staircase grid arrangement. A drop/particle that lands on the bed is assumed to be anchored there and to complete its remaining combustion stages on the bed surface.Mass and energy are exchanged between the bed and the gas within the cell first adjacent to the first bed gas phase cell. The bed is assumed to operate at steady state and the necessary mass and energy exchange is calculated from this assumption.

In early hot flow models with black liquor combustion, the liquor that reached the wall was assumed to stick to the wall surface and exchange mass and energy within the first neighboring gas phase cell. Later versions of the model compute the rate of combustion for the liquor that reaches the wall from the same rate equations used for the drop in-flight. If the rate of material striking the wall exceeds this rate, the excess material is moved to the bed.

Energy Balance

The black liquor spray model is coupled with the gas phase model. The gas phase variables (u, v, w, p, k, ε, T, c_i) are solved in a fixed coordinate system, for a steady state case, and are only a function of position. The properties of the black liquor phase are calculated in a moving frame of reference and are a function of time and location. The exchange of mass, momentum, and energy between the gas phase and the liquor phase is accounted for by source/sink terms added to the gas phase cells. The amount of thermal energy exchanged between the liquor particles and the gas phase is accounted for by source/sink terms in the gas-phase energy equation. The chemical energy is accounted for by the implicit enthalpy carried with the individual gas species transferring between the phases. In the version of the code available at the start of this current phase of this project, no attempt was made to have a thermodynamically rigorous heat balance for all interactions occurring between the phases. Thus the overall energy balance may not be rigorously closed.

STATUS OF BLACK LIQUOR BURNING MODELS

Black liquor burning models consist of two distinct parts, a drop burning model and a trajectory model. The drop burning model describes how the liquor drop interacts with the surrounding gas with respect to mass and energy. It includes an appropriate chemical description of the burning drop and means for tracking state changes (composition and temperature) in the drop, and rate equations that describe the exchange of mass and energy between the liquor and the gas. The drop burning model also provides means for handling the swelling and deswelling that occurs when black liquor burns. The rate equations that describe mass and energy exchange between the liquor and the gas are the basis for the gas-phase source/sink terms needed by the CFD part of the model.

Much of the work on black liquor combustion that provides the basis for drop burning models has been carried out at Oregon State University and Åbo Akademi. This work is summarized in detail in Appendix 2 and in DOE report DOE/CE/40936-T2 (DE96006558) "Sodium and Sulfur Release and Recapture During Black Liquor Burning". [4]

DROP BURNING MODELS

The minimum black liquor drop burning model for use in a CFD-based recovery furnace model, must have the following capabilities:

- decribe how the fuel content of the liquor is released as it burns in the furnace,
- describe the rate at which mass and density changes occur which influence trajectories and the ultimate fate of the drops, and
- incorporate all major factors that influence the overall energy balance.

This can be done with a liquor model which considers the liquor as consisting of liquid water, volatiles, and char. The drop burning model describes the rates at which liquid water is evaporated, volatiles are released and char formed by pyrolysis, and the rate at which char carbon is consumed. The inorganic smelt is assumed to remain with the burning drop, but transformations between sulfate and sulfide are allowed.

Such drop models are sometimes referred to as "earth, air, fire and water models". Both the first and second generation black liquor models were of this type. They are generally adequate for predicting carryover, doing the energy balances and energy transferrences needed to predict velocity and temperature fields from a hot flow model, and for predicting the concentration distributions of the main furnace gas components. They are not capable of describing formation of small aerosols, sulfur release and recapture, or concentrations of air emission species.

Early Burning Models

In the earliest models [5], black liquor burning was considered as occurring in distinct steps; drying, volatiles burning, and char burning. Drying and volatiles formation were treated as separate heat transfer controlled processes and char burning was treated as an oxygen mass transfer controlled process. Subsequent studies showed that in typical furnace atmospheres, gasification of carbon by reaction with CO_2 and H_2O was much more important than direct oxidation during the char burning step. Kinetic rate equations for these gasification reactions were developed and combined with external and internal mass transfer correlations to provide an overall rate equation for the char burning step. It was also recognized that evaporation of water and pyrolysis of black liquor organics occurred simultaneously because of the strong internal temperature gradients in burning droplets and a method of treating this was developed. Algorithms have also been developed for determining the extent of volatile formation during pyrolysis and for apportioning the volatiles to specific species for further reaction in the gas phase.

Development of these types of drop burning models is now substantially complete. However, the current model, as described in Appendix 2, still contains empirical parameters that are correlated in terms of variables that are not clearly defined in a recovery furnace environment, where drops are moving through a variable temperature and gas concentration field. This problem still needs to be resolved.

Elemental Transfer Models

More sophisticated black liquor burning models are needed to deal with air emissions and issues connected with boiler fouling and plugging. These can be referred to as elemental models because they deal with transfer of individual chemical elements between the liquor and gas phases.

The complete chemistry of black liquor is very complicated and undefined. The elemental composition of the liquor solids can be measured quantitatively in the laboratory, and this is the minimum information needed to describe the chemical reactions occurring in the furnace. Eight elements must be specified to provide the quantitative information on liquor composition needed to describe all of the critical air emission and plugging factors. These elements and typical ranges of composition are given below:

C	carbon	30-40%
H	hydrogen	3-4%
O	oxygen	30-40%
S	sulfur	3-6%
Na	sodium	17-20%
K	potassium	0.5-4%
Cl	chloride	0-4%
N_f	fuel nitrogen.	0.05-0.25%

The carbon and hydrogen are the main constituents of the organic fuel substances in the liquor. Oxygen is a major component of both the organic fuels and the inorganic compounds in the liquor. Sulfur is present as both organic sulfur and as inorganic sulfur compounds. The sodium and potassium are present as salts of organic acids and as inorganic salts. The chloride is present as NaCl and KCl. The fuel nitrogen is part of the organic material in the liquor.

The overall processes modeled in the elemental burning models are the same as those involved in simpler burning models namely drying, pyrolysis (and volatiles burning), and char burning. When elements are transferred between the liquor and gas phases, they do so as specific chemical species (with defined enthalpies as functions of temperature). The essence of the elemental burning model(s) is a set of algorithms defining the element - chemical compound transformations and rate equations for each of the transferrences. The individual elements in the black liquor solids are all converted to defined chemical compounds during pyrolysis, and all char burning reactions (including those that can take place when carbon is absent), occur as reactions between these defined chemical compounds.

The algorithms for transformations and interphase transfer for carbon, hydrogen, and oxygen are not greatly different from what they were in the simpler models. Pyrolysis converts the carbon in the liquor solids to elemental carbon and carbonate in the char and to volatiles such as CO, CO_2, and CH_4. It may be necessary to add additional C-containing species such as mercaptans and COS to handle sulfur transferrences. The hydrogen is usually considered to be completely converted to gaseous compounds during pyrolysis. These include, H_2, CH_4, and H_2O. It may also be necessary to add H_2S and mercaptans, etc. to handle sulfur transferences. Oxygen is converted to carbonates and sulfates in the char and also is transferred to the gas phase as CO, CO_2, and H_2O. The rate of pyrolysis can be considered to be heat transfer controlled as in the simpler models.

Data are available that describe the transformations of sulfur compounds during pyrolysis in a laminar entrained-flow reactor system. The pathways have been described, and the chemistry is partially understood, but algorithms suitable for use in a recovery furnace drop burning model have not yet been defined. The available data strongly indicate that sulfur transformations and release to the gas phase during pyrolysis are dependent on the specific sulfur compounds present in the black liquor. This means that the elemental composition of black liquor composition is an insufficient description of the liquor as far as sulfur behavior in the furnace is concerned. This is a considerable complication in a CFD-based furnace model, since it increases the amount of information that has to be carried with each drop and tracked.

Sulfur can also be transferred from the liquor phase to the gas phase during char burning through reactions such as
$H_2O + CO_2 + Na_2S = H_2S + Na_2CO_3$ and $2\ CO_2 + Na_2S = Na_2CO_3 + COS$.
Rate equations for these processes remain to be developed.

Sulfur reactions in the gas phase that lead to its ultimate capture as Na_2SO_4 fume must also be included. These include oxidation of H_2S, COS, and other sulfur gases to SO_2 and SO_3, and the reaction of SO_2 and SO_3 with sodium and potassium compounds to form Na_2SO_4. The path by which sulfate ultimately forms is not completely understood. There is some limited data available that suggests substantial sulfur recapture occurs in the superheater region, but this is not fully accepted. Two of the reactions that can occur are

$Na_2CO_3 + SO_2 + 1/2O_2 = Na_2SO_4 + CO_2$

$2NaCl + SO_2 + 1/2\ O_2 + H_2O = 2HCl + Na_2SO_4$

However, there are other possible paths and algorithms and rate equations for sulfur recapture are still incomplete.

Sodium release occurs during char burning. The possibility that significant sodium release takes place during pyrolysis has now been discounted. Two "reactions" are considered to be the primary ones responsible for sodium. These are the reduction of sodium carbonate to produce elemental sodium vapor, and the direct vaporization of NaCl. The reactions involved are generally considered to be

$Na_2CO_3 + 2C = 2Na + 3CO$ and

$NaCl_{(s,l)} = NaCl_{(v)}$.

There are algorithms and rate equations available for estimating the rates at which sodium is released by these reactions. Reduction of Na_2CO_2 is treated as a homogeneous reaction in the char phase. The current kinetic rate equation, however, is incomplete, since it is independent of carbon concentration and will not shut off when the particle runs out of carbon. This needs to be remedied. The vaporization of NaCl is treated as a purely mass transfer controlled process with the vapor pressure of the NaCl in the char determined by Raoult's Law and the pure component NaCl vapor pressure (which is a function only of temperature)

Potassium release is very similar to sodium release. It occurs primarily during the char burning stage and takes place through the reduction of potassium carbonate by carbon and by direct vaporization of potassium chloride. The reactions involved are generally considered to be

$K_2CO_3 + 2C = 2K + 3CO$ and

$KCl_{(s,l)} = KCl_{(v)}$.

There are no data currently available on the kinetics of the C– K_2CO_3 reaction. The method currently recommended is to use the same rate equation as for Na_2CO_3 reduction and multiply it by the molar ratio of K/Na in the liquor particle. This is at best an approximation, and a better rate equation is still needed. The vaporization of KCl is treated as a purely mass transfer controlled process with the vapor pressure of the KCl in the char determined by Raoult's Law and the pure component KCl vapor pressure (which is a function only of temperature)

All chloride release from the liquor phase is considered to take place by vaporization of NaCl and KCl. Since the relevant pure component vapor pressures are only functions of

temperature, and these substances are already present in the original liquor solids, some chloride release can occur during the higher temperature parts of the pyrolysis process. However, the bulk of the release takes place during char burning.

The NaCl and KCl in the dust can react with H_2O, SO_2, and O_2 in the furnace to form HCl which leaves the furnace with the other gases. A suitable algorithm and rate equation for this reaction is still needed. This reaction can be a significant chloride purge from the system and chloride contents in deposits have a large effect on recovery boiler fouling and plugging.

A good recovery boiler model must also be able to predict NO_x concentrations. It is the current concensus that NO_x in recovery boilers comes almost exclusively from nitrogen compounds in the black liquor solids (so-called fuel NO_x). Thus algorithms and rate equations for the release of fuel nitrogen, and for NO_x formation and destruction in the gas phase. There has been considerable research work done on aspects of this process, but a complete methodology for handling fuel NO_x predictions needs to be worked out.

DROP TRAJECTORY MODELS

The trajectory equations come from a force balance on the burning drop as it moves through the furnace. Forces acting on the drop include gravity and drag by the gas through which it is moving. The drag force depends on the vector velocity difference between the drop and the gas and is oriented in this direction. The initial condition for the drop trajectory as it enters the furnace comes from a model for the liquor spray. Typically, this sets the initial drop size and vector velocity. The drops continue on their trajectories until they reach the bed, strike a furnace wall, or are carried up out of the furnace.

Current means for describing drop trajectories are generally adequate. The drop moves according to its own inertia and as a result of forces from fluid drag and gravity. The only uncertainty in treating the drag forces lies with how to deal with turbulence in the gas. Some trajectory models ignore turbulence and use the average gas vector velocity at a given location in the calculation of the drag forces. This results in deterministic equations for the drop trajectory and all drops that start with the same initial conditions follow the same trajectories. Other trajectory models include a turbulent velocity fluctuation, U', in calculating the drag on the drop. The value for U' is a stochastic variable that is related to the local turbulence intensity, and is estimated from a probability function. In this stochastic treatment of drag, the trajectory equations are non-deterministic, and drops that start out at the same initial conditions follow different trajectories.

Simulations carried out using both approaches have showed that, at least when highly channeled gas flow fields exist, the stochastic treatment results in less physical carryover of burning drops up out of the furnace. The drops are more spread out and thus fewer are

likely to be caught in the narrow channeled gas updraft. The UBC model now uses the stochastic approach for estimating drag.

The biggest uncertainty in liquor drop trajectories arises from the liquor spray modeling which sets the initial conditions for the drops entering the furnace. The liquor drop size distribution and the vector velocity distribution for these drops as they enter the furnace are specified in terms of a model for the liquor spray itself. These are never directly measured quantities. The variables actually known about a liquor spray are, the type and size of gun used, gun locations, angular orientation of guns, liquor temperature and pressure, liquor solids, and possibly critical liquor properties such as the viscosity. An empirical model (partially based on laboratory data on sprays under somewhat similar conditions) is used to relate the model spray parameters to the actual spray variables.

In all of the models, the liquor is assumed to start out as a distribution of fully-formed, spherical droplets from a point on the boundary corresponding to the position of the liquor gun, and heat transfer for drying and volatiles formation begins immediately. The fact that real sprays develop gradually within the furnace and drops are not fully formed until some distance into the furnace is ignored. The likelihood that heat transfer from the hot gases affects the development of the sprays is also ignored.

CHAR BED MODELS

The char bed is a pile of partially combustible material that sits on the hearth of the furnace where it burns and releases molten smelt that drains out of the unit. The bed contains frozen and molten smelt, char (fixed carbon and inorganic compounds) and possibly unpyrolyzed liquor solids and unevaporated water. In the CFD-based furnace models, the material arriving on the bed comes from liquor drops landing there and from liquor drops that reach the walls and eventually sluff off and fall to the bed. In an actual furnace, these can be supplemented by slag falling off the convective sections of the boiler under the action of sootblowers.

The amount of combustion that can occur in the bed and the production of gaseous fuels from the bed must be accounted for in the models. The bulk of the bed is impervious to gas flow and so must be treated as a solid boundary for the gas flow. However, it is a boundary that is able to exchange mass (chemical species) and energy with the gas phase. The bed is able to act as a fuel reservoir and for any given set of furnace operating conditions, fuel may be accumulating or depleting in the bed. The shape of the bed can also influence gas flow patterns in the lower furnace.

The following are the critical items needed to set up a char bed model for use in a CFD-based furnace model:

- define the bed geometry,
- treat the chemical reactions between the bed and the gas phase,

- handle the heat exchange between the bed and the gas phase,
- carry out a bed heat balance to determine bed surface temperature, and
- address inventory accumulation or depletion.

Since the overall CFD model is set up on a rate basis, the char bed model that interfaces with it must also be set up on a rate basis.

Defining the bed geometry (size and shape) locates the boundary for the gas phase in the model and must be consistent with the grid structure used for the CFD calculations. Although the gas-bed interface is a smooth surface (on the scale of the CFD grids) in the real furnace, this is not necessarily the case in a CFD model. CFD codes may use fixed or body-fitted coordinates. Where a fixed (rectangular) grid system is used, the cells are rectangular blocks. In this case, the bed is made up of discrete blocks and is sometimes referred to as a staircase bed. With body-fitted coordinates, the cell shapes can be tailored to align with the actual gas-bed interface and the boundary is smooth and continuous. The UBC code uses a fixed, rectangular grid system, as do most other recovery furnace codes currently being used.

Although they are simpler to set up, the use of "staircase beds" has consequences that must be dealt with. The macroscopic gas-bed contact area is greater for a staircase bed than would actually be the case (by as much as 40%). In addition, the cell surfaces are oriented in either a horizontal or vertical direction, rather than parallel with the gas flows. This can affect how the gas flows impinge on the bed, the calculation of convective heat and mass transfer coefficients, and radiation view factors.

Bed models describe the chemical reactions and processes that occur during bed burning. In general, the description needs to include drying, devolatilization and char burning occurring in the active layer, since the material landing on the bed can be at any degree of completion of burning. Several issues need to be dealt with:

1. specifying the chemistry that is to be included,
2. determining how to handle drying, devolatilization, and char burning processes occurring in parallel rather than in sequence,
3. specifying the concentrations of the chemicals in the bed that appear in the reaction rate equations, and
4. defining the appropriate rate equations for each of the steps.

In the drop models, vaporization of water is assumed to occur simultaneously with pyrolysis (devolatilization) in a heat transfer controlled process. The same approach can be used in the bed burning model. Unpyrolyzed liquor solids reaching the bed are assumed to continue pyrolysis in a heat transfer controlled process. A transformation algorithm is required to define the gas species and char components (in quantitative amounts) that are produced by pyrolysis. This must be the same transformation algorithm used for describing devolatilization in the drop burning model. It is extremely unlikely that liquid water or unpyrolyzed liquor solids would accumulate indefinitely in a hot char

bed, so the rate of evaporation of water and the rate of pyrolysis of unpyrolyzed liquor solids can be assumed to match the rate at which they reach the bed surface. A distribution algorithm would determine how these materials are distributed over the surface of the bed by the primary air and the lower furnace gases.

The char is assumed to consist of four chemical species; C, Na_2CO_3, Na_2SO_4, and Na_2S. These can react with gases from above the bed and with each other. In addition, the combustible gases coming from the bed can react with oxygen in the gas boundary layer above the bed, and this can affect the rates of mass transfer between the bed and the gas phase. The following reactions are considered.

$$C + O_2 = CO_2$$
$$C + CO_2 = 2CO$$
$$C + H_2O = H_2 + CO$$
$$4C + Na_2SO_4 = 4CO + Na_2S$$
$$2C + Na_2CO_3 = 2Na + 3CO$$
$$Na_2S + 2O_2 = Na_2SO_4$$

The rate equations for the char burning reations can be taken from the paper by Wåg et al [6]. A rate equation for the homogeneous reaction between Na_2CO_3 and C needs to be added, while the equations for COS and H_2S formation can be ignored. In addition, Wåg's equations may need to be modified to include the effects of the combustion of volatiles from pyrolysis in the boundary layer.

The rate equations for char burning include terms that depend on the concentration of C, Na_2CO_3, Na_2SO_4, and Na_2S in the bed. This will require some sort of a mixing or reactor model for the surface layer to determine appropriate values for these concentrations. The appropriate algorithm for this still needs to be developed.

The bed model requires convective heat transfer coefficients and mass transfer coefficients at each position along the bed surface. These are functions of the gas velocity over the surface of the bed in the local region and the physical properties of the gas, and can be obtained from appropriate dimensionless correlations. However, the best way to define the gas velocity and characteristic length for the Reynolds number to be used in the correlations remains to be determined. The methodology employed by Karvinen, et al [7] may be the most appropriate for this purpose.

The active bed surface region is a monolayer of bed cells. A mass balance over the active burning layer is formulated for each bed cell. The terms making up the mass balance include:

- liquor species arriving as individual drops,
- liquor species sloughed off the walls and transported to that cell by a redistribution algorithm,
- CO_2, H_2O, and O_2 transferred from the gas above the bed into the active bed (which includes the reactive boundary layer),

- water vapor from drying leaving the bed,
- production of fresh char from continued pyrolysis and production of pyrolysis gases that enter the reactive boundary layer)
- gasification and pyrolysis gases leaving the active bed (which includes the reactive boundary layer),
- molten smelt leaving the bed (including any entrained carbon), and
- the inventory imbalance of char species.

The species in a simple bed model are water, unpyrolyzed solids, char carbon (C), Na_2CO_3, Na_2SO_4, and Na_2S. The mass balance simply requires adding these up for each drop that lands on the defined area (cell) as well as the amount coming in from the wall slough redistribution algorithm (or any other redistribution algorithm).

The rates of CO_2, H_2O, and O_2 transfer from the gas phase into the active bed zone are determined by mass transfer relations coupled with chemical reaction kinetics. The current approach uses the mass transfer rates that would occur from the gas to the surface if no reactions between O_2 and combustibles occurred in the boundary layer. The effects of such reactions on oxygen stoichiometry are included (and may veto any O_2 actually reaching the surface), but the effects of boundary layer oxidation increasing concentration gradients of H_2O and CO_2 are not included. This approach needs to be tested experimentally and modified if necessary.

The gasification and pyrolysis gases leaving the active zone are determined from the same basic set of equations that determined the mass rates for CO_2, H_2O, and O_2 transfer into the bed. In fact these two terms are best combined to give a net flux of gases entering or leaving the bed through devolatilization, gasification and combustion reactions. The gas species involved are O_2, CO_2, H_2O, CO, H_2, CH_4, and Na.

An arbitrary criterion is needed to relate the molten smelt release to the char carbon burning rate. There are several possibilities. The simplest is to assume all of the inorganic reaching the bed leaves as molten smelt and the carbon balance determines the amount of carbon in the smelt leaving. This approach would also automatically eliminate any bed inventory imbalance (although it would carry the possibility of having a negative carbon content in the smelt leaving). Another approach would use the carbon balance to determine if there were accumulation or depletion of bed in that region, coupled with a criterion that would tie the amount of inorganic inventory with the carbon inventory. An inorganic smelt balance would then determine the amount of smelt leaving (without any carbon in it). More complicated algorithms are also possible.

An energy balance over the active layer is used to determine the temperature of this layer, which is usually equated to the bed surface temperature. The following terms are involved:

- heat radiation from the gas to the bed
- heat radiation from the bed to the gas (and walls)

- convective heat transfer from gas to the bed
- sensible heat with arriving liquor phase material
- chemical (fuel) value of arriving liquor phase material
- sensible heat of net gas interchange with bed.
- heats of reactions occuring in bed (including the reactive boundary layer)
- latent heat in water evaporated from bed
- chemical (fuel) value in volatiles leaving bed (and reactive boundary layer)
- heat in smelt (and entrained char) leaving bed
- heat conduction into sub-surface bed region including heat absorbed by subsurface reactions.

The bed energy balance needs to be done carefully to ensure that it is compatible with the energy balance treatment in the drop burning model and ultimately is consistent with the energy present in the fuel value in the original black liquor solids. It may be easiest to formulate these balances in terms of enthalpies for each of the species involved. This would require developing an algorithm for determining the enthalpy of original black liquor solids as a function of temperature in a way that also correctly handles the measured black liquor heating value.

Heat and mass balances on the bed are inherently unsteady. There is no guarantee that bed burning rates will just match the rate at which material is being supplied to that portion of the bed. If the burning rates are lower than the rate at which bed material is being supplied to that portion of the bed, char will accumulate in the bed zone and the bed will grow. If the burning rates are greater than the supply rates, the converse is true. Char will be depleted, and the bed will decrease in size.

One way around this problem is to force the bed to operate at steady state so that all material that reaches the bed reacts and leaves. This approach ignores the chemical rate equations and bed rate processes. It is a simple approach that allows closure of material and energy balances, but it begs the question of whether the given operating state is actually possible. Thus it can allow "nice-looking" simulations that are not actually obtainable with the liquor spray and air supply conditions being used.

Material can be transferred along the surface of the bed by fluid drag from the gas flow across the surface. This can redistribute combustible material so that it does not burn at the point where it initially lands on the bed. Redistribution of char is particularly important for those firing practices that spray a large amount of liquor solids on the wall. Liquor drops that reach the wall dry, pyrolyze and burn while sticking on the wall. They accumulate on the wall until the weight becomes great enough that they slough off and fall to the hearth. This material tends to land around the perimeter of the bed and, if not redistributed, will either result in excessive bed growth right next to the wall, or very high temperatures, because of the large amount of fuel being burned in a small local area. Some sort of redistribution algorithm is needed to handle this in a bed model.

In an ultimate bed model, inventory balances would be used to determine bed shape in an iterative manner. In the areas where char is accumulating the bed would grow and in those areas where it was depleting, the bed would shrink. This information would be used to specify a new bed geometry and recompute the gas flow (and other) fields and combustion behavior to once again determine where the bed is growing and decaying. This could be repeated until bed burning approaches a steady state and the resulting bed shape would be fully compatible with the existing firing conditions. Indeed, such a bed shape would be a useful model output. However, such calculations would be very computationally intense, and no current bed model has this capability.

AEROSOL FORMATION MODELS

One of the functions of recovery furnace models is to predict the amounts of sodium and potassium salts that may be carried with the furnace gases through the convective sections of the boiler where they can contribute to fouling and plugging. These materials cover a very wide range of sizes from millimeter-sized carryover particles to submicron fume. The amount and composition of the macroscopic carryover particles is a predicted output of the CFD-based recovery furnace models. These predictions should be reasonable if the liquor sprays are properly described.

The fume particles are assumed to form by condensation of vaporous sodium and potassium species. The main precursor species (as discussed earlier in this chapter) are assumed to be $Na_{(v)}$, $K_{(v)}$, $NaCl_{(v)}$, $KCl_{(v)}$, and possibly $NaOH_{(v)}$ and $KOH_{(v)}$. The $Na_{(v)}$ and $K_{(v)}$ are assumed to be formed by reduction of sodium and potassium carbonates by carbon. This reaction will be kinetically limited except at very high temperatures. Limited rate equations are available, but they need modification and verification before they can be relied upon. The NaCl and KCl are assumed to vaporize as the salt and to follow Raoults Law in relating the vapor pressure to the concentration in the smelt. There is little data on NaOH and KOH release from burning black liquor and no rate equations or models are available for these processes. All in all, there is a good deal of uncertainty in the ability to predict the rate of fume precursor release in a furnace model.

The fume particles which deposit in the convective section or which reach the precipitator are primarily sodium and potassium sulfates, with lesser amounts of carbonate and chloride. The process by which sulfates form has been assumed to be as follows.

$$2\,Na_{(v)} + 1/2\,O_2 + CO_2 = Na_2CO_{3\,(s)}$$

and $$Na_2CO_3 + SO_2 + 1/2\,O_2 = Na_2SO_{4(s)}$$

However, some measurements made in recovery boilers suggest sulfation occurs rapidly in the superheater section. This does not seem to fit with what would be expected with the above reactions.

Verrill and Wessel [8] have suggested that fragmentation processes, as a black liquor drop burns, would produce tiny smelt drops (perhaps 5 - 20 microns) in the furnace and that these constitute a large fraction of the aerosols produced. Such particles would be very likely to deposit on superheater or generator bank tubes and contribute to fouling and plugging. There has been little direct indication that such particles exist in large quantities in the furnace, but then there have been very few measurements of particle size distributions of recovery furnace particulate further upstream than the generating bank outlet. It has further been suggested that these fragmentation particles are the main source of fume in recovery boilers because their very high surface area would favor vaporization. This has not been substantiated.

Cameron [9] showed that large quantities of Na_2CO_3 fume could be produced in the laboratory when sulfide in smelt was oxidized to sulfate. The importance of this process in recovery furnace fume formation has not been established.

Thus, at the present time, there is considerable uncertainty with respect to the ability to predict aerosol formation in the recovery furnace. This is one area where the black liquor combustion models need considerable improvement.

CRITICAL REVIEW OF RECOVERY FURNACE MODELS

Considerable effort has gone into the development of computational fluid dynamics (CFD) based recovery boiler models and applying these models to improve recovery boiler operation and design, both in this project and others. These models are now becoming recognized as engineering tools for evaluating design alternatives rather than as just an R&D novelty. It is very appropriate to assess the current state of the art of recovery boiler models and to determine what are the critical tasks that still need to be accomplished to make recovery boiler models a cost-effective tool for improving recovery boiler performance. Such a review was carried out as part of this project and was initially presented in a paper at the 1995 Tappi Engineering Conference [10]. The following is a summary of the results of that review.

USE OF RECOVERY BOILER MODELS

Recovery boiler models are not an end in themselves. The need is for an effective problem solving tool, not for "virtual reality" recovery boilers. Use of recovery boiler models must lead to improvements in recovery boiler operation and design and serve as a means for increasing the general understanding of recovery boiler operation.

One approach to the usefulness of recovery boiler models is to first identify the type of information needed to improve recovery boiler performance, and then look at whether or not the models can provide the necessary information. Recovery boiler designs and operating practices have already been optimized to a considerable extent through long experience. Thus if further improvements are to be obtained, changes in design or operation must deal directly with those factors that are the current limitations.

In order to improve recovery boiler performance, we need to understand the effects of furnace design, furnace operating variables, and liquor quality on the following:

1. fouling and plugging rates,
2. air emissions,
3. combustion stability and bed control,
4. corrosion and other boiler integrity issues,
5. steam and electric power production,
6. reduction efficiency.

The overall challenge is to define optimum operating strategies (liquor spray and air entry conditions) which will maximize liquor firing rates while

- achieving acceptable plugging rates,
- meeting air emission restrictions,
- maintaining a safe, stable operation.

Using the above list of information sought as a guide, we next need to look at what models can provide and what they cannot.

Fouling and Plugging

Fouling of heat transfer surfaces and plugging of gas passages ultimately limits firing rates on most recovery boilers. The material that causes fouling and plugging is usually divided into two classes; carryover and fume or dust.

Carryover is the name given to the macrosized remnants of burning liquor drops that are physically entrained in the gas stream leaving the furnace and carried into the convective sections of the boiler. These macrosized particles easily impact on the windward side of heat transfer surfaces and can freeze on tubes and form hard deposits. They have generally been considered a prime cause of plugging and the conventional wisdom is that carryover should be minimized.

Current CFD-based models are capable of predicting the amount, chemical composition, and physical state of the carryover material. Carryover prediction was a prime motivation for the original development of such models and is one of the most useful model outputs. In addition to the amount, chemical composition and physical state of the carryover material itself, other factors may also influence boiler plugging by carryover deposits. These additional variables include gas velocities, gas temperature, gas composition, furnace geometry, and sootblowing practices.

Fume or dust is the name given to the very small (micron-sized) particles produced by vaporization and condensation processes in the furnace. Recent experience indicates that many, if not most, recovery boiler plugging problems involve dust deposits. Thus for recovery boiler models to deal effectively with plugging problems, they must be able to deal with dust deposits. Unfortunately, the factors influencing dust formation, dust deposition rates, deposit hardening, and deposit removal are not well understood. The amount of dust leaving the furnace cavity, dust particle size, dust composition, gas velocities, gas temperatures, gas composition, convective section geometries, and metal temperatures may all be important factors. Current furnace models do not have the capability of predicting the amount, size, and composition of the fume or dust aerosols leaving the furnace. Furnace models do have the capability of predicting the distribution of gas velocities and temperatures out of the furnace. Current models do not have the capability of predicting all of the gas concentrations that might be relevant to deposit formation and hardening, but this capability is gradually becoming available.

There is a clear need to develop knowledge bridges that would relate the output of furnace models to the effects on convective section fouling and plugging. It is recognized that peak furnace exit gas temperature is an important parameter, but there are undoubtably others. It is also likely that furnace models may have to be enhanced to provide the capability of predicting the key information needed.

Air Emissions

Air emission constraints can limit recovery boiler operation. Thus useful recovery boiler models should have a capability of predicting the effects of operating changes on air emissions. Even if models prove incapable of accurately predicting absolute levels of each emission-limited substance, they should be capable of dealing with the effects of changes and with trade offs between different substances that might have emission limits.

Of the gaseous compounds potentially subjected to limits, TRS, CO and VOCs are all substances that are destroyed by oxidation. The destruction of these materials is essentially a stoichiometry and mixing issue. There may also be some kinetic limitations at lower temperatures but this is undoubtably a second-order effect. Current models are capable of predicting CO emissions. As a first approximation, other oxidizable substances could be proportioned to CO. More elaborate models with separate kinetic limitations could be used if it is found to be necessary.

The fundamental chemistry by which SO_2 is converted to sulfates within the furnace is gradually becoming understood as are the factors that govern sulfur release from the burning liquor drops. Algorithms for modeling SO_2 concentrations from the furnace should be available before the end of this project.

Considerable information on NO_x formation and destruction has been published within the last year and algorithms for predicting NO_x in recovery boilers should be available before the end of this project.

The basic information for predicting HCl concentrations is now available. However, since HCl formation depends on SO_2 concentrations, predictions of HCl concentrations require simultaneous prediction of SO_2.

The prediction of particulate emissions and/or opacity is more complicated. Particulate emissions depend on both the dust load and the precipitator collection efficiency and are, in fact, dominated by the precipitator performance. Furnace models have the potential for being able to predict dust loads (although this has not yet been implemented). There are no plans to model precipitators in current modeling programs.

Combustion Stability and Bed Control

Unstable combustion is potentially hazardous. Operating conditions that are conducive to black out, either local blacking out of primary air ports or a more general loss of fire, should be avoided. There is usually a close link between combustion problems and char bed behavior. Unstable char beds are often the main manifestation of combustion instability.

Although bed control is an important issue, it is hard to quantify. There is a need to define what constitutes a "good" bed. This is a somewhat subjective matter involving bed size, shape, surface temperature, burning rates, and stability. There are two factors that currently limit the ability of models to deal with these issues. One is a lack of an adequate bed model. The other is a lack of consensus on what constitutes a "good" bed, especially in a quantitative sense.

Auxiliary fuel usage can be effective in dealing with unstable char beds. However, auxiliary fuel use is not modeled in most current recovery boiler models. The assumption is made that an optimum recovery boiler should be operating autogenously on black liquor.

Corrosion and Boiler Integrity

Although corrosion, tube cracking, and other boiler integrity issues are critical to safe operation, they have not been a major focus of modeling. This is mainly because of a lack of sufficient understanding of the key underlying processes but also because at least some of these issues are not amenable to attack with steady-state furnace models.

Corrosion generally depends on three factors; local chemical environment, metal temperature, and metallurgy. Models have some capability of addressing the first two issues, but only in a limited fashion.

Furnace models can predict the heat flux distribution to the waterwalls. The heat flux has an effect on metal temperatures (along with boiler pressure, circulation and waterside deposits). In general, areas of higher heat flux would be more likely to have higher corrosion rates. Avoidance of local areas of high heat flux could be one criteria in seeking to optimize furnace performance.

Furnace models can predict the composition of some of the furnace gases that might be involved in corrosion. There is a problem in accurately predicting gas concentrations very close to a boundary without introducing an excessive number of computational elements. A more serious problem is that the relevant chemical environment is the one that exists at the metal surface and this surface is covered by frozen smelt and or char. The relationship between furnace gases and the local environment at the metal surface is currently not understood well enough to allow quantitative predictions.

Steam and Power Production

As far as steam production is concerned, CFD-based models are overkill. Steam efficiencies are determined by heat balance considerations and are dominated by externalities. Air emission constraints tend to require complete combustion so unburned fuel in gases is not a significant issue. The main variables affecting steam efficiency that

could have some relevance to models are the amount of excess air and the amount of residual carbon in the smelt. The latter quantity might be an output of a good bed model. Models could be used to determine how best to minimize excess air while meeting emission constraints.

Electric power production is affected by steam temperature and so is affected by the performance of the superheater. The extent of superheater fouling is probably the most important factor influencing steam temperature. Carryover would be expected to be significant here and carryover predictions are amenable to modeling. In addition, the furnace exit gas temperature and velocity distribution should be important and this is also amenable to model prediction. However, cleaning processes are also important and this is not addressed by current models.

Reduction Efficiency

Reduction efficiency is another parameter important to recovery boiler operation, although reduction efficiency has little economic significance once values in the +90% range are achieved. The overall reduction efficiency is dependent on the amount of reduction that takes place during black liquor pyrolysis and char burning and also on the amount of smelt reoxidation that occurs before the smelt flows out of the furnace. The sulfur chemistry during black liquor pyrolysis is becoming understood. New rate equations for sulfate reduction by carbon are available and have been incorporated in some black liquor burning models and char bed models.[6] Thus the capability to predict overall reduction efficiencies with furnace models is nearly in hand. Good bed models and good models of wall processes are necessary to do a decent job of predicting reduction efficiencies.

Summary of Critical Information

In summary, the output predictions of furnace models that are most important to improving recovery boiler performance are:

- amount of physical carryover,
- furnace exit gas temperature distribution,
- furnace exit gas velocity distributions,
- wall heat flux distributions,
- amount, size and composition of aerosols from the furnace,
- concentrations of air emission gases,
- bed size, shape, surface temperature distribution and burning rate distribution,
- some measure of bed stability and "goodness", and
- overall reduction efficiency.

Furnace models have the capability of providing the gas velocities, temperatures, turbulent intensity, and gas concentrations at very large number of points throughout the furnace volume. Most of this information is not used directly in addressing performance issues, although the patterns within the furnace can give insight into what is going on. Most of the key information needed is at the boundaries of the furnace.

TECHNICAL REVIEW

The previous section defined the specific technical information that CFD-based recovery boiler models are being asked to provide. The next step is to look at existing models from a technical standpoint to assess the degree that they are capable of providing the necessary information with reasonable accuracy and to define those areas where more development is needed.

As described earlier in this report, recovery boiler models generally consist of two parts; a CFD part and a black liquor combustion model. These two parts are coupled to provide the complete model. The CFD part solves the gas mass, momentum, and energy equations to provide gas velocity, temperature and concentration fields. The black liquor combustion models interact with the gas fields and provide source/sink terms to the CFD equations. Black liquor burning rates depend on the gas fields and in turn influence them through the source/sink terms.

Some recovery boiler models are limited to the furnace cavity itself and are terminated at the nose arch. Others carry flow and temperature calculations through the superheater. Still others carry the modeling through the furnace and the entire convective section. This discussion will basically be limited to the furnace.

CFD Aspects

Various CFD code platforms are in use for recovery boiler models. Some are based on the commercially available CFD codes, such as FLUENT and PHOENICS. Others, such as the model being developed at UBC and a model at Babcock &Wilcox, are based on internally-generated CFD codes. One of the technical issues is the adequacy of these various CFD platforms to handle the fluid dynamics important for recovery boilers. Do these codes give reasonable predictions of recovery boiler flows and the temperature and concentration fields? Do different CFD codes give similar results when applied to the same problem?

At the present time it appears that CFD codes are adequate for predicting the gas flows in the furnace. There have been limited attempts to compare predicted flows with measured flows and the agreement has generally been reasonable. Most of these comparisons have been done in isolation to verify the applicability of a particular code. There would be considerable value in a benchmarking exercise to compare the ability of different CFD

codes to predict the flow for the same cases, but this has not yet been done. Such benchmarking would add to the credibility of CFD predictions of recovery boiler flows and help pinpoint areas of weakness in flow prediction.

Empirical turbulence models are needed in the CFD models and the specific turbulence model used does affect flow predictions. This is another area where benchmarking could prove useful. There is a need for consensus on what is adequate for a turbulence model for recovery boiler flows.

Gas flows in recovery boilers are not necessarily stable, as has been shown both with CFD model calculations and by experimental measurements. This can be important when steady state solutions to the CFD equations are sought. When flows are unstable, the CFD calculations stall out at high residuals. If a transient case is then run, movement of the core flow can be seen. There are some indications that flows with circulation tend to be more stable.

It is not clear that unstable flows are inherently bad and should necessarily be avoided in real recovery boilers. If unstable flows are allowable in optimized recovery boilers, it is necessary to develop means for dealing with unstable flow fields in the models. Time-dependent solutions constitute an enormous calculation burden and are clearly not the complete answer. The time-average of an oscillating flow may not have the same properties as the actual unstable flow and may also not be the solution produced by the CFD code. Dealing with unstable flows remains an open issue.

Considering all the available information, current recovery boiler models generally appear to handle flow predictions adequately. Flow prediction no longer appears to be the modeling area with the greatest uncertainty, at least with respect to the information needed to improve recovery boiler performance.

The computational requirements to compute the flow field in a "hot" flow model with combustion are much greater than those needed to calculate isothermal flows. Limited comparisons between computed hot flow patterns and isothermal flows (at an appropriate average gas temperature) have been made and these have tended to show reasonable similarity. [11]

Differences between hot flows and isothermal flows come from volume flow sources and sinks. There are three sources/sinks for volume flow that result from black liquor combustion. These are:

- evaporation of water from the black liquor,
- gas mole changes resulting from black liquor combustion, and
- density changes associated with temperature gradients.

In many cases, these volume flow source sinks perturb, but do not dominate, the flow patterns. The flow pattern in the furnace itself tends to be determined primarily by air input conditions and furnace geometry. One area where isothermal and "hot" flows may

differ considerably is the flow in the superheater, where the gas density changes associated with temperature changes from heat absorption can induce recirculating flows.

The ability to accurately predict gas temperatures in the furnace depends on the ability to predict heat transfer rates to the waterwalls and properly handling all chemical reactions. There are some indications in published hot flow model results that gas temperature predictions in the lower furnace may be too high. Several papers have indicated gas temperatures in some regions in excess of 1600°C. [12,13] It is not evident that such high temperatures have ever been measured in a recovery boiler. This may be an indication that significant endothermic reactions are being neglected, that calculated gas reaction rates are too fast, or other problems in the models.

The ability to properly predict gas concentrations is merely a matter of putting into the models the proper stoichiometric relations and rate equations for the particular species in question. The CFD codes may put limits on the number of gas species that can be handled. If this is the case, then certain species cannot be predicted. One way around this problem is to consider only the main gas species that affect the mass and energy balances when doing the iterative CFD calculations of the gas fields. The minor constituents can then be calculated from a second, simpler model which uses fixed gas flow, temperature and concentration fields.

Black Liquor Burning Submodels

The black liquor combustion model is the second major component of a recovery boiler model. Black liquor burns in a number of different ways in the recovery furnace: as drops in flight, on the char bed, and on the wall. All of these must be accounted for in a recovery boiler model. At the present time, there is more uncertainty with respect to how key parts of the black liquor behavior should be modeled than there is with the CFD component of recovery boiler models.

Drop trajectory models

Black liquor is sprayed into the furnace as rather coarse drops which pass through the furnace gases and dry and burn as they move. The liquor drops eventually land on the hearth, reach a furnace wall, or are carried out of the furnace with the gases. Most current recovery boiler models use a Lagrangian approach for treating the black liquor. In this approach, the liquor droplets follow a deterministic path through the furnace dependent on the initial drop conditions and the gas fields through which the drop moves. In this approach all drops that start out with the same initial conditions follow the same path. Blasiak [14] has used a probablistic approach for modeling a dispersion of droplets. This method does not describe the detailed motion of each droplet. It describes the motion of the liquor phase by means of a probability distribution function. UBC has used an

approach which is partially stochastic. The black liquor drops follow deterministic trajectories as they move through the furnace, however, the gas velocity field contains a turbulent component which is described by a probability function. Thus a drop starting with the same initial condition will not experience the same gas flow field each time and so will not follow the same trajectory. Trajectory calculations directly determine the amount of carryover. Unpublished simulations have shown, at least for a gas flow pattern with a strong central updraft, that the amount of carryover calculated is less with the turbulence-affected trajectories.

The trajectories that individual drops follow are determined by initial vector velocities, gravity, and fluid drag. Trajectory models must account for the changes in mass and physical size of the drops as they burn. Current methods for calculating drop trajectories by force balance are adequate. The biggest uncertainties are associated with the proper assignment of initial velocities and drop sizes, and with the empirical treatment of the swelling and deswelling that accompanies liquor burning.

Drop burning models

There has been considerable improvement in black liquor burning models over the years. The initial models treated the liquor as containing four substances; water, volatiles, char carbon, and ash. These early models are sometimes referred to as "earth, air, fire and water" models. They were adequate for describing the weight changes and volumetric changes occurring during burning needed for trajectory calculations and carryover prediction. With appropriate assumptions and the proper treatment of char gasification as well as oxidation, they could be used to give a first approximation of the source/sink terms needed to predict hot flow fields. Black liquor drop burning models are now becoming available which give rate equations for the transfer of individual elements in the liquor to the gas phase. These elemental transfer models are gradually being incorporated into the drop burning models. They provide a much better basis for proper modeling of source/sink terms and for the prediction of aerosol formation and emissions behavior.

One of the most critical remaining problems is to develop and verify drop burning models specifically for recovery furnace conditions. Existing drop burning models are based on laboratory experiments. Most of these have been carried out with black liquor drops suspended in muffle furnaces. Others have been carried out in laminar entrained flow reactors. One issue is a proper description of the rate processes that depend on the particular environment in which the drop is present. Another is defining the stoichiometric partition factors and swelling factors that now are empirically linked to variables in the laboratory setups that do not have an obvious counterpart in the furnace. There remains a need to have an experimentally validated drop burning model that involves only those variables that are meaningful in a CFD furnace model.

Another issue is how to deal with liquor dependent parameters. The swelling tendency of a liquor depends on composition. Measurements of swelling made in the laboratory under arbitrary conditions can be used as a basis for describing swelling in the furnace, but there is a degree of uncertainty involved. The overall split of organic matter between volatiles and char is dependent on liquor chemistry as well as the time-temperature environment to which it is exposed. It is known that individual sulfur compounds in the black liquor behave differently during pyrolysis and this can affect the extent of reduction during pyrolysis and sulfur release to the gas phase.

Char bed models

The best current char bed models are capable of describing burning rates and interactions with the gas fields above the bed. However, better char bed models are clearly needed. Improvements are needed in treatments of surface and subsurface burning rates. There is also a need to have a means for predicting bed shape and stability. Several boiler manufacturers have indicated that they consider the ability to predict bed shape to be critical.

There is an inherent dichotomy in using a steady state furnace model to predict bed shape, since there is no guarantee that bed burning rates match the rate at which material is delivered to the bed. Some modelers have addressed this issue by arbitrarily assuming a bed shape and then assuming that everything that reaches the bed burns (as it must at steady state). While this approach allows closure of energy balances and does not greatly affect predictions of gas conditions leaving the furnace, it certainly begs the question of combustion stability and whether the operating conditions being modeled are actually feasible.

A proper bed model must allow a predicted bed geometry to be an outgrowth of the bed model integrated to the combustion processes occurring above the bed. It must not only provide bed burning rates, it should also allow for accumulation and depletion of material and physical transport of char along and off the bed surface in arriving at the ultimate size and shape.

The chemical basis for modeling bed burning rates is available. It is essentially the same as that used in the char burning step in the drop model. Char gasification by CO_2 and H_2O is included along with oxidation of product gases in the boundary layer in a combined mass transfer - chemical kinetics limited burning. Carbon consumption by reaction with sodium sulfate and carbonate can also be included. These latter reactions can occur subsurface. There are still questions about the proper way to handle combustible volatiles and water that reach the bed with incompletely dried and pyrolyzed black liquor. This isn't a problem with drop models, because these process occur in the sequence before char burning begins. However, the bed is a collection of many liquor drops in various stages of burning and all of the rate processes must be treated as occurring in parallel.

Effective means for providing for redistribution of char by physical transport along the bed surface have not yet been implemented in bed models. Where redistribution is done, it is done in a completely arbitrary manner.

There can be problems in setting up the heat balance for the surface region of the char bed for the purpose of predicting the bed surface temperature. In some approaches, an arbitrary reaction zone thickness is assumed and the calculated surface temperature is dependent on the value chosen for this thickness. Models must avoid making critical predictions that depend on arbitrarily chosen parameters.

Wall processes

The liquor drops that strike the walls of the furnace wall must be treated in a realistic manner. A variety of ways of handling liquor which reached the walls were used in early recovery boiler models. For example, when models were used only for carryover predictions, liquor which struck the walls was usually ignored. Another technique (not very realistic) was to assume that a liquor drop that reached the wall bounced off elastically. A more sophisticated way of handling wall processes, and one that did allow a steady state solution, was to assume that a particle that reached the wall continued burning at the same rate that it was burning at just before it reached the wall until all of the fuel was gone.

A realistic wall burning model must allow for the fact that in the furnace, liquor accumulates on the wall and then periodically sluffs off and falls to the bed. This can, in fact, be a very significant way that fuel and inorganic reach the bed. Recently, one boiler manufacturer has developed a wall model that treats the liquor burning rate on the wall in a similar manner to the burning rate on the char bed. If there is an inbalance between the rate at which liquor substances reach the wall and the burning rate, the excess is assumed to sluff off and fall to the bed. [15] This appears to be a reasonable way of treating wall burning.

Liquor Spray Modeling

Liquor sprays are modelled by setting up the initial conditions at which liquor drops enter the boiler. The key issues with liquor spray models are whether or not the finite length required to form drops should be dealt with and how to relate the drop specifications to the nozzle geometry and the actual variables (flow, liquor temperature, etc.) available to the operator. It is unclear whether or not spray drop size distribution data obtained under laboratory conditions are relevant to sprays formed in the high temperature environment of the furnace.

Liquor drops are usually assumed to originated from a point right at the wall with the drops fully formed and with a well-defined initial vector velocity. A mean drop size is

selected by the modeler (usually in a fairly arbitrary manner) and a size-distribution about this mean (often a square-root normal distribution) applied to give a discretized selection of initial drops. For example, if 10 drop size distributions were chosen, selection of the mean diameter and distribution function would determine the initial drop diameter for each of the 10 drop classes. The drops are also assigned an angle in both the horizontal plane and in the vertical direction and an initial velocity. If the liquor spray is a plate-type sprayer, the vertical angle might be chosen to be the same for all drops. Often, the same velocity is used for all of the drops.

The number of liquor drops actually modeled is normally kept rather small in order to keep down the amount of calculations required. The mass, heat and momentum transfer for each drop is then appropriately weighted to account for the total amount of liquor being fired. For example, if liquor was being fired in from 4 guns and there were 20 drop size classifications, a 120° spread in liquor divided into 5° increments, a single velocity and a single vertical angle, the total number of drops entering would be 4 x 20 x 25 = 2000 drops. Although this is a large amount of trajectories, it is actually a very sparse set of information from which to calculate source/sink terms. For example, if the furnace is modeled with 100,000 cells, and the average drop passes through 30 cells on its trajectory, the number of drops, on average, providing source/sink information to a given cell is 0.6. Even if a large number of drops are modeled, (say 100 size increments and each degree in angle, giving 4 x 100 x 121 = 48,400 drops) the average cell would only get source/sink information from about 15 drops. This coarse discretizing of the source/sink information may be one of the reasons for the prediction of apparently excessively high local temperatures in the lower furnace.

In the actual case, the spray is not fully formed into drops until the liquor has moved a significant distance into the furnace. The exposed surface will generally be smaller, during this formative stage, than when the drops are completely formed. Thus drying and devolatilization rates in the region near the liquor gun openings, will tend to be overpredicted.

In general, the way sprays are modeled, and the high degree of arbitrariness in selecting spray parameters, is one of the weaker areas in current recovery boiler models.

Heat Transfer Modeling

There currently is considerable uncertainty and disagreement with regard to how to handle radiant heat transfer in the furnace. Much of this has to do with the effect of fume and other furnace aerosols on radiation heat transfer. Some people believe fume may act like soot. Others consider it a minor matter.

It appears that there are good radiation models available. What is lacking is reliable data for radiation properties in a recovery boiler environment. This need is being specifically

addressed in the extended DOE recovery boiler modeling project. Babcock & Wilcox was brought in as a subcontactor on this project to obtain data on critical properties that affect radiative heat transfer in black liquor combustion and to develop strategies for accurate treatment of heat transfer in recovery boilers.

One of the key areas is the specification of the appropriate heat transfer boundary conditions for the waterwalls. The temperature is frequently taken to be equal to the melting temperature of the smelt. The reason for this assumption is that inorganic smelt will tend tend to reach the wall and freeze there and build up a frozen layer. The temperature drop over the frozen layer will increase until the outside temperature reaches the melting temperature (or the free-flow temperature) and this will then stop further growth of the frozed layer. Up until now, the emissivity has been chosen in an arbitary manner.

Overall Capability

The capability of CFD-based recovery furnace models has increased significantly over the past few years and they are at the point where they can be used as an effective tool. However, there remain some areas where further work is required.

Gap areas are those items where current models are inadequate to provide the information needed to improve recovery boiler performance. Critical technical enhancements needed for existing models include:

- drop burning models that are appropriate for recovery furnace conditions,
- models of aerosol formation in the furnace,
- good bed models with shape predicting capability,
- effective wall process models.

The capability to predict fouling and plugging is another gap area. Additional information needs to be obtained and integrated into a cohesive view of plugging processes in the furnace. It is probably not necessary to develop a computerized model of the fouling processes themselves. What is actually needed is a knowledge bridge between what a furnace model is able to predict (gas velocities, temperatures and composition leaving the furnace and aerosol amounts and characteristics) and the consequences in terms of fouling and plugging the convective sections. The effects of the amount, size, and composition of aerosols on plugging must be understood. It is also necessary to be able to interpret quantitatively how gas temperature, gas velocity, gas composition, and chemical reactions affect deposition rates and hardening. The essential question to be answered is "how does furnace operation, (i.e. how black liquor and air are put into the unit), affect fouling and plugging."

One critical need is to define the nature of the aerosol forming processes in the recovery boiler. A wealth of new information was presented at the 1995 International Chemical

Recovery Conference. This has to be interpreted. Sintering and hardening of deposits is also an essential element of the plugging and fouling process. There is considerable laboratory data on sintering and hardening rates as a function of composition. There is a need to tie this behavior more closely to field conditions.

Removal of deposits from heat transfer surfaces is an absolutely essential element of the plugging and fouling process. Recovery boilers would probably plug within 24 hours after liquor firing was initiated if sootblowers were not used. Thus, considerations of deposit removal must be incorporated into the knowledge bridge between furnace models and fouling and plugging of the upper furnace.

Excellent work on aerosol formation, deposition, hardening and removal is being carried out at the University of Toronto, Abo Akademi, VTT in Finland, Oregon State University, and at boiler manufacturers. This can be used to address fouling and plugging issues.

Modeling of corrosion processes in recovery boilers, as part of more general recovery boiler models, is probably not feasible at this time.There are no plans for modeling corrosion in this project.

APPLICATION ISSUES

Impediments

There are many impediments to the effective use of recovery furnace models. These include:

- the high computational intensity of calculations,
- the high degree of skill needed to set up problems and guide convergence,
- limited correspondence between the type of information needed to solve recovery boiler problems and the type of information a furnace model can produce,
- the immense amount of information developed by the models must be distilled and condensed and presented in a manner that the user can understand it,
- the inefficiency in re-solving the entire recovery boiler furnace field to see the effects of changing a single parameter,
- the lack of confidence in the reliability of model predictions.

Overcoming these impediments presents many challenges. Using faster, bigger computers may not be the only or even the best answer to the issue of high computational intensity. There is a clear need for simpler models to provide most of the answers sought, with full-blown models used only for confirmation purposes.

Compromises must sometimes be made in setting up a problem in order to describe the boiler geometry in a reasonable number of computational cells or elements. This may

result in air ports being moved in the model to fit grid lines lined up with other ports. Air port openings in the model may be larger than the real ports in order to fit a grid. This can be dealt with by introducing a port porosity but this will affect predicted flows. Primary ports are usually modelled as slots in order to keep the computational nodes reasonable. This usually has a minor effect on the flows, but it could influence bed burning rate predictions, especially close to the walls.

Critical Issues

In September 1994, a symposium on recovery boiler modelling was held, involving model developers, boiler manufacturers, and kraft pulp manufacturers. A summary of what model users felt were the most critical things needed included:

- model validation,
- good bed models,
- wall interactions models,
- fume, NO_x and S chemistry models,
- definition/criteria for stable combustion,
- means for treating radiation in dense, reacting, particle-laden flows, and
- how to define an optimum furnace.

It was generally agreed that it would be of great value to set up a program to benchmark various recovery boiler model codes against one another. If this benchmarking effort resulted in general agreement it would add greatly to model credibility. Where there were differences in model predictions, it would help point out critical issues that needed to be addressed. There was a general consensus that radiation and turbulence were not handled that well with current recovery boiler models.

Technology Transfer

It is clear that the benefits of recovery boiler models will only be fully realized if the models, submodels, approaches, etc. get into the hands of those who have a stake in improving recovery boilers and know enough about them to use the models effectively. In general, these are the boiler manufacturers and companies operating kraft mills.

There is also a need to use models to develop a better understanding of how boilers operate and provide general guidelines on firing practices and air supply. One of the long-range goals of the recovery boiler modeling effort is to provide guidelines for optimum liquor spray arrangements and air entry conditions. This might most appropriately be done through a series of simulations on a generic recovery boiler chosen for computational efficiency and ease of systematic altering of key parameters. Academic institutions might play a role here. It will be difficult to come up with general conclusions from isolated studies on individual boilers done on a piecemeal basis.

Credibility

Finally there is the challenge of model validation. This is essentially an issue of users having confidence in the predictions of the model. Validation has been an on-going part of this model development effort. Calculated flows from isothermal models have been tested against data from water flow models of two different recovery boilers with reasonable success. Model predictions have also been compared against limited cold flow data in recovery boilers. The results of these efforts indicate that overall flow predictions are reasonable. The black liquor combustion models that are being developed have been validated against single-drop black liquor burning data from laboratory systems, data from entrained flow reactors, and other laboratory systems.

It is clear that the global furnace model must also be validated against field data obtained on actual recovery boilers. Validation will be based on a comparison between model-predicted and measured results of cause-and-effect relations between selected operating variables and critical output variables. Thus validation will be intimately tied to what the models will be used for. Model validation at this level is not seen as something that requires breakthrough developments in sensors and measurement technology on recovery boilers. The necessary measurements can be made with existing methods, especially if the measurements need only be made for a limited time.

Every successful application of a recovery boiler model adds to credibility. Careless use of models for situations for which they are not appropriate can only destroy credibility. Benchmarking of predictions of one model against another could add considerably to the credibility of these types of models.

MODEL VALIDATION

The issue of validation rears its head whenever a computer model is developed. Predictions from mathematical models are met with considerable skepticism unless they can be shown to have been validated against "real" data. However, validation is a very fuzzy term and means different things to different people. In essense, model validation is a matter of users having confidence in the predictions of the model. The most critical objective of model validation is to convince ultimate users that model predictions can be relied on and that models are a useful tool for improving recovery boiler design and performance.

VALIDATION CONCEPTS

Computational fluid dynamics (CFD) is becoming increasingly used in industry because of its unique ability to predict complex, three-dimensional flows. Many computational codes exist and are currently in use. In the past, relatively little emphasis was placed on code validation, and as a result, confidence in CFD as a generic design tool has suffered. In the engineering environment, pressure may be strong to apply a code before it is thoroughly validated. Validation can be time-consuming and expensive. There have been no industry standard procedures for code validation.

NASA Approach

Because of the extensive use of CFD in the aerospace industry, NASA has recently developed a procedure and criteria for assessing CFD codes. This is described in NASA Tech Briefs MFS-29972 [16]. The procedure can be used with any computational code and can be customized for any application of interest. The four-phase validation procedure is flexible, allowing for various levels of validation. The level of validation may be incrementally upgraded as the need exists and time and funding permit. Phase 1 includes fundamental flows only. Phase 4 includes complex flows that directly represent the end application.

The four phases are:
1. unit problems,
2. benchmark cases,
3. simplified partial flowpath, and
4. actual hardware.

In Phase 1, the CFD code is exercised on unit problems. Unit problems are characterized by a single dominant flow feature and have available analytical solutions. Phase 1 validation would test the code on several unit problems, each representing one basic flow feature of the end application. All aspects of the code relevant to the end application are

exercised to verify accuracy, functionality and convergence characteristics. Grid sensitivity studies are conducted to assess relative error and to provide guidance in specifying computational grids for more complex cases.

In Phase 2, the code is tested on relevant benchmark cases. These benchmark cases are characterized by more than one flow feature. Physical models within the CFD code are exercised to verify operability and to quantify acuracy relative to benchmark data. Only data from the highest quality experiments should be used for comparisons with CFD solutions. Grid sensitivity studies are carried out to assess the refinement necessary to capture key physical effects. *A code validated through Phase 2, satisfying all established criteria, may be considered validated for conceptual design studies.*

Test cases selected for Phase 3 are simplifications of the final validation case, each representing multiple geometric and flow features of the final application. Data should be selected according to defined criteria, but these may be relaxed as necessary. The effects of grid topology and grid clustering are assessed and grid requirements to capture key physical effects established. Relatively few cases are run. *A code validated through Phase 3 may be considered validated for preliminary design studies.*

Cases for Phase 4 should be selected from tests conducted using actual hardware. All relevant geometric and physical effects should occur simultaneously. The best data sets should be used and deficiencies in the data identified. It is likely that only one or two cases will be run in Phase 4. *A code validated through Phase 4, satisfying all established criteria, may be considered validated for detail design studies.*

What is Possible in Recovery Boilers

It is of interest to try to apply the NASA procedure to the validation of CFD-based recovery boiler models. The essense of the NASA procedure is that confidence in the codes is built up systematically through assessment of the ability to predict results of simpler cases that are relevant to the actual recovery boiler situation. The complete, final validation is then confirmed by testing against a very limited number of "real cases". The model is not treated as a "black box" whose predictions have to be compared point-by-point with a tremendous amount of data from an actual recovery boiler. Instead, confidence is established in the pieces making up the complete model and then finally in the capability to make key predictions in the real boiler.

In the case of the recovery boiler model, the validation of the CFD model is first based on the ability to describe isothermal flow problems related to the types of flows expected in recovery boilers, and then this is expanded to cases with temperature differences and bouyancy forces. The black liquor combustion models that are interfaced with the CFD model must first be validated against experimental data on black liquor combustion processes. Only when these have been accomplished is it meaningful to attempt to validate the predictions of the combined hot flow model with black liquor combustion.

This latter step is sometimes seen as the only validation relevant and required. However, it is only one, final part of the total effort.

There are three basic elements in every validation exercise:

1. experimental data are acquired (or analytical solutions obtained) to define the conditions needed to set up a simulation for the case and to determine the actual results for the case,
2. one or more simulations are run on the case in question,
3. model predictions are compared to the actual data and judgements made with regard to the degree that predictions conform to reality.

In the case of recovery boiler model validation, the most difficult part is in acquiring data from actual operating recovery boilers. This includes both the data needed to define all of the input information needed to accurately set up a case as well as the boiler output data needed for comparison with model predictions. The environment inside a recovery furnace is very severe with respect to intrumentation for making the necessary measurements. In addition, access to the furnace is also limited to a rather small number of ports of different sizes and locations. This greatly restricts the amount of information that can be obtained on the gas flows, temperature and gas composition within the furnace.

The models have the capability of predicting a great deal of information about the processes occurring in the furnace. This includes gas velocity fields (all three velocity components), temperature fields, concentration fields for each of several gas species, the turbulence intensity field, and the trajectories and fates of the black liquor sprayed into the furnace. This is orders of magnitudes more information than can ever possibly be measured. There is no possibility whatsoever of actually making detailed measurements of the gas velocity, temperature, and gas concentration fields within the furnace for comparison with detailed model predictions. Validation to this level is not feasible now and is not likely to be feasible in the foreseeable future.

What needs to be done is to compress the output data set down to more manageable levels that contain only the most important information and are amenable to measurement on actual recovery boilers. Validation at this level is possible and ultimately needs to be done.

In order to do this, a certain amount of reliable data on process performance and operating conditions must be obtained on one or more recovery boilers. Once this data is obtained and made available in an accessable form, validation exercises can be done at any time. This allows the same set of information to be used to validate any number of different models, or for the same model to be validated at different times as it is updated and improved.

What is Needed for Recovery Boiler Model Validation

It is not only impossible, but also not necessary to verify that all of the model predictions about velocity, temperature and gas composition fields are in agreement with actual data. Most of the data generated by the models is not actually needed for improving furnace designs or performance. As was indicated in the critical review in the previous section, most of the important information needed is on the boundaries of the furnace. What goes on inside is only important if it affects the boundary information, i.e. the gas conditions leaving the furnace, bed conditions, wall heat fluxes, etc. The model can be considered validated for engineering purposes if it is capable of reliably predicting this "boundary information".

Critical information

The critical data needed is the information needed to set up a proper simulation, and the important furnace performance information needed to verify output predictions.

The conditions for setting up a simulation need to be accurately described. The information required is as follows:

1. geometry data on the boiler in question including furnace dimensions, locations and size of air ports and liquor gun openings, nose arch shape, etc. that are needed to set up the model grids,
2. data describing black liquor conditions including liquor flows, composition and heating value, and liquor spray characteristics, the latter of which may have to be inferred from the location, angle, and types of liquor guns, and the liquor temperature and pressure, and
3. data describing air conditions including air flows at different levels and distribution around the furnace, pressures, and temperatures.

Model validation must be intimately tied to what the models will be used for. As discussed in the previous chapter, the predicted furnace model output variables that are most critical to the use of models as a tool for improving furnace performance are:

- amount of physical carryover,
- furnace exit gas temperature distribution,
- furnace exit gas velocity distributions,
- wall heat flux distributions,
- amount, size, and composition of aerosols from the furnace,
- concentrations of air emission gases,
- bed size, shape, surface temperature distribution, and burning rate distribution,
- some measure of bed stability and "goodness", and
- overall reduction efficiency.

The important principle is that it is only necessary to validate the key predictions of the overall model. These are summarized above and thus these are the output variables that should be measured as accurately as possible and used for comparison against model predictions. Not all of them are measurable without an extensive probe development effort. Compromises may be needed with regard to the quality and quantitative nature of the information obtained, but the above list provides a clear focus for getting the needed information.

Cause and effect validation

One of the easier ways to obtain useful information on recovery boiler performance is to change one or more input variables and measure the changes in the performance variables. This can be used to obtain cause and effect relationships, and these cause and effect relationships are exactly the type of information needed to improve performance. However, cause and effect information is not in a form where it can easily be used for recovery boiler model validation. The reason lies in the nature of the CFD models and in the methodology used to obtain solutions.

In order to get a solution from a CFD model, a case is set up that defines the grid geometry and all of the input conditions (which come in as boundary conditions). An iterative solution procedure is then set up which gradually converges to give the final solution (the values of the gas field quantities at each grid point). This is a very computationally intensive process. If one input variable is changed, the entire solution process must be repeated. Experience indicates that starting from the solution set from one input condition does not give an appreciable shorter solution time for a second input condition. Thus establishing cause and effect relationships by simulations using CFD models is a very cumbersome and time-consuming procedure, even if only a few input variables are involved.

Despite the amount of computational work required, validation of cause and effect relationships is potentially one of the most effective ways of validating the recovery boiler models. At the very least, the model must be able to predict that output variable changes go in the right direction, even if it is not possible to measure all of the changes quantitatively.

VALIDATION APPROACH

The approach to model validation on this project closely follows the general concepts of the NASA validation approach, namely to do most of the validation and confidence building on the simpler level and minimize the amount of full-scale recovery furnace testing needed. The validation has proceeded in three distinct areas:

1. validation of flow predictions,
2. validation of the black liquor combustion models, and
3. validation of the integrated furnace model.

Flow Validation

What has been done

Flow validation has been an on-going part of this recovery boiler model development effort. The UBC isothermal flow model has been used to study the behavior of parallel and opposed jets in a confined cross-flow. Both steady-state and time dependent solutions have been obtained. The CFD code has also been tested against experimental data from small-scale water models of two different recovery boilers and has also been validated against limited cold flow data in a full-scale recovery boiler. These validation tests and results are discussed in considerable detail in Appendix 1. The results indicate that the computational model is capable of yielding velocity distributions that are representative of actual flow fields in recovery boilers.

Different CFD codes such as Fluent and Phoenics have been used as the basis for recovery furnace models. These have been widely used with success for many different types of fluid mechanics problems. However, there has been relatively little work done (at least in the open literature) testing the validity of employing these codes for the kinds of flow conditions that exist in recovery boilers or looking at the issue of grid sensitivity. The general flow patterns predicted for recovery furnace flows by all of the CFD models, including the UBC model, appear to be similar, at least superficially. No attempt has been made as yet to make detailed comparisons between the predictions of different CFD codes on the same recovery boiler flow problem. Lacking such comparisons, the UBC model must be considered to be the one most thoroughly validated for isothermal recovery boiler flows.

Outstanding issues

There remains some concern about the adequacy of the turbulence models used and the effect of using different types of turbulent models on the flow predictions.

There would be considerable value in comparing the predictions of different CFD codes on the isothermal flow in one or more recovery boiler cases. Similar flow predictions by several different codes would greatly enhance the believability of flow predictions in the models. On the other hand, if significant differences are found, the causes of the differences can be ascertained and problems corrected.

Finally, all of the validation that has occurred so far has been for isothermal flows. Validation of hot flow predictions, separate from the complication of the inclusion of the black liquor combustion model would be of value.

Black Liquor Model Validation

Various black liquor combustion models exist for describing the burning behavior of black liquor drops passing through the furnace and for char bed burning. The validity of these models is based on experimental data acquired in laboratory systems, which have similarities to and some significant differences from recovery furnace environments.

What has been done

Black liquor drop combustion models have been mainly derived from and validated against experimental data from laboratory single-drop muffle furnace systems and laminar entrained flow reactors. Some fundamental kinetic rate expressions have been obtained using TGA systems. The validation of black liquor drop combustion models is discussed in much greater detail in Appendix 2.

In the single-drop muffle furnace systems, a single drop of black liquor is suspended inside a muffle furnace and observed as it burns. The composition of the gas atmosphere inside the furnace can be controlled. The primary mode of heat transfer to the drop is initially by radiant heating from the walls of the muffle furnace. Most of the data have been obtained with furnace temperatures of 700-900°C, although there is some data at higher temperatures. Once volatile gases ignite, the drop is surrounded by a flame of burning gases and the radiation from these hot gases can be the dominant mode of heat transfer. Mass transfer is by natural convection that accelerates once a flame is established. The geometry changes as the liquor dries, pyrolyzes and burns can be followed with a camera system, and these geometry changes and the presence of a visible flame are used to mark the different burning stages. Most of the data on burning rates under heat and mass transfer controlled conditions have been obtained with this system.

However, there are some critical differences between this type of system and the furnace. In the furnace, the drops/particles are moving at a high velocity relative to the gas (at least in comparison to the stagnant gas environment that exists in the muffle furnace). This means that forced convection heat and mass transfer is important, and natural convection minimal. The combustible gases coming off the particle will tend to be stripped away and not form a localized flame around the particles. Radiation from the hot surrounding furnace gases as opposed to the walls will be the dominant heat transfer mechanism.

The laminar entrained flow reactor uses tiny particles of black liquor solids as feed. It can be a useful system for defining the relevant chemistry, but the very small particles make it impossible to get at heat and mass transfer effects and rates.

Thus, although the black liquor drop models are all based on experimental data, there are enough differences between real furnaces and the laboratory systems to raise questions

about the quantitative validity of the rate equations. In addition, empirical parameters are used in the models that have not been verified against data obtained from a recovery boiler. In some cases, these empirical parameters are correlated against variables that have meaning in the laboratory system, but which do not have a logical counterpart in a real furnace.

There has been very little validation of char bed models. The only experimental data available for validating char bed burning models is that of Grace et al [1]. This is a very limited data set.

Outstanding issues

The black liquor burning models need to be reformulated to eliminate empirical parameters that do not have physical significance and which can only be correlated in terms of system parameters that do not have recovery furnace couterparts. If empirical parameters remain, they must be based on data obtained in laboratory systems that more closely simulate actual recovery furnace environments.

The critical assumptions in the char burning model and in bed burning models must be tested experimentally. In particular the method of treating counterdiffusing oxygen and combustibles in the gas boundary layer during char burning needs experimental verification.

At the present time, there is considerable uncertainty with respect to the ability to predict aerosol formation in the recovery furnace. This is one area where the black liquor combustion models need considerable improvement.

Integrated Model Validation

What has been done

Very little has been done on validating the integrated CFD-based model incorporating black liquor combustion. Simulations have been done on actual recovery boilers, and in some cases, these have been coupled with experimental measurements to add credibility. However, no systematic acquisition of experimental data on an operating recovery boiler for the purpose of validation CFD-based model predictions has been carried out yet on this project. It has also apparently not been done elsewhere, at least as far as the open literature is concerned.

Even if the CFD flow code and the black liquor combustion models are fully validated, the integrated model combining both could still not be valid. There could be problems in properly interfacing the black liquor model with the rest of the code. Radiation heat transfer is very important in the real recovery furnace and in the integrated model, and is

not really validatable outside the integrated model. Mass and energy balance closure between the combined liquor and gas phases must be insured. Finally, the possibility that the source/sink terms coupling the liquor phase and the gas phase affect the flow in ways not thoroughly tested in isothermal validation must be considered. Thus the complete integrated furnace model must also be validated against field data obtained on actual recovery boilers.

Possible approaches

In looking at the possibility of validating the complete hot flow model incorporating black liquor combustion, use is made of the concept that integrated model validation should be directly tied to model end use. As discussed earlier, the most critical furnace output variables are:

- amount of physical carryover,
- furnace exit gas temperature distribution,
- furnace exit gas velocity distributions,
- wall heat flux distributions,
- amount, size, and composition of aerosols from the furnace,
- concentrations of air emission gases,
- bed size, shape, surface temperature distribution, and burning rate distribution,
- some measure of bed stability and "goodness", and
- overall reduction efficiency.

It is meaningful to consider the likelihood of being able to make the necessary nmeasurements.

The amount of physical carryover can be measured by sticking probes into furnaces for a predetermined time and measuring the amount collected. The problem with this approach is that only a very small portion of the furnace cross-section is being probed. There can be problems in using these data to estimate the total amount of carryover. Observations of deposits on sootblower lance tubes can provide information of a limited nature on the variability of carryover over different locations. Particle counters can provide information on the amount of carryover, but they are limited to counting glowing particles and have a limited field of view. By appropriate combinations of all available information, the amount of carryover can be estimated with some reliability.

The gas temperature in the upper furnace can be measured at various access points with suction pyrometers and/or shielded thermocouples. By using different probe depths and access points, a rough temperature profile can be obtained. Alternatively, acoustic pyrometry can be used to obtain a measured temperature profile in a given plane.

Furnace gas velocity measurements are very difficult to make with reliability, because of the amount of inorganic carried in the gas stream. Some indications of velocity can be

made by observations of burning particles moving with the gas, but these will tend to be confined to the region close to the wall openings.

Measurements of wall heat flux distributions would be very useful, since this is perhaps the best test of the capability of the model to accurately predict radiant heat transfer. This can be measured using thermocouples installed on the outside of membranes in membrane wall furnaces. Union Camp workers have described such a method [17] and a similar method has been used by boiler manufacturers. It takes a lot of thermocouples to do this and requires removal of skin casing and insulation to install the thermocouples. It may also be possible to get at heat fluxes using a cold-side IR scan with a sensitive scanner instead of thermocouples. This would also require removing of skin casing and insulation, but the need for extensive thermocouple installations would be eliminated with a scanner.

Measurements of the amount, size, and composition of aerosols at the entrance of the superheater would be very useful. Most available data on dust loads and composition are taken at the entrance to the economizer or further downstream. Limited data have been obtained in the hotter parts of the furnace [18], so the capability to make these measurements is becoming available. These would likely be costly measurements to make.

Measurements of the concentrations of various gases such as O_2, CO_2, TRS, SO_2, CO, NO_x, etc. could be used for verifying some of the combustion modeling and the treatments of formation and destruction of air emission gases in the furnace. The technology for making these measurements on stacks (downstream of the precipitator) is available commercially. Measurements in a dirty environment are much more difficult.

Bed camera technology is commercially available for measuring bed size, bed shape, and the surface temperature distribution. The pyrometer temperatures can be cross-checked against thermocouple probe measurements.

The reduction efficiency in the green or white liquor is routinely available. A smelt sample can be taken for analysis of reduction efficiency to account for any loss of reduction that occurs downstream of the furnace.

Thus most of the measurements needed to validate the most important predictions of the furnace model can be made with existing measurement technology. Model validation is not something that requires breakthrough developments in sensors and measurement technology on recovery boilers. The necessary measurements can be made with existing methods, especially if the measurements need only be made for a limited period of time. While it would be most desirable to make all of the measurements at one time on a single boiler, this is not absolutely critical to the validation effort. Several different boilers could be used and a partial data set obtained for each. Whatever data was obtainable could be used for validating the models on that particular boiler. The combination of the individual validation tests would provide substantial overall validation.

Data obtained from one or more validation tests could be made generally available for validating recovery boiler models. It appears that all of the people involved in modeling recovery boilers have standard information request sheets that define the information needed to set up a simulation. These can be acquired and combined to define a minimal information set needed to allow simulation set up whose acquisition would then be part of every validation test plan. The boiler performance data will be heavily dependent on access and availability of instrumentation. The most critical need is to make sure there is enough performance data to allow a legitimate comparison between simulation predictions and measured results.

It would be valuable to use different available recovery boiler models to simulate the same boiler and compare the resultant simulation predictions. If different models make essentially the same predictions, it would add to the credibility of the whole. This would most effectively be done in conjunction with a validation test on a boiler, since the same set up information would be available to everyone and there would also be performance data against which to compare the results.

It would also be useful to run sensitivity tests with the models. This would particularly be important with respect to empirical model parameters, since it would identify areas where better models are needed. It would also be useful to determine what set up values (e.g. mean drop diameter in the liquor sprays) are most important to define accurately, since this would provide a focus for obtaining the necessary setup data.

PLANS FOR ADDITIONAL VALIDATION

Additional validation efforts are a major element in the work remaining on this project. This includes not only full-scale furnace testing and validation, but also further validation of submodels.

Submodel Validation

Much of the remaining model validation must be on the submodels. The basic idea is that if the submodels are correct and are put together in a proper fashion, the integrated model predictions should have a reasonable chance to be correct.

One need is better validation of the drop burning model. There is a much more detailed drop burning model in existence that could be used to run simulations for comparison against the predictions of the more simplified models developed as part of this project. This could allow addressing the issues of whether we are properly handling internal temperature and concentration gradients as the drop burns and if our approach to treating the counterflow of oxygen and combustibles in the boundary layer is correct. One goal of such an effort would be to get rid of the empirical laboratory system parameters that now

exist in our black liquor models. Another is to gain insight into the type of experimental data that could provide further validation of the drop models.

There is also a need to acquire more information on fume formation processes and rate and to determine whether or not fragmentation processes during drop burning occur to a significant extent in the recovery boiler, and if so to develop models for these processes.

Integrated Hot Furnace Model Validation

It would be very desirable to have sets of validation data on a number of different boilers spanning a range of operating conditions. A strong case can be made for having three different boilers; a two-level air cyclonic flow boiler such as an older CE unit, a three-level air unit employing suspension burning or stationary firing, and a recovery unit where a large part of the liquor is sprayed on the walls.

It would be highly desirable to find a boiler that is not critical to production and which could be operated in a number of different ways for the specific purpose of generating data for model validation. A unit that might be used for this purpose has been identified. This could be used for cause-and-effect testing.

If possible, test units would be chosen to take advantage of information and data acquisition systems already in place. Units with high resolution IR bed cameras could provide very useful information on bed shape and temperature distribution and this information should be very useful in validating the bed models used in the recovery furnace models.

It would also be useful to use an IR camera with a periscope view looking down on the lower furnace from above. This can nicely define the spray and trajectory behavior of the liquor while it remains wet and cold. This could be very useful information for validating that portion of the black liquor in-flight model. The movement of suspended burning black liquor drops could also provide some information on internal gas flow patterns. Such a camera would be a very important component of any validation test.

SIMPLIFYING APPLICATIONS

As was discussed earlier in this report, there are a number of impediments to using CFD-based recovery boiler models that are directly associated with the complexity of the models. These impediments include;

- the extremely high computational intensity of calculations,
- the high degree of skill needed to set up cases and guide convergence,
- the inefficiency in re-solving the entire recovery boiler furnace field to see the effects of changing a single parameter, .
- the relatively high cost in time and money to solve problems through the use of models.

At the present time, the use of recovery boiler models is still not a very cost-effective way to solve problems related to design and operation. This is only partly due to the lack of complete confidence in model predictions. If the results of the model calculations are completely reliable, and if decisions can be limited to comparing a small number of cases (say 2 to 4), then the cost of model simulations could be easily covered through the returns from improved operation. However, models now provide basically qualitative information and the number of possible variables is very high. They complement, but do not replace more standard methods of troubleshooting operations and updating designs.

The keys to cost-effective use of models are;

- simplified methods for getting results must be developed,
- key problems must be solved once and the results then applied to many boilers, and
- models must complement other knowledge and not be used as a brute force means of overcoming a lack of understanding.

MODEL SIMPLIFICATION

Need for Simpler Models

Experience in applying models to actual recovery boilers has underscored the need to find methods for simplifying the calculation effort. The models provide an enormous amount of information on details of the flows, temperatures, and gas concentrations within the furnace and on the trajectories followed by liquor particles. However, most of this information is not used directly in applications aimed at improving performance. It can be displayed graphically and provide qualitative insights into what is happening in the furnace, but the critical quantitative model outputs are on boundaries of the furnace and much more limited in scope.

Another problem is that a complete new solution must be generated (which may take days to set up and compute) when any single variable (such as total black liquor firing rate or

liquor solids content) is changed. Experience has shown that simply starting with the gas fields from one solution provides any significant reduction in solution time for a second case which is a modification of the first. Solving the entire problem every time severely limits the number of cases that can be examined.

A third problem is one of dealing with the massive amount of information that is generated by the models. The common approach is to use graphical methods such as color mapping, contour lines or arrow diagrams to display the fields. These can be quite illustrative, but all tend to be qualitative or semi-quantitative in nature. It is very subjective to use such information to decide which of two cases is better. Often, these are just a way of reinforcing prejudices and reaffirming judgements already made, rather than as a clear cut decision-making tool. It would be very useful to have quantitative measures for making comparisons.

Flow Modeling

One way of simplifying the problem, particularly, where the interest is on the effects of possible changes in air flow arrangements, is to concentrate only on the flow in the furnace. It is much easier and quicker to solve an isothermal flow problem than it is to solve a complete, integrated hot flow model incorporating black liquor combustion. This approach does have value. Physical flow models were used by boiler manufacturers to gain insight into the effects of air flow variables, and CFD flow modeling simply adds to this capability.

Isothermal flow model solutions are not an unreasonable approximation of the actual flows. The gas flow is solved using properties corresponding to the average gas temperature and composition in the furnace. A scaling criterion, called the Thwing-Newby criterion is used to account for the fact that the air entering the furnace is at a significantly lower temperature than the furnace gases. This has well-established validity in the flow-modeling field.

The value of isothermal flow modeling depends to a large extent on the degree of correspondence between the flow patterns (velocity field) for the isothermal solution and for the real hot flow case. This correspondence has not been studied in a systematic manner, but experience to date indicates that there are strong qualitative similarities between isothermal flow fields and the hot flow fields. This suggests that isothermal modeling is a valid way of examining the effects of changing air arrangements on flow patterns.

Differences between hot flows and isothermal flows come from volume flow sources and sinks. There are three sources/sinks for volume flow that result from black liquor combustion. These are:

- evaporation of water from the black liquor,

- gas mole changes resulting from black liquor combustion, and
- density changes associated with temperature gradients.

In many cases, these volume flow source sinks perturb, but do not dominate, the flow patterns. The flow pattern in the furnace itself tends to be determined primarily by air input conditions and furnace geometry. The momentum transfer between the liquor spray and the gas has only a minor effect on the gas flow pattern, because the total momentum in the liquor entering is small compared to the momentum of the air entering the furnace.

One area where isothermal and "hot" flows may differ considerably is the flow in the superheater, where the gas density changes associated with temperature changes from heat absorption can induce recirculating flows. This is beyond the scope of furnace models.

If isothermal flow modeling is to be used to look at the effects of changing air arrangements in recovery boilers, there needs to be some criteria for evaluating the flow patterns produced. Typically, the criteria include the uniformity of the upward gas velocity at planes in the upper furnace and minimization of gas channelling in the furnace, the so-called "chimney effect". They may also consider mixing of the gases and turbulent intensity. There has not yet been an effort to use integrated hot models or other modeling approaches to see if these are valid criteria.

Fixed-Field Approach

In the integrated models, the black liquor combustion and the gas fields interact with one another in an iterative manner. The gas fields through which the liquor drops are moving affect the rates of burning and the trajectories followed, while the burning black liquor provides source/sink terms to the gas field equations. These interactions can be looked at non-iteratively to give simpler methods for looking at the behavior.

One type of simpler model is the "fixed-field" approach developed by IPST. [19] In this approach, the gas flow field is determined by an isothermal flow solution for the particular air flow conditions and boiler geometry, and the gas temperature and gas concentration fields are arbitrarily supplied. Then the behavior of liquor sprays can be determined with a fair degree of detail in a non-iterative manner. This greatly shortens the computational effort. This approach has been implemented into a code called IN-FLITE, which has proved to be useful in looking at the effects of black liquor spray variables.[20] The validity of the approach is strongly dependent on the degree that isothermal flow fields approximate hot flow fields, as well as the degree that details of the temperature and gas concentration fields influence black liquor combustion. This remains to be determined.

The IPST model uses the FLUENT code to carry out the isothermal flow solution and also as a platform to set up the grid geometry and information links to hold the gas field

information. The liquor behavior is then modeled in a Lagrangian format with computed trajectories and mass and size changes calculated as the drops burn in the furnace. Drops continue on their trajectories until they reach the bed, strike a wall, or get carried up out of the furnace.

This same approach could take the gas flow, temperature and gas concentration fields computed from a hot flow solution as a starting point. All that would be necessary would be to map the computed field solution onto the FLUENT grid. Then the effects of changing liquor spray variables could be examined. This could be a much more effective way of systematically studying liquor spray variables, provided that the gas fields remain representative of what a full solution would produce. This can be checked by computing the gas volume flow source/sink terms produced by each of the solution sets with changing liquor parameters, and running an occasional full solution to ensure that the temperature and gas concentration fields are not changed to greatly (or to demonstrate that liquor behavior is not strongly sensitive to the details of these fields.

The fixed-field approach as represented by the IN-FLITE model is probably most effectively used to look at carryover of partially burned liquor or smelt drops up out of the furnace. Where carryover is a significant contributor to a boiler plugging problem, this model can be used to determine how changing spray conditions might alleviate the problem. It would also be useful in examining the extent the gas channelling is important in carryover problems and to determine if channelling effects can be compensated for by adjusting liquor sprays. The IN-FLITE model is much less useful in dealing with boilers that have a plugging problem that is caused by fume deposits.

GENERIC MODELING

Up to now, most of the effort has gone into model development and most of the recovery boiler simulations that have been carried out by boiler manufacturers and others, including UBC and IPST, has been directed at specific boilers and operating conditions. The intent of these has been to look at a limited number of variables to try to improve the performance of a unit or to verify that a particular design is reasonable. The effort has not yet provided a lot of general insight into how recovery boilers perform.

One of the long-range goals of recovery boiler modeling efforts is to provide guidelines for optimum liquor spray arrangements and air entry conditions on recovery boilers. This might most appropriately be done through a series of simulations on a generic recovery boiler chosen for computational efficiency and ease of systematic altering of key parameters. It will be difficult to come up with general conclusions from isolated case studies of individual boilers done on a piecemeal basis.

Recovery boilers could be modeled generically and simulations done to determine the effects of classes of variables. The modeled boilers may not correspond to any particular real boiler. Such studies would go well beyond simple input-output comparisons or

determination of cause and effect relationships, although that would be part of what would be produced. The models would simply be used as a tool for generating a lot of information that would be analyzed in depth to obtain insights on why particular effects are obtained.

Some issues that could be addressed through generic modeling are:

- A thorough evaluation of air entry arrangements (location and size of air ports, injection velocity, etc.) and development of specific guidelines or criteria for air entry,
- Specification of liquor spray requirements. Definition of how these are tied into the load on the unit and the air supply arrangement,
- An evaluation of boiler geometry [cross-sectional area, length/width ratio, aspect ratio (height/cross-section$^{1/2}$), shape of bullnose, etc.] and development of specific guidelines,
- definition of optimum firing strategies,
- evaluation of the effects of liquor solids on furnace performance,
- insight into the effect of bed shape on gas flow patterns, and
- evaluation of the effect of and the need for air heating as a function of firing strategy.

TECHNOLOGY TRANSFER

This particular DOE supported program plays a three-fold role in advancing the capability of CFD-based recovery furnace models for improving recovery boiler design and operation.

1. It is developing a validated CFD-based recovery furnace model specifically tailored to deal with the particular geometries and flow effects characteristic of recovery boilers and incorporating the most reliable information of the relevant burning behavior of black liquor in a recovery boiler environment.

2. It is obtaining substantial fundamental information on the combustion of black liquor and on processes relevant to air emissions and aerosol formation, deposition, and removal in recovery boilers and making that information available not only for incorporation into the codes being specifically developed as part of the project but also to other developers of recovery furnace models.

3. It is advancing the confidence in using recovery furnace models by validating simulation predictions against actual data and disseminating the results.

For the industry to gain benefit from this work, they need to be able to have simulations of recovery boilers carried out with the codes developed as part of this project or to use other codes that have been enhanced because of the information and submodels developed and supplied from this effort. The industry can also benefit from the general knowledge about recovery boilers that has been obtained as a result of this project.

TECHNOLOGY TRANSFER PLAN

UBC has formed a "spin-off" company, Process Simulations Ltd. (PSL) and has licensed the UBC code to PSL for industrial application. A complete section (Section 6) of UBC's summary report (Appendix 1) is devoted to technology transfer and their technology transfer plan.

IPST has developed and used some simplified codes for looking at certain aspects of recovery boiler performance. These have been applied to several recover boilers in the state of Georgia [11] and have also been used to gain insight into some of the processes occurring in recovery boilers. However, past staff turnover problems have caused the IPST effort to be somewhat fragmented. The direction followed by IPST in this area in the future will depend on restaffing of the recovery group which is currently underway

It is clear that the benefits of improved recovery boiler models will only be fully realized if the models, submodels, approaches, etc. get into the hands of those who have a stake in

improving recovery boilers and know enough about them to use the models effectively. In general, these are the boiler manufacturers and companies operating kraft mills.

In order to move the information and codes developed on this project closer to the ultimate users, the following specific technology transfer tasks were built into the remainder of this project when it was restructured.

1. Transfer UBC codes to IPST to facilitate application of models to US recovery boilers.

2. Documentation of black liquor models and submodels in algebraic form including clear definitions of all parameters, assumptions and supporting validation data.

3. Documentation and transfer of codes that can be used in conjunction with available CFD codes or which can be directly utilized by the stakeholder.

4. Prepare a monograph on boiler plugging and fouling.

PUBLICATIONS

Much of the transfer of information developed through this project has been made available to industry through technical publications. Both UBC and OSU have included complete lists of their publications relevant to this effort in their summary reports which are included as Appendices 1 and 2. There is no need to repeat those lists here. The relevant IPST publications are listed below.

IPST Publications

Martin, D.M. and Malcolm, E.W., "The Impact of Black Liquor Composition on the Release of Nitrogen in the Kraft Recovery Furnace" Proceedings of the 1995 Tappi Engineering Conference, pp833-840, Sept. 1995

Grace, T.M., "A Critical Review of Computer Modeling for Kraft Recovery Boilers" Proceedings of the 1995 Tappi Engineering Conference, pp897-906, Sept. 1995

Lien, S.J. and Horton, R.R., "A Review of Recovery Boiler Model Applications", Preprints for 1995 International Chemical Recovery Conference, April 24-27, 1995, pA133

Thompson, L.M., Martin, D.M., Empie, H.J., Walcolm, E.W., and Wood, M., "The Fate of Nitrogen in a Kraft Recovery Furnace", Preprints for 1995 International Chemical Recovery Conference, April 24-27, 1995, pB225

Martin, D.M., Malcolm, E.W., and Hupa, M., "The Effect of Fuel Composition on Nitrogen Release During Black Liquor Pyrolysis" Presented at the Fall Technical Meeting of the Eastern States Section: The Combustion Institute, December 5-7, 1994, Clearwater FL

Empie, H.J., Lien, S., and Samuels, D.B., "Distribution of Mass Flows in Black Liquor Sprays" Presented at the AIChE Annual Meeting, November 15, 1994, San Francisco, CA

Verrill, C.L., Grace, T.M., and Nichols, K.M., "The Significance of Sodium Release During Devolatilization on Fume Formation in Kraft Recovery Furnaces", JPPS 20, 12:J354-J360, December 1994

Horton, R.R., Grace, T.M., and Adams, T.N., "The Effects of Black Liquor Spray Parameters om Combustion Behavior in Recovery Furnace Simulations" Proceedings of 1992 International Chemical Recovery Conference, pp 85-99, June 1992

Adams, T.N., and Horton, R.R., "The Effects of Black Liquor Sprays on Gas Phase Flows in a Recovery Boiler" Proceedings of 1992 Tappi Engineering Conference, pp81-101

Yang, W., Horton, R. R., and Adams, T. N., "Predictions of the Gas Flow Pattern and Mass Transfer to a Char Bed in a Recovery Boiler Lower Furnace Using Computational Fluid Dynamics", Proceedings of 1994 TAPPI Engineering Conference, pp799-808, Sept., 1994.

Grace, T. M., Wåg, K., Horton, R. R., and Frederick, W. J., "Sulfate Reduction and Carbon Removal During Kraft Char Burning", presented at Industrial Energy Conference, Houston, Apr., 1994

Horton, R.R., Slayton, D.J., Grace, T.M., and Adams, T.N.,"In-Flight Black Liquor Combustion Simulations Using a Three-Dimensional Computer Model: Sensitivity Studies", 1992 AIChE Forest Products Symposium Series, pp 27-48, (1993)

Yang, W., Horton, R. R., and Adams, T. N., "Effects of Boundary Geometries on CFD Simulations of Recovery Furnace Char Beds", TAPPI Journal 77,8:189, August 1994.

R. R. Horton and E. K. Vakkilainen, "Comparison of Simulation Results and Field Measurements of an Operating Recovery Boiler", TAPPI Engineering Conf. Proceedings, pp. 635-642, Orlando, Sept., 1993.

R.R. Horton, Slayton, D.J., Grace, T.M., and Adams, T.N.,"Sensitivity Studies of In-Flight Black Liquor Combustion Using a Three-Dimensional Computer Model", presented at Annual AIChE Conference., Miami, Nov. 1992.

E. K. Vakkilainen, T. N. Adams, and R. R. Horton, "The Effect of Recovery Furnace Bullnose Designs on Upper Furnace Flow and Temperature Profiles", 1992 International Recovery Conference Proceedings, pp.101-112 , June, 1992.

Grace, T. M., S. J. Lien and C. A. Brown, "Char Bed Burning - Laboratory Studies", International Chemical Recovery Conf. Proceedings, pp. 539-550, Seattle, June, 1992.

FUTURE NEEDS AND DIRECTIONS

Recovery boiler model development and application of these models will be an ongoing activity in the future as more information on black liquor processes are developed. This section will consider what remains to be done on this particular project and some directions for further developments.

CONTINUED WORK ON MODELING PROGRAM

Early in 1995, a critical review of recovery boiler modeling was carried out. This review is summarized in an earlier chapter in this report. As a result of this review and other factors, the project was restructured so as to bring it to closure in a manner that would maximize the value of the entire project to the pulp and paper industry. The restructured project was initiated at the end of October 1995 and is scheduled to be completed in January 1997.

The overall objective of the restructured project is to bring closure to this particular recovery boiler modeling project in an effective manner that maximizes the usefulness of the total effort to the kraft pulp industry. The specific objectives of the remaining work are as follows.

1. Complete the development of enhanced furnace models that have the capability to accurately predict carryover, emissions behaviour, dust concentrations, gas temperatures, and wall heat fluxes.

2. Establish the validity of these enhanced furnace models so that users will have confidence in the predicted results.

3. Obtain fundamental information on aerosol formation, deposition, and hardening so as to develop the knowledge base needed to relate furnace model outputs to plugging and fouling in the convective sections of the boiler.

4. Facilitate the transfer of codes, black liquor submodels, and fundamental knowledge to the US kraft pulp industry.

Statement of Work

The work will be carried out by the five organizations listed below. Major responsibilities are also indicated.

Institute of Paper Science & Technology (IPST) - leadership, bed modeling, validation.
University of British Columbia (UBC) - CFD code development, flow validation.
Oregon State University (OSU) - fundamental black liquor data, rate equations.
Babcock & Wilcox (B&W) - radiation heat transfer.
Tran Industrial Research (TIR) - fouling and plugging.

The Institute of Paper Scxience & Technology will have overall responsibility for the work. A more detailed description of the work to be performed is given below.

A: Development of Enhanced Furnace Models.

1. Modify CFD codes for recovery furnace processes to provide improved convergence, deal effectively with rotational flows, and provide for a better handling radiative heat transfer. Complete the development of a hot flow code fully incorporating black liquor combustion including char bed models and capable of prediction air emissions and aerosol formation. Specific tasks include:
   a. Implementation of convergence acceleration in smoothers for the Navier-Stokes equations,
   b. Investigation of rotational flows,
   c. Implementation of variable gas properties (based on composition, temperature and fume) on the radiation heat transfer and prediction of the wall radiant heat flux,
   d. Implementation of simplified heat/mass transfer from the char bed into the gas flow,
   e. Implementation of the enhanced chemistry and char bed models developed in program,
   f. Modeling of pressure drop and heat transfer in the convective sections to determine the extent that these affect flow and temperature fields in the furnace proper.

2. Provide an enhanced black liquor drop burning model. Specific tasks include:
   a. Complete the acquisition of fundamental data on release of sodium, potassium, sulfur, and chloride during black liquor burning and provide appropriate rate models for these processes,
   b. Develop the capability to model SO_2 formation and recapture, NO_x formation and destruction, and TRS concentrations,
   c. Develop an advanced model for black liquor drop combustion based on improved numerical methods for drop heat transfer. Use this advanced model to interpret laboratory data for application in global models.

3. Develop an improved char bed model. Specific tasks include:
   a. Incorporate proper surface and subsurface chemistry and proper handling of rate processes,
   b. Incorporate physical transport of char along the bed surface by air drag and reentrainment of char particles off the bed,
   c. Allow inventory imbalances and develop a methodology for using inventory imbalances to determine bed geometry,
   d. Develop a criteria for smelt release,
   e. Devise quantitative criteria for bed stability.

4. Obtain a consensus on the proper method for treating liquor which strikes the wall and for assigning appropriate wall thermal and chemical boundary conditions.

5. Provide a more accurate treatment of radiative heat transfer in recovery boilers. Specific tasks include:
   a. Complete the acquisition of data on critical properties that affect radiative heat transfer during black liquor drop combustion and develop methodologies for accurate treatment of burning black liquor drops and deposits of char, molten smelt, and saltcake,
   b. Measure the complex index of refraction of alkali salt mixtures over the infrared spectrum,
   c. Calculate radiative and scattering properties for submicron aerosols.

6. Provide the basis for incorporating aerosol formation into recovery boiler models. Specific tasks include:
   a. Develop the conceptual basis and provide experimentally validated rate equations for aerosol formation in recovery boilers that can predict the amount, size distribution and composition of aerosols,
   b. Develop codes and algorithms for incorporating aerosol formation into black liquor burning models.

<u>B: Establish Validity of Furnace Models.</u>

1. Develop a consensus comprehensive plan for model validation.

2. Validate key black liquor submodels through experimental measurements in laboratory, pilot equipment, and possibly actual recovery boilers.
   a. black liquor drop burning models,
   b. char bed models.

3. Validate flow predictions in recovery boiler geometries
   a. Summarize available comparisons between CFD flow predictions and measured flows in water models of recovery boilers and cold air flow tests in full-scale boilers,
   b. Establish the reliability of various CFD platforms for recovery boiler models through a benchmarking exercise for one or more isothermal flow cases. UBC would provide one set of boundary conditions and isothermal flow field measurements to the project for benchmarking and validation.

4. Validate key model predictions for the full hot flow model with black liquor combustion based on measurements on one or more recovery boilers.
   a. Measurements of critical output parameters on at least one recovery boiler as a function of different boiler operating conditions,
   b. Simulation of up to three cases of hot flow in recovery boilers for use in comparison with data collected in actual boilers,
   c. Simplified simulations to test cause and effect predictions against actual measurements.

C: Knowledge Base For Dealing With Fouling and Plugging:

1. Obtain fundamental data on fume deposition on heat transfer surfaces and on deposit hardening and removal.

2. Develop and integrate knowledge of aerosol deposition, deposit hardening, and deposit removal, to allow quantitative linkages between furnace model outputs and fouling/plugging rates and assess the current status of knowledge of fouling and plugging in convective sections.

D: Technology Transfer

1. Transfer UBC codes to IPST to facilitate application of models to US recovery boilers.

2. Documentation of black liquor models and submodels in algebraic form including clear definitions of all parameters, assumptions and supporting validation data.

3. Documentation and transfer of codes that can be used in conjunction with available CFD codes or which can be directly utilized by the stakeholder.

4. Prepare a monograph on boiler plugging and fouling.

Enhancement of Technology Transfer

The basic guideline with respect to the goal of maximizing the usefulness of the entire modeling program to the industry was to get the technical information and modeling capability into the hands of the stakeholders to as great an extent as possible. It was recognized that much of the continuing development of recovery boiler models themselves will be through boiler manufacturers. It was also recognized that they would not have the resources to do extensive research on black liquor combustion behavior. Finally, an attempt was made to package information in a way that it would be directly useful to paper companies with pulp mills operating recovery boilers.

The following specific deliverables from the remainder of the project are aimed at achieving this enhanced technology transfer.

A looseleaf notebook documenting black liquor drop burning models and other black liquor submodels in algebraic form will be produced. These models will be time-stamped and will include a clear definition of all parameters, assumptions and supporting data. This was requested by a boiler manufacturer and will be directly useful for upgrading existing models.

A variable density code with radiation and black liquor combustion models will be available at UBC and at IPST for running recovery boiler simulations. The code can also be licensed by UBC to prospective users.

A collection of water model experimental data and computational output from an isothermal model will be available for validation and benchmarking.

A compilation of experimental data on furnace output variables as a function of operating conditions and a full set of information needed to set up a simulation will be available from at least one recovery boiler for use in model validation.

A technical monograph on boiler plugging and fouling will be produced.

A comprehensive final report on the project.

FURTHER DEVELOPMENTS

There are several additional areas for enhancing the capability and application of recovery boiler models and for using models to increase the understanding of what happens in recovery boilers that are not encompassed by the work remaining on this project.

Much more work is needed to fully understand boiler fouling and plugging and eventually realize the full capabilities inherent in existing equipment. It is hoped that the

monograph on fouling that is produced in the remainder of this project serves not only to encapsulate existing knowledge on these important topics, but also to provide a roadmap to what remains to be done.

It would be useful to run sensitivity tests with the various recovery boiler models. These should include not only empirical model parameters to identify areas where better models are needed, but also model set up values (e.g. mean drop diameter in the liquor sprays) to determine which ones are most important to define accurately. It is particularly important to find out if critical model predictions are sensitive to arbitrary parameters or poorly defined variables.

Benchmarking of the various recovery boiler models against one another would be very useful. It would be valuable to try to arrange a round-robin series of modeling/simulation case studies among the various modelers and compare results. If there is general agreement in predictions among the different users it would greatly enhance model credibility.

The possibility of using the fixed-field approach in which the gas fields from one integrated hot flow simulation are used as the basis for developing cause and effect relationships for a wide-range of liquor spray variables should be explored.

Assess the value of isothermal flow modeling by studying the degree of correspondence between the flow patterns (velocity field) for isothermal solutions and for the real hot flow case in a systematic manner.

Recovery boilers could be modeled generically and simulations done in a systematic way to obtain insights on the behavior inside the furnace and to address at least some of the following issues.

- A thorough evaluation of air entry arrangements (location and size of air ports, injection velocity, etc.) and development of specific guidelines or criteria for air entry,
- Specification of liquor spray requirements. Definition of how these are tied into the load on the unit and the air supply arrangement,
- An evaluation of boiler geometry [cross-sectional area, length/width ratio, aspect ratio (height/cross-section$^{1/2}$), shape of bullnose, etc.] and development of specific guidelines,
- definition of optimum firing strategies,
- evaluation of the effects of liquor solids on furnace performance,
- insight into the effect of bed shape on gas flow patterns, and
- evaluation of the effect of and the need for air heating as a function of firing strategy.

REFERENCES

1. Grace, T.M., Lien, S.J., and Brown, C.A., "Char Bed Burning - Laboratory Studies", Proceedings of 1992 International Chemical Recovery Conference, pp. 539-550.

2. Magnussen, B.F., and Hjertager, B.H., "On Mathematical Modeling of Turbulent Combustion", 16th Symposium (Int.) on Combustion, The Combustion Institute, Pittsburg 719-729 (1976).

3. Karidio, I., Markovic, C., Uloth, V., Thorn, P., Abdullah, Z., Salcudean, M., Gartshore, I., and Zhang, K., "Cold Flow Velocity Measurements and Computations for CFD Validation. Part I: Interaction of Primary and Secondary Air Flows", Proceedings of 1995 TAPPI Engineering Conference, pp. 853-874.

4. Frederick, W.J., Iisa, K., Wåg, K., Reis, V., Boonsongsup, L., Forssen, M., and Hupa, M., "Sodium and Sulfur Release and Recapture During Black Liquor Burning", DOE/CE/40936-T2 (DE96006558) August 1995.

5. Walsh, A.R., and Grace, T.M., "TRAC: A Computer Model to Analyze the Trajectory and Combustion Behavior of Black Liquor Droplets", JPPS 15(3):J84-J89 (May 1989).

6. Wåg, K., Frederick, W.J., Sricharoenchaikul, V., Grace, T., and Kymäläinen, M., "Sulfate Reduction and Carbon Removal During Kraft Char Burning", Proceedings of 1995 International Chemical Recovery Conference, Book B, pp. B35-B50.

7. Siiskonen, P., Sutinen, J., Hyöty, P., and Karvinen, R., "A Numerical Study of Char Bed Burning Rates", Proceedings of 1993 TAPPI Engineering Conference, pp. 287-292.

8. Verrill, C., and Wessel, R., "Sodium Loss During Black Liquor Liquor Drying and Devolatilization - Application of Modeling Results to Understanding Laboratory Data", Proceedings of 1995 International Chemical Recovery Conference, Technical Section CPPA, Montreal, p. B89, (1995).

9. Cameron, J.H., "Vaporization from Alkali Carbonate Melts with Reference to the Kraft Recovery Furnace", JPPS 14(4):J76-J81 (1988).

10. Grace, T.M., A Critical Review of Computer Modeling of Kraft Recovery Boilers", Proceedings of 1995 TAPPI Engineering Conference, pp. 897-906.

11. Lien, S., and Horton, R., "A Review of Recovery Boiler Model Applications", Proceedings of 1995 International Chemical Recovery Conference, Technical Section CPPA, Montreal, p. A133, (1995).

12. Nowak, P., Matys, P., Sabhapathy, P., Abdullah, Z., and Salcudean, M., "Numerical Study of a Kraft Recovery Furnace", Proceedings of 1995 International Chemical Recovery Conference, Technical Section CPPA, Montreal, p. A149, (1995).

13. Chapman, P., and Jones, A., "Recovery Furnace Combustion Modeling Using Computational Fluid Dynamics", Proceedings of 1992 International Chemical Recovery Conference TAPPI, Atlanta, p. 71, (1992).

14. Blasiak, W., Miznov, V., and Collin, R., "Stochastic Modeling of Particulate Phase Dispersion in Two-Phase Flow" (Part 1 and 2), KTH, Värme- och Ugnsteknik, December 1991.

15. Wessel, R., Parker, K., and Verrill, C., *Paper to be presented at 1995 TAPPI Engineering Conference* "Three-Dimensional Kraft Recovery Furnace Model: Implementation and Results of Improved Black Liquor Combustion Model", TAPPI, Atlanta (1995).

16. "Procedure and Criteria for Assessing CFD Codes", NASA Tech Briefs MFS-29972.

17. Raymond, D.R., and Rauscher, J.W., "Heat Transfer Determination in Boiler Waterwall Tubes Using Fin Temperature Measurements", Tappi J. 67(7):76-79 (July 1984).

18. Mikkanen, P., Kauppinen, E., Jokiniemi, J., Sinquefield, S., and Frederick, W.J., "Bimodal Fume Particle Size Distributions from Recovery Boiler and Laboratory Scale Black Liquor Combustion", Tappi J. 77(12): (1994).

19. Horton, R.R., Slayton, D.J., Grace, T.M., and Adams, T.N.,"In-Flight Black Liquor Combustion Simulations Using a Three-Dimensional Computer Model: Sensitivity Studies", 1992 AIChE Forest Products Symposium Series, pp. 27-48, 1993.

20. Horton, R., Grace, T. and Adams, T., "The Effects of Black Liquor Spray Parameters on Combustion Behavior in Recovery Boiler Simulations", Proceedings of the 1992 International Chemical Recovery Conference, TAPPI, pp. 85-98 (June 1992).

APPENDIX I

BLACK LIQUOR COMBUSTION VALIDATED RECOVERY BOILER MODELING

1990 - 1994 Contract Report

Prepared by

Dr. Zia Abdullah
Dr. Paul Nowak
Dr. Jeff Quick
Paul Matys
Kegang Zhang
Dr. Martha Salcudean
Dr. Peri Sabhapathy
Peter Ajersch
Michael Savage
Dr. Ian Gartshore
Dr. Daniel Tse
Steve Ketler
Zhu Zhi Xiao

University of British Columbia

February 1995

Table of Contents

List of Figures

Section 1

Section 2

Section 3

Section 4

Section 5

SECTION 1: THEORETICAL FORMULATION OF THE UBC R.B.M.

Introduction

The programs 'geo' and 'mgfd' represent a stage in the development of a general purpose numerical algorithm for the calculation of flows in three dimensional recovery boiler geometries. For steady-state flows in the Cartesian coordinate formulation, their applicability is as wide as that of some previous codes such as TEACH ([Gosman and Ideriah 1976]), or the related codes TEMA ([Lai and Salcudean 1985]) and TURCOM ([Lai 1987]), but with much improved flexibility and robustness. In addition to recovery boiler flows, these codes can also be applied to other three-dimensional turbulent compressible flows with heat transfer and combustion.

As in many standard programs, the rectangular grids are used for discretization. In recovery boiler applications, the air ports at different elevations generally do not line up along the vertical direction, and the grids must be fine in the areas of strong variation of the flow field parameters. To avoid unnecessary grid refinement and to model the air ports at their correct locations, the programs 'geo'-'mgfd' allow the non-matching grids to co-exist in the adjacent parts of the flow field.

The convergence of the pressure correction method ([Patankar and Spalding 1972]) and of other iterative methods is usually rapid for calculation on a single grid at the beginning of the procedure, and deteriorates when the residues become smooth. As a remedy, a symmetrically coupled Gauss Seidel method is used with a nonlinear multigrid algorithm in the program'mgfd'. With these methods, a rapid convergence is achieved by "restricting" the smooth residues to coarser grids where they can be reduce more efficiently, and then "prolongating" the coarse grid corrections of the solution to the finer grids. Our nonlinear multigrid method was first presented by [Nowak 1984]. As a departure from the classical FAS method of [Brandt 1976, 1977]), the repetitive restriction of the solution is avoided, as well as the calculation of the residue after restriction. Instead of these restrictions, we use the converged coarse grid solutions, obtained during the preliminary phase of the solution refinement. The present method is simpler than the classical one, and at least equally effective for most applications.

Conservation equations

The governing steady-state conservation equations include the three momentum equations and continuity equation of the fluid dynamics:

$$\mathrm{div}\left(\rho u \bar{V}\right) = \mathrm{div}\left(\mu \mathrm{grad}\, u\right) - \partial p/\partial x + B_x + V_x \qquad (1)$$

$$\mathrm{div}\left(\rho v \bar{V}\right) = \mathrm{div}\left(\mu \mathrm{grad}\, v\right) - \partial p/\partial y + B_y + V_y \qquad (2)$$

$$\mathrm{div}\left(\rho w \bar{V}\right) = \mathrm{div}\left(\mu \mathrm{grad}\, w\right) - \partial p/\partial z + B_z + V_z \qquad (3)$$

$$\mathrm{div}\left(\rho \bar{V}\right) = 0 \qquad (4)$$

where $\bar{V} = (u,v,w)$ is the velocity, ρ is the density, μ is the viscosity, p is the pressure,

(B_x, B_y, B_z) is the body force per unit volume, and V_x, V_y, and V_z are the additional viscous transport terms due to turbulence.

The system may include a number of conservation equations of the form

$$\mathrm{div}(\rho\phi\overline{V}) = \mathrm{div}(x_\phi \ \mathrm{grad}\ \phi) + S_\phi \tag{5}$$

where ϕ represents a scalar quantity, x_ϕ is the diffusion coefficient, and S_ϕ is the source term. Such equations govern the turbulence energy k and its dissipation rate ε. The $k-\varepsilon$ system has the form ([Launder & Spalding 1974], Rodi 1984]):

$$\mathrm{div}(\rho k\overline{V}) = \mathrm{div}\left(\frac{\mu}{\sigma_k}\ \mathrm{grad}\ k\right) + G - \rho\varepsilon \tag{6}$$

$$\mathrm{div}(\rho\varepsilon\overline{V}) = \mathrm{div}\left(\frac{\mu}{\sigma_\varepsilon}\ \mathrm{grad}\ \varepsilon\right) + C_1\, G\varepsilon/k - C_2\ \rho\varepsilon^2/k + C_3\ \rho\varepsilon\mathrm{div}(\overline{V}) \tag{7}$$

where μ is the turbulent viscosity, defined as

$$\mu = c_\mu \rho k^2/\varepsilon \tag{8}$$

and often corrected by adding the laminar viscosity μ_i; σ_k, σ_ε, C_1, C_2, C_3 and c_μ are constants; G is the turbulent energy production rate, given by:

$$G = \mu\left\{2\left[(\partial u/\partial x)^2 + (\partial v/\partial y)^2 + (\partial w/\partial z)^2\right] + (\partial u/\partial y + \partial v/\partial x)^2 + (\partial w/\partial x + \partial u/\partial z)^2 + (\partial v/\partial z + \partial w/\partial y)^2\right\} - \tfrac{2}{3}\left(\mu\mathrm{div}(\overline{V}) + \rho k\right)\mathrm{div}(\overline{V}) \tag{9}$$

The usual values of the constants are

$c_\mu = 0.09$, $C_1 = 1.44$, $C_2 = 1.92$, $C_3 = 1.0$, $\sigma_k = 1.0$

and

$$\sigma_\varepsilon = \kappa^2/\left[(C_2 - C_1)c_\mu^{1/2}\right] \tag{10}$$

where $\kappa = 0.42$ is the Von Karman constant.

For turbulent flows, the pressure p in the momentum equations is understood as the "effective" pressure:

$$p = p' + \frac{2}{3}\left(\rho k + \mu\mathrm{div}\,(\overline{V})\right)$$

where p' is the sum of normal stresses, which is approximately the thermodynamic pressure for incompressible fluids. The additional viscous terms in the momentum equations are defined as

$$\begin{aligned} V_x &= \mathrm{div}(\mu\,\partial\overline{V}/\partial x) \\ V_y &= \mathrm{div}(\mu\,\partial\overline{V}/\partial y) \\ V_z &= \mathrm{div}(\mu\,\partial\overline{V}/\partial z) \end{aligned} \tag{11}$$

The energy equation for the steady-state low-velocity flow with negligible viscous dissipation has the form

$$\mathrm{div}(\rho T\overline{V}) = \mathrm{div}(x_T\ \mathrm{grad}\ T) + S_h/c \tag{12}$$

where T is the temperature, S_h is the volumetric rate of the heat generation, and c is the constant-pressure specific heat, assumed to be constant. If the flow is turbulent, then x_T is usually set equal or proportional to the viscosity. This practice is based on the experimental observation that the turbulent Prandtl number depends weakly on the flow condition. This number is about 0.9 in the near-wall flows, 0.5 in plane jets and 0.7 in round jets ([Rodi 1984, p. 19]).

The mass fraction M of a chemical species (the ratio of the mass of the species to the total mass of the mixture in a given volume) is governed by the conservation equation of the form (5), with S_M equal to the rate of generation of the species per unit volume. The density of a mixture is

$$\rho = \left(M_1/\rho_1 + M_2/\rho_2 + \cdots + M_n/\rho_n\right)^{-1}$$

where $M_1, M_2, \ldots, M_n$ are the mass fractions of the component species, and $\rho_1, \rho_2, \ldots, \rho_n$ are their densities.

Boundary conditions

The programs 'geo'-'mgfd' allow the division of the flow field boundary into rectangular "patches", and impose a variety of boundary conditions for the velocity components, the pressure, and other scalars on each patch. The types of the boundary conditions are specified in the input file 'geo.in' for the program 'geo'. The following types are available:

'v' condition ("value" or Dirichlet type):

When used for the velocity, this condition allows for prescribing the distributions of the components tangential to the boundary, and the distribution of the normal component or the mass flux on a patch. If the mass flux $f_n = \rho v_n$ is given, then $v_n = f_n/\rho$ is enforced. When used for scalars, the 'v' condition allows the distribution of value to be imposed.

'p' or pressure condition:

Allows for prescribing the pressure distribution on a patch.

'f' or "flux" condition:

When applied to the velocity, the 'f' condition allows for the imposition of the mass flux and the three momentum fluxes on a patch (the momentum flux in the x-direction is $j_u = f_n u$). For a scalar ϕ this condition allows for the imposition of the flux $j_\phi = f_n \phi$. The values of all the fluxes can be specified directly, or indirectly by providing the values of the velocity components or the scalars. In the latter case, the fluxes are calculated by 'geo' and enforced by 'mgfd'.

'w' or "wall" condition:

Is applied at the walls in turbulent flows. It imposes the tangential stresses and the values of k and ε, according to the theory of the Couette flows [Launder & Spalding, 1974].

The wall velocity in the tangential direction can be prescribed. The given mass flux is enforced exactly. The tangential wall velocity serves to determine the wall stress, which is enforced exactly.

's' or "symmetry" condition:

When applied for the velocity, it sets the normal component $v_n = 0$, and
$\partial v_s/\partial n = 0, \quad \partial v_t/\partial n = 0$
where v_s and v_t are the tangential components. For scalars it sets $\partial\phi/\partial n = 0$.

'g' or "gradient" condition:

For the velocity, it sets $\partial f_n/\partial n = 0$ as the 's' condition above. For scalars, it imposes Neumann condition $\partial\phi/\partial n = g$, where g is given on a patch. If $g=0$, then this is the same as the 's' condition.

'c' or "combined" condition:

This can be used for the scalars other than the pressure. It has the form
$j_\phi = \alpha\phi + \beta$ (13)
where j_ϕ is the scalar flux, and α, β are given on a patch. This condition is often imposed on free surfaces.

'i' and 'n' conditions:

These are imposed on the intersegmental boundaries and will be described in a separate section later in this chapter.

Discrete formulation

The flow region is divided into non-overlapping rectangular segments, covered with generally non-uniform staggered grids [Arakawa and Lamb 1977]. Figure 1 shows four sections of such a grid on a region composed of four segments. The staggered pattern of grid points is shown in Figure 2. The *u*, *v*, and *w*- velocity components are defined at the points denoted with O, ∇ , and • respectively. The pressure and other scalars are defined at the points denoted with *. The scalar points lie in the centers of the grid cells. Each segment may have its own grid, independent of the grids in the other segments. It is desirable, but not necessary, that the grids match at intersegmental boundaries.

Grid point values of *u*, *v*, *w*, *p* and other scalars are the solutions of the discrete system of the difference equations, obtained by integrating the original conservation equations over small volumes around the grid points. Two side views of a finite volume for the *u*-momentum equation are shown in Figure 3. For the *v*- and *w*-momentum equations, the volumes are defined similarly. The finite volumes for the continuity equation and the scalar equations coincide with the grid cells around the scalar points (Figure 4).

In order to avoid the numerical instability associated with the central difference approximation of the convection terms, the convection and diffusion terms are jointly approximated by the power law scheme ([Patankar 1980]). This scheme gradually replaces the central differences with the upwind differences when the cell Reynolds number is increased. As a consequence, the diagonal dominance of the discrete system matrix is preserved in each iteration of the solution procedure. This improve the stability and the convergence rate, and eliminates the unphysical "wiggles" from the converged solutions. The diagonal dominance is additionally increased by including the negative parts of the source terms into the diagonal terms.

Discretization of the scalar conservation equations

By integrating the scalar conservation equation (5) over the finite volume of Figure 4, we arrive at the following discrete equation (see [Patankar 1980, p. 98]):

$$(J_e - F_e\phi_p) - (J_w - F_w\phi_p) + (J_n - F_n\phi_p) - (J_s - F_s\phi_p) +$$
$$(J_t - F_t\phi_p) - (J_b - F_b\phi_p) = (S_c + S_p\phi)\Delta x\Delta y\Delta z \qquad (14)$$

where F_e, F_w,..., F_b are the mass flows (integrated fluxes) through the east, west, north, south, top and bottom sides of the volumes, and J_e, J_w, ..., J_b are the total (convection and diffusion) flows of ϕ through these sides; S_c, and S_p arise from the source term linearization of the form:

$$S_\phi = S_c + S_p\,\phi$$

with $S_p < 0$. Using the power law scheme, we obtain the following representation:

$$J_e, - F_e, \phi = a_e,(\phi_p - \phi_e)$$

where

$$a_e = D_e\, A(|Pe|) + \max(-F_e, 0) \qquad (15)$$
$$D_e = \Gamma\Delta y\Delta z/\Delta x_e$$
$$F_e = (pu)_e\Delta y\Delta z$$
$$P_e = F_e/D_e \quad \text{(Peclet number, or cell Reynolds number)}$$
$$A(|Pel|) = \max[0, (1 - 0.1|Pe|^5)]$$

and "max" denotes the larger of the two values which follow. Substituting the analogous expressions for the other terms in (14), we obtain the discrete equation of the form (see [Patankar 1980]):

$$a_p\phi_p = a_e\phi_p + a_w\phi_w + a_n\phi_n + a_s\phi_s + a_t\phi_t + a_b\phi_b + b \qquad (16)$$

where

$$a_p = a_e + a_w + a_n + a_s + a_t + a_b - S_p\,\Delta x\Delta y\Delta z \qquad (17)$$
$$b = S_c\Delta x\Delta y\Delta z$$

Discretization of the momentum equations

Laminar Flows

The discrete momentum equations additionally contain the components of the pressure forces acting on a finite volume (Figure 3). The u-momentum equation has the discrete counterpart:

$$a_p u_p = a_e u_e + a_w u_w + a_n u_n + a_s u_s + a_t u_t + a_b u_b + (p_w - p_e)\Delta y \Delta z + b \qquad (18)$$

where $a_p, \ldots, a_t$ are given by the formulas analogous to (15), p_w and p_e are the pressures on the west and east sides of the volume, and
$b = B_x \Delta x \Delta y \Delta z$

Turbulent Flows

We found that the additional viscous terms V_x, V_y and V_z, defined by (11) can cause numerical instability when discretized by the central difference scheme. For presentation of an alternative, let us consider the term:

$$V_x = \mathrm{div}(\mu \partial \bar{V}/\partial x) = \mathrm{div}\left(\partial(\mu \bar{V})/\partial x\right) - \mathrm{div}(\bar{V}\, \partial\mu/\partial x) = \partial\left(\mathrm{div}(\mu \bar{V})\right)/\partial x - \mathrm{div}(\bar{V}\partial\mu/\partial x)$$

Introducing the corrected "pressure":

$$\tilde{p} = p - \mathrm{div}(\mu \bar{V})$$

and a corrected "velocity" component:

$$\tilde{u} = u + \frac{1}{\rho}\frac{\partial u}{\partial x} \qquad (19)$$

we can rewrite the momentum equation (1) as:

$$\mathrm{div}\left(\rho \tilde{u} \bar{V}\right) = \mathrm{div}(\mu \,\mathrm{grad}\, \tilde{u}) - \partial\tilde{p}/\partial x + F_x - \mathrm{div}\left(\mu \,\mathrm{grad}\left(\frac{1}{\rho}\frac{\partial \mu}{\partial x}\right)\right) \qquad (20)$$

The last term on the right hand side can be neglected as a quadratic form of the small quantities, such as μ and its derivatives. Since (20) has the same form as the u-momentum equation for the laminar flows, its discrete form is:

$$a_p \tilde{u}_p = a_e \tilde{u}_e + a_w \tilde{u}_w + a_n \tilde{u}_n + a_s \tilde{u}_s + a_t \tilde{u}_t + a_b \tilde{u}_b + (\tilde{p}_w - \tilde{p}_e)\Delta y \Delta z + b \qquad (21)$$

The equation (19) is discretized with:

$$\tilde{u}_p = u_p + \frac{1}{\rho_p}\left(\frac{\Delta\mu}{\Delta x}\right)_p \qquad (22)$$

where $\left(\Delta\mu/\Delta x\right)_p$ is the central difference calculated at the u-point. Substituting (22) and the analogous formulas for $\tilde{u}_e, \tilde{u}_w, \cdots, \tilde{u}_b$ into (21), we obtain the discrete u-equation for the turbulent flows:

$$a_p u_p = a_e u_e + a_w u_w + a_n u_n + a_s u_s + a_t u_t + a_b u_b + (\tilde{p}_w - \tilde{p}_e)\Delta y \Delta z + b' \qquad (23)$$

where

$$b' = b + \frac{a_e}{\rho_e}\left(\frac{\Delta\mu}{\Delta x}\right)_e + \frac{a_w}{\rho_w}\left(\frac{\Delta\mu}{\Delta x}\right)_w + \frac{a_n}{\rho_n}\left(\frac{\Delta\mu}{\Delta x}\right)_n + \frac{a_s}{\rho_s}\left(\frac{\Delta\mu}{\Delta x}\right)_s + \frac{a_t}{\rho_t}\left(\frac{\Delta\mu}{\Delta x}\right)_t + \frac{a_b}{\rho_b}\left(\frac{\Delta\mu}{\Delta x}\right)_b - \frac{a_p}{\rho_p}\left(\frac{\Delta\mu}{\Delta x}\right)_p \qquad (24)$$

The difference between b and b' is small. Usually the schemes (18) and (23) have similar stability properties. An option is provided, which allows the correction of b, made in (24), to be neglected.

Discretization of the continuity equation

Integrating the continuity equation (4) over the finite volume of Figure 4, we obtain:

$$(\rho_e u_e - \rho_w u_w)\Delta y\Delta z + (\rho_n v_n - \rho_s v_s)\Delta x\Delta z + (\rho_t w_t - \rho_b w_b)\Delta x\Delta y = 0 \qquad (25)$$

Corrections of the discrete system for stability

Mass Imbalance Correction ([Gosman and Ideriah 1976])

It may happen, at an early stage of the calculation, that all the mass flows exit from a finite volume. If the outgoing velocities are sufficiently large, then the coefficients of (16) or (18) are equal to zero. The discrete equation becomes singular, and the solution procedure diverges immediately. To avoid such situations, the "false source" correction

$$c_f = \max\left(0,\ F_e - F_w + F_n - F_s + F_t - F_b\right)$$

is added to the diagonal coefficients a_p. Here, $F_e, F_w, \ldots, F_b$ are the mass flows through the sides of the finite volume. The free terms b are corrected accordingly, by adding $c_f\phi_p$ or $c_f u_p$. The corrected diagonal coefficient $a_p + c_f$ is always positive.

Correction for the Artificial Time Dependence ([Ramshaw and Mousseau 1990])

To improve the stability, the diagonal coefficients in (16) and (18) are increased by adding

$$c_t = \rho\,\Delta x\,\Delta y\,\Delta z\,/\Delta t$$

where $\Delta x\,\Delta y\,\Delta z$ is the volume of the control cell, and Δt is an artificial time step. The corresponding corrections $c_t\phi$ or $c_t u_p$ are added to the free term b. In this way, we included the time derivative terms $\rho\,\Delta\phi\ \Delta x\,\Delta y\,\Delta z/\Delta t$ and $\rho\,\Delta u\,\Delta x\,\Delta y\,\Delta z/\Delta t$ in the discrete equations ($\Delta\phi$ and Δu are the increments of ϕ and u during the time step). It must be mentioned, however, that for the *steady state formulation* reported here the accurate time dependence, which requires converged solutions at each time step, is not reproduced. Only one iteration of Vanka's method is made during each "time step". The correction is switched off by setting Δt equal to a large number. Time dependence is reproduced in the transient version of our code.

Damping Correction for the Mass Imbalance Rate of Change ([Ramshaw and Mousseau 1990])

Let δ denote the mass imbalance on the left hand side of the continuity equation (25). During the multigrid calculation, we are solving the equations:

$$\delta = r \qquad (26)$$

where r differs from 0 for the correction problems (Section IV). By adding the time derivative term, we obtain:

$$c_\delta \frac{\partial \delta}{\partial t} + \delta = r \qquad (27)$$

The solution of this equation has the form:

$$\delta = r + (\delta_0 - r)\exp(-t/c_\delta)$$

where δ_0 denotes the distribution of δ at $t = 0$. When t tends to the infinity, then the mass imbalance tends to the required limit (26), at the rate which depends on c_δ. A choice of $c_\delta > 0$ may stabilize the solution procedure. The discrete form of the equation (27) is:

$$\delta_{new} = \left(r + \frac{c_\delta}{\Delta t}\delta_{old} \right) \Big/ \left(1 + \frac{c_\delta}{\Delta t} \right)$$

which has the form (26), with a corrected right hand side.

Discretization of the internal boundary conditions

Let us consider the situation represented in Figure 5. For the completeness of the discrete system, discrete equations must be assigned to the *u*-points on the interface between segments. These equations depend on our choice of the internal boundary conditions.

Internal Boundary Conditions of the "Donor" Type 'i'

If the type 'i' is assigned to the interface of segment 1 in Figure 5, then the grid on this segment is extended to the right by including a layer of cells (Figure 6). If these cells have the same size Δx_2 as the boundary cells of segment 2, then *u*, *v*, *w*, *p* and the scalars at the added grid points can be determined by the interpolation between the values of these quantities at the grid points of segment 2, located in the same grid planes. The finite volume equation (18) or (23) can now be defined at the *u*-points on the interface of segment 1, since all the required "east" values of the flow field parameters are now available. Similar procedure is applied for the scalar quantities. The program 'mgfd' allows the size of the added cells to be different from Δx_2. However, the interpolations in the three space dimensions are then required, which may be less accurate.

Internal Boundary Conditions of the "Receiver" Type 'n'

If the grids of segments 1 and 2 do not coincide on the interface, then the interface of segment 2 must now be given the type 'n'. For this type, the *u*-values on the interface of segment 2 are determined by the mass preserving interpolation, using the *u*-values on the interface of segment 1. Let us consider the situation represented in Figure 7. The following discrete equation is defined at the *u*-point of segment 2:

$$a_0\rho_0 u_0 = a_1\rho_1 u_1 + a_2\rho_2 u_2 + a_3\rho_3 u_3 + a_4\rho_4 u_4 \qquad (28)$$

where ρ_1, ρ_2, ρ_3, ρ_4, u_1, u_2, u_3, and u_4, are the values of ρ and *u* at the nearest *u*-points of segment 1, labeled with 1, 2, 3 and 4 in Figure 7; the coefficients a_1, a_2, a_3, and a_4 are the overlap areas of the cell face, centered at 0, with the cell faces centered at 1, 2, 3 and 4 and $a_0 = a_1 + a_2 + a_3 + a_4$. The 'n' boundary condition (28) ensures the global mass conservation on the two segments. The 'n' condition is not used for the scalars.

Remarks

If the grids of the two segments coincide on the internal boundary, then the type 'i' can be assigned to both sides. If the types are not specified by the user, then the type 'i' is assigned by the program 'geo' to the interface of the segment with the lower label number (the segments have labels 1, 2, ...), and the type 'n' is assigned to the interface of its neighbor.

Discrete conditions on the flow field boundary

Boundary Conditions for the Normal Velocity Component

If the condition 'v', 's', 'w', or 'f' is imposed on the west boundary (Figure 8), then u_w is either prescribed in a data file ('v' condition), or set to 0 ('s' condition), or calculated as

$$u_w = F_w/(\rho_w \Delta y \Delta z) \tag{29}$$

where F_w is the given mass flow through the boundary ('w' and 'f' conditions).

For the 'f' condition, the momentum flux is additionally imposed. The discrete u-momentum equation, assigned to u_p, is written as:

$$a_e(u_p - u_e) - (J_{wp} - F_{wp}u_p) + a_n(u_p - u_n) + a_s(u_p - u_s) + a_t(u_p - u_t) + a_b(u_p - u_b) = (p_w - p_e)\Delta y \Delta z + b \tag{30}$$

where the contribution of the west side is expressed using the mass and momentum flows F_{wp} and J_{wp}. Since the west side of the finite volume of Figure 8 lies half-way between u_w and u_p, we put:

$$F_{wp} = (F_w + \rho_p u_p \Delta y \Delta z)/2$$

where F_w is the prescribed mass flow. Equation (30) can be written in the standard form (18) with the corrected coefficients

$$a'_p = a_e + F_{wp} + a_n + a_s + a_t + a_b \tag{31}$$
$$a'_w = 0$$
$$b' = b + J_{wp}$$

where J_{wp} is the prescribed momentum flow. In this way, we ensure that the required momentum flow enters the flow field. The required mass flow is enforced by (29). Let us note that the 'f' condition should not be used on the outflow boundaries, where the negative contribution of F_{wp} diminishes the diagonal coefficient (31).

For the 'g' condition we require that $\rho_w u_w = \rho_p u_p$

For the 'p' condition, the pressure p_w is prescribed at the p-point nearest to the boundary (Figure 8). As a consequence, the discrete continuity equation, normally assigned to p_w, must now be reassigned to u_w. This equation now plays the role of the boundary condition for u_w.

Boundary conditions for the tangential velocity components

For the 'v' condition on a south boundary (Figure 9), an extrapolated value u_s is defined outside the flow field:

$$u_s = u_{ps}\left(\Delta y_p + \Delta y_s\right)/\Delta y_p - u_p \Delta y_s / \Delta y_p$$

where u_{ps} is the prescribed value of u on the boundary. Substituting this into (18) we obtain a similar equation with the corrected coefficients:

$$a'_p = a_p + a_s \Delta y_s / \Delta y_p$$
$$a'_s = 0$$
$$b' = b + a_s u_{ps}\left(\Delta y_p + \Delta y_s\right)/\Delta y_p$$

The use of the 'v' condition increases the diagonal coefficient a'. For the 's', 'g' and 'p' conditions we set $u_p = u_s$, which gives rise to the corrections:

$$a'_p = a_p - a_s$$
$$a'_s = 0$$

For the 'f' and 'w' conditions we use the equation analogous to (30):

$$a_e(u_p - u_e) + a_w(u_p - u_w) + a_n(u_p - u_n) - (J_s - F_s u_p) +$$
$$a_t(u_p - u_t) + a_b(u_p - u_b) = (p_w - p_e)\Delta y \Delta z + b \qquad (32)$$

where F_s and J_s are the given mass and momentum flows. For the 'f' condition J_s is prescribed, and for the 'w' condition it is given by the formula:

$$J_s = \tau_x \Delta x \Delta z \qquad (33)$$

where τ_x is the x- component of the wall stress:

$$\tau_x = -\tau\,(u_p - u_{ps})/V_p; \qquad (34)$$

where u_{ps} is the x- component of the wall velocity, V_p is the resultant fluid velocity at P, relative to the wall, and τ is the resultant wall stress. Substituting this into (32) we obtain the equation of the standard form (18), with the corrected coefficients:

$$a'_p = a_e + a_w + a_n + F_s + a_t + a_b + \tau_x \Delta x \Delta z / V_p \qquad (35)$$
$$a'_s = 0$$
$$b' = b + u_{ps}\Delta x \Delta z / V_p$$

Boundary conditions for scalars

The 'v', 's' and 'f' conditions for scalars are discretized as for the tangential velocity components. The 'c' condition is similar to the 'f' condition. The 'g' condition $\partial\phi/\partial y = g$ is discretized using:

$$\phi_s = \phi_p - g(\Delta y_p + \Delta y_s)$$

where Δy_p, Δy_s are the same as in Figure 9. The resulting corrections in (16) are

$$a'_p = a_p - a_s$$
$$b' = b + a_s g(\Delta y_p + \Delta y_s)$$
$$a'_s = 0'$$

The 'w' condition is imposed on k and ε in the form of the explicit assignments (68) and (71) at the scalar points, nearest to the wall (see Appendix). If the 'w' condition was imposed on the velocity, then ε cannot be subjected to any other condition than 'w', but the condition for k can be 'w', 's', 'v', 'c', 'g' or 'f'.

The 'i' condition is imposed by the programs on all the internal boundaries.

Multigrid method

Two variants of the nonlinear multigrid method

The system of the finite volume equations, interpolation formulas on the internal boundaries and the discrete boundary conditions can be solved by the nonlinear multigrid methods. For these methods, the solution process is advanced on a sequence of successively finer grids, which will be labeled with $l = 1,2,\ldots, L$. For the introduction, let us consider the case of the two grids: $l-1$ and l. The discrete system on the finer grid l will be denoted by:

$$D_l(s_l) = r_l \qquad (36)$$

Let $\hat{s}$ be an approximate solution of (36), with the residue

$$e_l = D_l(\hat{s}_l) - r_l$$

and let

$$c_l = s_l - \hat{s}_l$$

be the required correction. Then

$$D_l(\hat{s}_l + c_l) - D_l(\hat{s}_l) = -e_l \qquad (37)$$

or

$$D_l(s_l - c_l) - D_l(s_l) = e_l \qquad (38)$$

The correction equations (37) and (38) give rise to the two multigrid methods.

<u>The FAS1 method</u>

The equation (37) is the basis of the classical FAS method (Full Approximation Storage, [Brandt 1977]). Here, the classical method will be called FAS1. For FAS1, the equation (37) is approximated on the coarse grid with

$$D_{l-1}(\hat{s}_{l-1} + c_{l-1}) - D_{l-1}(\hat{s}_{l-1}) = -e_{l-1} \qquad (39)$$

where D_{l-1},, $\hat{s}_{l-1}$ and e_{l-1} are some approximations of D_l, $\hat{s}_l$ and e_l. The easiest choice is to define D_{l-1} in the same way as D_l is defined on the fine grid, that is by using the same discretization procedure; $\hat{s}_{l-1}$ and e_{l-1} are the "restrictions" of s and e. Usually, the components of s and e at coarse grid points are calculated as weighted averages of the corresponding components of s and e at a certain number of the nearest fine grid points. We shall write

$$\hat{s}_{l-1} = R_l(\hat{s}_l) \text{ and } e_{l-1} = R_l(e_l),$$

where R_l denotes the restriction operator, which transforms the functions defined on the grid l into the functions defined on the grid l-1.

If D_{l-1}, $\hat{s}_{l-1}$ and e_{l-1} are sufficiently good approximations of D_l, $\hat{s}_l$ and e_l, then we can expect that the solution c_{l-1} of (39) is a good approximation of c_l in (37). An approximate solution $\hat{c}_{l-1}$ of (39) is found and then "prolongated" (usually, linearly interpolated) to the fine grid l to obtain an approximation $\hat{c}_l$ of c_l. We shall write

$$\hat{c}_l = P_{l-1}(\hat{c}_{l-1})$$

where P_{l-1} denotes the prolongation operator, which transforms the functions defined on the grid l-1 into the functions defined on the grid l.

We can expect that $\hat{s}_l + \hat{c}_l$ is an improved approximation of s_l. However, the prolongation introduced the slope discontinuities into $\hat{s}_l + \hat{c}_l$. These errors are reduced with a few cycles ("smoothings") of an iterative solution method ("smoother"), which begin with $\hat{s}_l + \hat{c}_l$ as the initial iterand. The final result now replaces $\hat{s}_l$, and the same correction cycle can be repeated.

The above procedure can be summarized as follows:

1. Choose initial $\hat{s}_l$. Usually, $\hat{s}_l$ is a prolongation of an approximate solution $\hat{s}_{l-1}$ of the coarse grid problem
   $D_{l-1}(s_{l-1}) = r_{l-1}$ (40)
   where r_{l-1} is the restriction of r_l.
2. Improve $\hat{s}_l$ with a few smoothings.
3. Calculate the residue of the improved solution $\hat{s}_l$:
   $e_l = D_l(\hat{s}_l) - r_l$
4. If e_l is sufficiently small, then terminate this procedure. Otherwise:
5. Restrict e_l and $\hat{s}_l$ to obtain e_{l-1} and $\hat{s}_{l-1}$ on the coarse grid, and calculate
   $d_{l-1} = D_{l-1}(\hat{s}_{l-1})$
6. Find an approximate solution $\hat{c}_{l-1}$ of the problem (39):
   $D_{l-1}(\hat{s}_{l-1} + c_{l-1}) = d_{l-1} - e_{l-1}$ (41)
7. Prolongate $\hat{c}_{l-1}$ to obtain $\hat{c}_l$ on the fine grid.
8. Replace $\hat{s}_l$ with $\hat{s}_l + \hat{c}_l$ and return to the operation 2.

The FAS2 method

The coarse grid approximation of the correction equation (38) can be written as

$$D_{l-1}(\hat{s}_{l-1} + c_{l-1}) - D_{l-1}(\hat{s}_{l-1}) = e_{l-1} \quad (42)$$

where $\hat{s}_{l-1}$ is a coarse grid approximation of the solution s_l. This gives rise to another multigrid method ([Nowak, 1984]), which can be summarized as follows:

1. Find an approximate solution $\hat{s}_{l-1}$ of the coarse grid problem
   $D_{l-1}(s_{l-1}) = r_{l-1}$ (43)
   where r_{l-1} is the restriction of r_l, and calculate
   $d_{l-1} = D_{l-1}(\hat{s}_{l-1})$ (44)
2. Prolongate $\hat{s}_{l-1}$ to obtain $\hat{s}_l$ on the fine grid.
3. Improve $\hat{s}_l$ with a few smoothings and calculate the residue
   $e_l = D_l(\hat{s}_l) - r_l$ (45)
   of the improved $\hat{s}_l$.
4. If e_l is sufficiently small, then terminate this procedure. Otherwise:
5. Restrict e_l to obtain e_{l-1} on the coarser grid.
6. Find an approximate solution $\hat{c}_{l-1}$ of the problem (42):
   $D_{l-1}(\hat{s}_{l-1} - c_{l-1}) = d_{l-1} + e_{l-1}$ (46)
7. Prolongate $\hat{c}_{l-1}$ to obtain $\hat{c}_l$ on the fine grid.
8. Replace $\hat{s}_l$ with $\hat{s}_l + \hat{c}_l$ and return to the operation 3.

Let us note that FAS2 avoids the repetitive calculation of $\hat{s}_{l-1}$ and d_{l-1}, which is a part of the operation 5 of FAS1. For FAS2, such functions are calculated once, during the initial operation 1.

Generalization of the FAS2 method

The 3-grid methods are derived when the coarse grid problems (40), (41) or (43), (46) are solved by the 2-grid methods. For that purpose, a third grid is introduced, coarser than the other two. Generalizations of the FAS1 method to 3 or more grids can be found in [Brandt 1976, 1977], [Hackbusch 1981] or [Stuben&Trottenberg 1981]. Here, we shall present a generalization of the FAS2 method.

Let L be the number of grids. For the presentation we shall need a lattice of triangles, which for L= 4 has the form shown in Figure 10. Let l and n denote the grid and the correction levels of this diagram. The correction level n=0 is the "solution level". At each node (l,n) a nonlinear problem
$D_l(s_{l,n}) = r_{l,n}$ (47)
will be solved approximately. At the apex $(L,0)$ this will be our discrete problem:
$D_L(s_{L,0}) = 0$ (48)
for which $r_{L,0}$=0. The form (48) is obtained when all the terms in the discrete equations are brought to their left-hand sides. The coarse grid operators D_l, with $l<L$, are the approximations of the finest grid operator D_L. On the solution level n=0 we shall have r=0 for all the grids l=1, 2, ..., L. On the correction levels n=1,2, ...,L-1, the right-hand sides $r_{l,n}$ are, in general, different from 0, as in (46).

At some nodes (l,n) an approximate solution $\hat{s}_{l,n}$ of (47) will be obtained by making a certain number, m, of smoothings, which may depend on (l,n) and on the current stage of

the multigrid calculation. We shall write:

$$\hat{s}_{l,n} := \tilde{D}_l(m; \hat{s}_{l,n}; r_{l,n}) \tag{49}$$

which denotes: "Make m smoothings for the problem (47), starting with $\hat{s}_{l,n}$ as the initial iterand, and assign the result to $\hat{s}_{l,n}$ (:= will denote the assignment). The one-grid algorithm (49) will be denoted by $A_l^{(l,n)}$.

If $l>1$ then the problem (47) can be solved by using the basic FAS2 method of the previous section. We shall introduce the following shorthand description of the basic method:

$$(B^{(l-1,n)} \rightarrow A_1^{(1,n)} \Leftrightarrow C^{(l-1,n+1)}) \tag{50}$$

where the opening bracket "(" represents the restriction:

$r_{l-1,n}=R_l(r_{l,n})$

and $B^{(l-1,n)}$ is a solution procedure for the problem (43):

$D_{l-1}(s_{l-1,n}) = r_{l-1,n}$

with the approximate result $\hat{s}_{l-1,n}$; the arrow represents the operation (44):

$d_{l-1,n} = D_{l-1}(\hat{s}_{l-1,n})$

and the prolongation

$\hat{s}_{l,n} = P_{l-1}(\hat{s}_{l-1,n})$;

$A_1^{(l,n)}$ is the smoothing (49) for the problem (47), with $\hat{s}_{l,n}$ as the improved result; the lower arrow represents the residue calculation (45):

$e_{l,n} = D_l(\hat{s}_{l,n}) - r_{l,n}$

followed by the test 4 and, if the procedure continues, the residue restriction:

$e_{l-1,n} = R_l(e_{l,n})$

and the calculation of the right hand side of (46):

$r_{l-1,n+1} = d_{l-1,n} + e_{l-1,n}$;

$C^{(l-1,n+1)}$ is a solution procedure for the problem (46):

$$D_{l-1}(s_{l-1,n+1}) = r_{l-1,n+1} \tag{51}$$

with the approximate result $\hat{s}_{l-1,n+1}$; the closing bracket ")" and the upper arrow represent the calculation of the approximate correction:

$\hat{c}_{l-1,n+1} = \hat{s}_{l-1} - \hat{s}_{l-1,n+1}$,

prolongation of the correction:

$\hat{c}_{l,n} = P_{l-1}(\hat{c}_{l-1,n+1})$,

calculation of the corrected solution on the finer grid:

$\hat{s}_{1,n} := \hat{s}_{l,n} + \hat{c}_{l,n}$

and the return to the operation 3 of the basic method.

The final result of (50) is stored in $\hat{s}_{l,n}$.

Using the notation (49) and (50) we can define the 2-grid method for the problem (47) as follows:

$$A_2^{(l,n)} = (A_1^{(l-1,n)} \rightarrow A_1^{(l,n)} \Leftrightarrow A_1^{(l-1,n+1)}) \tag{52}$$

Similarly, the 3-grid method could be defined as

$$A_3^{(l,n)} = (A_1^{(l-1,n)} \rightarrow A_1^{(l,n)} \Leftrightarrow A_1^{(l-1,n+1)}) \tag{53}$$

A consistent definition of the 4-grid method for our problem (48) on the grid level L=4 would be

$$A_4^{(4,0)} = (A_3^{(3,0)} \rightarrow A_1^{(4,0)} \Leftrightarrow A_3^{(3,1)}).$$

However, the correction equation (51) at the node (3,1) is then solved with a rather elaborate method $A_3^{(3,1)}$. In practice, we found that it is more efficient to use a simpler method

$$A_4^{(4,0)} = (A_3^{(3,0)} \rightarrow A_1^{(4,0)} \Leftrightarrow (A_3^{(2,1)} \rightarrow A_1^{(3,1)} \Leftrightarrow A_2^{(2,2)})) \tag{54}$$

Therefore, we finally adopted the following recursive definition of the general FAS2 method:

$$A_L^{(L,0)} = (A_{L-1}^{(L-1,0)} \rightarrow A_1^{(L,0)} \Leftrightarrow \tilde{A}_1^{(L-1,1)}) \tag{55}$$

where the correction equation solver is given by another recursive definition

$$\tilde{A}_l^{(l,n)} = (A_1^{(l-1,n)} \rightarrow A_1^{(l,n)} \Leftrightarrow \tilde{A}_{l-1}^{(l-1,n+1)}) \qquad \text{for } l=1, 2, 3, ... \tag{56}$$

and

$$\tilde{A}_1^{(1,n)} = A_1^{(1,n)} \tag{57}$$

For L=4 the definition (56) agrees with (54). In fact, (55) and (56) give

$$A_4^{(4,0)} = (A_3^{(3,0)} \rightarrow A_1^{(4,0)} \Leftrightarrow \tilde{A}_3^{(3,1)}) = (A_3^{(3,0)} \rightarrow A_1^{(4,0)} \Leftrightarrow (A_1^{(2,1)} \rightarrow A_1^{(3,1)} \Leftrightarrow \tilde{A}_2^{(2,2)}))$$

which is the same as (54), since by (56), (57) and (52) we have

$$\tilde{A}_2^{(2,2)} = (A_3^{(1,2)} \rightarrow A_1^{(2,2)} \Leftrightarrow A_1^{(1,3)}) = A_2^{(2,2)}$$

Using (53) and (52) we can split (54) into more elementary operations:

$$\begin{aligned} A_4^{(4,0)} &= ((A_2^{(2,0)} \rightarrow A_1^{(3,0)} \Leftrightarrow A_2^{(2,1)}) \rightarrow A_1^{(4,0)} \Leftrightarrow (A_1^{(2,1)} \rightarrow A_1^{(3,1)} \Leftrightarrow A_2^{(2,2)})) \\ &= (((A_1^{(1,0)} \rightarrow A_1^{(2,0)} \Leftrightarrow A_1^{(1,1)}) \rightarrow A_1^{(3,0)} \Leftrightarrow (A_1^{(1,1)} \rightarrow A_1^{(2,1)} \Leftrightarrow A_1^{(1,2)})) \\ &\quad \rightarrow A_1^{(4,0)} \Leftrightarrow (A_1^{(2,1)} \rightarrow A_1^{(3,1)} \Leftrightarrow A_1^{(2,2)} \Leftrightarrow A_1^{(1,3)}))) \end{aligned}$$

where, on the last right - hand side, only smoothings are present.

The restriction brackets "(" and the arrows, appearing in the last expression, are put on the operation diagram in Figure 10. For clarity, all $A_1^{(l,n)}$ are abbreviated to (l,n). The closing brackets ")" are attached to the oblique upper arrows. The procedure $A_4^{(4,0)}$ is started with the three restrictions "(((" of the zero right-hand side in (48) to the lower grids l=3, 2, 1 of the solution level n=0 (the results are 0), followed by the smoothing on the grid 1, the prolongation of the result $\hat{s}_{1,0}$ to the grid 2, the smoothing on this grid, the restriction of residue, the smoothing for the correction, the prolongation of the correction, next smoothing on the grid 2, and so on.

The flow chart of Figure 11 represents the practical implementation of the L- grid FAS2 method (55) in the program 'mgfd'. The parameters $m_{\tilde{L}}^{(1)}$, $m_{\tilde{L},n}^{(2)}$, $m^{(3)}$ and $m^{(4)}$ of this algorithm can be described as follows :

$m_{\tilde{L}}^{(1)}$: the number of smoothings for the solution (when $\tilde{L}=1$) or correction (when $\tilde{L}>1$) on the coarsest grid ;

$m_{\tilde{L},n}^{(2)}$: the number of the initial smoothings on the fine grids $l=\tilde{L}-n$ of the solution or correction levels n=0, 1, 2, ..., $\tilde{L}-2$; these smoothings precede multigrid cycles on these levels;

$m^{(3)}$: the number of smoothings on the coarse grids $l=\tilde{L}-n-1$ of the correction levels n=1, 2, ..., $\tilde{L}-2$; these smoothings give the approximate solutions of the problems (43);

$m^{(4)}$: the number of smoothings after adding a correction ;

$M_{\tilde{L},n}$: the number of the multigrid cycles for the solutions (if n=0) or corrections (if n>0) on the levels L=2, 3, ..., L and n=0, 1, ..., $\tilde{L}-2$; the variable $m_{l,n}$ is the counter of these cycles.

For the present implementation these parameters are fixed (read by 'mgfd' after each L-grid cycle). Obviously, the number of smoothings or multigrid cycles could be made dependent on the convergence rate, as it is often done for the FAS1 method ([Thompson and Ferziger 1989]). For example, the content of the box 12 of the flow-chart could be replaced with a more flexible criterion, especially on the finest grid (L,0). The program 'mgfd' allows to monitor the magnitude of the residues at all the nodes (l,n) of the operation lattice. The calculation can be stopped when the residues at (L,0) become sufficiently small, or continued as long as necessary by increasing the specified number $M_{L,0}$ of the L- grid cycles during the execution of the program 'mgfd'.

When appropriately programmed, the algorithm of Figure 11 can allocate the same memory space to the grid functions $d_{l,n}$, $r_{l,n}$ and $e_{l,n}$. The required memory size is then about two times larger than the size occupied by all the solutions $\hat{s}_{l,0}$, l=1, 2, ...,L. If N is the number of the grid point values in the finest solution $\hat{s}_{l,0}$, then we need space for about

$2 * (N + N/8 + N/64 + ...) = 16 * N/7$

real or double precision numbers. This memory requirement is not excessive.

Finally, as an example, let us set L=3 and M=1 (one multigrid cycle is made for the solutions and corrections). The sequence of operations is represented in Figure 12. The first numbers in the boxes determine the succession of operations, and the other numbers identify these operations on the flow-chart of Figure 11.

Components of the multigrid procedure

Grid refinement procedure

As shown in Figure 13, a finer grid is defined by dividing the sizes x, y, z of the coarse grid cells into the two parts (for irregular grids these parts are not equal, in general). As a consequence, each coarse cell contains eight finer cells. This procedure is not adaptive: finer grids are determined by the choice of the coarsest grid.

Restriction procedure

For the u-velocity component, 12 finite volumes of the fine grid overlap with one finite volume of the coarse grid (Figure 14)). The restricted residue e_o of the u- momentum equation is the weighted average of the 12 fine grid residues

$e_0 = (a_1 e_1 + a_2 e_2 + ... + a_{12} e_{12}) / a_0$

where a_1 , ..., a_{12} are the contributions of the 12 fine grid volumes into the coarse grid volume a_0. The same method is used for the residues of the v- and w- momentum equations.

For the continuity and the scalar equations, the coarse volume is composed of the eight fine volumes (Figure 12), and the restriction formula is

$e_0 = (a_1 e_1 + ... + a_8 e_8) / a_0$

The residues of the boundary conditions are restricted similarly, using the boundary cell face areas as the weighting factors. The approximation formulas on the internal boundaries, such as (28), are always satisfied exactly.

Prolongation procedure

The planes of the coarse grid p- points, perpendicular to the x-, y- and z- axes divide the flow field into the cells with these points at the corners. The coarse grid pressure distribution can be extended, in a unique way, to a continuous function, which is linear with respect to x, y and z inside each cell, and equal to the coarse grid pressures at the corners. For each cell this tri-linear interpolant is given by the formula

$$p = a + a_x x + a_y y + a_z z + a_{xy} xy + a_{xz} xz + a_{yz} yz + a_{xyz} xyz \quad (58)$$

where the eight coefficients a_x, ..., a_{xyz} are uniquely determined by fitting this interpolant to the pressure values at the eight corners of the cell. The prolongated pressures at the fine grid p- points inside the cell are defined by the formula (58). The same tri-linear method of prolongation is used for the other scalars, for the velocity components and for the coarse grid corrections of all the quantities.

Coarse grid operators

The coarse grid operators D_l (l = 1,2, ..., L-1) are defined by the same discretization formulas as the finest grid operator D_L . The distributions of boundary data, prescribed

on the finest grid, are transferred to the coarser grids by the area weighting restriction, used also for the residues of the boundary conditions.

Smoothing procedure

It was suggested by [Brandt 1984], and confirmed by [Vanka 1986] and [Thompson and Ferziger 1989], that good smoothing rates can be obtained if the velocity components and pressure are updated in a locally coupled manner. In particular, the locally coupled smoothing method, proposed by [Vanka 1986], proved to be superior to the SIMPLE method ([Patankar and Spalding 1972]), which treats u, v,w and p separately.

As an introduction, let us briefly outline the point version of Vanka's method. Each grid cell around a p- point contains 7 grid points associated with 7 values of u, v, w, p and 7 finite volume equations of the form (18) or (25). The coefficients and the free terms in these equations are always calculated using the "old" values of u, v, w, p and other scalars. Assuming that the old values are also substituted into (18) and (25), except at these 7 points, we arrive at the system of 7 linear algebraic equations with 7 unknowns. By solving this system we obtain the "new" values of u, v, w and p on a cell. All grid cells are visited during one iteration of Vanka's smoother.

This cell-by-cell method was found to be inefficient for grids with aspect ratios larger than 4 ([[Vanka 1987]). For higher aspect ratios the line-by-line or the plane-by-plane iterative methods perform better ([Fuchs and Zhao 1984]). For the line Vanka's smoother the system of equations is set up on a line of cells (Figure 15). Let us consider a line of N cells. The u- momentum equation (18) assigned to u_i can be written in the form:

$$a_i u_i = r_i + \Delta y \Delta z (p_{i-1} - p_i),$$

or

$$u_i = r_i / a_i + \Delta y \Delta z (p_{i-1} - p_i) / a_i \qquad (59)$$

where a_i is the diagonal coefficient, and r_i is the sum of all the remaining terms present in (18). The other momentum equations for the i-th cell can be written as

$$u_{i+1} = r_{i+1} / a_{i+1} + \Delta y \Delta z (p_i - p_{i+1}) / a_{i+1} \qquad (60)$$

$$v_i^s = r_i^s / a_i^s - \Delta x_i \Delta z \, p_i / a_i^s \qquad (61)$$

$$v_i^n = r_i^n / a_i^n + \Delta x_i \Delta z \, p_i / a_i^n \qquad (62)$$

$$w_i^b = r_i^b / a_i^b - \Delta x_i \Delta y \, p_i / a_i^b \qquad (63)$$

$$w_i^t = r_i^t / a_i^t + \Delta x_i \Delta y \, p_i / a_i^t \qquad (64)$$

where r_i^s , r_i^n , r_i^b and r_i^t include parts of the pressure terms. Substituting these explicit formulas into the continuity equation (25) for the i - th cell :

$$\Delta y \Delta z (\rho_{i+1} u_{i+1} - \rho_i u_i) + \Delta x_i \Delta z (\rho_i^n v_i^n - \rho_i^s v_i^s) + \Delta x_i \Delta y (\rho_i^t w_i^t - \rho_i^b w_i^b) = r_i^p$$

($r_i^p = 0$ on the solution level), we obtain the following equation for the pressure:

$$\alpha_i p_{i-1} + \beta_i p_i + \gamma_i p_{i+1} = \delta_i \qquad (65)$$

where

$$\alpha_i = -\rho_i (\Delta y \Delta z)^2 / a_i$$

$$\gamma = -\rho_{i+1} (\Delta y \Delta z)^2 / a_{i+1}$$

$$\beta_i = -\alpha_i - \gamma_i + (\Delta x_i \Delta z)^2 (\rho_i^n / a_i^n + \rho_i^s / a_i^s) + (\rho_i^t / a_i^t + \rho_i^b / a_i^b)$$

$$\delta_i = r_i^p + \Delta y \Delta z (\rho_i r_i / a_i - \rho_{i+1} r_{i+1} / a_{i+1}) + \Delta x_i \Delta z (\rho_i^s r_i^s / a_i^s - \rho_i^n r_i^n / a_i^n) + \Delta x_i \Delta y (\rho_i^b r_i^b / a_i^b - \rho_i^t r_i^t / a_i^t)$$

The equations (65) with $i = 1, 2, ..., N$, represent a tri-diagonal system with dominant diagonal coefficients. For completeness, boundary conditions must be added at the ends $i = 0$ and $i = N+1$ of the line. If the line begins or ends in the interior of the flow field, as it happens on the segmental interfaces (or the "block" interfaces) then the given values of p_0 or p_{N+1} are substituted into the first and the last equation (65), and the system becomes complete. Let us assume that the line begins at the boundary of the domain, where the 'v' condition is imposed. Then the equation (59) with $i=1$ is replaced by $u_1 = g$, with given g. Unlike (59), this equation does not contain p_0. As a consequence, p_0 will disappear from the first equation (65). Similarly we can show that p_0 and p_{N+1} can be removed from the system (65) for all the other boundary condition types described previously.

The system (65) is solved by the Gauss elimination, and then u_i, v_i^s, v_i^n, w_i^t and w_i^b are found from (59) - (64) at all the grid points on the line. All the lines parallel to x, y and z-axes are treated by this procedure. For each direction, the even numbered lines are treated first, and then the procedure is applied to the odd numbered lines. This alternating zebra - sweeping was found to be better than other choices for the case of flow around the backward-facing step [Thompson and Ferziger 1989].

The tri-diagonal systems (65) are solved together with the similar systems for the scalars:

$$-a_i^w \phi_{i-1} + a_i^p \phi_i - a_i^e \phi_{i+1} = r_i^\phi \qquad (i = 1, 2, ..., N) \qquad (66)$$

where r_i^ϕ is the sum of the remaining terms, present in (16).

For better efficiency, the lines of cells are connected to form rectangular "blocks" (Figure 16). For each block, the coefficients and the independent terms of the discrete system are calculated first, and then the zebra - line procedure is applied. This saves computational time, which would be spent on the discretization, if all the lines were treated separately. Since the number of elements for the coefficients and the right - hand sides of the discrete system is about 8 times larger than the number of the grid point values, the block sizes may be limited by the size of the computer memory. During one iteration of Vanka's smoother all the blocks are visited in a three-dimensional checkerboard order.

Treatment of the turbulence equations

The treatment of the k-ε system by the multigrid methods is difficult. The difficulties are due to the dominance of the source terms and their strong ($1/k$) nonlinearity. The 'w' boundary condition is not amenable to the treatment by the solution methods presented in the last section. Some of the difficulties are discussed in [Vanka, 1987]. For the present version of the programs we decided to delete the discrete equations for k and ε from the discrete systems for the corrections ($n > 0$). Since no corrections are added to the fine grid distributions of k and ε , the solution procedure for these quantities is reduced to the application of the zebra-line smoother on the finest grid. The program 'mgfd' allows for the exclusion of the specified scalars from the multigrid correction process, during a given number of the initial multigrid cycles.

References:

1. A. Arakawa and V. R. Lamb, Computational design of the basic dynamical processes of the UCLA general circulation model, Methods Comput. Phys., Vol. 16, 173 - 263, 1977.
2. A. Brandt, Multi - level adaptive techniques (MLAT) I. The multi - grid method, Research Report RC. 6026, IBM T. J. Watson Research Center, Yorktown Heights, NY, 1976.
3. A. Brandt, Multi - level adaptive solution to boundary value problems, Math. Comp. 31, 333 - 390, 1977.
4. A. Brandt, von Karman Institute, Lecture Series 1984 - 04, 1984.
5. A. K. Cline, Scalar- and planar- curve fitting using splines under tension, Comm. ACM 17, 4, 218 - 220, Apr. 1974.
6. L. Fuchs and H. - S. Zhao, Solution of Three Dimensional Viscous Incompressible Flows by a Multigrid Method, Int. J. for Numer. Meth. in Fluids, Vol. 4, 539 - 555, 1984.
7. A. D. Gosman and F. D. K. Ideriah, TEACH - 2E : A general computer program for two dimensional turbulent recirculating flows, Int. Rep., Dept. Mech. Eng., Imperial College, Univ. of London, United Kingdom, 1976.
8. W. Hackbusch, Multi - grid convergence theory, Multigrid Methods, Proceedings, Cologne, Springer - Verlag, 1981.
9. K. Y. M. Lai and M. Salcudean, TEMA: A computer program for two - phase, multi - dimensional, turbulent recirculating flows, Int. Rep., Dept. Mech. Eng., Univ. of Ottawa, Canada, 1985.
10. K. Y. M. Lai, TURCOM: A computer code for the calculation of transient, multi - dimensional, turbulent, multi - component chemically reactive fluid flows, Div. of Mech. Eng., National Research Council Canada, Technical Rept. TR - GD - 011, 1987.
11. B. E. Launder and D. B. Spalding, The Numerical Computation of Turbulent Flows, Computer Methods in Applied Mechanics and Engineering, Vol. 3, 269 - 289, 1974.
12. Z. P. Nowak, Calculation of transonic flows around single and multi-element airfoils on a small computer, Report 84 - 48, Delft Univ. of Technology, 1984.
13. S. V. Patankar, Numerical Heat Transfer and Fluid Flow, Series in Computational Methods in Mechanics and Thermal Sciences, 1980.
14. S. V. Patankar and D. B. Spalding, A calculation procedure for heat, mass and momentum transfer in three - dimensional parabolic flows, Int. J. Heat and Mass Transfer 15, 1787 - 1806, 1972.
15. J. D. Ramshaw and V. A. Mousseau, Accelerated artificial compressibility method for steady - state incompressible flow calculations, Computers and Fluids, Vol. 18, No. 4, 361 - 367, 1990.
16. W. Rodi, Turbulence models and their applications in hydraulics, The state of art review, Institut fuer Hydromechanik, Univ. of Karlsruhe, 1984.
17. W. Rodi, Experience with two - layer models combining the k - model with a one - equation model near the wall, 29 - th Aerospace Sciences Meeting, Jan. 7 - 10, Reno, Nevada, 1991.

18.M. C. Thompson and J. H. Ferziger, An Adaptive Multigrid Technique for the Incompressible Navier - Stokes Equations, Journal of Comput. Physics 82, 94 - 121, 1989.
19.K. Stuben and U. Trottenberg, Multigrid Methods : Fundamental Algorithms, Model Problem Analysis and Applications, Multigrid Methods, Proceedings, Cologne, Springer - Verlag, 1981.
20.S. P. Vanka, Block Implicit Multigrid Solution of Navier Stokes Equations in Primitive Variables, Journal of Comput. Physics 65, 138 - 158, 1986.
21.S. P. Vanka, Block - Implicit Computation of Viscous Internal Flows -Recent Results, AIAA 25 - th Aerospace Sciences Meeting, Jan. 12 - 15, Reno, Nevada, 1987.
22.J. Zhou, A Multigrid Method for Computation of Film Cooling, M. Sc. Thesis, Dept. Mech. Eng., Univ. of British Columbia, Vancouver, Canada, 1990.
23.J. Zhou and M. Salcudean, A Multigrid Local Mesh Refinement Method for Computation of Recirculating Flows, Proceedings of the 11 - th Annual Meeting of the Canadian Applied Mathematics Society, Halifax, N. S., 1990.

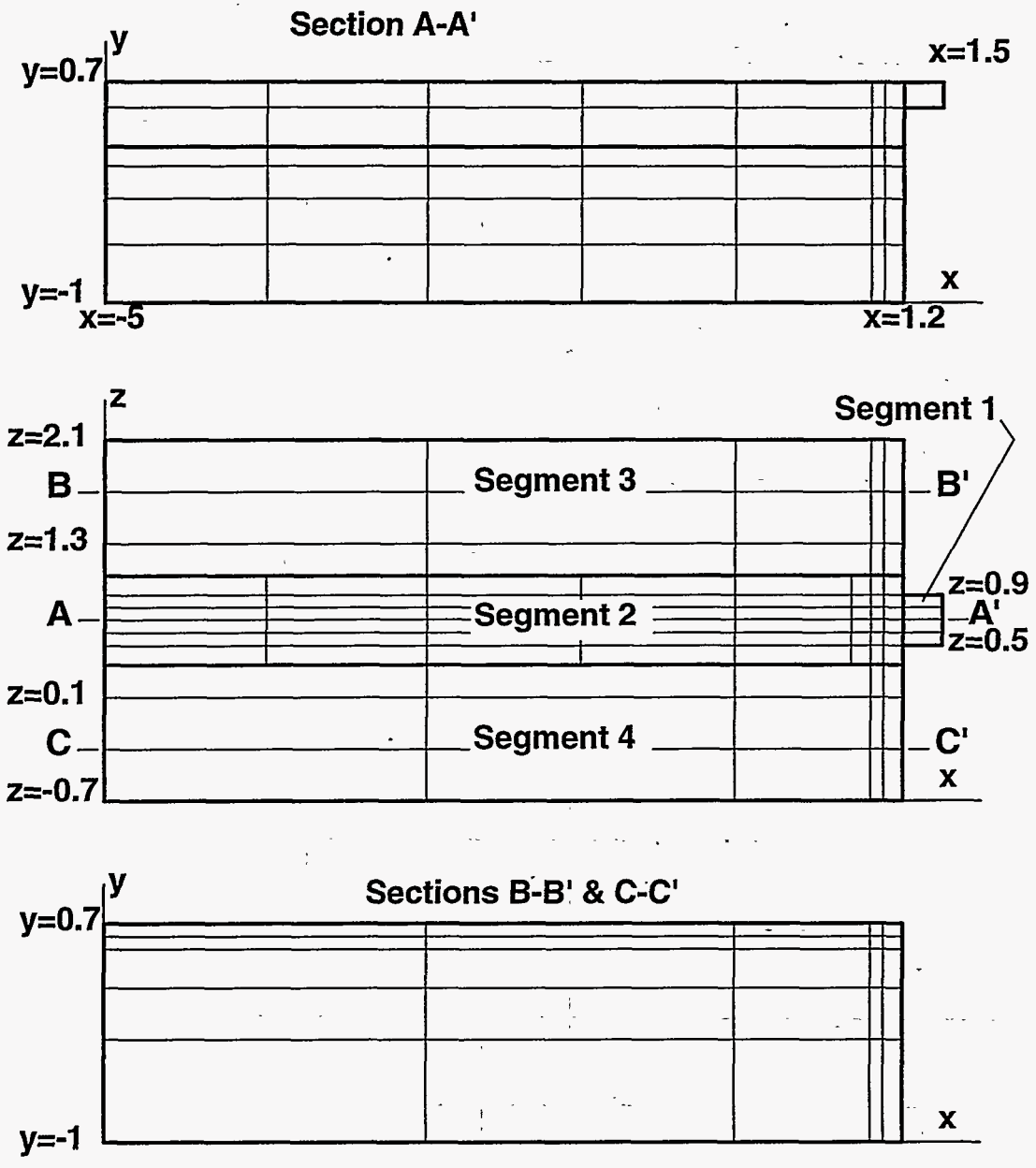

Figure 1: Scalar grid cells on a domain composed of 4 segments.

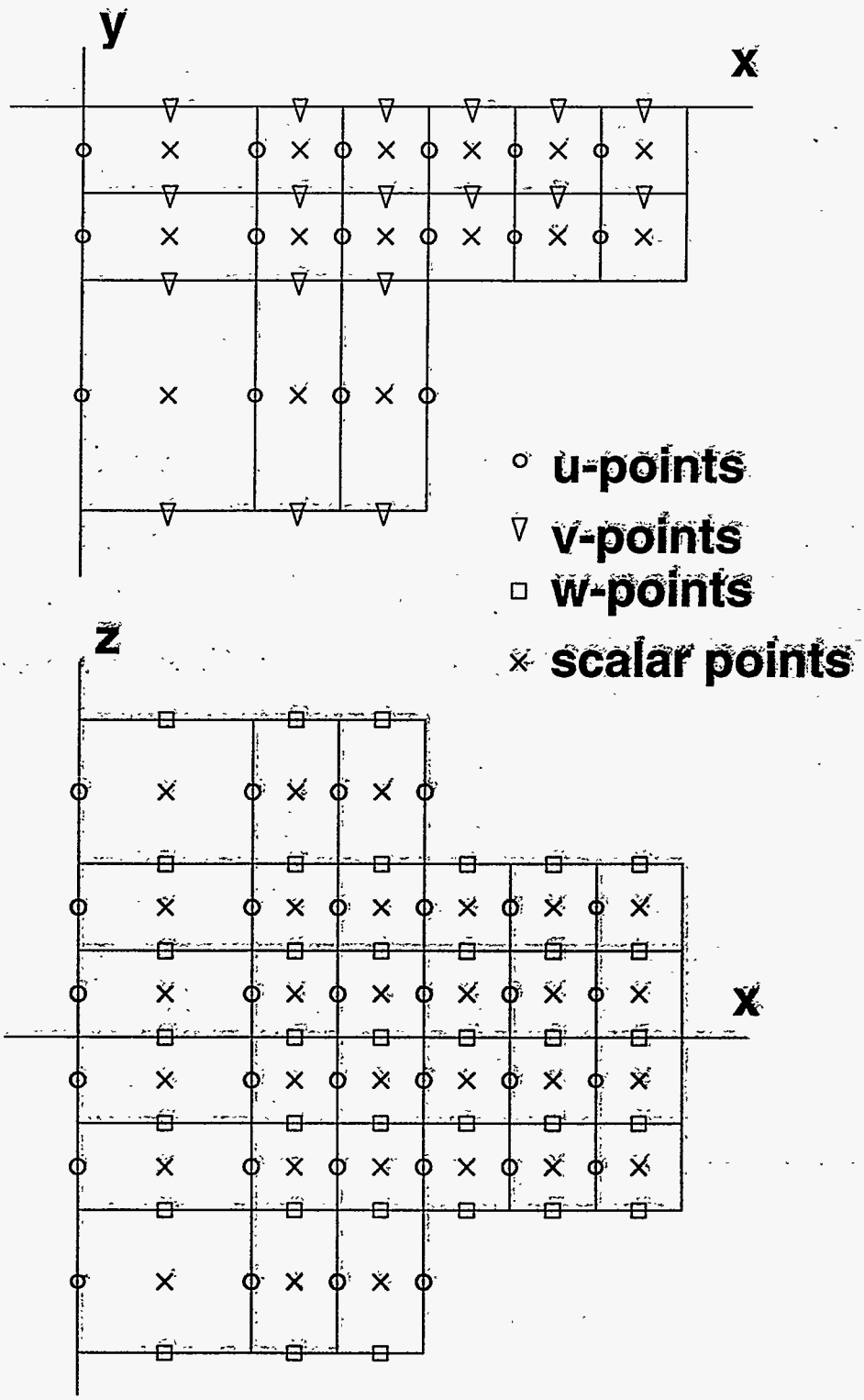

Figure 2: Two views of the grid.

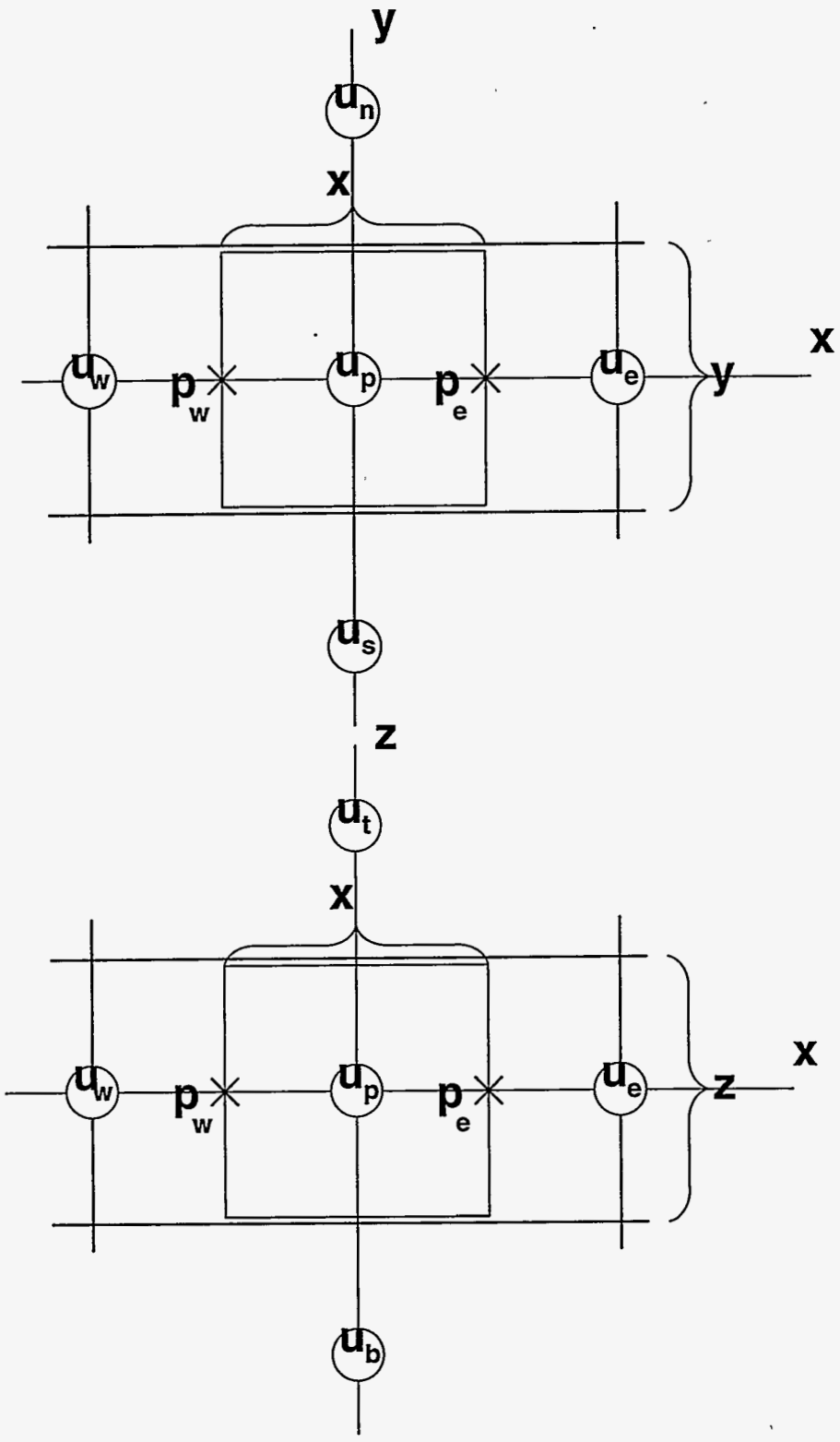

Figure 3: Finite volume for the u momentum equation (Broken Lines).

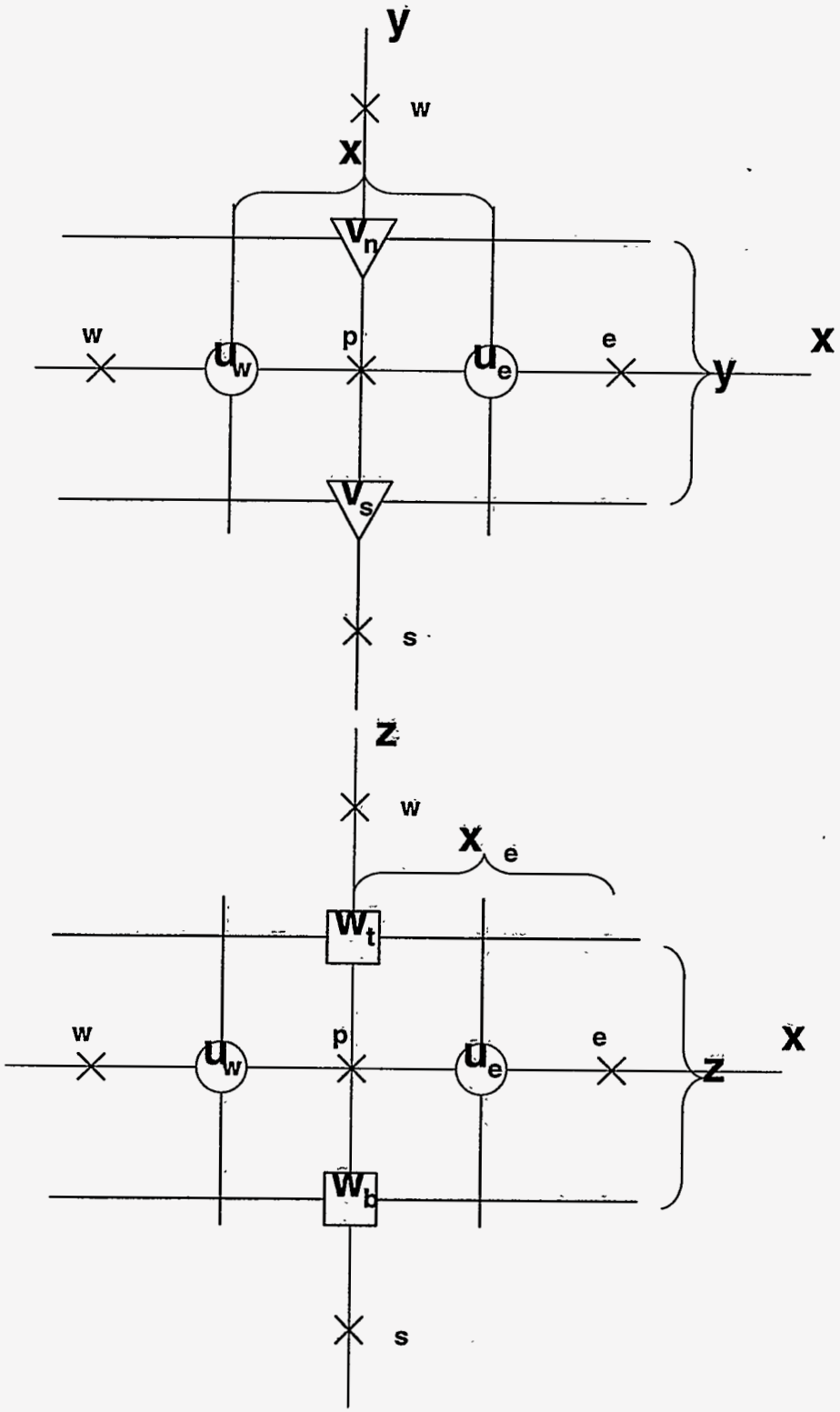

Figure 4: Finite volume for the continuity equation and the scalar equations.

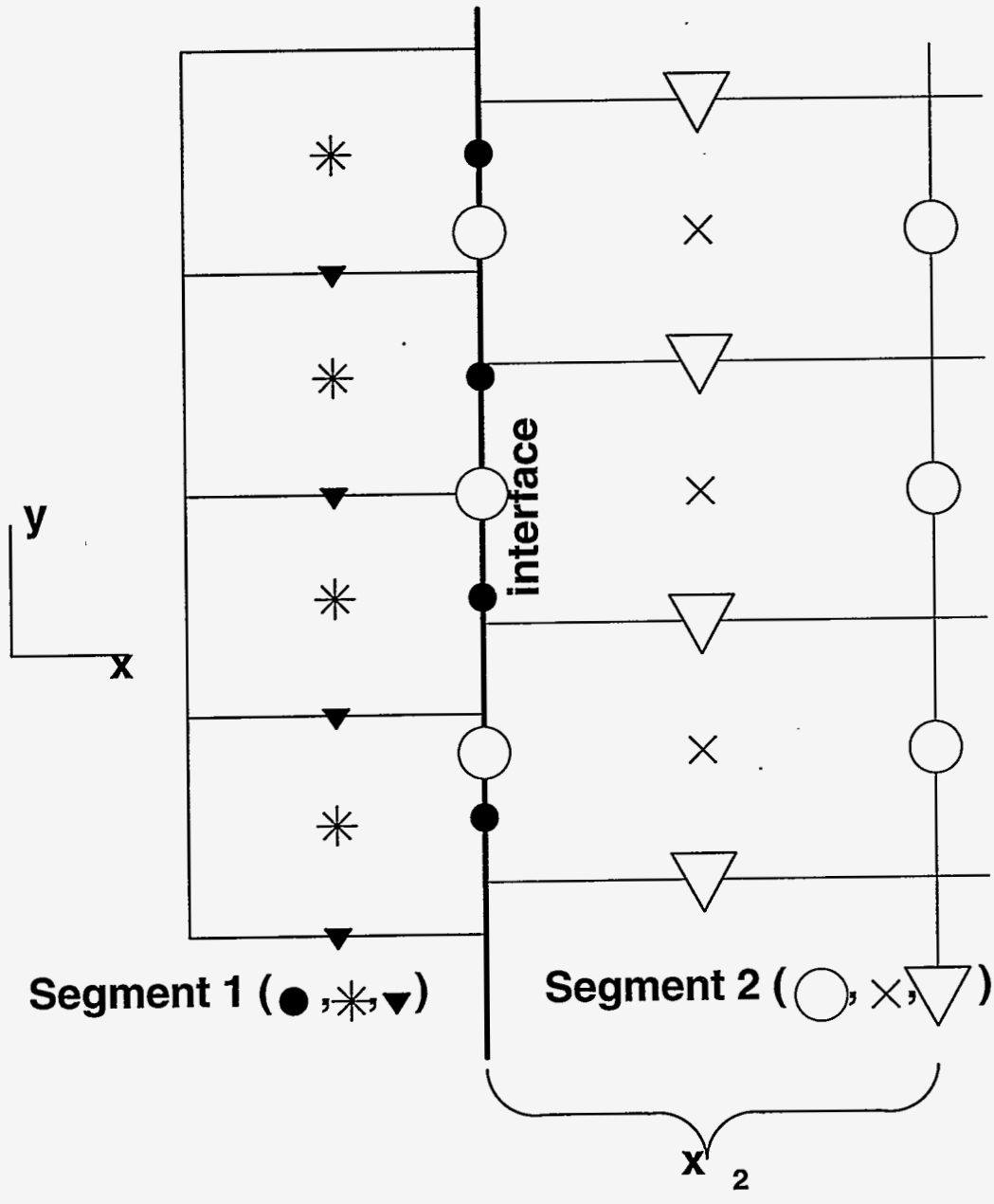

Figure 5: Interface between segments.

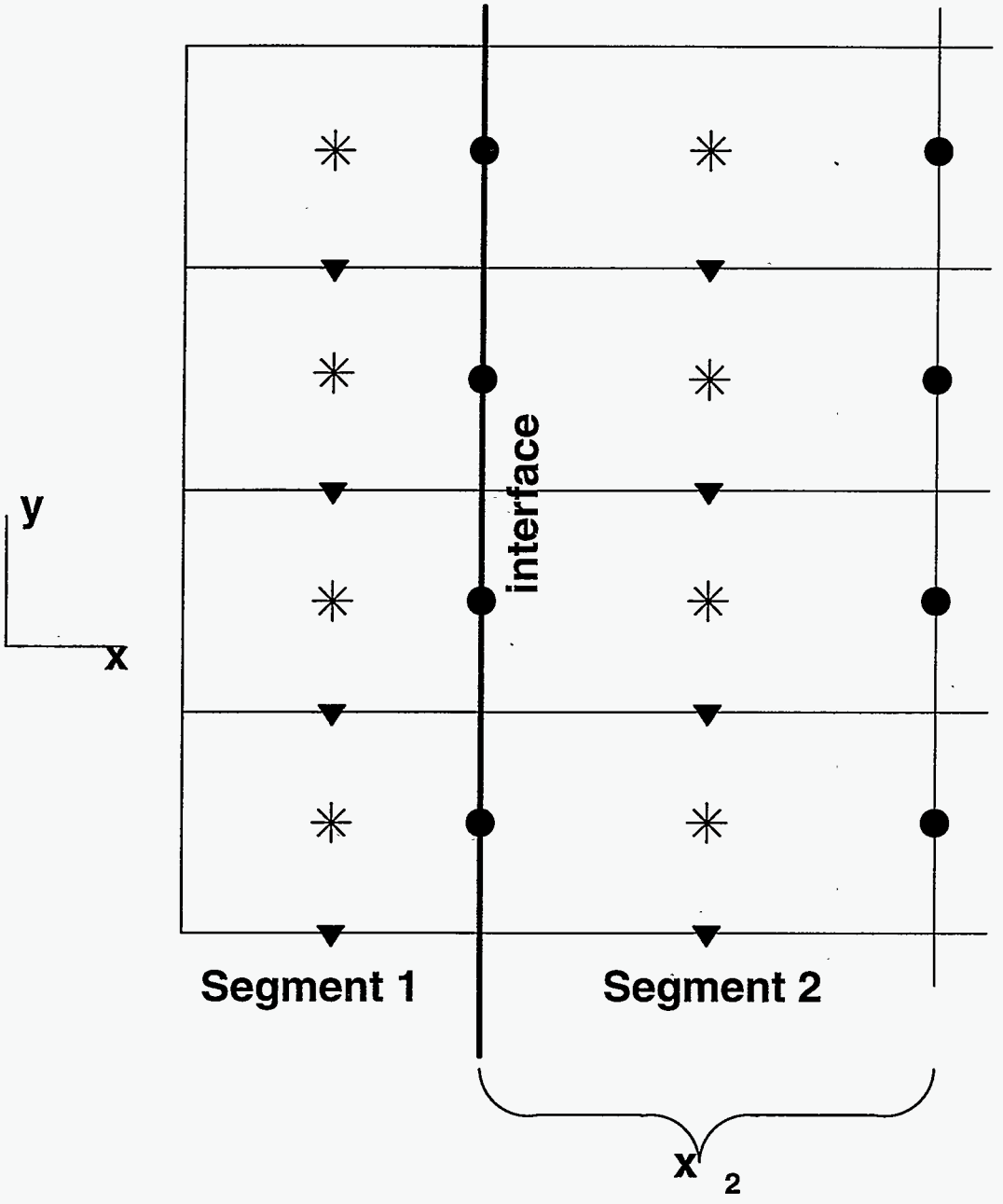

Figure 6: Extended grid near the interface.

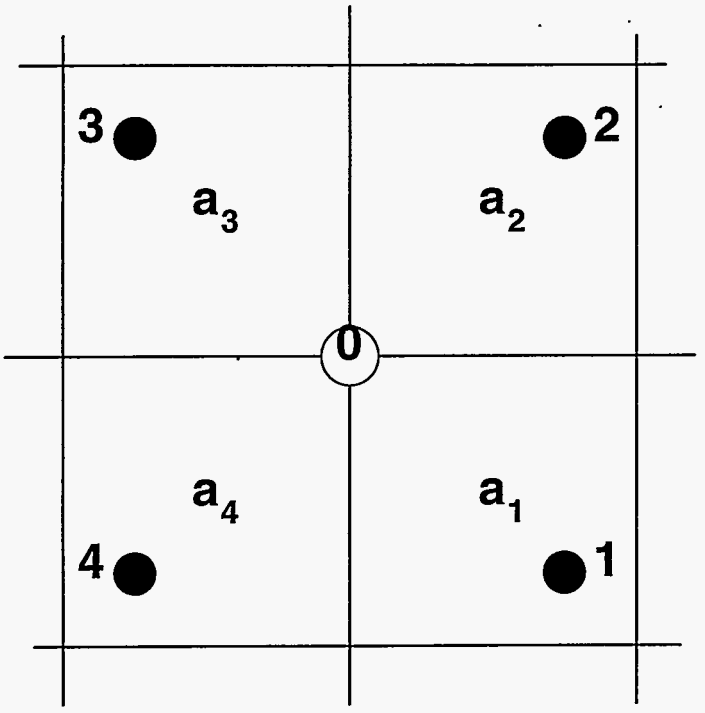

Figure 7: View of the interface.

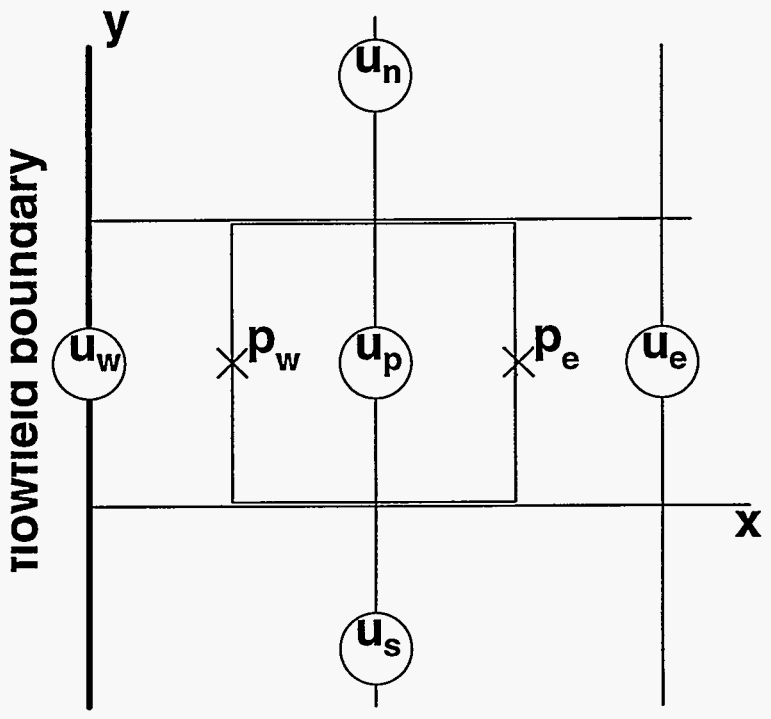

Figure 8: Finite volume for the normal velocity component near the boundary.

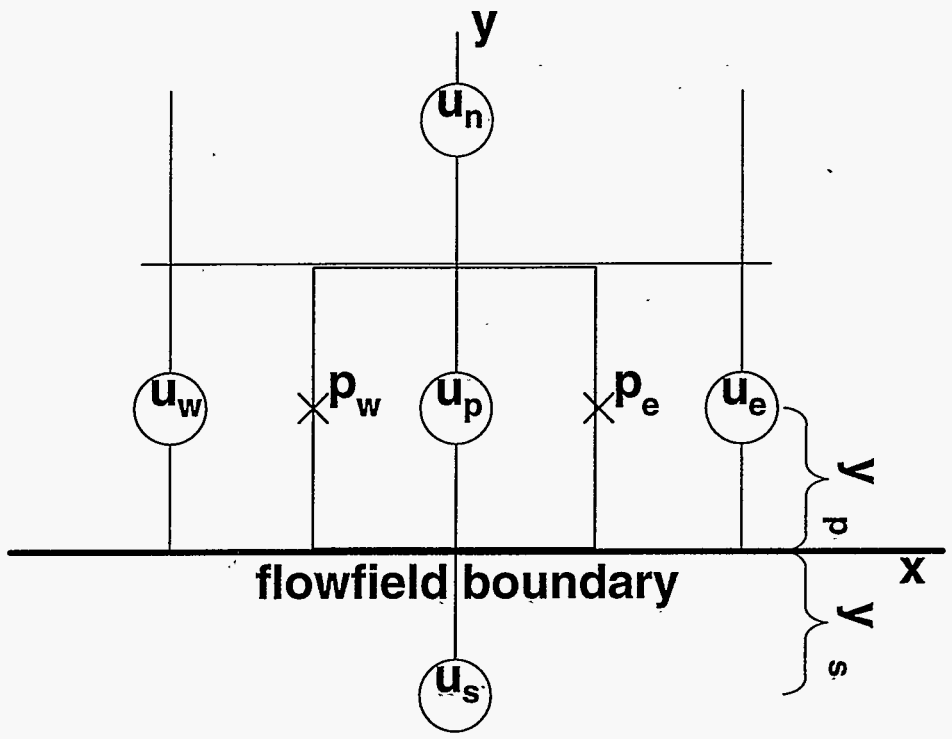

Figure 9: Finite volume for the tangential velocity component near the boundary.

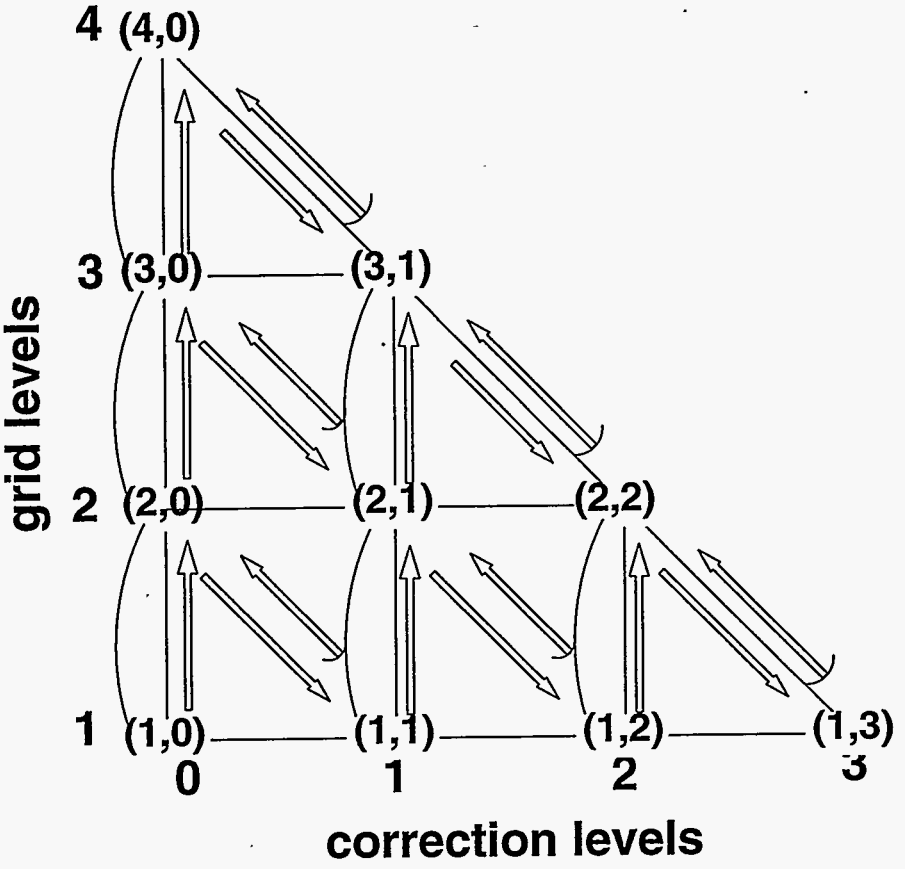

Figure 10: Operation method for the 4-grid FAS2 method.

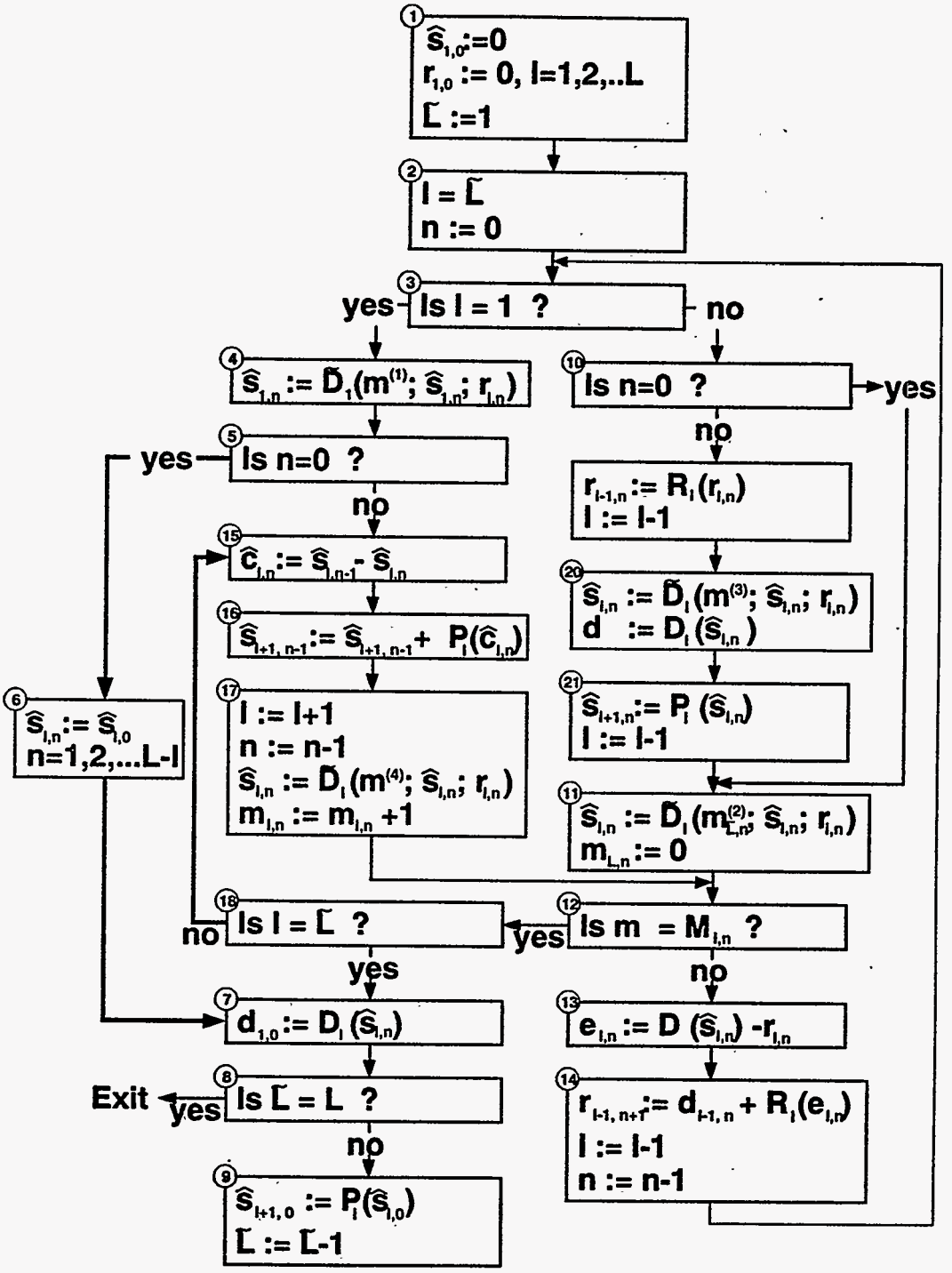

Figure 11: Flow chart for the L grid FAS2 method.

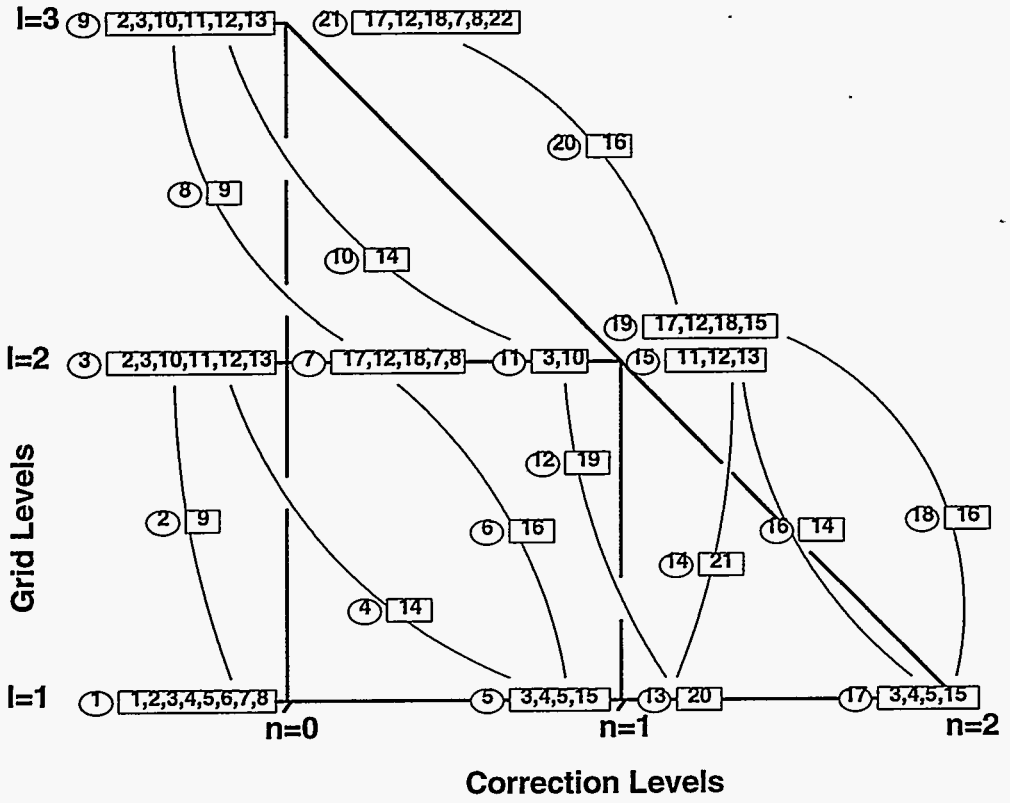

Figure 12: Sequence of operations for the 3 grid FAS2 method.

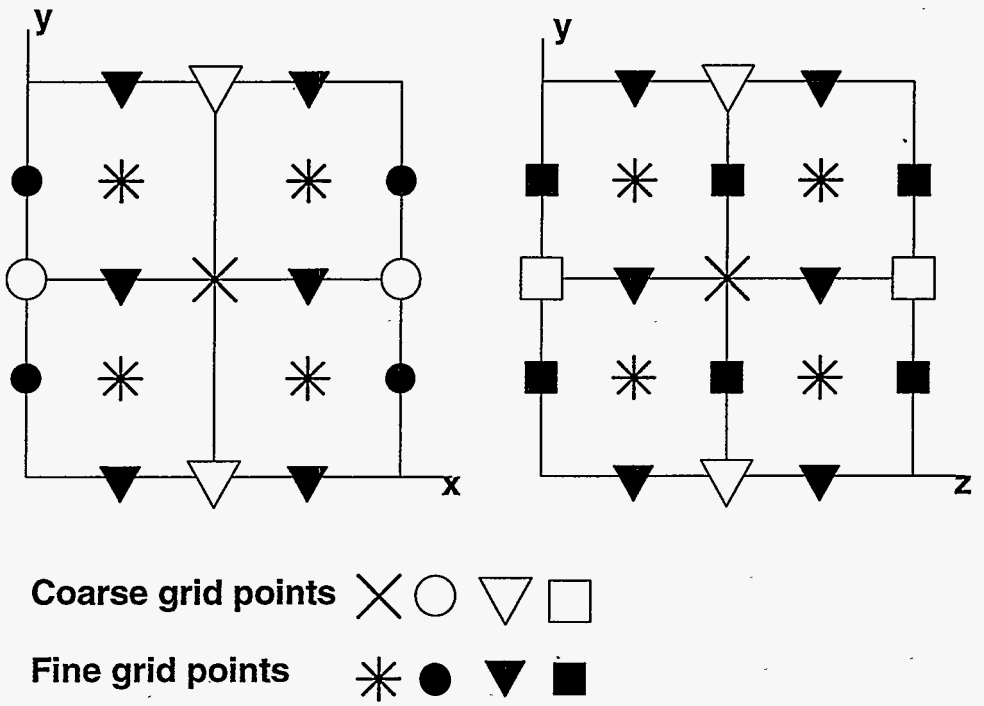

Figure 13: Coarse grid cell and its partition into fine grid cells (broken lines).

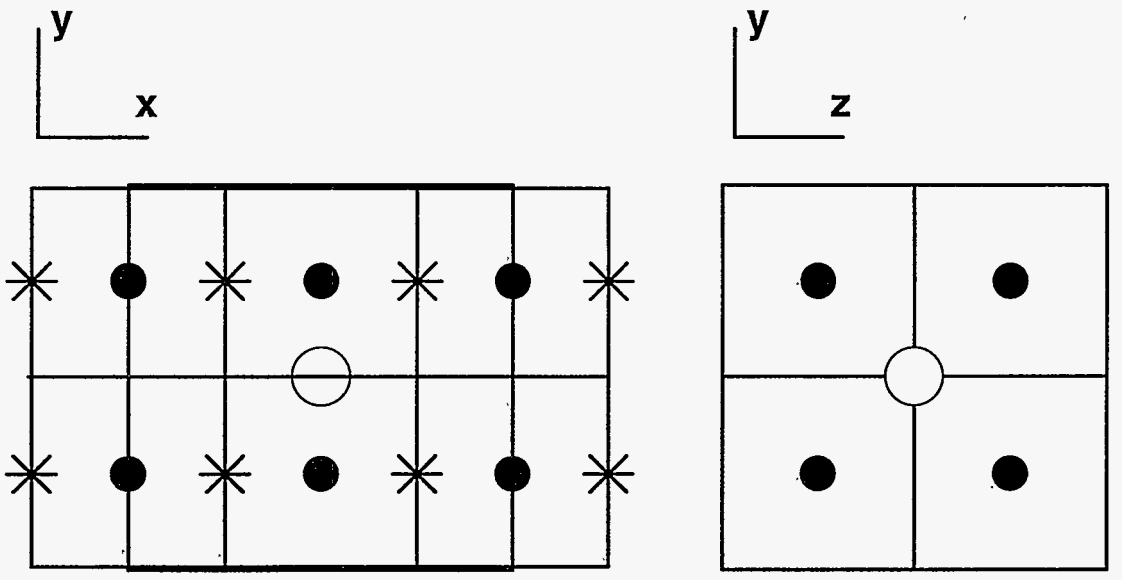

Figure 14: Finite volumes around the u points of the coarse and fine grids.

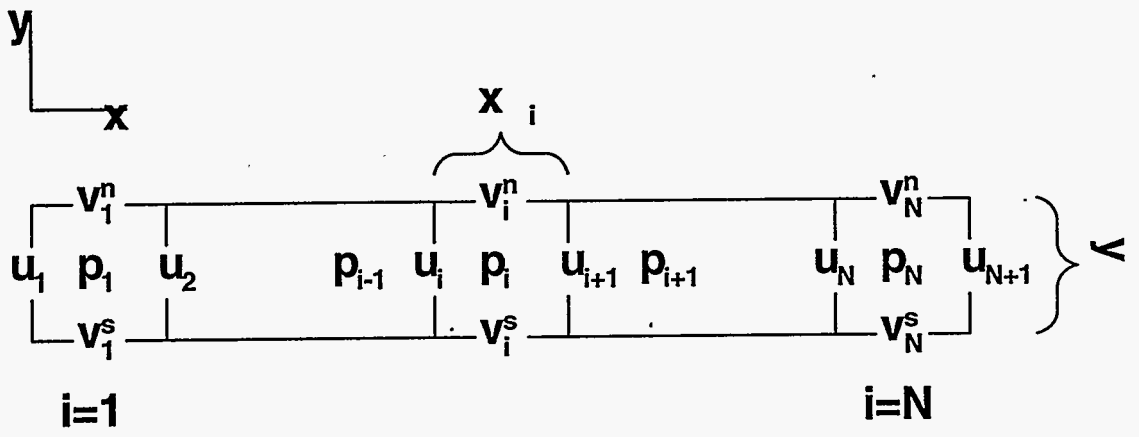

Figure 15: x-y projection of a line of cells.

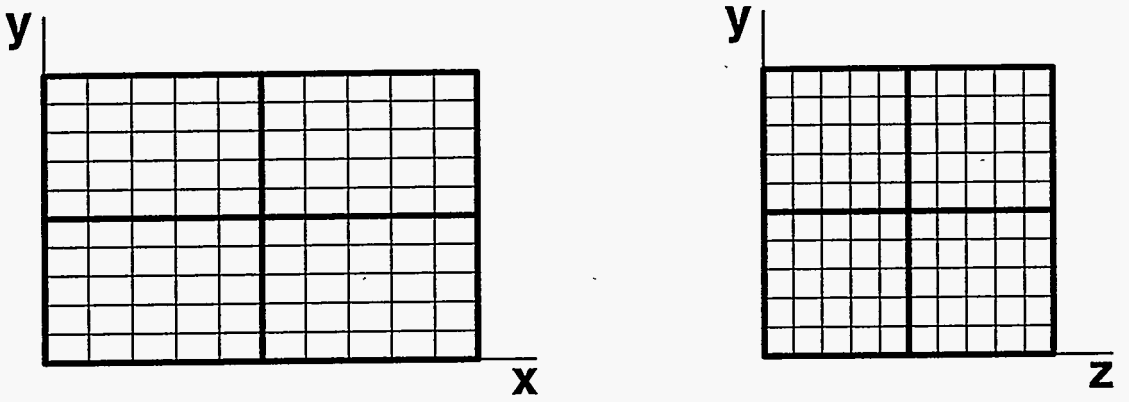

Figure 16: Partition of a segment into blocks.

SECTION 2: COMPUTER CODES 'GEO' AND 'MGFD'

The equations and solution method described previously have been coded into a series of FORTRAN computer programs at UBC. These codes are machine independent and we have run them successfully on Silicon Graphics, SUN, IBM, HP and Cray computers. The program set consists of three main codes: a pre-processing program 'geo', a discretization and solution program 'mgfd', and a post-processing program 'prnt'. Figure 1 shows the connections between these programs.

Program 'geo':

This program consists of the main file, and the files 'geo.par' and 'dens', included into the main file by the 'include' statements (example: include 'dens'). The file 'geo.par' contains one parameter statement, which specifies the array dimensions for 'geo'. The file 'dens' provides the definition of the density as a function of the pressure and other scalars. This definition is ignored when the density is constant. The file 'dens' is also included into the program 'mgfd'.

The program 'geo' reads the data from the file 'geo.in'. Among other things, this file defines

- the geometry of the grid,
- the geometry of the boundary patches,
- the boundary data types ('v', 's', etc.),
- the boundary data values, if these values are constant over their patches.
- Variable distributions of the boundary data are specified by the subprogram 'cbv', which is a part of 'geo'.

The main objectives of 'geo' are:

1. to generate the sequences of the grid point coordinates,
2. to generate the sequences of the boundary data types and values,
3. to generate the sequences, which define the allocation of the mass flows from the "donor" cells to the "receiver" cells on the intersegmental boundaries,
4. to generate the sequences, used by 'mgfd' for the continuation of the flowfield parameters across the segmental boundaries (such continuation is necessary at interfaces between segments; it also simplifies the discretization on the outer boundaries),
5. to write all these sequences into the file 'geo.mgfd', for use by 'mgfd',
6. to calculate the array sizes for 'mgfd' and write them into the file 'mgfd.par' in the form of a parameter statement (included into 'mgfd'),
7. to write the sequences, which define the grid geometry, into the file 'geo.prnt', for use by post-processing programs,
8. to write the sizes of these sequences into the file 'prnt.par', in the form of a parameter statement for post-processing programs.

The program 'geo' produces the diagnostic file 'geo.out', which serves to detect the errors in 'geo.in'. Additionally, when errors are detected, 'geo' displays diagnostic messages on

the screen of the computer terminal. These messages indicate the sources of errors and the corrective action.

The array sizes for 'geo', recorded in 'geo.par', are difficult to determine in advance. They depend on the number of the segments and the grid levels, on the geometry of the boundary patches and on the boundary data types. Therefore, for each new flow case 'geo' must be run twice. The file 'geo.par', used for the first run, must contain safely large values of the array sizes. For example, this first 'geo.par' could be the copy of a permanent file 'geo.init', containing such sizes. The program 'geo' is compiled and run. During the first run, 'geo' calculates the minimum array sizes for 'mgfd', the post-processing programs and for itself, and writes them into the files 'mgfd.par', 'prnt.par' and 'geo.par' in the form of the parameter statements. Now, 'geo' must be recompiled and run again. During the second run, the data sequences of the minimum size are written to the files 'geo.mgfd' and 'geo.prnt'. After the second run of 'geo' we can compile and run 'mgfd'.

If the computer memory is not an important consideration, then we could use a permanent executable file for the first run of 'geo'.

Program 'mgfd':

The program 'mgfd' reads data from the files 'fas.in' and 'mgfd.in'. The file 'fas.in' contains:

- the output control parameters,
- the parameters of the multigrid procedure,
- the parameters of the smoothing procedure,
- the description of tables of the flow field parameters.

The file 'fas.in' is read by 'mgfd' before starting the multigrid procedure and after each multigrid cycle on the finest grid. This allows for updating its content and for controlling the progress of the solution process during the execution of 'mgfd'. In particular, the execution can be stopped, and the latest results for the distribution of the flow field parameters can be written to the file 'o.#', where # is the number of the last multigrid cycle, completed on the finest grid. The files 'o.#' may be used for restarting 'mgfd' from the cycle no. #, or for the analysis of the results by post processing programs. These files can be generated also during the execution of 'mgfd', in regular intervals of #.

The file 'mgfd.in' contains fixed data, which cannot be corrected during the execution of 'mgfd', such as the number # of the last multigrid cycle for restarts, the initial constant values of the flow field parameters (ignored during restarts), etc.

In addition to the files 'o.#', the program 'mgfd' produces a similar file 'init', which contains the distributions of the flow field parameters on all the grid levels, except the finest. This file is needed for restarting runs.

An output file 'res.out' contains the list of the maximum and r.m.s. residues for all the conservation equations on all the segments, grids and correction levels. It is used by the post processing program 'res.f' for plotting the convergence history. The same information, in the form of tables, is written at the same time to the diagnostic file 'mgfd.out'.

The content of 'mgfd.par' and 'geo.mgfd' is not affected by a run of 'mgfd'. Therefore, no reruns of 'geo' are needed before a new run of 'mgfd' with corrected data in 'mgfd.in' or 'fas.in'. However, if a new flow case requires other boundary values (but not data types), then the required changes should be made in 'geo.in', and 'geo' should be rerun without recompilation. If the changes affect the data types or the grid geometry, then the two compilations and runs of 'geo' are necessary, as explained earlier.

Post-processing programs:

Grid data for these programs are stored in 'geo.prnt', and the array sizes are recorded in the parameter statement of 'prnt.par'. The distributions of the flow field parameters are read from the files 'o.#'.

A common post-processing application is to display these distributions in the form of contour plots, vector plots, streamlines, etc. The post-processing program 'prnt' produces the file 'plot.dat', which contains the list of the grid point coordinates and the values of the flow field parameters at these points. The list can be used by standard computer graphics softwares, such as 'Tecplot'.

The program 'prnt' reads the data file 'prnt.in', which specifies the name 'o.#' and the position of the flow field section for display.

Use of the programs:

As an example, let us consider a case of turbulent flow of fluid with variable temperature and density, inside the domain of Figure 2. This figure shows the coarsest grid on the four constituent segments. The boundary patches with their data types and values are represented in Figures 3-6, which closely correspond to the boundary data in 'geo.in'. The patches are labeled with 1, 2, ...

Figure 3 represents the data for the velocity and pressure. The patch labels and their data types must be specified on the entire flow field boundary and on the interior boundaries with the 'i' conditions on both sides. The pairs of the 'i'-'n' patches need not be specified. By default, the type 'i' is assigned to the interface of the segment with the lower label, and 'n' to the interface of its adjacent neighbor. A specification overrides the default. It is advisable to assign the type 'i' to the interface with the finer grid cell faces. The following types are allowed on the outer boundary: 'v', 'p', 'f', 'w', 's' and 'g'. If the patches overlap, then the overlap area is assigned the type of the patch with the largest label. Thus, the type 'v' overrides 'w' inside the patch 8. The types 'i' and 'n' always override other types. The same rules are adopted for the scalar patches.

Variable distribution: $w = 20+40(0.5-\tilde{x})(1.5+\tilde{x})$ with $\tilde{x} = (x+1.9)/6.2$ was imposed on the bottom patch #20 of the segment 4 (see Figure 3). Since $-0.5 < \tilde{x} < 0.5$ on this patch, w decreases from 60 on the west symmetry plane to 20 on the east wall.

For the scalar quantities (Figures 4-6) the patch labels and data types need not be specified for

- the internal boundaries and
- the parts of the outer boundary, which have the same type as the coinciding patches of Fig. 18.0 and either no boundary values are needed ('s' and 'w' conditions) or these values are 0.

In our example, the patch labels are not specified on the west side of the segment 1, because it is an internal boundary, and on the south side for k and ε , because it has the same type 'w' as the corresponding "velocity" patch of Figure 3. The patch label had to be specified for the temperature on the south side, because it has the different type 's', and for k and ε on the east side, because non-zero boundary values are imposed.

Boundary values for k and ε are usually calculated from the formulae:

$$k = 1.5u^2 I^2$$

$$\varepsilon = c_\mu^{3/4} k^{3/2} / l$$

where the turbulence intensity I is given a value $0.02<I<0.05$ and the turbulence length scale l is set equal to a small fraction of the inlet size. For our example, we set I=0.05 for k on the patch 21 (Figure 4) and l= 0.04 (10 times less than the dimensions of the inlet) for ε on the patch 23 (Figure 5). By default, $k = \varepsilon = 0$ on the 'v'-strip of the east side of the segment 2, because no boundary values are given. Type 'w' can be specified only for k and ε . Other types for the outer boundary are: 'v', 'f', 's', 'g' and 'c'. The type 'n' is not allowed.

Use of 'geo':

We include here the input file 'geo.in' for our example.

Example of 'geo.in'

```
'Single jet'

'Number of scalar conservation laws                :',3
'Is density constant or variable  ?                :','variable'
'Density, if constant                              :',0.245
'or, if variable, density depends on scalars no.   :       '
'* * * * * * * * * * * '
 3
'Type of flow (turbulent/laminar)                  :','turbulent'
'Wall type (rough/smooth or E value)               :','smooth'
'Number of segments                                :',4
'Number of grid levels                             :',3
'Tension factor for X-grids                        :',4.0
'Tension factor for Y-grids                        :',4.0
```

```
'Tension factor for Z-grids                    :',4.0
'Scaling factor                                :',1.0
'Block sizes for the x, y and z- directions    :',20,20,20

        'Grid data for X - coordinate'
'Segment number                :', 1
'Cell size at lower end as in segment :', 0
'Cell size at upper end as in segment:', 0
' No. of cells      Node   Cell size   or prop. to   Corrected   Refine'
'in prec. piece      X      constant   size in seg   tens. fact.  grid '
' ****.*****    -*.****d-*     y          ***        ***.***      n '
              1.2000d+0
    3.0       1.5000d+0

'Segment number                :', 2
'Cell size at lower end as in segment :', 0
'Cell size at upper end as in segment:', 1
' No. of cells      Node   Cell size   or prop. to   Corrected   Refine'
'in prec. piece      X      constant   size in seg   tens. fact.  grid '
' ****.*****    -*.****d-*     y          ***        ***.***      n '
             -5.0000d+0
    6.0       1.0000d+0
    2.0       1.2000d+0                      20.0

'Segment number                :', 3
'Cell size at lower end as in segment :', 0
'Cell size at upper end as in segment:', 0
' No. of cells      Node   Cell size   or prop. to   Corrected   Refine'
'in prec. piece      X      constant   size in seg   tens. fact.  grid '
' ****.*****    -*.****d-*     y          ***        ***.***      n '
             -5.0000d+0
    3.0       1.0000d+0                   2
    2.0       1.2000d+0                   2

'Segment number                :', 4
'Cell size at lower end as in segment :', 0
'Cell size at upper end as in segment:', 0
' No. of cells      Node   Cell size   or prop. to   Corrected   Refine'
'in prec. piece      X      constant   size in seg   tens. fact.  grid '
' ****.*****    -*.****d-*     y          ***        ***.***      n '
             -5.0000d+0
    3.0       1.0000d+0                   2
    2.0       1.2000d+0                   2
```

```
'    Neighbour segments for X - direction                    '
'Segment    is preceded by    and followed by                 '
           segment          segment
' ***         ***              ***                            '
   1           2
   2                           1

        'Grid data for Y - coordinate'
'Segment number                :',  1
'Cell size at lower end as in segment :',  0
'Cell size at upper end as in segment:',  0
' No. of cells       Node    Cell size   or prop. to   Corrected   Refine'
'in prec. piece       Y      constant    size in seg   tens. fact.   grid '
' ****.*****    -*.****d-*     y          ***         ***.***       n '
              0.5000d+0
    2.0       0.7000d+0

'Segment number                :',  2
'Cell size at lower end as in segment :',  0
'Cell size at upper end as in segment:',  0
' No. of cells       Node    Cell size   or prop. to   Corrected   Refine'
'in prec. piece       Y      constant    size in seg   tens. fact.   grid '
' ****.*****    -*.****d-*     y          ***         ***.***       n '
             -1.0000d+0
    6.0       0.5000d+0
    2.0       0.7000d+0      y

'Segment number                :',  3
'Cell size at lower end as in segment :',  0
'Cell size at upper end as in segment:',  0
' No. of cells       Node    Cell size   or prop. to   Corrected   Refine'
'in prec. piece       Y      constant    size in seg   tens. fact.   grid '
' ****.*****    -*.****d-*     y          ***         ***.***       n '
             -1.0000d+0
    3.0       0.5000d+0                  2
    1.0       0.7000d+0                  2

'Segment number                :',  4
'Cell size at lower end as in segment :',  0
'Cell size at upper end as in segment:',  0
' No. of cells       Node    Cell size   or prop. to   Corrected   Refine'
'in prec. piece       Y      constant    size in seg   tens. fact.   grid '
' ****.*****    -*.****d-*     y          ***         ***.***       n '
             -1.0000d+0
```

```
    3.0        0.5000d+0              2
    1.0        0.7000d+0              2

'   Neighbour segments for Y - direction                                '
'Segment    is preceded by    and followed by                          '
'            segment          segment                                  '
' ***          ***              ***                                    '

        'Grid data for Z - coordinate'
'Segment number                :',  1
'Cell size at lower end as in segment :',  0
'Cell size at upper end as in segment:',  0
' No. of cells       Node    Cell size   or prop. to   Corrected   Refine'
'in prec. piece       Z      constant    size in seg   tens. fact.   grid '
' ****.*****    -*.****d-*     y          ***        ***.***       n '
              0.5000d+0
    4.0       0.9000d+0

'Segment number                :',  2
'Cell size at lower end as in segment :',  0
'Cell size at upper end as in segment:',  0
' No. of cells       Node    Cell size   or prop. to   Corrected   Refine'
'in prec. piece       Z      constant    size in seg   tens. fact.   grid '
' ****.*****    -*.****d-*     y          ***        ***.***       n '
              0.1000d+0
    1.0       0.3500d+0
    1.0       0.5000d+0
    4.0       0.9000d+0      y
    1.0       1.0500d+0
    1.0       1.3000d+0

'Segment number                :',  3
'Cell size at lower end as in segment :',  2
'Cell size at upper end as in segment:',  0
' No. of cells       Node    Cell size   or prop. to   Corrected   Refine'
'in prec. piece       Z      constant    size in seg   tens. fact.   grid '
' ****.*****    -*.****d-*     y          ***        ***.***       n '
              1.3000d+0
    2.0       2.1000d+0

'Segment number                :',  4
'Cell size at lower end as in segment :',  0
'Cell size at upper end as in segment:',  2
' No. of cells       Node    Cell size   or prop. to   Corrected   Refine'
```

```
'in prec. piece      Z      constant   size in seg  tens. fact.   grid '
' ****.*****    -*.****d-*     y        ***       ***.***       n '
            -0.7000d+0
    2.0       0.1000d+0

'    Neighbour segments for Z - direction                                '
'Segment   is preceded by    and followed by                             '
'           segment          segment                                     '
' ***         ***              ***                                       '
   2           4                3
   3           2
   4                            2

'     Geometry of boundary patches and boundary data types               '
Sc Pch Seg  Side          Coordinates of lower and upper corner        Type
                xl      yl      zl      xu      yu      zu
** *** *** ****** +*.***d+* +*.***d+* +*.***d+* +*.***d+* +*.***d+* +*.***d+* *
   1   1   east                                                        v
   2   1  south                                                        w
   3   1  north                                                        s
   4   1 bottom                                                        w
   5   1    top                                                       w
   6   2   west                                                       s
   7   2   east                                                       w
   8   2   east                0.350d+0                1.050d+0 v
   9   2  south                                                       s
  10   2  north                                                       s
  11   3   west                                                       s
  12   3   east                                                       w
  13   3  south                                                       s
  14   3  north                                                       s
  15   3    top                                                       g
  16   4   west                                                       s
  17   4   east                                                       w
  18   4  south                                                       s
  19   4  north                                                       s
  20   4 bottom                                                       f
 1 21   1   east                                                      v
 1 22   4 bottom                                                      v
 2 23   1   east                                                      v
 2 24   4 bottom                                                      v
 3 25   1   east                                                      v
 3 26   1  south                                                      s
 3 27   1 bottom                                                      s
```

```
 3 28  1   top                                  s
 3 29  2  east                                  s
 3 30  3  east                                  s
 3 31  4  east                                  s
 3 32  4 bottom                                  v

'       Non - zero boundary data                                        '
'Patch Number   Flow Variable   Boundary Value
'  ***      ***************    +*.***************d+*                    '
     1        u velocity      -1.0000d+2
    20        w velocity
    21         k value         0.4000d+2
    22         k value         6.0000d+0
    23         e value         1.0000d+3
    24         e value         5.0000d+0
    25         t value        4.2300d+2
    32         t value         1.2730d+3
```

Comments

'geo.in' starts with a two-line title.

Since the density is variable, the constant value 0.245 is ignored by 'geo'. In our example, the density depends only on the temperature, which is the scalar 3. Here, it should be mentioned that the scalars have labels 0, 1, 2, ... The pressure is always labeled with 0, and k and ε with 1 and 2. Other scalars are assigned the labels 3, 4, ... for turbulent flows and 1, 2, ... for laminar flows.

Accordingly, the value vs(3) is used for the definition of the density in the file 'dens'. For our example, 'dens' has the form:

```
c
c*************************************************************************
c  Formulas for variable density using the values of scalars VS(0:NSCALS)
c  VS(0) : pressure
c  VS(1), VS(2),..., VS(NSCALS) : other scalars
c  Here, perfect gas law is used with gas constant 296.9407 (air); pressure
c  was set equal to 9.81D+4 Pascals
                dens=330.36899d0/vs(3)
c  where VS(3) is the absolute temperature.
c
c*************************************************************************
c
```

The wall type can be 'rough' or 'smooth' or defined by a value of the roughness parameter E, such as: '5.25'. Smooth and rough walls have E = 9.8 and E = 1.14, respectively. E < 1.14 is not allowed.

The number of the grid levels must be larger than 0. When this number is 1, then only one grid is generated on each segment. The solution procedure of 'mgfd' is then reduced to the smoothing on one grid. If this number is larger than 1, then finer grids are generated, and the stage is set for the multigrid calculation.

The data for the tension factors are needed for the grid generation, based on the tensioned spline interpolation.

The next line determines the scaling factor, which multiplies all the Cartesian coordinates, provided in 'geo.in'. If these coordinates are given in feet, then setting the scaling factor equal to 0.304 makes 'geo' produce the final coordinates in meters.

The last line of the first part of 'geo.in' determines the maximum block sizes for the smoothing procedure, that is, the maximum number of the grid increments (scalar cells) along the three edges of a block, parallel to the x, y and z- axes.

The second part of 'geo.in' defines the geometry of the coarsest grid. Before its presentation we must explain the grid generation method used by 'geo'.

Let x(i) denote the x- coordinate of the i-th plane of the u-points, with i =0, 1, 2, ..., I between the west and east sides of a segment. Let i(x) be the inverse function, that is the number of grid increments between the west side and a grid plane x = const. The function i(x) is defined by fitting the linear or tensioned spline pieces to the data given in the second part of 'geo.in'. Analogous functions y(j), j(y), z(k) and k(z) are defined for the y- and z- grids.

Let us consider the case of the x - grid on the segment 2, defined under the titles " 'Grid data for X - coordinate' and 'Segment number:', 2." As shown in Figure 7, the range $-5.0 < x < 1.2$ of this segment is divided into the 2 intervals $x(0) < x < x(6)$ and $x(6) < x < x(8)$, containing 6 and 2 grid increments. The values of x(0), x(6), x(8) = -5.0, 1, 1.2 are listed in 'geo.in' under the title 'Node X'. The numbers of the grid increments are listed under the title 'No. of cells in prec. piece'.

In the simplest case, the physical coordinates x(0), x(1), ..., x(8) of all the grid planes are determined by fitting the tensioned spline interpolant i(x) to the data (i,x) = (0,-5.0), (6,1.0) and (8,1.2), with the tension factor given in the first part of 'geo.in'. However, in order to produce an acceptable (single-valued) interpolant it was necessary to increase the tension factor to 20. The corrected tension factors are listed under the titles 'Corrected tens.fact.'. In order to diminish the range of this tension factor we could put another tension factor in the preceding line. If a multi-valued interpolant is generated then 'geo' displays the message of the form:

> Spline slope = 0 in piece 2 of X-grid on seg: 2
> Increase tens. fact. in line 3 of X-data for seg. 2

and ends the calculation.

For increased accuracy of the discretization we may prefer constant grid increments in certain parts of the grid. This choice was made for the y and z- grids on the segment 2, in the area of the orifice: $0.5 < y < 0.7$, $0.5 < z < 0.9$ ('y' under the title 'Cell size constant'). As a consequence, this area will be divided into the cell faces of the size 0.1 in both

directions. The j(y) and k(z) interpolants include a linear piece (Figure 8). The interpolation still preserves the continuity of the derivatives dj/dy and dz/dk (that is, the grid increments vary smoothly). Obviously, if 'y' appears in 2 successive lines, then the smoothness cannot be preserved in general.

For better accuracy, it is desirable to match the grids on the internal boundaries. In order to match the grids on the common side of the segments 2 and 3, we put 2 under the title: 'or prop. to size in seg.' in the x and y- grid data for the segment 3. The grid cell faces in the area $-5.0 < x < 1.0$, $-1.0 < y < 0.5$ are twice as fine on the interface of the segment 2 then on the interface of the segment 3, and identical in the area $1.0 < x < 1.2$, $0.5 < y < 0.7$. The matching of grids reduces the interpolation errors on the interface. In our example, the grids are matched on all the internal boundaries.

Grid smoothness in the direction perpendicular to the common side of the segments 1 and 2 is enhanced by setting:

'Cell size at upper end as in segment:', 1

in the header of the x- grid data for the segment 2. Then 'geo' enforces the continuity of di/dx across the interface. As a consequence, the x- grid increment varies smoothly between the segments 1 and 2. Here, we refer to the grid increments inside segments. As mentioned previously, exterior cells are added to the segments for the continuation of the solution. We noticed that the errors of such continuations are diminished when the size of the exterior cells, measured in the direction perpendicular to the interface, is the same as the size of the first interior cell of the adjacent segment (see Figure 6 in the chapter related to the theoretical formulation of the UBC program). To enforce the agreement of these sizes, 'geo.in' provides the lists of 'Neighbor segments'. The list of the 'Neighbor segments for X - direction' identifies the segments 1 and 2 as neighbors. Similar list for the z- direction provides information about the relative position of the segments 2, 3 and 4. The list for the y- direction is empty, since there are no internal boundaries $y = \text{const}$. If a pair of adjacent segments does not appear in a list of 'Neighbor Segments', then the exterior grid increments are set equal to the derivatives dx/di, dy/dj or dz/dk (the exterior cell size is the extrapolation of the interior size).

We now proceed to the presentation of the third part of 'geo.in', entitled 'Geometry of boundary patches and boundary data types'. It is easy to see the close correspondence between figures 3-6 in the chapter on the theoretical formulation and the list under this title. Each figure corresponds to a different scalar label 'Sc'. If the 'Sc' field is empty in a line of data, then this line defines a velocity or pressure condition and corresponds to one of the patches of Figure 3. If the 'Sc' field contains a scalar label 1, 2 or 3, then the line of data refers to one of the scalar patches in Figure 4, Figure 5 and Figure 6, respectively.

If the x- range $xl < x < xu$ of a patch is identical to the x- range of the segmental side, to which the patch belongs, then xl and xu need not be specified. The same convention is adopted for the ranges $yl < y < yu$ and $zl < z < zu$. In our example we had to provide zl and zu for the patch 8, which is not the same as the east side of the segment 2.

The last part of 'geo.in', entitled 'Non-zero boundary data', determines the boundary values, which are constant and different from 0 over their patches.

The following 'Flow Variables' are allowed for the velocity patches of the 'v' or 'w' type:

mass flux, u velocity, v velocity, w velocity

However, either the mass flux or the normal velocity component can be specified, but not both quantities simultaneously. If the normal velocity is specified, then 'geo' calculates the mass flux using the local value of the density. The mass fluxes and the tangential velocity components on all the cell faces are collected in a sequence 'bdat' and stored in 'geo.mgfd'. For the 'w' patches, the tangential components define the wall velocity rather than the fluid velocity.

For the velocity patches of the 'f' type we also allow the 'Flow Variables':

u momentum flux, v momentum flux, w momentum flux

If not provided directly, the mass and momentum fluxes are calculated using the given values of the velocity components and density. For all the cell faces of the 'f' type, the four fluxes are stored in 'bdat'.

The only flow variable needed for the 'p' condition is pressure. The conditions 'g', 's', 'i' and 'n' do not require any boundary values.

One 'Flow Variable' is required for the scalar 'f' condition. It must contain one of the words: 'flux' or 'value'. Examples: T flux, k value. If the value is specified, then the scalar flux is calculated using the given mass flux.

One 'Flow Variable' is required for the scalar 'v' and 'g' conditions. Its name is an arbitrary text constant of no more than 15 characters. Examples: e value, T gradient. The scalar 's' and 'i' conditions ('n' is not allowed) and the 'w' conditions for k and ε do not require any 'Flow Variables'.

Two 'Flow Variables' are needed for the 'c' condition: 'coefficient' and 'free term'. They represent the coefficient α and the free term β in (13).

The 'Flow Variables' directly or indirectly define the boundary data collected in 'bdat', for use by 'mgfd'. If the required 'Flow Variables' do not appear in the list of the 'Non-zero boundary data', then 'geo' sets them equal to 0 on respective patches. If they appear in this list with a non-zero 'Boundary Value' then 'geo' sets them equal to this value on the entire patch. If a 'Flow Variable' appears in this list, but the 'Boundary Value' is empty or 0, then it is assumed that this 'Flow Variable' is non-constant on the patch.

The distributions of such 'Flow Variables' are defined by the subprogram 'cbv' of 'geo'. For our example, the following subprogram defines the 'w velocity' on the patch 20.

```
      function cbv(n,fv,x,y)
c
c  Calculation of a boundary value for the flow variable FV on the data patch
c  no. N at the point with the normalized patch coordinates X and Y; normalized
c  coordinates are obtained by shifting and scaling the physical coordinates;
c  in normalized coordinates patch occupies the square -0.5 < X, Y < 0.5.
c
      implicit double precision (a-h,o-z)
```

```
      character fv*15
c
c  Insert the definition of CBV between the lines of stars
c**********************************************************************
      if (n.eq.20.and.index(fv,'w velocity').ne.0) then
            cbv=20.0d0+40.0d0*(0.5d0-x)*(1.5d0+x)
      endif
c**********************************************************************
      return
      end
```

For more complex problems, 'cbv' may contain the definitions of boundary values for more patches and flow variables, involving input operations, the interpolation of the input data, calls of other subprograms, etc. As mentioned in the comment to 'cbv', the boundary value is expressed as a function of the normalized coordinates -0.5 < X, Y < 0.5. Here, (X, Y) may denote the shifted and scaled physical coordinates (x,y), (x,z) or (y,z).

The file 'geo.in' ends with a line of blanks.

Examples of 'geo.par'

For the first run 'geo' was compiled with the file 'geo.par', which we print here together with comments:

```
c  Constants - array sizes - for the programs GEO and MGFD.
c
c  Before the first run of GEO put safely large values of constants (below)
c  and copy this file to GEO.PAR. Compile and run GEO.
c  GEO finds the precise values of constants, and writes them to GEO.PAR and
c  MGFD.PAR, included in subprograms of GEO and MGFD.
c  GEO should then be recompiled and run again, before the compilation and
c  runs of MGFD.
c  In this way the memory requirements of GEO and MGFD are minimized.
c
c  INIT        : here, always 0 (becomes 1 after the first run of GEO)
c  MXSEG       : number of segments
c  MAXLEV      : number of multigrid levels
c  MXSC        : number of scalar conservation laws
c  MXCELL      : number of fine grid cells in one coarse grid cell
c  MXPT        : total number of 'data patches' on segmental boundaries
c  NODX        : maximum number of data points (spline nodes), defining the X-grid
c          on a segment
c  NODY, NODZ          : the same for Y and Z - grids
c  MXPX        : maximum number of points of the finest grid along X - edge of
c          a segment
c  MXPY, MXPZ          : the same for Y and Z - edges
c  MXDX        : total number of all X - grid cells on all segments and multigrid
c          levels
c  MXDY, MXDZ          : the same for Y and Z - grids
c  MXBLK       : maximum number of the smoothing blocks along an edge of a segment
c  MXBLKS      : maximum total number of smoothing blocks on all the grids
```

```
c MXNR          : total number of "non-receiver" boundary cell faces on all levels
c           except finest
c INTPS         : total number of 'donor' cell faces on segmental boundaries on all
c           levels
c NGPTS         : total number of 'receiver' cell faces on segmental boundaries
c MXBCS         : total number of scalar boundary cell faces on all segments and
c           grid levels
c MXBDAT        : total number of boundary data values on all segments and grid
c           levels
c MXFPS, MXCPS, MXCF        : sizes of the sequences NF1,NF2,N1,N2,MC and CF to
c            be used by the program MGFD for the continuation of velocity
c            components and pressure across segmental boundaries
c
      parameter(
c
     +     init = 0  ,
     +     mxseg = 5  , maxlev = 3  , mxsc  =  5 ,
     +     mxcell= 8  , mxpt  = 1000,
     +     nodx  = 200 , nody  = 200 , nodz  = 200 ,
     +  mxpx  = 1000, mxpy  = 1000, mxpz  = 1000,
     +  mxdx  = 5000, mxdy  = 5000, mxdz  = 5000,
     +  mxblk = 200 , mxblks = 10000,
c Other constants are usually larger:
     +  mxnr  = 50000 , intps  = 50000 , ngpts  = 50000 ,
     +  mxbcs = 500000, mxbdat = 500000,
     +  mxfps = 1000000, mxcps  = 1000000, mxcf  = 1000000
c
     + )
```

As a result of the first run, 'geo.par' is changed to

```
      parameter (init=1,mxseg=  4,maxlev= 3,
     +mxsc= 3,mxcell=  4,mxpt=  33,nodx=  3,
     +nody=  3,nodz=  6,mxpx=  33,mxpy=  33,
     +mxpz=  33,mxdx=  195,mxdy=  174,mxdz=  160,
     +mxblk=  2,mxblks=  19,
     +mxnr= 2700,intps=  2856,ngpts=  2856,mxbcs=  68476,
     +mxbdat=  26718,mxfps=  70363,mxcps=  45505,
     +mxcf=  135104)
```

This time, init = 1, and the other parameters have the minimum allowable values. Similar files 'mgfd.par' and 'prnt.par' are generated for 'mgfd' and 'prnt'. Now, 'geo' must be recompiled with the new parameters. As a result of the second run, the grid geometry and boundary condition data are written to the files 'geo.prnt' and 'geo.mgfd' for use by 'mgfd' and other post-processing programs.

Diagnostic output: 'geo.out'

Each run of 'geo' generates 'geo.out'. Among other information, this file contains the lists of the calculated grid point coordinates for all the segments and grid levels. An example of such a list:

Z - grid on segment 3
Multigrid level: 3

Cell no.	Length	Midpoint	Endpoint
0	0.620446D-01	0.119232D+01	0.122334D+01
1	0.766579D-01	0.126167D+01	0.130000D+01
2	0.105391D+00	0.135270D+01	0.140539D+01
3	0.102943D+00	0.145686D+01	0.150833D+01
4	0.101441D+00	0.155905D+01	0.160977D+01
5	0.100376D+00	0.165996D+01	0.171015D+01
6	0.994389D-01	0.175987D+01	0.180959D+01
7	0.983924D-01	0.185878D+01	0.190798D+01
8	0.970038D-01	0.195648D+01	0.200498D+01
9	0.950151D-01	0.205249D+01	0.210000D+01
10	0.937500D-01	0.214687D+01	0.219375D+01
11	0.937500D-01	0.224062D+01	0.228750D+01

Let us note that the exterior cells 0, 1 and 10, 11 are added on both sides of the segmental range $1.3 < z < 2.1$. The reasons for using the 2 - cell margins are technical, and is explained elsewhere. Often, an excessive irregularity of the grid causes difficulties during the solution phase. Therefore, it is advisable to study the contents of 'geo.out' or plot the grids before running 'mgfd'.

Use of 'mgfd'

Example of 'mgfd.in:'

```
'Restart after mg-cycle no. (start: empty string)                    :' '
'Direction of gravity (x, -x, y, -y, z, -z or empty)                 :' '-z'
'Include terms DIV(MU*DU/DX) in the momentum equations (y/n)         :' 'n'
'Laminar dynamic viscosity coefficient                               :' 2.0d-5
'Starting value of U - velocity component on coarsest grid           :' 0.0
'Starting value of V - velocity component on coarsest grid           :' 0.0
'Starting value of W - velocity component on coarsest grid           :' 20.0
'Starting value of pressure on coarsest grid                         :' 0.0
'Starting value of turbulence energy on coarsest grid                :' 6.0
'Starting value of turbulence dissipation on coarsest grid           :' 5.0
'Starting value of temperature on coarsest grid                      :' 1.273d+3
'

'Fixed pressure values and finest grid coordinates of their locations
'Segment    Pressure at    I    J    K
' ***      +*.***d+*     ***  ***  ***
```

Comments:

Solution procedure is started from the coarsest grid when the string at the end of the line 'Restart after mg-cycle ...' is empty. When this string is '0', then 'mgfd' reads the files 'init' and 'o.0', produced by a previous run, which ended with the first series of smoothings on the finest grid. Next, 'mgfd' continues the first multigrid cycle on the finest grid. When this string is '1', '2', ..., then 'mgfd' restarts the calculation after the specified number of cycles, using the data stored in 'init' and 'o.1','o.2',...

'Direction of gravity' is ignored when the density is constant, or when the string, which follows, is empty.

'Include terms ...' is ignored when the flow is laminar. For the turbulent flows 'y' or 'n' in this line switches on and off the correction of the free term in (24), due to the turbulent sources in the momentum equations. The influence of these terms is usually small.

'Starting values ...' define the initial constant distributions of the flowfield parameters. They are ignored when the string, which follows 'Restart...', is not empty.

The last part of 'mgfd.in' serves to impose the values of pressure at the p- points with the finest grid coordinates I, J and K (I = 1, J = 1, K = 1 correspond to the first p-planes inside a segment). For example, in the case of a channel flow with the 'g' condition at both ends, two pressure values must be imposed to ensure the uniqueness of the solution. With the present version of 'mgfd', no more than 2 pressure values can be imposed on a segment. The pressure is adjusted, after each smoothing, by adding a constant or linear correction on a segment. The point-pressure option should be used with caution. Let us note that it is impossible to fix arbitrary values of pressure at 2 or more points of the flowfield of Figure 3. Only one point value can be imposed in this case. If the density does not depend on the pressure, then this value is arbitrary, and need not be imposed at all. The pressure is then allowed to evolve freely during the solution phase. Usually, this results in better convergence rates.

The file 'mgfd.in' ends with a line of blanks.

Example of 'fas.in'

```
'    OUTPUT CONTROL PARAMETERS                                    '
'Do you want to stop before the next mg-cycle (y/n)                :' 'n'
'Do you want to store final results (y/n)                          :' 'y'
'Do you want to display residue norms after smoothing (y/n)    :' 'y'
'Write residue norms if smoothing no. is divisible by              :'  0
'Store results if mg-cycle no. is divisible by                     :'  100
'                                                                  '
'    PARAMETERS OF THE MULTIGRID PROCEDURE                        '
'No of smoothings for solution on coarsest grid                :'  300
'No of smoothings for corrections on coarsest grid, except highest     :'  50
'No of smoothings for corrections of highest order             :'  50
'No of initial smoothings for solutions on intermediate grids      :'  10
'No of initial smoothings for solution on finest                   :'  10
'No of initial smoothings on fine grids of correction levels   :'  10
'No of smoothings on coarse grids of correction levels         :'  50
'No of smoothings after adding a correction                        :'  10
```

```
'No of mg-cycles for solutions on intermediate grids      :' 10
'No of mg-cycles for solution on the finest grid                :' 40
'No of mg-cycles for corrections                                :' 2
'Multigrid procedure for energy equation starts from mg-cycle no.  :' 0
'
'   PARAMETERS OF THE SMOOTHING PROCEDURE                                '
'Artificial time step on coarse grid                            :' 1d15
'Mass defect fluctuation damping coefficient on coarse grid     :' 0.0
'Artificial time step on intermediate grids                     :' 1d15
'Mass defect fluctuation damping coefficient on intermediate grids  :' 0.0
'Artificial time step on finest grid                :' 0.05
'Mass defect fluctuation damping coefficient on finest grid     :' 0.0
'
'Underrelaxation factor for turbulence quantities near walls    :' 1.0
'Turbulence production underrelaxation factor       :' 1.0
'
'Velocity underrelaxation factor on coarsest grid   :' 0.6
'Pressure underrelaxation factor on coarsest grid   :' 0.8
'Turbulence energy underrelaxation factor on coarsest grid      :' 1.0
'Turbulence dissipation underrelaxation factor on coarsest grid :' 1.0
'Temperature underrelaxation factor on coarsest grid :' 1.0
'Constant correction of dynamic viscosity on coarsest grid      :' 0.0
'
'Velocity underrelaxation factor on intermediate grids  :' 0.6
'Pressure underrelaxation factor on intermediate grids  :' 0.8
'Turbulence energy underrelaxation factor on intermediate grids  :' 1.0
'Turbulence dissipation underrelaxation factor on intermediate grids  :' 1.0
'Temperature underrelaxation factor on intermediate grids  :' 1.0
'Constant correction of dynamic viscosity on intermediate grids  :' 0.0
'
'Velocity underrelaxation factor on finest grid                  :' 0.8
'Pressure underrelaxation factor on finest grid                  :' 0.8
'Turbulence energy underrelaxation factor on finest grid         :' 1.0
'Turbulence dissipation underrelaxation factor on finest grid    :' 1.0
'Temperature underrelaxation factor on finest grid   :' 1.0
'Constant correction of dynamic viscosity on finest grid  :' 0.0
'
'                    PRINTOUT DESCRIPTIONS                           '
'                    Bounds for grid coordinates                     '
```

						Iteration no			I		J		K	
R	Sc	Name	Seg	Lev	Cor	First	Last	Step	First	Last	First	Last	First	Last
C	**	******	***	*	*	***	***	***	***	***	***	***	***	***
		U	2	3	0	5	10	5	16	33	8	16	16	16
		V	2	3	0	5	10	5	16	32	8	17	16	16
		W	2	3	0	5	10	5	16	32	8	16	16	16
		P	2	3	0	5	10	5	16	32	8	16	16	16
	1	K	2	3	0	5	10	5	16	32	8	16	16	16
	2	E	2	3	0	5	10	5	16	32	8	16	16	16
R		P	2	3	0	5	10	5	0	-1	8	16	16	16
C		P	2	2	1	5	10	5	0	-1	8	16	16	16

Comments:

As mentioned earlier, this file is read by 'mgfd' at the beginning of the calculation and at the end of each multigrid cycle on the finest grid. Therefore, it allows to control the output and the parameters of the solution procedure during the execution of 'mgfd'.

By putting 'y' at the end of the first line of data we can stop the execution of 'mgfd' at the end of the current multigrid cycle, after completing a prescribed series of smoothings on the finest grid.

If the second line ends with 'y', then the final results are stored in the file 'o.#', where # is the number of the last cycle. These final results are obtained either by stopping the execution of 'mgfd' in the manner described above, or by completing the precribed 'No of mg-cycles for solution on the finest grid', which is one of the 'PARAMETERS OF THE MULTIGRID PROCEDURE'.

'mgfd' writes the maximum and r. m. s. residues for all the conservation equations, on all the segments and all the grid and correction levels, into the file 'mgfd.out', after completing each series of smoothings, whose number on various levels is prescribed in the 'PARAMETERS OF THE MULTIGRID PROCEDURE'. The residues are simultaneously displayed on the screen of the computer terminal, if the question 'Do you want to display residue norms after smoothing' is answered with 'y'.

The residues can be written to 'mgfd.out' more frequently. The number of smoothings between the successive additions to 'mgfd.out' is prescribed in the line 'Write residue norms if smoothing no. is divisible by:'. One smoothing is a complete sweep of the flowfield with the zebra-line procedure described previously.

In addition to the final output, the complete distributions of the flowfield parameters can be stored in the files 'o.#' in regular intervals of #, prescribed after the title 'Store results if mg-cycle no. is divisible by:'.

Let us proceed to the explanation of the 'PARAMETERS OF MULTIGRID PROCEDURE':

'No of smoothings for solution on coarsest grid' is the parameter $m_0^{(1)}$ of the flow-chart in ZZFig. 11.

'No of smoothings for corrections on coarsest grid, except highest' is the parameter $m_{\tilde{L}}^{(1)}$ for $\tilde{L} = 2, ..., L - 1$ (ignored when the finest grid level $L < 3$).

'No of smoothings for corrections of highest order' is the parameter $m_L^{(1)}$ (ignored when $L = 1$).

'No of initial smoothings for solutions on intermediate grids' is the parameter $m_{L,0}^{(2)}$ for $\tilde{L} = 2, 3, ..., L-1$ (ignored when $L < 3$).

'No of initial smoothings for solution on finest grid' is the parameter $m_{L,0}^{(2)}$ (ignored when $L = 1$).

'No of initial smoothings on fine grids of correction levels' is the parameter $m^{(2)}_{\tilde{L},n}$ for $\tilde{L}$ = 3, 4, ..., L and n = 1, 2, ..., $\tilde{L}$ - 2 (ignored when L < 3).

'No of smoothings on coarse grids of correction levels' is the parameter $m^{(3)}$ (ignored when L < 3).

'No of smoothings after adding a correction' is the parameter $m^{(4)}$ (ignored when L = 1).

'No of mg-cycles for solutions on intermediate grids' is the parameter $M_{\tilde{L},0}$ for $\tilde{L}$ = 2, 3, , L - 1 (ignored when L < 3).

'No of mg-cycles for solution on the finest grid' is the parameter M (ignored when L = 1).

'No of mg-cycles for corrections' is the parameter $M_{\tilde{L},n}$ for $\tilde{L}$ = 3, 4, ..., L and n = 1, 2, , $\tilde{L}$ - 2 (ignored when L < 3).

The multigrid procedure for the specified scalars can be postponed until a prescribed number of cycles for the momentum and continuity equations has been completed on the finest grid. Until then, the solution procedure for these scalars is reduced to smoothing on the finest grid. In our example:

'Multigrid procedure for energy equation starts from mg-cycle no. : ' 0,

so that the multigrid procedure is applied from the beginning as for the fluid-dynamic equations. As mentioned earlier, k and ε are always excluded from the multigrid correction procedure. Therefore, the last lines of the 'PARAMETERS OF THE MULTIGRID PROCEDURE' should define the starting cycle for the successive scalars, except k and ε.

The next part of 'fas.in' defines the 'PARAMETERS OF THE SMOOTHING PROCEDURE'. If the finest grid level is L = 1, then the parameters for the intermediate and finest grids are ignored. The intermediate grid parameters are ignored also when L = 2.

'Artificial time step on coarse / intermediate / finest grid' is the value Δt in the stabilizing correction of Section III.5.2.

'Mass defect fluctuation damping coefficient on coarse /intermediate / finest grid' is the coefficient c_δ of the stabilizing term in (27).

The data, which follow, specify the underrelaxation factors for the flowfield parameters on all the grids (including all the scalars in their prescribed order) and the constant corrections, added to the dynamic viscosity coefficient. The small corrections of the turbulent viscosity may improve the convergence, without seriously affecting the converged results. They may be needed when the turbulent viscosity becomes unrealistically small in certain parts of the flowfield, as it sometimes happens with the present k - ε model.

The grid distributions of the flowfield parameters, the residues or the multigrid corrections for chosen parts of the flowfield can be written, in the form of tables, to the file 'mgfd.out' during the execution of 'mgfd'. For our data, the distributions of u, v, w, p, k, ε and T on the grid level 3, correction level 0 (solutions) inside or on the boundary of the quarter $16 < I < 32$, $8 < J < 16$ of the cross-section $K = 16$ of the segment 2 (area around the middle of the orifice) are tabulated after the 5th and 10th multigrid cycle. Setting 'First' grid coordinate larger than the 'last' results in the tabulation within its entire range. Thus, the residues ('R') of the continuity equation (identified with the name 'P') are tabulated inside the whole strip $8 < J < 16$ of the cross-section $K = 16$. The multigrid corrections 'C' of the pressure ('P') are tabulated for this strip on the grid 2, correction level 1, before prolongation. In this way, the possible failures of the multigrid method can be investigated very closely by an experienced user.

The file 'fas.in' ends with a line of blanks.

Use of the restart option: examples:

The program 'mgfd' was compiled and the first run was made with
'Restart after mg-cycle no. :' ' '
in 'mgfd.in' and
'No of mg-cycles for solution on the finest grid : ' 5
in 'fas.in'. As a result, the files 'init' and 'o.5' were generated. For the next run we put
'Restart after mg-cycle no. :' ' 5 '
and
'No of initial smoothings for solution on finest grid : ' 0
since sufficient number of 10 smoothings was made at the end of the previous run, after adding the correction. The final results are now stored in 'o.10'.

The restart option allows to investigate the performance of 'mgfd' on chosen grids and correction levels. For example, in order to examine the performance of the smoother on the finest grid, the first run could be made with
'No of mg-cycles for solution on the finest grid : ' 0
and
'No of initial smoothings for solution on finest grid : ' 10
During this run, the multigrid process is completed on the coarser grids, 10 smoothings are made on the finest grid, and the results are written to 'o.0'. We can now
'Restart after mg-cycle no. :' ' 0 '
with, for example,
'No of initial smoothings for solution on finest grid : ' 20
and
'No of initial smoothings on fine grids of correction levels : ' 0
'No of smoothings on coarse grids of correction levels : ' 0
'No of smoothings after adding a correction : ' 0
'No of mg-cycles for solution on the finest grid : ' 1
'No of mg-cycles for corrections : ' 0

One cycle, made in the second run, is reduced to 20 additional smoothings on the finest grid. The results are stored in 'o.1', which can be used for the next
'Restart after mg-cycle no. :' ' 1 '.

As another example, we could reduce the cycle, made in the second run, to 20 smoothing on the grid 2, correction level 1, by choosing
'No of initial smoothings for solution on finest grid :' 0
'No of initial smoothings on fine grids of correction levels :' 20

For very complex or unstable flows the multigrid method, when not applied correctly, may not yield convergence. A remedy is to run 'geo' with 'Number of grid levels' equal to 1 in 'geo.in'. As mentioned earlier, the solution procedure of 'mgfd' is then reduced to the smoothing on one grid, which is slow, but often more reliable. All the 'PARAMETERS OF THE MULTIGRID PROCEDURE' are then ignored, except 'No of smoothings for solution on coarsest grid'. If this number is 100, for example, then the results are stored in 'o.100'. We could now
'Restart after mg-cycle no. :' ' 100 '

The results of the second run are written to 'o.200'. New series of smoothings may use different sets of the 'PARAMETERS OF THE SMOOTHING PROCEDURE' for the coarsest grid (other parameters are ignored). By comparing residues, tabulated in 'mgfd.out' or displayed on the screen, we can optimize these parameters. The optimized parameters could now be used for the improved multigrid calculation. In difficult cases such optimization may also be needed on the finer levels.

Exchangeable parts of 'mgfd':

By changing the formula for the density in the file 'dens' and the formulas for the diffusivity coefficients and the source terms in the conservation equations, it is possible to adapt the system 'geo'-'mgfd' to a wide variety of practical problems. For convenience, the exchangeable parts of 'mgfd' are separated from the other parts by the lines of stars. One of these parts defines the viscosity (here, the formula (8) is used):

```
c*********************************************************************
c CMU          : was set equal to 0.09
c RHO(i,j,k)   : density
c SCL(i,j,k,1) : kinetic energy of turbulence
c SCL(i,j,k,2) : its dissipation
c TVISC(i,j,k): turbulent viscosity
c
                 te=scl(i,j,k,1)
                 tvisc(i,j,k)=cmu*rho(i,j,k)*te*te/scl(i,j,k,2)
c*********************************************************************
```

The definition of the diffusivity coefficient in the energy equation is given by another exchangeable part:

```
c*********************************************************************
c Definition of the diffusivity coefficient for the non-turbulent scalars.
c Here, Prandtl's number is assumed to be 1.
c FLOW         : 'laminar' or 'turbulent'
```

```
c DIFF(i,j,k)     : values of the diffusivity for these scalars
c TVISC(i,j,k):  values of the turbulent viscosity
c VLAM            : laminar viscosity
c
                  if (flow.eq.'turbulent') then
                        diff(i,j,k)=tvisc(i,j,k)+vlam
                  else
                        diff(i,j,k)=vlam
                  endif
c*********************************************************************
```

The buoyancy term B_1 is included into the z- momentum equation (3) by using the exchangeable part:

```
c*********************************************************************
c  Source term in the w-momentum equation at (i+1/2,j+1/2,k) is defined as:
c        WSRC + WSRP * W(i,j,k)
c  In our example :
c
                  wsrp=0.0d0
c  and
                  wsrc=-9.81d0**(rho(i,j,k)-rho0)
c  where RHO0 is a constant (initial value of the density).
c*********************************************************************
```

The source terms in the other conservation equations are defined similarly, as sums of the form $S_C + S_P \phi$.

Diagnostic output: 'mgfd.out':

An example of the output after a series of smoothings:

Residues inside segment: 2

Variable	Max. residue at	I	J	K	Rms residue
U	.529D-09	26	32	24	.966D-11
V	.254D-09	31	27	26	.721D-11
W	.234D-09	24	31	26	.112D-10
P	.481D-11	25	30	24	.259D-12
1	.142D-07	25	32	24	.118D-09
2	.811D-05	32	24	16	.688D-07
3	.417D-08	26	32	24	.159D-09

Residues and Y+ on the boundary of segment: 2

Side	Var	Type	Max residue at	I	J	K	Rms residue	Min Y+	Max Y+	Mean Y+
east	U	w	.595D-59	33	32	29	.797D-60	.185D+03	.535D+03	.370D+03
east	1	w	.209D-12	32	23	29	.494D-13			
east	2	w	.464D-10	32	23	29	.112D-10			
bottom	w	i	.378D-10	5	31	1	.593D-11			
top	w	i	.807D-10	22	24	33	.687D-11			

Mass flows through sides of segment : 2

east	-0.62481132859359D+01
bottom	0.12772796147616D+03
top	0.13397607476209D+03
total:	-0.17053025658242D-12

The grid coordinates I, J and K are counted starting from the first grid planes, which belong to the segment or to its boundary. For example, I = 1 in the line with 'U' as the 'Variable' would refer to the maximum residue of the u- momentum equation on the west side of the segment, while with 'P' as the 'Variable' this would be the reference to the maximum residue of the continuity equation on the first interior plane of the p- points.

In the last part, only non-zero mass flows are listed.

Use of the post-processing programs and the associated files:

Example of the input file 'prnt.in' :

```
'Plot title:'  'Paul Nowak Test case            : 1'
'Data file containing solution vector           :' 'o.40'
'Slicing plane (xy, zx, yz, or 3d)              :' 'xy'
'Physical coordinate of the xy, xz or yz slice  :'  0.7
'Problem type (laminar/turbulent)               :' 'turbulent'
'Additional TECPLOT scalar variable labels      :' ' ,temp  '

  'List of participating'
  'segments in the slice'
      **
              1
              2
```

The program 'prnt' reads the flowfield data from 'o.40', and produces the file 'plot.dat', containing the list of the (x, y) - coordinates of the grid points in the section z = 0.7 of the segments 1 and 2, and the values of the flow variables at these points. The program was modified for the use with the plotting package TECPLOT.

The file 'plot.dat' is used directly by TECPLOT. For our example it contains the list of the (x, y)- coordinates and the values of u, v, w, p, k, ε , kinetic turbulent viscosity, turbulence length scale, turbulence intensity, defined as $(2 * \sqrt{k} / 3) / u$, and temperature. On the finest grid in the section z = 0.7, the vector plot of the velocity distribution, projected onto the section, and the contour plots of all the specified scalars are shown in Figure 9 to Figure 16. Discussion of these results will be given elsewhere.

For our example, the convergence history during 40 three-grid cycles is presented in Figure 17. The residues on the grid 3 are reduced at the steady rate of about three orders of magnitude per 150 work units (one work unit is equivalent to one smoothing on the finest grid). Figure 17 was plotted using another post-processing program resv5.f, which reads the residue norms from the file 'res.out', produced by 'mgfd'.

Structure of 'geo'

Figure 18 shows the dependence structure of the various parts of the program 'geo' and its associated files.

Subprograms of 'geo':

Subroutine 'grid' calculates the parameters, which define the piecewise linear or tensioned spline interpolants i(x), j(y) and k(z) of the grid coordinates i, j and k as functions of the physical coordinates x, y and z (Figure 7, Figure 8). The grid point coordinates are read from 'geo.in'.

Subroutine 'divbl' divides segments into blocks. The x, y and z- ranges of the segments are divided into intervals, which define the size of the blocks. The blocks are ordered in a checkerboard fashion by the main program 'geo'.

Logical function 'defect' becomes .true. when the slope of a tensioned spline interpolant equals 0 within its physical range. Near such points, the grid increments degenerate to 0 or become negative. A message is then displayed, which indicates the corrective action (a local increase of the tension factor) and the execution of 'geo' is stopped.

Subroutine 'tenspl' interpolates data using tensioned splines. This subroutine is a modification of the subroutine 'curv1', published by [Cline, 1974].

Function 'valspl' calculates the value of a tensioned spline at a point of its range; 'valspl' is a modification of the function 'curv2' from [Cline, 1974].

Function 'derspl' calculates the derivative of a tensioned spline at a point of its range.

Subroutine 'coord' calculates the physical coordinates x(i), y(j) or z(k) of the finest grid points along a grid line in a segment. The interpolants i(x), j(y) or k(z) are inverted for this purpose.

Function 'root' inverts the functions i(x), j(y) or k(z) by Newton's method.

Subroutine 'stagrd' generates the sequences of coordinates for the u, v, w and p- points.

Subroutine 'bdata' reads boundary data from 'geo.in' and generates the sequences 'type', 'bdat' and 'ndat', which contain the data types, values and pointers to these values, for rapid access by 'mgfd'.

Function 'cbv' calculates the boundary data, which are variable over corresponding boundary patches. An example of 'cbv' was presented earlier.

Subroutine 'intfac' allocates the mass flows from the "donor" cells (type 'I') to the "receiver" cells (type 'n') on the segmental interfaces. The interface cells are indexed. The indices for the donor-receiver cell pairs and the mass flow allocation ratios for such pairs are stored in the sequences 'ngnr' and 'wght'.

Subroutine 'segnrs' determines all the segments, which contain a given point (x, y, z) in the inerior or on the boundary.

Subroutine 'grcrd' determines the grid coordinates (i, j, k) of a given point (x, y, z) in a segment.

Function 'xk' solves the equation (75) for b on the outer boundary of the laminar sublayer.

Function 'q' solves the equation (80) for q outside the laminar sublayer. In the main program 'geo' this equation is solved at about 500 values of α and then the piecewise cubic interpolant is fitted through the points (α, $q(\alpha)$). The coefficients of this interpolant are stored in the sequence 'a'.

Examples of included files 'dens' and 'geo.par' were previously.

Structure of 'mgfd':

Figure 19 represents the information flows during the execution of 'mgfd'.

Subprograms of 'mgfd':

Subroutine 'inifas' reads the data file 'fas.in', containing the control parameters for the output and the solution procedure; 'inifas' is called before the beginning of the multigrid procedure ('fas') and then inside 'fas', after each cycle on the finest grid.

Subroutine 'fas' is the implementation of the multigrid method FAS2 for an arbitrary number of grid levels (Fig. 11). It reads the control parameters from 'fas.in', through 'inifas'. For restarts, previous results are read from 'init' (the solutions on the coarser grids), and 'o.#' (the finest grid solution after the cycle no. #). Current results are written to 'init' before starting the first cycle on the finest grid, and to the files o.# in regular intervals of # or at the end of the calculation.

Subroutine 'iofas' is called from 'fas' to read or write 'init' or 'o.#'.

Subroutine 'smtrsd' : smoothing or calculation of the residues. These operations are performed "block - by - block", in the checkerboard order prescribed by 'geo'.

Subroutine 'contin' is called inside 'smtrsd' before smoothing or calculation of residues; 'contin' continues the distributions of the flowfield parameters into the segmental margins (one or two exterior grid planes), updates the density inside the flowfield and the mass flows on the segmental interfaces.

Subroutine 'block : one smoothing by the zebra-line methods of Section IV.3.5 or calculation of residues inside a block.

Subroutine 'line': Vanka's procedure for the velocity components and the pressure, and the inversion of the tri-diagonal systems for the scalars on a grid line; 'line' is used by 'block' in an alternating zebra pattern, for all the lines parallel to the three space directions.

Function 'coeff' : correction of the discrete momentum equations at the edges of the flowfield, which belong to the segmental interfaces with the 'i' condition on both sides; a small correction is required, since otherwise two different discrete equations are generated at the same edge point when the two adjacent segments are visited for smoothing.

Subroutine 'pfix' : calculation of the pressure correction, constant or linear on a segment; this correction is added to enforce the point - pressure values, prescribed by 'mgfd.in'.

Subroutine 'errors' : output of the maximum and r. m. s. residues to 'mgfd.out', 'res.out' and to the screen. Calculation and output of the mass flows through the segmental boundaries, and of the total mass imbalance.

Subroutine 'uvwprt' : writes tables of the flowfield parameters, residues or multigrid corrections to 'mgfd.out', as specified by 'PRINTOUT DESCRIPTIONS' of 'fas.in'.

Subroutine 'restr' : restriction of residues for 'fas' by the "full weighting".

Subroutine 'prolon' : prolongation of the solutions or corrections by the tri-linear interpolation.

Logical function 'criter' : provides convergence criterion for the multigrid correction procedure. The present version of 'mgfd' uses fixed numbers of cycles M on all the grid and correction levels (l, n).

Input files for post-processing programs

File 'geo.prnt'

The file 'geo.prnt', generated by 'geo', provides the description of the flow field and grid geometry. It contains:

nlevs : number of the grid levels (> 1);

nsegs : number of segments;

nscals : number of the scalar conservation equations;

npx(nsegs) : for each segment this sequence contains the number of nodes listed under the title 'Node X' in 'geo.in'.

npy(nsegs), npz(nsegs) : analogous sequences for the other directions.

nu(nsegs, nlevs): defines the position of the u- values in the global solution sequence 'u0' (Section V.4.2); the first u- value on the segment m and the grid l occupies the position nu(m,l) + 1 in this sequence;

nv(nsegs,nlevs), nw(nsegs,nlevs), nscl(nsegs,nlevs,0:nscals) : contain analogous pointers to the first values of v, w and scalars, including pressure (scalar 0);

ndz(nsegs,nlevs): defines the position of the z- coordinates in the sequences 'zws' and 'zus' (see later comments); the first z- coordinates of the w and u-points on the segment m and the grid l, occupy the position ndz(m,l) + 1 in the corresponding sequences 'zws' and 'zus';

ndy(nsegs,nlevs): provides such pointers to the y- coordinates of the v and u-points in the corresponding sequences 'yvs' and 'yus';

ndx(nsegs,nlevs): provides such pointers to the x- coordinates of the u and v-points in the corresponding sequences 'xus' and 'xvs';

ims(nsegs,nlevs) : the integer ims(m,l) is the number of the grid increments on the grid l, within the x- range of the segment m;

jms(nsegs,nlevs), kms(nsegs,nlevs): contain analogous numbers for the y and z-ranges;

neq(nlevs): the integer neq(l) is the number of all the grid points on the grid l, including the segmental margins; grid points for each scalar are counted separately;

zus(mxdz): the sequence of all the z- coordinates of the u- points (or scalar points) on all the grid levels; mxdz is a parameter from 'prnt.par'. As mentioned earlier, 'zus' is divided into pieces, which contain the z- coordinates for various segments and grid levels. The elements zus(ndz(m,l)+1) and zus(ndz(m,l)+2) are the z- coordinates of the two u- points inside the bottom margin (two scalar cells) of the segment m on the grid l. The z-coordinates of the interior points occupy the positions: ndz(m,l)+3, ndz(m,l)+4, ..., ndz(m,l)+kms(m,l)+2. Next follow the z- coordinates of the two u- points inside the top margin;

yus(mxdy) : the analogous sequence of the y- coordinates of the u- points (or scalar points); mxdy is provided by 'prnt.par'; the pointers to the y- coordinates in 'yus' are given by the sequence 'ndy';

yvs(mxdy) : the sequence of the y- coordinates of the v- points; yvs(ndy(m,l)+1) is the y-coordinate of the single exterior v- point on the south margin of the segment m, grid l. The y- coordinates of the boundary and interior v- points occupy the positions: ndy(m,l)+2, ndy(m,l)+3, ..., ndy(m,l)+jms(m,l)+2. Next follows the y- coordinate of the exterior v- point on the north margin;

xus(mxdx) : contains analogous sequence of the x- coordinates of the u- points;

mxdx is provided by 'prnt.par';

xvs(mxdx) : contains x- coordinates of the v- points; in analogy with the sequences 'zus' and 'yus', the segmental margins (west and east) contain two exterior v- points;

zws(mxdz) : contains z- coordinates of the w- points; in analogy with 'yvs' and 'xus', the segmental margins (bottom and top) contain one exterior point;

x(-1:nodx+2,nsegs) : contains the x- coordinates read from 'geo.in' ('Node X');

nodx is the maximum number of such coordinates for a segment, given in

'prnt.par'; the two auxiliary nodes are added by 'geo' on the west and east margins.

y(-1:nody+2,nsegs), z(-1:nodz+2,nsegs): the analogous sequences of the y- and z-coordinates from 'geo.in', with four nodes added by 'geo';

vx(-1:nodx+2,nsegs) : values of the finest grid coordinate i(x), corresponding to the physical coordinates x in the array x(-1:nodx+2,nsegs);

cbx(-1:nodx+2,nsegs), cex(-1:nodx+2,nsegs), sgx(-1:nodx+2,nsegs) : define the linear or tensioned spline pieces between the interpolation nodes;

vy, cby, cey, sgy (-1:nody+2,nsegs), vz, cbz, cez, sgz (-1:nodz+2,nsegs) : the analogous data for the interpolants in the y- and z- directions.

For the calculation of the grid-point coordinates, it is advisable to follow the example of the program 'prnt', which uses the same subprograms 'segnrs', 'grcrd' and 'valspl' as the program 'geo'.

Files 'o.#'

The main content found in the files 'o.#' is the grid distributions of all the flowfield parameters, written by 'mgfd' after # cycles on the finest grid. The content of 'o.#' contains the following arrays:

u0(maxeq) : the global solution sequence on the finest grid, that is, the sequence of the values of u, v, w, p and scalars at all the points of the finest grid, including the points on the segmental margins; its size 'maxeq' is given in 'prnt.par'. As mentioned earlier, the values of u on a segment m occupy the part of 'u0', which begins with u0(nu(m,nlevs)+1). The ordering of data in this part follows the rules of Fortran for an array u(i,j,k) with $1 < i < im + 3$, $1 < j < jm + 2$, $1 < k < km + 2$, where im = ims(m,nlevs), jm = jms(m,nlevs) and km = kms(m,nlevs). Fortran arrays are stored in column order, that is the first subscript increases most rapidly in ascending order of storage sequence. The u-values, which belong to the segment or to its boundary have the indices $2 < i < im + 2$, $2 < j < jm + 1$, $2 < k < km + 1$. The other values belong to the segmental margin. Similarly, the first value of v can be found in 'u0' at the position nv(m,nlevs) + 1. The ordering of the other values follows the rules of Fortran for an array v(i,j,k) with $1 < i < im + 2$, $1 < j < jm + 3$, $1 < k < km + 2$. The values of v inside the segment or on its boundary correspond to $2 < i < im + 1$, $2 < j < jm + 2$, $2 < k < km + 1$, and the other values belong to the segmental margin. The ordering of w is such as in an array w(i,j,k) with $1 < i < im + 2$, $1 < j < jm + 2$, $1 < k < km + 3$, with the first value at the position nw(m,nlevs)+1. The interior or boundary values correspond to $2 < i < im + 1$, $2 < j < jm + 1$, $2 < k < km + 2$. The first value of the scalar n in 'u0' occupies the position nscl(m,nlevs,n)+1, and all the values are ordered as in an array s(i,j,k) with $1 < i < im + 4$, $1 < j < jm + 4$, $1 < k < km + 4$, Interior values have the indices $3 < i < im + 2$, $3 < j < jm + 2$, $3 < k < km + 2$. Other records of 'o.#' contain:

bdat: the sequence of all the boundary values,

gens: the sequence of all the values of the turbulence generation (9) on the finest grid (for the turbulent flows),

wu : number of the work units in # multigrid cycles.

These three records are needed mainly for restarting the program 'mgfd'.

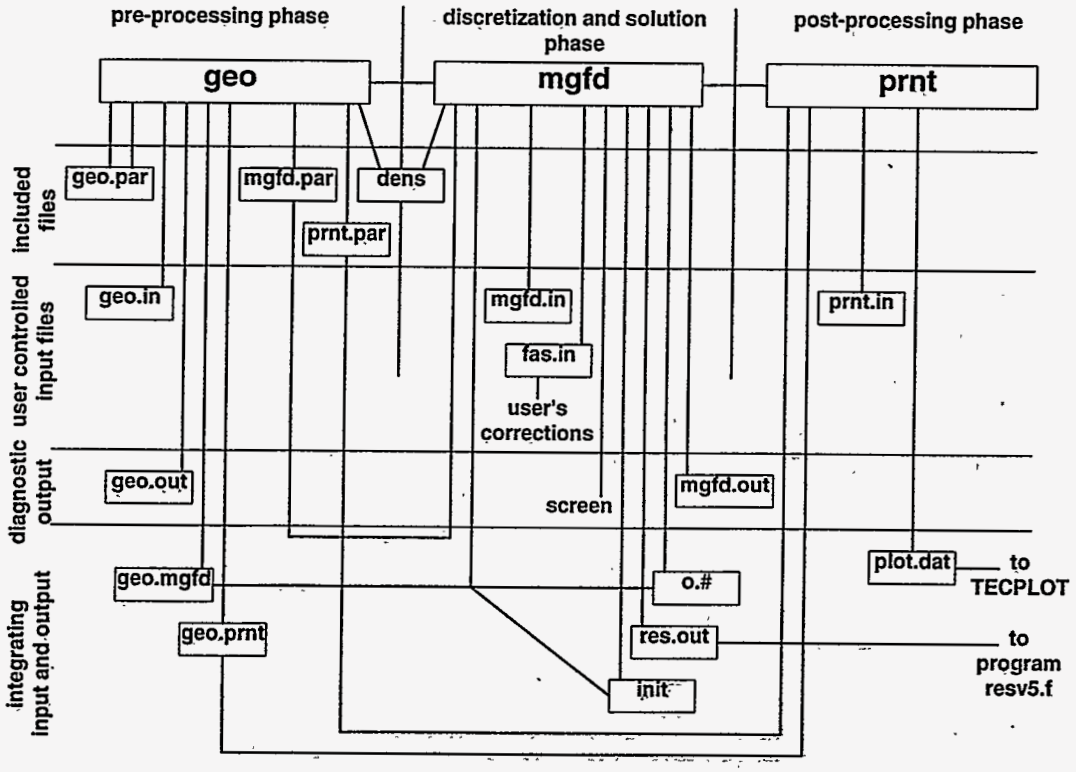

Figure 1: Flow chart for the sequence of programs.

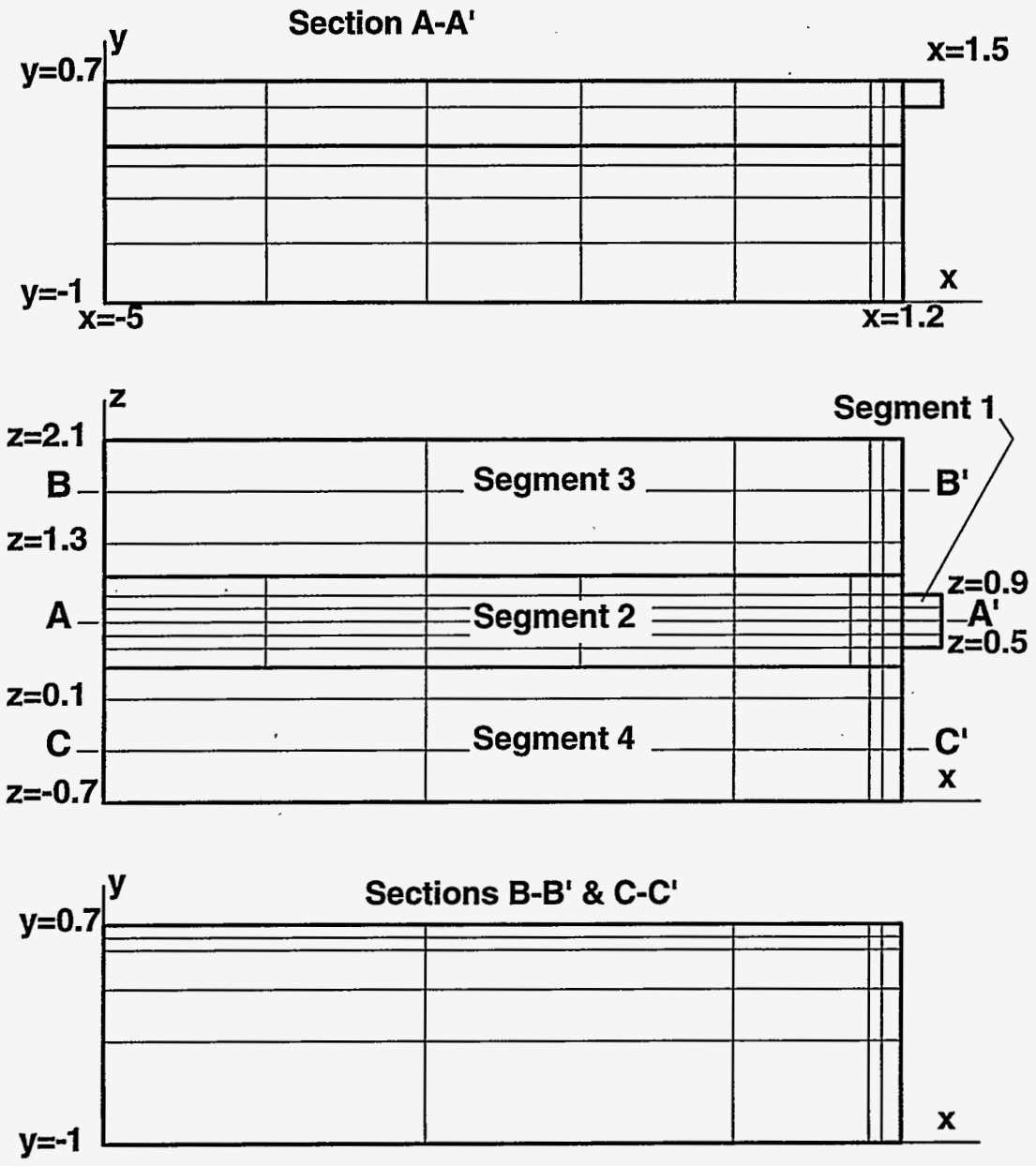

Figure 2: Scalar grid cells on a domain composed of 4 segments.

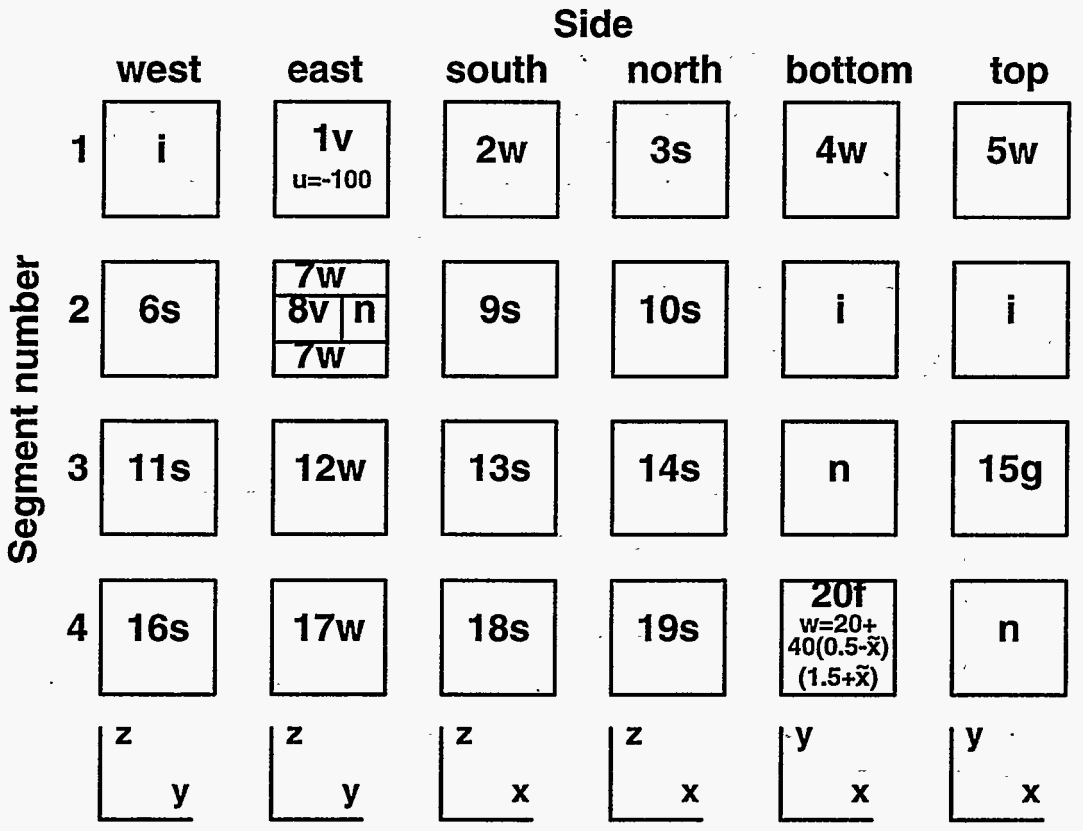

Figure 3: Boundary data for the momentum and continuity equations: Case of a jet in a cross flow.

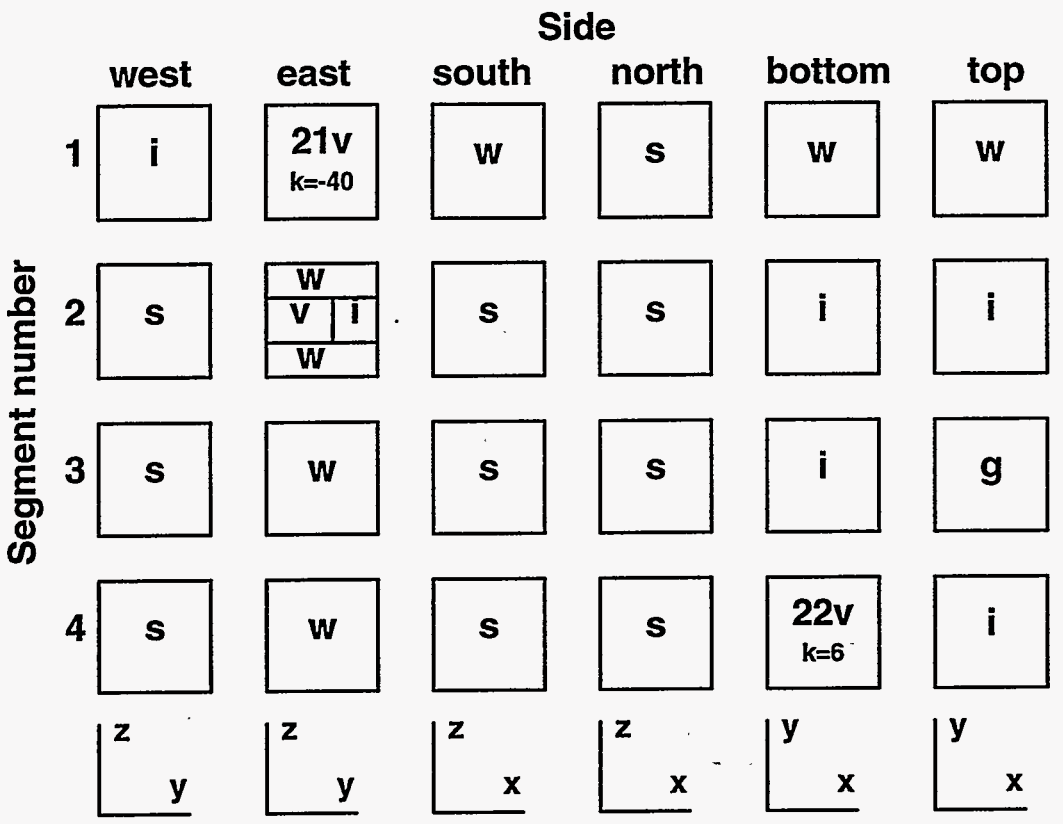

Figure 4: Boundary data for the turbulence energy equation.

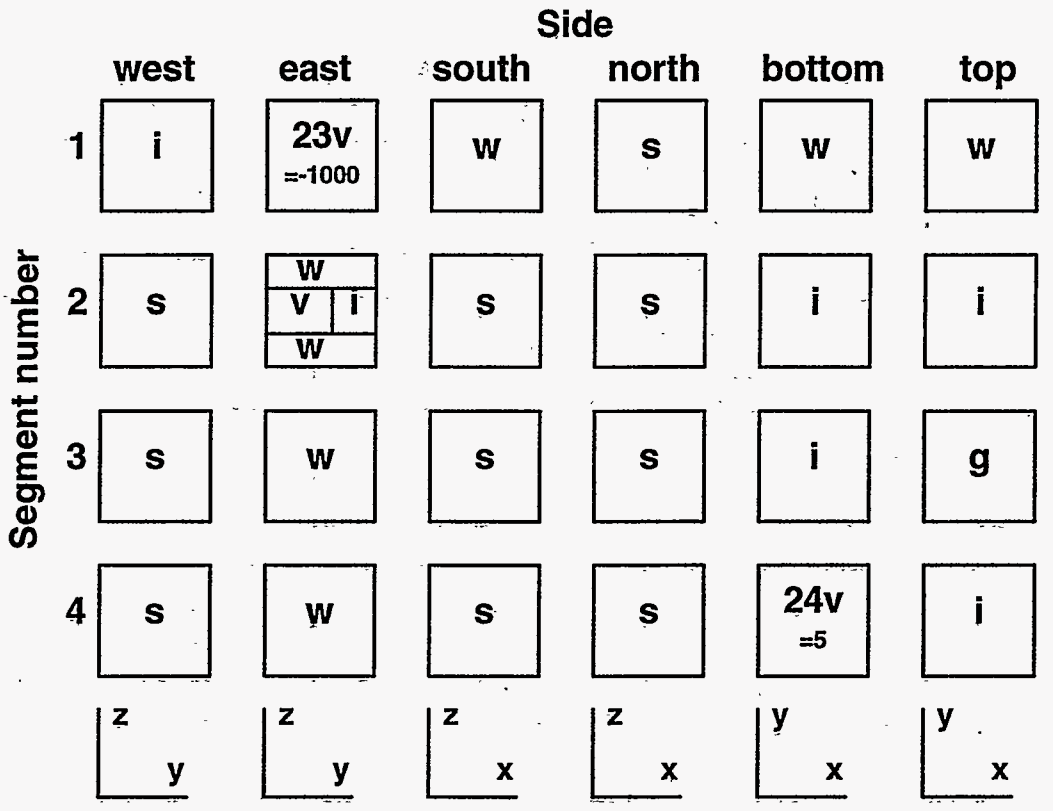

Figure 5; Boundary data for the turbulence energy dissipation equation.

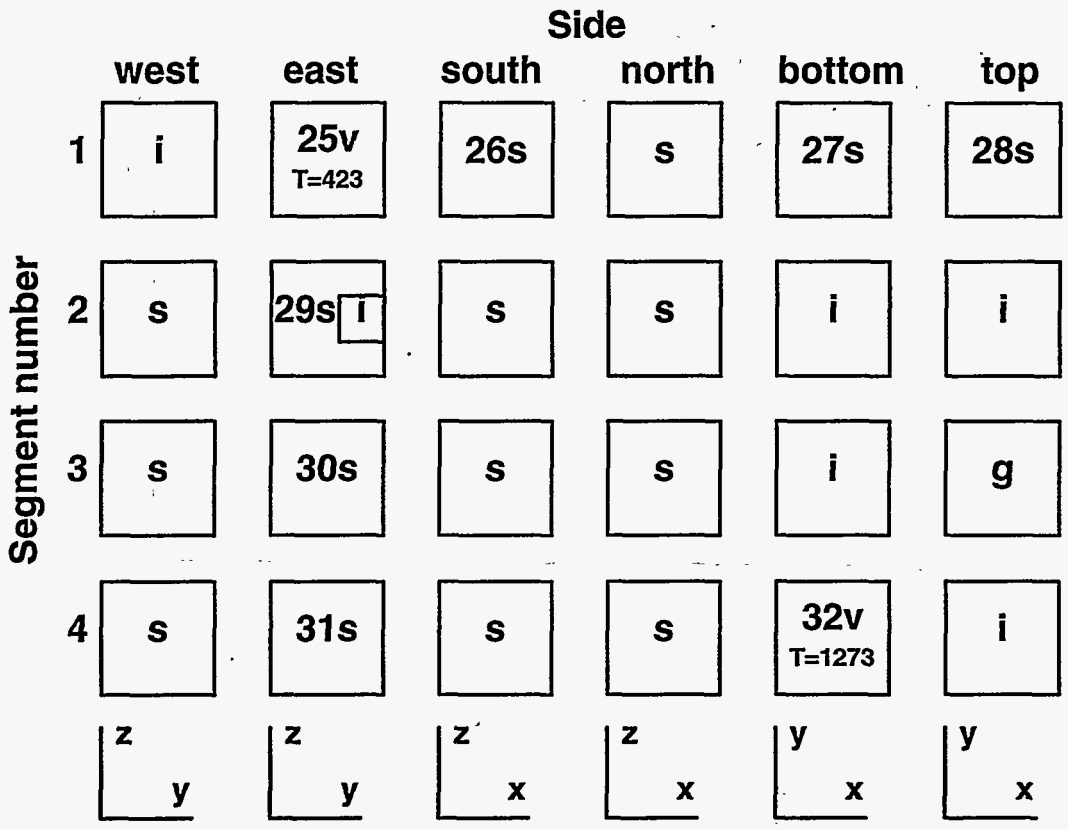

Figure 6: Boundary data for the energy equation.

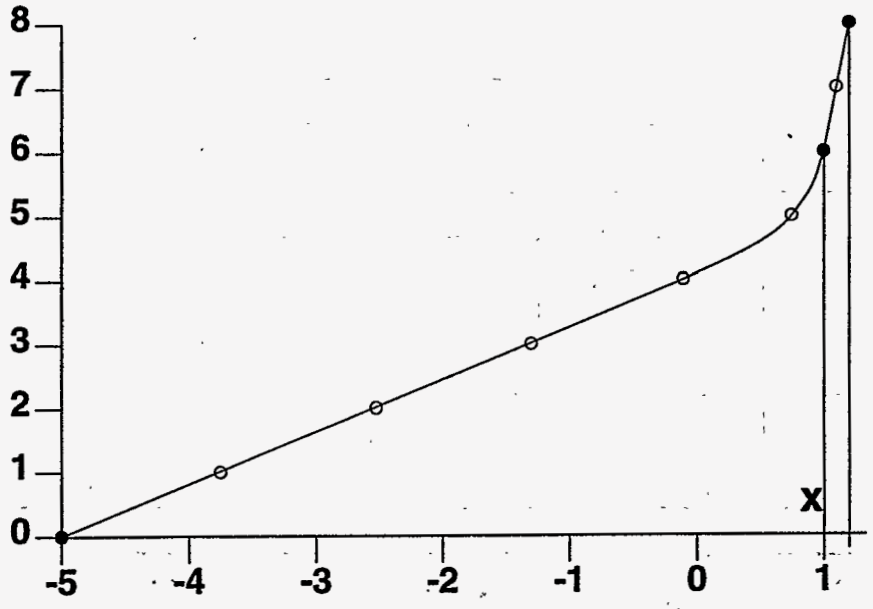

Figure 7: Tensioned spline interpolation of the grid data (•: Data points for the x-grid on segment 2).

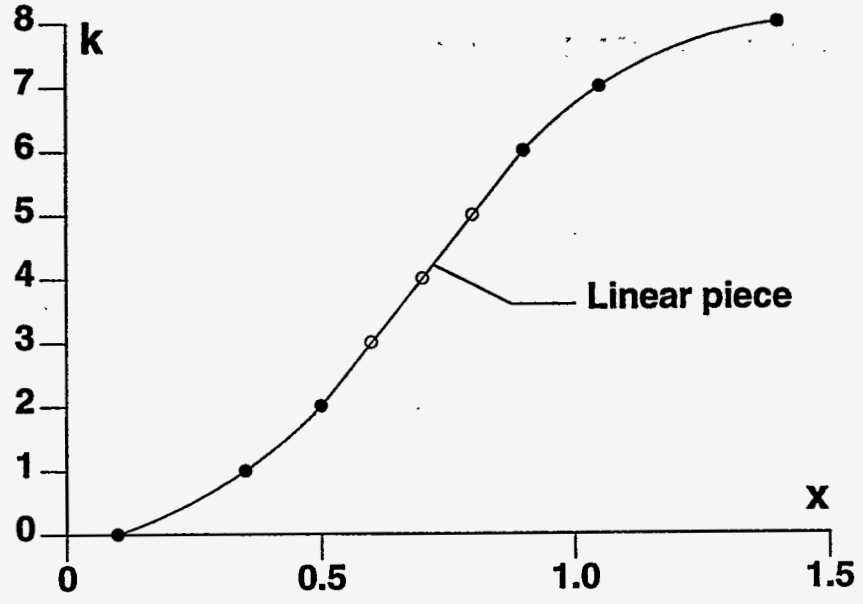

Figure 8: Combined interpolation of the grid data. (•: Data points for the z-grid on segment 2).

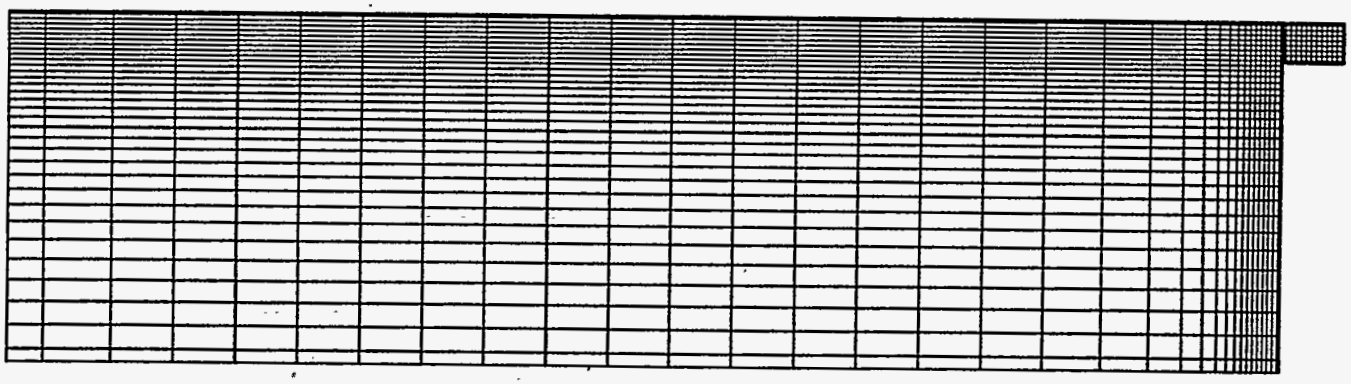

Figure 9: The finest grid on section Z=0.7.

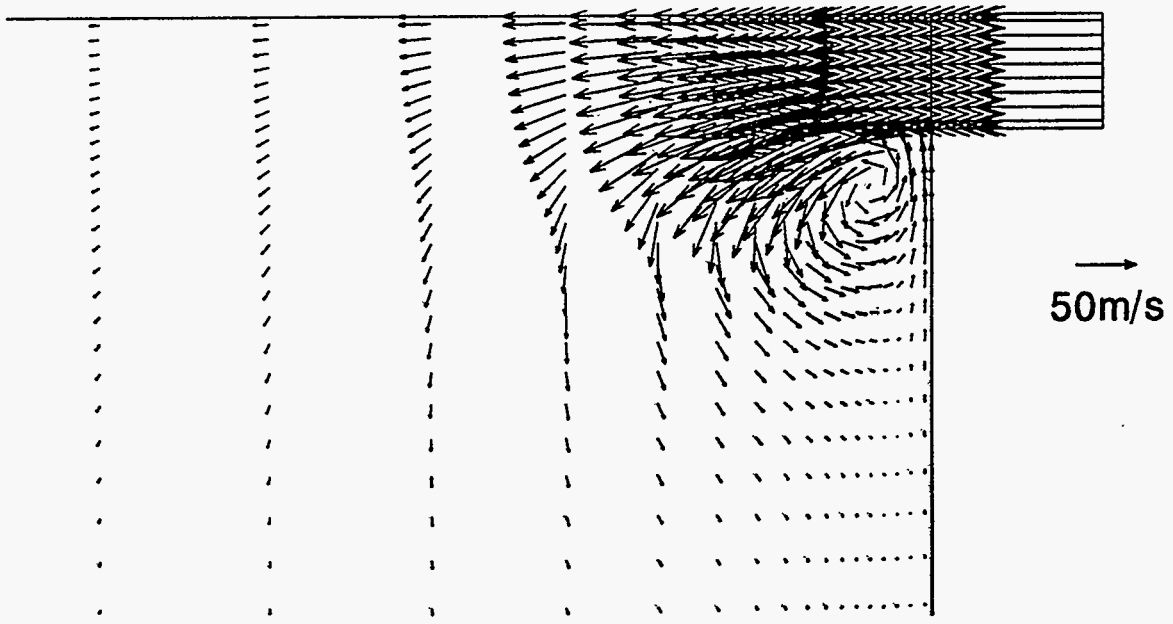

Figure 10: Vector plot of projected velocity.

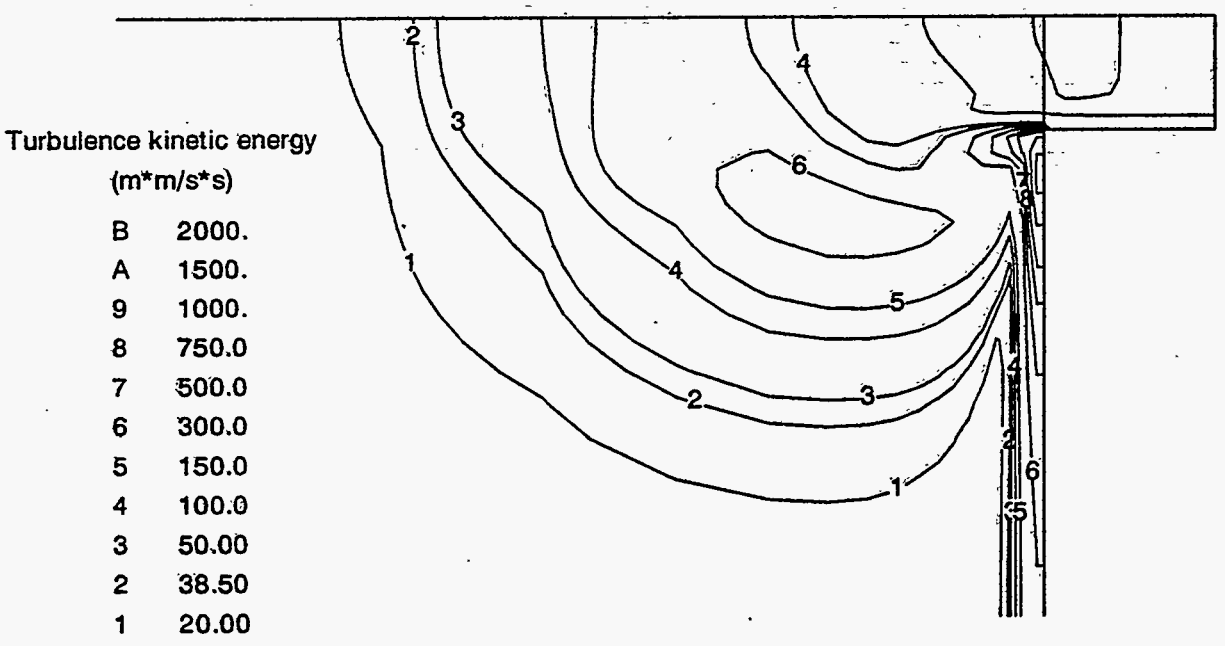

Figure 11: Contour plot of turbulence kinetic energy.

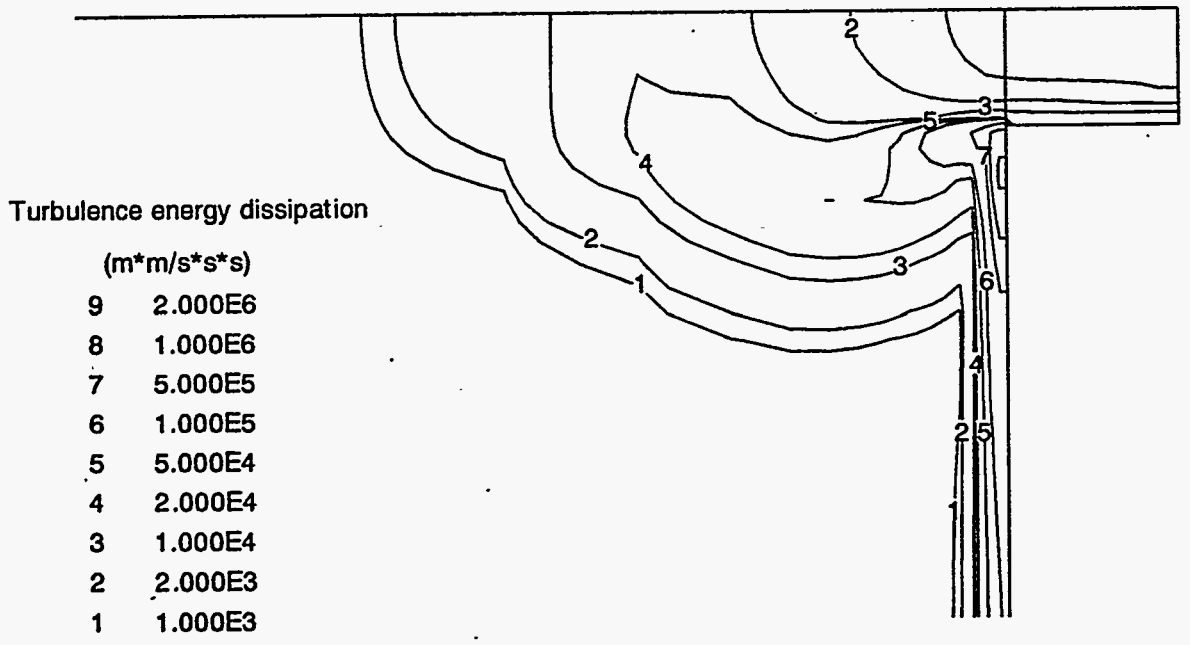

Figure 12: Contour plot of turbulence energy dissipation.

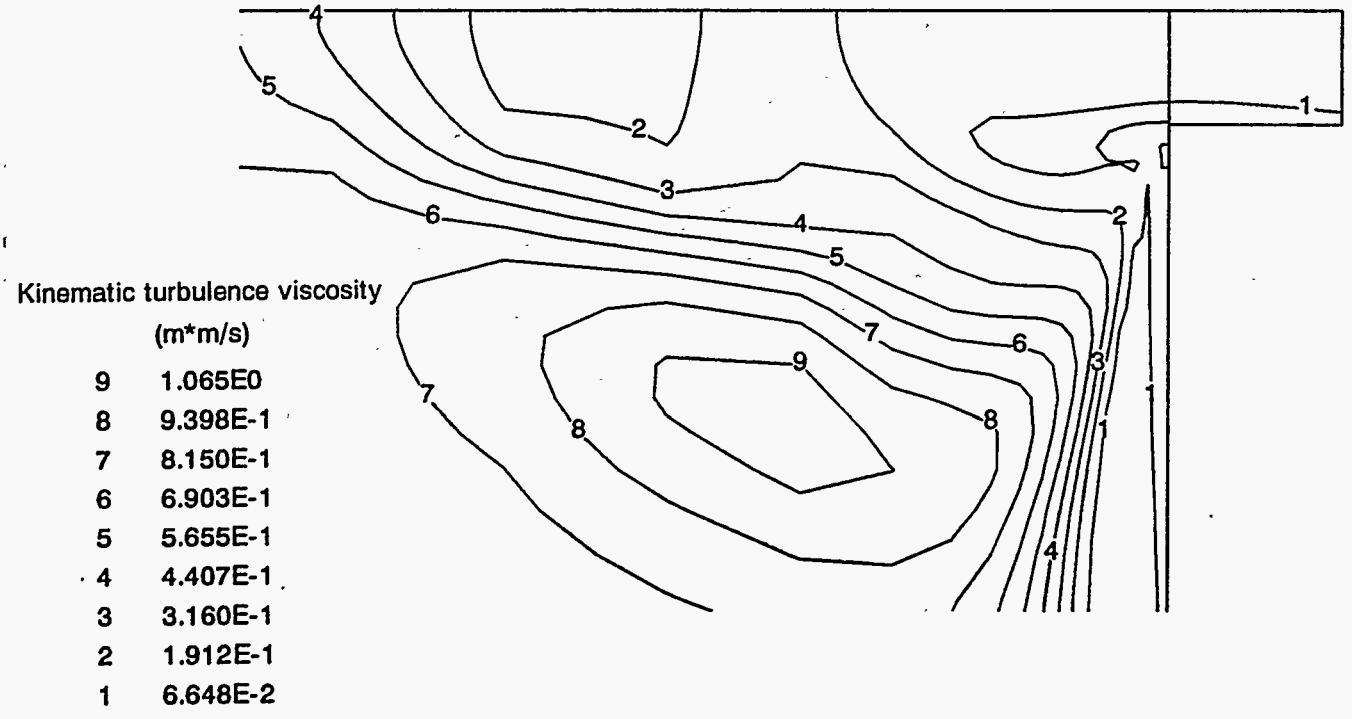

Figure 13: Contour plot of the kinetic turbulence viscosity.

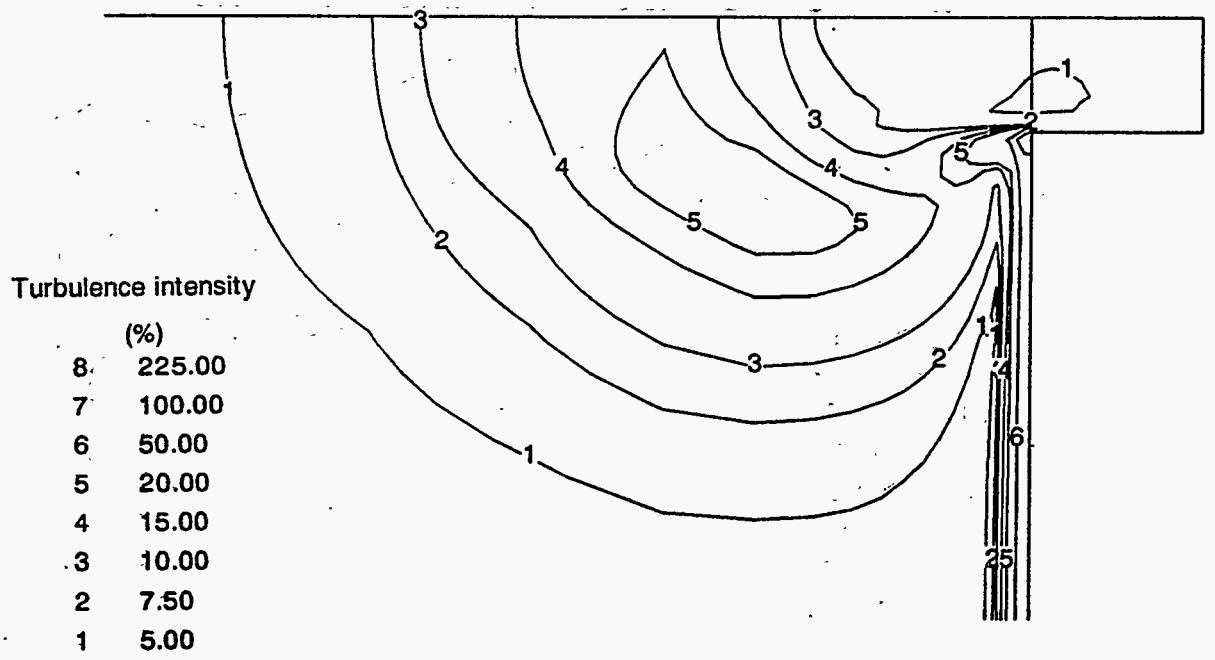

Figure 14: Contour plot of the turbulence intensity.

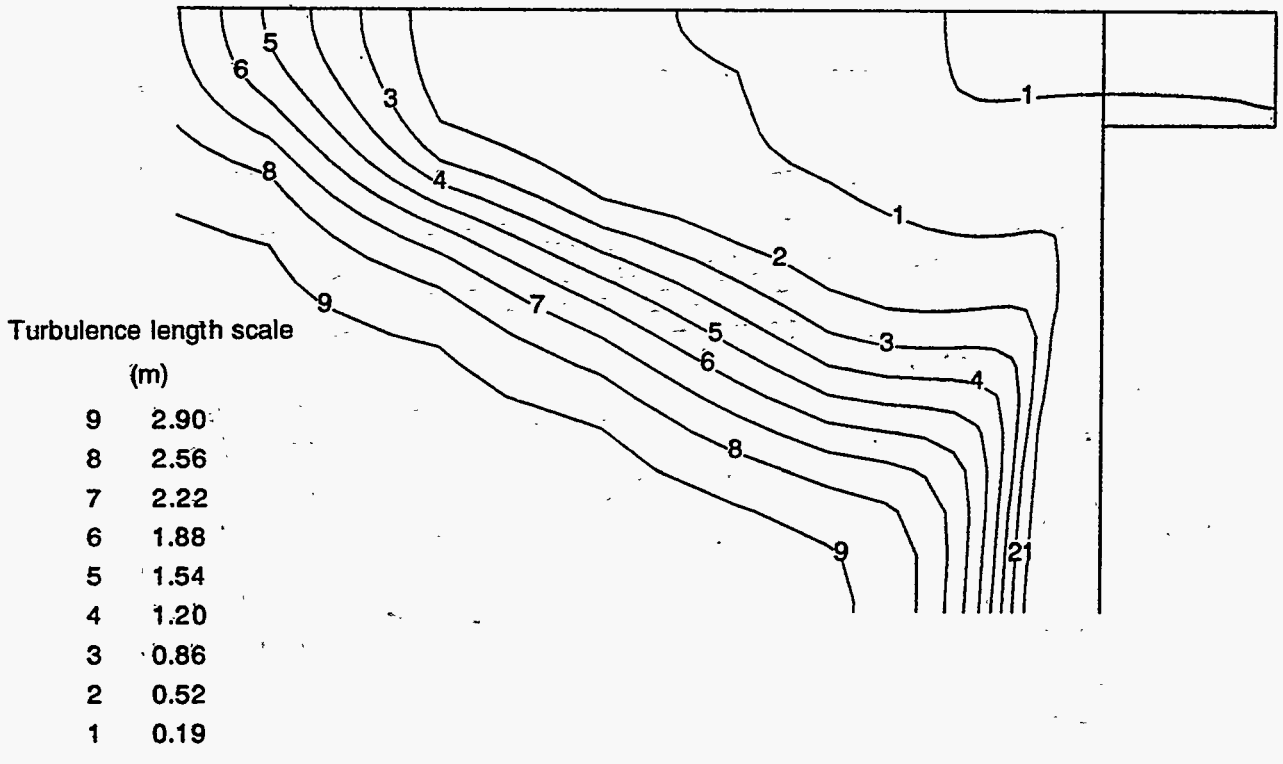

Figure 15: Contour plot of the turbulence length scale.

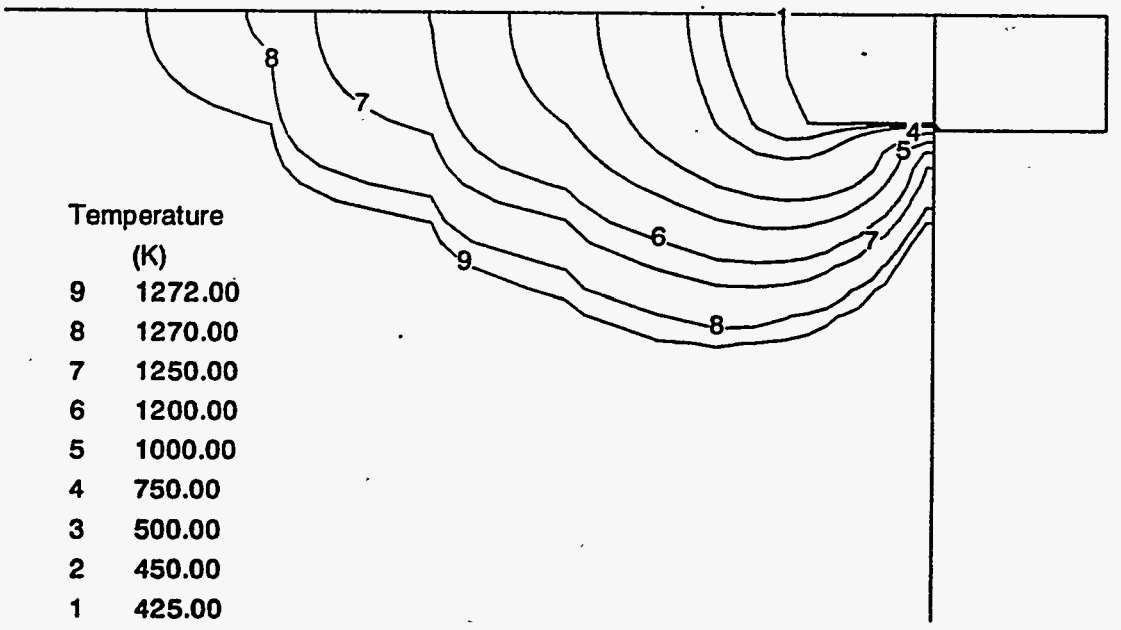

Figure 16: Contour plot of the temperature.

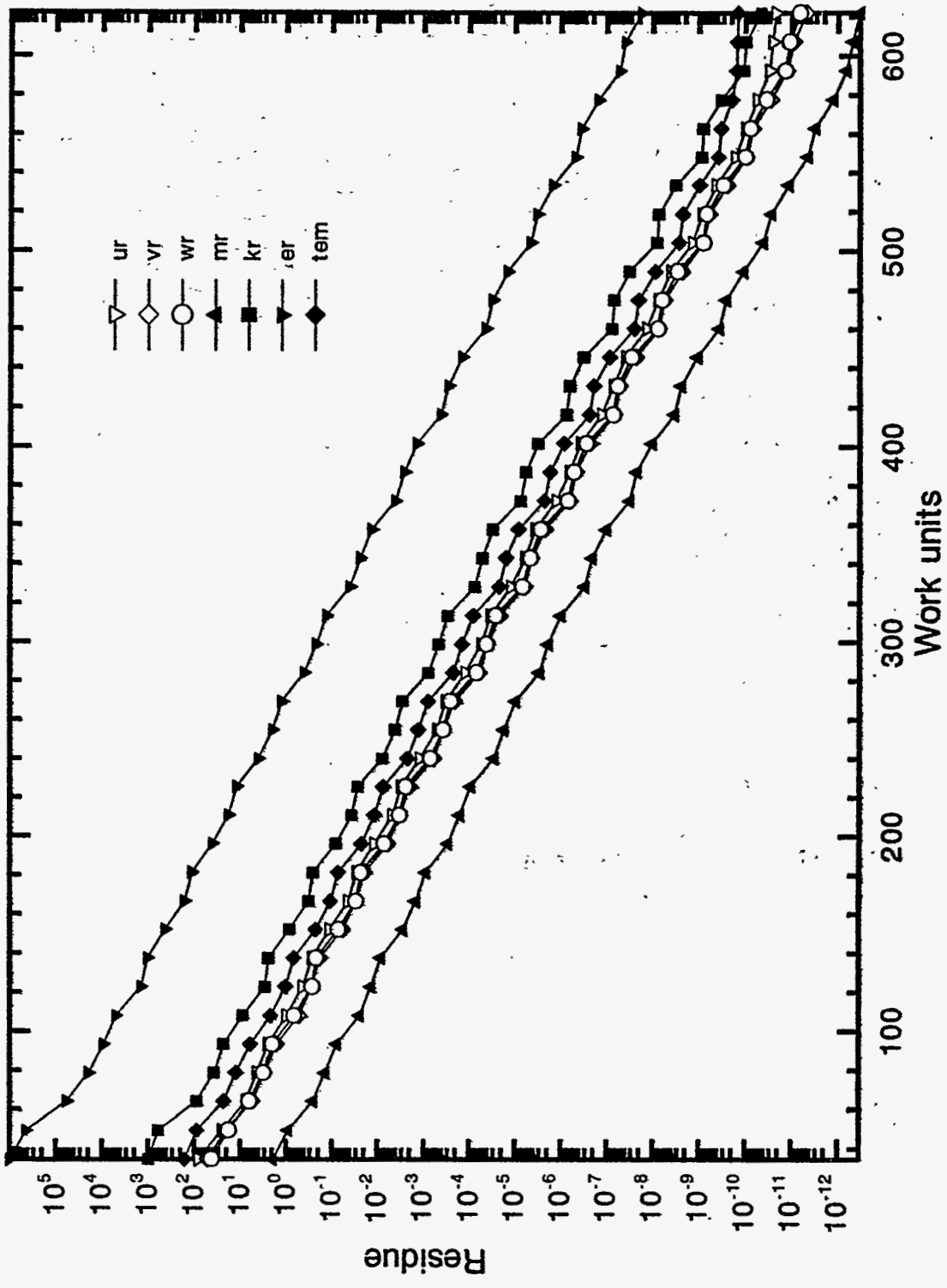

Figure 17: Convergence history for the 3-grid FAS2 method.

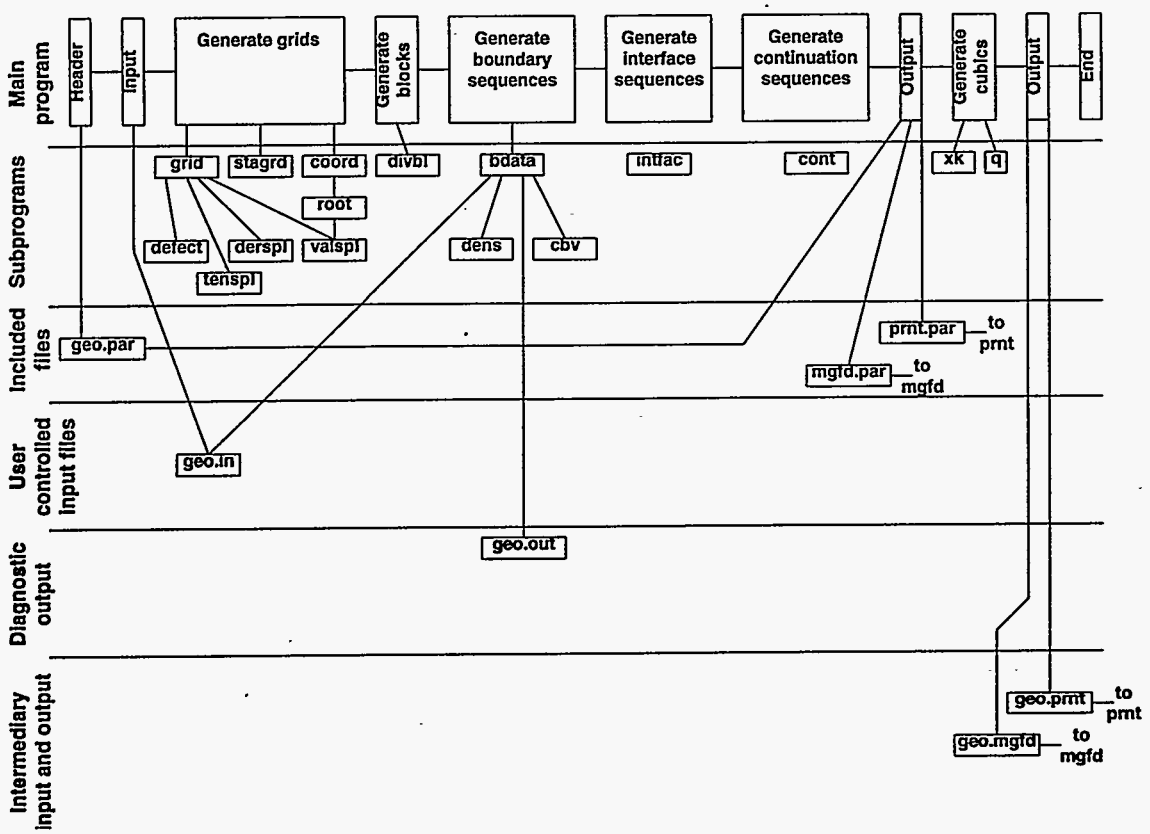

Figure 18: Flow chart for geo.f.

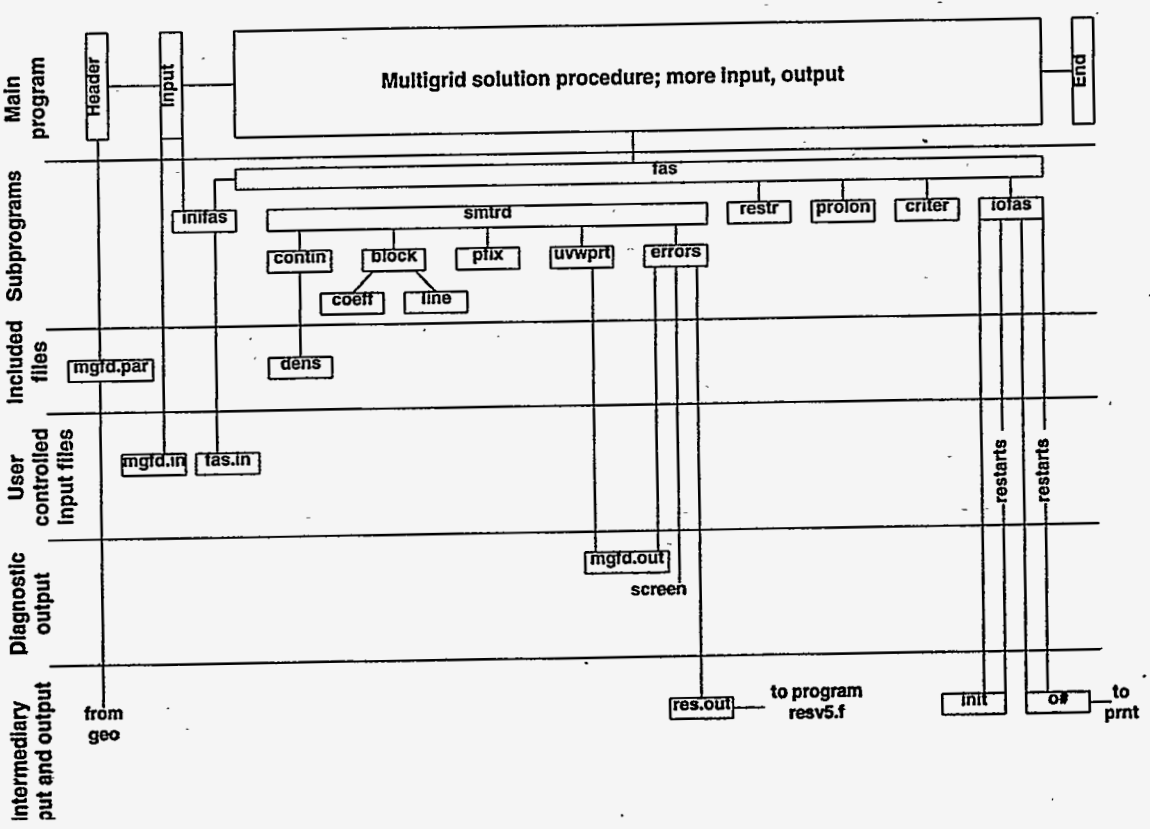

Figure 19: Flow chart for mgfd.f.

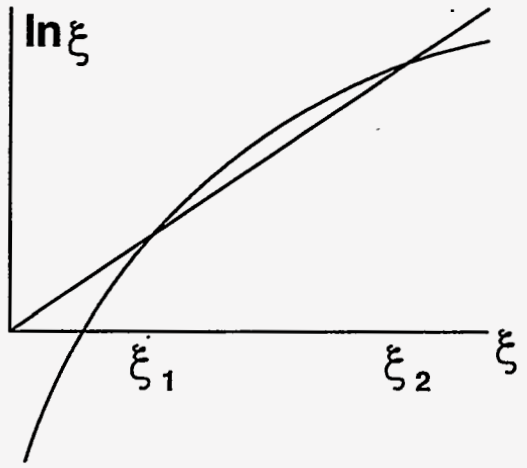

Figure 20: Two sides of eq.(77).

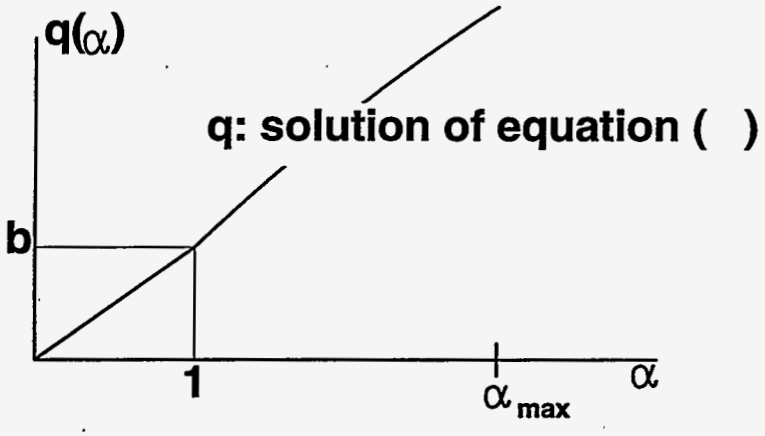

Figure 21: The function q(α).

SECTION 3: PHYSICAL MODELING OF RECOVERY BOILERS

Introduction

Flow measurements are being conducted at the University of British Columbia using isothermal scale water models of recovery boilers. The purpose of this work is to evaluate the relative merits of different air system designs, to compare the results with full-scale measurements, as well as with computational simulations of similar conditions.

Two physical models of recovery boilers were integrated into a flow modeling facility in the Pulp and Paper Centre on the campus of the University of British Columbia. These models are both of operational Weyerhaeuser boilers, developed with that firm's cooperation and assistance. The first model is of an Asea-Brown-Boveri design with a lower furnace rebuild by Götaverken, located in the Weyerhaeuser mill at Plymouth, North Carolina, while the second is of a Babcock and Wilcox design located in the Weyerhaeuser mill at Kamloops, British Columbia. These will be subsequently referred to as the ABB and B&W recovery boiler models respectively.

Modelling of physical phenomena such as flow in recovery boilers may be undertaken using one or more of three approaches: analytical, computational, or experimental. Due to the complexity of the flow in a kraft recovery boiler, analytical solutions are not possible, and computations of the flow inside are an attractive alternative due to their flexibility, amount of information provided, and modest cost. While experimental measurements made in a full-scale operating recovery boiler would potentially be the most realistic, they are expensive, and impractical to make due to the inhospitable environment in terms of temperature, fouling, and accessibility. Measurements may be made much more easily in a scale model of a recovery boiler which is operating isothermally without combustion. While such measurements neglect the effects of buoyancy, liquor and smelt flow, and the gas flow off of the bed, they can provide insight into flow patterns and characteristics of various geometries and flows, and may be used for validation of isothermal computational fluid dynamics studies.

For the physical models developed at UBC, water was chosen as the working fluid due to its suitability for both point velocity measurements and flow visualization. This would permit a closed-loop water circuit to be used, as opposed to a vented balanced-draft air model. The use of a scale model of a boiler for experiments requires that the velocities measured in the model be scaled, via some method, to equivalent values in the full-scale boiler. For experimental modelling of fluid flows, a customary dimensionless parameter used is the Reynolds number

$$Re = \frac{UL}{\nu}$$

which is a measure of the ratio of inertial to viscous forces. At high enough

Reynolds number, provided wall shear is not an important parameter, the large scale motions become independent of viscosity, and therefore of Reynolds number.

There is no possibility of equating the Reynolds number of a small water model to that of an operating furnace; the model will have a Reynolds number, defined in any convenient way, at least an order of magnitude smaller than that of an actual furnace. However, provided that both flows are fully turbulent, and viscous effects at walls are not important, the Reynolds number should not be a significant parameter, and the velocity at which the model is run can be set for the convenience of the test apparatus and not to satisfy any similarity requirement. Tests were completed with identical flow percentages between port levels, but different Reynolds numbers. Results of the test showed comparable non-dimensional velocities, within experimental accuracy, for the two Reynolds numbers.

In an actual furnace, the combustion air enters at a temperature of approximately 150°C, while the temperature in the furnace is about 1000°C. The density change which the combustion air in the full-scale furnace undergoes cannot be simulated in an isothermal water model. In both the ABB and the B&W boiler models, the ratios of area and mass flux between port and cross-section are preserved from the full-scale to the model. With subscripts "p" and "v" denoting port flow and vertical cross-flow respectively, the ratio of velocities between model and full-scale are:

$$\left(\frac{U_p}{U_v}\right)_{\text{full-scale}} = \left(\frac{\rho_v}{\rho_p}\right)_{\text{full-scale}} \left(\frac{U_p}{U_v}\right)_{\text{model}}$$

It should be noted that this scaling method does not preserve momentum flux between port and cross-sectional flow.

Experimental Modelling Facilities

A physical recovery boiler modelling facility was constructed at the UBC Pulp and Paper Centre. It consists of two 1:28 isothermal, scale water models of kraft recovery boilers, the full-scale versions of which are both owned and operated by the Weyerhaeuser Paper Company. A centrifugal pump draws water from a 5600 litre reservoir, sending it vertically into three header pipes feeding the primary, secondary, and load-burner or tertiary model ports respectively. Gross flow control is achieved by adjusting four gate valves which control a bypass line and the flow into each of the three headers. A total of 59 lines of 1.6 cm diameter flexible hose each transport water from the header pipes through a valve and an orifice-plate flowmeter. The hoses then lead to manifolds feeding between four and nine ports each in the case of the primaries and secondaries, and which directly feed the load-burner and tertiary ports. The models were typically run at set flowrates of between 100 and 200 US gallons per minute. To set a given flow condition, a portable differential pressure meter is attached to each orifice-plate in turn and the corresponding valve adjusted to achieve the desired flowrates. A plan view of the experimental facility is shown in Figure 1.

The full-scale boilers are approximately 43 metres high by 11 metres per side, and both employ one liquor gun on each wall. The models are constructed of 4.8 mm thick Plexiglas, and all ports present in the full-scale boilers are modelled. Liquor flow into, and smelt flow out of, the boiler are not modelled. It is assumed that each port on a given level of the boiler has the same mass flow passing through it. In addition, it is assumed that the influence of the liquor droplets and their combustion products on the flow patterns or velocities may be neglected. Representations of the screen tubes and the convective heat transfer section were included in both the ABB and B&W boiler models. The floor of the ABB boiler is flat, while the B&W model floor slopes towards the rear wall at the same rate as the full-scale. A representation of the char bed shape was created for the B&W model, which may or may not be included in a given test.

Table 1 gives the heights of the horizontal measurement planes above the model floors, non-dimensionalized by the respective boiler width. For the B&W boiler, the middle of the sloping floor was taken as datum. These non-dimensional heights were intended to roughly correspond between boiler models, but were constrained somewhat by differences in geometry and accessibility.

Table 1. Non-dimensional Measurement Level Heights

Level	ABB z/d	B&W z/d
3	1.82	1.93
2	1.41	1.29
1	0.66	0.64

The configuration of the models and the locations of the vertical planes used for quantitative flow visualization are shown in Figures 2 and 3, for the ABB and B&W

A statistical test of the flow errors was initiated for each of the 59 orifice-plate/valve packages used in the facility. During an experimental run, flowrates were measured by connecting a portable differential pressure meter across each orifice-plate in turn. The meter measures pressure differential, but has a dial calibrated by the manufacturer which reads in US gallons per minute. The error in a port flowrate is

$$\varepsilon_{total} = fn\left(q_{set}, time\right) \qquad \text{or} \qquad \varepsilon_{total} = fn\left(\varepsilon_{meter}, \varepsilon_{drift}\right)$$

where ε_{meter} refers to the error between the meter reading and the true flowrate, which may be a function of time, and ε_{drift} measures the change in the meter reading, which may be a function of time and the flowrate set. The expected values and variances of each error source were separately estimated through experimentation and statistical analysis.

Considering meter error in the ABB model only, for a typical run of 150 US gpm total set flowrate, a 95% confidence interval for the expected value of the total flowrate was given by (148.9, 157.3) US gpm. If both meter and drift error are considered, for the same typical run, a 95% confidence interval for

the expected value of the total flowrate is given by (130.9, 149.5) US gpm. The major source of error in setting the model flowrate is due to the drifting of valves from the set values. The errors in setting flows in the B&W model showed similar results.

Measurement Techniques

Due to the expected high turbulence level of the flow, a non-intrusive measurement technique capable of recording the instantaneous velocity direction and magnitude in multiple components would be preferable. Multi-hole pitot-static tubes cannot resolve highly turbulent flows, are disruptive to the flow, and have low temporal resolution. Measurement devices such as the pulsed hot-wire or hot-film anemometer are capable of distinguishing instantaneous velocity vectors, but are still disruptive to a highly turbulent flow of this nature and are rather fragile.

A method capable of accurate measurement of unsteady velocities, while not physically altering the flow, is the laser-Doppler velocimeter (LDV). The LDV is able to simultaneously measure multiple components of velocity at a single point, with both high temporal and spatial resolutions. The technique requires that light be scattered from small particles which accurately follow the flow. A limitation of the LDV technique is that the velocities may be measured at only one point at a time. In a flow which changes over time, or exhibits low-frequency unsteadiness, such a point velocity survey may not accurately represent the actual flow. A measurement technique which can give a succession of two-dimensional representations of the velocities in a plane is particle-image velocimetry (PIV). This methods determines the velocity of small particles in the flow which are illuminated by a high-power sheet of light.

Both of the above methods were used to measure velocities in the recovery boiler water models, and so the ability of small particles to accurately follow the flow is of considerable importance. For the LDV experiments, the naturally occurring sediment in the tap water yielded acceptable results. The sediment was assumed to be between 10 and 50 μm in diameter, with a specific gravity of about 4. While performing PIV experiments, polystyrene-latex beads, commonly used in the manufacture of styrofoam cups and insulation, were added to the flow. These were industrial quality particles with a mean diameter of approximately 400 μm, and specific gravity of 1.05. The compatibility of a flowfield and tracer particle may be evaluated by examining the difference between the flow and particle velocity estimated as

$$\left(\frac{\Delta u}{u}\right)^2 \approx \left(\frac{\Delta \rho}{\rho}\right)^2 \frac{d^2 f}{56\nu}$$

where

u = instantaneous fluid velocity
Δu = velocity diff. between particles and fluid
ρ = fluid density

$\Delta\rho$ = density diff. between particles and fluid
d = particle diameter
f = typical fluctuation frequency
ν = kinematic viscosity

Assuming an arbitrary maximum frequency in the model velocities of 10 Hz, the velocity difference between the water sediment used in LDV experiments and the flow would be 0.4%, while the same difference using PSL particles would be 0.8 percent. Such an analysis shows that the particle tracking error may be neglected unless regions of high frequency flow motion are encountered.

Laser-Doppler Velocimetry

The laser-Doppler velocimeter used for making measurements was a two-component differential beam system using a burst-correlator processor. A continuous-wave 5-watt argon-ion laser was used as the coherent light source. Vertical and horizontal velocities, including negative and near-zero velocities, could be measured simultaneously at nearly any point within the model. The beam from the laser was split into two lines of 514.5 and 488.0 nm wavelength, and each line was split again, with one being shifted by a user-selected frequency in order to measure negative velocities. The four beams then were directed into fibre-optic couplers connected to single-mode polarization-preserving optical fibres, which led to a portable barrel probe. This probe focused the beams to a waist at the measurement volume, and received light scattered back by the particles passing though the measurement volume. The separation of the beams and focal length of the probe were 50 and 350 mm respectively.

For the two laser velocimeter components used, parameters of the measurement volume are summarized in Table 2, which assumes that the collimator is not in use. Actual measurements may be recorded from particles passing through any portion of the football-shaped measurement volume.

Table 2. Measurement Volume Parameters

	488.0 nm		514.5 nm	
Measurement volume diameter	85.8	μm	90.5	μm
Measurement volume length	1.24	mm	1.31	mm
Fringe spacing	3.54	μm	3.73	μm
Maximum number of fringes	24.2		24.2	

The experimental arrangement of the physical modelling facility used for laser-Doppler measurements is shown in Figure 4.

The flow was not seeded with artificial particles to enhance data rates during LDV experiments. It was found that unfiltered tap water possessed suitable scattering particles of approximately 10-50 μm in diameter. With natural seeding, data rates of between 50 and 5000 samples per second were

attained, depending on the laser power, optical efficiency, and measurement location within the model. To maintain adequate laser power at the model, it was necessary to realign the fibre-optic couplers using the laser power meter prior to, and during, every run. The software which controlled the processors did not permit selection of measurement times, but only the total number of Doppler bursts between the two processors. This required that the approximate data rate be observed at each location, and the sample size adjusted to approximate the desired record length.

The measurement duration was desired to be approximately two and one-half minutes, which was chosen to obtain reasonable expected values of the statistical moments in the presence of very low frequency oscillations in the velocity. However, the software limited the maximum number of data points per measurement to about 30,000. In order to stay within this limit, the laser power often had to be reduced, sometimes to minimum levels, to lower the data rates. Data rates, and amplifier gain levels, could also be modified by selecting different bandpass filters in the processor of varying gains, but which still bracketed the expected Doppler frequencies. This procedure did not affect the actual velocities measured but only the signal to noise ratio of the Doppler signal.

Simultaneous measurements were made of the instantaneous velocity components in the x (horizontal front-rear) and z (vertical) directions. Two-dimensional velocity information was obtained on three different horizontal planes of 36 points each, as shown in Figures 2 and 3. Horizontal planes were divided into 6×6 grids of equal area, the centre of each being the measurement location. These levels are seen to be near the liquor guns, above the tertiaries, and below the bullnose.

Mean and root-mean-square velocities, as well as turbulence kinetic energies, were found by averaging the data over the entire length of the available data record. Velocity moments such as the mean, standard deviation, skewness, and flatness coefficients, were estimated by excluding data points lying outside 3 times the mean value from all velocity statistics. Bias in the estimates of velocity moments arises due to faster particles having higher probabilities of traversing the measurement volume than do slower particles. Methods have been proposed for correction of bias in the measured u_i values, using various weighting functions as estimators of the true moments:

$$\hat{u}^{<n>} = \frac{\sum_i u_i^n b_i}{\sum_i b_i}$$

where

$\hat{u}^{<n>}$ = estimator of the n-th statistical moment of velocity
b_i = weighting value for the i-th measurement

For cases of low data rates, such as in the experimental facility used in this research, the most appropriate choice for the weighting function b_i is the residence time of the i-th particle in the measurement volume. While processors used were unable to record residence times, they do record multiple measurements per particle as a result of the use of frequency shifting. The number of measurements recorded per particle is inversely correlated with velocity, reducing somewhat the effects of velocity bias. Ensemble averaging, where $b_i = 1$ for all i, was used for estimation of all velocity statistics in this work. This approach was felt to be acceptable in light of the agreement shown between bulk flowrates measured by the orifice-plate flowmeters and the laser-Doppler velocimeter. Both two-dimensional vector plots of velocity and contours of vertical velocity, non-dimensionalized by the expected bulk vertical velocity, were generated from the LDV data at each measurement level.

The kinetic energy in all fluctuating components of velocity may be used as a tool for evaluating the potential for mixing and combustion at a particular location. Although only two components of velocity were recorded at each location, the turbulence kinetic energy may be estimated by assuming that the fluctuating velocity in the y direction is approximately equal to that in the x direction. With superscript "^" denoting an estimator of the quantity underneath, the standard representation of turbulence kinetic energy may be modified as

$$K \approx \hat{K} = \frac{1}{2}\left(2 \cdot \overline{u'u'} + \overline{w'w'}\right)$$

Contour plots of $K^{1/2}$ were generated, again non-dimensionalized by the expected bulk vertical velocity at level three, for each horizontal measurement plane.

Particle Image Velocimetry

Particle image velocimetry (PIV) is a quantitative flow visualization technique that can provide two-dimensional velocity information on a gas or liquid flowfield through optical recording and analysis of the motion of small tracer particles added to the flow. A light sheet is used to illuminate a two-dimensional region within the experimental apparatus, in which the motion of the particles is recorded using film or videotape. These recordings could then be analyzed using particle tracking, auto- or cross-correlation methods, or some combination of the above. The result is a time series of two-dimensional velocity vectors which may be averaged over time and space before being presented in static or animated form. The four components essential to any implementation are: illumination, particles, recording, and analysis. The present application of a correlation technique is the first known use of particle image velocimetry to study an industrial flowfield such as that in a recovery boiler.

The illumination source chosen was the same 5-watt continuous-wave argon-ion laser used for the LDV experiments. The laser beam was sent through a fibre-optic cable to the experimental apparatus, and spread into a sheet using a plano-concave cylindrical lens. The light sheet was then introduced into the models through their clear Plexiglas sides or bottom. The configuration of the experimental facility for the PIV experiments is shown in Figure 5.

The particles used must follow the flow accurately, and be highly reflective. Due to the large water reservoir used in these experiments, an inexpensive and common particle was needed. Polystyrene-latex (PSL) beads of approximately 400 μm diameter, commonly used in the manufacture of styrofoam cups and insulation, were selected.

Accuracy of the PIV analysis technique will be dependent on the resolution of the optical recording device. While photographic film has very high resolution, it is expensive to develop thousands of images, and difficult to transfer the information to a computer for analysis. A commonly available Super-VHS (S-VHS) digital camera-recorder was chosen, which provides more than 400 horizontal lines of resolution. The exposure and aperture of the camera were set to give high-contrast stop-action images of the particles with as little streaking and blurring as possible. The camera recorded 30 frames per second, each frame being a single 1/100 second exposure of the particles in the flow.

An advantage of the sequential, single-exposure image recording method is the lack of directional ambiguity present in double-exposure images. However, as the flow speed increases, the method is limited by the frame rate of the recording camera. The images on the S-VHS videotape were transferred to the hard drive of an IBM-compatible 486 computer using a real-time digitization boards which digitizes a video signal at 30 frames per second with a resolution of 752×480 pixels. This frame rate was felt to be adequate for the expected velocities in the model boiler cavity of less than one metre per second. Custom software was written by the investigators to permit definition of a region of interest in each frame, and to specify a threshold brightness level. The software automatically queries each frame, and writes to a file the location of each pixel having a brightness greater than the threshold value. This process results in a digital representation of the tracer particle positions, with the threshold value reducing the background noise in the images.

The three-dimensional nature of the turbulent flow in a recovery boiler requires the analysis method to be tolerant of particles appearing and disappearing from the light sheet. Such images may be effectively analyzed using optical Young's fringe, digital Fourier transform, or correlation methods, all of which are equivalent in principle. In digital form, the brightness of each camera element, or pixel, is recorded as a gray-scale function between 0 and 255. The two-dimensional cross-correlation value may be defined as:

$$r_i(\overline{s}) = \int \int g_i\left(\overline{x}\right) \cdot g_{i+1}\left(\overline{x} + \overline{s}\right) d\overline{x}$$

where

r_i = cross-correlation between images i and i+1

g_i = digital gray scale function of image i

$\overline{x}$ = two-dimensional location vector

$\overline{s}$ = two-dimensional displacement vector

An identical grid of cells is superimposed on each image, and the integration was carried out for the local area enclosed by each sampling cell, in which the average velocity is to be determined. The average velocity in each cell is defined by the vector $\overline{s}$ at which the cross-correlation function r is maximized, divided by the image separation time. The time taken to compute the cross-correlation function may be decreased by taking advantage of the correlation theorem

$$R_i(\overline{s}) = G_i G^*_{i+1}$$

where

R_i = two-dimensional Fourier transform of r_i

G_i = two-dimensional Fourier transform of g_i

G_i^* = complex conjugate of G_i

The overall accuracy of this implementation of the PIV technique was examined using simulated data, and was found to decrease in regions of very low velocity, due to the limited resolution of the S-VHS camera. For regions in which the average particle displacements were half of the cell size or more, the error in the velocity magnitude was less than 10 percent. Accuracy at low velocities could be improved by employing a camera with greater spatial resolution.

Cases Run

A summary of the port flow conditions for all of different measurements made in the two physical recovery boiler models is shown in Table 3. Unless noted otherwise, all runs were made without use of a char bed shape. While some ratios of flow between primary, secondary, and tertiary levels were chosen to simulate industrially run combinations, others, such as those using only primaries and secondaries only, were run to investigate the effects of those flows in isolation. Mass flows were approximately evenly divided between the port levels used in a given run. Laser-Doppler velocimetry measurements were made in two components of velocity on three horizontal planes. Particle image velocimetry cases refer to videotapes made of the flow, not all of which have been analyzed using the PIV method.

Table 3. Physical Boiler Model Cases Run

	←——ABB——→		←——B&W——→	
	LDV	PIV	LDV	PIV
Primaries & Secondaries	√	√[1]	√	√[2]
Primaries & Secondaries w/ Bed				
Primaries & Secondaries +/- 10%	√			
Primaries, Secondaries & Tertiaries	√		√	√[3]
Primaries, Secondaries & Tertiaries w/ Bed				√[4]
Primaries, Secondaries & Load Burners	√			

[1] Bullnose level, central slice
[2] Bullnose level, 3 slices; Lower level, 7 slices; All B&W experiments use starter burner as per full-scale
[3] Bullnose level, 3 slices; Mid level, 7 slices; Lower level, 7 slices
[4] Bullnose level, 3 slices; Mid level, 7 slices; Lower level 7 slices (murky water)

PIV cases analyzed as of October 7, 1994 are shown in Table 4.

Table 4. PIV Cases Analyzed

	ABB	B&W
Primaries & Secondaries	- Bullnose level, central slice	- Bullnose level, central slice
Primaries, Secondaries & Tertiaries		- Bullnose level, ¼ depth slice
		- Mid level, ¼ depth slice
Primaries, Secondaries & Tertiaries w/Bed		- Mid level, ¼ depth slice

Typical Results

As a check of the set velocities, bulk vertical velocities at the three measurement planes were found by integration of measured LDV vertical velocities. In the ABB model, these erred from the set values by mean errors of 6.8, 4.8, and 3.2 percent for levels one, two, and three respectively.

Typical plots of velocity vectors, non-dimensionalized vertical velocity, and turbulence kinetic energy for cases measured in the ABB and B&W models are shown in Figures 6 through 11. The crosses at the base of each vector in Figure 6 represent the local root-mean-square velocity in each component.

Plots of 30-second averages of the velocity field returned through particle image velocimetry are shown in Figures 12 and 13, for the ABB and B&W models respectively. Consecutive 5-second averages of the same fluctuating flowfields, showing a time series of the changes in the same data, are shown in Figures 14 and 15.

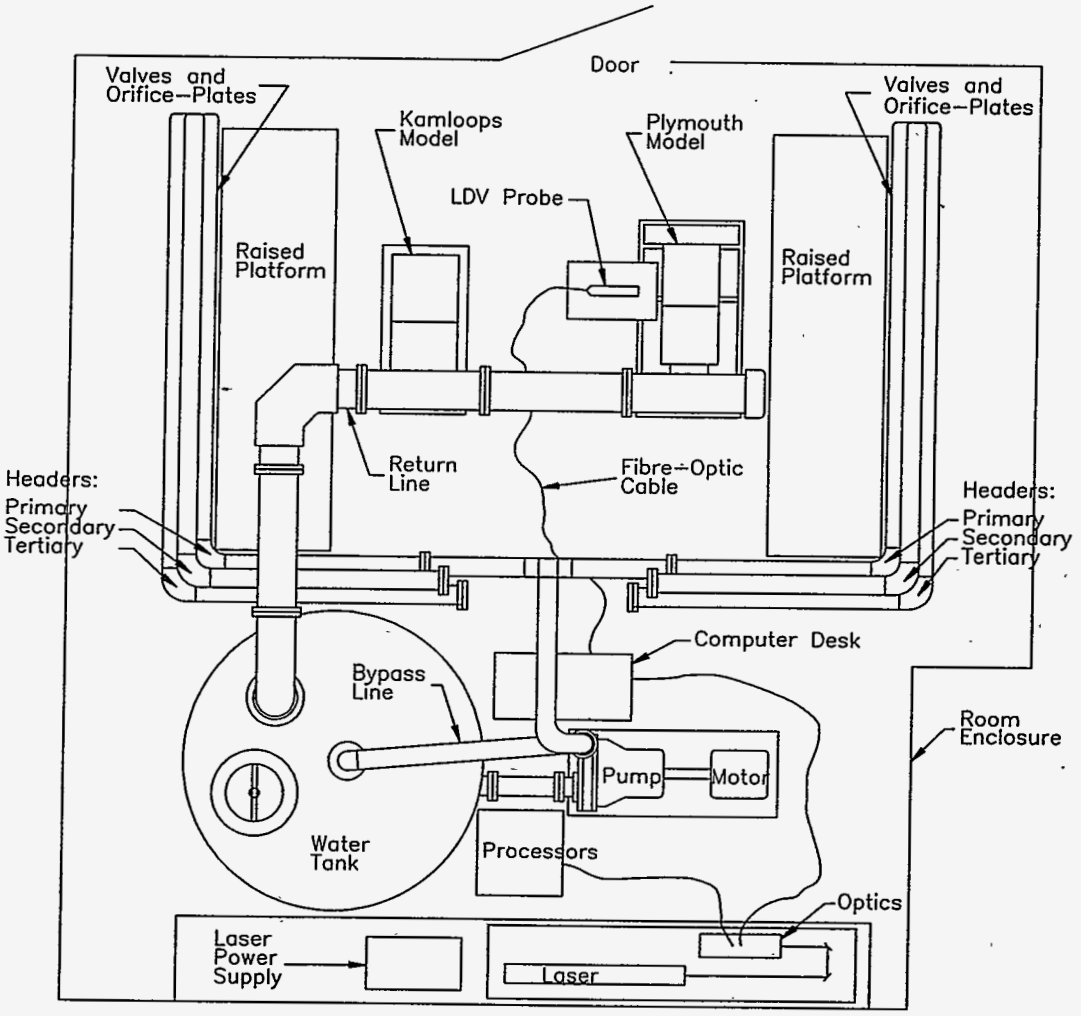

Figure 1: Recovery Boiler Water Model Experimental Facility.

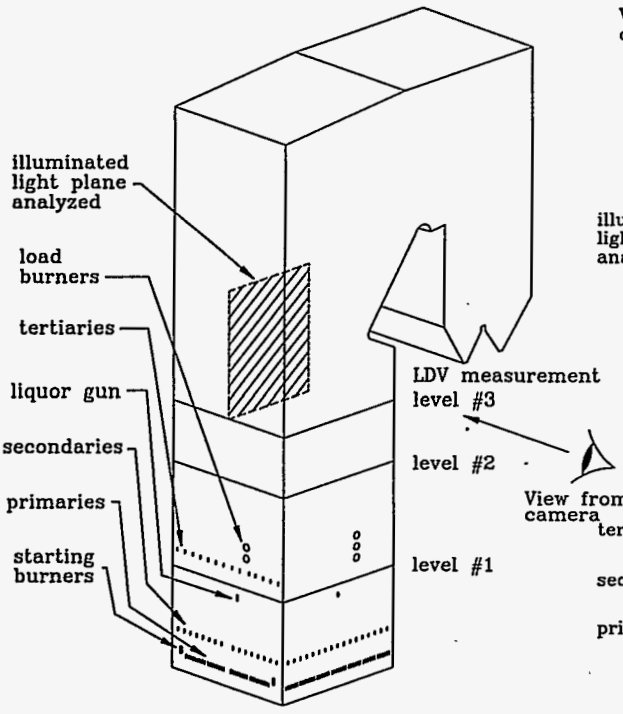

Figure 2: ABB Recovery Boiler Model.

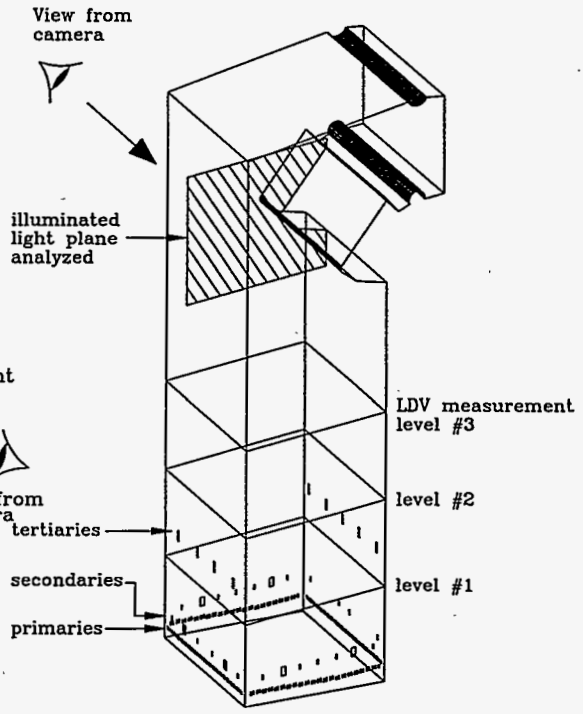

Figure 3: B&W Recovery Boiler Model.

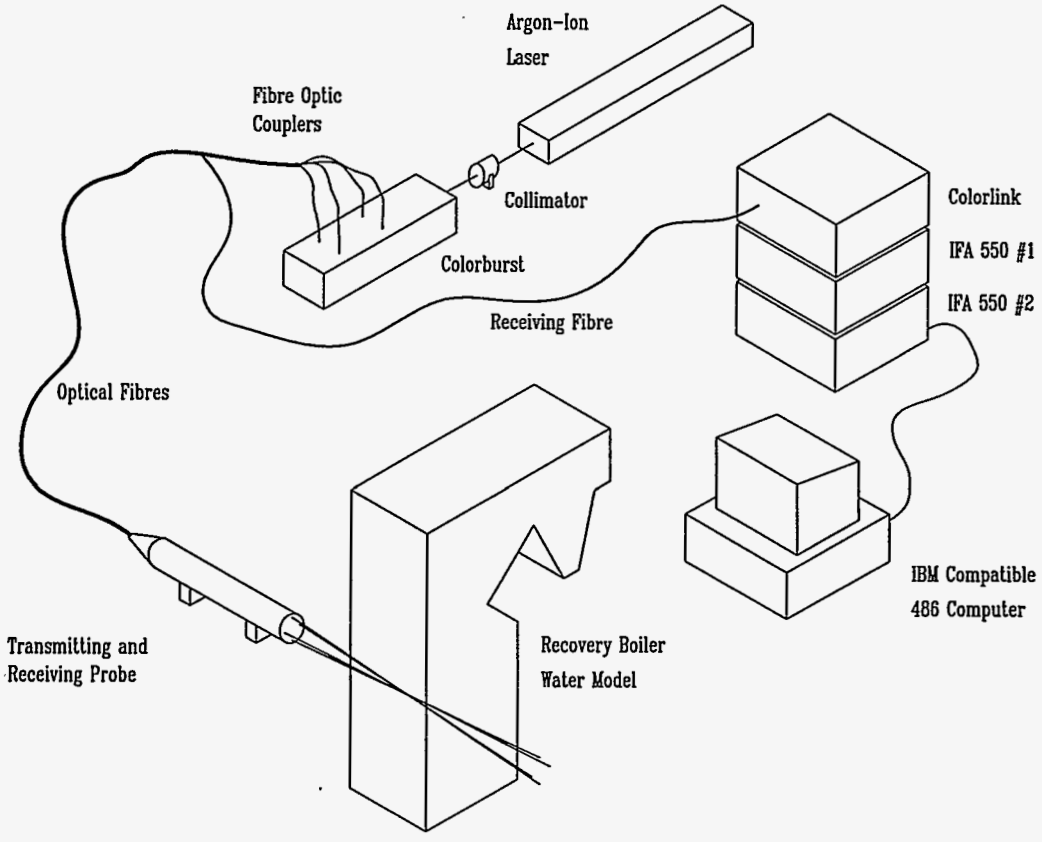

Figure 4: Laser Doppler Velecimetry Experimental Arrangement.

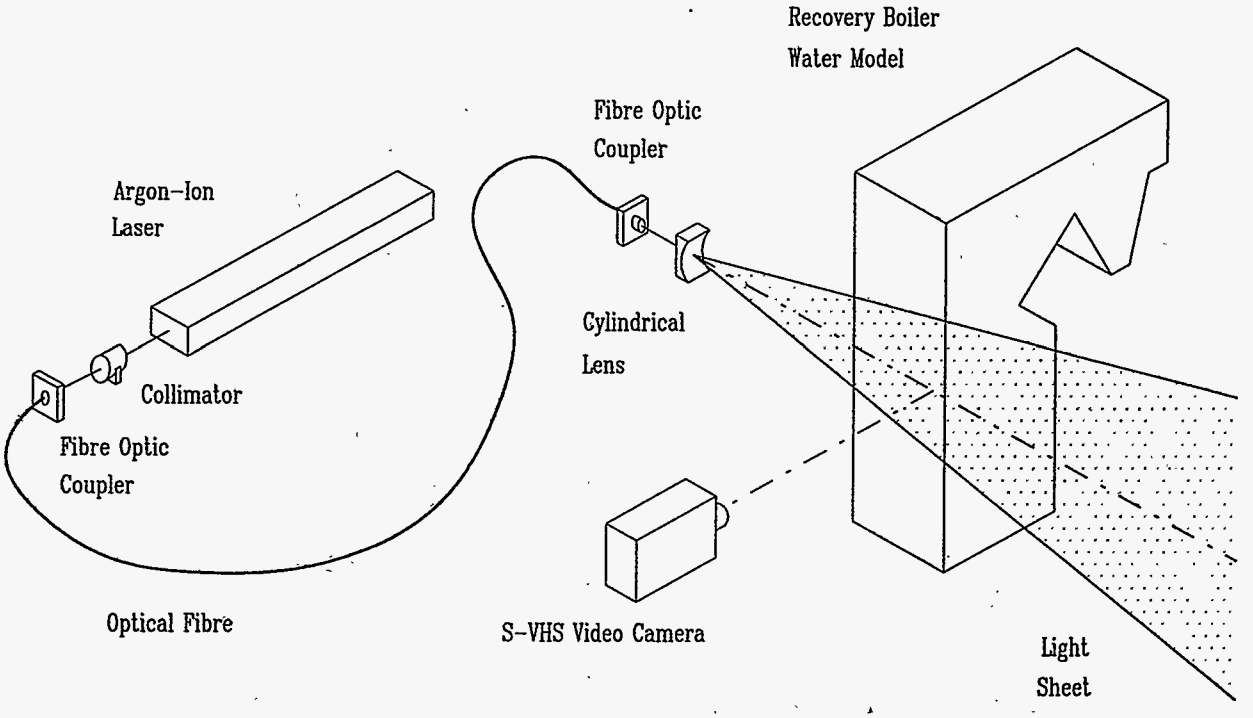

Figure 5: Particle Image Velocimetry Experimental Arrangement.

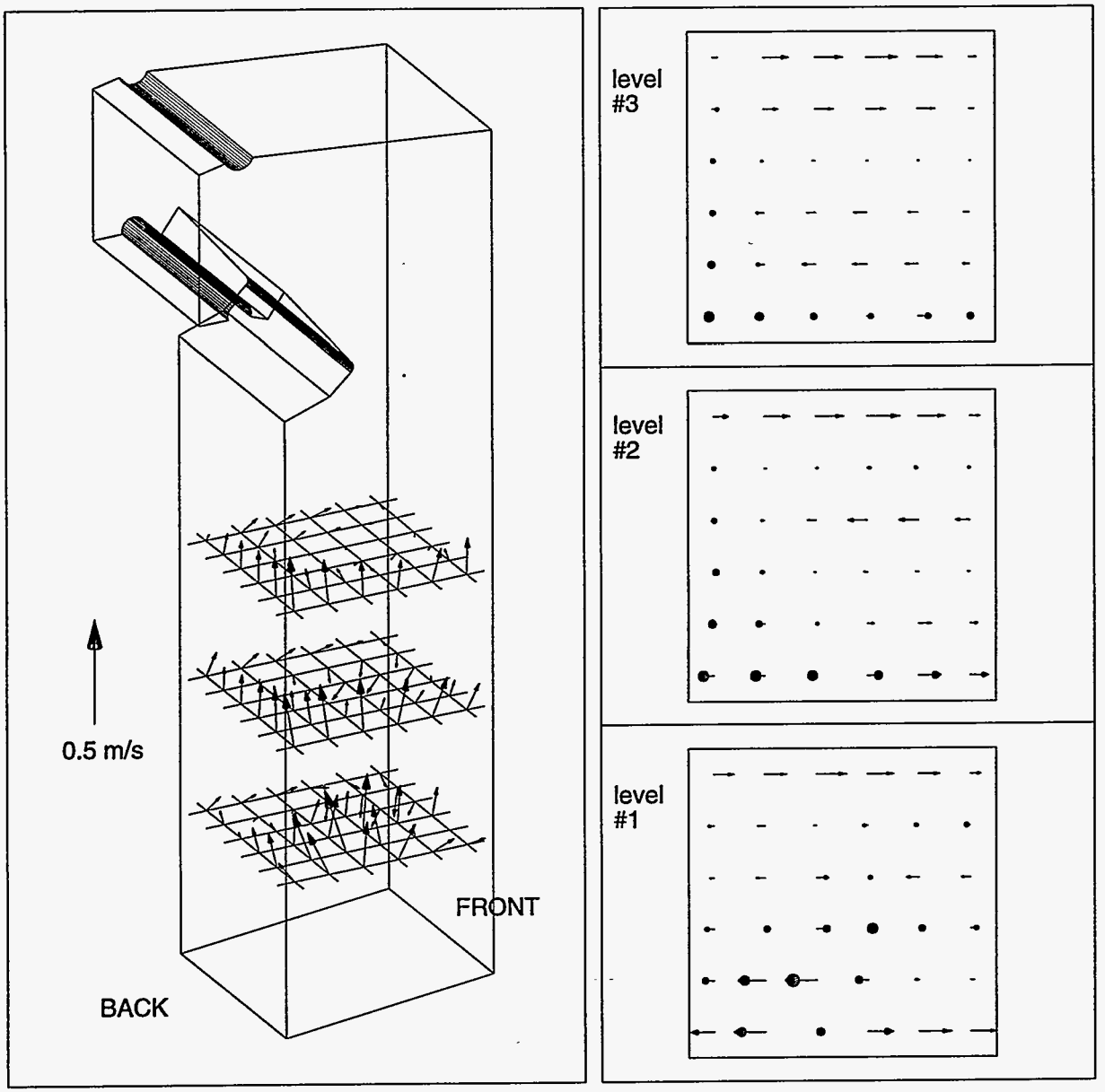

Figure 6: Two Components of Mean Velocities - B&W Primary & Secondary Ports .

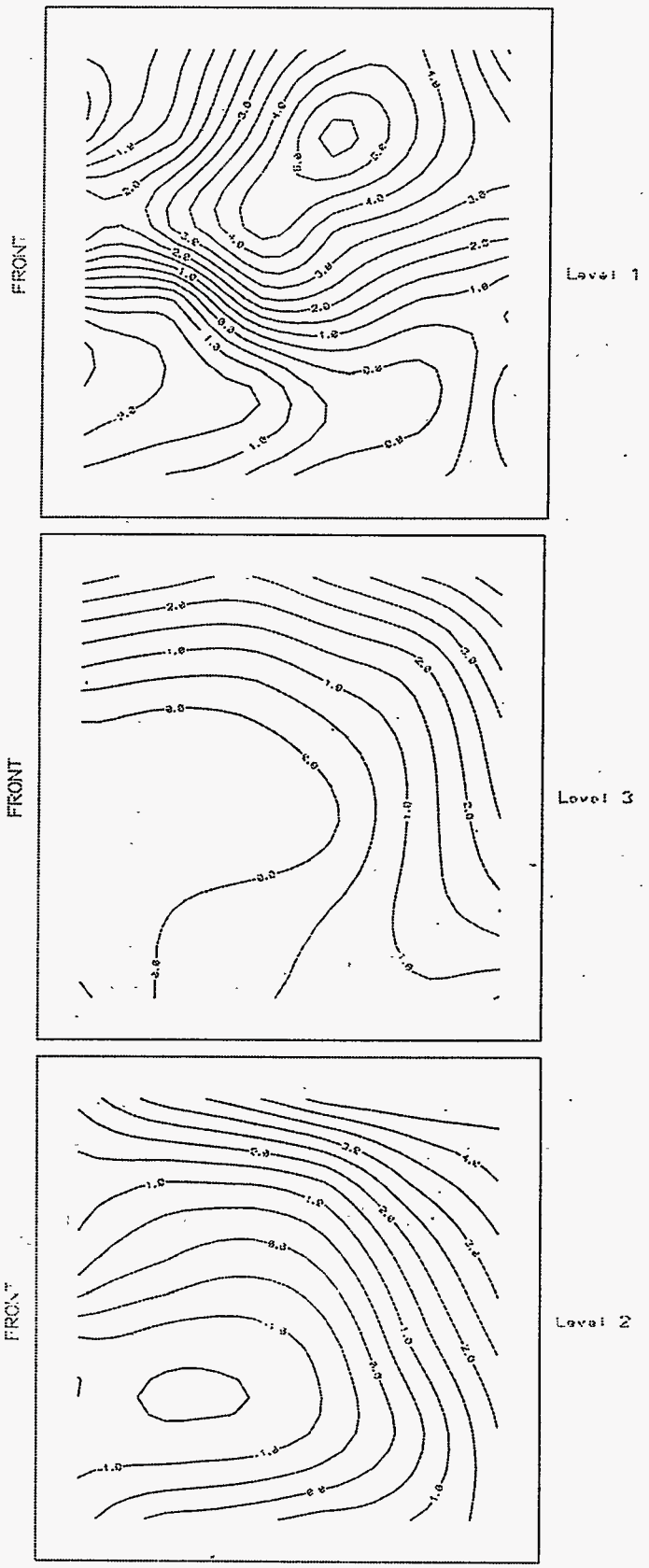

Figure 7: Contours of Non-dimensionalized Vertical Velocity - B&W Primary & Secondary Ports.

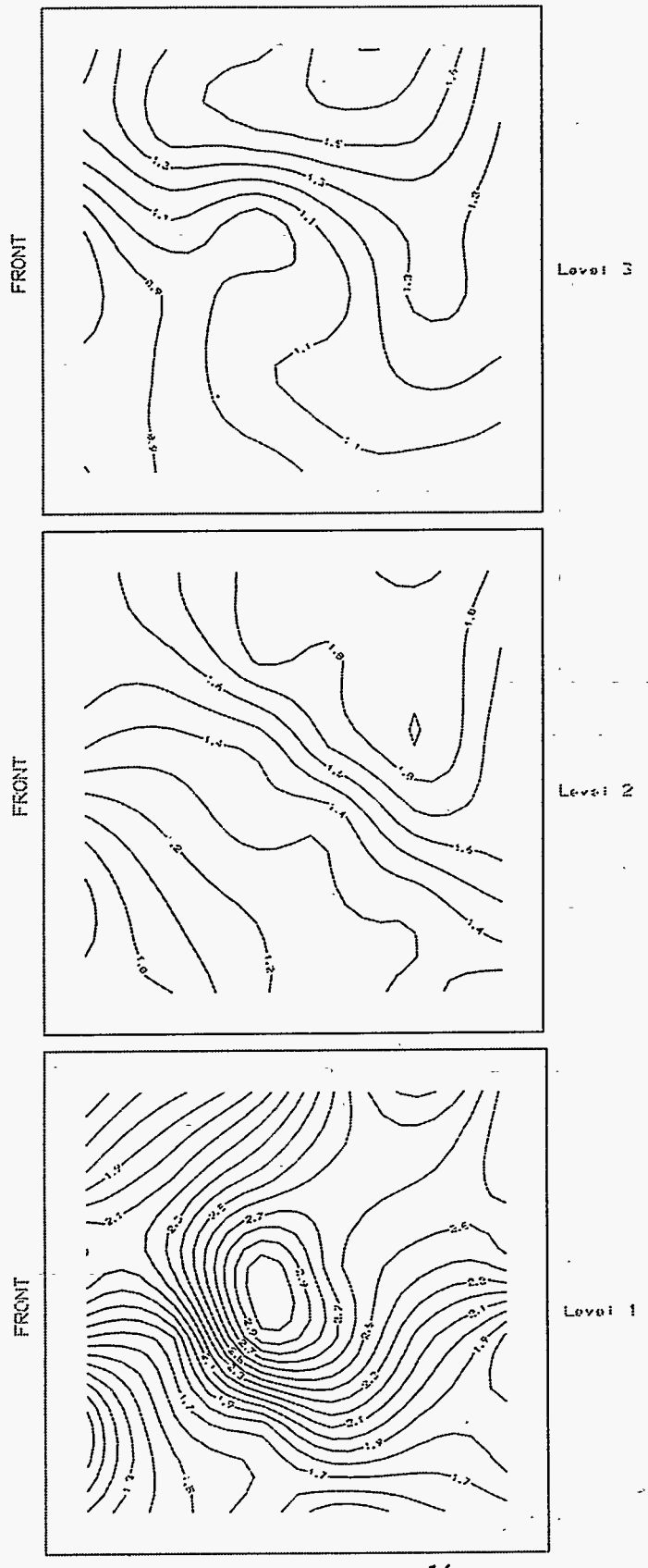

Figure 8: Contours of Non-dimensionalized $K^{1/2}$ - B&W Primary & Secondary Ports.

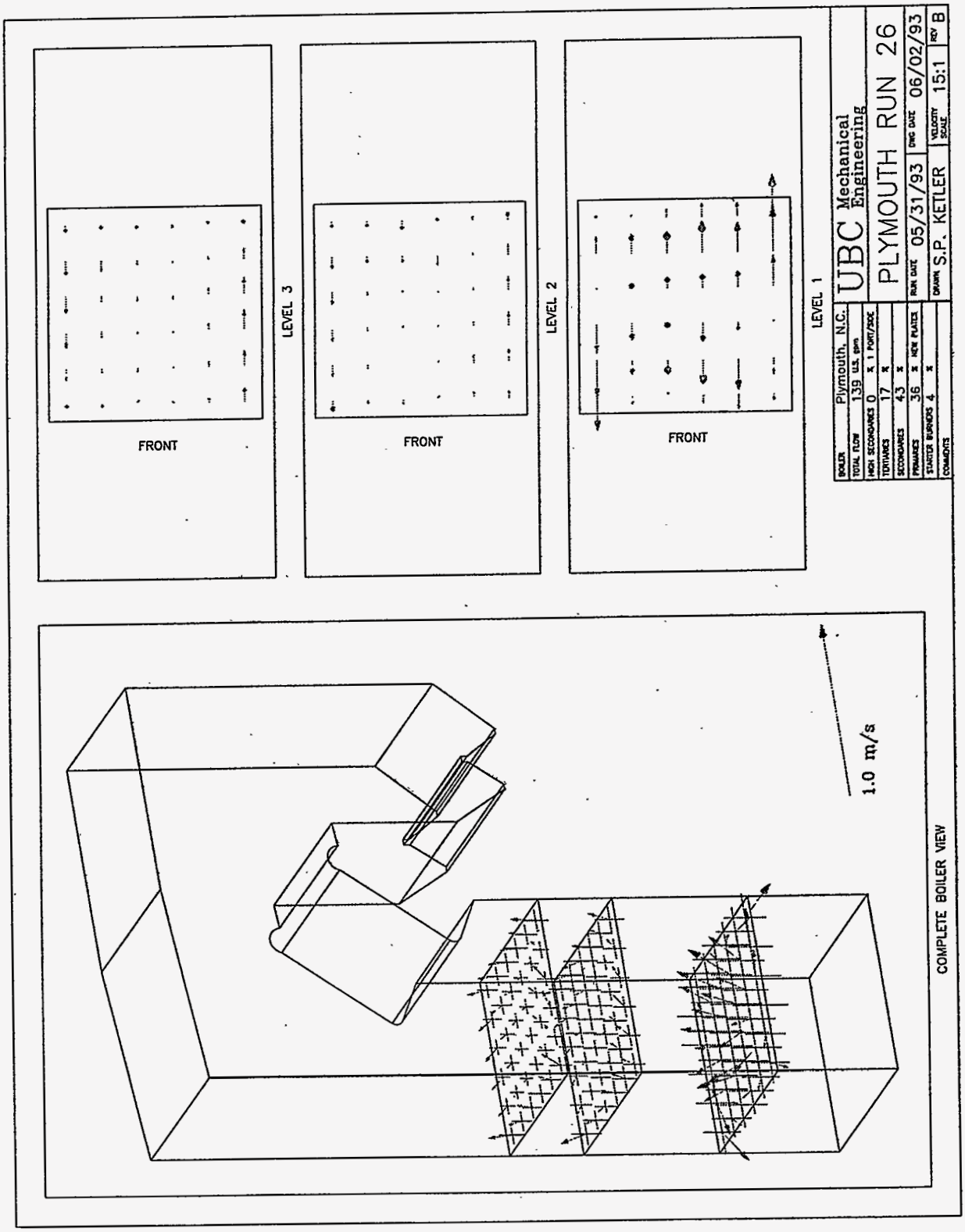

Figure 9: Two Components of Mean and RMS Velocities - ABB Primary, Secondary & Tertiary Ports.

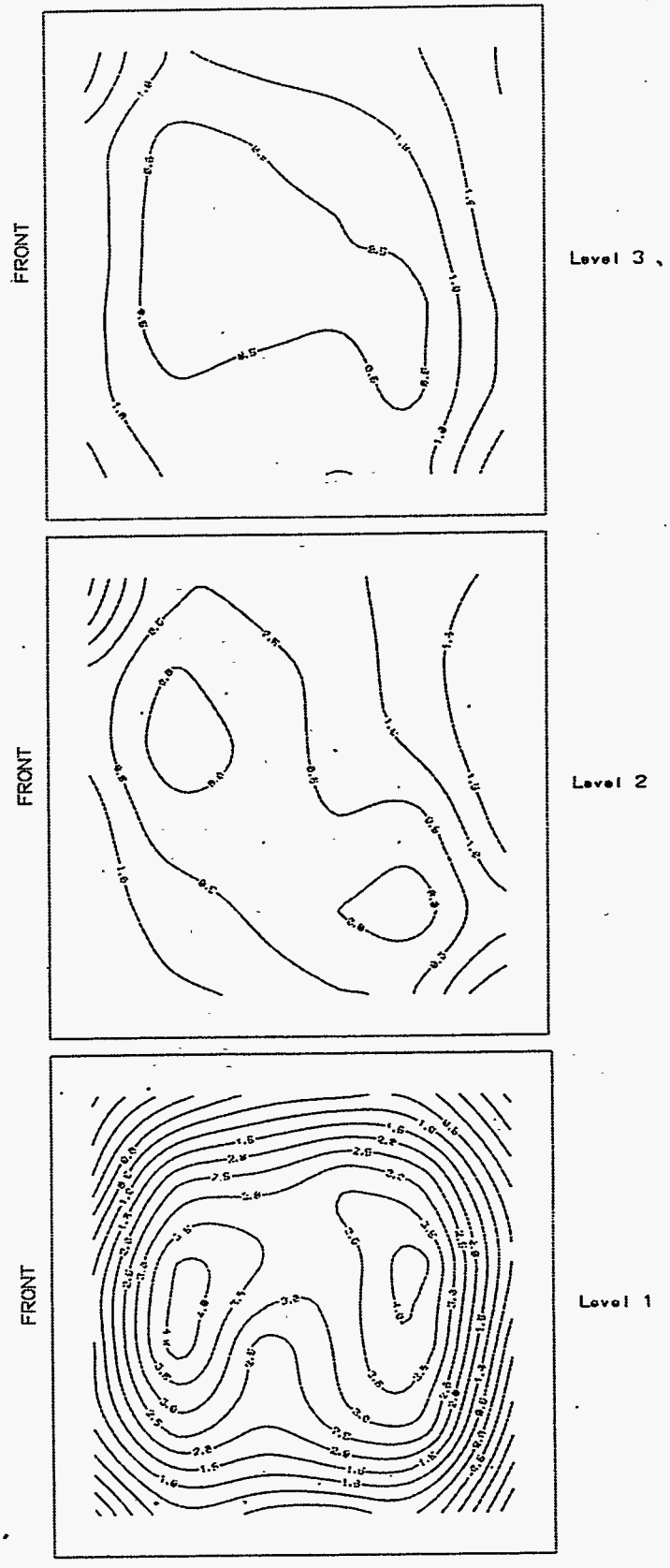

Figure 10: Contours of non-dimensionalized vertical velocity - ABB primary, secondary and tertiary ports.

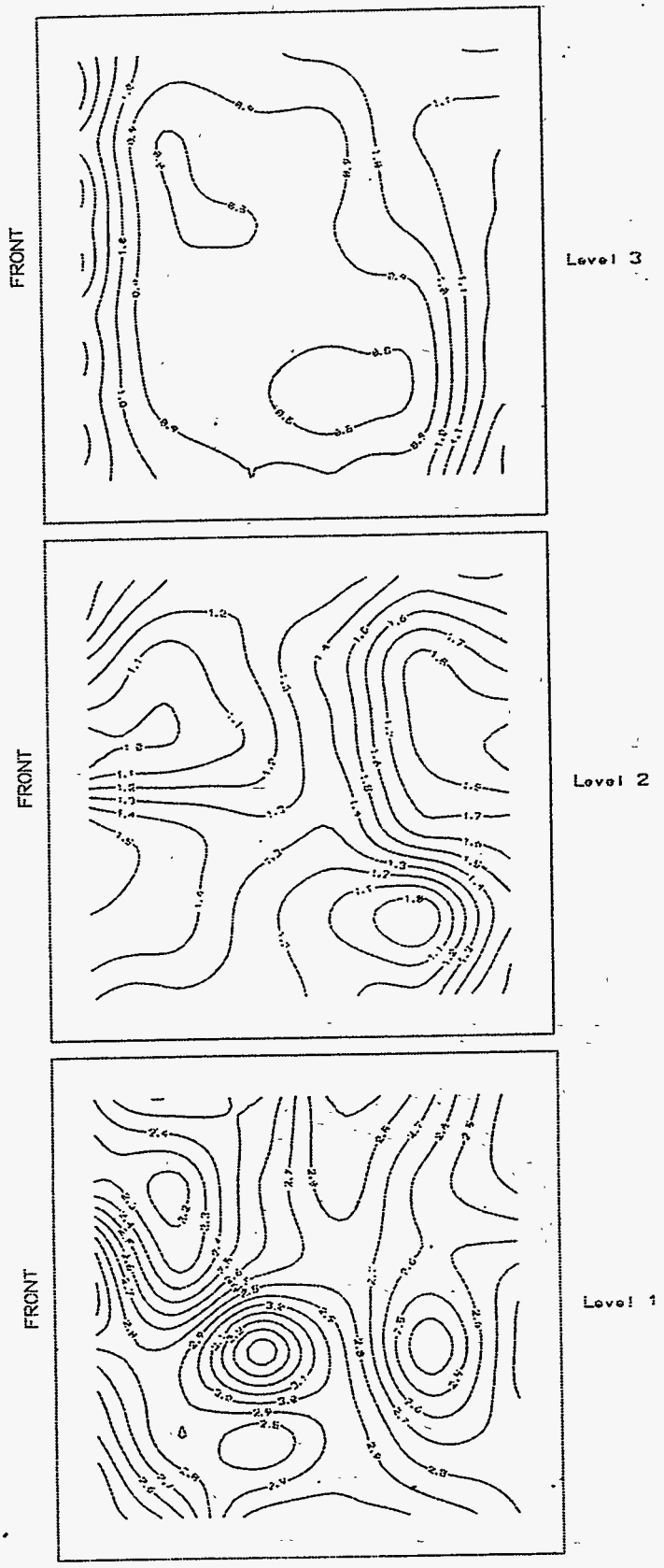

Figure 11: Contours of Non-dimensionalized $K^{1/2}$ -ABB Primary, Secondary & Tertiary Ports .

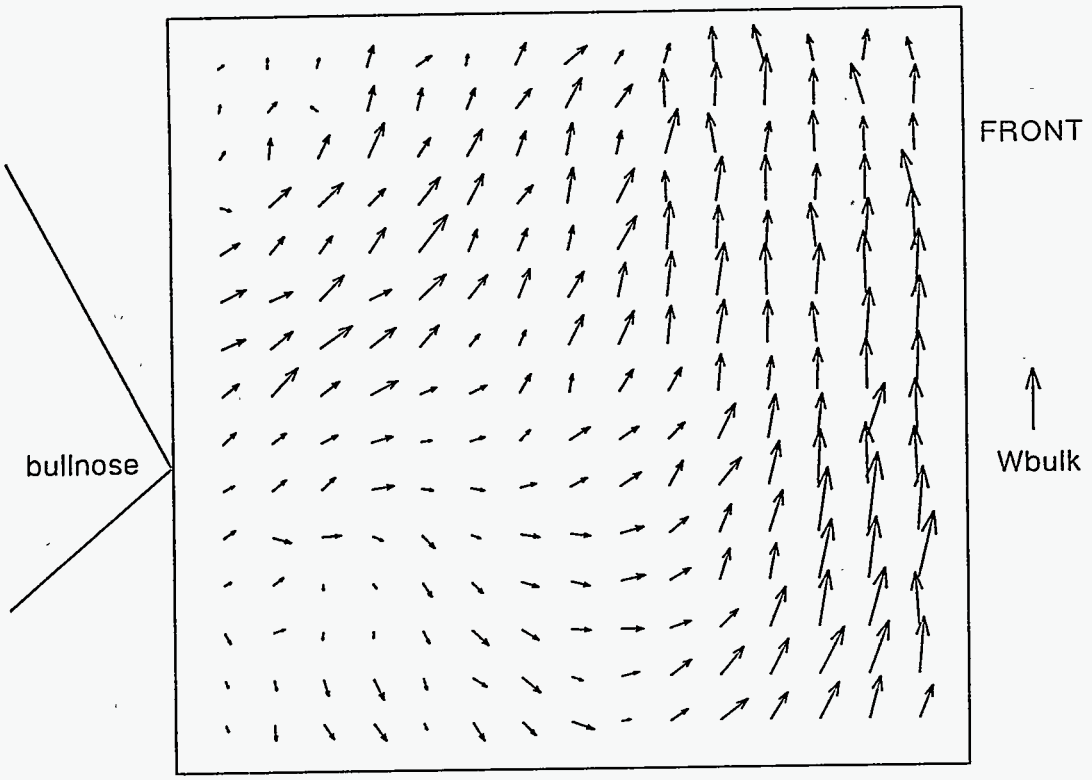

Figure 12: 30 Second Velocity Average - ABB Primary & Secondary Ports.

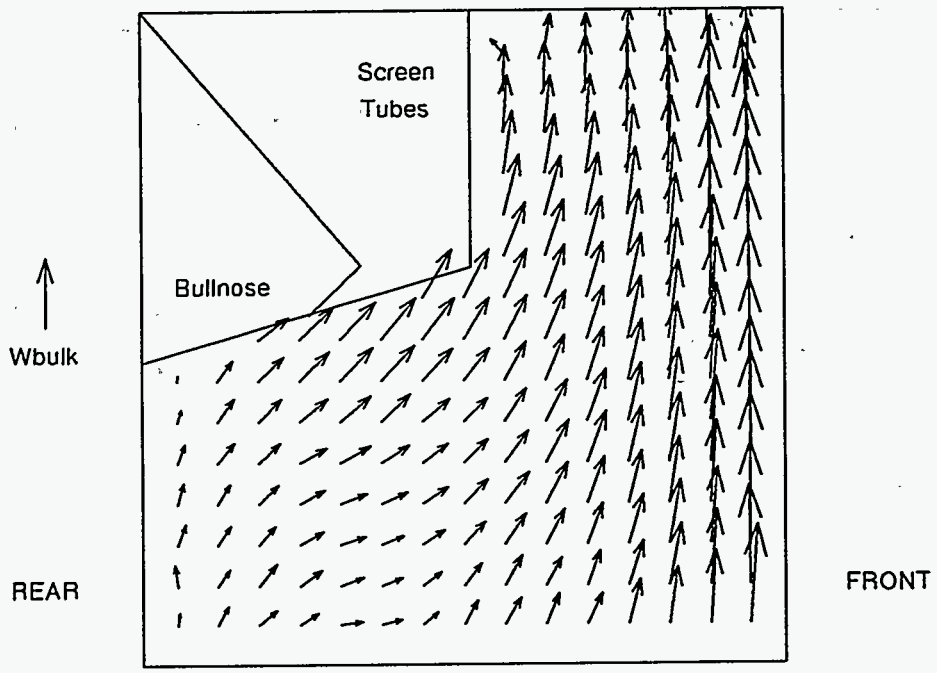

Figure 13: 30 Second Velocity Average - B&W Primary, Secondary & Tertiary Ports.

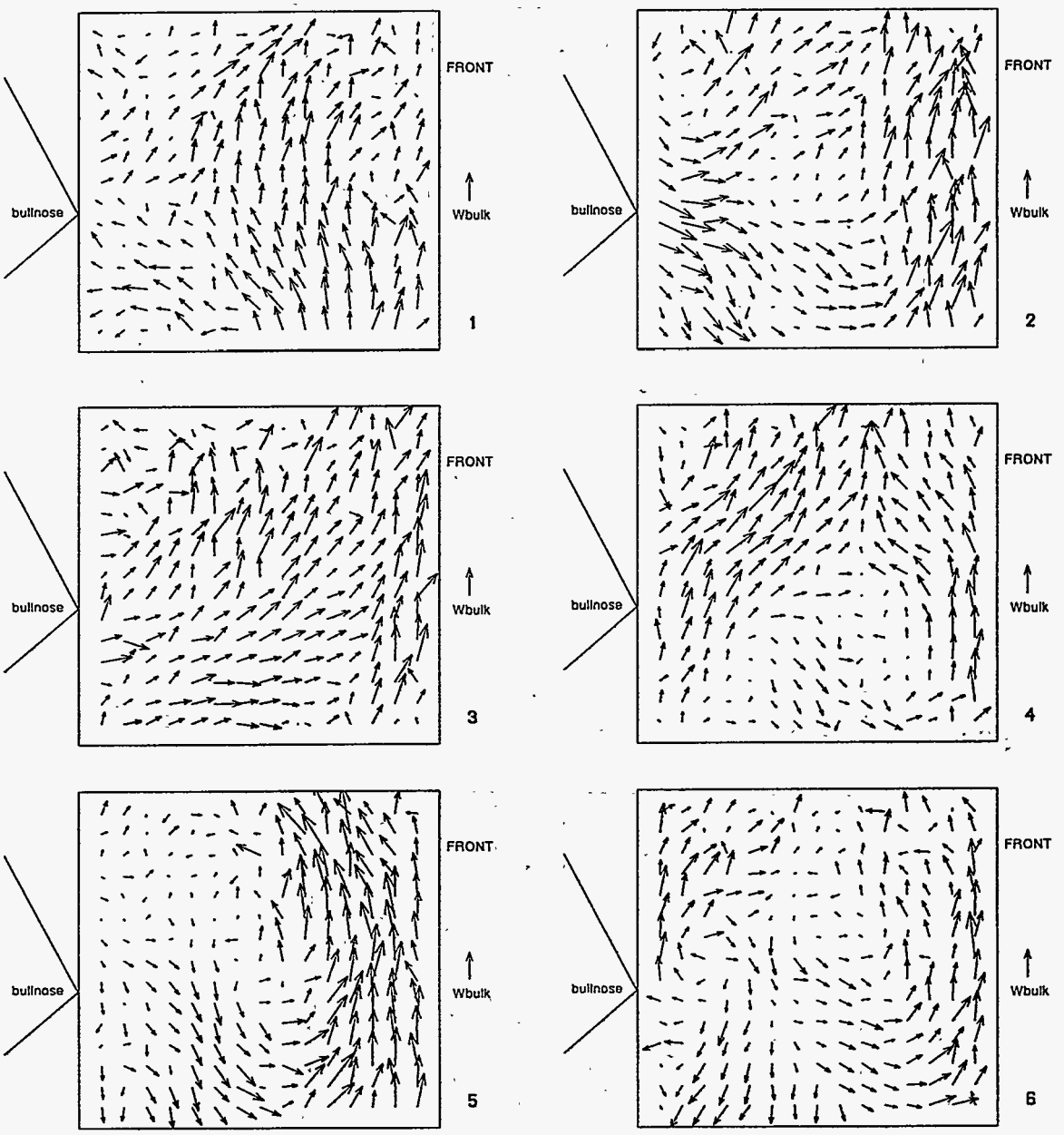

Figure 14: Consecutive 5 Second Velocity Averages - ABB Primary & Secondary Ports .

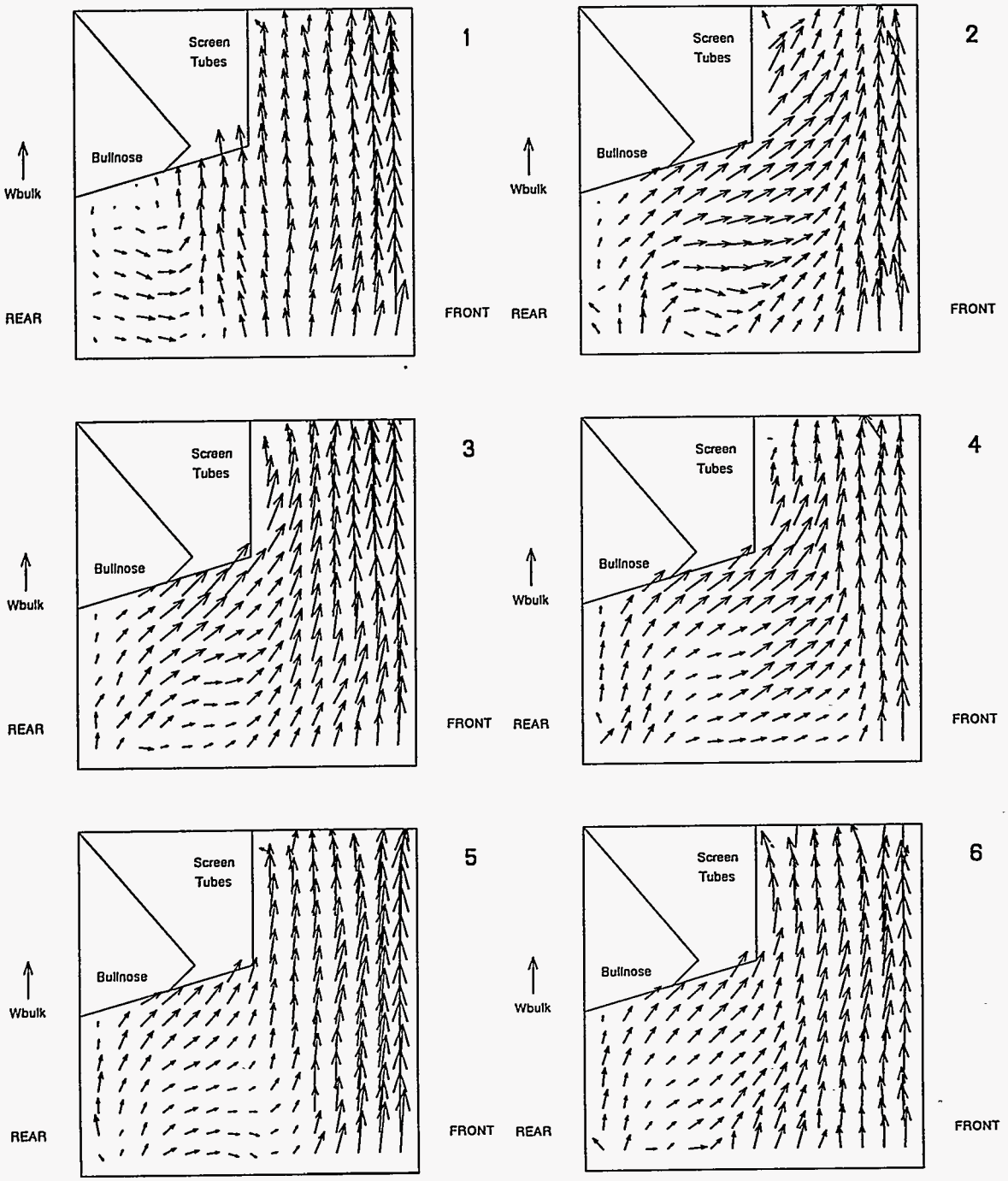

Figure 15: Consecutive 5 Second Velocity Averages - B&W Primary, Secondary & Tertiary Ports.

SECTION 4: UBC RECOVERY BOILER MODEL VALIDATION

Introduction

In this part of the report we address the need for increasing the confidence level of industry in the mathematical modeling work being carried out at UBC. This is done by directly comparing the cold flow velocity distributions obtained by actual physical measurements and by mathematical modeling. The air splits for the cases investigated are shown in table 1. The physical measurements of the flow are done at three locations: a) in the water model of the CE recovery boiler (Weyerhaeuser Plymouth), b) in the water model of the B&W recovery boiler (Weyerhaeuser Kamloops), and c) in an actual recovery boiler. It is demonstrated that mathematical modeling of the flow can yield velocity distributions which are representative of the actual flow field.

The validation work reported in this chapter represents the initial part of this activity at UBC. Additional water model measurements and cold flow trials with radical variations in combustion air distribution are planned; measurements under operating conditions will also be attempted by Paprican as part of the validation procedure. We hope that the combined series of validation tests will increase industry confidence by demonstrating that the UBC mathematical model predicts flow patterns that are realistic and show the same trends observed in an actual boiler.

Physical modeling:

Water models:

Extensive physical modeling work has been carried out using the water modeling facility at UBC. This facility consists of approximately 1/30 scale Plexiglas water models, one of a CE boiler with a lower furnace rebuilt by Götaverken, and one of a B&W boiler, and associated pumps, plumbing, valves, flow measurement devices and a water tank. These measurements have been carried out using two techniques: laser Doppler velocimetry and particle image velocimetry. The water models and measurement techniques have been described in detail elsewhere in this report. Comparison with the water model results will be presented in a subsequent section.

Full scale measurements:

Physical measurements of the cold flow in the B&W recovery boiler are being carried by Paprican and Weyerhaeuser. Funding to Paprican is being provided by the BC Science Council. Figure 1 shows a schematic of the boiler, with the primary, secondary and tertiary air ports. The air flow in the boiler at the liquor gun level was measured for several sets of flow conditions with air flow through the ports at the primary and

secondary. There was no air flow through the tertiary ports for the full scale measurement runs reported in this chapter.

The hot wire anemometers used for the velocity measurements are direction dependent; the instruments indicated different flows depending on whether the large or small element was facing the flow. During the trials the probes were positioned with the small element facing the floor of the furnace. Flow measurements in the boiler were made in a horizontal plane at the liquor gun level. The hot wire anemometer probes were attached to extension tubes and inserted through the liquor gun openings and the observation ports at the liquor gun level. Figure 2 shows the measurement locations at the liquor gun level. The direction of the flow was determined from the orientation of a brightly colored paper ribbon attached close to the hot wire probes. Pressure measurements at the primary and secondary wind boxes were also made to calculate the flow through the individual air ports. This information is necessary to establish the boundary conditions of the mathematical model of the flow in the boiler. In order to determine the flow distribution across an air port opening, pitot tube measurements were carried out for selected air ports where this was possible. Flow velocities in the primary and secondary air ducts were also measured using pitot tubes. This information is helpful in cross checking the measurements at each air port. To eliminate outlying data points resulting from measurement error, flow unsteadiness and instability, RMS velocities were plotted as a function of position to create velocity profiles across the furnace for the various traverses conducted during both trials. Points that showed significant deviation from the smoothed profile were discarded.

It can be seen from Figure 2 that velocity measurements could not be made in some regions at the liquor gun level. Velocities in these regions were interpolated on the basis of neighboring velocity profiles, and by comparing the total integrated up flow at the liquor gun level to the measured total air flow in the primary and secondary ducts. Agreement between the total flow through the ducts and the integrated up flow at the liquor gun level was within 30%. The authors consider this level of agreement to be quite good, considering the sources of errors, for example, the large scale of the measurement volume, the sparse regions where the measurements were taken and the flow unsteadiness.

Mathematical modeling

The mathematical modeling work was done using the UBC code described elsewhere. The rows of primary air ports at each wall were modeled as slots, however each secondary and starter burner port was modeled individually. The computational domain extended up to the top of the boiler and included the bull nose. The superheaters and boiler tube banks were not modeled. The boundary conditions are specified as follows:
Inflow: This condition was applied to all the air port openings. Values of all the variables were specified except the pressure. The turbulent kinetic energy was estimated from the inflow velocities, and the turbulence energy dissipation rate was estimated from a characteristic length scale using standard methods.
Outflow: A zero stream wise gradient condition was imposed for all variables at the exit

of the computational domain, located close to the boiler tube bank.
Wall conditions: This condition is applied at all the walls of the domain. Zero values for the normal and tangential velocities were used, in conjunction with conventional wall function treatment for the turbulence quantities and the wall stresses.

Results and discussion:

Full scale comparisons

The full scale validation work is carried out for a relatively large B&W recovery boiler (rated capacity 4 million lb. of black liquor solids/day; approximately 12 m in cross section). The measurement grid shown in Figure 2 was quite sparse, with large regions where it was not possible to obtain data. Velocities in these regions were estimated by interpolating between measured data points. In addition, it was not possible to directly measure the velocity at most of the air ports. The velocity at the air ports was calculated from wind box pressures, which were obtained by inserting a probe into small access openings in each wind box. These pressure readings varied considerably as they depend on the orientation of the flow to the pressure measurement probe. The velocity distributions across the port could not be obtained for most air ports. The hot wire probes were accurate to five percent if the flow was reasonably aligned with the probe under the controlled steady conditions of a wind tunnel. However, the flow in the boiler had an unsteady component, which caused the ribbons to flutter, and made accurate determination of the flow direction difficult in some regions. Due to these difficulties, a 30% difference was noted between the total flow calculated from the wind box pressures and the calculated total upward flow integrated at the liquor gun level. Although the 30% tolerance seems large, it should not be too surprising, considering the factors outlined above and the problems associated with hot wire anemometer calibration noted earlier. The 30% variation is also well within the variation in velocity measurements at a given location observed in this and earlier studies. The degree of agreement between the measured and the predicted results should thus not be expected to be quantitative. At best, we should expect a qualitative agreement, as the computations are based on the velocity boundary conditions calculated on the basis of the wind box pressures. With this in mind, the measured and the computed results are presented in this section.

Case(FS-a): October 1992 Trial 1, Flow through the primary and secondary air ports

Figure 3 shows the measured and computed upward velocity distributions at the liquor gun level for case (FS-a), with air flow through both the primary and the secondary ports. The measurements indicate a strong up flow core, mostly in the central region, but deflected somewhat toward the rear-left corner. A fairly strong down flow region exists along the right wall. The down flow is more pronounced in the front right corner. Weak downward flow was also measured in the front left corner. The down flow was weaker along the rear-right corner. Some fluctuation of the flow direction was observed at the rear left corner during the measurements, however the averaged flow measurements,

plotted in Figure 3 indicate a weak up flow in this region. The computed velocity distribution, shown on the right panel of Figure 3 is very similar to the measured velocity distribution. The upward and downward flow and the zero velocity regions are at similar locations. The computed results indicate a weak down flow in the rear left corner, however the zero velocity contour is also close to this location. In actual physical measurements, one would expect very low velocities (and even reversal in flow direction) in such a region. Weak flow reversals were noted during the measurements in this region. Analysis of the computed flow patterns at the secondary level (not shown here) indicates a strong interaction of the air entering from the secondary and starter burner ports. The flow from the starter burner ports, especially from the front right port, is very strong and penetrates deeply into the domain. This flow then turns upward and forms part of the upward flowing core. The displacement of the upward flow towards the left wall is because of the deep penetration of the flow from the starter burner port at the front left region.

Case(FS-b): October 1992 Trial 2, Flow through the secondary air ports only

Steady state computations did not yield a converged solution for case (FS-b), in which air flow was through the secondary ports only. A transient algorithm yielded a converged solution which varied with time. The computations were carried out to simulate a real time period of 170 seconds, and a converged solution was obtained for each time step, however no periodicity in the solution was observed during this computation. It should be mentioned that considerable unsteadiness was observed in the cold flow measurements for this case. It appears that the primary air flow stabilized the flow field considerably. It should be noted that UBC has already reported on the unsteady interaction of opposed jet configurations elsewhere in this report. Figure 4 shows the measured results, as well as the converged computed results for one time step for case (FS-b). Since the flow measurements were carried out over a period of several hours, the measured velocity distribution represents a form of an average of the time dependent flow field. It can be seen that the average vertical velocity in a fairly large region close to the rear-left wall is approximately zero. In fact, considerable flow reversals were noted in this region during the actual measurements. The up flow is mainly in the center, and in the front left corner. There is down flow along the right and rear walls. The computed velocity field for one time step is also shown in the same figure. It can be seen that there are many similarities between the measured and the computed fields. The computed field also indicates up flow to be along the front left corner and down flow along the right and rear walls. The strongest down flow appears to be along the rear wall for the time step shown in Figure 4. This strong down flow region moves along the rear and side walls as the time is advanced in the transient computations. Figure 5 shows the computed vertical velocity field at the liquor gun level at different times. The transient nature of the flow field can be seen. The change of direction of the flow along the left wall can also be seen as the time is advanced.

Analysis of the velocity distribution showed that there is considerable down flow under the secondary jets as the flow from the primary ports is not present to help deflect the

secondary flow upward. The down flow from the secondary ports deflects upward from the floor of the boiler and interacts with the air from the secondary ports.

Case(FS-c): May 1993 Trial 2, Flow through the primary and secondary air ports

This case is similar to case (FS-a), with the main difference that there is a side to side imbalance in the secondary air flow. The air flow from the secondary ports on the right side is 20% higher than that on the left side wall. The secondary level flow from the front and rear walls is balanced, and the flow from the primary level is balanced on all four walls. Figure 6 shows the velocity distribution at the liquor gun level. We see that the upward flow has been pushed toward the left side of the boiler and there is downward flow along the right side wall. The computed results show very similar features as those of the measurements. The upward flow is along the left side wall, and the downward flow is along the right side wall. The location of the zero vertical velocity contour is very similar for both the computations and the measurements. The peak values of the upward and the downward velocities are also very similar. The overall velocity flow patterns in the boiler show features similar to those in case (FS-a).

Case(FS-d): May 1993 Trial 3, Flow through the primary and secondary air ports

The flow in this case was set up with balanced four wall primaries, balanced front and rear wall secondaries, and coarsely interlaced (small-large) side wall secondaries. The resulting flow pattern is shown in figure 7. We see that there is a bias of the upward flow toward the left side wall. There is downward flow close to the right side wall. The computational results show similar features with upward flow close to the left wall and downward flow close to the right wall. In this case, as well, the locations of the zero vertical velocity contours are very similar. The measurements do not show the peak upward velocity contour of 4m/s, however a parametric analysis (not shown here) has indicated to that the computed flow pattern could be made to resemble the measured flow pattern much better by modifying the secondary jet flows by less than 5%. Since the boundary conditions (flow rates at the ports) are not known to such high accuracy, we can conclude that the agreement between the measurements and the computations is reasonable.

Water model comparisons

The water model measurements and computations were done for both the B&W boiler model of the Weyerhaeuser Kamloops BC recovery boiler and for the Götaverken modified ABB-CE boiler model of the Weyerhaeuser Plymouth NC recovery boiler. Figures 8 and 9 show schematics of the water models, with the measurement planes for the laser Doppler velocimeter system. Velocity measurements were taken at three horizontal planes, "level 1", between the secondary and the tertiary elevations, "level 2", just above the tertiary elevation, and "level 3", under the bull nose arch. It should be noted that the ABB-CE boiler model reflects the lower furnace refit by Götaverken. Even though the boiler is of a vintage CE design, it has four wall primaries, four wall

secondaries, two wall (front rear interlaced) tertiaries, and the original CE load burners. We now show the measured and computed results for some of the water model tests.

Case(WM-a): Kamloops B&W water model, primary and secondary:

Figures 10, 11 and 12 show the results for the Kamloops water model for the case with flow from the primary and secondary levels only. This water model test was done to show the similarities between the full scale measurement case (FS-a) and the water model measurements. Figure 10 shows the velocity distribution at "level 1", above the secondary elevation. Flow features similar to those in figure 3 can be seen. There is upward flow close to the left side wall, and downward flow along the right wall, closer to the front wall. The small circles on the left image indicate the 6 by 6 measurement grid. The upward flow core closer to the left side can be seen. The computed and the measured fields are quite similar. Figure 11 shows the vertical velocity distribution at level 2. Similar features in the flow fields can be seen, i.e. upward flow in the rear left half of the model, and downward flow in the front right half. Figure 12 shows the velocity distribution at level 3, under the bull nose. The measurement contours are very irregular, which indicates that it was not possible for the contouring routine to plot smooth contours with the available values. This is because the measured values were somewhat inconsistent due to flow fluctuations. A comparison at level 3 could not be carried out.

Case(WM-b): Kamloops B&W water model, primary, secondary and tertiary:

The second case considered for the Kamloops water model simulated air input under normal operating conditions. Ports on all three levels (primary, secondary and tertiary) were active. The water model was set up as symmetrically as possible, with 4 wall primary and secondary, and two wall tertiary. The measured and computed results are shown in figures 13-15. As before, the small circles indicate the measurement locations. Figure 13 shows the vertical velocity at level 1, above the secondary elevation. The velocity values have been non dimensionalized by the average upward velocity. The measured and computed flow fields look quite similar. The measured flow field is not as symmetrical as the computed flow field. This demonstrates that it is very difficult to attain a high degree of symmetry in setting up a water model (or a real boiler). Figure 14 shows the vertical velocity distribution at level 2, above the secondary level. The flow fields are similar. The computed flow fields show a somewhat higher peak velocities as compared to the measurements. Figure 15 shows the velocity distribution at level 3, under the bull nose. We see similar velocity fields for both cases, with upward flow in the rear left side and downward flow in the front right side.

Case(WM-c): Plymouth ABB-CE water model, primary, secondary and tertiary:

Measurements and computations have also been done for the Plymouth water model. This is a vintage ABB-CE boiler, with a lower furnace rebuild by Götaverken. For the present case, the boiler is operated with four wall primary, four wall secondary and two

wall interlaced tertiary. Figures 16-18 show the results for the vertical velocities. Figure 16 shows the vertical velocity at level 1, above the secondary elevation. Fairly good agreement can be seen between the measurements and the computations, with a central upward flow. Figure 17 shows the flow at level 2, above the tertiary level. Good agreement is obtained here as well, with upward flow close to the front and rear walls, and very little upward flow in the central region. Figure 19 shows the flow under the bull nose. Good agreement can be seen here as well with low velocity in the central region and higher velocities close to the walls.

Conclusions

Isothermal flow measurements and computations were carried out for a number of flow configurations in water models of B&W and ABB-CE boilers, and in an actual B&W boiler. For all cases, qualitative agreement was obtained between the computed and the measured results. The up flow and down flow regions were correctly predicted. The zero upward velocity contours have a similar shape across most of the cross section, both for the physical measurement results and the mathematical modeling results. The peak values of the up flow and down flow velocities were similar for the measurements and the modeling in most cases. This validation work indicates that the computations are able to capture the essential features of the flow fields for a wide variety of operating conditions investigated.

Table 1: Flow distribution for the cases investigated

No	Case	Primary	Secondary	Tertiary
1	FS-a	61	39	
2	FS-b		100	
3	FS-c	63.5	36.5	
4	FS-d	61	39	
5	WM-a	61	39	
6	WM-b	33	33	33
7	WM-c	36	47	17

Note: FS indicates full scale runs
WM indicates water model runs

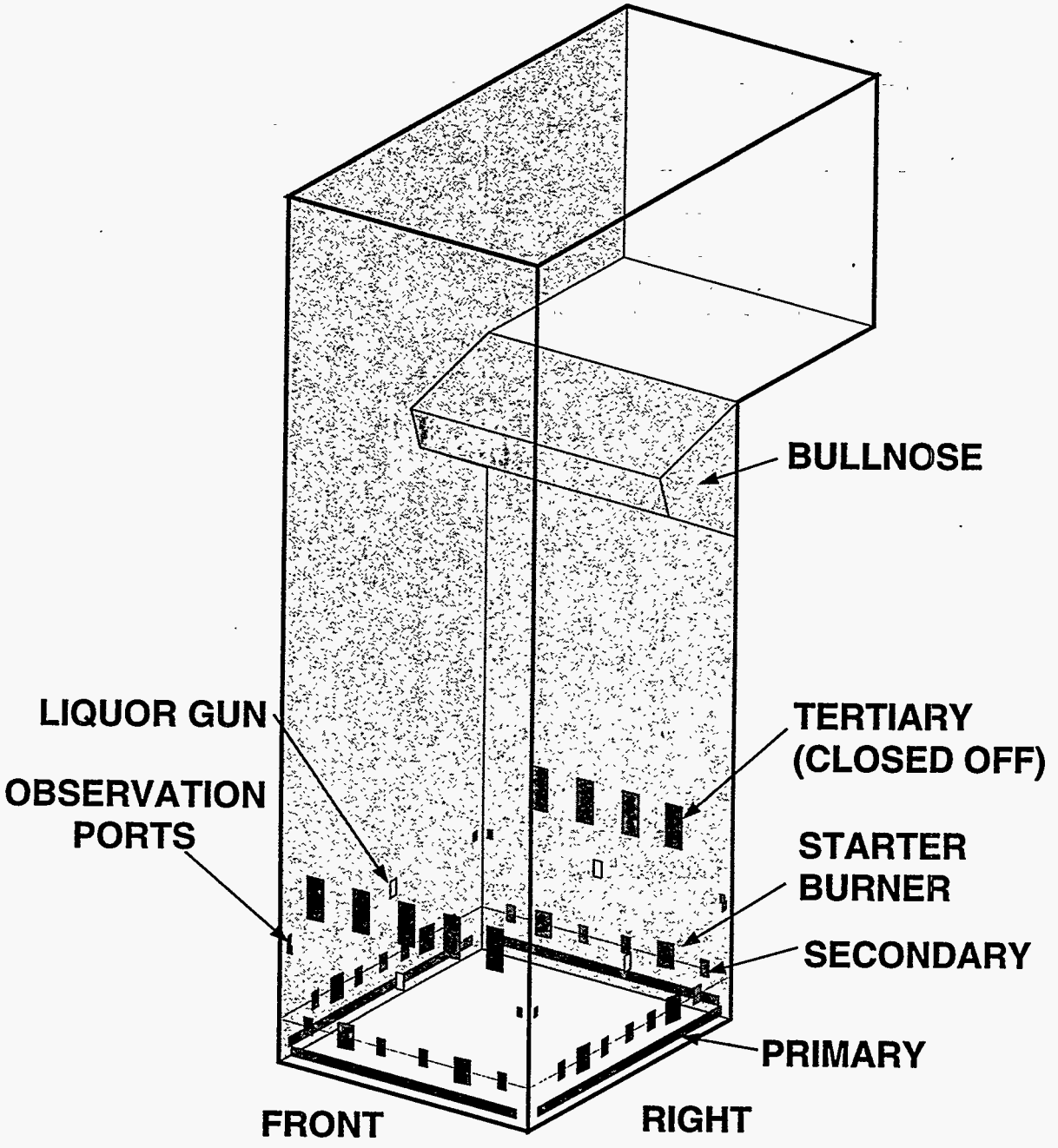

Figure 1: Schematic of the boiler showing the air and liquor gun ports..

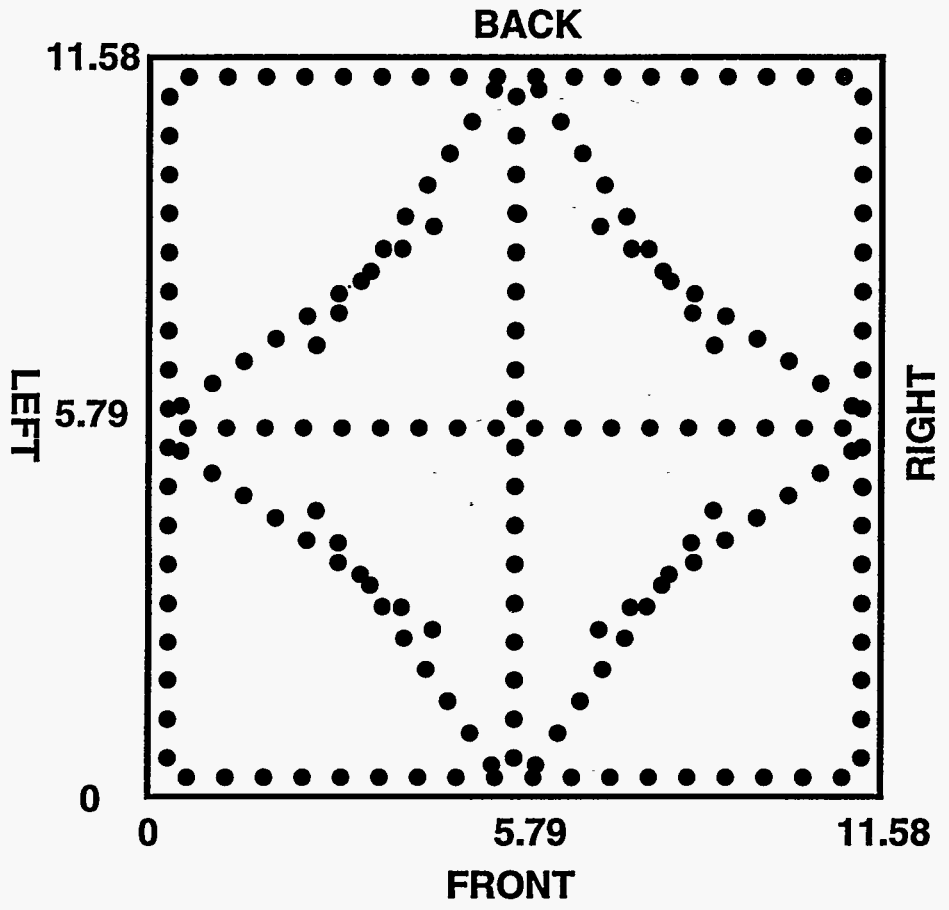

Figure 2: Typical velocity measurement locations at the liquor gun level (dimensions in (m)).

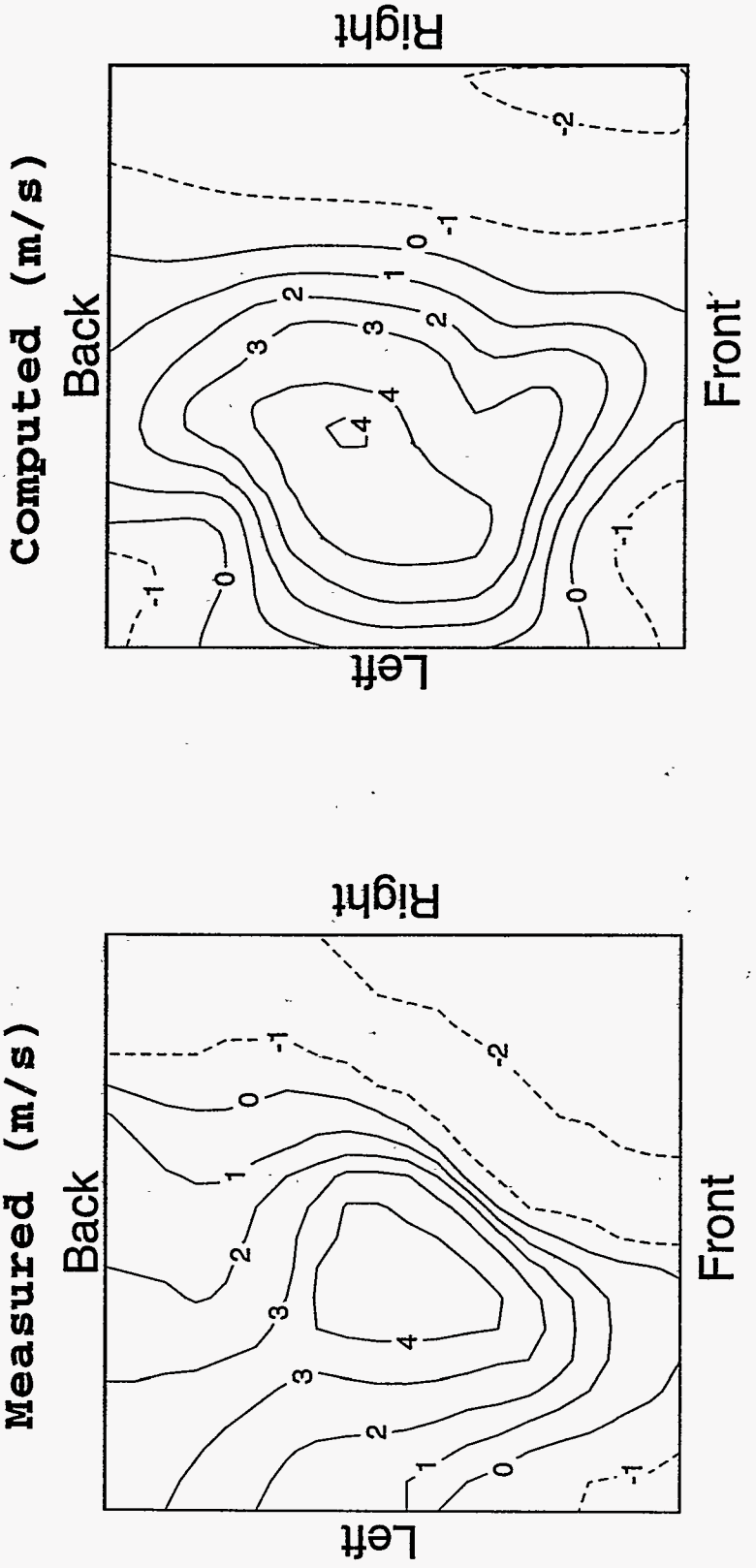

Figure 3: Measured and computed vertical flow (in m/s) at the liquor gun level (case (FS-a), inflow through primary and secondary ports. Positive values indicate upward flow, negative values indicate downward flow.)

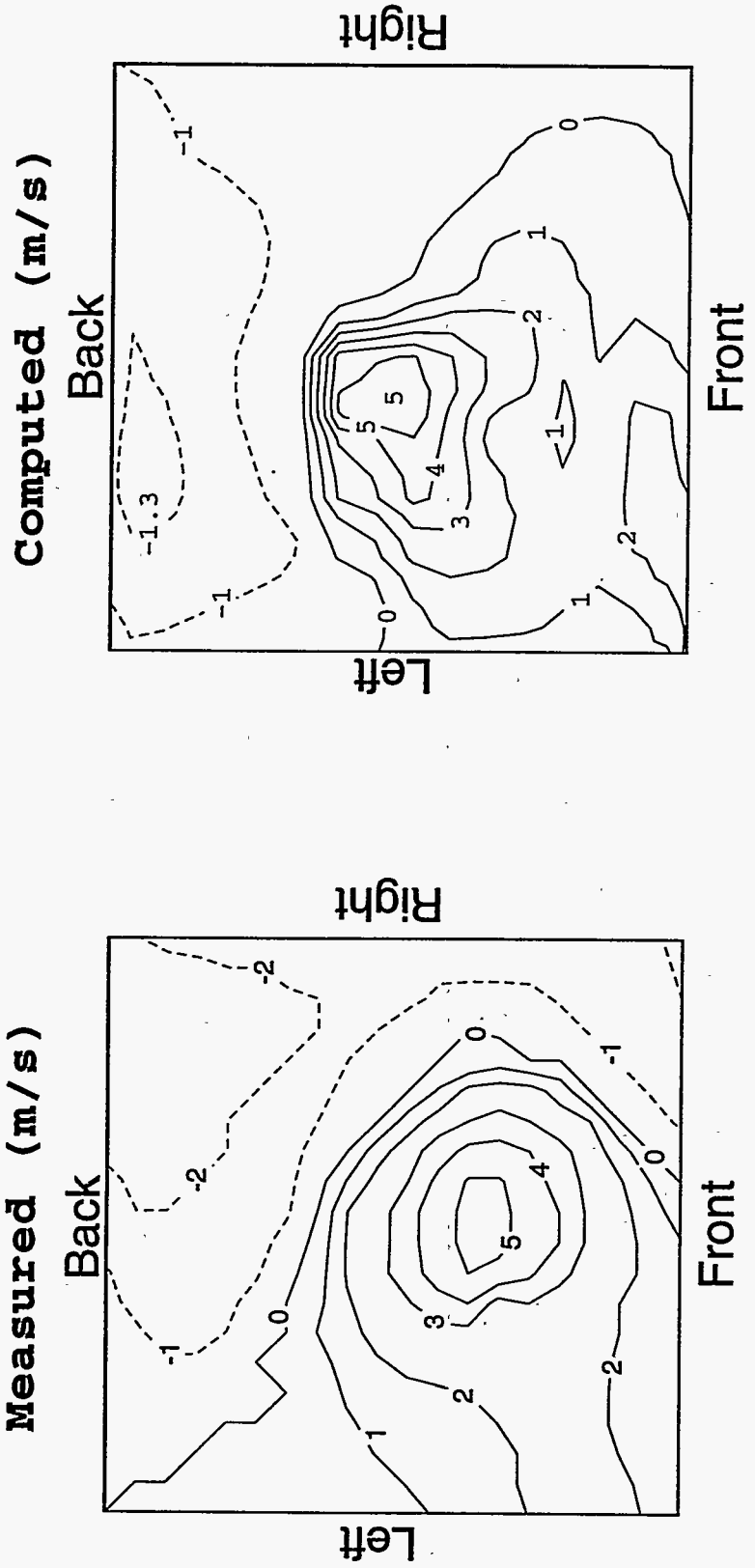

Figure 4: Measured and computed vertical flow (in m/s) at the liquor gun level (case (FS-b), inflow through secondary ports only. Positive values indicate upward flow, negative values indicate downward flow.)

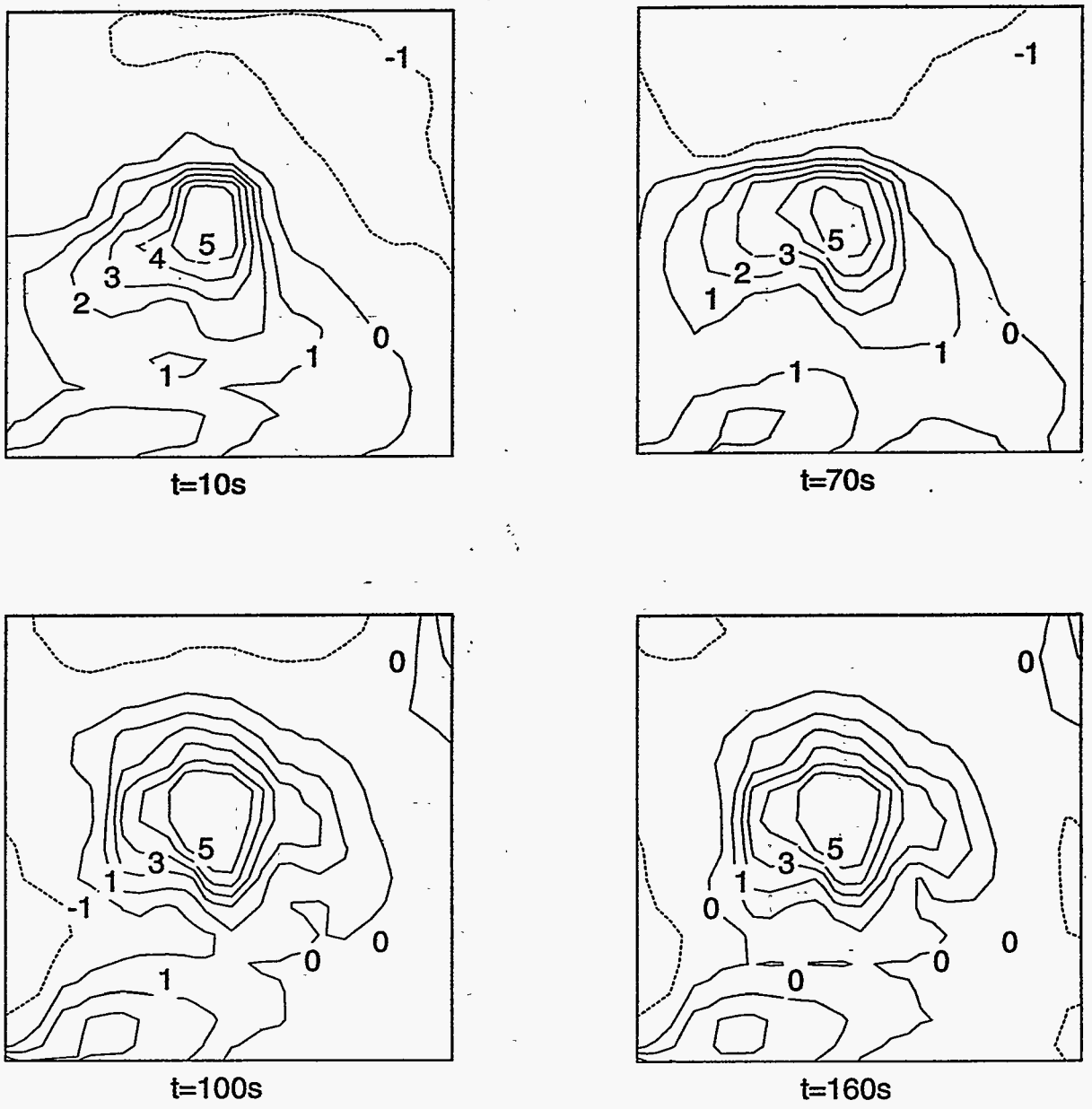

Figure 5: Vertical velocity distribution (in m/s at the liquor gun level at different times).

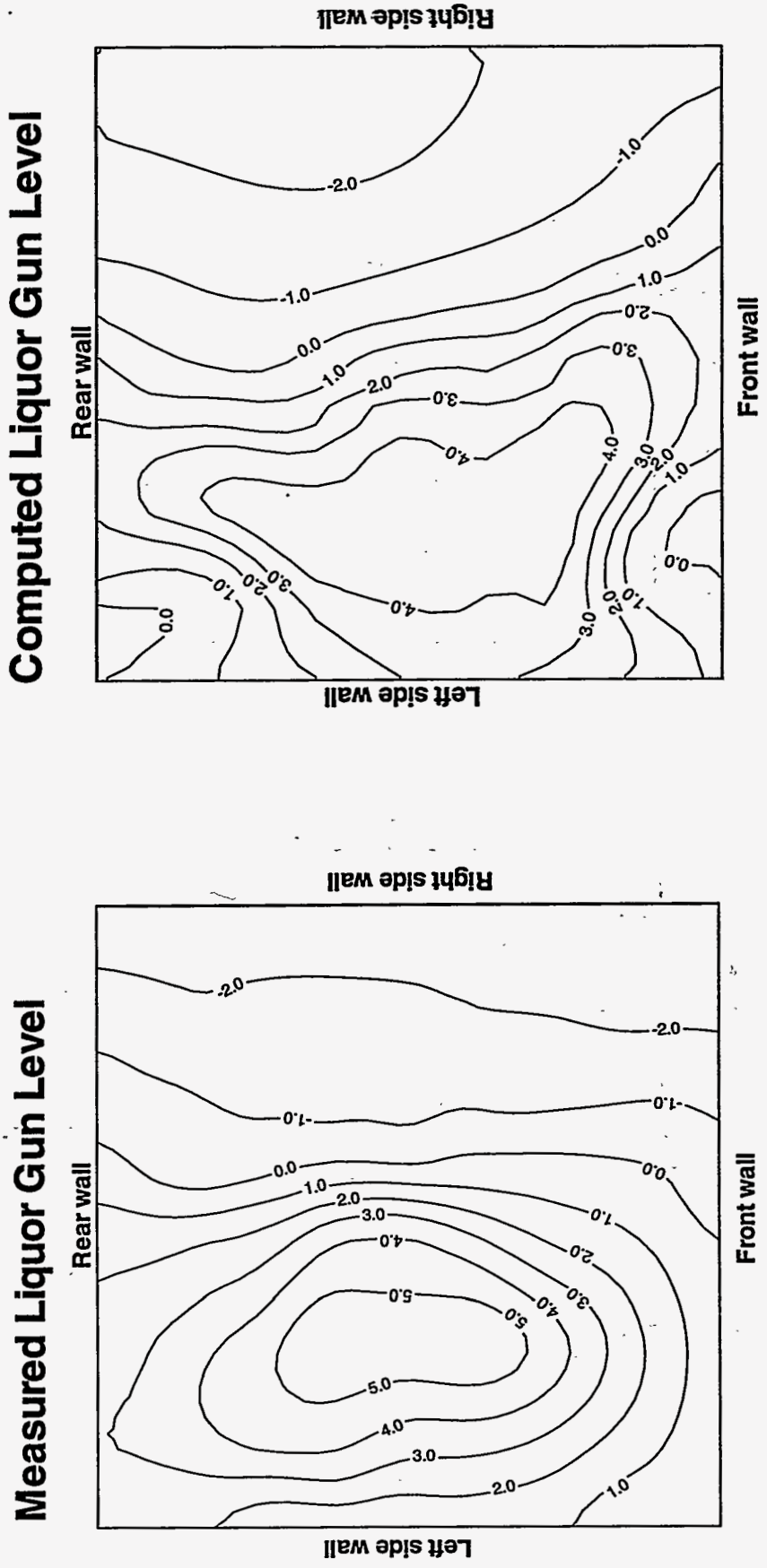

Figure 6: Measured and computed up flow (in m/s) at the liquor gun level (case (FS-c), inflow through primary and secondary ports. Secondary flow on right side wall +20%, secondary flow on left side wall -20%) .

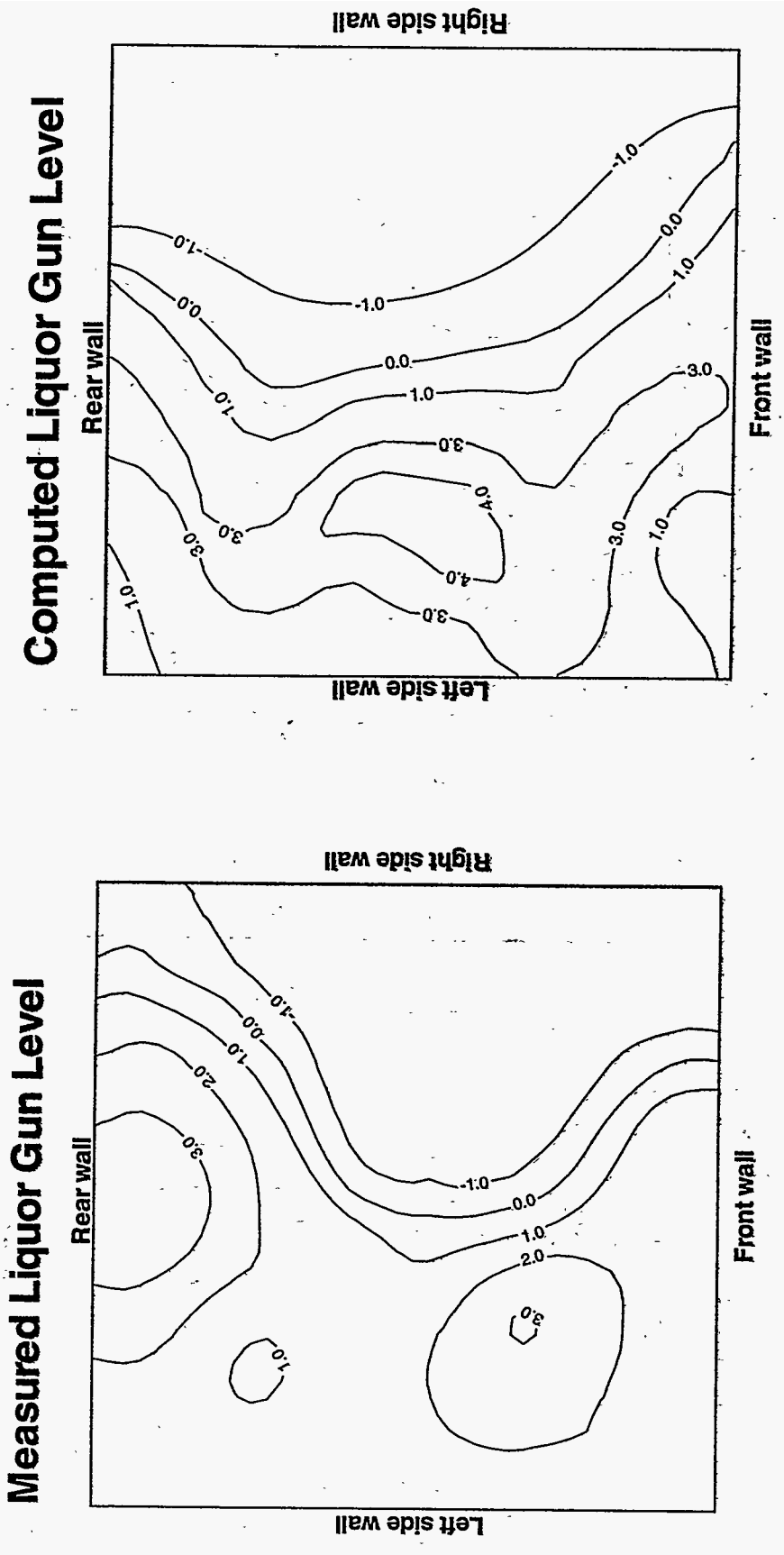

Figure 7: Measured and computed up flow (in m/s) at the liquor gun level (case (FS-d), inflow through primary and secondary ports. Coarsely interlaced (small-large) side wall secondaries.

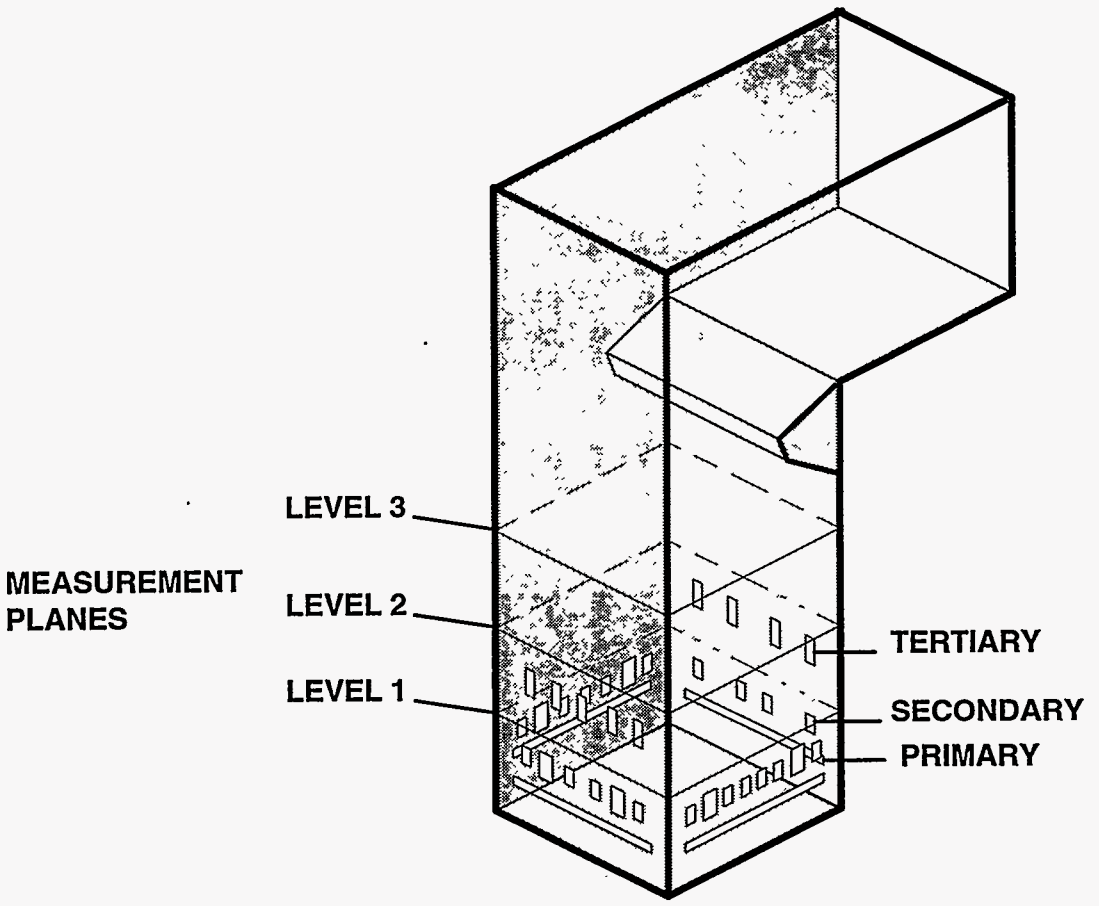

Figure 8: B&W Recovery boiler water model (Weyerhaeuser Kamloops Recovery Boiler).

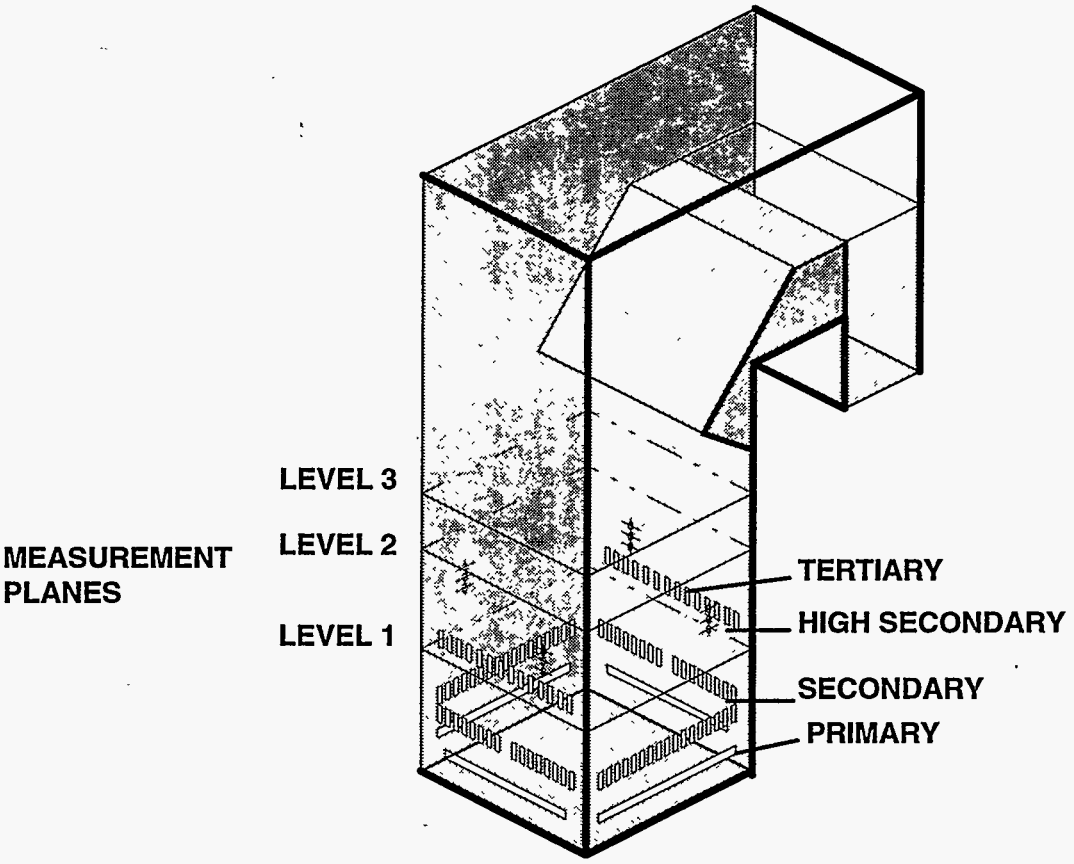

Figure 9: ABB-CE Recovery boiler water model with lower furnace rebuilt by Götaverken (Weyerhaeuser Plymouth Recovery Boiler).

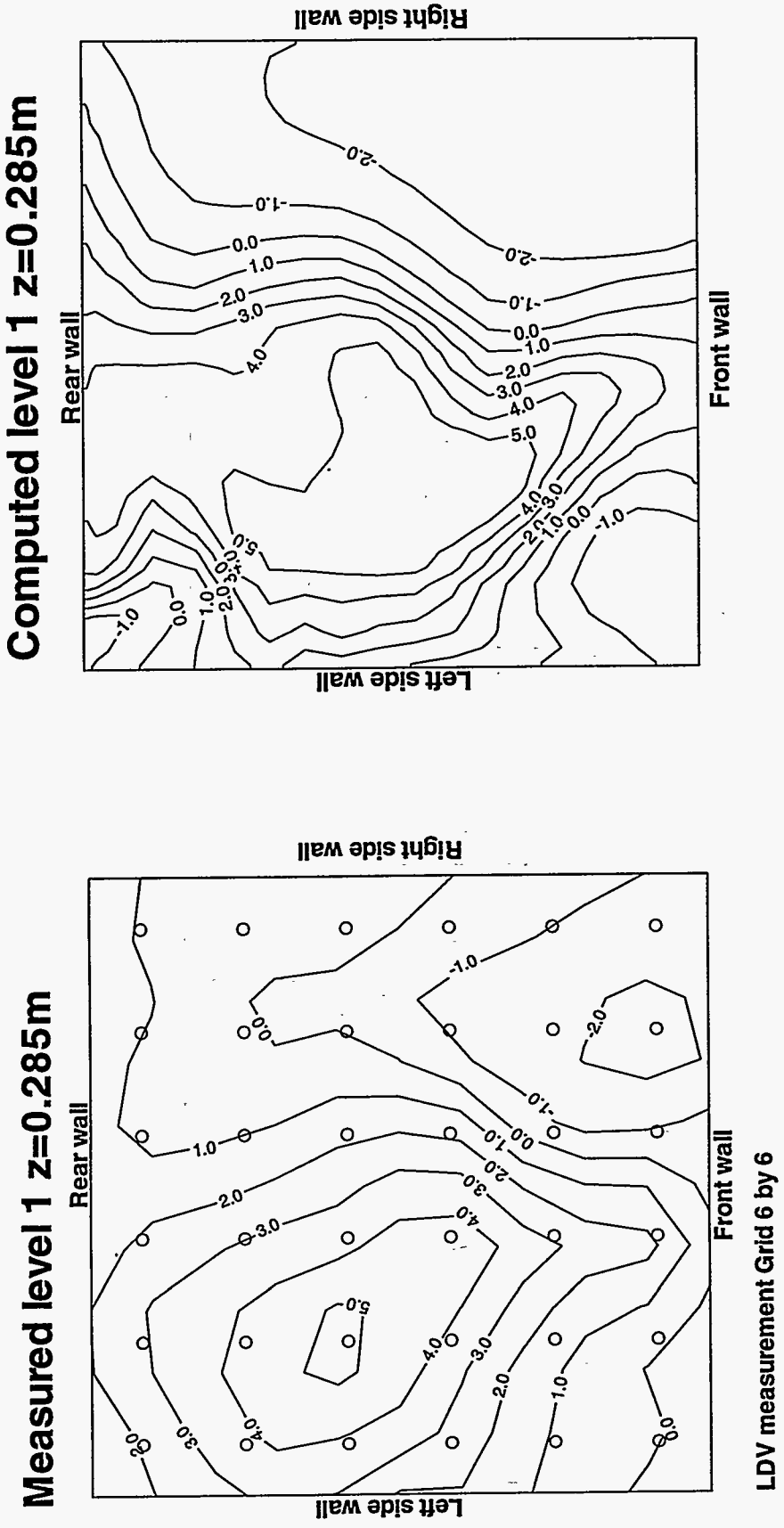

Figure 10: Kamloops boiler water model, measurements and computational results, primary and secondary, level 1. (Case (WM-a))

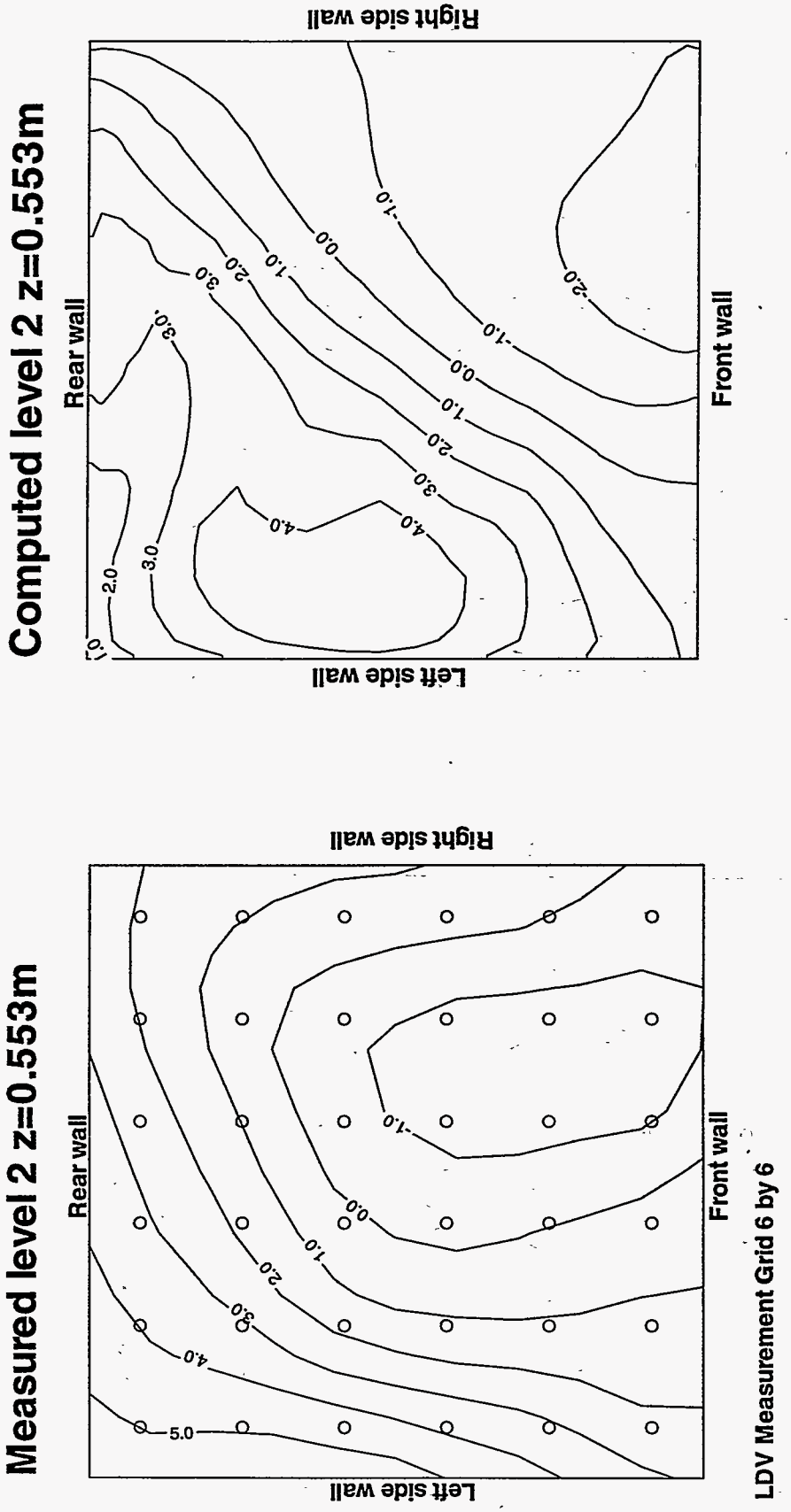

Figure 11: Kamloops boiler water model, measurements and computational results, primary and secondary, level 2. (Case (WM-a))

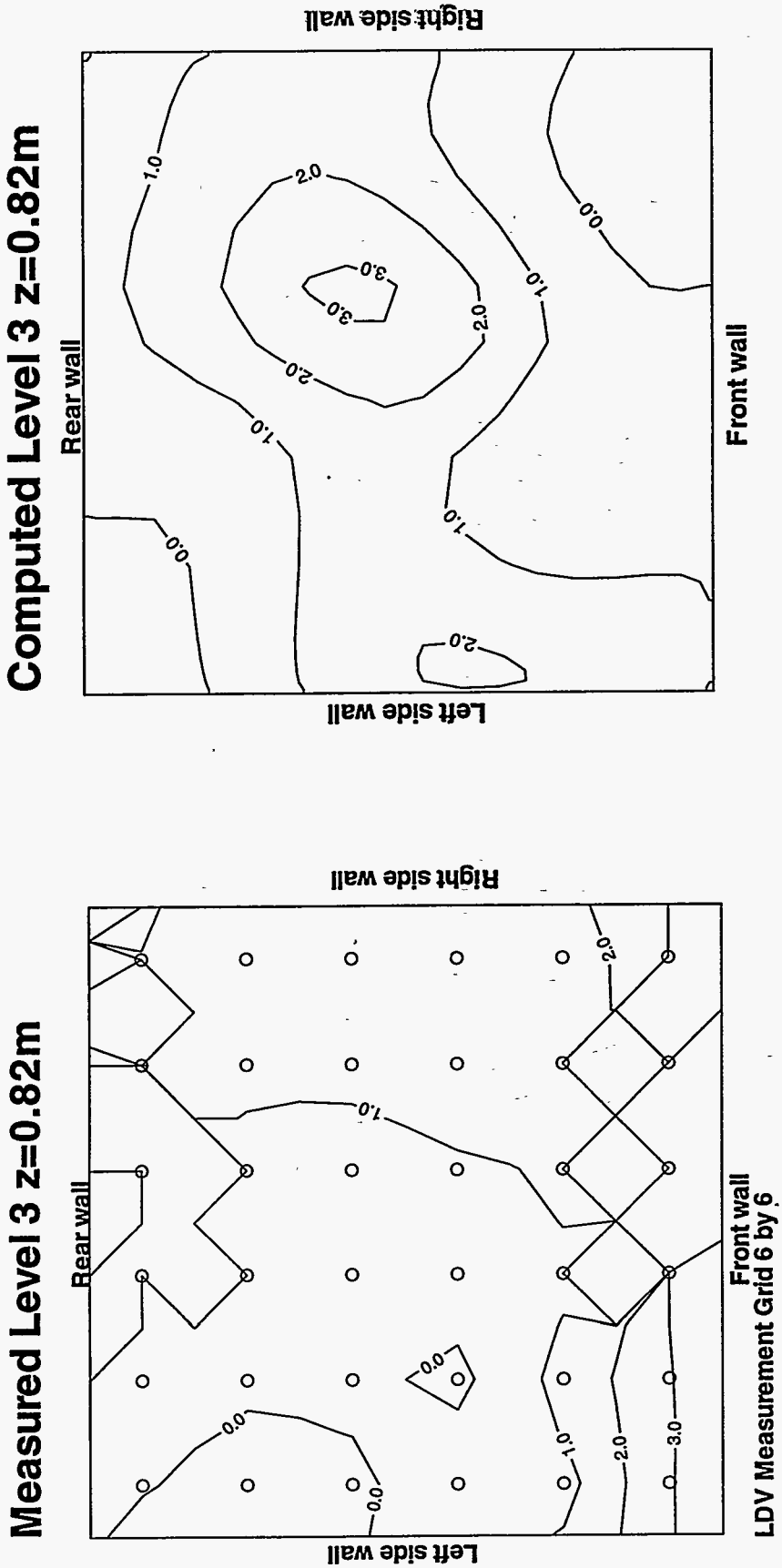

Figure 12: Kamloops boiler water model, measurements and computational results, primary and secondary, level 3. (Case (WM-a))

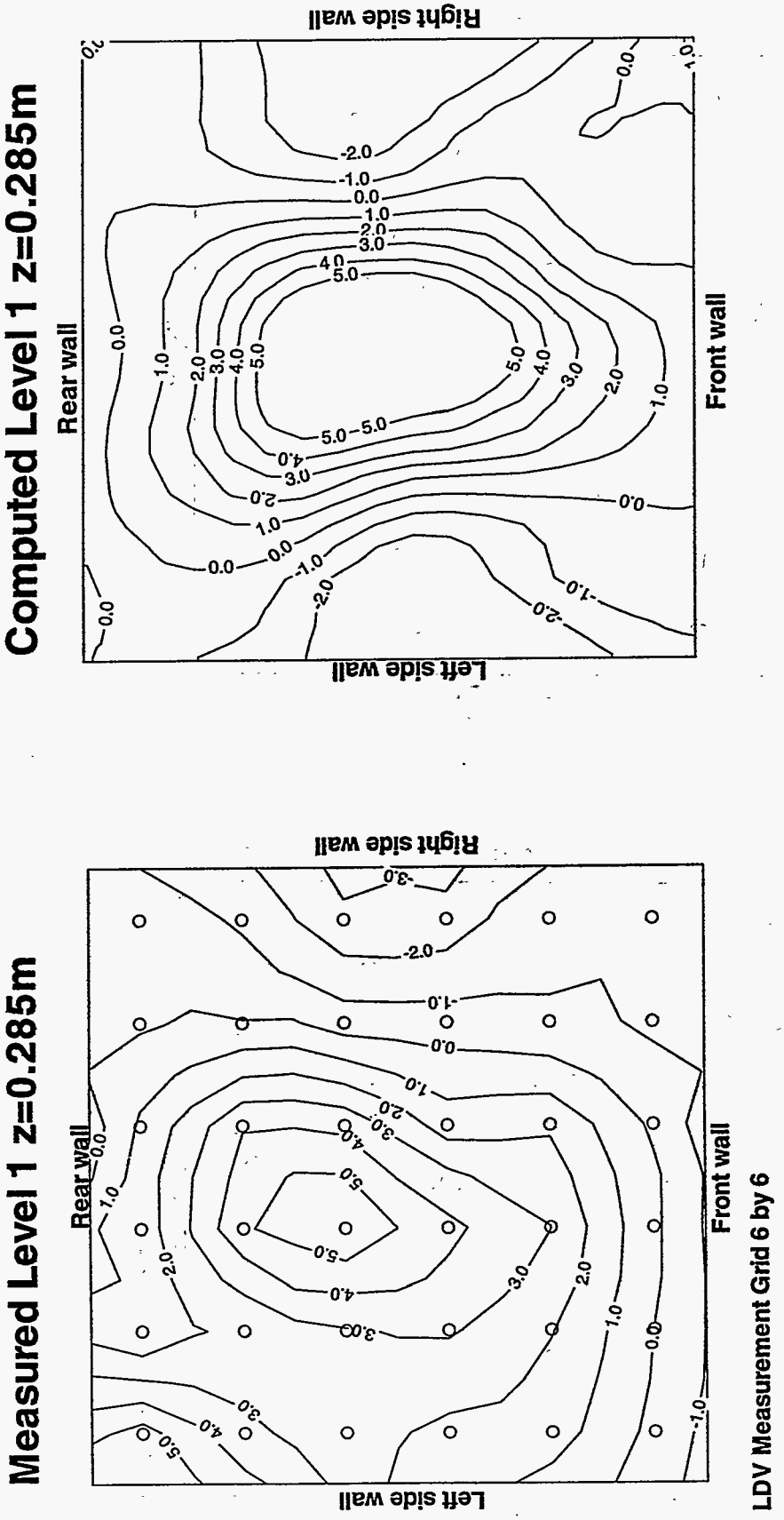

Figure 13: Kamloops boiler water model, measurements and computational results, primary, secondary and tertiary, level 1 (Case (WM-b)).

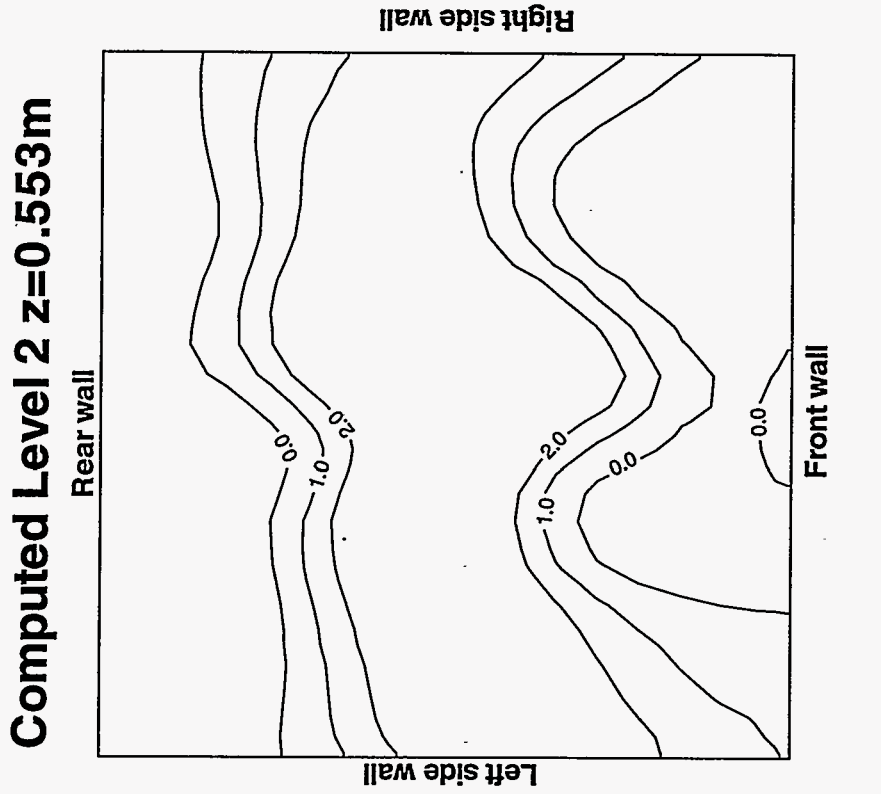

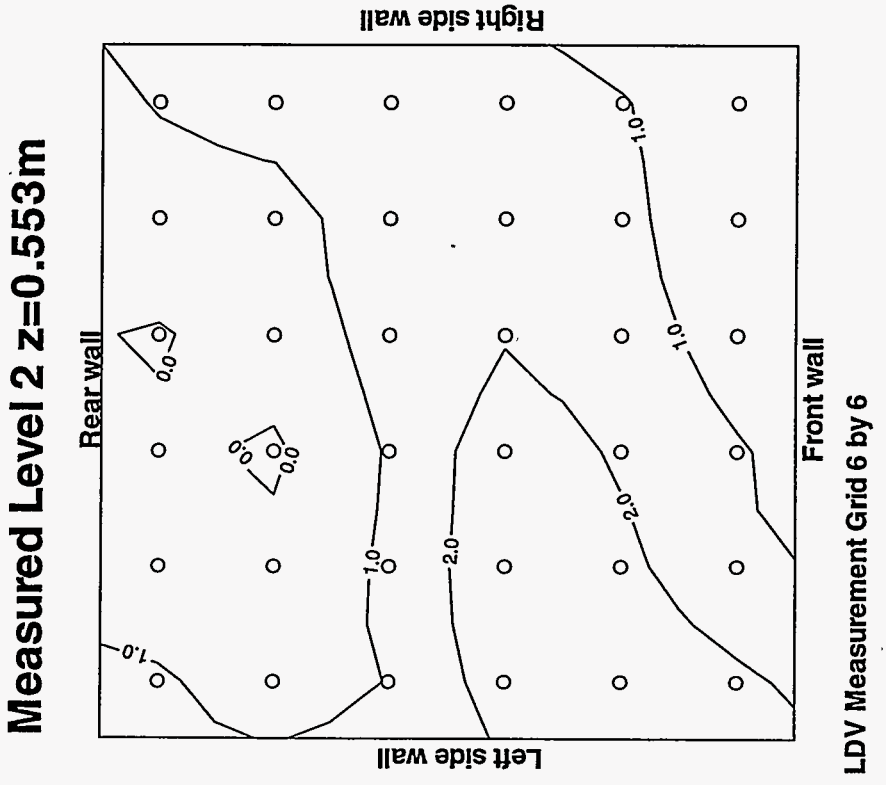

Figure 14: Kamloops boiler water model, measurements and computational results, primary, secondary and tertiary, level 2. (Case (WM-b)).

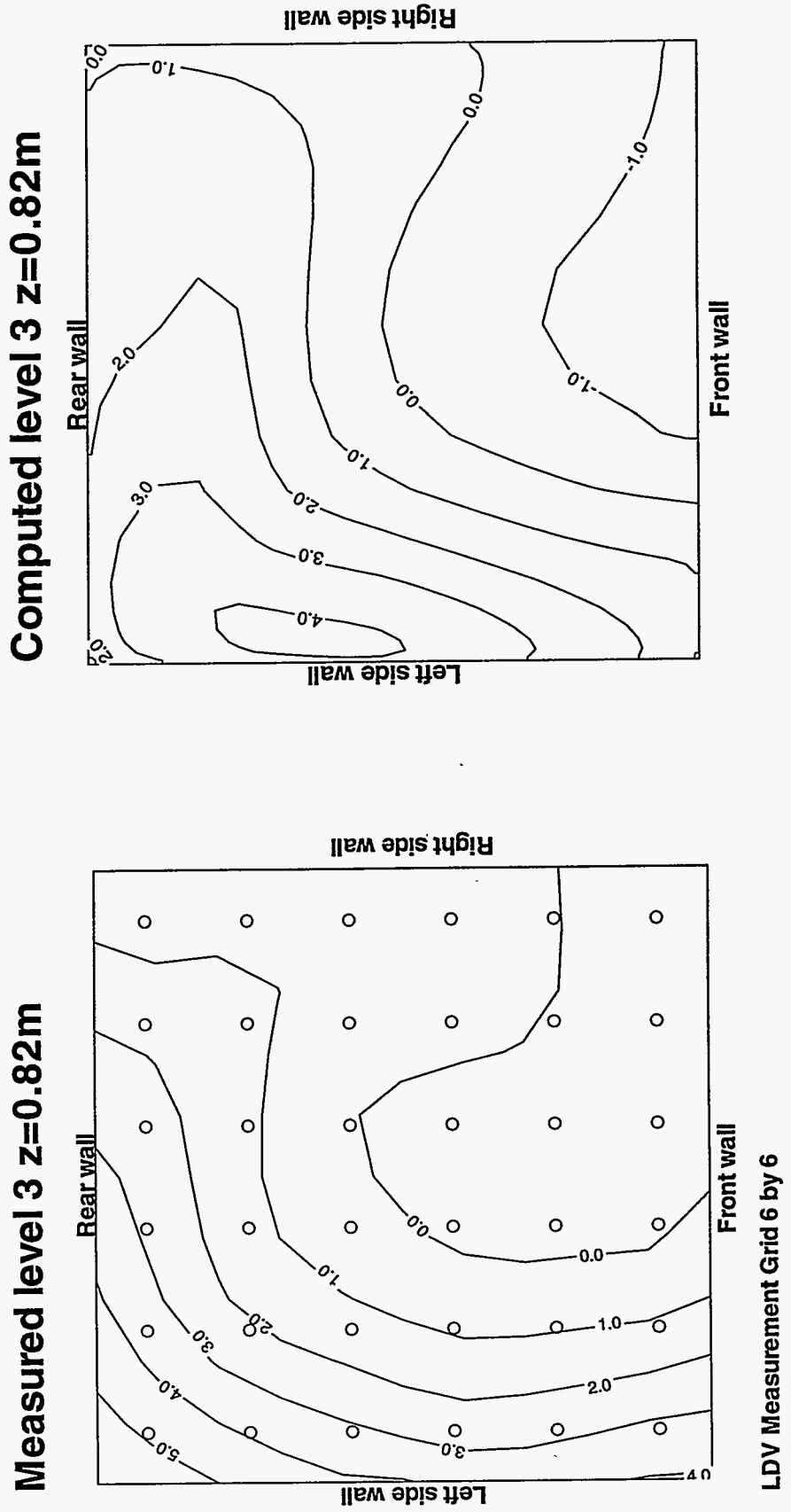

Figure 15: Kamloops boiler water model, measurements and computational results, primary, secondary and tertiary, level 3. (Case (WM-b)).

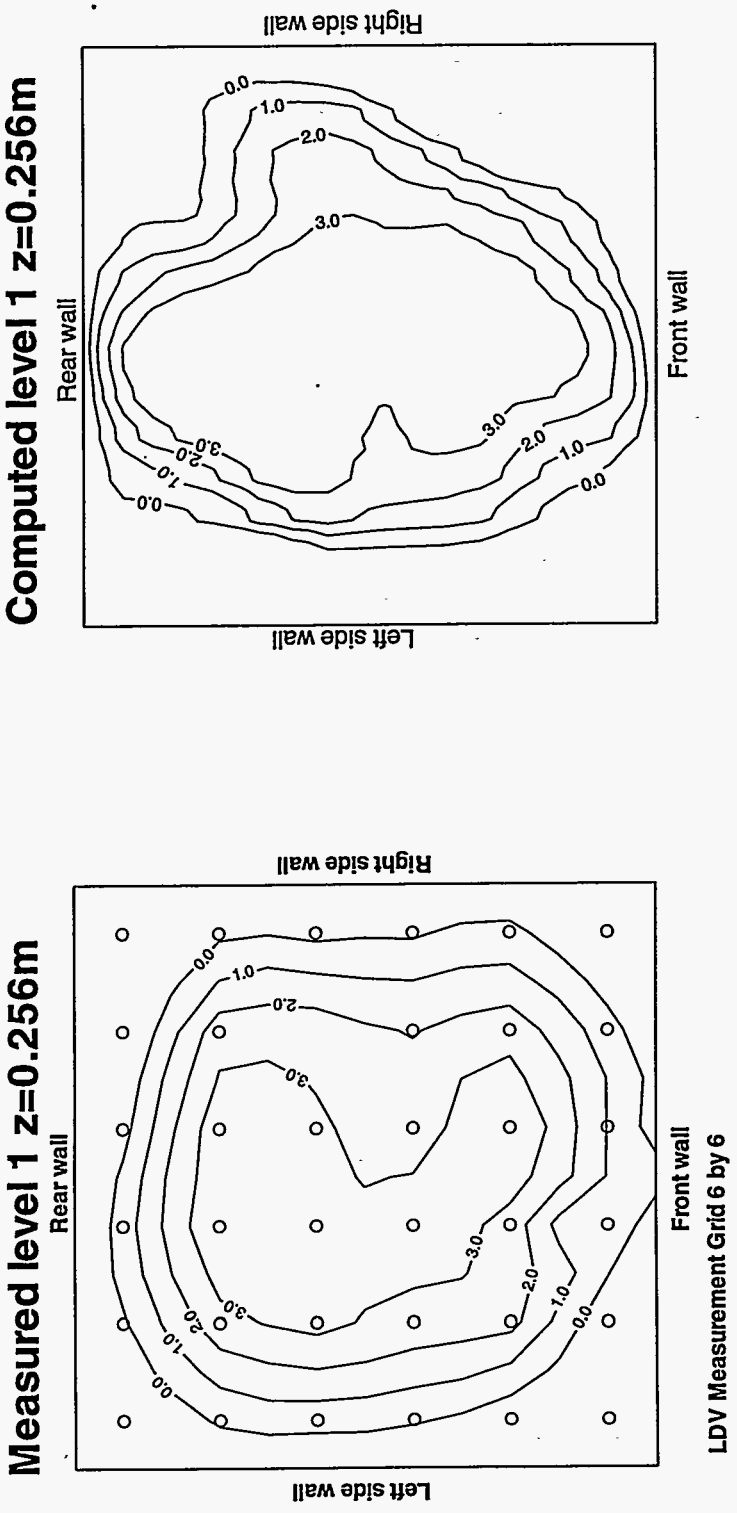

Figure 16: Plymouth boiler water model, measurements and computational results, primary, secondary and tertiary, level 1. (Case (WM-c)).

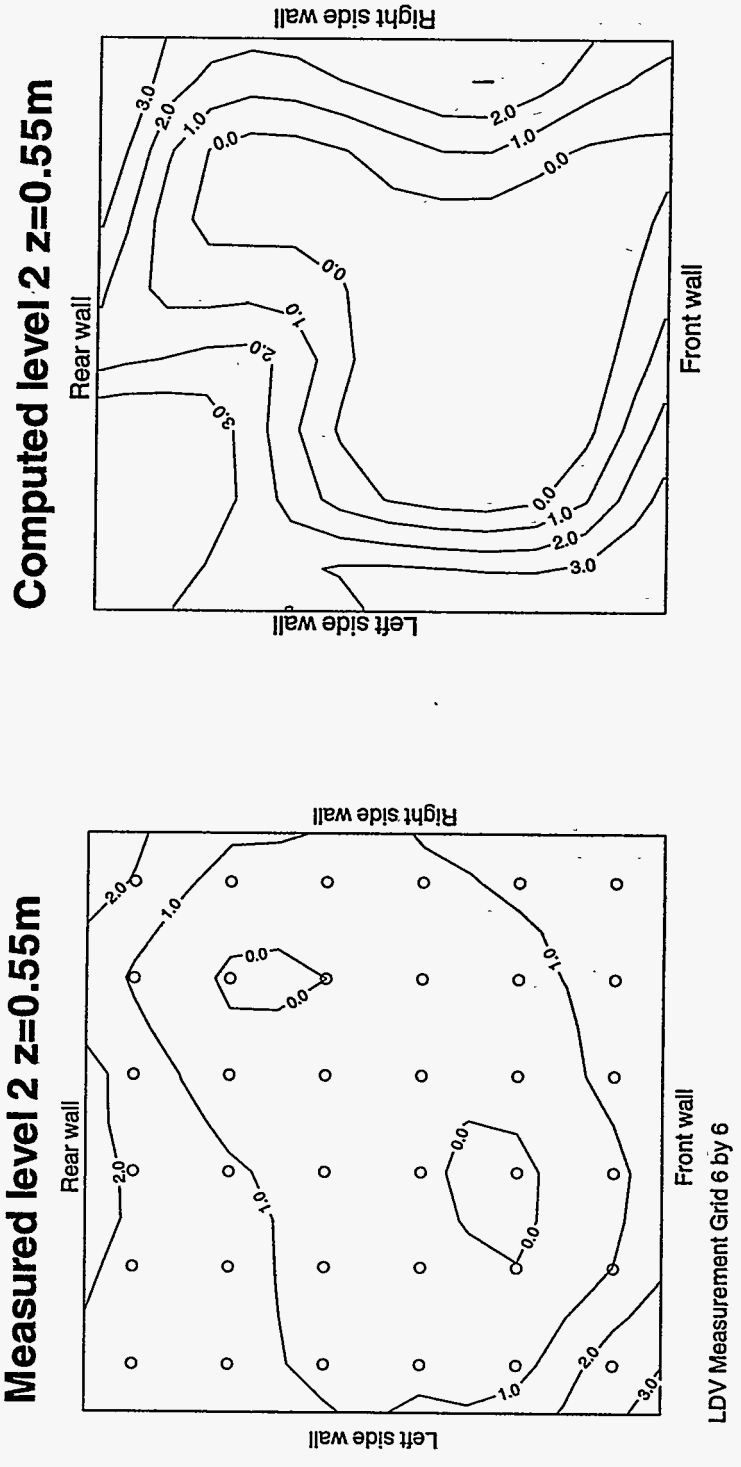

Figure 17: Plymouth boiler water model, measurements and computational results, primary, secondary and tertiary, level 2. (Case (WM-c)).

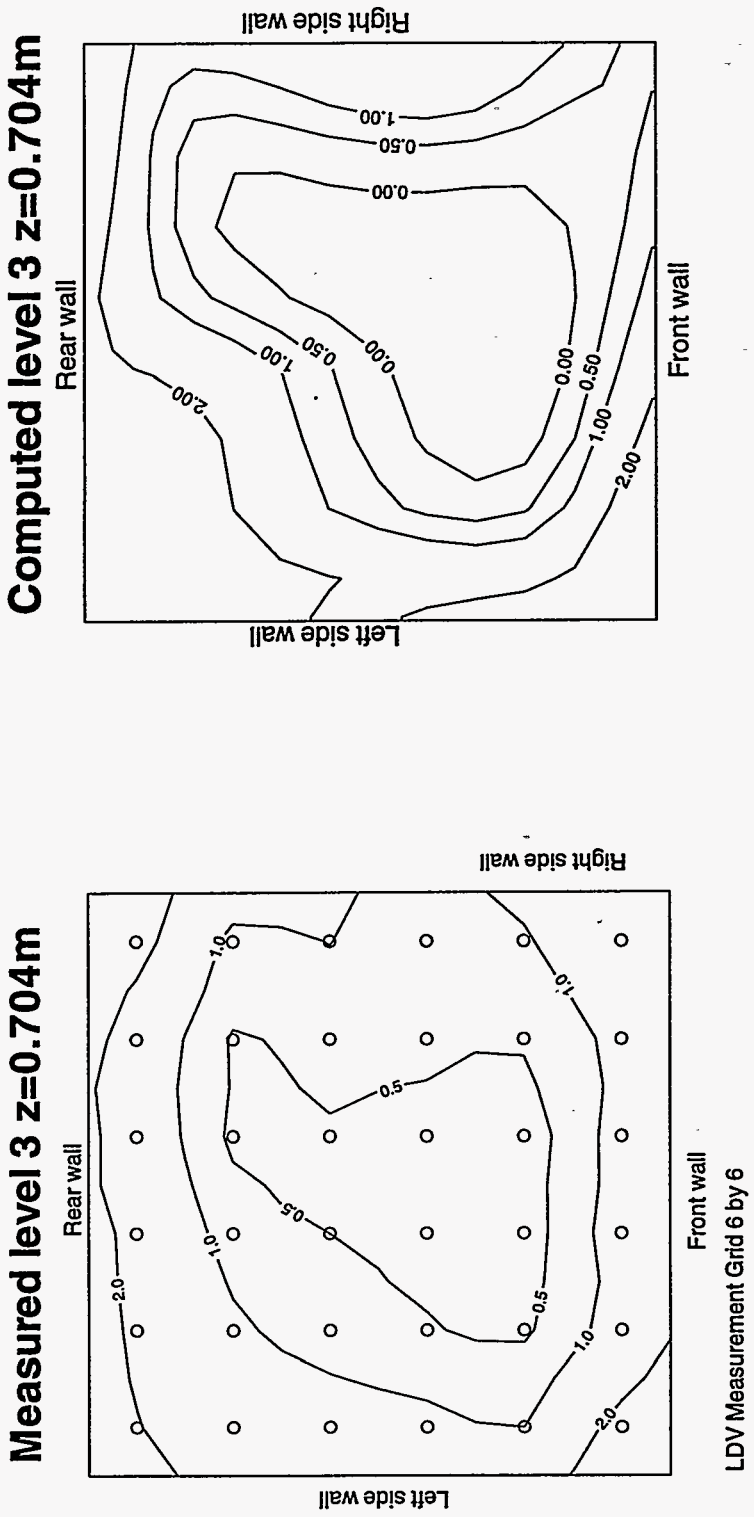

Figure 18: Plymouth boiler water model, measurements and computational results, primary, secondary and tertiary, level 3. (Case (WM-c)).

SECTION 5: MULTIPLE JET INTERACTION WITH RELEVANCE TO RECOVERY BOILER FLOW FIELDS[1]

Introduction

In a recovery boiler furnace, the velocity and geometric arrangement of air jets (their size, spacing, orifice shape, and position) have a large effect on the performance of the unit. Calculations of the complete flow pattern are necessary and becoming possible [Chapman and Jones 1990, Salcudean et. al. 1992], but a simplified geometry (see Figure 1) facilitates an understanding of the aerodynamics, giving a general picture of the more significant effects of variables such as the orifice width (W), the furnace width (H), the jet momentum ratio (J), and jet orifice shape or aspect ratio $AR=L/W$, where L is the orifice length.

As noted in [Adams 1988], the results for an isolated jet in an infinitely large uniform cross flow are not very applicable to our understanding of the jet arrays typical of recovery boilers. A single jet penetrates further into an infinite cross flow than it would into a confined furnace and the interaction between multiple jets provide further variations not predictable from single jet behavior. Physical experiments in recovery boiler models by [Perchanok et al., 1989] and full scale measurements by [Blackwell et al., 1989] suggest that there can be large scale unsteadiness in recovery boiler flows at rather low frequencies, of the order of one hertz.

This chapter is aimed at investigating the interaction of parallel and opposed jets into a confined cross flow, which may be non-uniform or be zero. The geometry and kinematic variables are related using a basic non-dimensional formulation which was suggested from experiments performed elsewhere, and which can be tested using numerical simulations. This work helps in the analysis and understanding of the flow modeling work presented elsewhere in this report. Isothermal constant density flow is considered, on the assumption that Thring-Newby scaling can compensate for much of the expansion effects of cold jets entering a hot cross flow (see [Perchanok 1989]).

Interaction of parallel jets

A Non-dimensional Relationship

Holdeman and Walker [Holdeman et. al. 1977] and Holdeman, Srinivasan and Berenfeld [Holdeman et. al. 1984] (hereafter HSB) studied the dilution mixing of a row of round jets entering a hot cross flow, with application to combustion chamber design. From their experiments, they observed that the most important parameter affecting the jet penetration was the jet-to-mainstream momentum flux ratio J, defined as $J=\rho_J U_J^2/\rho_C U_C^2$ (ρ is density, U is velocity, and subscripts J and C indicate jet and cross flow variables, respectively).

[1] The work reported in this chapter was done mostly by Daniel Tse and Jeff Quick as part of their Ph.D. thesis projects. Further details can be obtained from their theses and related publications.

The experiments of HSB were grouped to define `desirable' mixing in which the jet center-line was bent by the cross flow so that it traveled down the center of the confining chamber. This strategy seems to be reasonable for applications related to combustion, where it is desirable to have air jets penetrating into the interior of the chamber without significant over-penetration or under-penetration. In any specific application of course the desirable mixing is problem dependent, but similar non-dimensional relationships are likely to exist in most cases. The grouping suggested by HSB was:

$$S/H = C/\sqrt{J} \qquad (1)$$

where S is the center-line spacing of the jets in a long array, H is the cross dimension of the confining chamber (see Figure 1), and C is a dimensionless parameter whose value for round cold jets entering a hot cross flow was found to be 2.5. Equation (1) implies that more widely spaced jets (S/H large) require a lower momentum to penetrate to the center-line of the chamber, or conversely that closely spaced jets (S/H small) require more momentum to penetrate to the chamber center-line. Equation (1) can also be viewed as a correlation of jet penetration: for $(S/H)\bullet\sqrt{J}=2.5$, jets penetrate to the center of the chamber; for $(S/H)\bullet\sqrt{J} >> 2.5$ the jets will penetrate more deeply than the center; for $(S/H)\bullet\sqrt{J} << 2.5$ the jets will not penetrate as far as the center-line. In this work, we consider primarily penetration from one side to the chamber center-line, following HSB in considering this a `good' mixing arrangement.

Equation (1) can be valid only when the ratio S/W (jet spacing divided by jet width) is neither too small (very closely spaced jets) nor too large (essentially isolated jets). Closely spaced jets coalesce and the resulting lack of three dimensional entrainment increases the penetration so that equation (1) is no longer appropriate. The validity of equation (1) for a range of jet sizes and shapes will be investigated here using numerical simulations. The possible implications of the correlation for recovery furnaces will then be considered.

The geometry for one-sided injection is illustrated in Figure 1. The flow field is obtained by using the UBC multigrid program described elsewhere in this report. A unit of an inert tracer is injected with the jet to indicate the disbursement of the jet fluid. Previous studies on laterally spaced jets using the k-ε model show that the model is generally accurate in predicting the gross features of the flow field [Claus 1985].

To extend Holdeman's well-mixing criterion to the case of rectangular jets of different aspect ratios, we will perform numerous simulations with different values of S/H and J to examine the appropriate choice of C for each case. The control parameter we employ is the jet-to-mainstream mass flow rate M, which for constant density flow is evaluated from the relationship

$$M = \left(LW/HS\right)\left(V_{jet}/U_c\right) = AR\bullet W^2/HS\bullet\sqrt{J}$$

This quantity is significant in combustion application, where its value is fixed by the stoichiometric requirement for air. In our simulations, at the same value of J, M is held fixed when we compare the injection from orifices of the same aspect ratio but with a different spacing ratio S/H, or when the orifice aspect ratio is varied.

Results for Uniform Cross flow

Square Jets

Turbulent flow simulations were carried out to emulate the experiments of [Holdeman et al. 1984]. The results should not be affected significantly by changes in actual size or Reynolds number, provided other dimensionless ratios are kept constant. Thus, the non-dimensional correlation derived should be useful in describing the flow structures in larger devices.

The values for the geometric and operational parameters considered are listed in Table 1. Two values of J are chosen to reflect the cases where the jet has momentum that is low or moderate. For each value of J, three values of S/H are chosen to study the effects of varying the jet spacing. A value of M is then chosen and the jet width W can be determined. We choose a larger value of M for J=25 so that the corresponding value of W will not be too small for each choice of S/H.

Table 1: Parameters chosen for simulations of square jets, H=0.1016m (4"), U_C=15m/s

J	M	S/H	W/H
6	0.15	0.25	0.1250
		0.5	0.1768
		0.75	0.2165
25	0.31	0.10	0.0394
		0.20	0.0557
		0.30	0.0682

The results are plotted as concentration contours in the jet center-plane (Z=0) like those of Figure 2. A value of $C \approx 1.5$ correlates the results for desirable jet penetration for square jets in constant density flow. This value is about one half that recommended by HSB. Our lower value for C may be due to the use of isothermal flow in the present calculations.

Rectangular Jets

Similar calculations were made for orifices whose aspect ratio $AR=L/W$ was 3 and 6, using the value J=6 and M=0.15 as before. Again the jet fluid concentration contours were plotted for Z=0 and a value of C was found for which the jet center-line lay close to the center of the confining chamber. For the cases we tested, large aspect ratio jets were found to penetrate deeper into the cross flow, all other conditions being equal, so that values of C for high aspect ratio jets are smaller than for square jets. Quantitatively, we

estimate C to be 1.0 and 0.65 for aspect ratios of 3 and 6, respectively, in every case requiring that jet penetration be such as to bring the concentration maxima to the approximate center of the chamber. The estimates we have obtained are listed in Table 2. For jets whose aspect ratio is between 1 and 6, its corresponding optimal value of C may be obtained by interpolation.

Table 2: Optimal values of C for orifices of different aspect ratios

AR	Optimal C
1	1.3
3	1.1
6	0.65

Implications for Recovery Boilers

In an idealization of the tertiary air system of a recovery boiler, we consider an array of jets coming from orifices of aspect ratio 4 (common in recovery boilers) and mass flow input 20\% of the cross flow mass (M=0.20). A rearrangement of equations (1) and (2) leads to

$$J = \left(C \bullet M/AR\right)\left(H^2/W^2\right)$$

so that, for fixed C, M, AR, and H, the jet momentum varies as $1/W^2$. This implies that small jets, for which W=0.1m (say) require much higher velocity to achieve good penetration than do larger jets of W=0.2m. Choosing typical recovery boiler values of U_C=3m/s and H=10m, corresponding jet velocity values may be calculated easily if we take C=0.8 as a value appropriate for jets of aspect ratio 4. This value of C is obtained by interpolating the values listed in Table 2.

The jet penetration for the three cases W=0.1, 0.15 and 0.2m (corresponding to U_J = 60, 40 and 30m/s respectively) was observed to be similar, with the jet propagating mid-way down the chamber in each case. The results given here are a great simplification of actual tertiary jets; isothermal jets from one side of a chamber (of size H) have been correlated, and jet penetration to the center of the chamber has been identified. For actual furnace tertiary jets which are interlaced or opposed, other effects may appear, such as oscillation or other forms of instability (and the effective H or parameter C may need modifications. With adjustments such as these, however, the formulae given here suggest trends in the mixing behavior and penetration desirable in an actual recovery boiler.

The relation that J varies as $(H/W)^2$ for a given shape of jet orifice and required mass input, is of interest, suggesting that large, low speed jets can penetrate as deeply and have similar mixing effects as small, high speed jets. The spacing of such jets may also be estimated. Again rearranging equations (1) and (2) we obtain:

$$S/W = \sqrt{C \bullet AR/M}$$

which implies that S/W is a constant for given AR and M. For the values chosen here

(M=0.20, AR=4, C=0.8), S/W becomes equal to 4, so that small jets must be more closely spaced (i.e. S is small) than large jets (for which S is larger), the ratio of S/W remaining constant.

Non-uniform Cross flow

In practice, the upward flow approaching actual tertiary jets is not likely to be uniform and some studies were done to simulate the effect of cross flow non-uniformity. To do this a peaked cross flow profile with a flat top, given by:

$$U_c\left(Y/H\right) = \left[U_o\ A\right] \Big/ \left[A + \left\{2\left(Y/H - 1/2\right)\right\}^4\right]$$

was chosen, where $U_C = U_o$ when Y/H=1/2 so that U_o is the peak velocity and $U_C(Y/H)$ is symmetrical about Y/H=1/2. The values of U_o and A are chosen so that the integrated mean velocity U_{mean} for the profile is the same as before, that is 3 m/s, and that the minimum velocity, found at Y/H=0 or 1 at the inlet, is 10% of the peak velocity U_o. With these two criteria, the peak velocity U_o is 1.65 times U_{mean} or 4.95 m/s, and A=1/9. It is remarked that this non-uniform velocity profile has a value of standard deviation equal to 1.68 m/s. A sketch of this profile is shown in Figure 3.

The calculation was performed with the same choices of jet parameters and chamber width as done in the previous section. The resulting jet fluid concentration profiles, obtained with this non-uniform cross flow, were similar to those obtained when the cross flow was uniform. We conclude that the non-uniformity of the type examined does not change the semi-empirical relationships (1), (3) and (4) linking the momentum and penetration to geometric parameters. This observation will have to be validated for a more complex flow generated by the interaction among primary, secondary, and tertiary jets in a boiler.

Interlaced Jets from Both Sides of the Chamber

The experimental results of HSB also suggest that interlaced jets provide very effective mixing. The interlacing is introduced by placing alternative jets on opposite walls, so that in our previous simulations where the jet spacing was S/W=4, the interlaced arrangement would lead to S/W=8 on either wall.

Simulations were carried out with the same three jet sizes and velocities previously. The jets acted on the same non-uniform cross flow profile given in equation (5). It was verified that these interlaced jets penetrate adequately to the middle of the chamber. The velocity distributions in the chamber downstream of the jets are now rather different for the different sizes of jets, and the velocity uniformity at downstream locations is investigated. The standard deviation of the streamwise velocity component from its average value was computed for each of the three cases. A low standard deviation indicates a more uniform outflow than a high value.

The results are shown in Figure 4 for the variation of the standard deviation of the streamwise velocity component with the downstream position X/H for the three types of

jets. All values are non-dimensionalized by the value of the standard deviation in the original non-uniform profile (1.68m/s). The largest, lowest momentum jets provide the most uniform outflow (smallest standard deviation at large *X/H*). Hence the following conclusion may be made: for interlaced jets interacting with the type of non-uniform cross flow prescribed, large jets at a low momentum could satisfy the mass flow requirement and would create less flow non-uniformity far downstream.

Interaction of opposed jets

The target problem considered here is that of two symmetrically opposed jets injected normally into a uniform cross-flowing stream of like fluid, as shown in Figure 5. In an alternative case the cross flow is set to zero and a floor is placed at the bottom of the cavity at a height D_1 below the jets. There is a two dimensional limiting case of two conceptually infinite opposing slot jets of height h and infinite width, and the three dimensional case of two opposing discrete jets as illustrated in the figure. In the latter case, the flow is bounded on either side of the jets by free slip walls, which may be interpreted as planes of symmetry in a conceptually infinite array of opposing jets. The spacing S between these boundaries is equivalent to the spanwise spacing between jets in the corresponding array.

In the computations, the flow is assumed to be incompressible and of constant density. The boundary conditions are specified as free slip duct walls. The inlet and outlet velocity profiles are set to uniform. This outlet condition is the simplest way to allow use of a duct length comparable to real furnaces, which is too short for a fully developed flow assumption at the exit. In a real furnace, the pressure drop across the convective heat transfer section tends to make the flow more uniform, so the uniform flow assumption in this model is believed to be a good one for the present purpose. The inlet turbulence intensity is set to 10% and length scale is set the square root of the area of one jet for the jet flow, and one half the cross-flow duct width for the cross-flow. Results are not very sensitive to the turbulence boundary values, since turbulence generated by shear within the calculation domain dominates.

Results for opposed jets

Specific cases for the target problem are described by a set of parameters. The geometry is described in terms of a reference length scale equal to the square root of the flow area of one jet ($b=\sqrt{hw}$). The geometric parameters are then the jet aspect ratio (AR=h/w); spanwise spacing ratio (S/b), cross-flow duct half width ratio (B/b), and duct length ratios (D_i/b). A jet Reynolds number ($Re_J = V_J b/\upsilon$) relates the reference length, jet velocity and molecular viscosity. A final specifying parameter is the ratio of momentum flux of one jet to that of half the cross-flow;

$$M = \frac{(hw)V_J^2}{SBV_C^2}$$

$$\text{or } M = \frac{1}{(S/b)(B/b)}\left(\frac{V_J}{V_C}\right)^2$$

which can be simplified for a 2D slot as;

$$M = \frac{1}{(B/b)}\left(\frac{V_J}{V_C}\right)^2$$

2D Case: B/b=10, $Re_J=10^6$, M=10

The two dimensional case has been reported previously by the authors [Quick et al., 1991]. The importance of momentum flux ratio is demonstrated there. At low M, < 2, the jets interact very weakly or not at all and each is deflected by the cross-flow in a symmetric manner, i. e. the flow field obeys the symmetry of the firing geometry. At M ≥ 2 the jets interact resulting in a bifurcation. It is shown that a symmetric flow exists, which is unstable and can only be computed by enforcing symmetry mathematically at the geometric symmetry plane. This halves the computation domain and is often used by CFD practitioners to reduce cost. However, in the case of bifurcation it is shown that there exist two asymmetric, stable steady flow fields, mirror images of one another with respect to the duct walls, and very different from the symmetric solution.

The most important features of the 2D asymmetric flows are the two unequal spanwise recirculation zones adjacent to the walls downstream of each jet, which are associated with reattachment to each wall. Also, the jets do not collide head-on, as they are rapidly deflected by the cross-flow fluid which must pass between them in the 2D flow.

3D Reference Case: AR=4, S/b=5, B/b=10, $Re_J=10^6$, M=20

This case approximates conditions at the tertiary level in a recovery furnace. The numerical grid has 48 nodes along the duct axis, 32 along the jet axis and 14 along the spanwise axis. Two level multigrid is used, so a coarser grid of one half the number of nodes in each coordinate direction is also used in the calculations.

As found in the 2D work, a symmetric steady state flow can only be obtained by enforced symmetry calculations. This flow is significantly different from the 2D results, in that there is a strong, head-on impingement of the jets. This can occur because the jets are deflected less by the cross-flow which is able to flow around either side in a 3D flow. From the impingement region there is radial flow outwards in all directions, which actually penetrates quite far upstream against the cross flow. This produces some spanwise recirculation upstream of the jets, however, owing to the three dimensionality of the flow, there is no reattachment of the jets to the walls as observed in the 2D flows. These characteristic features of the 3D flow are similar to the RIM laminar flow fields described by [Wood et al. (1991]. The symmetrical flow is unstable in a full calculation through both jets.

Unlike the 2D work, stable steady state flow fields can not be found. For repeated iteration of the solver, the root mean square residual error in the equations will not decrease below a level of about 10^{-3}, made dimensionless with respect to V_J and b. At successive iterations the current flow field will be asymmetrical and varying from one side of the duct to another.

A time dependent run initiated from one of these unconverged steady state results converges rapidly to lower residuals. A dimensionless time step ($\Delta t/(b/V_J)$) of 10.0 is used, and two multigrid iterations are performed in each time step. The root mean square (RMS) dimensionless residual error at the end of each time step is 10^{-6} to 10^{-7}, or three to four orders of magnitude lower than for the unconverged steady state runs. The result is an oscillation, which becomes periodic following the decay of an initial transient. The periodic solution is shown as a time series in Figure 6 which plots U velocities, parallel to the jet axes, at three points on the cavity center line as indicated in Figure 5. A time scale based on the jet momentum flux $J=b^2U_J$, and cavity dimension B, is defined as $B^2/J^{1/2}$.

The oscillation period is then expressed as $T^*=T/(B^2/J^{1/2})=4.22$ in dimensionless units. A Strouhal number can be defined as the inverse of the dimensionless period, $St=fB^2/J^{1/2}$, equal to .237. In terms of a typical recovery furnace with a jet velocity of 69.2 m/s, b = 0.567 m, and B = 5.670 m the real calculation time step is .082 s, and the oscillation period is 3.50 s.

It is observed from Figure 6 that the U velocities at these three elevations are out of phase with one another. They are never zero simultaneously and so the flow is never symmetrical. Transient flow fields are shown in Figures 9 and 10 when U_2 is at zero and maximum magnitude respectively.

The time average flow computed over one cycle of the oscillation is symmetrical as shown in Figure 11. The time average result is also quite distinct from the enforced symmetry steady state in that gradients in velocity are generally much smoother in the time average picture.

The instantaneous behavior of the unsteady, periodic flow can be observed using computer animation. A view of the flow field such as the 2D slice of Figures 9 and 10 can be taken. One period of oscillation is animated by displaying the flow field with vectors at successive time steps. This process can be repeated in a loop to observe continuous oscillations. A video sequence of the computer has been shown by the UBC group in previous DOE review meetings.

Variations from the Reference Case

To investigate the effect of differences in plenum pressures to opposed jets, arising due to small variations from control set points, a case was run for a pressure differential of 5.0%, or a 2.5% difference in jet velocities. The result is only a very slight shift of the flow to one side with the main features and frequency of the motion essentially unchanged. Actual recovery boilers may also have slight asymmetries in alignment, but it is reasonable to expect that these too will have a weak effect on the flow and bifurcation behavior.

For sufficiently weak jets, relative to the cross flow, the bifurcation disappears and there is a stable, symmetric steady flow field. This transition or bifurcation point occurs for the reference case geometry at a value of M between 1.25 and 5.0.

Increasing the jet spacing by a factor of two to S/b=10, which changes M to 10, gives a different behavior entirely. One jet passes to the side of the other and the flow is symmetrical in the vertical center plane. There is only a very weak fluctuation, and the jets do not oscillate from one side to another. A reduction in jet spacing to S/b=4, which changes M from 20 to 25, increases the frequency by 25% as well as increasing the amplitude of the motion. A case with S/b=4 and velocities adjusted to preserve M = 20 has a frequency 28.6% higher. Calculated Strouhal numbers are summarized in Table 1.

Table 3: Summary of calculated Strouhal Numbers

S/b	$M=J/(SBV^2_C)$	$St=fB^2/J^{1/2}$
5	20	.237
4	25	.296
4	20	.305
4	Closed floor	.229

Closed Floor Cavity AR=4, S/b=4, B/b=10, $Re_J=10^6$, $D_1=15.5$

This case is representative of the geometry in the physical experiments described previously. There is a closed floor in the cavity at $D_{1/b}=15.5$ below the jets. There is no momentum flux parameter, and the only flow parameter is the Reynolds number, upon which the CFD results are essentially independent at these high values. The result is shown in the same format as for the reference case, as a time series plot in Figure 7, and instantaneous flow fields in Figures 12 and 13. The main feature of the transient flow field is that the recirculations below the jets can grow to a size limited by the floor. The calculated Strouhal number of St=.229 is lower than for the cases presented having a cross flow (e.g. S/b=4, M=20) which is probably due to the larger recirculations below the jets.

Physical Experiments

The physical model is a 1:28 scale, isothermal recovery furnace model using water as the working fluid. This model has been described elsewhere in this report. Only the tertiary level of a three level air system is used, which has been modified from an interlaced design to fire 5 jets from each of the front and back walls, symmetrically, and directly opposed. Each jet has an aspect ratio of 4.3 and characteristic size b = 19.8 mm. Each bank of five jets is located on a wall of width W/b = 21, and the cavity depth between opposite banks of jets is 2B/b = 20.74. The spacing ratio between center and first neighbor jets is $S_1/b=4.2$, that between first and second neighbors is $S_2/b=4.6$ and the side

walls are $S_3/2b=1.7$ from these. The floor slopes from the front wall at $D_{1F}/b=15.5$ downward toward the back wall at $D_{1B}/b=17.5$. Each jet is a sharp edged orifice cut in a 5 mm thick plate. The flow is supplied through a 10 diameter long straight section of 1.5 in circular pipe to a small rectangular plenum ahead of the jet orifice. This is the original design of the furnace model used, with the exception that the authors have increased the feed pipe diameter to give a three to one contraction ratio from the feed pipe to the jet. The flow rates used give a jet Reynolds number of 2×10^4, and a time scale of $B^2/J^{1/2}=2.21$s.

Measurements are made using a back scatter, two component laser doppler velocimetry (LDV) system powered by a 7 W argon ion laser described elsewhere in this report. A time trace for the U velocity at point 2 (see Figure 5 for location) between the center pair of jets is plotted in Figure 8. The mean and rms velocities are given by $\underline{u}/U_J=.026$ and $\sqrt{(\underline{u}^2)}/U_J=.277$ respectively. Oscillations at relatively low frequency can be distinguished from the turbulence, although the amplitudes of the turbulence are of comparable magnitude. The oscillation period is not constant, and appears to range from about a factor of two higher and lower than the constant calculated value of $T^*=4.22$.

Flow visualization is done with a laser light sheet from a cylindrical lens and polystyrene seed particles in the flow. The particle motion is recorded in real time with a Super VHS video camera at 30 frames per second (fps) and a shutter speed of 1/60 s or faster. A still camera with a motor winder is used to record sequences of streak photographs at 2.25 fps and a slow shutter speed of 1/4 s. The reference time scale of $B^2/J^{1/2}=2.21$ s gives a 1/4 s shutter speed equal to .113 in dimensionless units. Each frame captures a flow pattern over the shutter opening time as in Figure 14, for a vertical plane through the center pair of jets, where the jet impingement point is maximally off center. As observed by LDV, the oscillations are somewhat irregular in time, and so are the patterns observed. Figure 14 is chosen as a pattern that best represents the calculated result of Figure 13. The asymmetric geometry of the sloping floor does not seem to have a large influence as the flow behavior is nearly symmetrical.

The nearest neighbor jets on either side of center exhibit similar behavior when viewed with a vertical light sheet through their centers. In vertical planes between neighbor jets the large recirculating patterns also appear, as seen in the calculations, which tends to suggest that this part of the motion is closely in phase along the array. However, when viewed in a horizontal plane through all the jets, the impingement points do not always move together in phase, but appear to be moving, at times, up to 90° out of phase with one another. This result is not surprising in such a highly turbulent flow.

Conclusions and Recommendations

Our results parallel jets indicate that Holdeman's formula (1) is useful in correlating conditions upon which the jet trajectory in the center-plane is similar. For a certain choice of the value of *C*, we can obtain conditions that will give rise to effective transport of jet fluid into the chamber. The choice of *C* depends on the aspect ratio of the jet orifice and decreases as aspect ratio increases. Estimates of the optimal values of *C* are shown in

Table 2. A value of $C = \sqrt{J} \bullet S/H$ that is a factor of two larger than the optimal value would mean over-penetration, and vice versa. Also, for two-sided interlaced jets, the effective orifice spacing would be half the actual spacing. Keeping these items in mind, formula (1) can be used as a `back-of-an-envelope' type calculation tool to estimate how jets will penetrate into a confined cross flow. To be cautious, we need to remember that the formula only applies in situations where lateral jet interaction is significant and where jet spacing is not too small. Also, for cold jets entering a hot cross flow, we need to use the Thring-Newby scaling criterion first to account for the effects of jet expansion before we can apply the above strategy to estimate the jet penetration.

In our study of mixing with interlaced jets, the following trend was revealed: at a given mass flow ratio or stoichiometry, less velocity non-uniformity in the cross flow is observed with the use of bigger jets at a lower momentum ratio. When applying our results, however, we need to realize that the actual flow in the recovery boiler is significantly more complex than our idealized conditions. Moreover, our focus has been on the jet penetration, which is only one criterion and does not necessarily reflect the many parameters which need to be accounted for in the optimization of the design of the boiler. Nevertheless, the present study provides an estimate of the trends with different parametric variations, and these trends could be used as guidelines for air system development.

As one might expect intuitively, there is a physical instability when opposing jets collide, either in the presence of a weak cross flow or with a closed floor cavity. This instability produces a bifurcation to several steady state flows or an oscillatory flow that can be captured by a suitable numerical method, using a simple two equation turbulence model. The calculations give a perfectly periodic result for the mean flow, while there is more variation in the oscillations observed in the physical experiments. The use of more sophisticated turbulence modeling would not be likely to alter the periodic nature of the calculations, although there might be a change in the flow field and frequency to a presumably more accurate result. The calculated results represent an ensemble mean flow, which may be realizable also from physical experiments, in theory, but difficult to achieve in practice. The traditional experimental technique of making individual point measurements over sufficiently long record times would give a mean flow, and fluctuations with respect to the mean, analagous to the calculated time average flow, and fluctuations due to the superposition of the calculated ensemble mean flow and turbulence fields.

References:

1. Chapman, P.J. and Jones, A.K., "Recovery Boiler Secondary Air System using Experimental and Computational Fluid Dynamics" Proc. TAPPI Eng. Conf., Vol 3, pp.193-203, 1990.

2. Salcudean, M., Nowak, P., and Abdullah, Z., "Mathematical Modeling of Recovery Furnaces" TAPPI Proceedings, International Chemical Recovery Conference, pp.197-208, Seattle, June 1992.

3. Adams, T.N. and Frederick, W.J., Kraft Recovery Boiler Physical and Chemical Processes, Ch.6, American Paper Institute, New York, 1988.

4. Perchanok, M.S., Bruce, D.M., and Gartshore, I.S., "Velocity Measurements in an Isothermal Scale Model of a Hog Fuel Boiler Furnace" Journal of Pulp and Paper Science, Vol.15, No.6, pp.J212-J219, Nov. 1989.

5. Holdeman, J.D. and Walker, R.E., "Mixing of a Row of Jets with a Confined Crossflow," AIAA Journal, Vol.15, pp.243-249, Feb. 1977.

6. Holdeman, J.D., Srinivasan, R., and Berenfeld, A., "Experiments in Dilution Jet Mixing," AIAA Journal, Vol.22, No.10, pp.1436-1443, Oct. 1984.

7. Claus, R.W., "Numerical Calculation of Subsonic Jets in Crossflow with Reduced Numerical Diffusion." NASA Technical Memorandum 87003, 1985.

8. Quick, J.W., Gartshore, I.S., and Salcudean, M., "The Bifurcation of Steady States for Opposing Jets in Cross Flow; Application to Recovery Boilers." Proceedings of the Thirteenth Canadian Congress of Applied Mechanics, CANCAM 91, June 2-June 6, 1991.

9. Blackwell, B., Oliver, R., Brisco, B., "Physical flow modelling of a vintage Combustion Engineering Kraft recover boiler." CPPA Technical Section Conference, May, 1989.

10.Launder, B.E., Spalding, D.B., "The numerical computation of turbulent flows" Computer methods in Applied Engineering, 3:269-289, 1974

11.Wood, P., Hrymak, A., Yeo, R, Johnson, D., Tyagi, A., "Experimental and computational studies of the fluid mechanics ain an opposed jet mixing head", Physics of Fluids, A, 3(5):1362-1368, May 1991

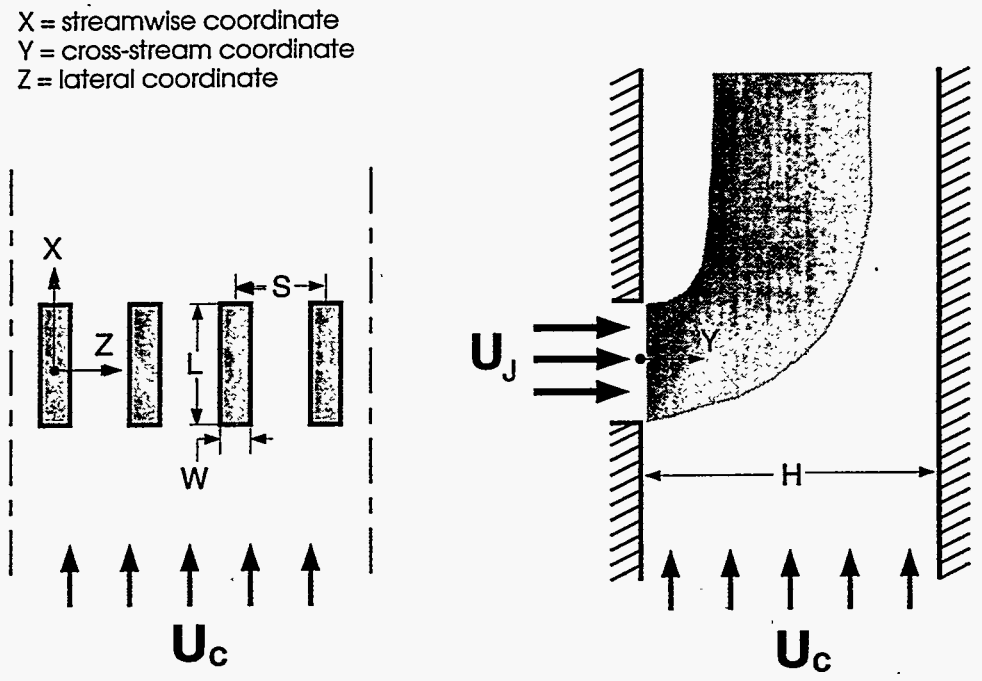

Figure 1: A schematic description of the domain for one-side injection. The side view illustrates a desirable jet mixing scheme in which the bulk of the jet fluid is propagating down the middle of the chamber.

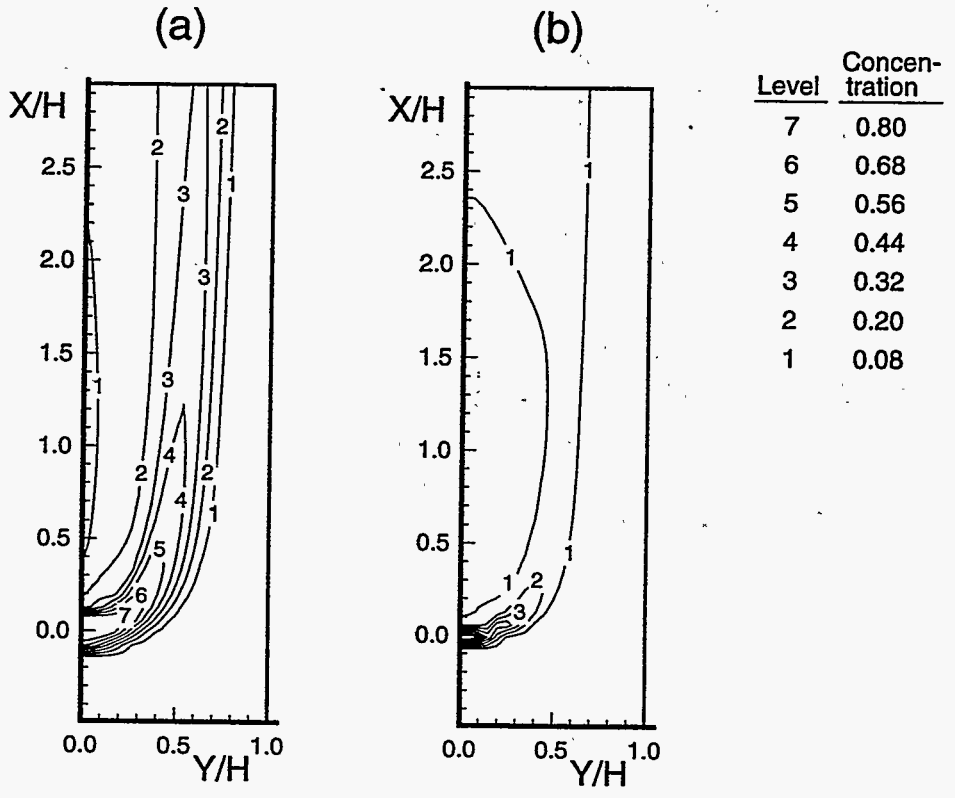

Figure 2: Jet concentration profiles in the jet center-plane Z=0 for square jets. (a) *J*=6, *S/H*=0.5; (b) *J*=25, *S/H*=0.3.

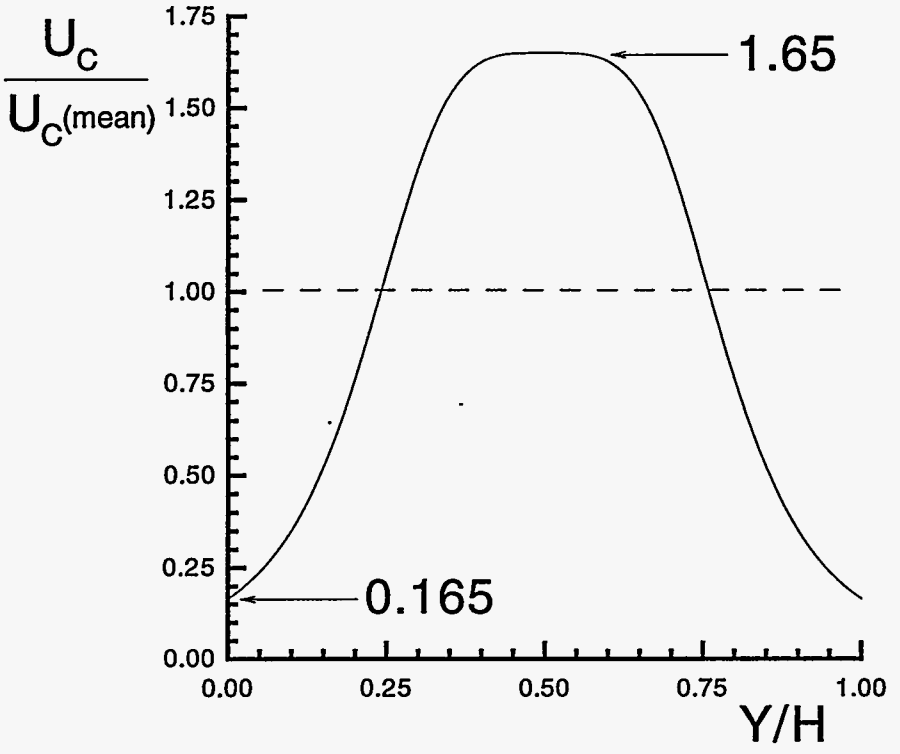

Figure 3: Velocity profile of the peaked crossflow.

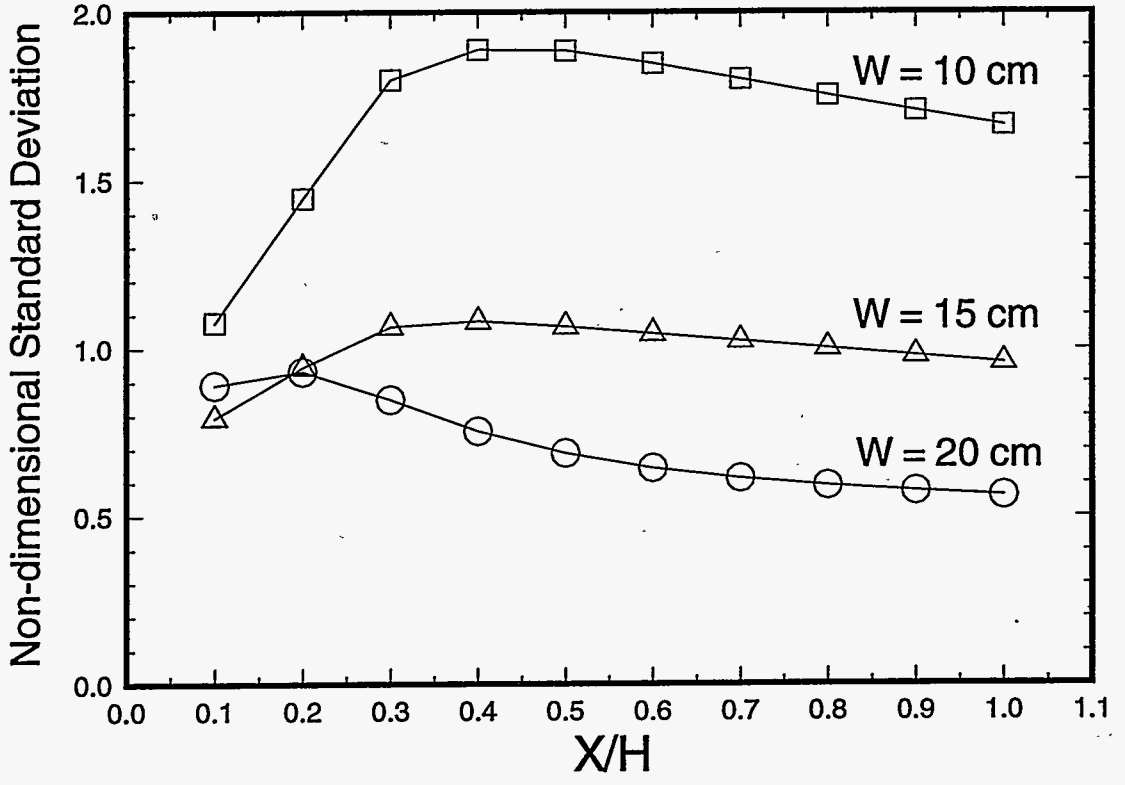

Figure 4: Non-dimensional standard deviation of the streamwise velocity component at various downstream positions for three sizes of interlaced jets.

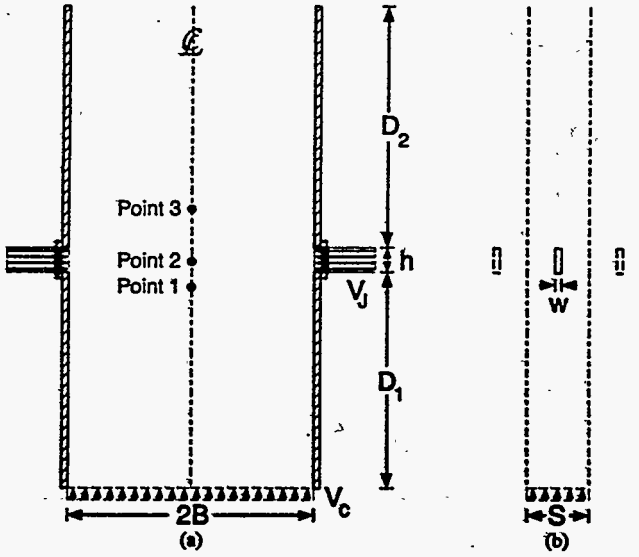

Figure 5: Computational domain for opposed jets.

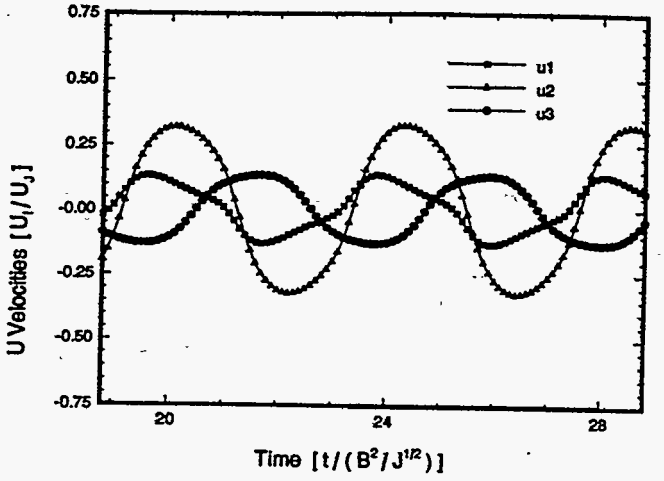

Figure 6: Reference case time series.

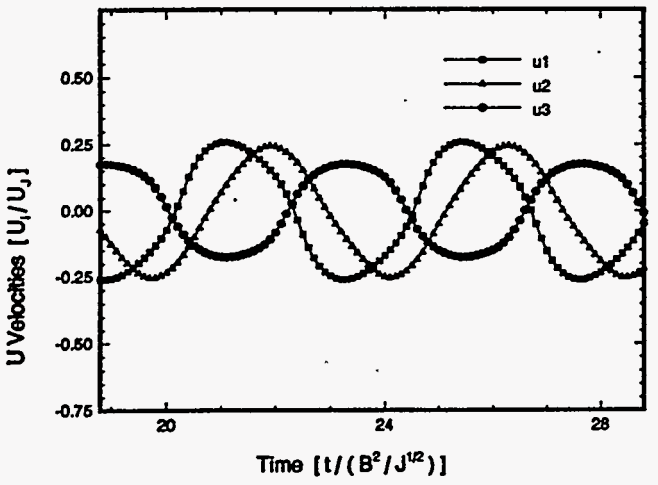

Figure 7: Closed floor time series.

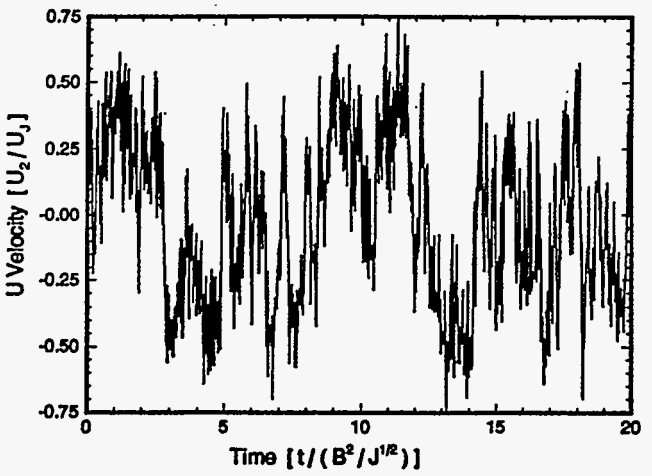

Figure 8: Physical experiment time series.

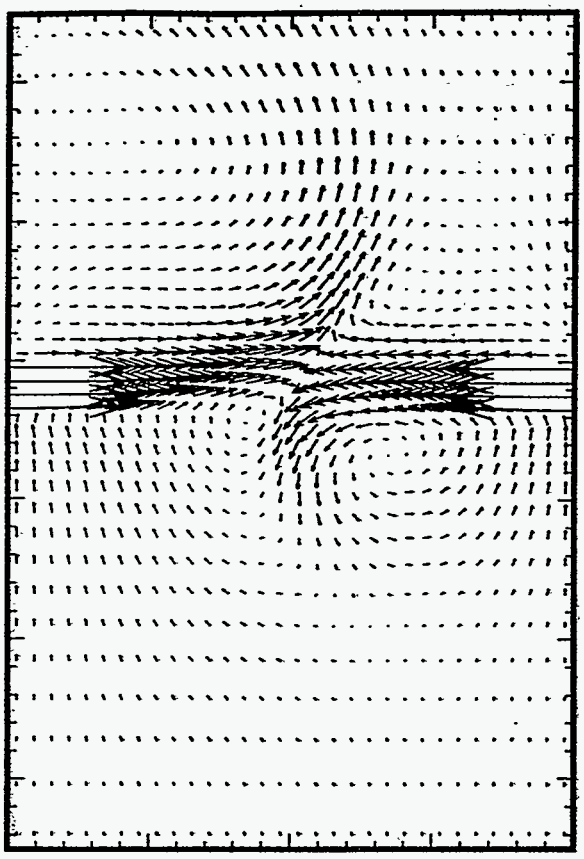

Figure 9a: Reference case flow when U_2=0. Plane through jets.

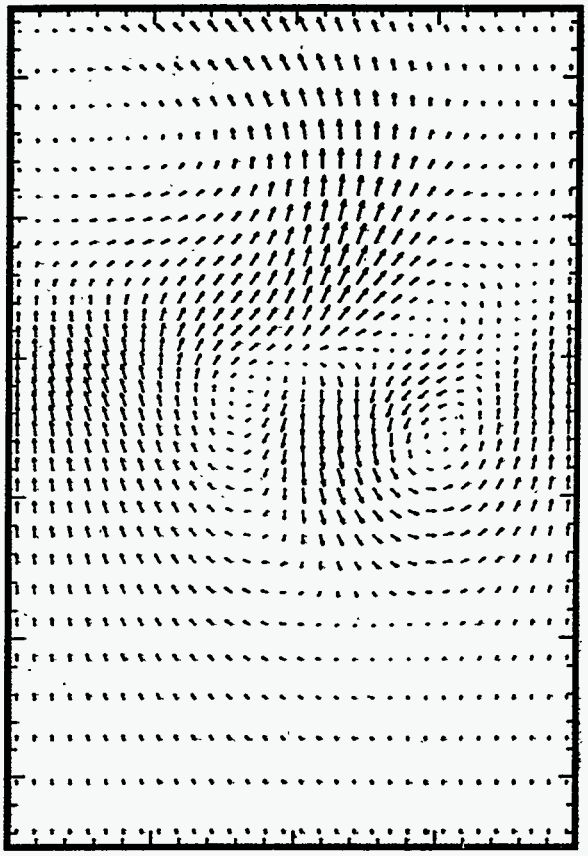

Figure 9b: Reference case flow when U_2=0. Symmetry plane (between jets).

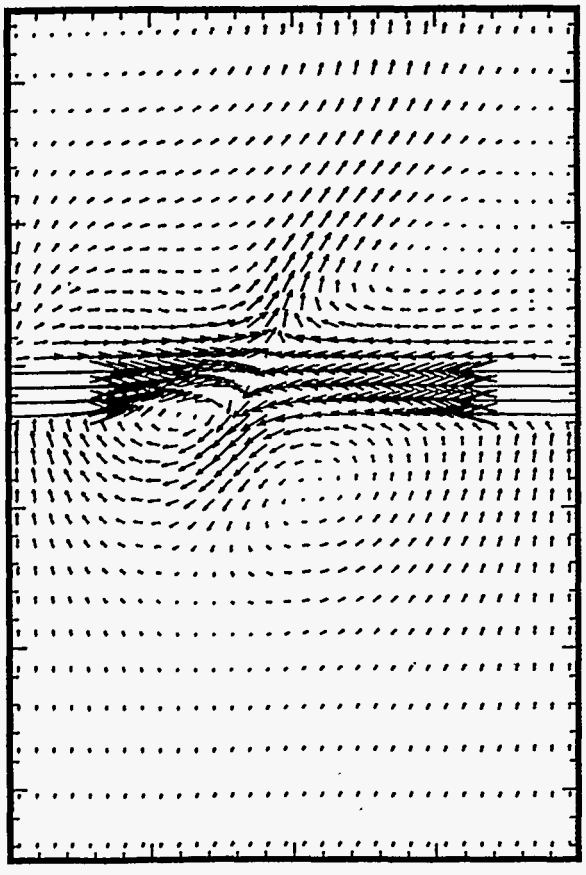

Figure 10: Reference case flow when U_2=*maximum*. Plane through jets.

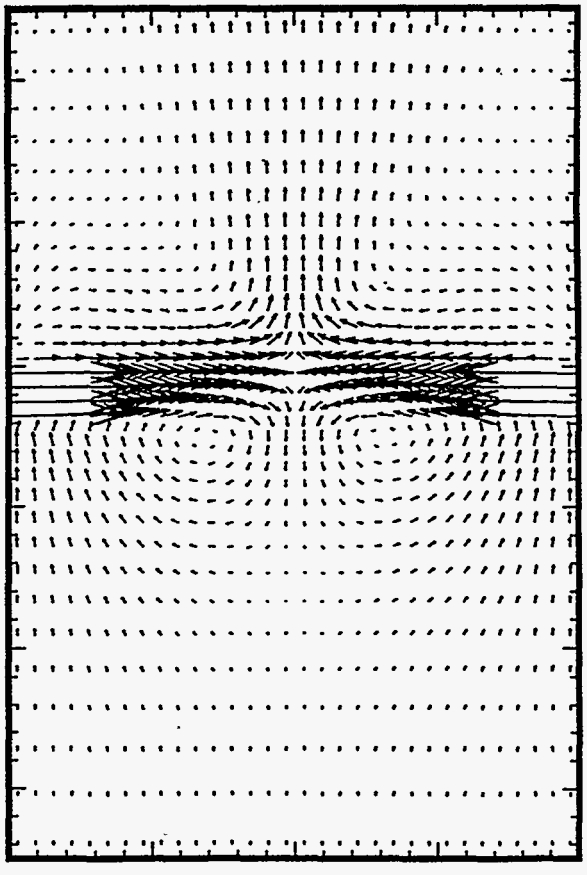

Figure 11: Reference case time average flow when. Plane through jets.

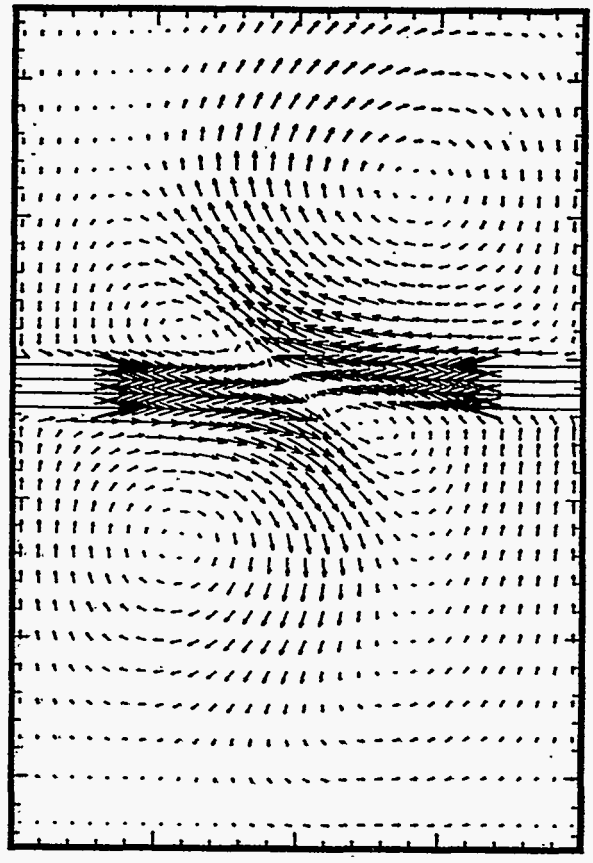

Figure 12a: Closed floor case when U_2=0. Plane through jets.

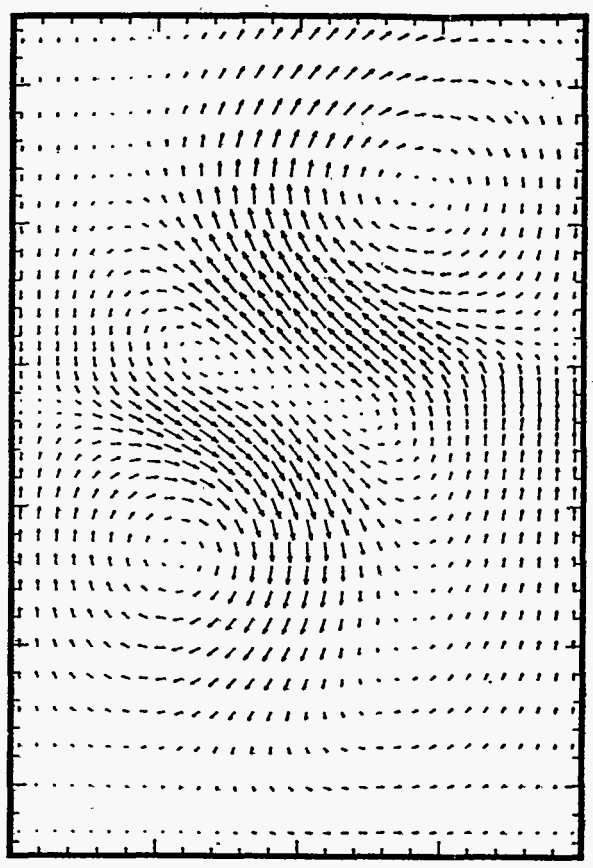

Figure 12b: Closed floor case when U_2=0. Symmetry plane (between jets).

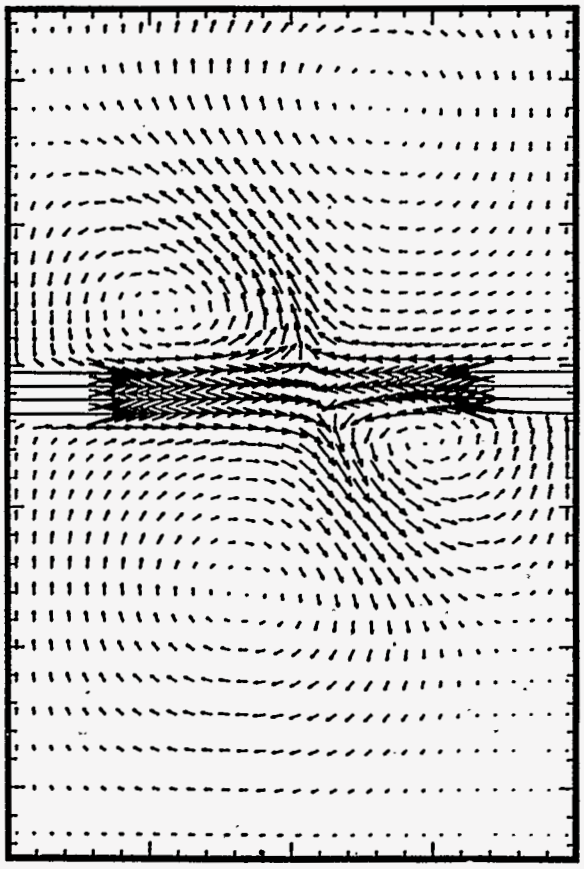

Figure 13: Closed floor case when U_2=*maximum*. Plane through jets.

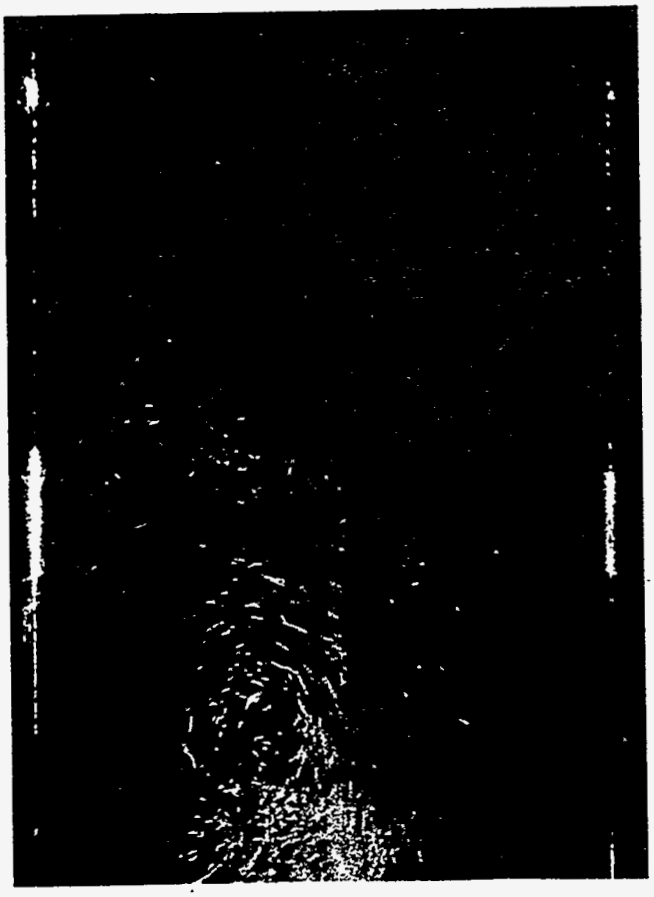

Figure 14: Physical experiment. Streak photograph when jet impingement point is maximally off center.

SECTION 6: TECHNOLOGY TRANSFER

UBC Technology transfer Plan

Code transfer:

A number of considerations were taken into account in the development of a technology transfer plan for the UBC recovery boiler model. Some of these include:

1. The model has been developed under significant funding from a number of different agencies (including the US DOE, CANMET EMR, Industry Canada, NSERC, BC Science Council, UBC internal funding and Weyerhaeuser) and therefore ownership of the model cannot simply and easily be transferred to any single external funding agency.
2. The model requires continuous development as new and better CFD methods and sub-models become available.
3. The model is very complex and requires the attention of knowledgeable and experienced users both to obtain converged solutions, and to interpret the solutions.
4. The size of a single output file can be of the order of 100 megabytes, and hence post processing and possible animation of the results is not a trivial task.
5. The modeling expertise of the potential users covers a wide range. Potential users may include CFD modeling specialists who would like to use the code themselves and only require limited assistance. There are also potential users who may have an engineering background but no CFD modeling expertise. These users would like to use the final results, with somebody else doing the modeling work.
6. Confidentiality is an important issue to some industrial clients.

UBC, as an educational institution, is not suitable for providing confidential consulting and code maintenance services to industry. UBC does have a strong group in the area of mathematical model research and development, and would like to continue to incorporate state of the art solution techniques and sub-models into the code. These fundamental research activities are suited to an educational institution. Many paper companies do not have large R&D departments, and in order to get this segment of the industry to use the new technology it is necessary to take a pro-active role in it's use. In order to address these difficulties UBC has decided to use the following technology transfer mechanism:

1. The basic model development work is being done and will continue to be done at UBC.
2. UBC will retain ownership of the code and the models.
3. UBC has granted a royalty free license to IPST to use the code. As a deliverable of the DOE contract extension, this license will also be extended to include the hot flow code and the global model when these are available. IPST will be free to use the code and apply it to industrial problems, however it will not have the right to sub-license the code to third parties..

UBC has formed a "spin-off" company, Process Simulations Ltd. (PSL), and has licensed the code to PSL for industrial application.

Process Simulations Ltd.:

Process Simulations Ltd. (PSL) is a registered corporation in the Province of BC, Canada. UBC researchers who worked on the recovery boiler mathematical model development are the principals of PSL. The three PSL principals (Dr. Z. Abdullah, Dr. M. Salcudean, Dr. I. Gartshore) have 50 years of CFD modeling experience between them. PSL has been granted a 20 year license of the recovery boiler model by UBC. Under this license, PSL will provide confidential modeling services to industry. PSL will also have the right to sub-license the code, and provide the necessary training, support, maintenance and upgrade services to the sub-licensees.

PSL has already been active in providing consulting services to the industry. Present clients include Weyerhaeuser Paper Co., Kværner (Sweden) and Götaverken (USA). UBC is also working on an ongoing modeling project with Georgia Pacific which precedes the formation of PSL.

Steps in a typical modeling activity with PSL:

Representatives of the paper industry do not have to be knowledgeable in CFD modeling to get their boiler modeled. Typical information which is required includes the boiler dimensions, bull nose shape, and air port locations and dimensions. PSL can obtain this information directly from the manufacturer's drawings. Air and liquor temperatures and flow rates or wind box pressures and damper positions are required. This information is readily available from boiler operators.

The model output includes animation of the flow field. Analysis of the gas flow field is presented with the mechanical carryover at the convective sections. The flow field analysis addresses such issues as excessive carryover, flow instability, air impingement on walls, uneven temperature distribution across the convective sections, etc. PSL will also be able to model black liquor combustion in 1995, and can help in the evaluation of different air injection techniques. PSL has modeled recovery boilers by most major boiler manufacturers of the world.

A typical isothermal flow analysis presently costs US$30,000. This includes the setup of the basic air system and three additional parametric variations (or firing strategies) of the basic air system. Additional studies can be done for lower cost. For further information, please call Zia. Abdullah at (604)-822-2672, or fax at (604) 822-2403.

Workshops:

UBC organizes regular workshops at the Paprican Vancouver Laboratories on a semi-annual basis. These workshops are attended by representatives of paper companies, boiler manufacturers, consultants and academia. The objectives of these workshops are to present and discuss ongoing activities in recovery boiler model development and application and to obtain feedback from the participants. Informal presentations are made not only by UBC and Paprican, but also by any other interested participant. UBC intends to continue this activity in the future, and anybody who is interested in recovery boiler modeling is welcome to attend. For further information please contact Ian Gartshore, at

the Department of Mechanical Engineering, UBC (Ph. 604-822-3770, Fax: 604-822-2403.).

Publications:

The following is a list of UBC publications related to recovery boiler modeling. Copies of these publications are available from Martha. Salcudean, Department of Mechanical Engineering, UBC, 2324 Main Mall, Vancouver, BC., Canada, (604) 822-2196, Fax: (604) 822-2403.

Theses:

1. Aghdasi, Fariba, "Effect of Buoyancy on Jets in Crossflow - Application to the Kraft Recovery Boiler", Ph.D. Thesis, Department of Mechanical Engineering, UBC, 1994
   This thesis presents an analysis of the effect of buoyancy forces on jets in a cross flow, with specific emphasis to Kraft Recovery furnaces. Both experimental and numerical studies are presented. It is found that for horizontal jets in an upward cross flow, excluding the buoyancu forces from the momentum equations results in under prediction of the jet penetration and spread. Numerical simulation of the flow in a recovery furnace showed that the gross features of the gas flow field with or without buoyancy forces are similar.
2. Ketler, Stephen, P., "Physical Flow Modelling of a Kraft Recovery Boiler", M.A.Sc. Thesis, Department of Mechanical Engineering, UBC, 1993
   This thesis presents the water modelling work carried out at UBC. It describes the physical modelling facility, the water models, the data acquisition system, and some results for the CE (Plymouth) water model.
3. Quick, Jeffrey, William, "The Interaction of Opposing Jets" Ph.D. Thesis, Department of Mechanical Engineering, UBC, 1994
   This thesis investigates the time dependant interaction of opposing jets in geometries similar to those of recovery boilers. This work is relavent to flow instabilities in recovery boilers. Both computational as well as experimental work is presented.
4. Tse, Daniel, "Multiple Jet Interactions with Special Relevance to Recovery Boilers", Ph.D. Thesis, Department of Mechanical Engineering, UBC, 1994
   This thesis investigates the interaction of parallel jets in geometries similar to those of recovery booilers. The work is applicable to analysis of primary level air ports, and closely spaced secondary ports.

Other publications

5. D. Tse, M. Salcudean and I. Gartshore, "Multiple Jet Interaction with Relevance to Recovery Boiler Flow Fields", Pulp and Paper Canada, Vol. 95, No. 2, pp. T79-T82, 1994.
   This paper disscusses issues related to parallel jet and interlaced interaction in recovery boiler like flows.

6. Z. Abdullah, M. Salcudean, P. Nowak, Z. Xiao, M. Savage, C. Markovic, V. Uloth, P. Thom, "An Initial Validation of a Cold Flow Mathematical Model of a Recovery Boiler", 1993 TAPPI Engineering Conference, published in Tappi Journal, Vol. 77, No. 5, pp. 149-157, May 1994.
This paper presents results of initial validation of the UBC CFD model against data from the Weyerhaeuser Kamloops Recover Boiler.

7. S. Ketler, P. Ajersch, I. Gartshore, "Particle Image Velocimetry Investigation of Recovery Boiler Flows", Proceedings of the TAPPI Engineering Conference, SanFrancisco, September, 1994
This paper describes the Particle Image Velocimetry (PIV) technique applied to flow measurements in recovery boiler water models. This technique can be used to visualiza and subsequently analyze the unsteady flow field in an entire plane.

8. M. Salcudean, Z. Abdullah, and P. Nowak, "Cold Flow Computational Model of a Recovery Boiler", Journal of Pulp and Paper Sciences. Vol. 19, No. 5, September 1993.
This paper presents an isothermal simulation of a B&W recovery boiler with the UBC code.

9. S. Ketler, M. Savage, I. Gartshore, "Physical Modelling of Flows in Black Liquor Recovery Boilers", TAPPI Journal, Vol. 76, No. 9, pp. 97-106, September 1993
This paper describes the physical model of the ABB-CE Plymouth Recovery boiler, and the Laser Doppler Velocitmeter measuring techniques.

10. S. Ketler, M. Savage, I. Gartshore, "Recovery Boiler Sensitivity to Secondary Level Flows", TAPPI Proceedings, 1993 Conference, pp.271-285
This paper shows the great sensitivity of the flow field in the ABB-CE boiler model to minor changes in the secondary level boundary conditions.

11. J. Quick, I.S. Gartshore and M. Salcudean, "Interaction of Opposing Jets with Relevance to Recovery Furnaces", Paper 6-4, Ninth Symposium on Turbulent Shear Flows, Kyoto, Japan, Aug. 16-18, 1993.
This paper presents results of an investigation of the unsteady interaction of opposed jets in recovery boiler like geometries. This paper demonstrates clearly, how the flow in recovery boilers can be unsteady.

12. D. Tse, I. Gartshore, and M. Salcudean, "Mixing and Vorticity Characteristics of a Row of Rectangular Jets in a Confined Cross Flow", Proceedings of the 14th Canadian Congress of Applied Mechanics (CANCAM '93), Volume 1, pp. 313-314, Queen's University, Kingston, Ontario, May 30 - June 4, 1993.
This paper presents an evaluation of some formulae in the literature that can be used to evaluate jet spacing in recovery boiler design and operation.

13. D. Tse, I. Gartshore, and M. Salcudean, "Compete Numerical Simulation of Primary Jets for Kraft Recovery Boilers", Proceedings of the 14th Canadian Congress of Applied Mechanics (CANCAM '93), Volume 1, pp. 311-312, Queen's University, Kingston, Ontario, May 30 - June 4, 1993. .

This paper evaluates the "Slot assumption" for modelling of primary jets in recovery boilers.

14.Z. Abdullah, P. Nowak, M. Salcudean and I.S. Gartshore, "Investigation of Interlaced and Opposed Jet Arrangements for Recovery Furnaces", Proceedings of the 1992 TAPPI Engineering Conference, Boston, Mass., Sept. 14-17, 1992, pp. 103, 122. *This paper evaluates two different secondary air arrangements in recovery boiler air system design.*

15.J. Quick, I.S. Gartshore and M. Salcudean, "Interaction of Opposing Jets with Relevance to Recovery Furnaces", Proceedings of the 1992 TAPPI Engineering Conference, Boston, Mass., Sept. 14-17, 1992, pp. 123-134.
This paper presents results of an investigation of the unsteady interaction of opposed jets in recovery boiler like geometries.

16.D. Tse, I. Gartshore and M. Salcudean, "A Study of Multiple Jets with Attention to Recovery Boiler Flow Fields", Proceedings of the 1992 International Chemical Recovery Conference, Seattle, WA, Book 1, pp. 181-196, June 7-11, 1992.
This paper disscusses issues related to parallel jet and interlaced interaction in recovery boiler like flows.

17.M. Salcudean, P. Nowak and Z. Abdullah, "Mathematical Modelling of Recovery Furnaces", Proceedings of the 1992 International Chemical Recovery Conference, Seattle, WA, Book 1, pp. 197-208, June 7-11, 1992.
This paper presents some initial cold flow modelling results from UBC.

18.I. Gartshore, F. Aghdasi and M. Salcudean, "Physical Modelling of Recovery Boilers: Problems and Prospects". 41st Canadian Chemical Engineering Conference, Vancouver, October 1991.
This paper presents results and discussion on water modelling at UBC.

19.M. Salcudean, I.S. Gartshore, P. Nowak, Z. Abdullah, D. Tse and J. Quick, "Mathematical Modelling of Flow Patterns in Recovery Boilers". Paper accepted for presentation at the 41st Canadian Chemical Engineering Conference, Vancouver, October 1991.
This paper presents some initial cold flow modelling results from UBC.

20.I. Gartshore, M. Salcudean and J. Quick, "Bifurcation of Flow Pattern from Opposing Jets Confined in a Cavity". Paper presented at the 13th CANCAM, 1991.
This paper presents an analysis of the interaction of two dimensional opposing jets. It can also apply to three dimensional closely spaced jets.

21.J. Zhou and M. Salcudean, "A Multi-grid Local Mesh Refinement Method for Recirculating Flows", 11th Int. Annual Conf. of CAMS, Halifax, N.S., Canada, 1990, pp. 587-594.
This paper presents early results from the UBC multigrid development program.

APPENDIX II

BLACK LIQUOR COMBUSTION VALIDATED RECOVERY BOILER MODELING: CHEMICAL PROCESSES IN BLACK LIQUOR COMBUSTION

1990-1994 Contract Report

Prepared by

Dr. Wm. James Frederick
Dr. Thomas M. Grace
Mr. Scott A Sinquefield
Mr. Lerssak Boonsongsup
Mr. Victor V. Reis
Mr. Sheng-Liang Wu
Dr. Kristiina Iisa
Mr. Kaj J. Wåg
Ms. Aimee C. Carangal
Mr. Narongsak Jivakanun
Mr. Viboon Srickaroenchaikul

Oregon State University

March 1995

TABLE OF CONTENTS

LIST OF FIGURES

LIST OF TABLES

CHAPTER 1. INTRODUCTION

In 1990, prior to initiation of the current project, a study of the phenomena involved in the combustion of black liquor droplets was completed and a numerical model for the combustion of single black liquor droplets was developed (1). The objective of this work had been to develop a computational model for burning of black liquor droplets which predicted the rate of drying, devolatilization, and char burning at conditions typical of recovery boilers, with the constraint that the model be computationally simple enough to be used in computational fluid dynamic (CFD) codes for recovery boilers. This model became the basis for the droplet combustion submodels used in the CFD models for recovery boilers that are available or under development today.

During the development and application of these droplet combustion models, the key needs for understanding black liquor combustion were identified. these formed the basis for the first four years of black liquor combustion fundamentals and modeling work under DOE contract AC02-83CE40637. It also became clear that the simple, four component model developed in 1990 would not be adequate to handle the formation and conversion of important species such as TRS gases, fume species, HCl, and NOx. The experimental and droplet burning modeling work in the first four years of the current project was therefore focused on developing a chemical element-based model for black liquor burning, and on obtaining experimental data on which to base and with which to test the model.

In this section, we review briefly the single droplet burning model reported in 1990. We then present a summary of the results obtained in the first four years of the current project, showing how the current version of the model was developed.

1.1 Status of droplet burning model in 1990

The black liquor droplet burning model reported in 1990 treated black liquor as consisting of four components: water, volatiles, char, and inorganic. The model accounted for total mass as the sum of these four components, but did not account for the individual chemical elements. Burning was modeled as occurring in the four stages (drying, devolatilization, char burning, and smelt reactions) observed by Hupa et al. (2), with each stage treated as occurring separately from the rest. The following summarizes the model as reported by in 1990 (1).

1.1.1 Drying

The rate-controlling step was assumed to be heat transfer from the surroundings to the droplet. Both external and internal heat transfer resistances were considered.

$$\frac{dQ}{dt} = \frac{(T_g - T_s)}{R_{tot}} \qquad (1\text{-}1)$$

The total resistance to heat transfer, R_{tot}, was calculated as

$$R_{tot} = \frac{1}{A} \left[\frac{1}{h'} + \frac{D}{(6\, k_{drop})}\right] \quad (1\text{-}2)$$

The surface area of the droplet was calculated as

$$A = \frac{P\, D_o^2\, DR_i^2}{6} \quad (1\text{-}3)$$

where DR_i,the swelling factor during drying, is 1.54.

The apparent heat transfer coefficient, h', was calculated as

$$h' = \{h_c + q_r/(T_g - T_s)\} \quad (1\text{-}4)$$

where q_r is the net radiative heat flux between the droplet surface and the surroundings and h_c is the convective heat transfer coefficient.

The heat transfer coefficient for Eq. 2 includes both natural and forced convection. The heat transfer coefficient is obtained from the Nusselt number, Eq. 5. It accounts for both forced and natural convection effects.

$$Nu = 2 + 0.39\, Gr^{0.25} + 0.37\, Re^{0.6} \quad (1\text{-}5)$$

The apparent thermal conductivity of the droplet during drying was assumed to be a linear function of the solids content of the droplet

$$k_{drop} = (k_{0bl} + (k_{bls} - k_{0bl}) \left(\frac{S - S_0}{1 - S_0}\right) \quad (1\text{-}6)$$

The thermal conductivities of the black liquor droplet at the initial solids content (k_{0bl}) and black liquor solids (k_{bls}) were estimated from (3)

$$k = \frac{0.00144\, T - 0.335\, S + 0.58}{DR_i^3} \quad (1\text{-}7)$$

The DR_i^3 term in Eq. 7 accounts for the effect of volume expansion on the thermal conductivity.

The total heat requirement for drying is

$$Q_{tot,d} = M_o \{C_p (T_i - T_o) + h_{fg} (1 - S_o/S_i)\} \quad (1\text{-}8)$$

where T_o and T_i are determined from a correlation for boiling point rise data, Eq. 9.

$$T = 100 + 50\, S_o^{2.74} \quad (1\text{-}9)$$

The water/solids ratio in the droplet was assumed to vary linearly with the fraction of the total heat that had been supplied, or

$$(1\text{-}S)/S = Q/Q_{tot} \tag{1-10}$$

The surface temperature, T_s, is calculated from Eq. 11

$$T_s = T_g - \frac{dQ/dt}{h'A} \tag{1-11}$$

1.1.2 Evaluation of the drying model

Figure 1-1 compares calculated versus measured times to ignition times for individual droplets of three different liquors from the Åbo Akademi data base. The solids content at ignition (S_i) was assumed to be 1.0 for these calculations. Measured values of the swelling factors (DR_i) were available for each data point. For this data, the model overestimates the time to ignition by about 5%. A slight decrease in S_i, to 0.95, improves the agreement between the data and model.

Figure 1-2 compares predicted versus experimental times to ignition for droplets of different sizes for a single kraft liquor. The drying time was calculated assuming that the droplets were completely dry at ignition ($S_i = 1.0$). The model agrees very well with the time to ignition data for this liquor.

Figure 1-3 compares predicted versus experimental time to ignition data at different furnace temperatures for a different kraft liquor. The calculations were made assuming $S_i = 1.0$. The model estimates the drying time accurately at 600°C, but predicts too long a time to ignition at higher temperatures. Figure 1-4 shows how S_i would have had to vary with furnace temperature to force the two-resistance model to agree with the experimental data. The trend is reasonable. It suggests that ignition would have occurred before the droplets were completely dry.

Figure 1-5 compare the drying times for sixteen Finnish and North American liquors with values predicted by the drying model. The droplets are larger (8 mg) than the 2.5 mg droplets used to obtain the data in Figures 1-3 and 1-4 . The model provides a reasonable estimate of the average drying time when S_i is assumed to be about 0.8. There is no difference in drying behavior among the four types of liquors.

1.1.3 Devolatilization

As with drying, the rate-controlling step was assumed to be heat transfer from the surroundings to the droplet as per Eq. 1-1. The total heat input required to devolatilize a droplet is

$$Q_{tot,v} = M_i \{C_p (T_{max} - T_i) + h_{fg} (1 - S_i)\} + M_o S_o \Delta H_{pyr} \tag{1-12}$$

and the time required for devolatilization is obtained by integrating Eq. 1 from the end of the drying stage until the incremental heat transferred equals $Q_{tot,v}$.

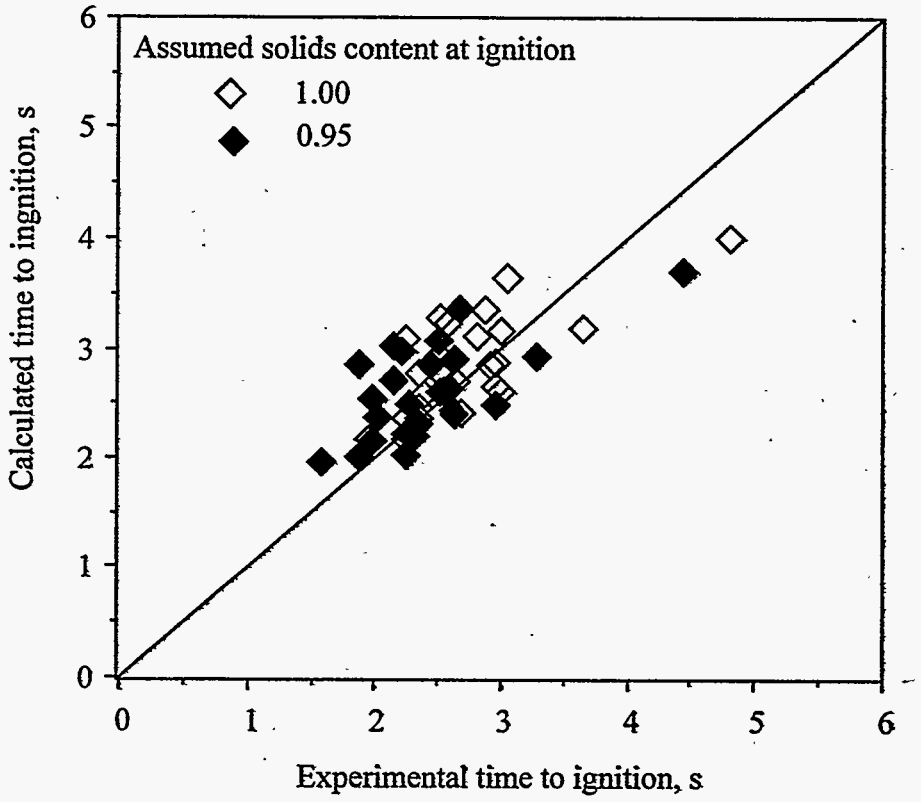

Figure 1-1. Calculated versus experimental time to ignition for three kraft black liquors using a two resistance heat transfer model. Droplet size 5-9 mg, 700-850°C furnace temperature, 60% initial dry solids content.

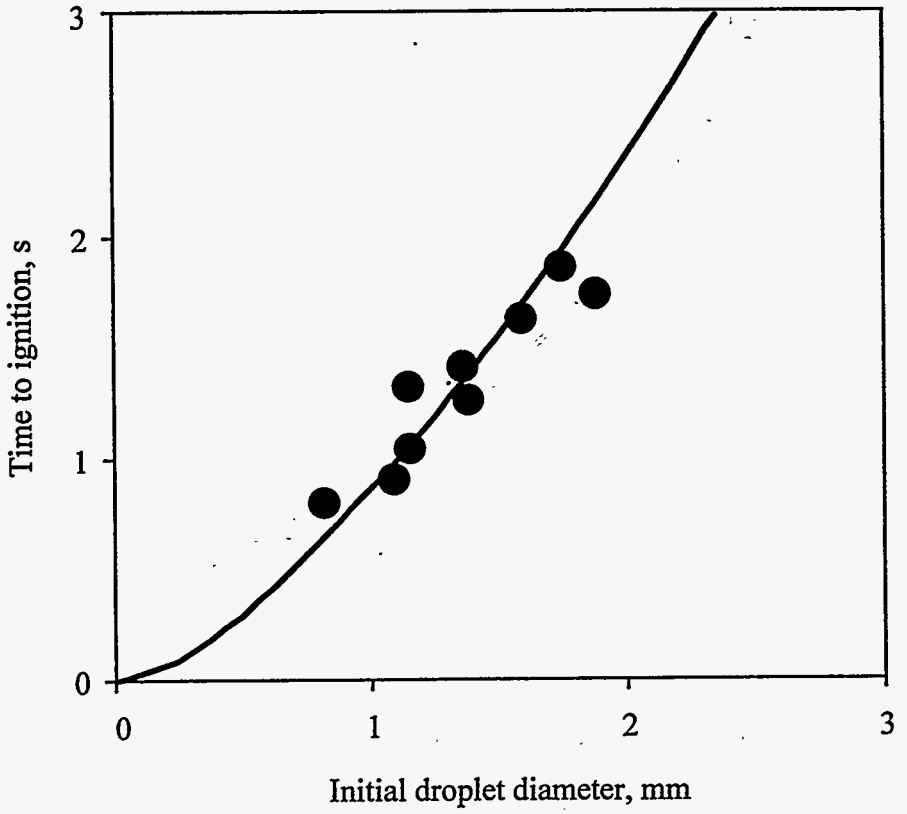

Figure 1-2. Time to ignition versus droplet size for a kraft black liquor. Data are from Hupa et al. (2).

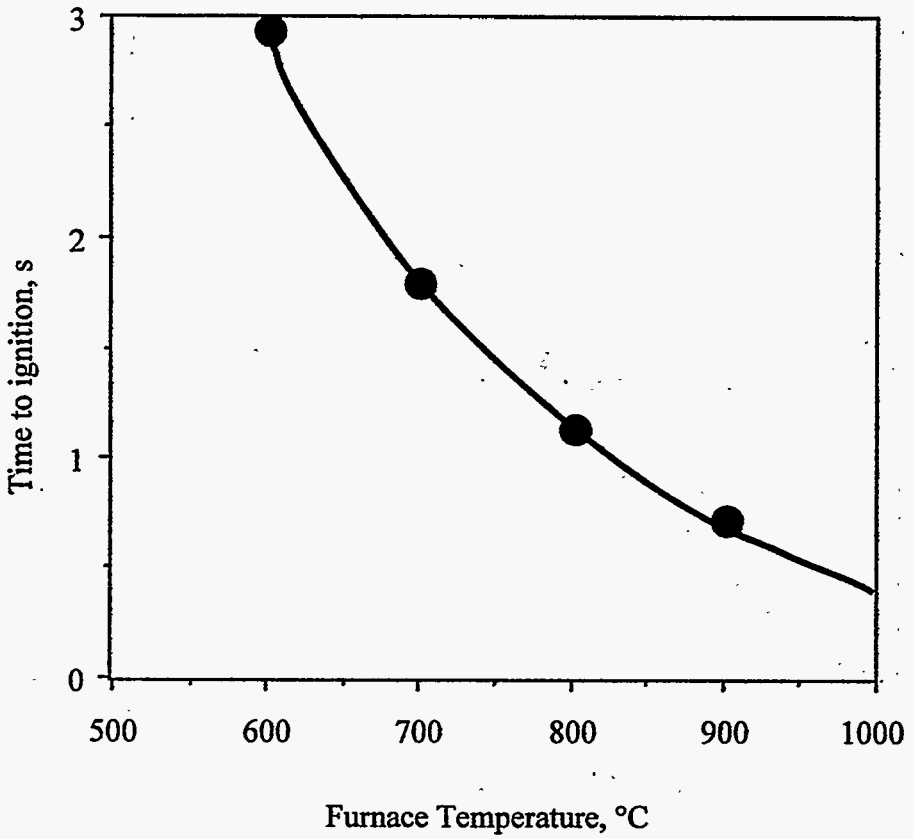

Figure 1-3. Time to ignition versus furnace temperature for one kraft liquor, 1.5 mm droplets, 60% initial solids content. Data are from Hupa et al. (2).

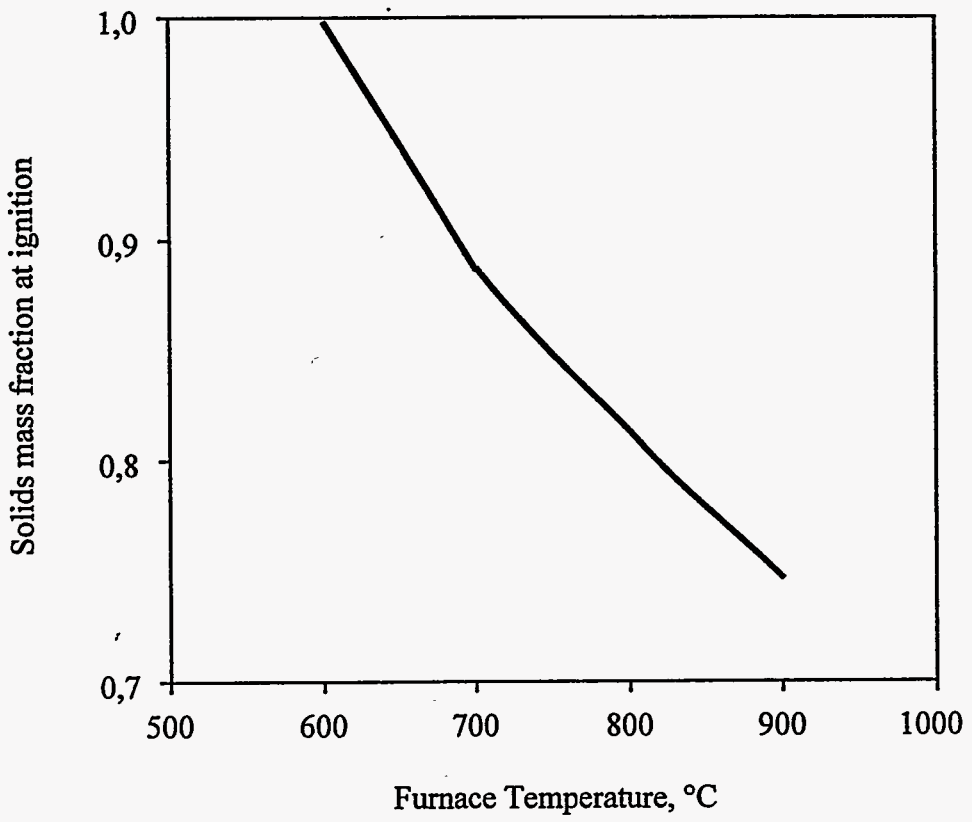

Figure 1-4. Calculated solids mass fraction at ignition to force agreement between the data and model in Figure 1-3.

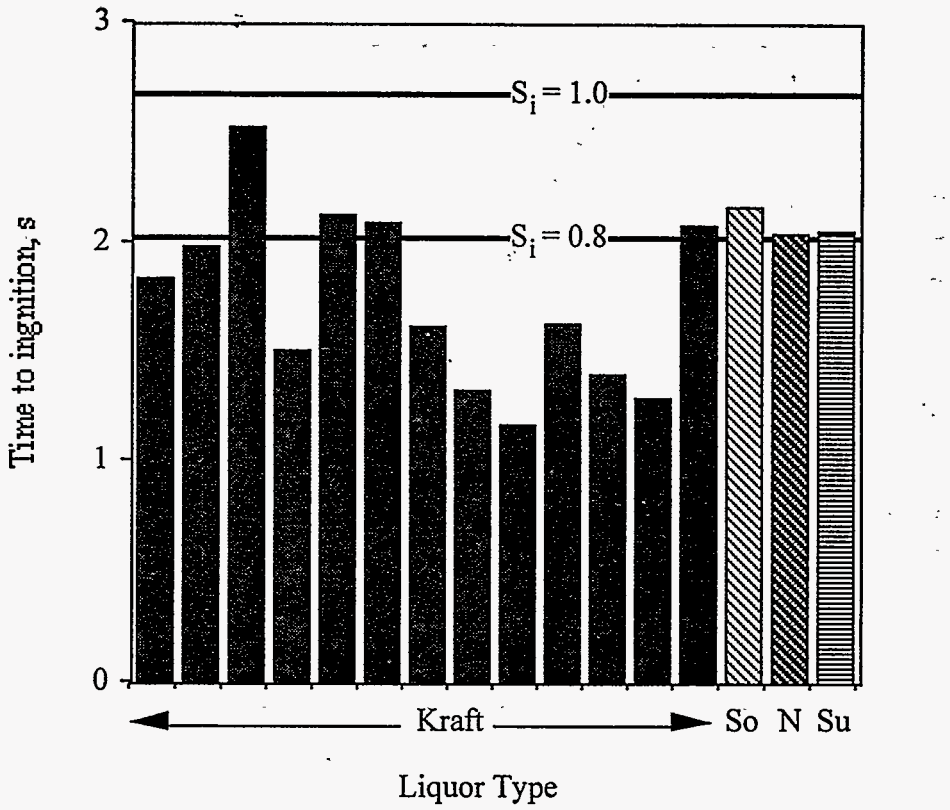

Figure 1-5. Time to ignition for 8 mg liquor droplets in an 800°C furnace. Horizontal lines are calculated times to ignition. So indicates a soda liquor, N indicates an NSSC liquor, and Su indicates a sodium-base sulfite liquor.

The gas temperature used to calculate the convective heat transfer rate was the mean temperature of the flame surrounding the droplet from Eq. 1-13:

$$T_g = T_{go} + \frac{0.232\ \Delta H_{comb}}{P_{O_2}\ C_{pg}} \tag{1-13}$$

Figure 1-6 compares measured versus calculated elapsed time between ignition and maximum swelling (devolatilization time) for sixteen kraft and three NSSC liquors at two furnace temperatures. The model predicts reasonably well the devolatilization time for the kraft liquors but overestimates the time required for some of the NSSC liquors.

1.1.4 Char Burning

The char burning model was based on the assumption that oxygen, CO2, and water vapor react directly with char at the surface of the char particle. The rate of mass transfer of oxygen to the particle surface was assumed to be the rate-controlling step. The rate equation for char burning was given as Eq. 1-14:

$$\frac{dM_c}{dt} = -(k_{ox}\ C_{ox} + k_{CO_2}\ C_{CO_2} + 0.5\ k_{H_2O}\ C_{H_2O})\ A\ (\frac{M_{ctot}}{M_{oxtot}}) \tag{1-14}$$

The total mass of oxygen required for char combustion is

$$M_{ox,tot} = M_{c,tot}\left[\frac{16}{12}\frac{CO}{C_{tot}} + \frac{32}{12}\frac{1\text{-}CO}{C_{tot}}\right] \tag{1-15}$$

where $M_{c,tot} = M_o S_o X_c$.

Equations 1-16 - 1-18 were used to describe the change in droplet diameter during drying, devolatilization, and char burning respectively. They were obtained empirically from experimental droplet swelling data (1).

Drying stage:

$$D/D_o = 1.54 \tag{1-16}$$

Devolatilization stage:

$$(D - D_i)/(D_{max} - D_i) = (Q/Q_{tot})^{0.8} \tag{1-17}$$

Char combustion stage:

$$(D^3 - D_{max}^3)/(D_{max}^3 - D_s^3) = 1 - M_c/M_{tot} \tag{1-18}$$

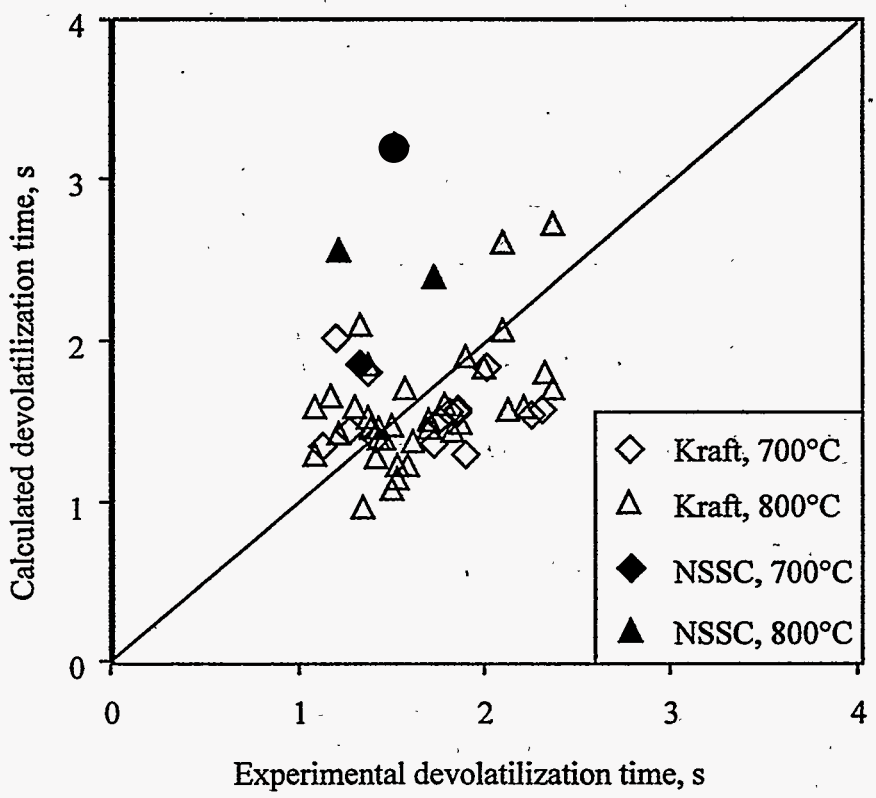

Figure 1-6. Measured versus calculated elapsed time between ignition and maximum swelling (devolatilization time) for sixteen kraft and three NSSC liquors at two furnace temperatures. The model predicts reasonably well the devolatilization time for the kraft liquors but overestimates the time required for some of the NSSC liquors.

Figures 1-7 and 1-8 compare the measured versus calculated char burning times. When the carbon content of the char following devolatilization (X_c) is adjusted, the model predicts very well the char burning times. X_c was at this point an important but unknown parameter that apparently varied from liquor to liquor.

Figure 1-9 shows the measured versus calculated particle diameter for a char particle during burning in air. Here also the measured and calculated values agree well.

1.1.5 Times to Ignition, End of Devolatilization, and Char Burning

At the time the 1990 model was reported, the available reliable data on black liquor burning were limited to observed times to ignition, to maximum swelling (end of devolatilization), and end of char burning. These were used to evaluate the droplet burning models summarized here. The times to ignition and to the end of devolatilization were obtained by integrating Eq. 1-1 until the total heat transferred equaled $Q_{tot,d}$ and $Q_{tot,d} + Q_{tot,v}$ respectively. The char burning time was obtained by integrating Eq. 1-14 until the total oxygen transferred (as O_2, CO_2, and H_2O) equaled $M_{ox,tot}$.

1.1.6 Assessment of the 1990 Model

The model gave reasonable estimates of the sum of the time to complete drying and devolatilization. and for char burning in air and other O_2/N_2 mixtures. However it predicted increasingly too long a time to ignition and too short a devolatilization stage as furnace temperature increased. This suggested that the stages of burning cannot be treated as completely independent - the droplets probably were not dry when they ignited, and char burning may have begun before devolatilization had been completed.

The three burning stage models described by Eqs. 1-1 - 1-18 required various physical properties data and combustion parameters. While it was possible to estimate the physical properties correlations and constants from available data, there was little or no information available for most of the combustion parameters.

A sensitivity analysis of the models (1) showed that the combustion parameters which significantly impacted burning and for which data or correlations were not available were the particle diameter at maximum swelling (DR_{max}), the extent to which the droplet had dried prior to ignition, the effects of temperature and heating rate on the yield of volatiles and fixed char carbon (X_c), and the ratio of CO/CO_2 produced during char burning. In addition, the temperature of the droplet residues during devolatilization and char burning, which can affect the rates of these processes, was not known.

Because the model treated black liquor as four components instead of as chemical elements, it was not possible to model the transitions of specific chemical species such as sulfur compounds, alkali metals, chlorides, HCl, and NO_X.

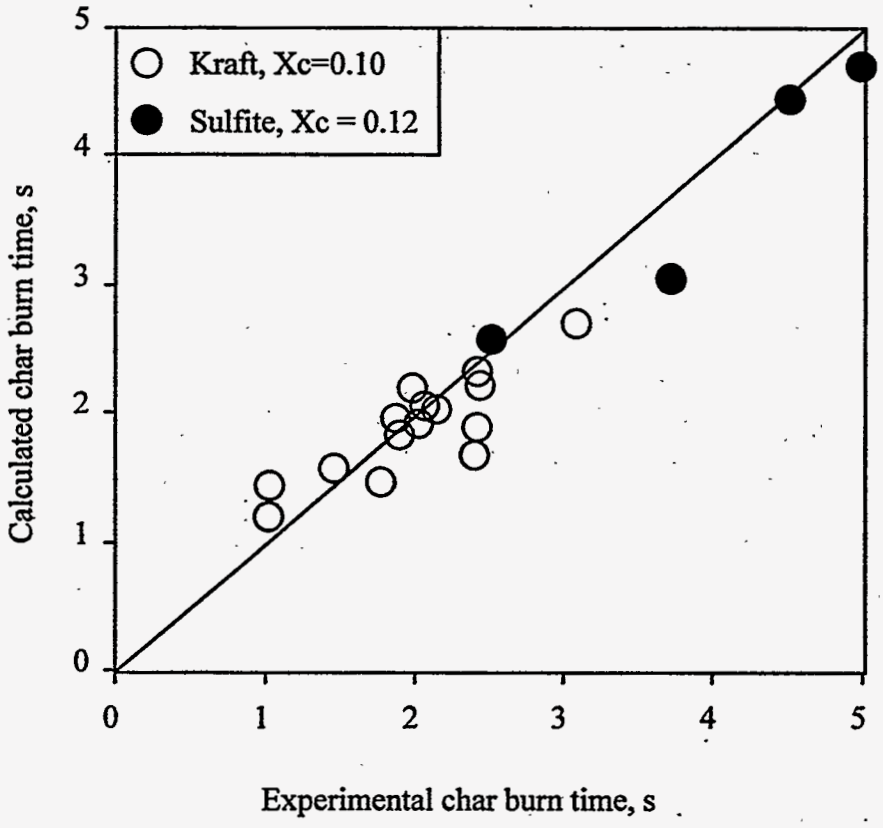

Figures 1-7. Measured versus calculated char burning times for kraft and sulfite liquors burned in air. X_c was adjusted to the values indicated.

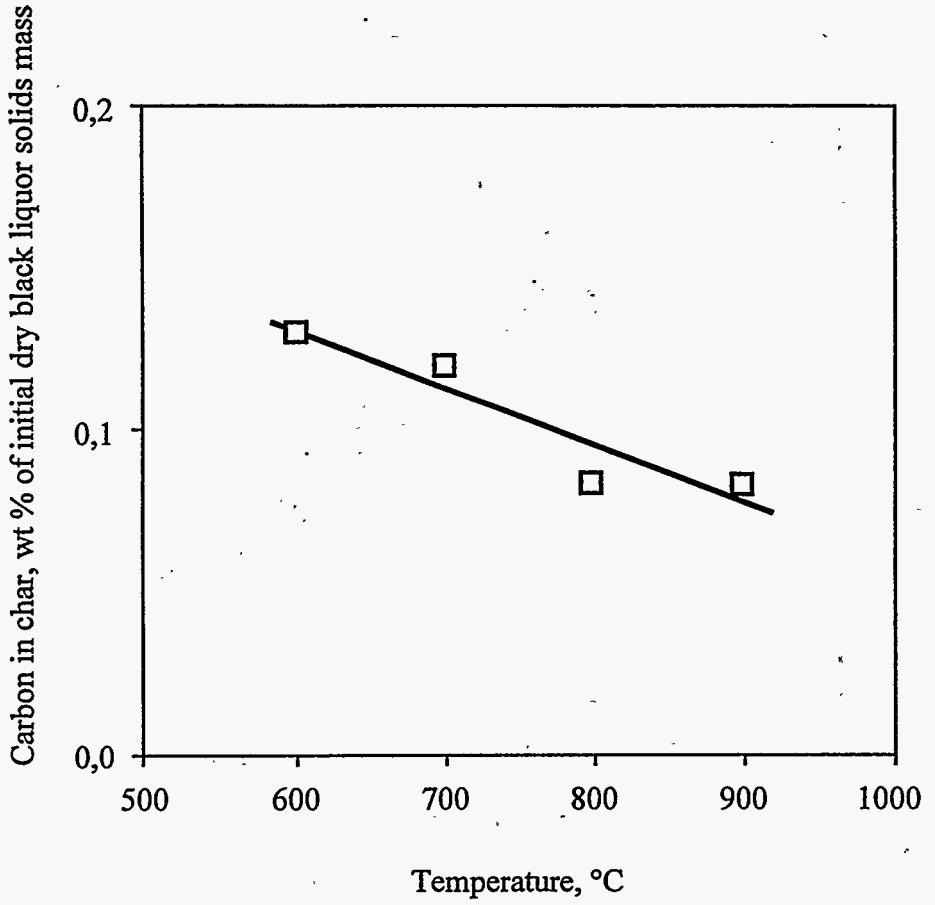

Figure 1-8. Measured versus calculated char burning times versus furnace temperature. In the calculations, X_c was adjusted at each temperature from 0.13 at 600°C to 0.085 at 900°C.

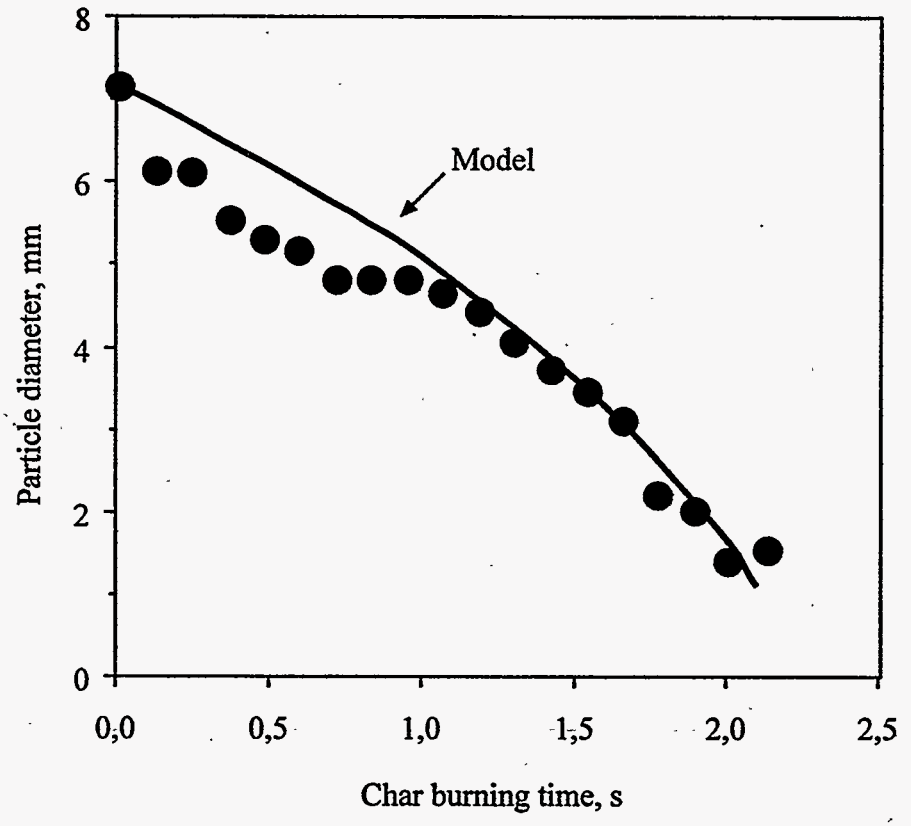

Figure 1-9. Particle diameter versus time for a hardwood kraft char burned in air at 800°C.

1.2 OBJECTIVES FOR YEARS 1-4

While the 1990 droplet burning model provided an adequate description of water and volatiles release and char burning, it was not able to address important questions such as TRS gases, fume species, HCl, and NO_X. The overall objective of the current project was to develop an advanced droplet burning model that could account for the chemical species transitions of importance in recovery boilers. To accomplish this objective, the following tasks were defined:

1. to develop a chemical element-based model which can predict the fate of all chemical species of interest during burning of black liquor. The chemical elements to be included were C-H-O-S-Na-K-Cl-N. The model was to account for closure of each chemical element and energy

2. to obtain the key experimental data needed to model key processes during the entire burning process at furnace conditions (i.e. at temperatures between 900-1200°C and in the presence of O_2, CO_2, and water vapor), to develop sub-models for each, and to incorporate those sub-models into the overall droplet burning model. The key processes are

   a. the conversion of carbon-containing species to CO, CO_2, and other carbon-containing gases

   b. the release of sulfur gases during burning and their recapture by fume and droplet residue

   c. the reduction of sulfur species in char.

   d. the release of sodium, potassium, and chloride

   e. the release of nitrogen, and the formation and destruction of NO_X

Results of the work accomplishments during the first four years of the current project are summarized in Chapters 2-6 of this section of the report. Publications and reports that resulted from this work are listed in Appendix 1.

1.3 REFERENCES

1. Frederick, W.J., "Combustion processes in black liquor recovery: analysis and interpretation of combustion rate data and an engineering design model," US DOE Report DOE/CE/40637-T8 (DE90012712), March, 1990.

2. Hupa, M., Solin, P., Hyöty, P., "Combustion Behavior of Black Liquor Droplets" *JPPS*, 13(2):J67-72 (1987).

3. Adams, T.N., Frederick, W.J. *Kraft Recovery Boiler Physical and Chemical Processes*, American Paper Institute (1988).

CHAPTER 2. CARBON CONVERSION

2.1 INTRODUCTION

In Chapter 1, we pointed out several weaknesses in the 1990 black liquor burning model. These included the lack of key combustion parameters describing devolatilization and char burning, inability of the droplet swelling model to predict the effects of gas composition and environment temperature on swelling, and a lack of data on droplet temperatures during burning in different gas atmospheres.

In the current project, experimental measurements of carbon conversion during devolatilization and char burning were made in four types of experiments at Åbo Akademi University and Oregon State University as part of the current project. Additional swelling measurements and modeling of swelling during devolatilization and the temperature of black liquor char particles during devolatilization and char burning were also completed. This chapter summarizes the results obtained for carbon conversion during devolatilization, swelling during devolatilization, carbon conversion during char burning, and black liquor particle temperatures during burning, and presents updated models for carbon conversion and swelling during black liquor burning.

2.2 EXPERIMENTAL PROCEDURES

2.2.1 Single Droplet Techniques

Pyrolysis, gasification, and combustion experiments were performed at Åbo Akademi University with single black liquor droplets in two different experimental setups, described as follows.

Combustion experiments were conducted by suspending single droplets of spent pulping liquors in a stagnant gas within laboratory muffle furnaces (Figure 2-1), using a method developed earlier by Hupa and co-workers (Hupa et al. 1987; Noopila and Hupa, 1988). The furnace per se was placed in an enclosure, and a gas mixture of controlled composition flowed through the enclosure to isolate the furnace from the ambient environment.

In the experiments, droplets of black liquor at solids contents of 60% or greater and weighing 5-20 mg were suspended on a platinum hook and weighed, lowered into the furnace through a hole on the top and allowed to remain in the furnace for the desired time. The pyrolyzed droplets were then removed and cooled in the nitrogen purge chamber at the exit to the furnace, weighed, and analyzed for sulfur, carbon and sodium content. The thermal event for each droplet was recorded using a video camera. The elapsed times for each combustion stage were read from the video recordings. Droplet dimension versus time data were also obtained from the recordings.

In some of these single droplet burning and gasification experiments, droplet surface temperatures were recorded using a two-color optical pyrometer with an optical probe [28,29]. An optical probe consisting of a 1 mm diameter all-quartz fiber guide encapsulated in a stainless steel tube was inserted through a sealed port in the furnace and positioned about 2 cm from the position where the droplet would be when it entered the furnace. The signal from the probe was sent to a radiometric unit in which the signal was split into visible and IR components by a dichroic mirror. Interference filters of 10 nm bandwidth were used to select the spectral bands at 650 and 1050 nm which optimize the sensitivity of the method and are not affected by the emission or absorption of radiation by gases surrounding the particle [28]. The

narrow bandwidth radiation was received by silicon photo diode detectors, and the signals from the detectors were recorded and further processed by computer.

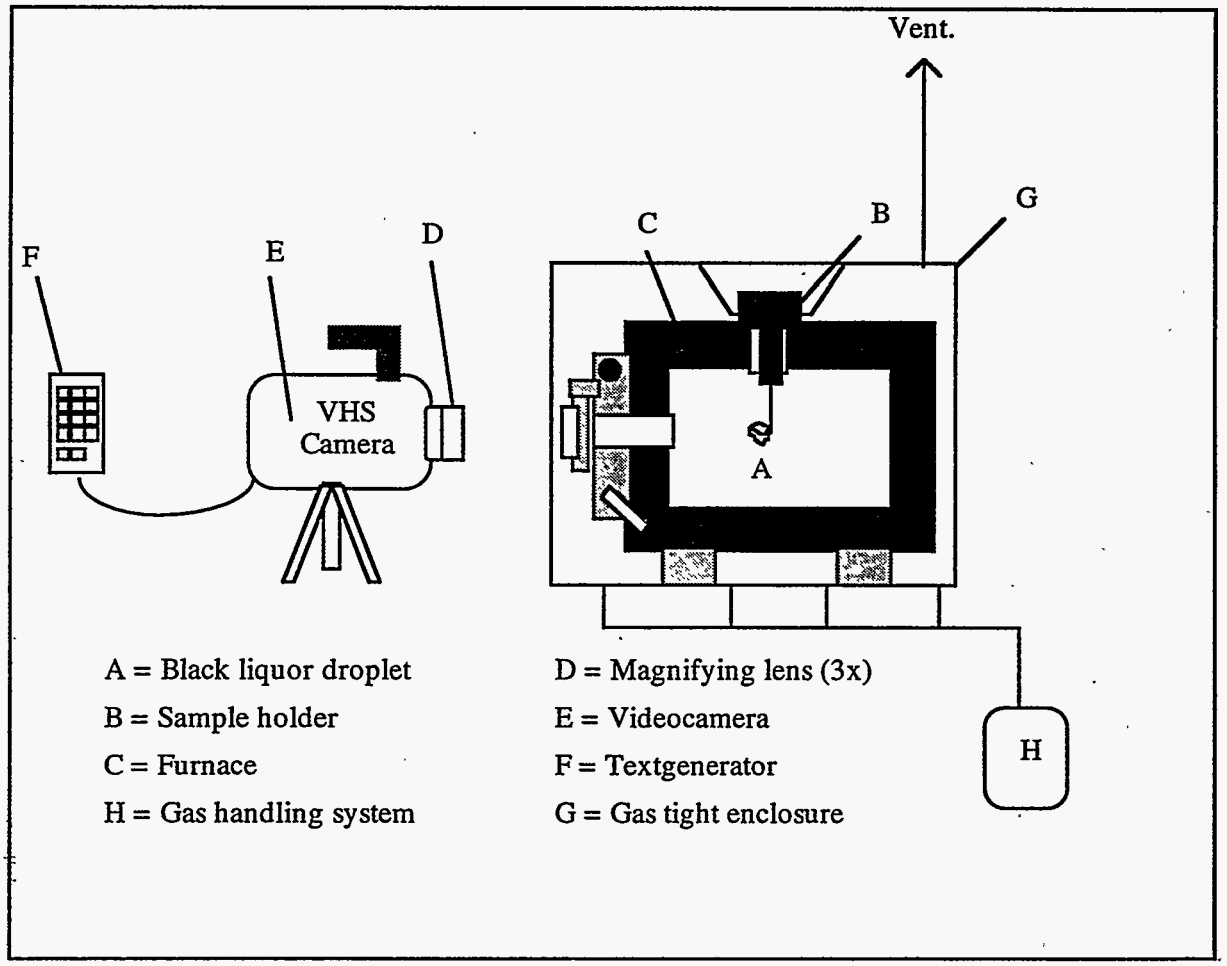

Figure 2-1. Diagram of the Abo Akademi single droplet/stagnant gas reactor.

The second droplet burning reactor consisted of a gas preheater, a pyrolysis reactor, oxidizer, gas sampling pump, SO_2 and CO_2 analyzers (all shown in Figure 2-1) and a computer for data collection. The droplet reactor per se consisted of a quartz tube, 25mm in diameter, in a tube furnace.

Droplets of black liquor were pyrolyzed/ pyrolyzed and gasified in the reactor. The quartz reactor was purged with desired gas composition and in that way isolated from the ambient gas environment. The gas mixture leaving the pyrolysis zone was mixed with air downstream of the tube furnace. The mixture then passed through an oxidizer where the sulfur and carbon gases were converted to SO_2 and CO_2 respectively. SO_2 and CO_2 where analyzed with gas UV- and IR analyzers. The char was lifted up in a nitrogen purge, weighed and analyzed for sodium, sulfur and carbon.

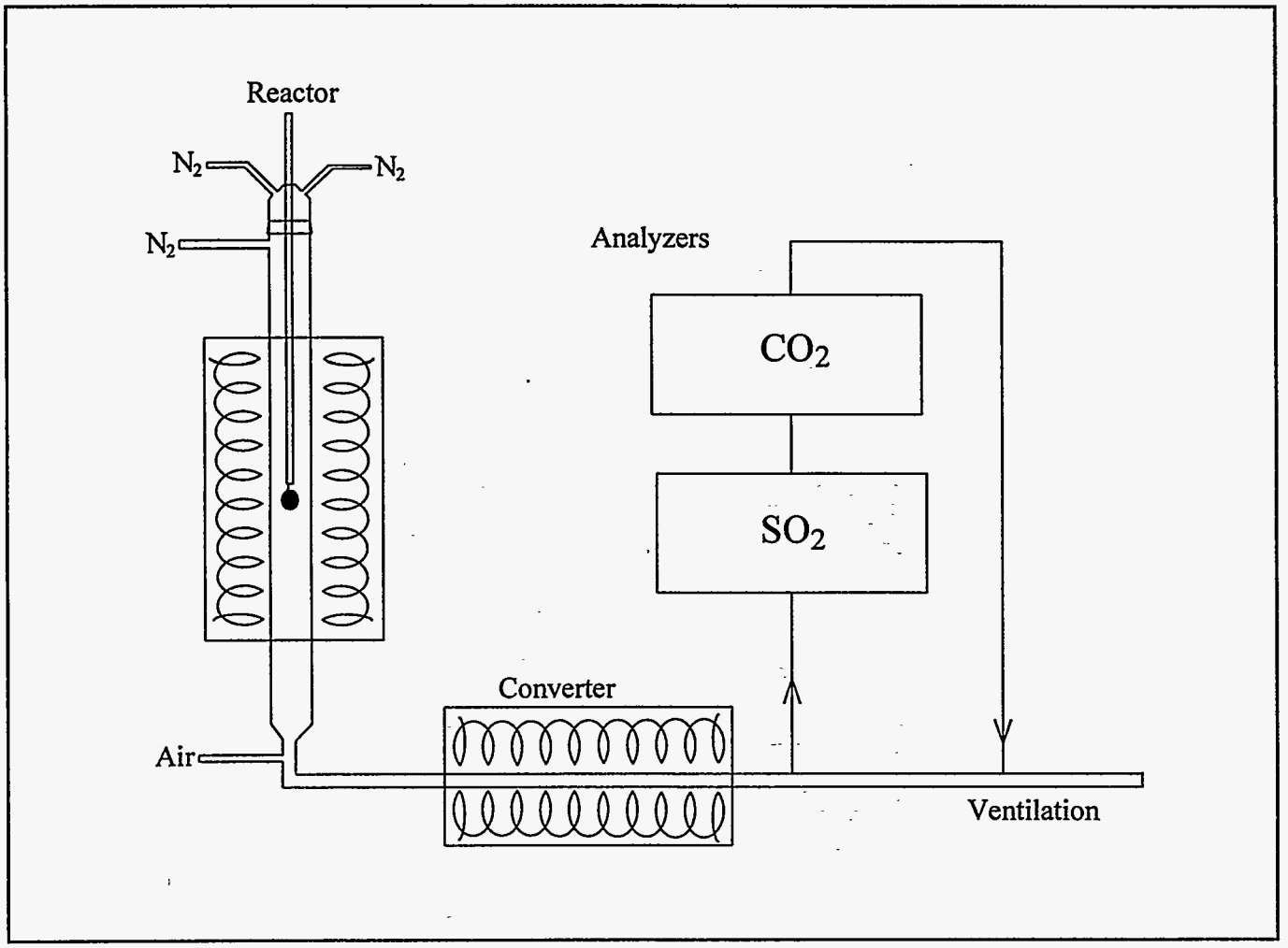

Figure 2-2. Diagram of the Abo Akademi single droplet/flow reactor.

2.2.2 Laminar Entrained-Flow Reactor

Pyrolysis and combustion experiments with black liquor were conducted at Oregon State University in a laboratory scale laminar entrained-flow reactor (LEFR). This type of reactor has two features that are important when obtaining fundamental pyrolysis and combustion data: they provide very rapid heating, and use particles that are small enough so that temperature gradients within the particles are small. Another important advantage is that all aspects of pyrolysis or combustion, e.g. carbon volatilization, char formation, sulfur release, sulfate reduction, and volatilization of sodium, potassium, and chloride, and the formation and destruction of nitrogen species, can be studied in a single experiment

A schematic of the OSU laminar entrained-flow reactor used in the experiments reported here is shown in Figure 2-3. The LEFR consists of a vertical 3-zone high temperature electrical furnace with two ceramic tubes inside. It operates with a downward flowing gas stream at temperatures to 1150°C and laminar conditions. The primary flow, a low temperature gas stream, is injected at the center of the

reactor. The secondary flow is preheated to the reactor temperature and injected coaxially with the primary flow. The small particles are heated rapidly (~10,000°C/s) by the high temperature secondary gas and radiation from the hot walls of the reactor. After passing through the reactor, the particles and gases enter a water-cooled, gas-purged collector where they are quenched with nitrogen to stop the chemical reactions. After the quench, the particles larger than 3 μm in diameter (char) are removed by a cyclone and the fine particles are collected on a nylon membrane filter (0.5 μm pore size) located before the exhaust duct. The cyclone/filter setup is shown in Figure 2-3. Residence times of 0.3-2.0 seconds were achieved in the experiments reported here.

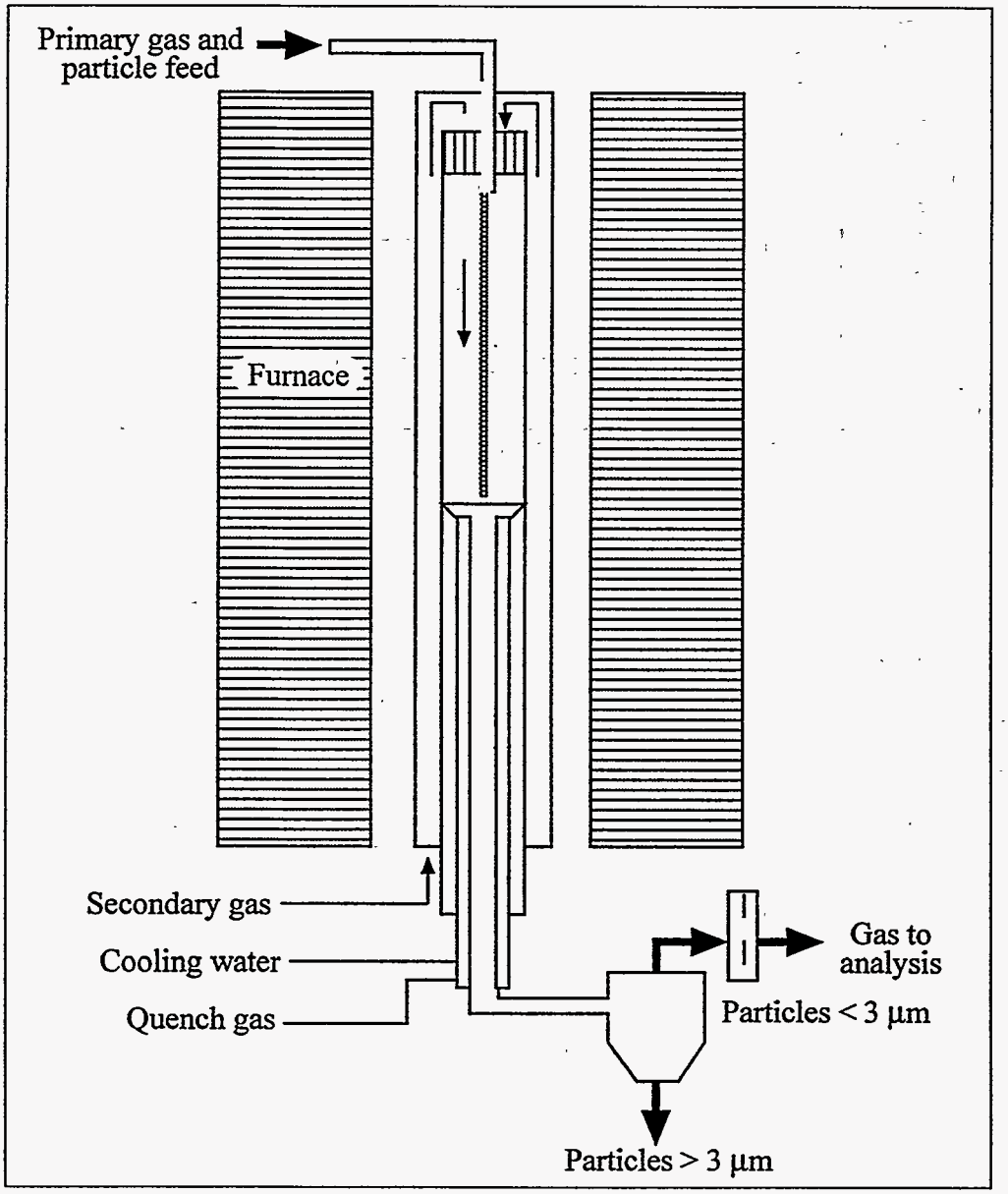

Figure 2-3. Schematic of the OSU laminar-entrained flow reactor.

2.3 CARBON VOLATILIZATION AND CHAR BURNING RESULTS

Devolatilization occurs very rapidly when black liquor solids are heated rapidly to temperatures substantially above 200°C. Figure 2-4 shows experimental data for char collected in pyrolysis experiments in a laminar entrained-flow reactor. The data, for 100 μm particles heated at rates of 4400-13,000°C/s, indicate that devolatilization is complete essentially as fast as heat can be supplied to the particles The amount of char collected was 30-70% of the mass of the dry black liquor solids fed. The amount of char decreased with increasing reactor temperature and with increasing reaction time. The shortest reaction time in these measurements was 0.3 seconds. The relatively slow decrease in char collected with reaction time after 0.3 seconds indicates that the loss of volatile gases via pyrolytic decomposition of the organic matter was complete in less than 0.3 seconds. Further loss of char mass is attributed to the formation of CO and CO_2 via sulfate and carbonate reduction (Cameron and Grace, 1985; Li and van Heiningen, 1990).

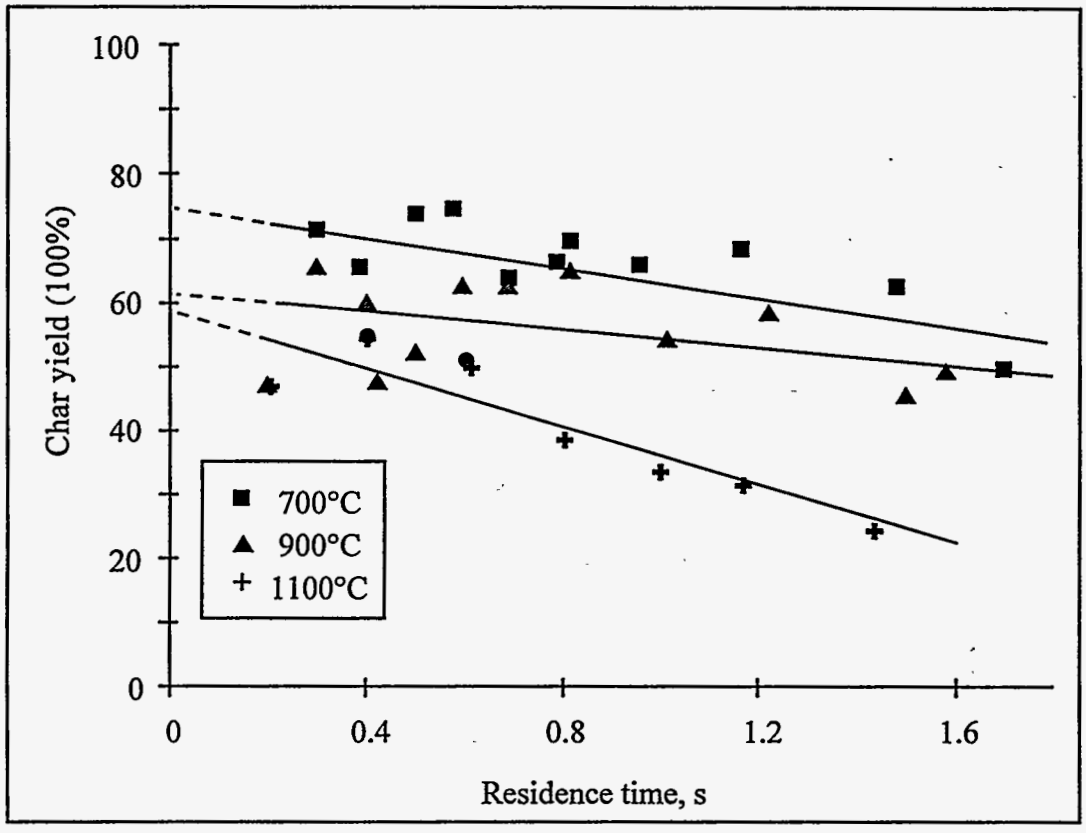

Figure 2-4. Char collected versus furnace temperature and residence time for 100μm dry black liquor particles in a laminar entrained flow reactor.

Figure 2-5 shows the particle temperatures versus residence time as calculated with a computational fluid dynamic and heat transfer model for entrained flow reactors developed by Flaxman (42). The calculations are for the same conditions at which the data in Figure 2.4 were obtained. The times for completion of pyrolysis at each temperature were estimated based on (a) the data of Li and van Heiningen (43) who showed that pyrolysis of black liquor was complete by 460°C at heating rates of

20°C/min, and (b) the correlation of Frederick and Hupa (3) between the average droplet temperature at the completion of devolatilization and the furnace temperature for 2-3 mm black liquor droplets at heating rates in the order of 100°C/s. The small particles used in this study would have heated more uniformly than those of 2-3 mm droplets, so that devolatilization would have been complete somewhere between 460°C and the higher limit predicted by the Frederick and Hupa correlation. According to *Figure 2-5*, devolatilization would have been complete in less than 0.14 s at 700°C and less than 0.06 s at 1100°C. These estimates indicate that the loss of volatile gases produced by pyrolytic decomposition of the organic matter in black liquor is complete before the particles reach their final temperature, and that this process would be complete long before the shortest particle residence time for the data in Figure 2-4 (0.3 seconds) was reached.

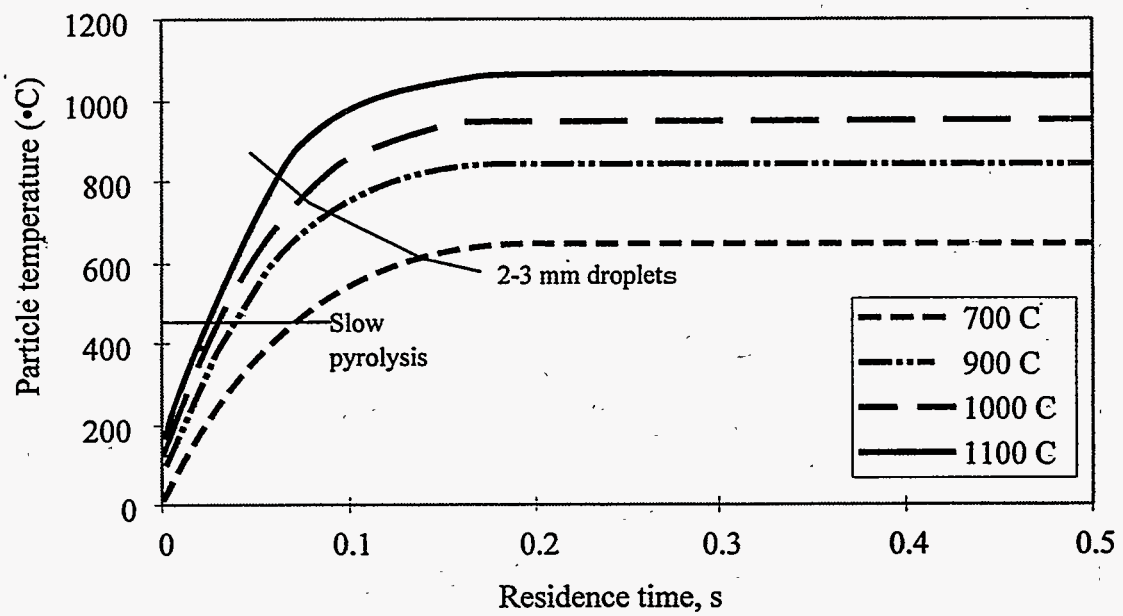

Figure 2-5. Particle temperatures versus residence time at the four reactor temperatures used in this study as estimated with Flaxman's model (1986). Conditions are for 100 μm dry black liquor particles, a diameter swelling factor of 3.0, primary gas flow rate 0.1 l/min NTP, secondary gas flow 20 l/min NTP, and injector diameter 3.3 mm ID.

An important difference between the pyrolysis behavior of the small particles in Figure 2-4 and those of the 0.5-5 mm black liquor droplets typically fired in recovery boilers is that the temperature within the particles should be more uniform within the smaller particles. The temperature profiles shown in Figure 2-6 were calculated using a detailed particle burning model for black liquor developed by Verrill and Wessel et al. [17]. The profiles show that there are temperature gradients within the 100 μm particles used in this study during the early stages of pyrolysis. However, the temperature is more uniform than within the larger black liquor droplets typically fired in recovery boilers. The steep local temperature gradients at the outer surface of the larger droplets indicate that devolatilization tends to occur in an outer shell of expanding thickness for the larger droplets. By contrast, devolatilization occurs much more uniformly throughout the smaller particles used in this study.

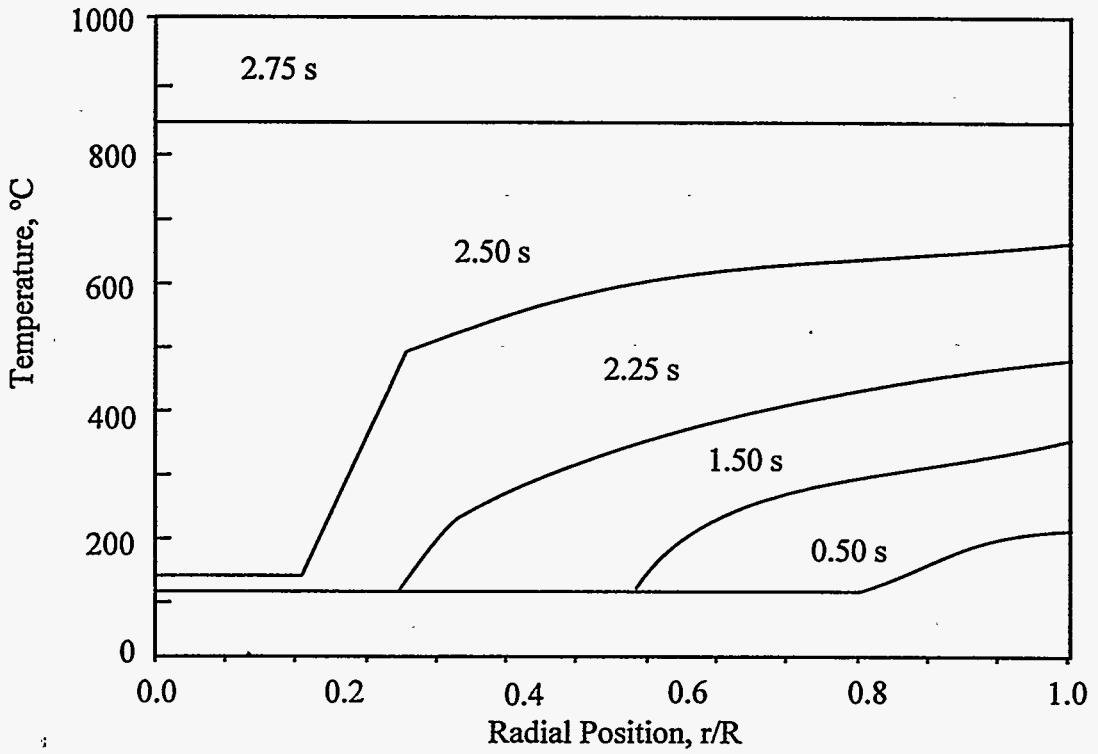

Figure 2-6a. Predicted radial temperature profiles for 2 mm captive drop (70% initial solids in 100% N_2 at 900°C with no forced convection). (Verrill and Wessel, 1995)

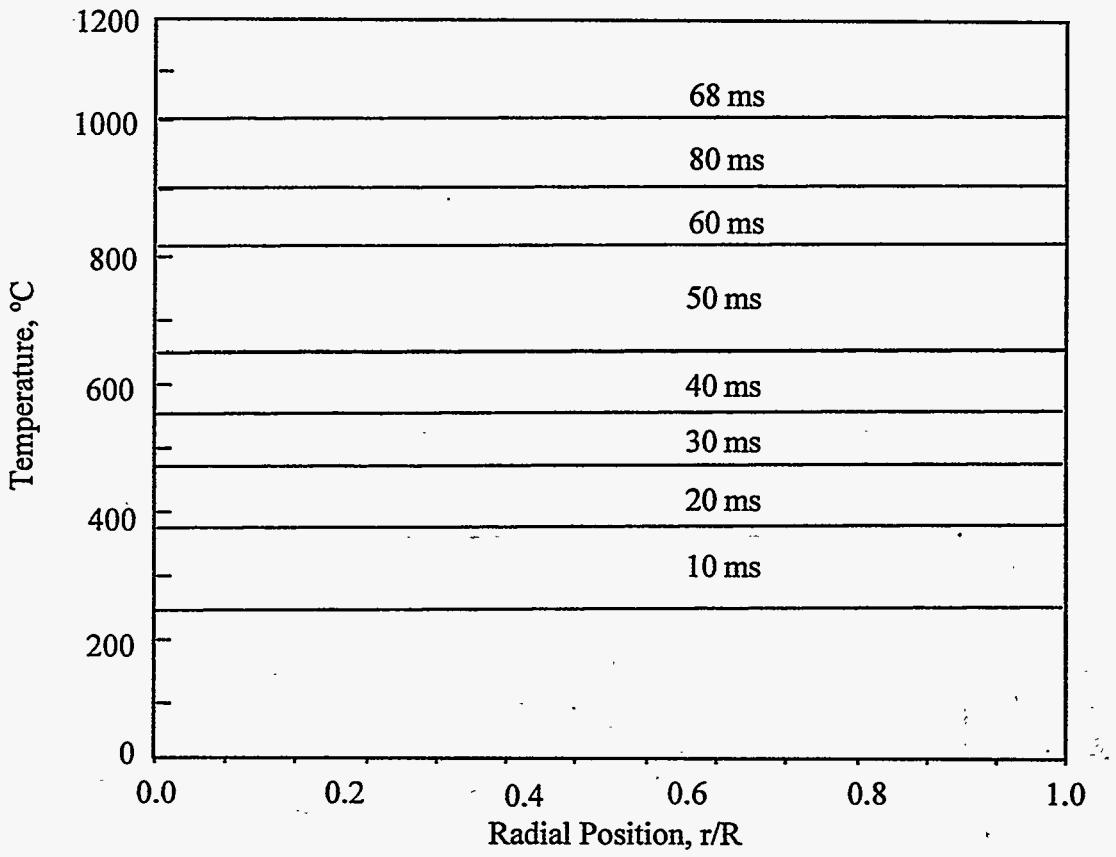

Figure 2-6b. Predicted radial temperature profiles for 100 μm falling particle (100% initial solids in 100% N_2 at 900°C with 0.28 m/s gas velocity). (Verrill and Wessel, 1995)

For most fuels, the yield of char from devolatilization decreases with increasing furnace temperature and heating rate. Figure 2-7 compares the char residue mass (fixed carbon + inorganic) retained immediately after release of the volatile pyrolysis products. The data for the 100 μm particles was obtained by extrapolating the data in Figure 2-4 and similar data at intermediate temperatures to zero residence times. The char yield decreases as the reactor temperature increases from 700°C to 900°C, but remains essentially constant at higher temperatures. The data for single droplets (~2 mm diameter, ~100-200°C/s heating rate) were obtained by exposing the droplets to a hot furnace environment for 10 seconds. The data at the lower temperatures agree well with data from single droplet experiments (3). However, at higher temperatures, the char yields are much lower.

Figures 2-8 and 2-9 show the fixed carbon in the char versus time and the fixed carbon remaining in the char residue at the end of devolatilization. The trends are similar to those for the char residue - the fixed carbon decreases with increasing furnace temperature but more slowly for the 100 μm particles, and seems to approach an asymptotic value near 50% at higher furnace temperatures. As with the char residue mass data in Figure 2-7, the fixed carbon remaining in the larger droplets continues to decrease as temperature increases.

Drying and devolatilization end well before 10 seconds, and the additional mass loss is due to reactions that occur in the char [30], carbonate reduction, and the accompanying loss of sodium [32,44]), and possibly by shedding of char fragments [22], all of which occur after devolatilization is complete. Because of these effects, the char residue and fixed carbon yield data with the smaller particles is considered to be more reliable. The data in Figures 2-7 and 2-9 indicate that black liquor char residue and char carbon yields do not decrease significantly with increasing furnace temperature above 900°C, and that they are not sensitive to heating rate in the range ~100-10,000°C/s.

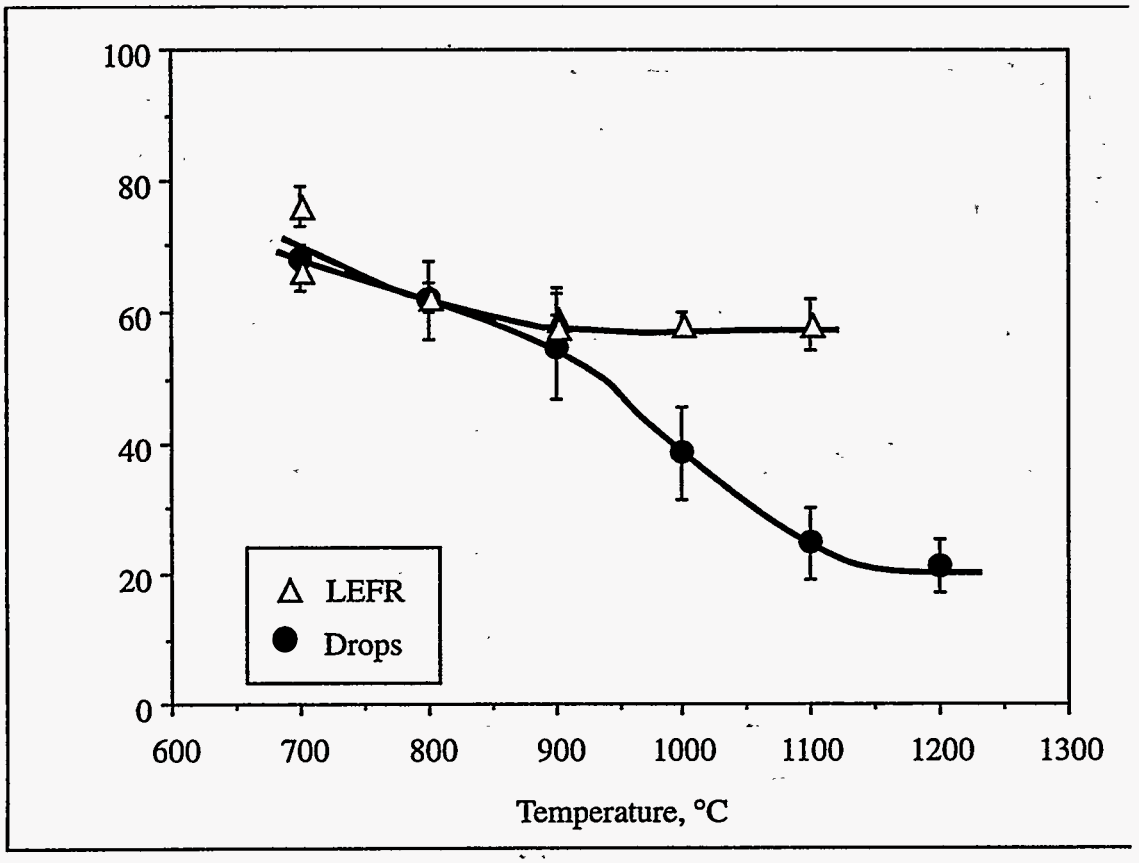

Figure 2-7. Comparison of char yields obtained from LEFR experiments and experiments with single droplets.

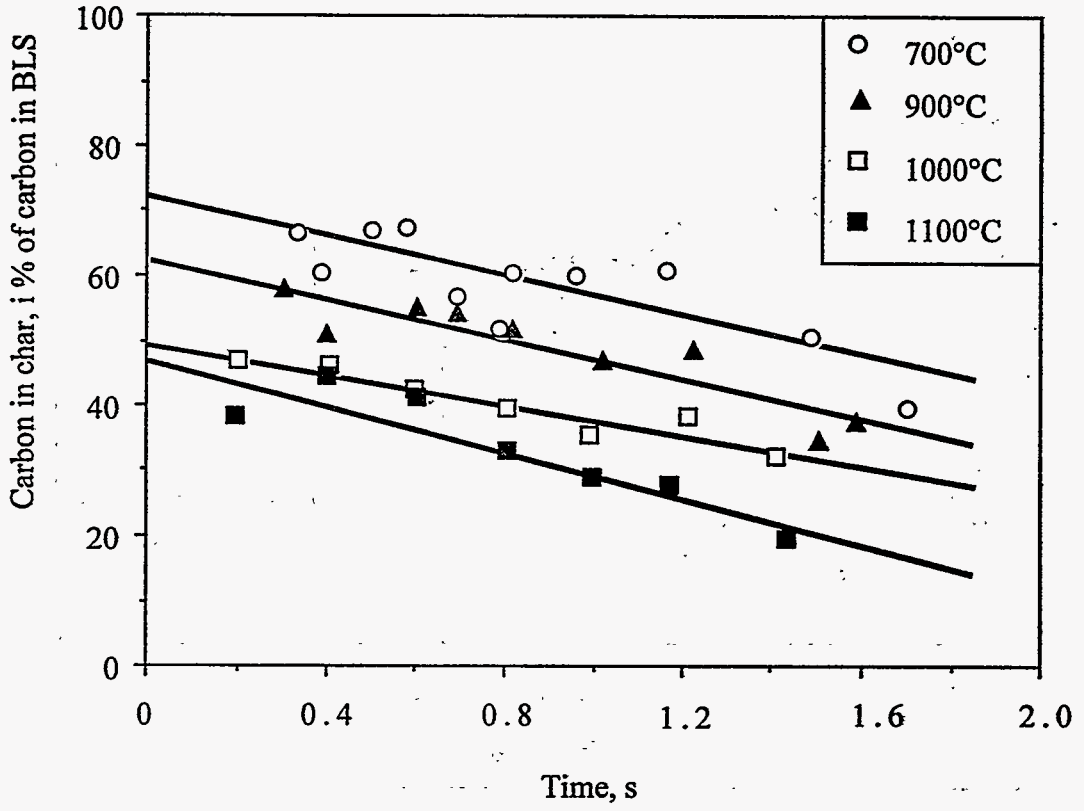

Figure 2-8. Fixed carbon in char collected versus furnace temperature and residence time for 100 μm dry black liquor particles in a laminar entrained flow reactor.

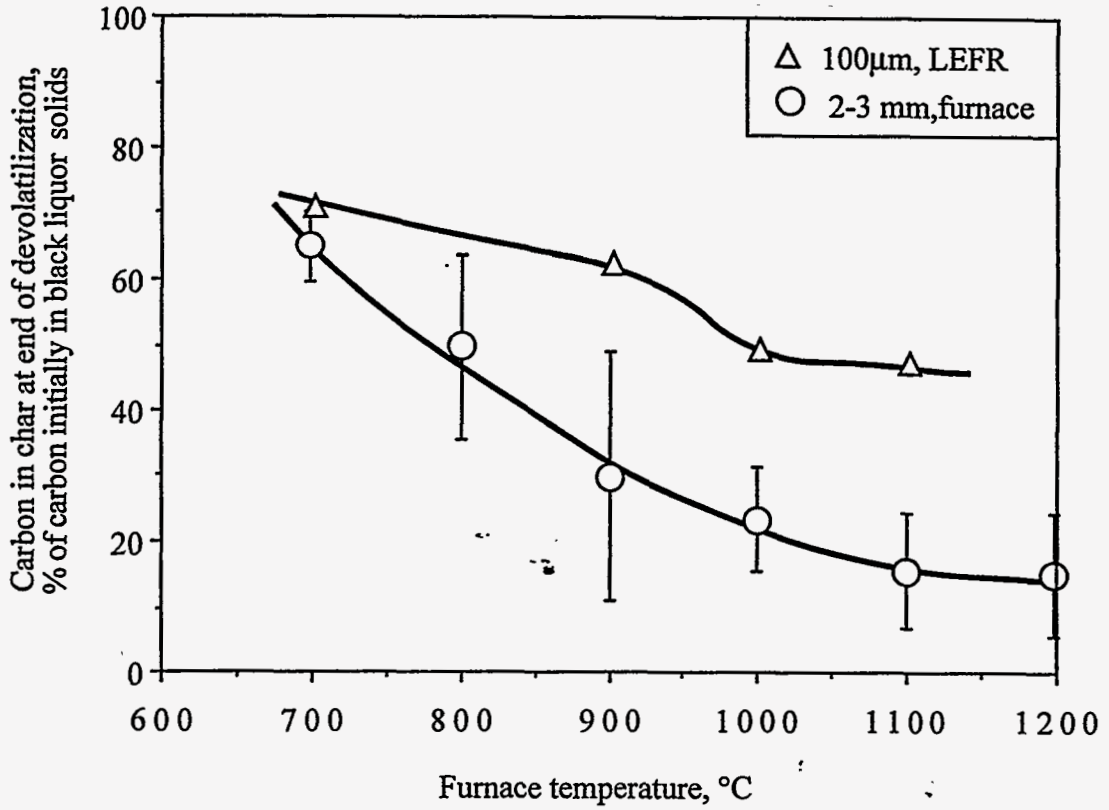

Figure 2-9. Comparison of fixed carbon in char obtained from LEFR experiments and experiments with single droplets.

During black liquor combustion, the processes of drying and devolatilization are clearly not separate and distinct. They can overlap considerably depending on the droplet size and heat flux to the droplet surface. Figure 2-10 shows the predicted average droplet solids content at ignition versus heat flux based on the model developed by Frederick and Hupa (1993). These conclusions are based on an analysis of time to ignition data for droplets burned in air and detailed modeling of single droplet combustion. The results show that smaller droplets and droplets in lower temperature environments are more likely to dry completely before devolatilization begins. The data in Figures 2-6 and 2-10 together suggest that, at conditions applicable to recovery boilers, droplets dry and begin to devolatilize at the outer surface with little or no drying of the mass within the droplet.

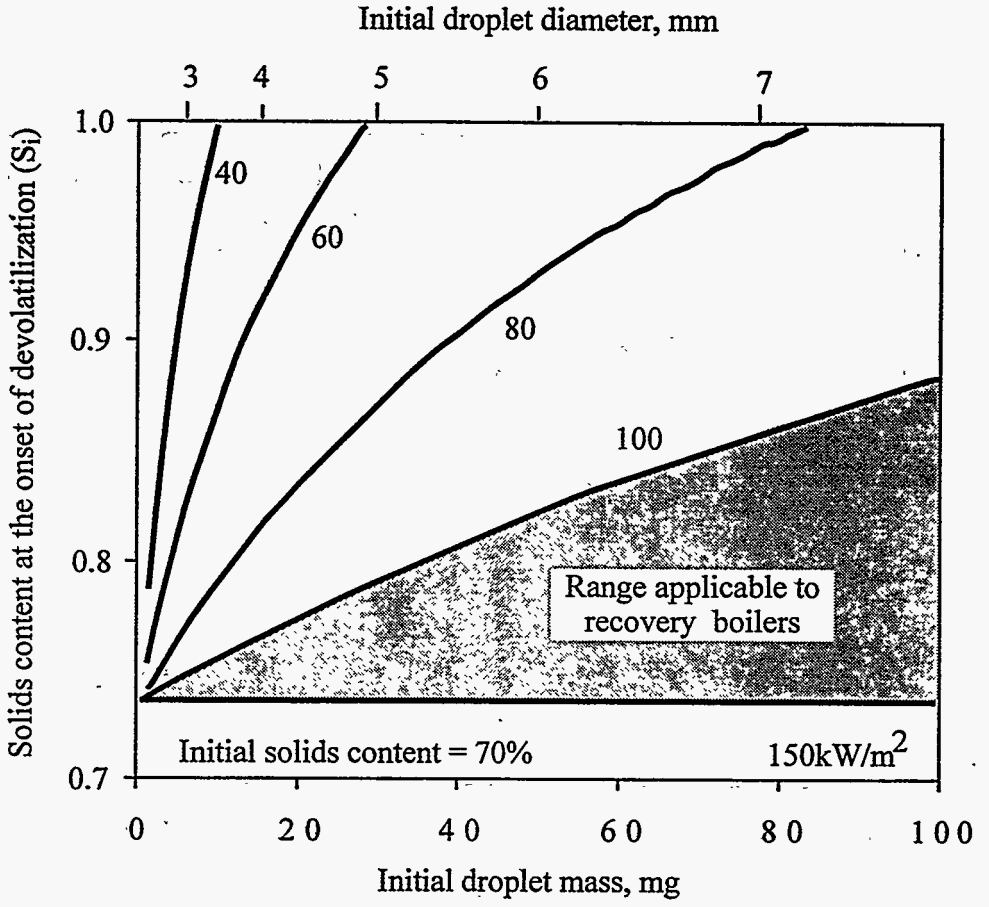

Figure 2-10. Effect of initial droplet mass and heat flux to droplet on the solids content at the onset of devolatilization for droplets initially at 70% dry solids content.

The fixed carbon in char is converted to CO by oxidation with O_2, CO_2, and water vapor. At furnace conditions, all three reactions can be important. Oxidation with elemental oxygen is limited by the rate of film mass transfer at furnace conditions (Figure 2-11), while the rate of carbon oxidation by CO_2 and water vapor is also influenced by diffusion of these gases into the char particles (Figures 2-12, 2-13).

The data of Grace et al. (39) suggest that oxidation of char carbon by O_2, CO_2, and water vapor does not occur simultaneously, but that CO and hydrogen produced at the char surface consume O_2 in the boundary layer. They presented a criterion for estimating the rate of carbon consumption when all three gases are present.

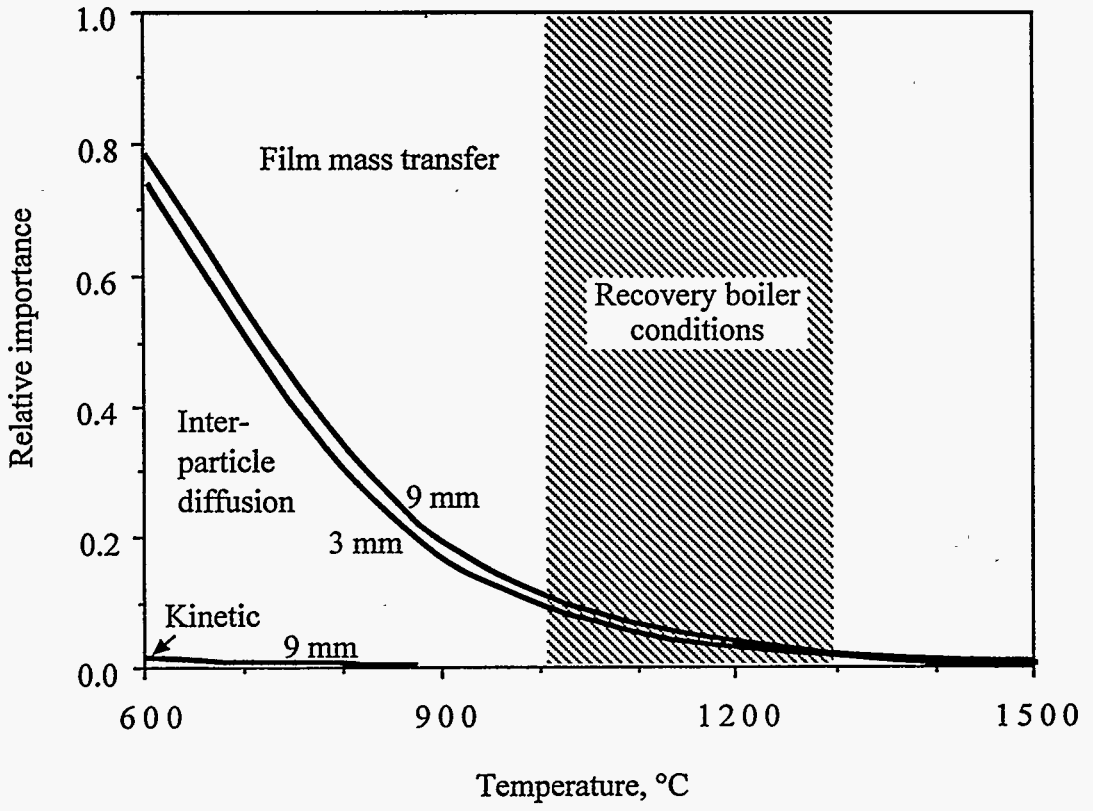

Figure 2-11. Relative importance of the chemical kinetic, interparticle diffusion, and film mass transfer resistances to the overall rate of char carbon oxidation for 3 and 9 mm char particles in a gas environment containing 5% O_2, 122 m^2/g char carbon specific area. The droplet surface temperature is assumed to exceed the furnace temperature by 50°C in these calculations.

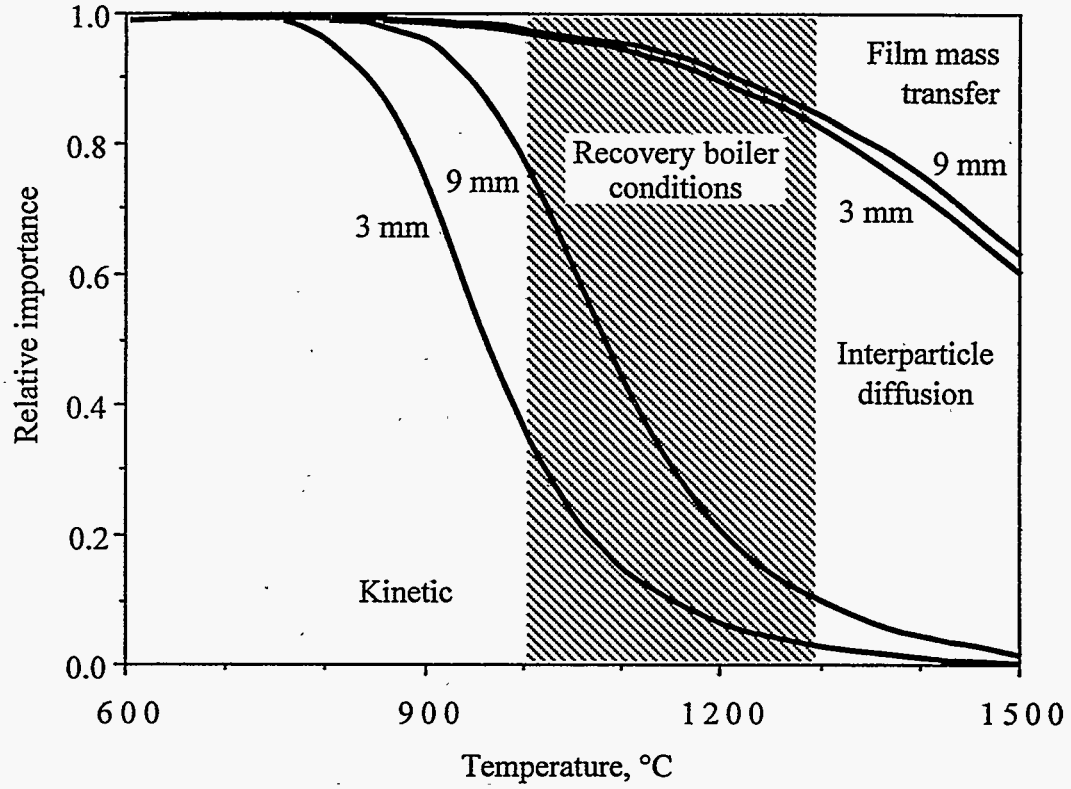

Figure 2-12. Relative importance of the chemical kinetic, interparticle diffusion, and film mass transfer resistances to the overall rate of char carbon gasification with CO_2 for 3 and 9 mm char particles in a gas environment containing 13% CO_2, 5% CO. 122 m^2/g char carbon specific area. The droplet surface temperature is assumed to exceed the furnace temperature by 50°C in these calculations.

The results in Figure 2-13 for char carbon gasification with water vapor fall in between the results for char oxidation and gasification with CO_2. Both interparticle diffusion and film mass transfer are important, with film mass transfer becoming dominant above 1400°C. The kinetic rate is not very important at combustion temperatures, and dominates only at temperatures below 600°C. This agrees well with experimental observations for 2-3 mm black liquor char particles gasified in water vapor/N_2 mixtures at 700-900°C.

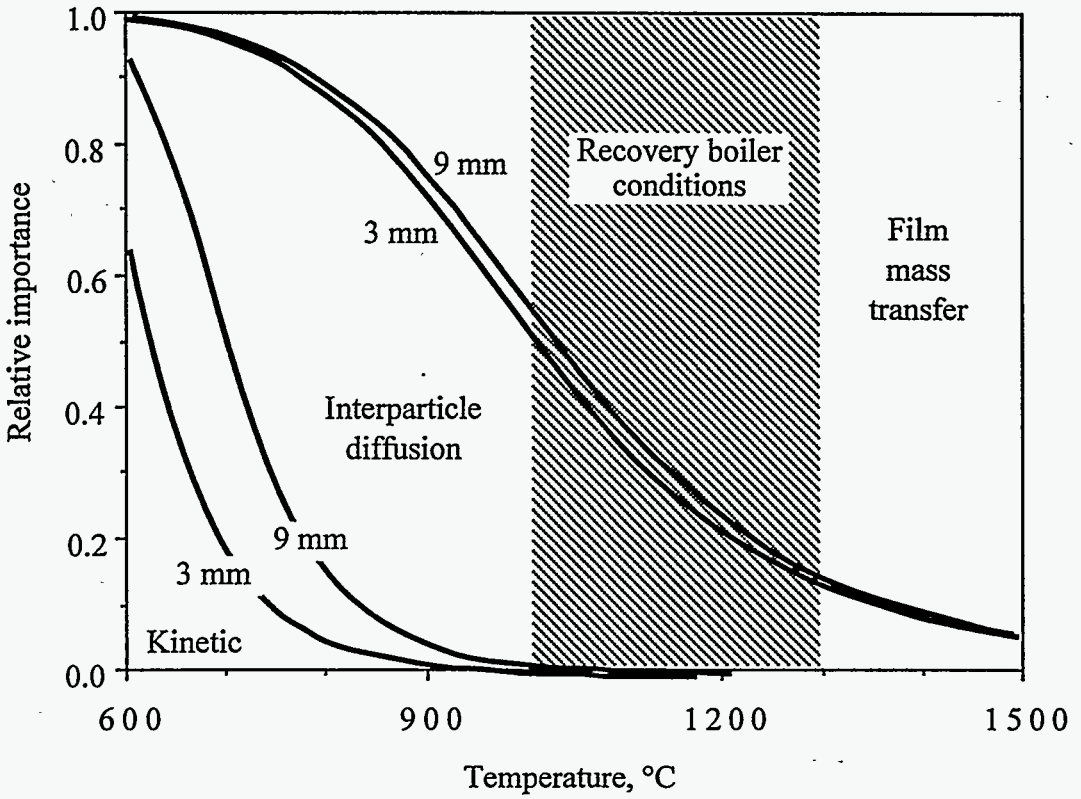

Figure 2-13. Relative importance of the chemical kinetic, interparticle diffusion, and film mass transfer resistances to the overall rate of char carbon gasification with water vapor for 3 and 9 mm char particles in a gas environment containing 18% H_2O, 3% H_2. 122 m^2/g char carbon specific area. The droplet surface temperature is assumed to exceed the furnace temperature by 50°C in these calculations.

2.4 SWELLING DURING DEVOLATILIZATION VERSUS FURNACE TEMPERATURE AND GAS COMPOSITION

As discussed in Chapter 1 of this section, the effects of furnace temperature and gas composition on swelling during devolatilization had not earlier been established to the point where these effects could be accounted for in modeling of black liquor burning. Experimental data on the maximum swelling observed at the end of devolatilization were obtained with five black liquors from commercial pulp mills. Four were kraft liquors and the fifth was an NSSC liquor. The origin, properties, and available composition data for the five liquors are listed in Table 2-1.

Most of the droplets were burned in gas mixtures containing 2-21% O_2, 0 or 20% CO_2, with the balance N_2, at muffle furnace temperatures of 600-900°C. In these measurements, CO_2 was included in part because of the observation of Miller et al. (10) that the presence or absence of oxidizing gases influenced the character of the external surface of the char particle. CO_2 was chosen as a representative oxidizing gas other than O_2, and a concentration of 20% was chosen as a concentration high enough so that its influence, if different than that of the other gases present, could be observed experimentally. A few additional measurements were made in 20% CO_2/80% N_2 and 20% water vapor/80% N_2 mixtures, in the

absence of O_2. By comparison, typical concentrations of the major oxidizing gas species above the char bed are 5% O_2, 13% CO_2, and 4% water vapor [16].

Table 2-1. Source and composition data for the five black liquors used in this study.

Liquor		A	B	C	D	E
Liquor type		Kraft	Kraft	Kraft	Kraft	NSSC
Wood species		D. fir	D. fir	Pine	Birch	Birch
Solids content	%	62	60	60	60	60
Heating value	MJ/kg	13.7	14.9			
Residual effective alkali	% as Na_2O	3.2	3.4			
Sulfated ash	% as NaOH	36.8	34.0			
Na	%	20.4	18.0			
Na_2SO_4	%	8.2	5.6			
Na_2CO_3	%	7.4	6.3			
NaOH	%	2.7	2.9			
NaCl	%	2.7	2.4			
Na_2S	%	2.8	2.7			

Swelling measurements were made with enough droplets to obtain 6 to 12 reliable measurements at each muffle furnace temperature and gas composition. The apparent diameters of the particles were determined as they swelled by measuring the minimum and maximum particle dimensions (L_1, L_2) from the video recordings as shown in Figure 2-14 A body of known length, also recorded by video when suspended in the muffle furnace, was used as a reference standard for calibration. The apparent diameter (D) was approximated as

$$D = (L_1 \times L_2)^{1/2} \tag{2-1}$$

Because only two of the three axes for each droplet could be measured, a more accurate approximation of the droplet diameter was not considered necessary.

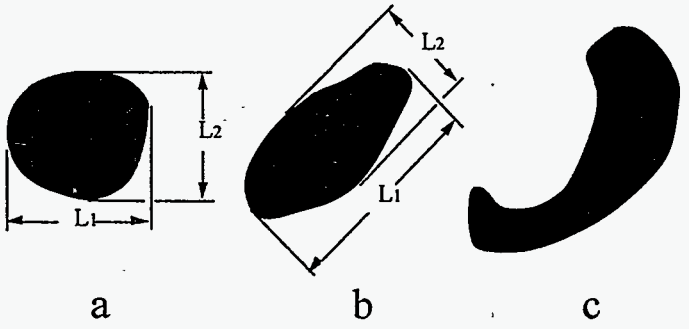

Figure 2-14. Typical shapes of char particles observed in this study and the method used for measuring them. Only particles similar in shape to those labeled "a" and "b" were measured. Elongated particles or those with irregular shapes, as depicted by particle "c" were discarded.

SV_{max}, the specific volume of the swollen droplet at the end of devolatilization is defined as the ratio of the particle volume at maximum to the initial dry solids mass, and is related to the maximum particle diameter (D_{max}) as:

$$SV_{max} = \frac{1}{r_{BL} S_o} \left[\frac{D_{max}}{D_o}\right]^3 \qquad (2\text{-}2)$$

where D_o is the initial diameter of the unswollen black liquor droplet, r_{BL} is its density, and So is the initial dry solids content of the liquor. SV_{max} is also referred to as the maximum swollen volume. This method was used by Noopila and Hupa [11].

Table 2-2 shows a typical set of measurements with ten droplets. In this data set, the range of L_1/L_2 varied from 1.00 to 1.88 with a mean $\pm$ standard deviation of 1.27 ± 0.27.

Table 2-2. A typical set of swelling measurement data - Liquor A, 61.8% solids content, 700°C, burned in air.

Mass, mg	Initial diameter, mm	L_1, mm	L_2, mm	L_1/L_2	Swelling factor (D/D_o)	SV_{max} cm^3/g BLS
5.9	2.00	7.90	6.32	1.25	3.52	50.7
7.7	2.19	9.48	8.42	1.13	4.08	78.6
4.3	1.80	8.42	7.37	1.14	4.37	96.5
8.5	2.26	9.48	8.42	1.13	3.95	71.2
4.5	1.83	7.90	4.21	1.88	3.15	36.2
5.0	1.90	7.37	7.37	1.00	3.89	68.0
6.9	2.11	8.42	6.32	1.33	3.46	47.8
7.4	2.16	8.95	8.42	1.06	4.02	75.1
6.2	2.04	8.42	5.27	1.60	3.27	40.4
5.6	1.97	8.42	7.37	1.14	4.00	74.1
Average				1.27	3.77	63.9
Standard deviation				0.27	0.38	18.3
Coefficient of variation, %				21	10	29

Uncertainty in the individual experimental values of droplet diameter and maximum swollen volume due to error in measurement of the individual droplets were estimated from the measurement errors in the experimental data. The error in measuring the dimensions of the swollen droplets was due to the difficulty in determining the actual location of the edge of the droplet on the video screen. This resulted from lack of clarity of the picture and lack of contrast between the droplet surface and the muffle furnace wall when droplets were burned in low O_2 content gases or were gasified. The droplet dimensions were

read from the video display with an uncertainty of 10-20% at the maximum swollen volume. The greater uncertainty corresponds to smaller droplets.

The initial droplet diameter was determined from the droplet mass, typically 5-15 mg, which was measured with an accuracy of $\pm$0.2 mg. The corresponding uncertainty in initial droplet diameter as determined from the initial droplet mass is 0.3% to 1.5% depending upon initial droplet mass.

The uncertainty in SV_{max}, calculated by differentiating Equation 2 and substituting the uncertainties of D_o and D_{max}, is 25-59%. Variation in the measured maximum swollen volumes were 25-40% when expressed as coefficients of variation. These experimental coefficients of variation agree well with the expected uncertainties based on measurement error.

2.4.1 Effect of Furnace Temperature and Gas Composition

Muffle furnace temperature, oxygen concentration, CO_2 concentration, and water vapor concentration have all been shown to affect SV_{max} [2,19,21]. Figure 2-15 shows maximum swollen volumes for two different kraft liquors burned at different muffle furnace temperatures and various furnace gas compositions. Data for one of the liquors were obtained at both 5% O_2 and 21% O_2 at muffle furnace temperatures of 600-900°C. Data for the second liquor were obtained at a muffle furnace temperature of 800°C in gases containing 20% CO_2 and 2-17% oxygen. The oxygen concentration which corresponds to each data point for this liquor is also shown in Figure 2-15. These data illustrate clearly the large differences in SV_{max} that can be obtained at different laboratory conditions with the same liquor but at different combustion conditions.

The data in Figure 2-15 show that liquor droplets swell less both in higher temperature environments and when oxygen concentrations are higher. These two variables may not be independent since a higher oxygen concentration means that the volatiles leaving the particle will burn more intensely near the particle surface, increasing the temperature to which the droplet is subjected.

We tested the hypothesis that it is the gas temperature immediately surrounding the droplet that determines how much it swells. Since it was not possible to measure accurately the gas temperature near the particle surface [20], we used a non-adiabatic combustion temperature equation, Eq. 1-13 to estimate it instead. With numerical values for the combustion properties substituted, Eq. 1-13 becomes

$$T_g^* = T_g + 1980\ Y_{O2} \qquad (2\text{-}3)$$

where Tg and T_g^* are in °C, Y_{O2} has units of mole fraction O_2, and the numerical constant has units of °C/mole fraction. The slope in Equation 2-3, 1980, is valid for the experimental conditions employed here. In modeling of black liquor combustion in recovery boilers, it should be decreased to account for the higher heat capacity of the combustion gas which results mainly from the presence of water vapor.

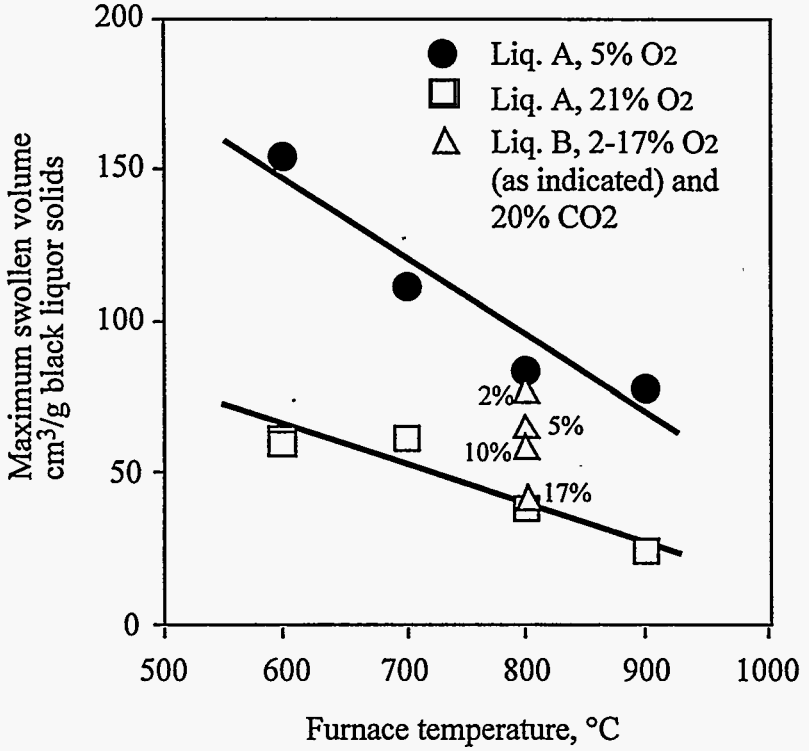

Figure 2-15. Effect of furnace temperature and gas composition on the maximum swollen volume for two kraft black liquors burned under different conditions in a laboratory furnace.

The SV_{max} data from Figure 2-15 are plotted in Figure 2-16 versus the gas temperature near the droplet surface. When plotted this way, the data for each liquor fall on separate straight lines.

It has been reported earlier [21] that the relative change in the swollen volume with degree of conversion of the devolatilization process was the same for all liquors, independent of liquor type, solids content, and laboratory furnace conditions employed. In that study, the swelling factors were converted to a dimensionless form, $(D - D_i)/(D_{max} - D_i)$, where D_i was the droplet diameter at the onset of devolatilization and D_{max} was the droplet diameter at maximum swelling. In the work reported in the present study, we have attempted to reduce the data to a single correlation for all kraft liquors by assuming that the relative change in the swollen volume with temperature is the same for all liquors. Here, the dimensionless swollen volume is calculated as $SV_{max}(T_g^*)/SV_{max}(800°C)$ where $SV_{max}(T_g^*)$ is the maximum swollen volume at the laboratory furnace temperature and gas composition of interest and $SV_{max}(800°C)$ is the maximum swollen volume when $T_g^* = 800°C$. We interpolated or extrapolated the available data for each liquor to find the value of SV_{max} when $T_g^* = 800°C$; the values obtained are listed in Table 2-3.

Table 2-3. Values of SV_{max} at Tg* = 800°C obtained by extrapolation of SV_{max} versus T_g* data for four kraft and one NSSC liquors.

Liquor	SV_{max} at T_g* = 800°C
A	115
B	77.0
C	50.4
D	39.3
E	34.7

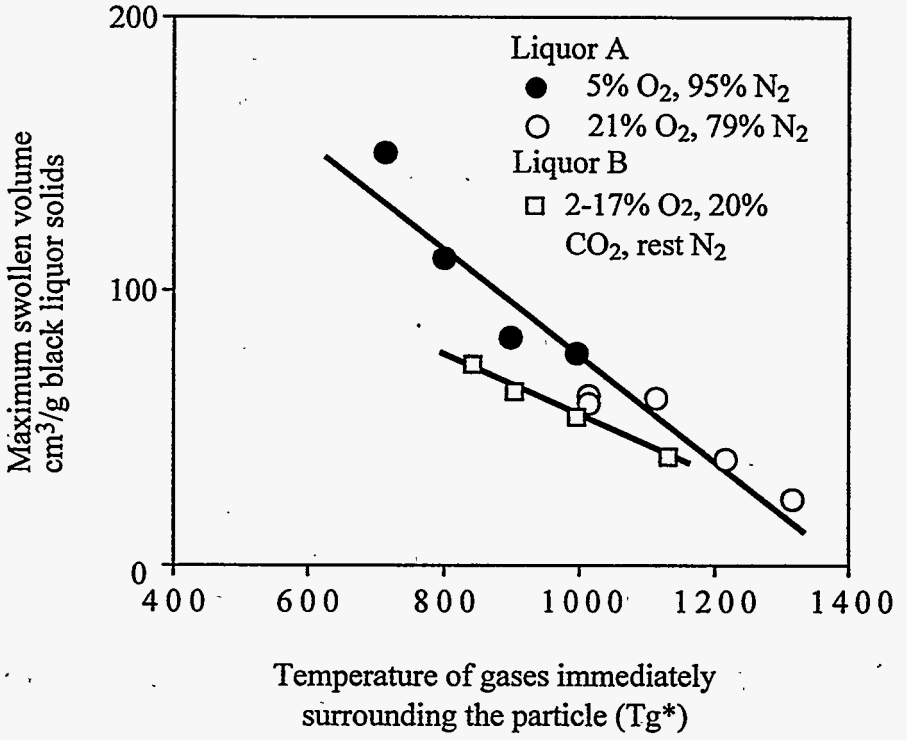

Figure 2-16. Maximum swollen volumes versus T_g* for the two liquors in Figure 2-15. The gas temperature environment (T_g*) was estimated from Equation 2-3. Both are Douglas fir kraft liquors.

The data from Figure 2-15 are plotted in this reduced form in Figure 2-17. Also included are data for three other liquors, two kraft (liquors C,D) and one sodium-base neutral sulfite semichem (NSSC) liquor (E), from an earlier study [29]. The kraft data fall on or near a single curve when plotted on semi-logarithmic coordinates. There is no difference between the data in air and at lower O_2 concentrations, and CO_2 per se has no effect. These results indicate that our assumption, that the relative change in swelling with temperature for kraft liquors is liquor independent, is adequate for modeling purposes. It also indicates that the effect of gas composition on SV_{max} when oxygen is present can be accounted for

as a temperature effect. The fact that there is no difference between the measurements in O_2/N_2 versus $CO_2/O_2/N_2$ environments indicates that the results can be generalized to recovery boiler conditions as long as some oxygen is present.

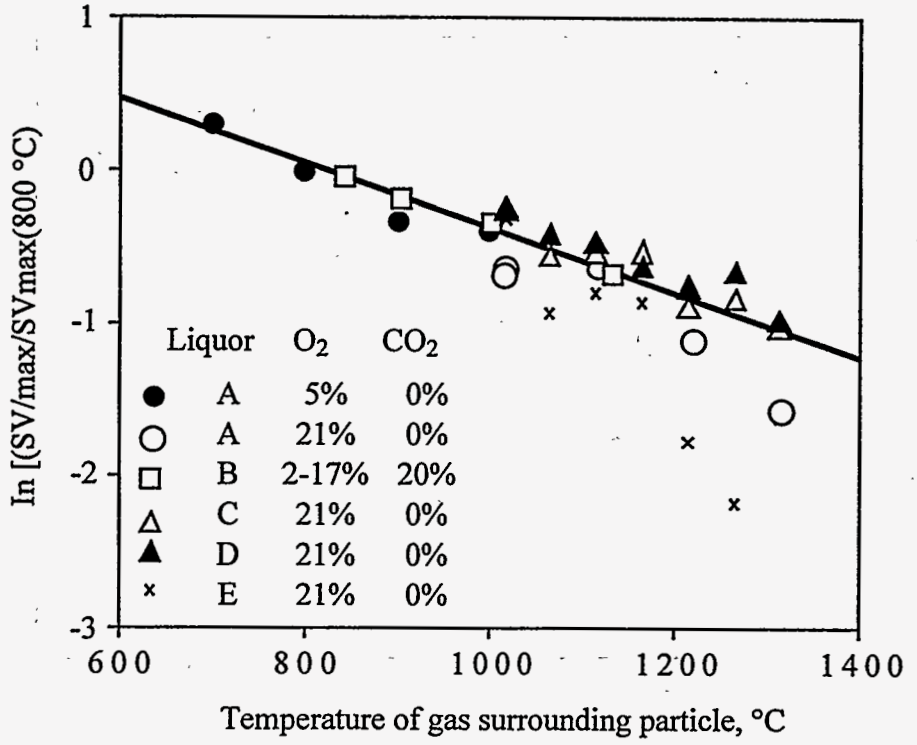

Figure 2-17. The effect of the temperature of the gases immediately surrounding a black liquor droplet on SV_{max}. The gas temperature environment (T_g*) was estimated from Equation 2-3. The liquors are A,B - Douglas fir kraft, C - pine kraft, D - birch kraft, E - sodium base sulfite semichem. Liquors A and C-E were at 60% dry solids content and liquor B at 68%.

Equation 2-4, the correlation shown in Figure 2-17, is a regression fit to the kraft liquor data only - the NSSC data were not used to generate it.

$$\ln [SV_{max}/SV_{max}(800°C)] = 1.724 - 0.00210T_g^* \quad (2\text{-}4)$$

The NSSC data fall below the kraft data in Figure 2-17, and appear to have a steeper temperature dependence, but they are too limited to develop a correlation for NSSC liquors in general. Equation 2-4 is also restricted to conditions where oxygen is present, i.e. combustion conditions. Figure 2-18 shows that, for liquor A, swelling is less when oxygen is absent although the trend of decreasing swelling with increasing T_g* is the same. The reason for this difference in behavior in the presence or absence of oxygen is not known.

The data for the four different kraft liquors devolatilized at a wide variety of different furnace temperatures and gas compositions collapsed to a single straight line (Figure 2-17) when presented in the form of Equation 2-4. This implies that this method is a useful empirical tool for estimating SV_{max} at

conditions other than at which it was measured. While we do not fully understand the underlying phenomena, there does indeed seem to be a similar swelling behavior based on the nondimensional basis indicated in Equation 2-4.

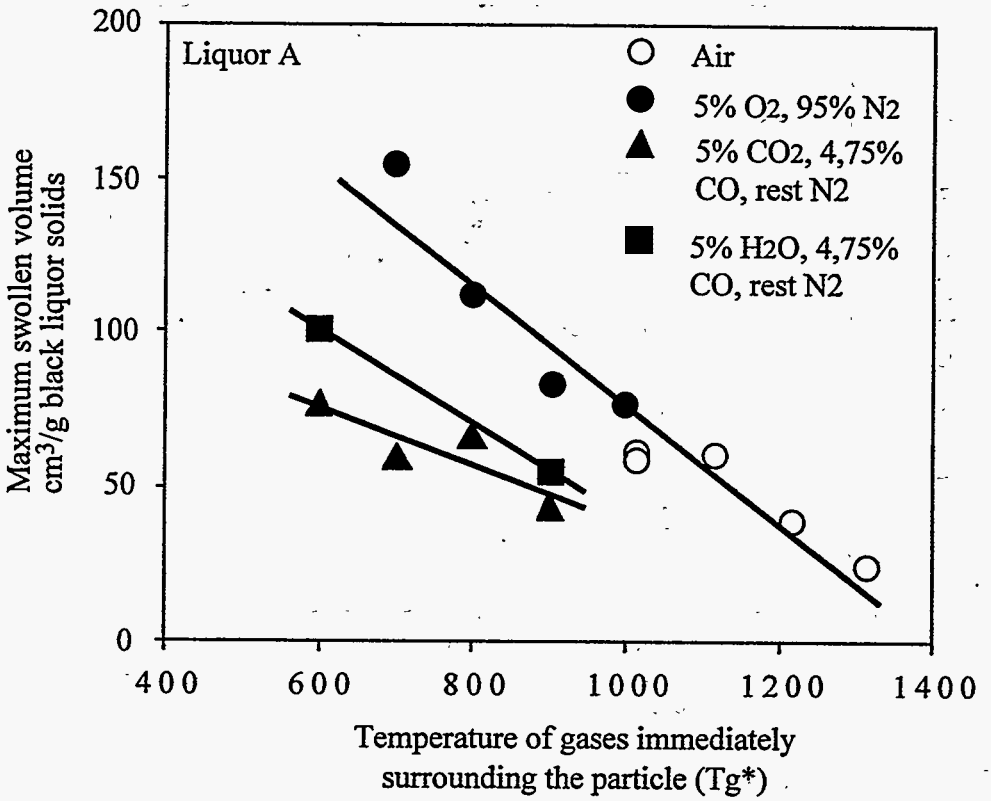

Figure 2-18. The effect of CO_2 and water vapor on the maximum swollen volume for black liquor droplets devolatilized at different temperatures.

To test Equation 2-4, we used the SV_{max} at $T_g^* = 800°C$ data in Table 2-3 with Equation 2-4 to predict the values of SV_{max} at all values of T_g^* for which data were available for each of the four kraft liquors. The differences between the predicted and experimental values, expressed as a percentage of the experimental values, are shown in Figure 2-19. The average of the absolute value of the differences for all of the data is 15%. 93% of the predicted values are within ±30% of the experimental values.

$SV_{max}/SV_{max}(800°C)$ was also correlated with Tg* using a linear correlating equation, but the fit was slightly poorer than with the semi-logarithmic equation (Equation 2-4). The mean square value for the relative difference between the measured value and that predicted by the correlation, calculated as

$$\text{mean square} = \frac{1}{n}\sum\left[\frac{\text{predicted } SV_{max} - \text{measured } SV_{max}}{\text{measured } SV_{max}}\right]^2 \qquad (2\text{-}5)$$

was 4.15 for the semi-logarithmic correlation (Equation 2-4) versus 4.43 for the linear correlating equation. In equation 2-5, n is the number of experimentally measured values. Also, 93% of the points fell within ±30% of the correlation with the semi-logarithmic correlating equation versus 81% for the linear correlating equation.

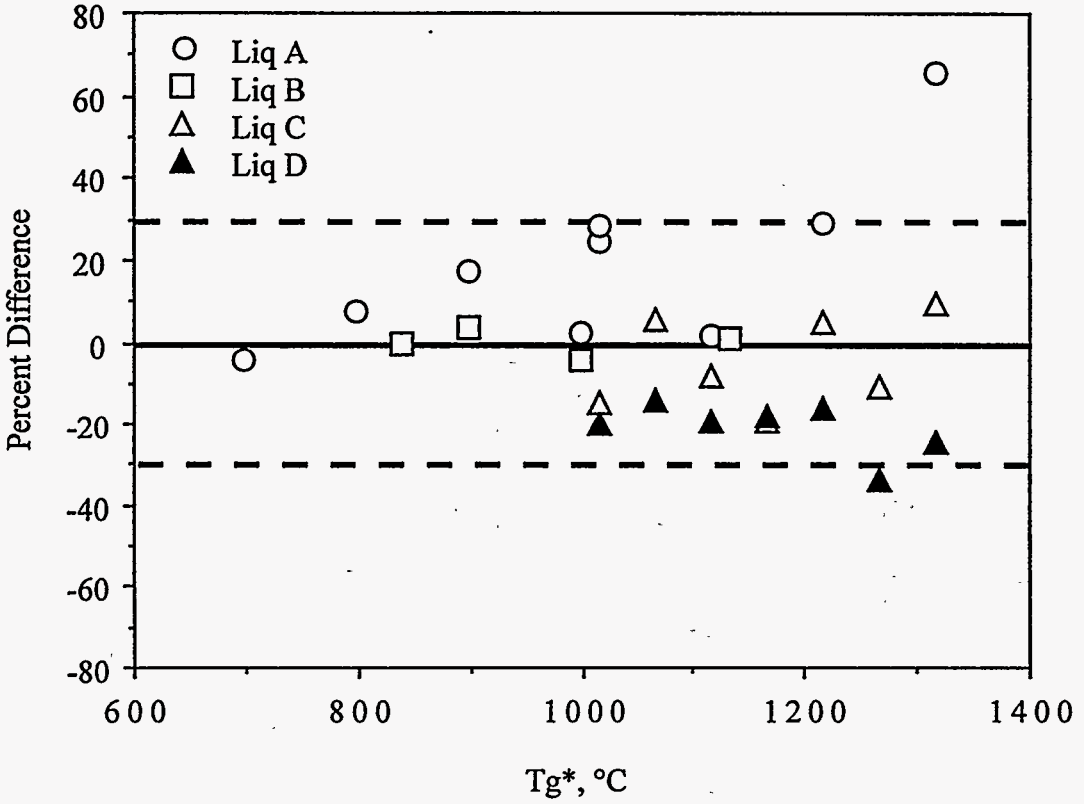

Figure 2-19. Differences between predicted and experimentally measured SV_{max} versus T_g* for the four kraft liquors in Figure 2-17. The differences are expressed as a percentage of the experimental values.

2.5 BLACK LIQUOR PARTICLE TEMPERATURES DURING BURNING

Two-color optical pyrometry has been used in various applications to measure the surface temperature of burning particles [29,34,35]. The method is based on the detection of radiation emitted at different wavelengths from the particle surface. In the work reported here, the method developed by Hernberg, Stenberg, and co-workers [28,29] was used for measuring the surface temperature of black liquor droplets during combustion. Details of the method used in these experiments is summarized by

Frederick and Hupa (1993), and only the results obtained are reported here.

2.5.1 Surface Temperatures During Combustion

Figure 2-20 shows the indicated temperature for a black liquor droplet burned in air at 800°C. The times that correspond to ignition, the end of devolatilization, and the end of char burning, obtained by visual observation of the video recording of this experiment, are also indicated.

The indicated temperature is below that of the furnace prior to ignition. This was not always detected and may be due to the problem of measuring temperatures lower than the surroundings [28].

The indicated temperature rises steeply at ignition (1.8 - 2.7 s in Figure 2-20), and very high values were obtained during the early part of devolatilization. These high temperature values were apparently the result of soot particles in the flame surrounding the droplet during the early stages of devolatilization. These temperatures were not very reproducible. The presence of soot particles in the flame can result in indicated temperatures several hundred degrees higher than either the soot or char particle temperatures [36,37].

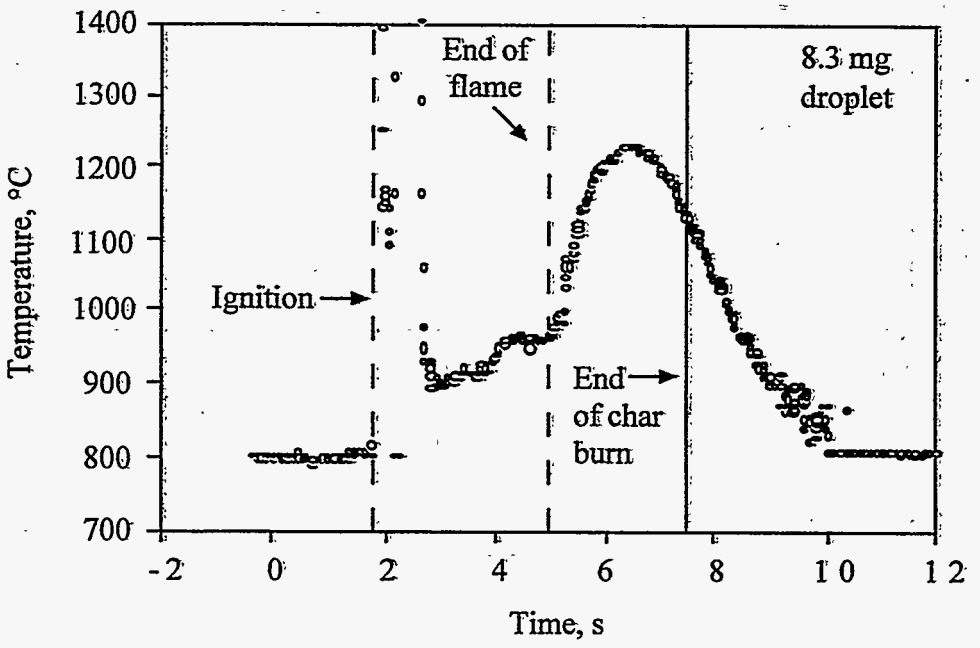

Figure 2-20. Indicated temperature versus time for a black liquor droplet burned in air at 800°C. Experimentally observed times to ignition, disappearance of the flame, and the end of char burning are also shown.

After this first temperature peak, the indicated temperature during devolatilization is greater than the furnace temperature and increases with time (2.7 - 4.9 s in Figure 2-20). This may occur because the pyrolysis products burning near the droplet surface heat the particle surface to above the ambient gas temperature. However, the indicated temperature during this time interval may be influenced by the volatiles flame surrounding the particle thus be higher than the particle surface temperature.

The rise in indicated temperature continues into the char burning stage. The rate at which it rises increases at the onset of char burning. The particle surface temperature rises steadily through a maximum about 400°C above the furnace temperature and then declines slowly. The surface temperature is still more than 200°C above the furnace temperature when char burning ends. The rate of decrease in temperature following char burning is slowed by the strongly exothermic oxidation of Na_2S which can comprise 20-30% of the inorganic residue after char burning. The particle finally reaches the furnace temperature a few seconds after char burning is complete.

Figure 2-21 shows the surface temperatures for several droplets burned in air at 800°C. The temperature curves are shifted upward by multiples of 200°C so that they can be distinguished from one another more clearly. The surface temperature always rises during devolatilization (following the temperature spike associated with ignition), goes through a maximum, and then decreases with time. The change in rate of temperature increase at the onset of char burning is generally greater with larger droplets. For larger droplets, the maximum is very distinct and, in an 800°C furnace, the maximum surface temperature can be more than 400°C greater than the furnace temperature. For smaller droplets, there is a less distinct temperature rise during char burning. The particle surface temperature is higher at the end of devolatilization, and it is more uniform throughout char burning.

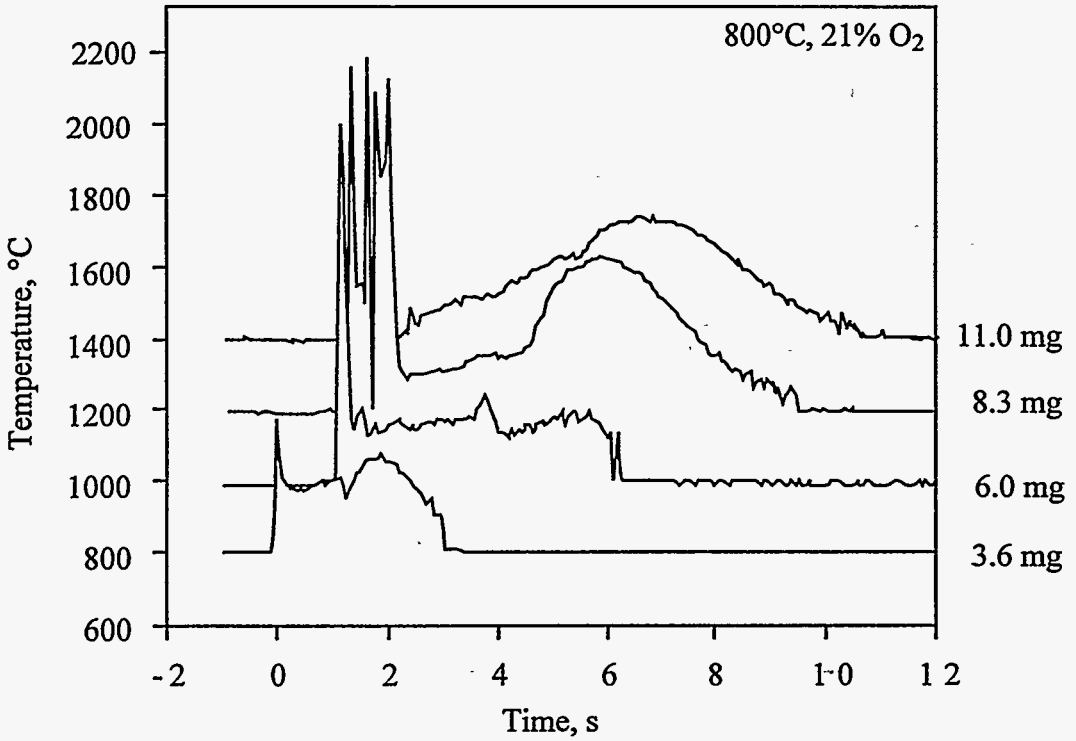

Figure 2-21. Surface temperature versus time for four droplets burned in air at 800°C. All of the curves start at 800°C but those for the 6.0, 8.3, and 11.0 mg droplets are shifted upward respectively by 200, 400, and 600°C for clarity.

The maximum surface temperatures during char burning for data in air are compared in Figure 2-22 with the maximum internal droplet temperatures measured earlier by Solin and Hupa (1984). With one exception the surface temperatures are either lower or about the same as the range of the internal droplet

temperatures. The internal temperature can only exceed the surface temperature if some oxidation occurs within the droplet, generating heat there. The internal and surface temperature data in Figure 2-22 were measured for separate droplets of different liquors, so some caution must be used when drawing conclusions about the relative temperatures.

At lower oxygen contents, the temperature versus time profiles during char burning are much flatter. The maximum difference between the droplet surface and furnace temperatures in 15.8% oxygen is 100-150°C and the maxima in the temperatures during devolatilization are less reproducible than in 21% O_2 (Figure 2-23). There is a much less distinct maximum in temperature with time during char burning, and the maximum surface temperature does not increase measurably with increasing initial droplet mass. The data in lower oxygen contents show an even smaller difference between the maximum droplet and furnace temperatures.

The difference between the average value for the maximum surface temperature during char burning and the furnace temperature is plotted in Figure 2-24 at each oxygen content along with the range for each oxygen concentration. The maximum surface temperature increases more rapidly than linearly with increasing oxygen content. It exceeds the furnace temperature on average by more than 300°C and by as much as 500°C for droplets burned in air.

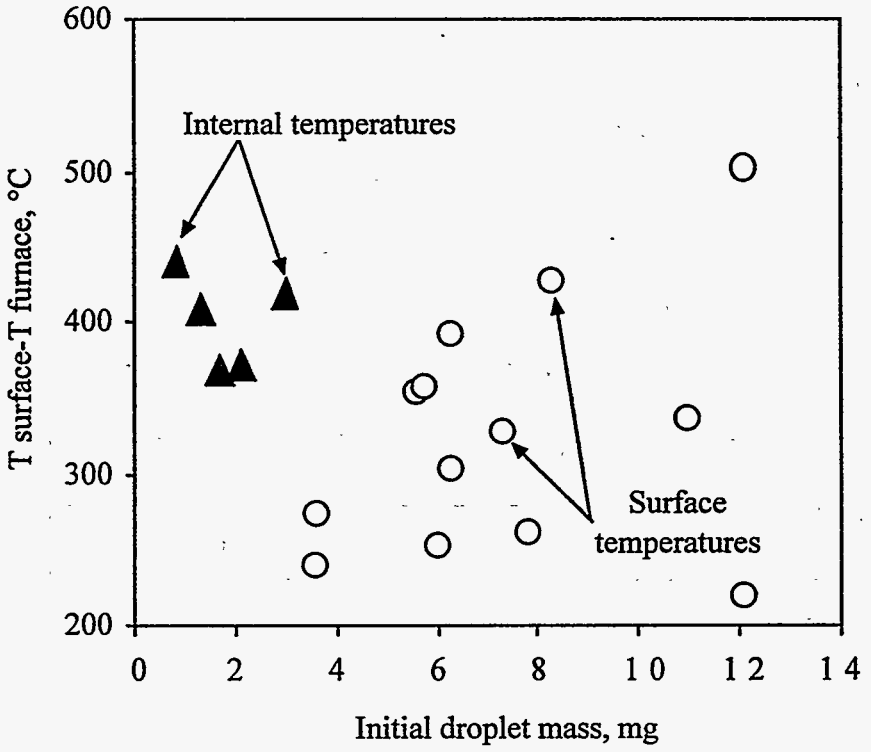

Figure 2-22. Comparison of maximum surface temperatures measured in this study with maximum internal droplet temperatures measured earlier by Solin and Hupa[38]. Both data sets are for kraft black liquor droplets burned in air in an 800°C furnace.

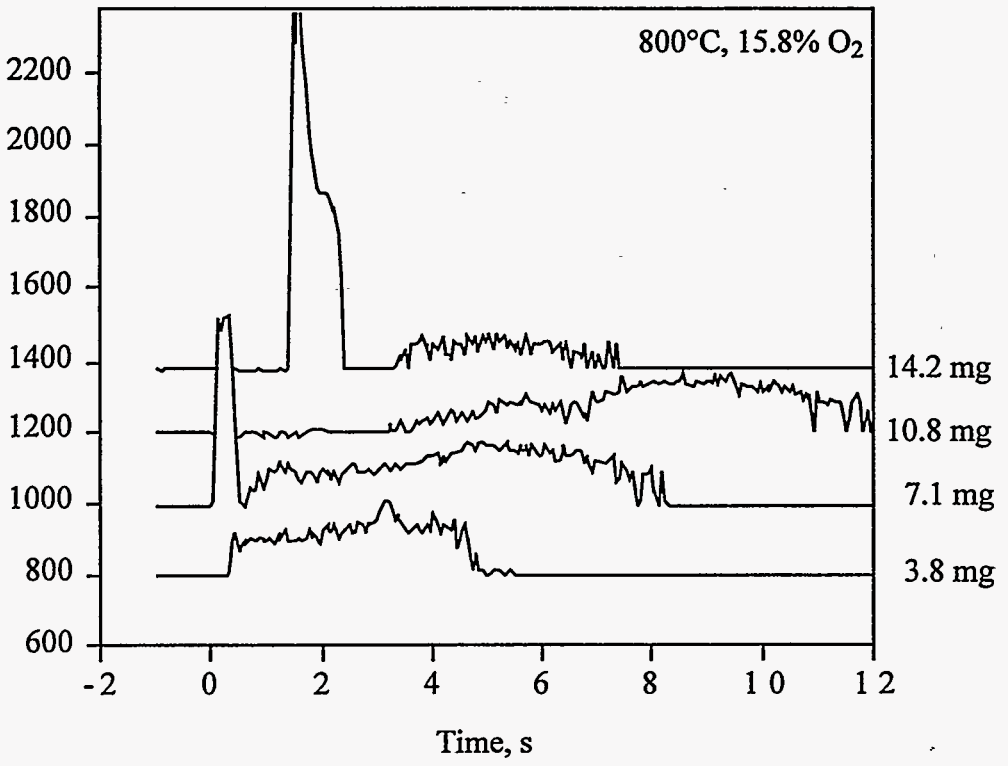

Figure 2-23. Surface temperature versus time for four droplets burned in 15.8% O_2 at 800°C. All of the curves start at 800°C but those for the 7.1, 10.8, and 14.2 mg droplets are shifted upward respectively by 200, 400, and 600°C for clarity.

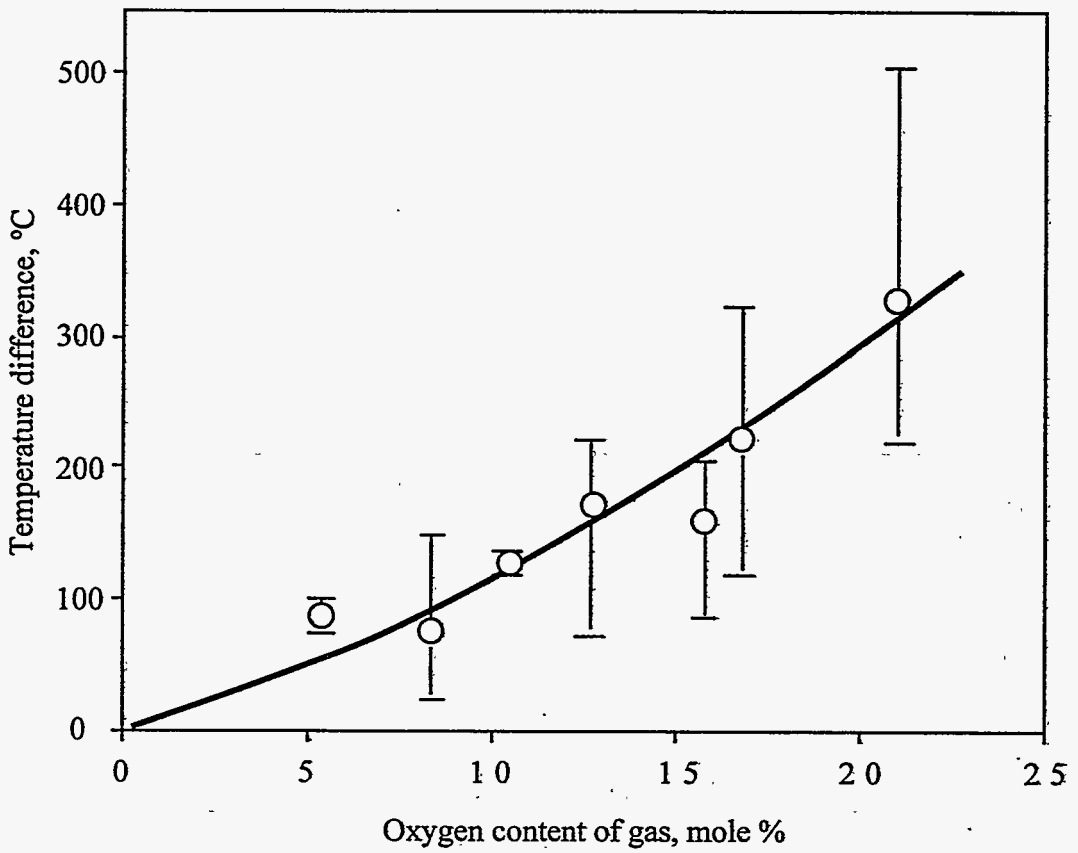

Figure 2-24. Difference between the surface temperature and furnace temperature during char burning versus oxygen content of the surrounding gas for droplets burned in O_2/N_2 mixtures in an 800°C furnace. Error bars indicate the minimum and maximum temperature differences at each oxygen content. The solid line corresponds to the regression equation $\Delta T = 883\ P_{ox} + 2966\ P_{ox}^2$ where P_{ox} is the oxygen partial pressure in bar and ΔT is the temperature difference in °C.

Comparison of data for droplets burned at 750 versus 800°C in 10.5% O_2 indicates a smaller increase in surface temperature (90°C) at 750°C relative to the furnace temperature as compared with 130°C in an 800°C furnace. This would only occur if the rate of combustion increased as temperature increased. Under conditions where film mass transfer completely dominates the overall rate of combustion, the rate would not increase significantly with increasing temperature. These experimental results imply that at least some combustion is occurring within the pores at this oxygen concentration and these furnace temperatures. The difference between the surface and furnace temperatures may be even greater at higher furnace temperatures, although the fourth power dependence of radiant energy exchange on temperature would be offsetting.

2.5.2 Surface Temperatures in a CO_2/N_2 Atmosphere

The surface temperature for droplets pyrolyzed in N_2/CO_2 (Figure 2-25) reach a temperature somewhat below the furnace temperature during devolatilization and remains there as long as char gasification continues. After devolatilization, the carbon in the char undergoes an endothermic reaction with CO_2 to

yield CO. The surface temperature remains below the furnace temperature until gasification is complete. The difference between the furnace and surface temperatures is a result of the endothermic gasification process. At 800°C, complete gasification of black liquor char requires about 60 seconds, and the temperature increase when gasification is complete is not shown in Figure 2-25. For six droplets gasified in an 800°C furnace in 20% CO_2, the surface temperature during gasification was 762°C with a standard deviation of 10°C.

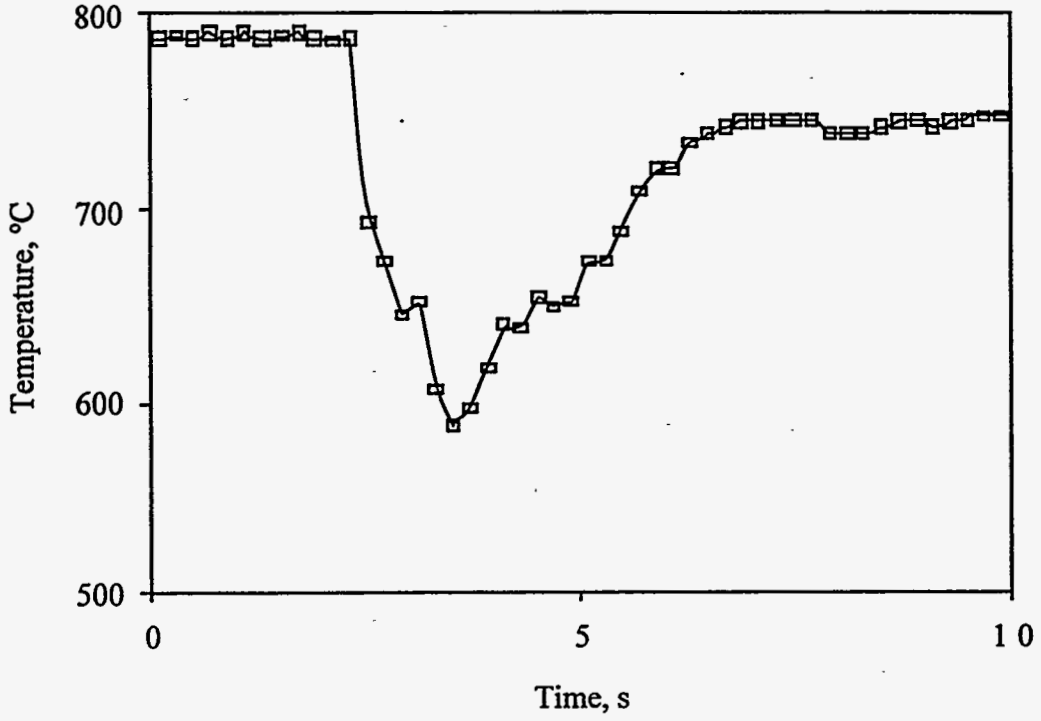

Figure 2-25. Surface temperature versus time for a 15 mg droplet in 20% CO_2/80%N_2 at 800°C.

2.5.3 Summary of Temperature Measurement Data

The temperature of a black liquor droplet burned in air is well above the furnace temperature for the entire char burning stage. The two-color optical pyrometer measurements show that the surface temperature for droplets burned in air is typically 200°C higher than the furnace temperature at the end of the devolatilization stage and increases to 220-500°C above the furnace temperature during char burning. Internal droplet temperatures measured in separate experiments and reported earlier indicate that the internal droplet temperature typically increased from about the furnace temperature at the end of devolatilization to 400°C above it during char burning for droplets burned in air.

At the lower oxygen contents typically found in recovery boilers, the droplet surface temperature is always greater than the furnace temperature during char burning. The difference is about 65°C for droplets burned in 5% O_2 in an 800°C furnace, and this difference increases with increasing oxygen content.

Particle size apparently has relatively little effect on particle temperature during char burning. Hurt and Mitchell (25) reported that coal particles with 106-125 m initial diameter have a surface temperature of

about 200°C higher than the gas temperature when burning in 12% O_2. Black liquor solids may burn even hotter because of the presence of sodium and sulfur compounds that act as catalysts. For the same oxygen content, 12%, and a larger particle size, Frederick et al. found a difference of about 150°C. The similar temperatures may be because the rate of char burning is limited by the rate of transport of O_2 across the gas film surrounding the char particles, and that heat transfer and mass transfer have similar dependences on particle size. Therefore, we can use the data reported here to estimate the temperature of black liquor particles of any size char burning.

During the devolatilization stage, the droplet surface temperature may exceed the furnace temperature when oxygen is present in the bulk gas. This is a result of heat transferred to the droplet from the volatiles which burn near the droplet. In the presence of CO_2 and the absence of oxygen, the droplet surface temperature is below the furnace temperature until essentially all of the carbon has been gasified.

2.6 MODELS

2.6.1 Devolatilization

The rates of both drying and devolatilization are modeled as heat transfer driven processes as described by Eqns. 1-1 to 1-13. The analysis of Frederick (4) showed that this is a valid approach for evaporation of water prior to the onset of devolatilization, and gives reasonable estimates of the time required for drying and devolatilization to be completed. More recent data on the release of sulfur gases (45), and of carbon, sulfur, and fuel nitrogen during rapid pyrolysis of black liquor (46,47) support this approach.

The results in Figure 2-6 show that, at the temperatures encountered in recovery boilers, droplets begin to devolatilize before very much drying has occurred. We therefore model drying and devolatilization as a single stage, where the droplets are assumed to swell immediately by a factor of 1.54 (Eq. 1-16) and then continue swelling according to Eq. 1-17. They are referred to as the overall devolatilization stage.

The rate the overall devolatilization stage is calculated from Eqns 1-1 to 1-13. The total energy input to the droplet required to complete devolatilization is the sum of Eqns. 1-8 and 1-12, or

$$Q_{tot,d/d} = (M_o - M_{char})\, C_{p,avg} \frac{(T_{max} + T_o)}{2} + M_{char} \{C_{p,avg} (T_{max} - T_o) + M_o h_{fg} (1 - S_o) + S_o \Delta H_{pyr}\} \quad (2\text{-}6)$$

In Eqn. 2-6, both the particle temperature and the fraction of the volatile organic matter and water are assumed to increase linearly with the fraction of $Q_{tot,d/d}$ transferred to the droplet. ΔH_{pyr} is nearly zero for wood and other biomass materials (Frederick, 1990), and a value of zero is used in the model. A correlation for T_{max}, the average droplet temperature at which devolatilization is complete, versus furnace temperature is

$$T_{max} = 1.072 \times 10^5 \,(1 - \exp(-7.424 \times 10^{-6}\, T)) \quad (2\text{-}8)$$

where T and Tmax are in °C. This correlation is based on the experimental data of Solin and Hupa (1984).

The split of carbon between volatiles and char residue is estimated according to the data for 100 μm particles in *Figure 2-9* and the point fixed carbon in char = 100% at T = 200°C. A correlation that approximates this data is

$$\begin{aligned} &C = 100, T<200°C \\ &\quad 112.31 - 5.8903\times10^{-2}, 200<T<1100°C \\ &\quad 47.5, T>1100°C \end{aligned} \qquad (2\text{-}9)$$

where C is the total carbon in the char at the end of devolatilization and T is the furnace temperature.

The ratio of the rates of evaporation of water and volatilization of organic matter is assumed to be constant with time in the current version of the model. This is an assumption and is not based on experimental evidence. It needs to be tested and perhaps modified.

2.6.2 Char Burning

The net rate of mass transfer of O_2 to the particle surface is determined by calculating the O_2 mass transfer rate in the absence of gas phase reactions and then subtracting the rate of O_2 consumption in the boundary layer. The following considerations apply.

- Each CO_2 that reacts in the particle produces 2 CO which then react with one O_2 in the boundary layer. Thus each CO_2 that reacts consumes one O_2 in the boundary layer.
- Each H_2O that reacts in the particle produces one H_2 and one CO which subsequently react with one O_2 in the boundary layer. Thus each H_2O that reacts consumes one O_2 in the boundary layer.
- Each CO produced by sulfate reduction consumes 1/2 O_2. The amount of O_2 consumed is then $2f/(2-f)\ R_{SO4}$.

These considerations are valid as long as there is sufficient O_2 to consume all of the combustibles produced. If there is insufficient O_2, the net oxygen flux at the surface will be zero and there will be some net production of combustibles. The net O_2 rate to the smelt/char particle is then:

$$R'_{O2} = R_{O2} - R_{CO2} - R_{H2O} - 2f/(2-f)\ R_{SO4} \qquad \text{where } R'_{O2} > 0 \qquad (2\text{-}10)$$

The O_2 reaching the surface can react with either Na_2S or C. The relative amount of oxygen reacting with each is specified by a partition parameter, "p", the fraction of O_2 reaching the surface that reacts with C. The use of an arbitrary partition parameter is necessary because there are no kinetic data on carbon burnup and sulfide oxidation occurring in parallel on which to base an estimate of the partition parameter. It was set equal to the mole fraction carbon in the particle, i.e. p = C/(C + I). This approach has the advantage that all of the O_2 will react with sulfide as the carbon becomes depleted.

The parameter "f" is the fraction of CO in the gas produced by the sulfate reduction reaction. Cameron's data [30] indicates that CO_2 is the major product of this reaction, and therefore f was assumed to be 0.

The rate of carbon burnup is then given by:

$$R_C = 4/(2-f)\ R_{SO4} + R_{CO2} + R_{H2O} + p\ R'_{O2} = -\,d[C]/dt \qquad (2\text{-}11)$$

The reduction efficiency, E, is defined as the smelt reduction, the fraction of the sulfur in the smelt that is sulfide.

$$E = [Na_2S] / [Na_2S + Na_2SO_4] \qquad (2\text{-}12)$$

where $0 < E < 1$.

The smelt reduction efficiency in the particle is calculated from a sulfide balance. Sulfur is assumed to be present as sulfide, sulfate, COS and H_2S.

$$\text{Change of overall reduction efficiency} = \frac{\text{[sulfide formed - sulfide consumed]}}{\text{[total sulfur present]}} \qquad (2\text{-}13a)$$

$$S\ I\ dE/dt = R_{SO4} - R_S - R_{COS} - R_{H2S} = R_{SO4} - (1-p)/2\ R'_{O2} - R_{COS} - R_{H2S} \qquad (2\text{-}13b)$$

where "S" is the total sulfur in the inorganics, and the inorganics, "I", is the sum of sulfide, sulfate, and carbonate.

If all oxygen is depleted in the boundary layer ($R'_{O2} = 0$), the rate of carbon consumption then becomes through substitution of Eq. 2-13b into Eq. 2-11:

$$R_C = R_{CO2} + R_{H2O} + 4/(2-f)\ \{ S\ I\ dE/dt + R_{COS} + R_{H2S} \} \qquad (2\text{-}14)$$

However, if there is an abundance of oxygen, all CO will be consumed in the boundary layer and, hence, the rate of carbon consumption reduces to:

$$R_C = R_{O2} + 2\ \{ S\ I\ dE/dt + R_{COS} + R_{H2S} \} \qquad (2\text{-}15)$$

If there is no change in the reduction state of the particle and the formation of COS and H_2S is neglected,

$$R_C = R_{O2} \text{ or } R_{CO2} + R_{H2O}, \qquad (2\text{-}16)$$

whichever is greater.

This is the same result as that which had been obtained earlier by Grace [39] in the treatment of bed burning when reduction state changes were neglected.

The key expressions for the char burning model are Equations 2-10, 2-12, and 2-13. To solve them, rate equations for R_{O2}, R_{CO2}, R_{H2O}, and R_{SO4} and values for the parameters "f" and "p" are needed.

The overall rates of consumption of CO_2 and $H_2O_{(v)}$ were calculated as:

$$1/R_i = 1/R_{mi} + 1/(hR_{ci}) \quad (2\text{-}17)$$

where rates of consumption of gas species i under film mass transfer limited conditions were calculated as:

$$R_{mi} = k_{gi} A_p C_i \quad (2\text{-}18)$$

The mass transfer coefficient was estimated from [15?]:

$$Sh = k_g D / D_p = 2 + 0.569 (Gr\ Sc)^{1/4} + 0.347 (Re\ Sc^{1/2})^{0.62} \quad (2\text{-}19)$$

and diffusion coefficients for the reacting gas species were estimated by the Chapman-Enskog equation using Neufeldt's correlation to estimate the diffusion collision integral.

The rates under chemical kinetic controlled conditions were calculated from the rate equations of Li and van Heiningen (40,41) for black liquor char.

$$R_{CO2} = 6.310^{10} [C] P_{CO2}/(P_{CO2} + 3.4 P_{CO}) \exp(-30070/T) \quad (2\text{-}20)$$

$$R_{H2O} = 2.5610^{9} [C] P_{H2O}/(P_{H2O} + 1.42 P_{H2}) \exp(-25300/T) \quad (2\text{-}21)$$

The rate limiting effect of interparticle diffusion was accounted for with a Thiele modulus-based effectiveness factor.

$$h = \tanh(M_{Ti})/M_{Ti} \quad (2\text{-}22)$$

where

$$M_{Ti} = D/6 (k_i/D_i)^{1/2} \quad (2\text{-}23)$$

and

$$k_i = R_{ci}/(V_p C_i) \quad (2\text{-}24)$$

The overall rate of consumption of O_2 was assumed to be limited by the rate of film mass transfer and was calculated from Equation 2-18.

The rate equation for reduction of sulfate is

$$R_{SO4} = 3790\,[C]\,[SO_4]^{1.4}\exp(-18700/T) \qquad (2\text{-}25)$$

2.6.3 Estimating Swelling Factors During Devolatilization

Equation 2-26 is an empirical relationship between the diameter of a black liquor particle during devolatilization and the extent of conversion of the devolatilization stage that was reported previously (4).

$$\frac{D - D_i}{D_{max} - D_i} = X_{DEVOL}^{0.8} \qquad (2\text{-}26)$$

In Eq. 2-26, D is the equivalent diameter of the particle and D_i is the droplet diameter at the onset of the devolatilization stage, equal to $1.54D_o$ [6]. D_{max} is the diameter at maximum swelling which always occurs at the end of the devolatilization stage. The devolatilization process is treated as a heat transfer driven process and X_{DEVOL} is the degree of completion of the devolatilization stage. It has the values 0 at the onset of devolatilization and 1 at the end.

It is not yet possible to estimate SV_{max} for a given liquor based on its composition. It is necessary therefore in modeling to begin with experimentally measured SV_{max} data for the liquor of interest. To obtain SV_{max} data, we recommend the procedure described by Noopila and Hupa [11] because of its simplicity and the decoupling of flow and combustion phenomena during the experiments. We also recommend that the droplets be burned in air at several temperatures (e.g. 600-900°C) and at the solids content of interest.

To obtain SV_{max} at other temperatures and gas compositions, $T_g^{*}{}_{(exp)}$ is first calculated for each measured value of SV_{max} using Equation 2-3 and the experimental muffle furnace temperature and gas composition. SV_{max} at $T_g^* = 800°C$ is then obtained by interpolation or extrapolation of experimental data if several experimental data points are available. The Tg* value in the left side of Equation 2-27 corresponds to the furnace temperature and oxygen concentration for the modeling calculations. The value obtained, $SV_{max}(T_g^*=800°C)$ can then be used with Equation 2-27 to estimate SV_{max} at other values of T_g^*.

When an experimental value SV_{max} is available at a single temperature and furnace gas composition, SV_{max} at other conditions can also be estimated as

$$\ln[(SV_{max}(T_1, Y_{O2,1})/SV_{max}(T_2, Y_{O2,2})] = 0.00210(T_g^*{}_2 - T_g^*{}_1) \qquad (2\text{-}27)$$

where $(T_1, Y_{O2,1})$ and $(T_2, Y_{O2,2})$ are respectively the bulk gas temperature and oxygen mole fraction at (1) the conditions of interest and (2) the conditions at which SV_{max} data are available.

The swelling factor during devolatilization is calculated as

$$SF_{vol} = D/D_o \qquad (2\text{-}28)$$

where D is obtained from Equations 2-2 and 2-27, and D_0 is the initial droplet diameter before drying begins.

2.6.4 Droplet Temperature Estimation

The maximum temperature difference between a burning black liquor char particle and the surroundings, as measured in this work, is given as a function of gas-phase oxygen content by Eq. 2-29:

$$DT = 883\ P_{O2} + 2966\ P_{O2}^2 \qquad (2\text{-}29)$$

where P_{O2} is the oxygen partial pressure in bars and T is the temperature difference between the particle and surroundings in °C,

The droplet particle temperature data during char burning were fitted to quadratic equations to estimate the particle temperature as a functrion of carbon conversion. The equation is of the form

$$T_p = T_f + A + B\ X - C\ X^2 \qquad (2\text{-}30)$$

where X is the fractional conversion of the fixed carbon in the char to gases, T_f i the furnace temperature, °C, Tp is the particle temperature, and A, B, and C are empirical constants given by the following polynomials:

$$A = 5.19 + 2.48\ O_2 + 0.137\ (O_2)^2 \qquad (2\text{-}31)$$

$$B = 24.66 + 13.06\ O_2 + 0.693\ (O_2)^2 \qquad (2\text{-}32)$$

$$C = 19.08 + 10.25\ O_2 + 0.537\ (O_2)^2 \qquad (2\text{-}33)$$

where O_2 is the mole percent oxygen in the gas phase.

2.7 REMAINING NEEDS FOR MODELING OF CARBON CONVERSION

The devolatilization and char burning models as presented here are essentially complete and are now being used in comptational fluid dynamic codes for modeling recovery boilers. The remaining data needed to improve these models are

1. experimental data on the relative rates of release of water versus organic volatiles from droplets versus conversion during the drying/pyrolysis stage

2. pyrolysis kinetic data at short residence times

3. measurement of the heat of devolatilization of black liquor solids

4. experimental data on the rate of char carbon gasification at furnace temperatures in mixtures of O_2, CO_2, and water vapor.

The effects of temperature and oxygen concentration on the swelling factor for black liquor droplets during devolatilization in oxygen-containing gases can be estimated as long as the temperature of the environment is constant. There is currently no way to account for the effect of a changing temperature environment, as would be encountered by a droplet sprayed into a recovery boiler, on swelling.

2.8 REFERENCES

1. Hupa, M., Backman, R., Hyöty, P. "Investigation of fireside deposition and corrosion in sulphate and sodium bases sulphite recovery boilers," *Proc. Black Liquor Recovery Boiler Symposium 1982*, Helsinki (August 31 - September 1, 1982).

2. Hupa, M., Solin, P., Hyöty, P., "Combustion Behavior of Black Liquor Droplets" *J. Pulp Paper Sci.* 13(2), J67 (1987).

3. Frederick, W.J., Hupa, M., "Combustion Parameters for Black Liquor." Report to the U.S. Department of Energy, US DOE Report DOE/CE/40936-T1 (DE94007502), April, 1993.

4. Frederick, W.J. Combustion processes in black liquor recovery: analysis and interpretation of combustion rate data and an engineering design model. US DOE Report DOE/CE/40637-T8 (DE90012712), March, 1990.

5. Walsh, A., Grace, T.M., *J. Pulp Paper Sci.*, 15(3), J84 (1989).

6. Frederick, W.J., Noopila, T., Hupa, M., "Swelling of pulping liquor droplets during combustion," *J. Pulp Paper Sci.*, 17(5),J164 (1991).

7. Clay, D.T., Lien, S.J., Grace, T.M., Macek, A., et al.: Fundamental Studies of Black Liquor Combustion, Report No.2, US DOE Report DE88005756, January 1987.

8. Miller, P.T., Clay, D.T. "Swelling of kraft black liquor during pyrolysis," *AIChE For. Prod. Div. Symp.* 1, 152 (1986).

9. Clay, D. T., Grace, T. M., Kapheim, R. J., Semerjian, H. G., Macek, A., Charagundla, S. R., "Fundamental study of black liquor combustion. Report No. 1–Phase 1," US DOE report DOE/CE/40637-T1 (DE85013773), Jan. 1985.

10. Miller, P. T., Clay, D. T., and Lonsky, W. F. W., "The influence of composition on the swelling of kraft black liquor during pyrolysis," TAPPI Engr. Conf., Seattle, Sept. 1986.

11. Noopila, T. and Hupa, M., "Measuring the Combustion Properties of Black Liquors by Different Techniques", *Combustion Chemistry Research Group Report 88-5*, Abo Akademi, Turku, Finland (1988).

12. Noopila, T., "The influence of droplet size and kappa number on black liquor burning behaviour - a study in a convective gas environment," *Combustion Chemistry Research Group Report 89-17*, Abo Akademi, Turku, Finland (1989).

13. Frederick, W.J., Noopila, T., Hupa, M., "Combustion behavior of black liquor at high solids firing conditions," *Tappi J.*, 74(12), 163 (1991).

14. Alén, R., Hupa, M., Noopila, T., *Holzforschung* 46, 337 (1992).

15. Hupa, M., Frederick, W.J., "Combustion of black liquor droplets," *Proc. 1991 TAPPI Kraft Recovery Operations Seminar*, TAPPI Press, Atlanta (1991), p. 191-200.

16. Borg, A., Teder, A., Warnqvist, B. *Tappi*, 57(1), 126 (1974).

17. Verrill, C.L., Wessel, R.A. *Sodium Loss During Black Liquor Drying and Devolatilization-Application of Modeling Results to Understanding Laboratory Data.* Proc. 1995 Intl. Chem. Recovery Conference, Toronto, April 24-27, p. B89-B103.

18. Verrill, C.L. Inorganic aerosol formation during black liquor droplet combustion. PhD Thesis, The Institute of Paper Science and Technology, Atlanta (1992).

19. Adams, T.N., Frederick, W.J. *Kraft Recovery Boiler Physical and Chemical Processes*, American Paper Institute (1988).

20. Frederick, W.J. and Hupa, M., *Tappi Jl.*, 1991, 11:192.

21. Frederick, W.J., Forssén, M., Hupa, M., Hyöty, P. Proc. 1992 TAPPI - CPPA International Chemical Recovery Conference, TAPPI Press, Atlanta, June 7-11, p. 599-608.

22. Verrill, C.L., Nichols, K.M. Proc. 1992 TAPPI - CPPA International Chemical Recovery Conference, TAPPI Press, Atlanta, June 7-11, p. 609-616.

23. Anderson, P.H., Jackson, J.C., Tappi Jl., 1992, 74(1):115-118.

24. Aho, K., Nikkanen, S., Hupa, M., Proc. 1993 TAPPI Eng. Conf., TAPPI Press, Atlanta, p. 377-384.

25. Hurt, R.H., Mitchell, R.E., Twenty-fourth Symp. (Intl.) on Combustion/The Combustion Institute, 1992, pp. 1233-1241.

26. Hurt, R.H., Mitchell, R.E., Twenty-fourth Symp. (Intl.) on Combustion/The Combustion Institute, 1992, pp. 1243-1250.

27. Wall, T.F., Tate, A.G., Bailey, J.G., Jenness, L.G., Mitchell, R.E., Hurt, R.H., Twenty-fourth Symp. (Intl.) on Combustion/The Combustion Institute, 1992, pp. 1207-1215.

28. Stenberg, J., Frederick, W.J., Bostrom, S., Hernberg, R., Hupa, M., Optical pyrometric measurement of the temperature of black liquor particles during pyrolysis, combustion and gasification. In press.

29. Hernberg, R., Stenberg, J., Zethræus, B. Simultaneous in situ measurements of temperature and size of burning particles in a fluidized bed furnace by means of fiber optic pyrometry. In press.

30. Cameron, J. H. and Grace, T. M., *I&EC Fundamentals*, 1985, 24(4): 443.

31. Milanova, E. and Kubes, G. J., *J. Pulp Pap. Sci.*, 1986, 12(6): J187.

32. Li, J., van Heiningen, A.R.P.,*Ind. Eng Chem. Res.*, 1990, 29(9), 1776-85.

33. Frederick, W.J., Wåg, K., Hupa, M., Rate and Mechanism of Black Liquor Char Gasification with CO_2 at Elevated Pressures. *Ind. Eng. Chem. Research*, 32(8):1747-1753 (1993).

34. Macek, A., Bulik, C. Twentieth Symp. (Intl.) on Combustion/The Combustion Institute, 1984, pp. 1213-1221.

35. Tichenor, D.A., Mitchell, R.E., Hencken, K.R., Niksa, S. Twentieth Symp. (Intl.) on Combustion/The Combustion Institute, 1984, pp. 1213-1221.

36. LaFollette, R.M., Hedman, P.O., Smith, P.J., *Combustion Sci. and Tech.*, 1989, 66, 93-105.

37. Grosshandler, W.L., *Combustion and Flame*, 1984, **55**, 59.

38. Solin, P., Hupa, M., Black liquor combustion studies in a laboratory furnace IV (in Finnish). Internal Report, Åbo Akademi, Turku, Finland (1984).

39. Grace, T.M., Lien, S.J., Brown, C.A., Char bed burning - laboratory studies. Proc. 1992 TAPPI-CPPA Intl. Chem Recovery Conf., TAPPI Press, Atlanta, p. 539-549 (1992).

40. Li, J., van Heiningen, A.R.P., Kinetics of CO_2 Gasification of Fast Pyrolysis Black Liquor Char. *Ind. Eng Chem. Res.*, 29(9):1776-1785 (1990).

41. Li, J., van Heiningen, A.R.P., Kinetics of Gasification of Black Liquor Char by Steam. *Ind. Eng Chem. Res..*, 30(7):1594-1601 (1991).

42. Flaxman, R.J. (1986) Flow and particle heating in an entrained flow reactor. MSc thesis, University of Ottawa, Ottawa, CANADA.

43. Li, J., van Heiningen, A.R.P., *Tappi Jl.*, 74(3):237-239 (1991).

44. Reis, V.V., Frederick, W.J., Wåg, K.J., Iisa, K., Sinquefield, S.S. Potassium and Chloride Enrichment During Black Liquor Combustion. Paper 104c, 1994 AIChE Spring National Meeting, Atlanta, April 17-21, 1994.

45. Forssén, M., W.J. Frederick, M. Hupa, and P. Hyöty, "Sulfur release during pyrolysis from single black liquor droplets." AIChE 1991 Forest Products Symposium Proceedings, TAPPI Press, Atlanta, p. 11-22 (1992).

46. Sricharoenchaikul, V., Frederick, W.J., Grace, T,M., Thermal Conversion of Tar to Light Gases During Black Liquor Pyrolysis. Paper 3.b.2, 1995 TAPPI-CPPA Intl. Chem. Recovery Conf., Toronto, April 24-27.

47. Iisa, K., Carangal, A., Scott, A., Pianpucktr, R., Tangpanyapinit, V. , Nitrogen Oxide Formation and Destruction in Recovery Boilers. Paper 7.b.4, 1995 TAPPI-CPPA Intl. Chem. Recovery Conf., Toronto, April 24-27.

CHAPTER 3. SULFUR REDUCTION, RELEASE, AND RECAPTURE

3.1 EXPERIMENTAL

Experimental data on sulfur release were obtained from two types of experiments. Some of the data were obtained in single particle pyrolysis and burning experiments at Åbo Akademi University. The experimental apparatuses for the pyrolysis and burning experiments are described in Chapter 2. In these experiments, the total sulfur in the char residue was measured and the amount of sulfur released was assumed to be the difference between the initial and final sulfur masses in the particle. In some of these experiments, the sulfur gases released were oxidized to SO_2 and the SO_2 content of the product gas was analyzed to determine the fraction of the sulfur initially in the particle that as released.

The other type of experiments were conducted at Oregon State University using a laminar entrained-flow reactor, also described in Chapter 2. In these experiments, the sulfur species in the cyclone catch (char) were analyzed with a Dionex Model CES-1 capillary ion analyzer. Sulfur species in the product gases, with the exception of H_2S, were analyzed by FTIR. The H_2S produced was analyzed by wet scrubbing and titration. Sulfate reduction rate data was also obtained by this method.

The kinetics of sulfation of NaCl were measured in a fixed bed reactor consisting of a vertical quartz tube (2 cm ID) inside a tube furnace (Figure 3-1). The NaCl used reagent grade NaCl, ground and sieved to fractions of 63-90, 90-125 and 125-250 mm. The total surface area of NaCl particles, obtained from BET analysis with N_2 gas, were 0.289, 0.181 and 0.134 for the 63-90, 90-125 and 125-250 mm particles. Rate data was obtained by passing a gas stream containing SO_2, O_2, and water vapor over a preheated bed of NaCl particles. The experiments were run at gas flow rates high enough so that the rate of sulfation was independent of gas flow rate. The rate of reaction was monitored by absorbing the HCl generated in deionized water and measuring the chloride ion concentration with a specific ion electrode. The residual solids in the fixed bed were also analyzed for chloride and sulfate content at the end of several experiments. The conversions calculated from the two analytical methods agreed well.

3.2 SULFUR RELEASE DURING DEVOLATILIZATION

The amount of sulfur released during pyrolysis has been shown in this project and in earlier studies to go through a maximum with furnace temperature (Figure 3-2). The data from this project, obtained with 2-3 mm droplets in the Åbo Akademi University single droplet furnaces, indicate that the amount released is not strongly dependent on initial droplet size. The maximum in release rate with furnace temperature can be explained qualitatively in terms of competing release and recapture mechanisms; this concept remains to be tested quantitatively.

The rate of release of sulfur gases during devolatilization is controlled by the rate of heat transfer to the droplet at temperatures of importance in recovery boilers. This is based on data which show that the apparent activation for sulfur release during devolatilization is the same as the apparent activation energy for heat transfer, 11 kJ/mole (Figure 3-3). The release of sulfur occurs in proportion to or slightly faster than the release of carbon gases.

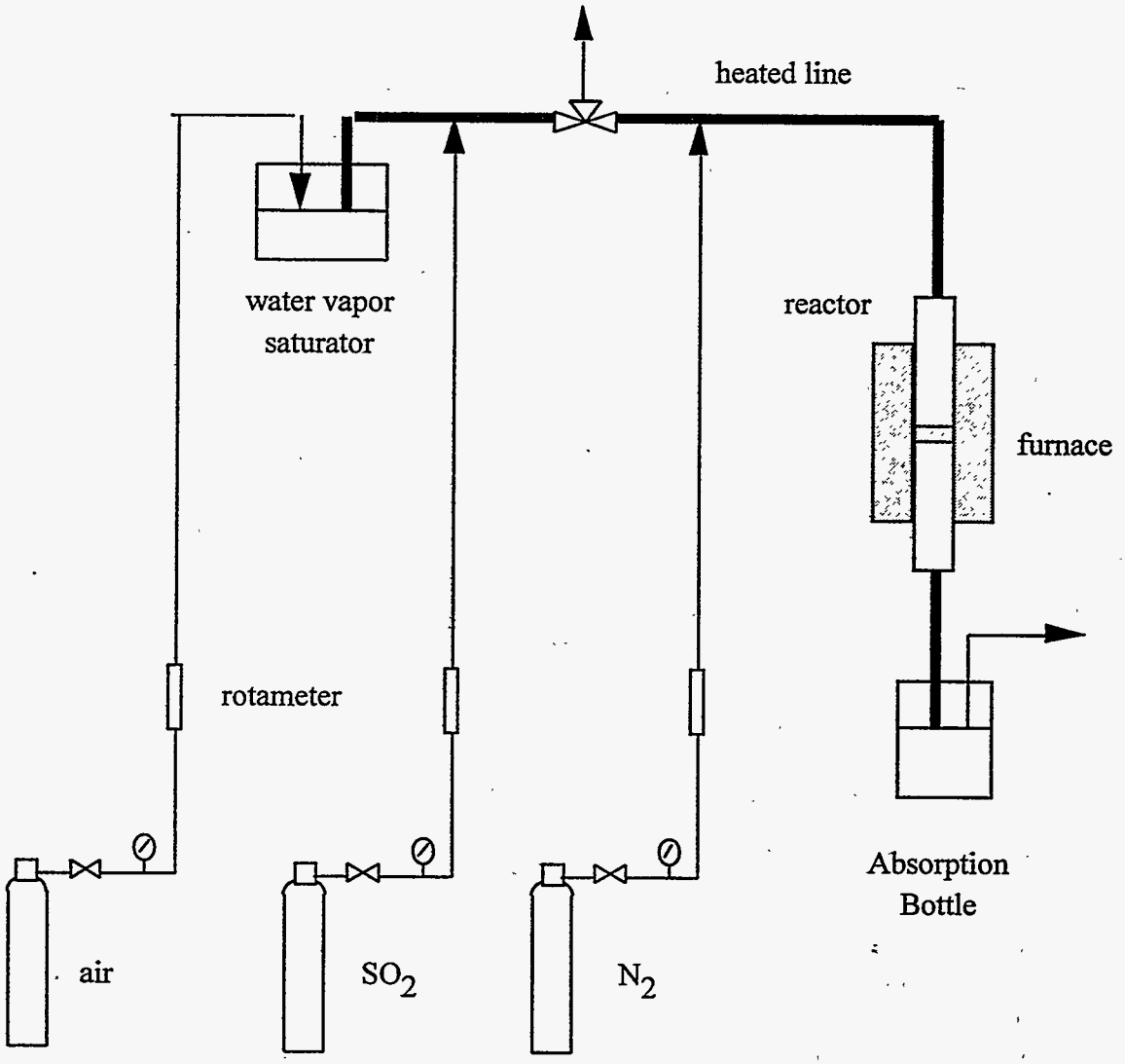

Figure 3-1. Experimental apparatus for sulfation of solid NaCl.

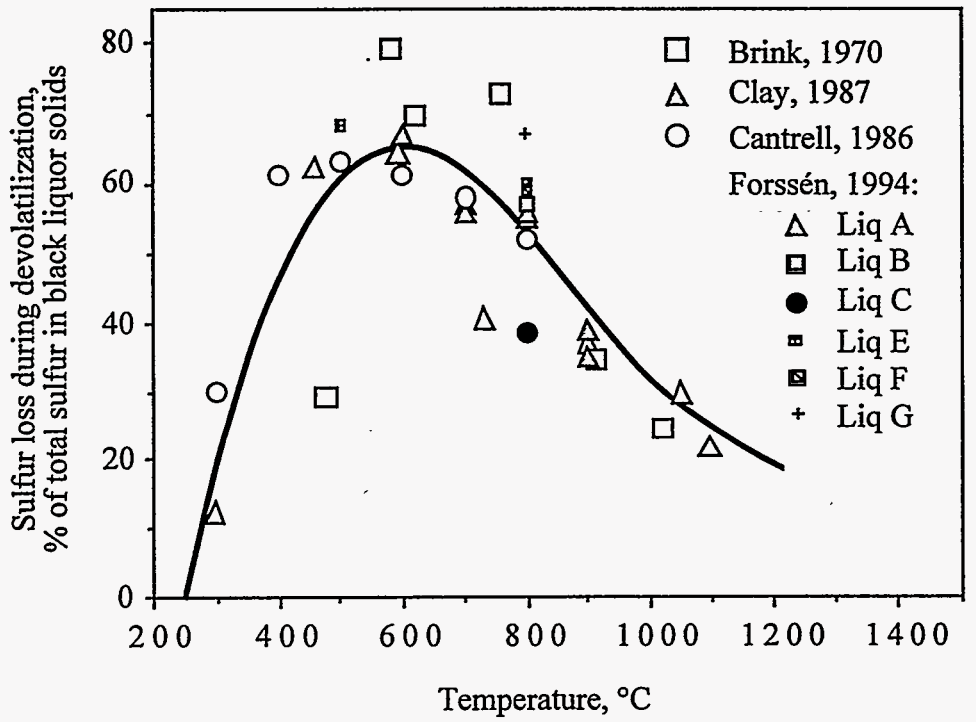

Figure 3-2. Fraction of total sulfur released from black liquor droplets pyrolyzed at temperatures between 300°C and 1100°C.

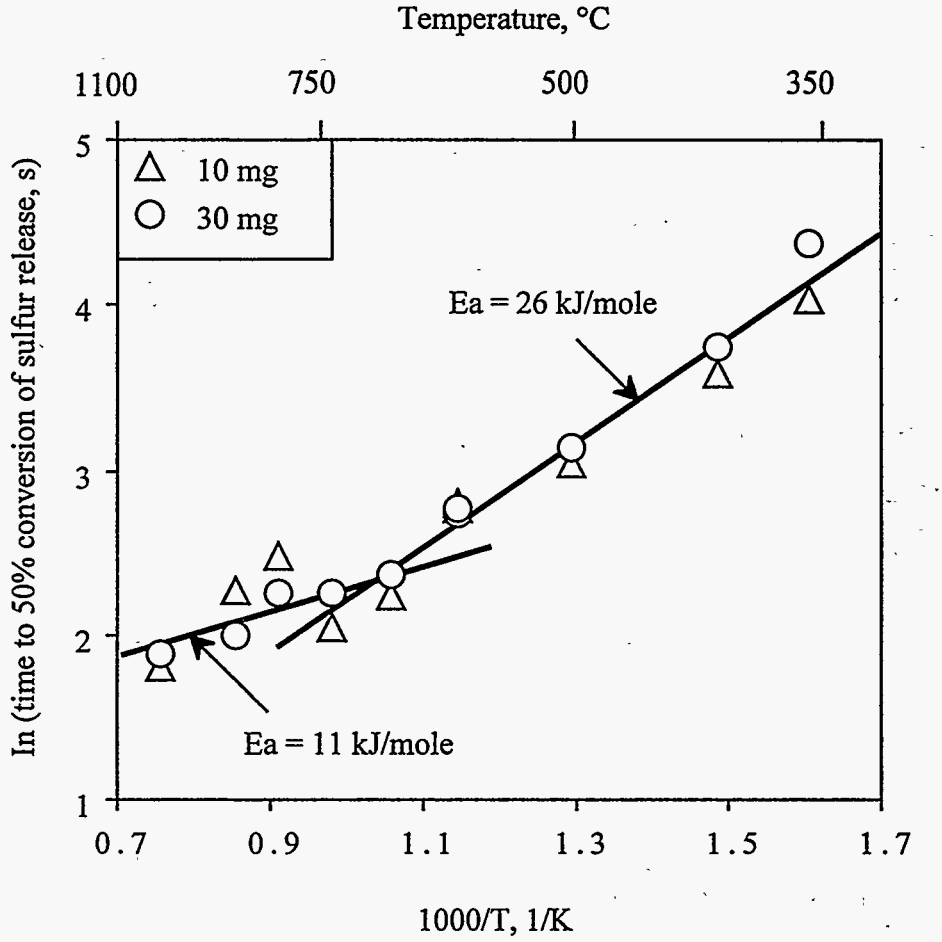

Figure 3-3. Time to 50% completion of the sulfur release process versus furnace temperature for 10 and 30 mg black liquor droplets.

Figure 3-4 compares data from experiments at Åbo Akademi University on sulfur release from black liquor during devolatilization taken at different furnace temperatures and gas concentrations. These data suggest that there is no difference in sulfur loss during devolatilization in N_2 versus other gases for CO_2 and water vapor partial pressures not exceeding 0.05 bar. The droplets were inserted in the furnaces for 15 seconds which is longer than the time required for complete devolatilization (98.6 seconds at 700°C; 4.2 seconds at 900°C) at these temperatures, so that some of the sulfur loss may have occurred during the char reactions stage.

3.2.1 Sulfur Species Transitions Under Pyrolysis Conditions

In the LEFR experiments, dried black liquor particles (100 μm) were pyrolyzed at temperatures of 700-1100°C. The sulfur-containing pyrolysis products measured quantitatively were COS, CS_2, SO_2, and H_2S. Organosulfur compounds (mercaptans, sulfides, disulfides) were also measured but because of their very similar infrared absorption bands it was not possible to quantify each compound. The sum of these organosulfur compounds is therefore reported as "mercaptans."

Figure 3-5 shows the distribution of gaseous sulfur species versus time for black liquor particles pyrolyzed at 900°C. These data show that most of the sulfur released is present as mercaptans or H_2S at short residence times, while much smaller quantities of SO_2 are also produced in this time frame. Some of these species are subsequently converted to CS_2 and COS. In these experiments, the total sulfur present as gaseous species drops to nearly zero in less than 2 seconds. These trends were also found at other temperatures in the range investigated.

The sulfur species remaining in the char at 900°C are shown in Figure 3-6. Almost all of the thiosulfate initially present in the black liquor solids had disappeared in less than 0.3 seconds in these experiments. The sulfite content of the char increases to a flat maximum between 0.3 and 0.8 seconds, and then decreases to zero. The sulfate content is nearly constant for the first 0.8 seconds but then decreases, nearly disappearing after 1.6 seconds. The sulfide content remains at zero until after 0.7 seconds, and then increases rapidly. The total sulfur in the char (not shown) increases very slightly from 0.3 seconds to about 0.8 seconds, and then increases rapidly. Part of this increase in char sulfur may be due to reabsorption of H_2S, forming Na_2S. The apparent initiation period for Na_2S formation, followed by a rapid rise in char Na_2S content, was observed at 1000°C and 1100°C as well, as were the trends for the other sulfur species shown in Figure 3-6.

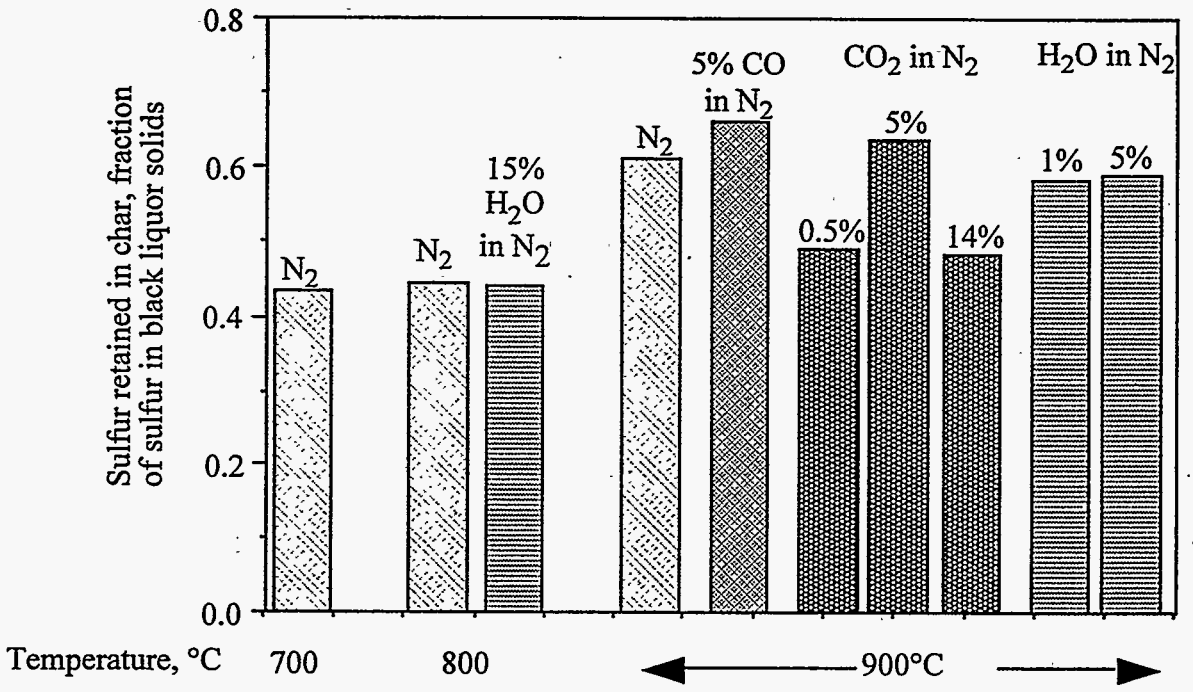

Figure 3-4. Sulfur retained in the char for droplets of liquor A inserted for 15 seconds in gas environments of different temperatures and gas compositions.

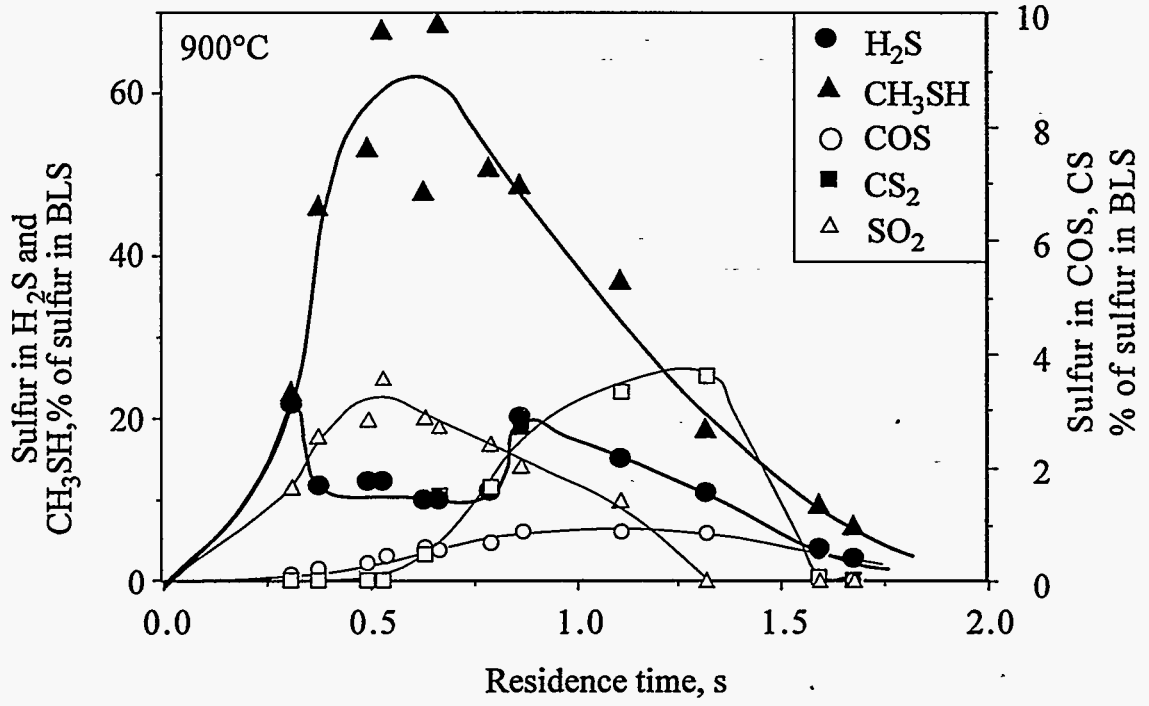

Figure 3-5. Amounts of sulfur-containing gases versus time for pyrolysis of an oxidized kraft black liquor at 900°C.

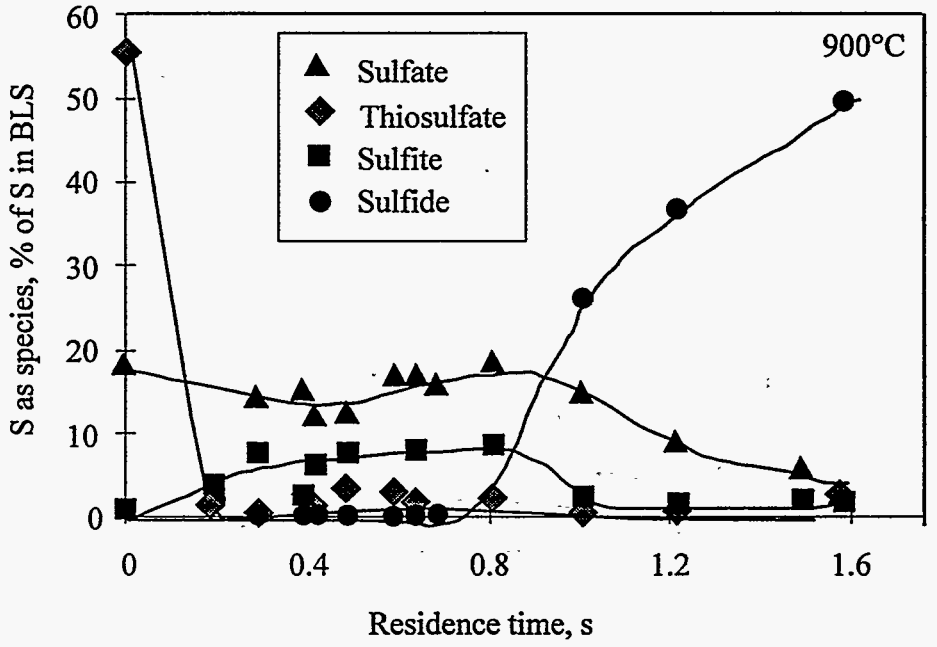

Figure 3-6. Distribution of sulfur species in char versus time for pyrolysis of an oxidized kraft black liquor at 900°C.

3.3 SULFUR RELEASE DURING CHAR BURNING

While much of the sulfur release during black liquor combustion or gasification occurs during devolatilization, sulfur release continues to occur from char during char burning, gasification, and even during heating in non-reactive gases. Durai-Swamy et al. (1991) found that nearly 90% of the sulfur recovered in their steam reforming of black liquor studies was converted to H_2S, with less than 1% of the sulfur recovered as COS and no CH_3SH detected. Li (1989) reported that, in CO_2 gasification of black liquor char at 750°C and below, nearly all of the sulfur released was as COS. He also reported that H_2S was the only sulfur species released during gasification of black liquor char with water vapor in the presence of H_2O at 600-700°C. The following reactions were indicated to be responsible for COS and H_2S formation at the higher temperatures used in the study

$$Na_2S_{(s,l)} + 2CO_2 \Rightarrow Na_2CO_{3(s,l)} + COS \quad (3\text{-}1)$$

$$Na_2S + H_2O + CO_2 \Rightarrow Na_2CO_3 + H_2S \quad (3\text{-}2)$$

Li suggested that, in the absence of water vapor, the COS concentrations in the char were at thermodynamic equilibrium at relatively low CO_2 partial pressures and high temperatures, and that the rate of COS release was controlled by film mass transfer. When water vapor was present, Li indicated that the partial pressure of H_2S within the particle would be at equilibrium and that the rate of H_2S release was controlled by film mass transfer.

Li found that the fraction of Na_2S in black liquor char that had been converted to H_2S at the point when gasification was complete decreased with increasing temperature as shown in Figure 3-7. This indicates that the rate of Na_2S conversion to H_2S became slower relative to the rate of carbon conversion as temperature increased.

3.3.1 Experimental Sulfur Release From Char Data From This Study

The average sulfur retained for liquor A in experiments where the CO_2 or H_2O content of the gases did not exceed 5% is shown in Table 3-1. These data were obtained in the Åbo Akademi droplet/flow reactor. The sulfur retained increases with increasing reactor temperature. We use these values of sulfur in the char at the end of devolatilization to find by difference the sulfur loss during char reactions for droplets that remained in the reactor for longer residence times.

Table 3-1. The average sulfur retained for one kraft liquor in experiments where the CO_2 or H_2O content of the gases did not exceed 5%.

Temperature °C	Sulfur retained in char, % of sulfur originally in the black liquor solids
600	33.0
700	43.0
800	44.3
900	62.1±3.4

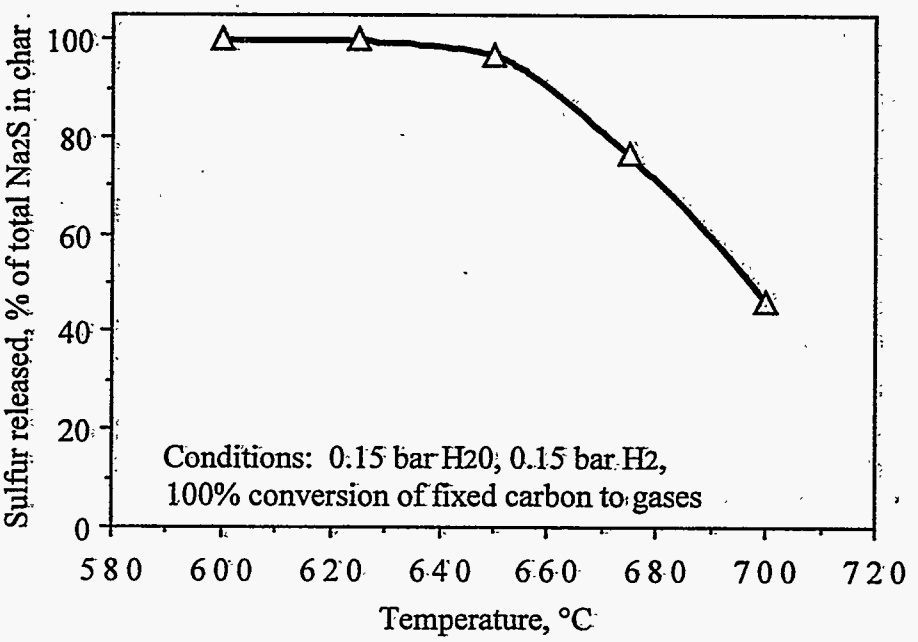

Figure 3-7. Percentage of the sulfur in black liquor char that is converted to gases during char gasification with water vapor at temperatures between 600 and 700°C. Data are from Li (1989).

The effects of gas components on sulfur release during char burning or gasification, based on data obtained from the Åbo Akademi University experiments, are summarized as follows.

Effect of CO: there was in general a greater sulfur loss during the char reactions stage at 900°C and above as the CO partial pressure increased. It is possible that CO was converted to CO_2 via an alkali metal-catalyzed reverse Boudouard reaction and the CO_2 converts Na_2S in the char to COS.

Effect of CO_2: Sulfur loss during char gasification with CO_2 was low at temperatures below 700°C and moderate (~10-20% of initial sulfur in char) at higher temperatures. The sulfur loss during char gasification generally increases with increasing temperature, CO_2 partial pressure, and reaction time.

Effect of water vapor: sulfur loss during char gasification with H_2O generally increased with increasing temperature, H_2O partial pressure, and reaction time. 20% of the sulfur initially in the black liquor solids was released within 15 seconds from char at 900°C in a 0.15 bar water vapor.

Effect of O_2: Sulfur loss during char combustion with O_2 was low at temperatures of 800°C and below except at higher O_2 partial pressures. The sulfur loss was much higher at 900°C, about 50% at 0.04-0.07 bar O_2 partial pressures. The sulfur loss during char oxidation generally increased with increasing O_2 partial pressure and reaction time. This may be due to the CO_2 and water vapor partial pressures created at the particle surface during char burning.

3.3.2 Comparison of the data from this study with Li's data.

In the data reported here, the sulfur release at 600-700°C was very low, usually within the uncertainty of the data. The amount of sulfur released generally increases with temperature, and there seems to be a threshold between 700-800°C where sulfur release began to increase rapidly. Also, reaction time was more important than gas concentration in determining sulfur release. More sulfur was released from droplets in O_2/N_2 than in other gases, but this could be a result of higher particle temperatures for those burned in O_2/N_2 mixtures. Overall, these results suggest some kinetic influence and a non-gas phase reaction.

The effect of temperature on the data reported here does not agree with that reported by Li (1989). Li found a decrease in sulfur release as temperature increased, while the data reported here generally indicates the opposite. The main differences in the experimental conditions are between the experiments reported here and those of Li's are:

1. Li's chars were pre-reduced, so the only sulfur species that they contained was Na_2S. The sulfur species in the chars used in this study were determined by the initial sulfur species distribution in the black liquor and the reactions that occurred during devolatilization and char burning. It is unlikely that the only sulfur species present after devolatilization would have been Na_2S.

2. The temperature range for the data reported here was higher than Li's, 600-900°C versus 600-700°C for H_2S and 675-750°C for COS. Also, our experiments involved molten rather than solid sodium salt species at 800°C and above.

3. The reaction times for the data reported here were generally shorter than in Li's experiments.

The rate of sulfate reduction may be an important factor in explaining the differences between our data and Li's. Sulfate reduction proceeds very slowly at 600-700°C but significant reduction can occur in the time frame of our experiments at higher temperatures. The increase in the amount of sulfur released from char with increasing furnace temperature in our experiments may be because much more sulfide was formed at the higher temperatures and therefore available to be converted to H_2S by water vapor and CO_2.

Another important factor in explaining the differences between our data and Li's is that H_2S may react to form SO_2, CS_2, or other sulfur gas species. Removal of H_2S by chemical reaction would increase its concentration gradient near or within the particle. This would increase the rate of transport of H_2S from the particle and therefore increase the overall rate of sulfur release from the particles.

A third factor is the effect of temperature on the rate of gasification of carbon and the reduction of Na_2CO_3. Conversion of Na_2S to H_2S requires both CO_2 and water vapor as reactants. In our experiments with water vapor at 900°C, gasification proceeds rapidly at 900°C, producing CO, and Na_2CO_3 is reduced at an appreciable rate, producing CO and possibly CO_2. The char is a very effective catalyst for the water gas shift reaction,

$$CO + H_2O \iff CO_2 + H_2 \qquad (3\text{-}3)$$

so that CO_2 would certainly be available along with water vapor to react with Na_2S at 900°C and above. In Li's experiments, the temperatures were too low for appreciable Na_2CO_3 reduction and gasification proceeds much more slowly. The CO_2 partial pressure would therefore probably be lower within the particles in Li's experiments, contributing to a slower rate of H_2S formation.

In summary, it is clear that the data reported earlier by Li and van Heiningen do not fully account for the rate of release of sulfur from black liquor droplets at higher temperatures. A better understanding of the chemistry and physical processes involved in sulfur release is needed. This work is now under way.

3.4 SULFATE REDUCTION

Sulfate reduction data obtained in LEFR experiments with four different liquors in Table 3-2 are shown in Figure 3-7 and 3-8. Figure 3-7 shows the moles of sulfate reduced per gram black liquor solids versus reaction time for the four liquors whose initial sulfate content is given in Table 3-2. When compared on this basis, the rate of reduction apparently varies by an order of magnitude and increases with increasing sulfate content of the black liquor solids. The only rate equation available for predicting sulfate reduction in black liquor char is that of Cameron and Grace *[1]*. The moles of sulfate reduced versus time as estimated with Cameron and Grace's equation is also plotted in Figure 3-7. Their model predicts that sulfate reduction is essentially zero order in sulfate and occurs more slowly than the data for three of

the four liquors. When the experimental data are compared on the basis of fractional conversion of sulfate (Figure 3-8), they follow roughly the same conversion versus time relationship.

Table 3-2. Composition of black liquor chars used in the model calculations.

Liquor	A	B	C	D
Carbon in char, g/g BLS	0.164	0.166	0.158	0.134
Na in char, g/g BLS	0.226	0.192	0.213	0.234
SO_4 in char, g/g BLS	0.0158	0.0321	0.0504	0.136
Initial [C], mole/mole Na_2	2.77	3.30	2.84	2.19
Initial [SO_4], mole/mole Na_2	3.36×10^{-2}	8.01×10^{-2}	1.13×10^{-1}	2.78×10^{-1}

A rate equation could be of the form of Equation 4, which was fitted to the available experimental data. An apparent activation energy of 78.1 kJ/mole was obtained from the time to 50% conversion of sulfate obtained from the data of Sricharoenchaikul et al. (23) for liquor A (Table 3-3). The equation was then fit to the data in Figure 3-7 to obtain values of A = 3790 and n = 1.40. In the fitting procedure, the rate of sulfate reduction and of carbon conversion were accounted for by integrating Equation 3-4, using a stoichiometric ratio of 3 moles carbon consumed/mole sulfate reduced. The initial carbon and sulfate concentrations in the char ([C] and [SO_4]), expressed as moles per mole total inorganic (as Na_2) are given in Table 3-3. Four of the lowest experimental values of sulfate conversion in Figures 3-7 and 3-8 for several of the liquors (one for liquors A and B, two for liquor D) were not included in the optimization The justification for this is that reoxidation of sulfide is expected to be the greatest source of error and would result in low experimental values of reduction, while nothing other than random experimental error would result in too high values.

$$R_{SO4} = - A [C] [SO4]^n \exp(-E_a/RT) \qquad (3\text{-}4)$$

The predicted and experimental sulfate conversions, shown in Figure 3-9, agree reasonably well.

Table 3-3. Time to 50% conversion of sulfate versus reaction temperature for liquor A.

Temperature, °C	Time, s
900	1.37
1000	0.80
1100	0.43

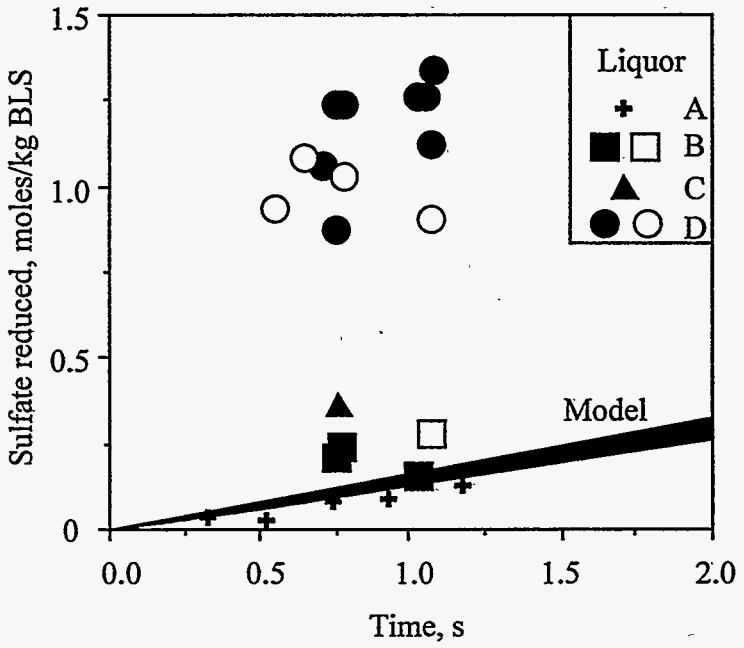

Figure 3-8. Moles of sulfate reduced per gram of black liquor solids versus time at 1000°C for four kraft black liquors, comparing LEFR results and predicted conversions based on Cameron and Grace's model. The band marked "model" indicates the range of predictions for the four liquors.

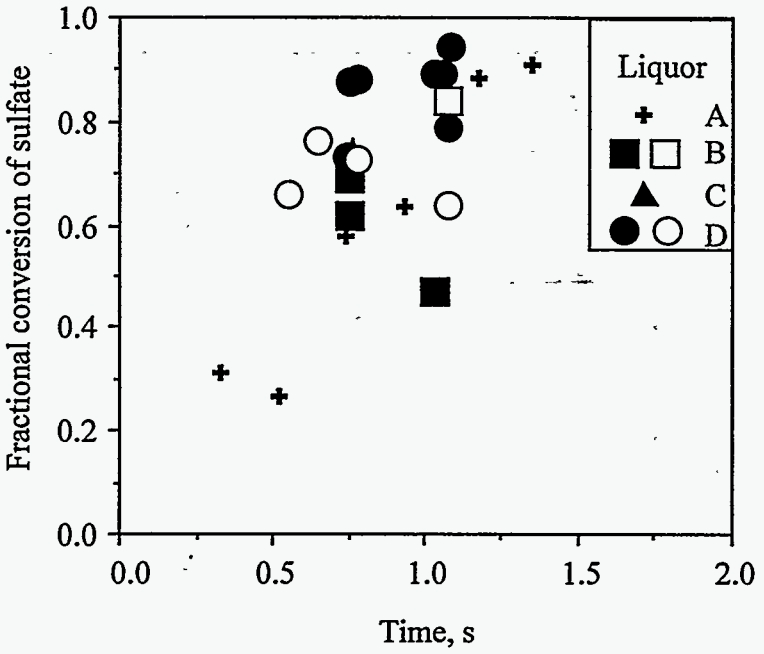

Figure 3-9. Fractional conversion of sulfate versus time at 1000°C for four kraft black liquors, comparing LEFR results and predicted conversions based on Cameron and Grace's model.

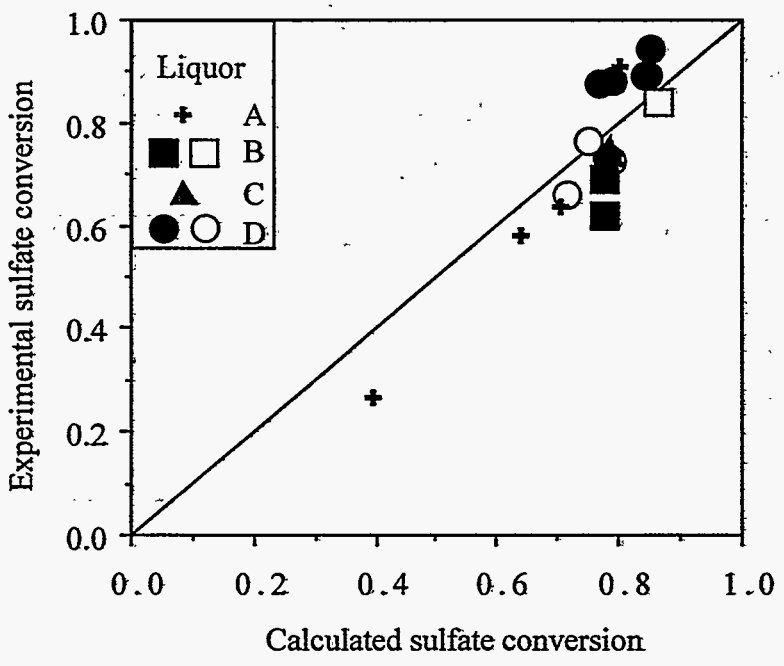

Figure 3-10. Comparison of experimental and predicted degrees of sulfate conversion for the four liquors listed in Table 3-2.

3.5 SULFUR CAPTURE

SO_2 Capture by Na_2CO_3

In black liquor combustion, sulfur dioxide may be captured by the sulfation of sodium carbonate. The reaction is

$$Na_2CO_3\,(s,l) + {}^1/_2\,O_2 + SO_2 \text{ ----> } Na_2SO_4(s,l) + CO_2 \qquad (3\text{-}5)$$

In this section, we analyze existing kinetic data. We also develop a model for predicting the rate of sulfation of solid sodium carbonate based on that data.

3.5.1 Analysis of the Existing Rate Data

Data on the kinetics of the SO_2 - Na_2CO_3 reaction in the presence of oxygen have been reported by Backman et al. [9], Maule and Cameron [10] and Keener and Davis [6]. All of these studies were made at temperatures below the melting point of Na_2CO_3.

Figure 3-10 compares the reaction rates as reported in these three studies. There is considerable discrepancy in the rates reported - they differ by as much as a factor of more than 100 when compared at the same temperature. Both the materials and the gas concentrations used in the studies varied considerably as shown in Table 3-4. The greatest difference is that Keener and Davis used a much more porous Na_2CO_3 than did Backman et al. or Maule and Cameron.

Table 3-4. Experimental conditions employed in previously reported Na_2CO_3 sulfation studies.

	Keener and Davis (6)	Backman et al. (9)	Maule and Cameron (10)
Particle size, mm	20, 90, 200	55	0.25-1.0
Temperature, °C	121-344	350-700	120-246
Specific surface area, m^2/g	1.72 (20 mm) 1.25 (90 mm) 0.91 (200 mm)	0.132	6.56
Ratio of total to external surface area	14.3 (20 mm) 46.9 (90 mm) 75.8 (200 mm)	3.03	1.71
SO_2, %	2.45	1-5	0.25-0.43
O_2, %	4.9	5-20	0.34-2.15

We determined the chemical reaction and the diffusion rates from all of the studies and compared them. We determined the chemical reaction rates from the initial rates as well as both the chemical reaction and the product layer diffusion rates using the shrinking unreacted core model for Backman et al. [9] and Maule and Cameron [10] data. An example of the fit of the shrinking unreacted core model is shown in Figure 3-11.

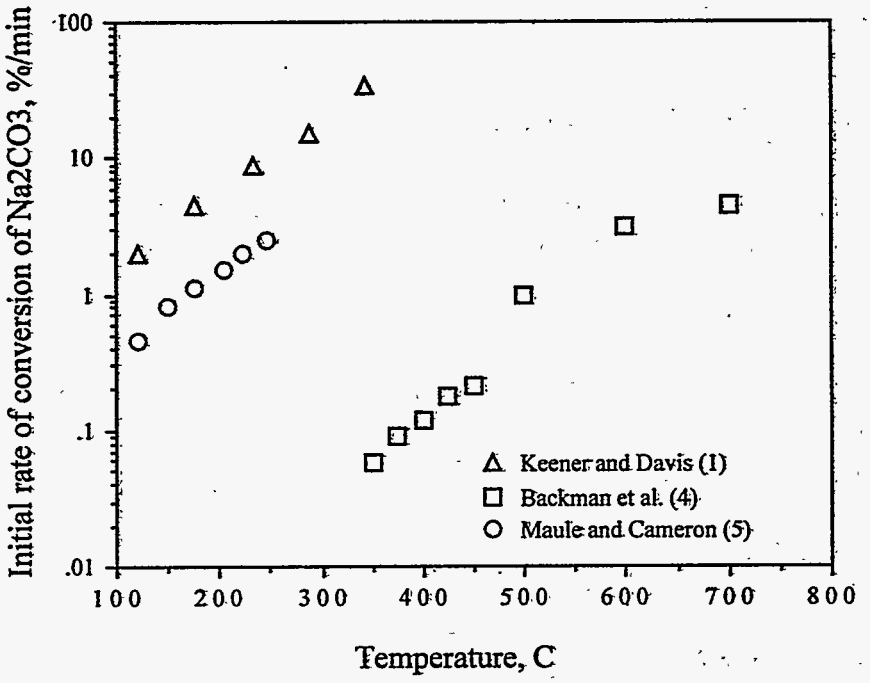

Figure 3-11. Initial rates of sulfation of Na_2CO_3 as reported by Backman et al. [9], and as estimated from the Keener and Davis [6], and Maule and Cameron [10].

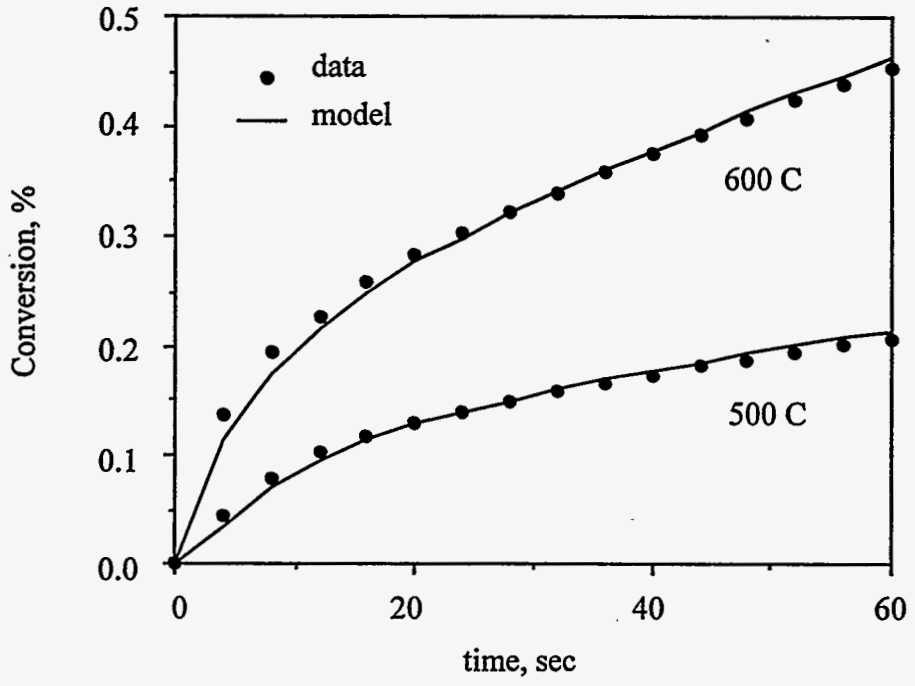

Figure 3-12. The fit with shrinking unreacted core model with both chemical and diffusion control with Backman et al. [9] data at 500 and 600 ^{o}C.

For the Keener and Davis [6] data, we used the general model for gas solid reaction [13-15] to determine the chemical reaction and the diffusion rate. This general model accounts for both interfacial and intraparticle gradients within the particle. The shrinking unreacted core modelis a special case of this model.

In the initial rate analysis we assumed that the total surface area of the particles was available for the reaction. The chemical reaction rate constants thus determined are presented in Figure 3-12. The agreement of these studies is improved. The range of variation was reduced by an order of magnitude when compared with the data in Figure 3-11.

3.5.2 Temperature Dependence

The activation energies of both the chemical reaction kinetics and the product layer diffusion were determined from Arrhenius plots of the rate constant and apparent diffusivity versus reciprocal absolute temperature. The activation energies are presented in Table 3-5.

Table 3-5. The activation energies of the chemical reaction and product layer diffusion in the sulfation of Na_2CO_3.

Study	Chemical Reaction, E_a	Diffusion, E_a
Backman et al. (4)	67 kJ/mol	98 kJ/mol
Keener and Davis (1)	66 kJ/mol	51 kJ/mol
Maule and Cameron (5)	25 kJ/mol	37 kJ/mol

The activation energies of the chemical reaction rates for the Backman et al. and the Keener and Davis data agree very well. The activation energies from the study of Maule and Cameron [10] were, however, considerably lower for both of the processes. Maule and Cameron [10] used very fine particles which sintered during sulfation, and this probably accounted for their lower activation energies. The data of Maule and Cameron [10] may be relevant for fume particles in deposits in which sintering is important. However, the data may not be applicable for sulfur capture by fume particles in-flight.

Based on the shrinking unreacted core modeling, the major limiting step of this reaction was diffusion through the product layer [16]. The apparent activation energies of the diffusion process were too high for bulk gas diffusion or Knudsen diffusion and indicate that the diffusion mechanism may be solid state diffusion. This is supported by the non-linear dependence of the overall sulfation rate on SO_2 and O_2 partial pressures.

The apparent activation energy of the product layer diffusion determined from the data of Keener and Davis was again approximately one half of the activation energy from Backman et al. data. If the rate in the study of the Keener and Davis was limited by both solid state and gas phase diffusion in the pores, the method would give one half of the true activation energy of the solid state diffusion process. The assumption of both pore diffusion and solid state diffusion control in the Keener and Davis [6] study is supported by the fact that the diffusion rate from Keener and Davis [6] data was considerably higher than in the other studies [16].

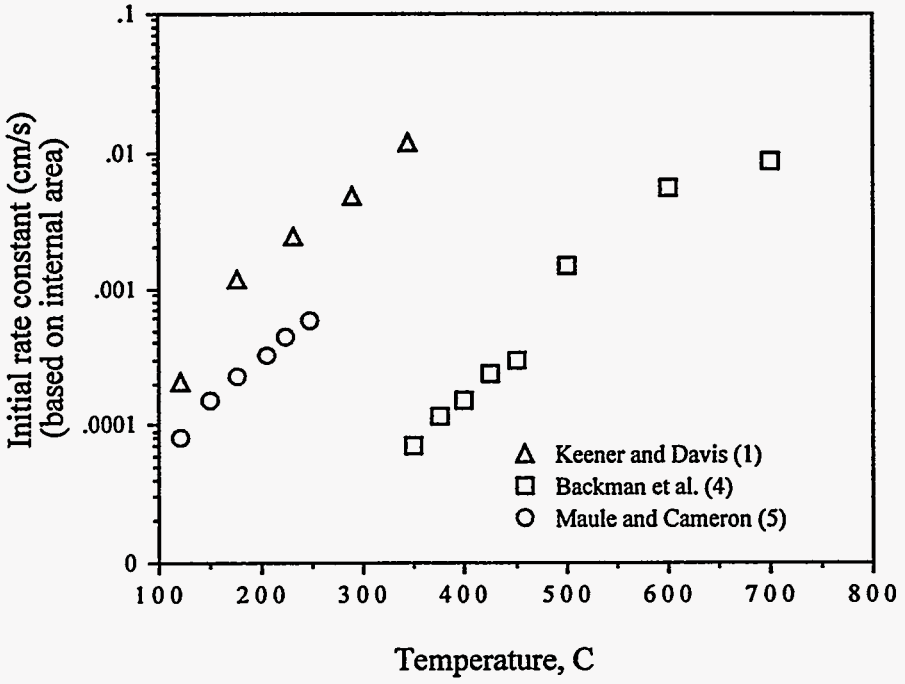

Figure 3-13. The chemical reaction rate coefficients determined from the initial rate data for the sulfation of Na_2CO_3.

3.6 SULFUR CAPTURE BY NaCl

The reaction of SO_2 with NaCl in the presence of water vapor and oxygen is shown in Equation 3-6. This reaction is important in the capture of sulfur gases in black liquor combustion and in purging of chlorides from the soda cycle in kraft pulp mills. It produces HCl emissions which, in addition to detrimental environment effects, can cause corrosion in the boiler.

$$NaCl\ (s,l) + {}^1/_2\ SO_2 + {}^1/_4\ O_2 + {}^1/_2\ H_2O \ \text{---> } HCl + {}^1/_2\ Na_2SO_4\ (s,l) \qquad (3\text{-}6)$$

The kinetics of reaction 3-6 have been studied Henriksson and Warnqvist [17] from 500 to 800°C in ceramic boats placed inside a muffle furnace. There were probably mass transfer effects in their rate data as a result of the experimental procedure used. Fielder et al. [8] followed this reaction in SO_3-SO_2 mixtures from 100 to above 650°C they reported that the sulfation reaction was first order with respect to SO_3 and also first order with respect to water vapor. The overall rate of reaction was reported to be controlled by the chemical reaction step. Almost all of the Fielder et al. [8] were obtained at anhydrous conditions. The effect of SO_2 on the reaction was not clarified because of the presence of SO_3 in the gas mixture. A rate equation could be obtained from their data.

3.6.1 Experimental Results

Particles of different sizes, 125-250, 90-125 and 63-90 mm, were used to evaluate whether intraparticle diffusion was important. Chemical kinetic rates ($mol/m^2.atm.min$) of different particle sizes, based on total surface area, were calculated to determine the effect of porosity [16]. The results, in Table 3-6, show that the kinetic rates for different particle sizes were almost the same. This implies that intraparticle diffusion has no significant effect on the measured rate.

The conversion versus time data for the sulfation of NaCl at different temperatures from 400-600 °C are shown in Figure 3-14. The rate of SO_2 capture by NaCl was not strongly temperature dependent, increasing by slightly more than a factor of two over the temperature range 400-600 °C. The activation energy of reaction was determined to be 17.3 KJ/mol. This is quite low for a chemical kinetic-controlled process and suggests that a physical process such as adsorption or desorption was the rate-controlling step.

Experiments were made in the SO_2 concentration range 0.3 - 1.1 mole %. The conversion versus time data for different SO_2 concentrations are shown in Figure 3-15. These data show that the rate increases more rapidly with increasing SO_2 partial pressure at lower SO_2 partial pressure than at higher SO_2 partial pressure.

Table 3-6. Comparison of total surface areas and rate constants of different particle sizes at flow rate of 15 cm^3/s (20 °C, 1 atm) total flow rate, 500 °C, 0.3 % SO_2, 5 % O_2, 10 % H_2O and 2 g of NaCl

Particle Size Range (mm)	Total SurfaceArea (m^2/g)	Rate Constant ($mol/m^2.atm.min$)
63- 90	0.289	$1.53x10^{-3}$
90-125	0.181	$1.21x10^{-3}$
125-250	0.134	$1.21x10^{-3}$

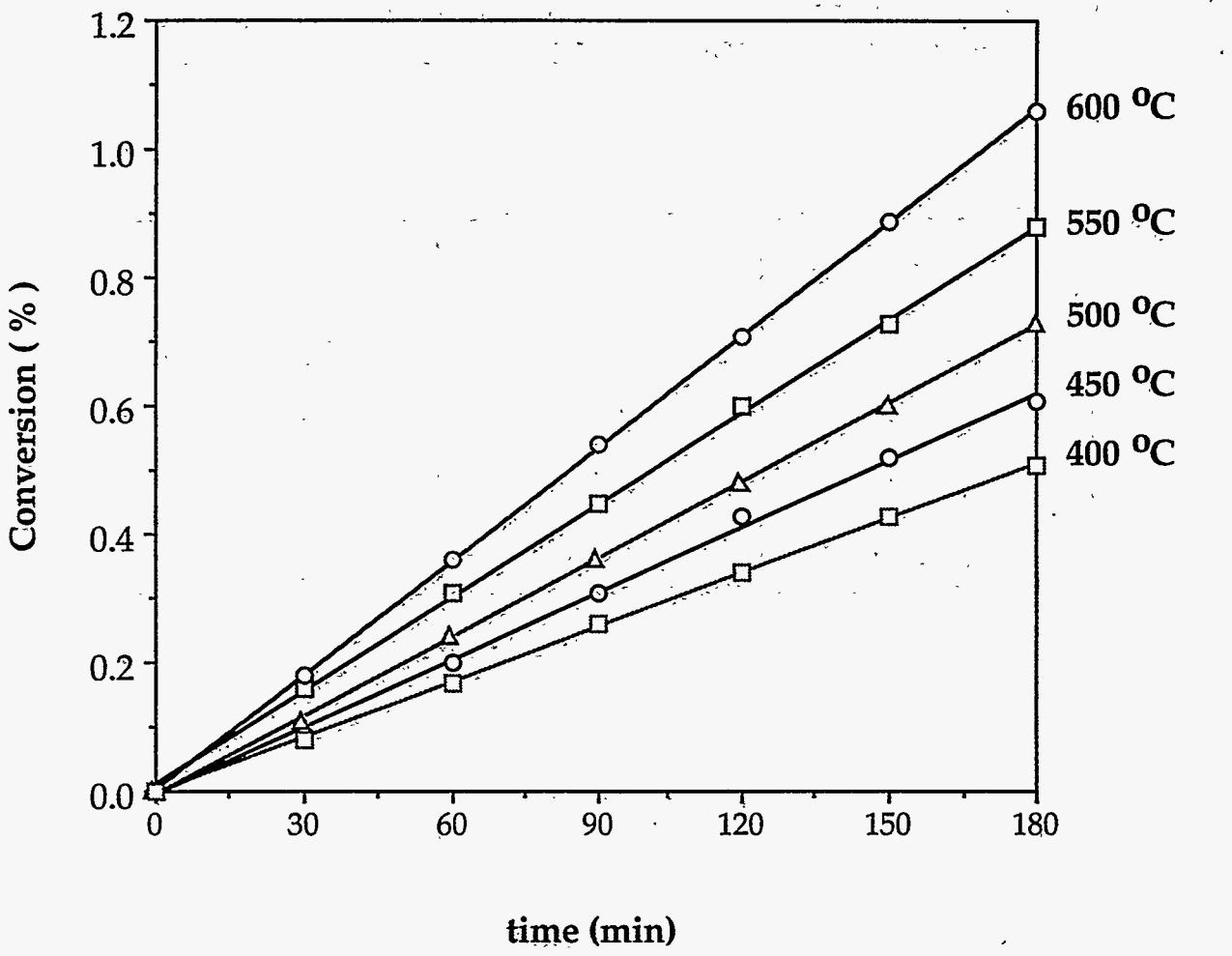

Figure 3-14. The conversion versus time data of temperature 400, 450, 500, 550 and 600 °C at 15 cm^3/s (20 °C, 1 atm) total flow rate, 0.3 % SO_2, 5 % O_2, 10 % H_2O and 2 g of 125-250 mm NaCl.

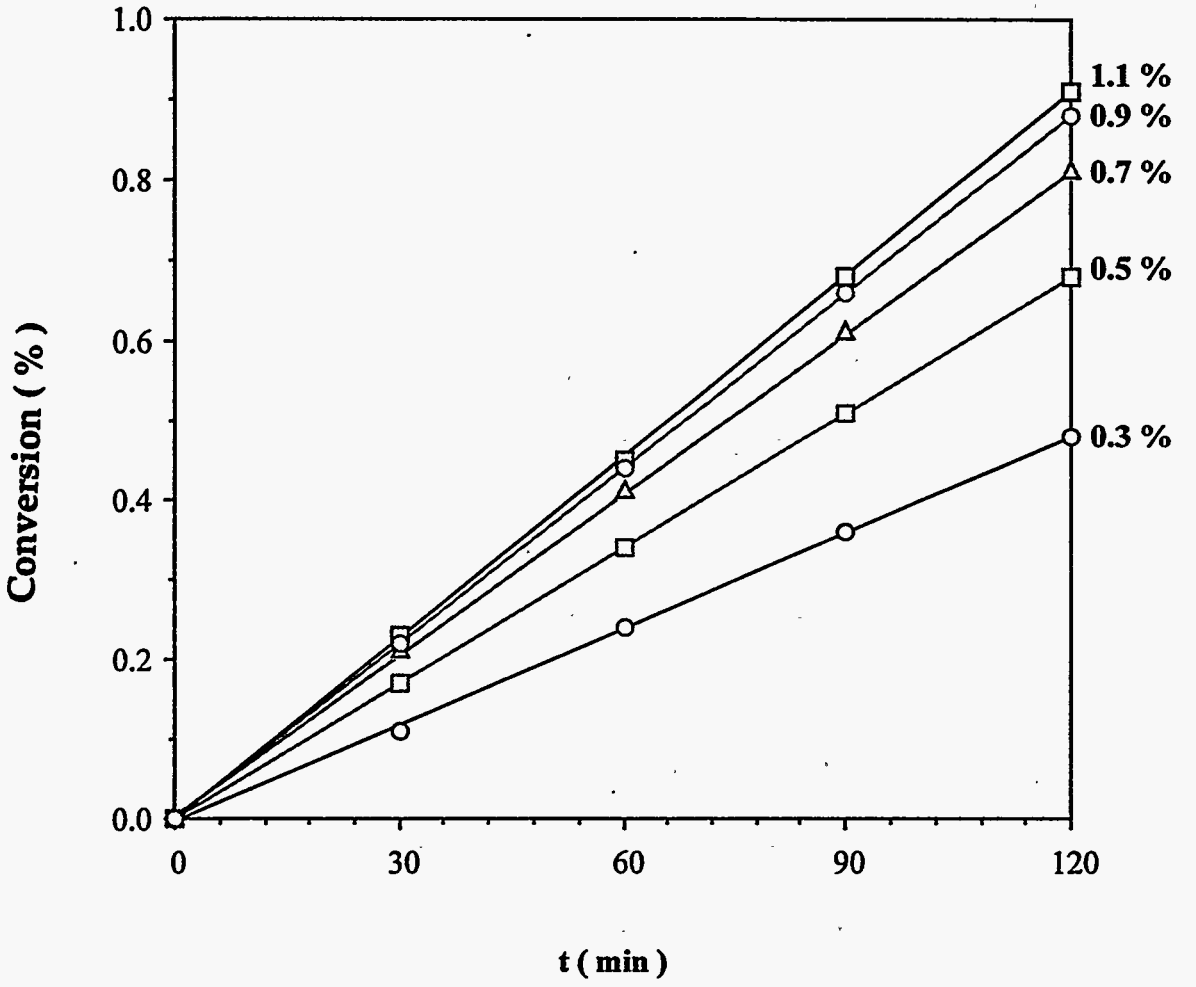

Figure 3-15. Conversion versus time data of 0.3, 0.5, 0.7, 0.9, and 1.1 % SO_2 concentrations at 15 cm3/s (20°C, 1 atm) total flow rate, 500°C, 5% O_2, 10% H_2O and 2 g of 125-250 mm NaCl.

The data in Figure 3-15 were analyzed further to find the reaction order with respect to SO_2. To find this reaction order, the logarithm of the chemical kinetic rate was plotted against the logarithm of the SO_2 concentration as shown in Figure 3-15. The chemical kinetic rate increased with SO_2 concentrations and was less dependent on SO_2 concentration at higher SO_2 concentrations. The slope of this curve, which was the order of the reaction with respect to SO_2, decreased from 0.67 at the lowest SO_2 concentrations used to 0.16 at the highest. The nonlinear dependence of the rate on SO_2 concentration in Figure 3-16 indicates that the rate is not first order in SO_2 but that SO_2 is involved in the rate limiting step of the reaction.

The O_2 and H_2O(v) concentration ranges studied were from 3 - 11 % and from 0.5 - 20 % respectively. The conditions of these studies were 15 cm^3/s (20 ^oC, 1 atm) total gas flow rate, 500 ^oC, 0.3 % SO_2, 5 % O_2 or 10 % H_2O and 2 g of 125-250 mm NaCl. The reaction rate was independent of O_2 and H_2O concentration at the conditions employed. It indicated that oxygen and water vapor were involved in a fast reaction step which did not control the overall rate of reaction.

3.6.2 Mechanism and Rate Analysis

The mechanism of the sulfation of NaCl by SO_2 in the absence of SO_3, suggested by Henriksson and Warnqvist [17], is as follows:

$$SO_2\ (g) \text{ <-----> } SO_2\ (ads)$$

$$O_2\ (g) \text{ <-----> } O_2\ (ads)$$

$$H_2O\ (g) \text{ <-----> } H_2O\ (ads)$$

$$SO_2\ (ads) + {}^1/_2\ O_2\ (ads) \text{ -----> } SO_3\ (ads)$$

$$SO_3\ (ads) + H_2O\ (ads) \text{ -----> } H_2SO_4\ (ads)$$

$$H_2SO_4\ (ads) + NaCl\ (s) \text{ ------> } HCl\ (g) + NaHSO_4\ (ads)$$

$$NaHSO_4\ (ads) + NaCl\ (s) \text{ ------> } Na_2SO_4\ (s) + HCl\ (g)$$

In this mechanism, SO_2 (g), O_2 (g) and H_2O (g) are first adsorbed on the surface of NaCl and then SO_2 (ads) reacts with O_2 (ads) to form SO_3 (ads). H_2O (ads) reacts with SO_3 (ads) to form H_2SO_4 (ads). The products, Na_2SO_4 and HCl, are obtained from the reaction between H_2SO_4 (ads) and NaCl.

The apparent activation energy of the overall reaction was quite low which is consistent with a physical adsorption-desorption process as the rate-controlling step in this reaction. SO_2 was involved in the rate limiting step of this reaction whereas O_2 and H_2O were not. The rate limiting step of this reaction should therefore be the adsorption-desorption of SO_2 (g) on the surface of NaCl. Additional support for this conclusion was that the chemical kinetic rate increased with increasing SO_2 concentration and was less dependent at higher SO_2 concentrations. This is also Langmiur adsorption type behavior [15].

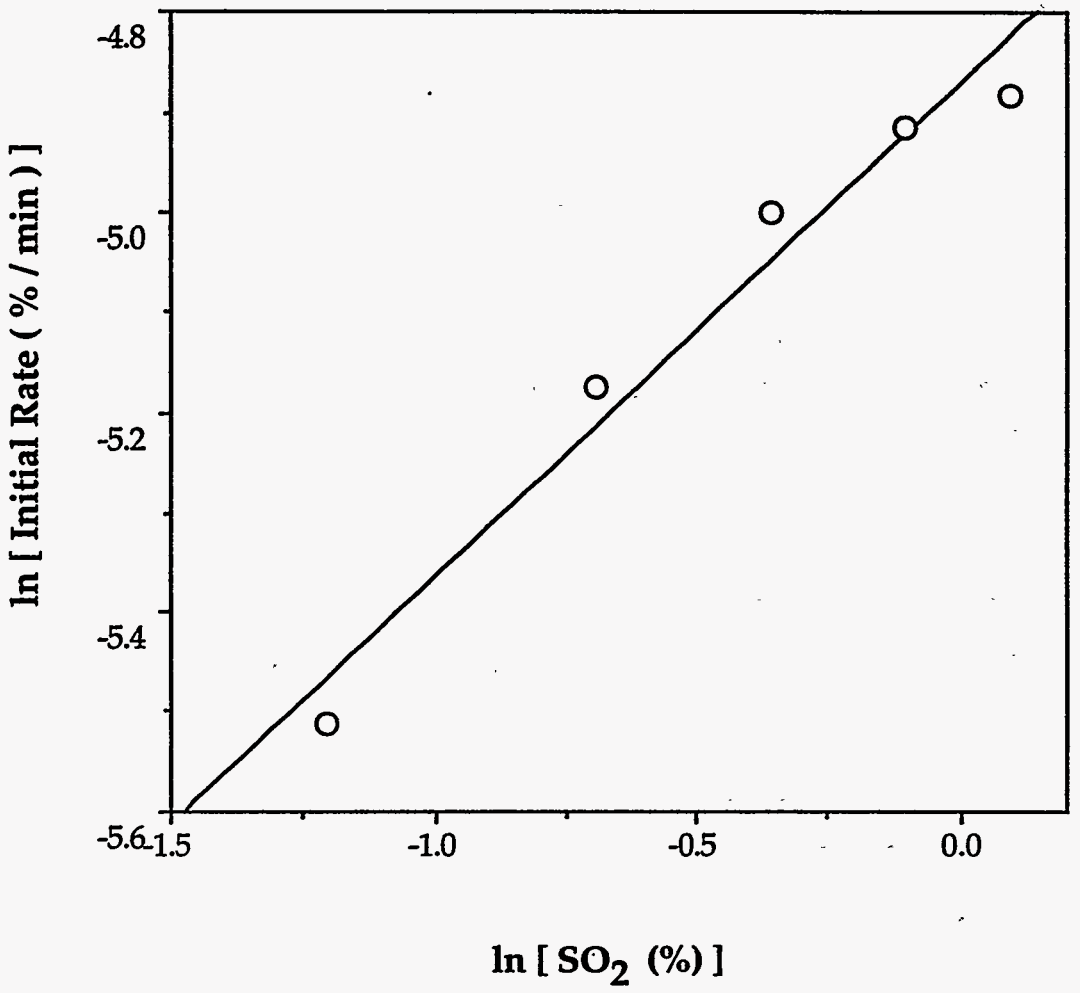

Figure 3-16. The plot of ln (rate (%/min)) and ln (SO_2 (%)) at 0.3-1.1 % SO_2, 5 % O_2 and 10 % H_2O.

The overall rate of reaction can be approximated by the rate of adsorption of SO_2 (g) which can be described by a Langmuir isotherm. The model is based on the assumption that the surface is energetically ideal and that forces of interaction between adsorbed species are negligible. The adsorption rate is assumed to be proportional to the partial pressure of the adsorbed species and the fraction of the solid surface unoccupied. The resulting rate equations is then :

$$-r_{SO_2} = S' \frac{k P_{SO_2}}{1 + K_1 P_{SO_2} + K_2 P_{O_2} + K_3 P_{H_2O}} \qquad (3\text{-}7)$$

where r_{SO_2} = rate of deformation of SO_2, mol/min.

k = reaction rate constant, mol/m^2.min.atm

P_{SO_2} = partial pressure of SO_2, atm

S' = internal surface area, m^2/g

K_1 = adsorption equilibrium constant of SO_2, atm^{-1}

K_2 = adsorption equilibrium constant of O_2, atm^{-1}

K_3 = adsorption equilibrium constant of H_2O, atm^{-1}

$$K = K_o \exp [\, Q/RT \,] \qquad (3\text{-}8)$$

where Q = heat of adsorption

If $K_2 P_{O_2}$ and $K_3 P_{H_2O}$ are much less than 1 and $K_1 P_{SO_2}$ this reaction rate will be :

$$-r_{SO_2} = S' \frac{k P_{SO_2}}{1 + K_1 P_{SO_2}} \qquad (3\text{-}9)$$

from the overall reaction stoichiometry, $2 r_{SO_2} = r_{NaCl}$

so that
$$2 S' \frac{k P_{SO_2}}{1 + K_1 P_{SO_2}} = \frac{1}{M} \frac{dX}{dt} \qquad (3\text{-}10)$$

or
$$\frac{2S'M}{(dX/dt)} = \frac{K_1}{k} + \frac{1}{k P_{SO_2}} \qquad (3\text{-}11)$$

In Figure 3-17 the plot between 2S'M/(dX/dt) and $1/P_{SO_2}$ is linear which shows good agreement between this model and the data. The values of K_1 and k at 500 °C, calculated from the plot in Figure 3-18, are 172 atm^{-1} and 1.21×10^{-3} $mol/m^2.atm.min$ respectively. Thus the kinetic rate equation of this reaction at 500 °C was :

$$r = -r_{NaCl} = r_{HCl} = -2\, r_{SO_2} = S' \frac{2.42 \times 10^{-3}\, P_{SO2}}{1 + 172\, P_{SO_2}} \quad (3\text{-}12)$$

3.6.3 Implications

From the results of sulfation of both Na_2CO_3 and NaCl, SO_2 capture in solid particles is not significant in the boiler and generator banks. This implies that nearly all of the sulfation of fume particles in recovery boilers occurs as reactions in the molten phase or before the particles solidify. Figure 3-18 shows data on SO_2 concentration in a boiler provided by Babcock and Wilcox Company. The SO_2 concentration was measured from boiler bank entrance, superheater entrance and boiler stack. It shows that there is no change in SO_2 concentration between the boiler bank inlet and stack, but that there is a significant change across the superheater. This agrees very well with the data of sulfation of solid Na_2CO_3 and NaCl.

The rates of sulfation of both Na_2CO_3 and NaCl in solid particles are fast enough, however, to account for significant sulfation of Na_2CO_3 and NaCl in deposits from heat transfer surface in recovery boilers.

3.7 MODELS

3.7.1 Devolatilization

The sulfur loss during devolatilization from black liquor droplets is estimated from the data in Figure 3-1. Correlations that fit this data are as follows:

for 250°C<T<1018°C,

$$S_{vol} = -163.27 + 0.9171T - 1.150 \times 10^{-3}T^2 + 4.283 \times 10^{-7}T^3 \quad (3\text{-}13)$$

for T>1018°C,

$$S_{vol} = 458.85 \exp(-2.666 \times 10^{-3}T) \quad (3\text{-}14)$$

where S_{vol} is the percentage of sulfur in the black liquor that was volatilized and T is the furnace temperature in °C.

In modeling sulfur release during devolatilization, the rate of sulfur release is proportional to the rate of carbon release, while the total amount of sulfur released is a fraction of the total sulfur in black liquor that depends only on furnace temperature.

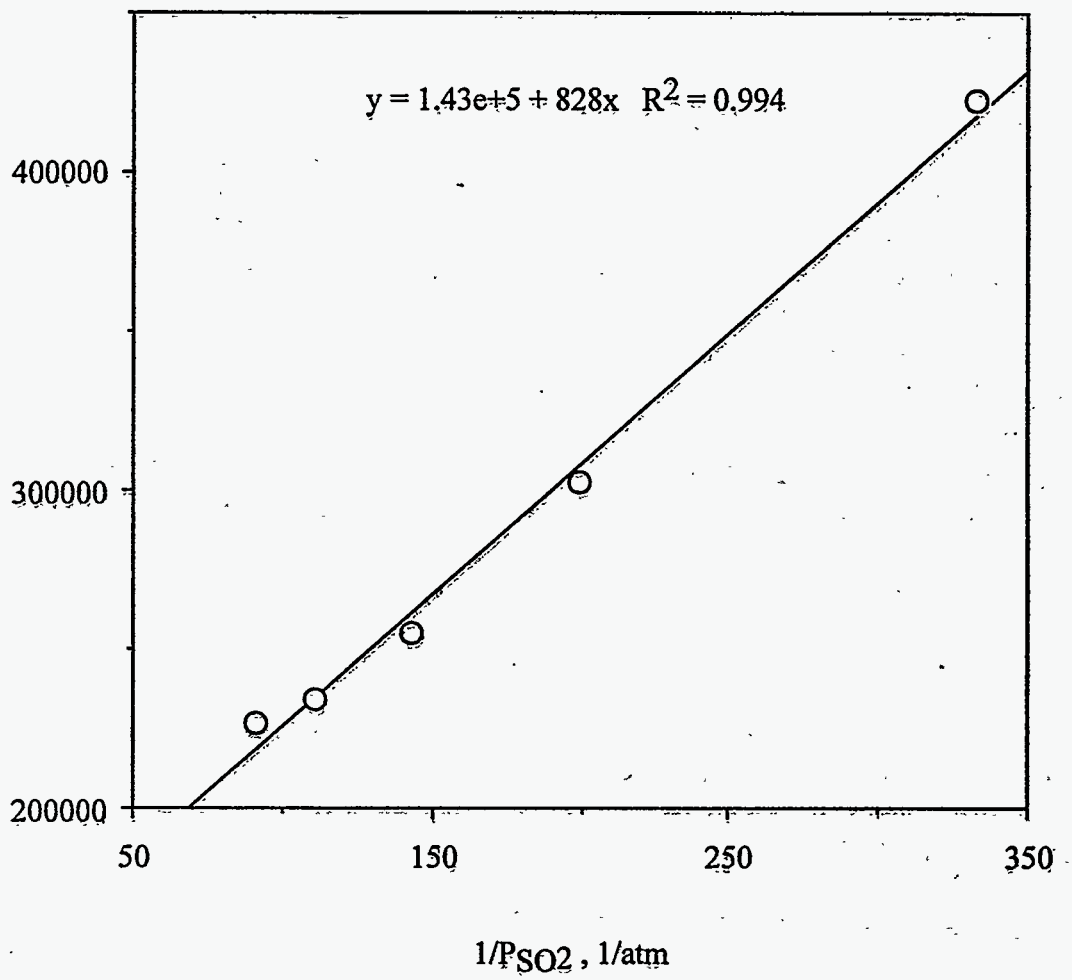

Figure 3-17. Plot of 2S'M/ (dX/dt) and $1/PSO_2$.

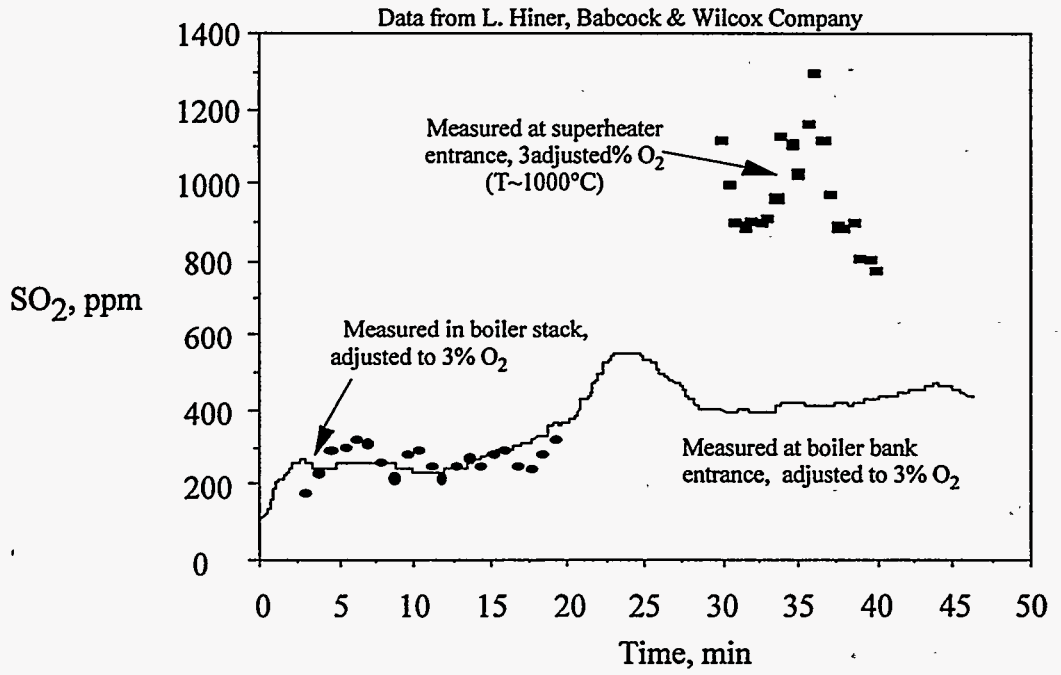

Figure 3-18. SO_2 concentration in boiler from Babcock and Wilcox company at boiler bank entrance, superheater entrance and boiler stack.

3.7.2 During Char Conversion

In the presence of both CO_2 and water vapor, the rates of H_2S and COS release when both are mass transfer limited are given by

$$\frac{dN_i}{dt} = k_g A_{ext} [C_i]_{eq} \tag{3-15}$$

where

N_i = moles of species i (H_2S or COS)
kg = mass transfer coefficient
A_{ext} = external surface area of the char particle
$[C_i]_{eq}$ = equilibrium concentration of species i (H_2S or COS) at the existing partial pressures of CO_2 and water vapor

The equilibrium partial pressures of H_2S and COS are calculated from the equilibrium expressions as

$$[COS]_{eq} = \frac{K_{COS} P_{CO2}^2}{RT} \tag{3-16}$$

where

$$K_{COS} = \frac{P_{COS}}{P_{CO2}^2} = \exp(-16.0739 + 12307/T) \tag{3-17}$$

and

$$[H_2S]_{eq} = \frac{K_{H2S} P_{H2O} P_{CO2}}{RT} \tag{3-18}$$

where

$$K_{H2S} = \frac{P_{H2S}}{P_{H2O} P_{CO2}} = \exp(-16.4674 + 16507/T) \tag{3-19}$$

concentrations are in mol/m^3, pressures in bar, and temperatures in K.

This model predicts that the rate of COS release decreases with increasing temperature because the equilibrium P_{COS} decreases. It might account for the higher sulfur release observed in colder lower furnaces in recovery boilers, although the measured rate of sulfur release becomes much slower than the predicted H_2S release rate at realistic furnace temperatures.

3.7.3 Sulfate Reduction

The rate of sulfate reduction in black liquor char is estimated as

$$R_{SO4} = -3790\,[C]\,[SO4]^{1.4}\exp(-9394/T) \qquad (3\text{-}20)$$

where the sulfate reduction rate has units of moles $SO_4^{=}$/kg BLS s and the initial carbon and sulfate concentrations in the char ([C] and [SO_4]) are expressed as moles per mole total inorganic (as Na_2). Equation 20 is based on data at temperatures between 900°C and 1100°C.

3.8 Remaining Needs

The data available on sulfur release during devolatilization are adequate for modeling black liquor burning with one important exception: it is not possible to predict the effect of changes in furnace temperature during devolatilization on the amount of sulfur released.

The mechanism of sulfur release during char burning is conceptually clear, i.e. H_2S and COS are produced by the reaction of Na_2S with water vapor and CO_2. Data at temperatures below 800°C suggest that the rates of these reactions are controlled by chemical equilibrium (which determines the partial pressures of H_2S and COS within the particles) and transport across the gas film surrounding the particles. However, data at the temperatures of interest in recovery boilers indicate that the rate of sulfur release from char is higher than the equilibrium/mass transfer models would predict. The products H_2S and COS can be converted to other sulfur species which would increase the effective sulfur release rate within the char particles. The chemistry and rates of these reactions of gaseous sulfur species need to be better understood.

The kinetic data on sulfate reduction are rather limited and the current sulfate reduction model is very approximate. Additional sulfur species transition and sulfate reduction data, especially with liquors whose initial sulfur species distribution is quite different, need to be obtained, and a mechanistic model of the sulfur species transitions and sulfate reduction needs to be developed.

The rates of sulfation of solid NaCl and Na_2CO_3 are too slow to account for the low SO_2 emissions from recovery boilers. Very limited preliminary data obtained with the OSU laminar entrained-flow reactor indicates that the rates are much faster with liquid salts, and that the formation of Na_2SO_4 from NaCl vapor, SO_2, O_2, and water vapor is very fast. The rates of sulfation of NaCl vapor and liquid NaCl need to be measured.

3.9 REFERENCES

1. Cameron, J. H. and Grace, T. M., "Kinetic study of sulfate reduction with kraft black liquor char," *Ind. Eng. Chem. Fundamentals* 24(4): 443(1985).
2. Durai-Swamy, K., Mansour, M.N., Warren, D.W., Pulsed combustion process for black liquor gasification. US DOE Report DOE/CE/40893-T1 (DE92003672), February, 1991.
3. TAPPI-CPPA Intl. Chem. Recovery Conf., TAPPI Press, Atlanta, p. 531-538.

4. Li, J. "Rate processes during gasification and reduction of black liquor char," PhD thesis, McGill University, October, 1989.
5. Whitty, K.J. Gasification of black liquor char with H_2O under pressurized conditions. M.S. Thesis, Åbo Akademi University (1993).
6. Keener, T. and Davis, W., "Study of the Reaction of SO_2 with $NaHCO_3$ and Na_2CO_3", *J.Air Pollution Control Assoc.*, 34:651-654 (1984)
7. Kirk-Othmer, *Encyclopedia of Chemical Technology*, 3rd Edition, Volume 12, p. 996, John Wiley & Sons
8. Fielder, W., Stearns, C. and Kohl, F., "Reaction of NaCl with Gaseous SO_3, SO_2 and O_2", *J. Electrochem. Soc.*, Vol.131, NO.10:2414-2417 (1984)
9. Backman, R., Hupa, M., Usikartano, T., "Kinetics of Sulphation of Sodium Carbonate in Flue Gases", Proc. 1985 International Chemical Recovery Conference, TAPPI Press, Atlanta, 1985
10. Maule, G. and Cameron, J., "Reaction of Na_2CO_3 Fume Particles with SO_2 and O_2", IPC Technical Paper Series, number 317, January 1989.
11. Lloyd-George, I., "The sulfation of sodium carbonate: the significance of pyrosulfate, potassium, and chloride", M.S. thesis, University of Toronto, 1985
12. Levenspiel, O., "*Chemical Reaction Engineering*", 2nd Edition, p. 361-373, John Wiley & Son, 1972
13. Wen, C. Y., "Noncatalytic Heterogeneous solid Fluid Reaction Models", *J. Ind. and Engr. Chem.*, Vol. 60, No. 9, 34-54, 1968
14. Ishida, M. and Wen, C.Y., "Comparison of Kinetic and Diffusional Models for Solid-Gas Reactions", *AIChe J.*, 14(2), 311-317, 1968
15. Froment, G.F. and Bischoff, K. B., "*Chemical Reactor Analysis and Design*", p. 201 - 207, John Wiley & Son, 1979
16. Boonsongsup, L., "SO_2 Capture and HCl Release at Kraft Recovery Boiler Conditions", M.S. thesis, Oregon State University, 1993
17. Henriksson, M. and Warnqvist, B., "Kinetics of Formation of HCl(g) by the reaction between NaCl(s) and SO_2, O_2, and H_2O(g)", *Ind. Eng. Chem. Process*, Des. Dev. 18(2):249-254 (1979)
18. Anderson, A., "Mechanism for forming Hydrogen Chloride and Sodium Sulfate from Sulfur Trioxide, Water and Sodium Chloride", *J. Am. Chem. Soc.*, Vol. 106, NO.21:6262-6265 (1984)

CHAPTER 4. SODIUM RELEASE

4.1 INTRODUCTION

Black liquors typically contain about 20% sodium. Part of the sodium is volatilized during combustion, forming fume and contributing to fouling of heat transfer surfaces, plugging of gas passages, corrosion, and emissions of particulates and acid gases. The reactions between sulfur and sodium compounds provide an important trap for sulfur gases which results in their recycle within the process.

Neither the mechanism of fume formation in kraft recovery boilers nor the relative amount formed during the various stages of black liquor combustion are well understood. Various researchers have attempted to describe the mechanism of sodium volatilization which leads to fume formation, or to predict the amount of fume formed. Borg et al. (1) and Pejryd and Hupa (2) used a chemical equilibrium approach to estimate the fume content of gases in the lower furnace. Cameron et al. (3) showed that sodium can be volatilized by a mechanism involving the oxidation of Na_2S in the smelt. None of these has provided an acceptable way of modeling fume generation in recovery boilers.

This chapter deals with sodium release during all three stages of black liquor burning: devolatilization, char burning, and smelt reactions.

4.2 EXPERIMENTAL

The data reported here was obtained in experiments at Åbo Akademi University and at Oregon State University. The single droplet apparatuses and the laminar entrained-flow reactor (LEFR) described in Chapter 2 were used in obtaining the data. In the single droplet measurements, the sodium retained in the droplet residues after pyrolysis, gasification, or combustion was measured, and the difference between the sodium initially in the droplet and that measured in the residue was assumed to be volatilized. In the LEFR experiments, the sodium volatilized was collected as fine particles after passing through a cyclone with a 3 μm cutoff.

Additional experiments were made at Åbo Akademi University in the experimental apparatus shown in Figure 4-1. The reactor was operated in a semi-batch mode, in which stationary char particles were contacted with a preheated upward flowing gas. The reactor was maintained at temperatures between 700 and 1000°C. The fume particles produced were collected on a filter at the gas exit, from the tubing connecting the reactor to the filter, and from the walls of a ceramic insert above the char particles. These particles and the residue from the char were analyzed for sodium content.

In some of the LEFR experiments, the particle size distribution for the fine particles which passed through the 3 μm cutoff cyclone were measured using a Berner low pressure impactor. These measurements were made by the Aerosol Technology Group of the Technical Research Centre of Finland. The particles collected were analyzed for sodium, potassium, chloride, and sulfate, yielding chemical species distributions as well as the particle size distributions. Details of the experimental method are available from Kauppinen et al. (4).

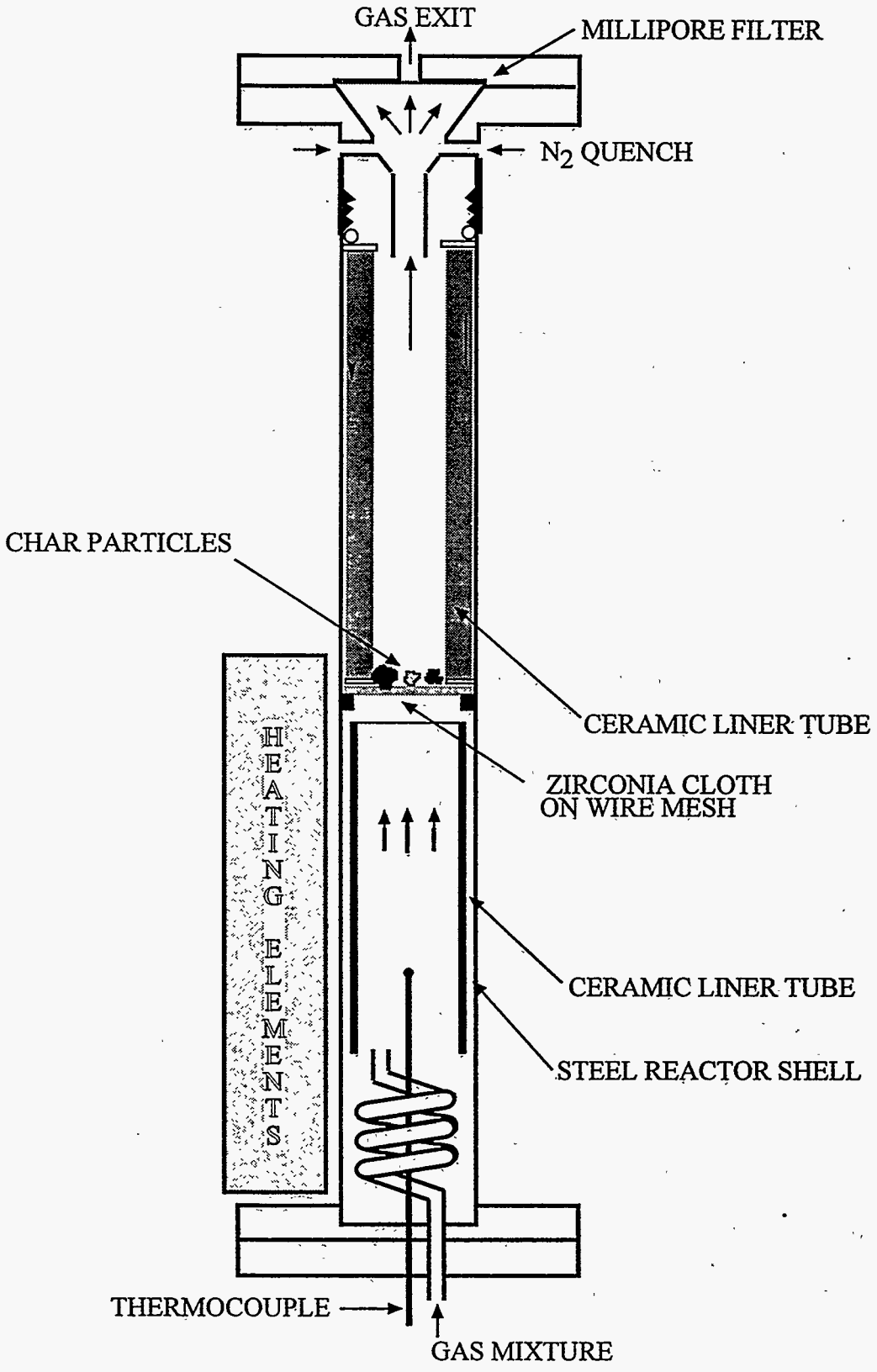

Figure 4-1. Fume generation reactor used at Åbo Akademi University.

4.3 SODIUM RELEASE

Figures 4-2 and 4-3 show sodium loss versus time data for single black liquor droplets suspended in a muffle furnace at four different temperatures. The dashed line in Figure 4-2 indicates the time at which devolatilization ends, and the insert indicates the amount of sodium lost from the droplet residue at the end of devolatilization versus furnace temperature. The sodium retained in the char particle, expressed as a percentage of the initial sodium mass in the droplet, decreased by 13-20% of the initial sodium content during devolatilization. The sodium loss during devolatilization was similar for the seven liquors of three different types that we tested.

After devolatilization was complete, there was no significant sodium loss in up to 55 seconds at 800°C and below. However, at higher temperatures, the sodium content of the particles continued to decrease with time beyond the end of devolatilization, and the rate of loss was greater as temperature increased. This data indicates that sodium fume generation from the char is strongly temperature dependent. Similar results - a significant loss of sodium from the droplet residue during devolatilization, with loss of sodium leveling off at 800°C and below but continuing at 900°C and above - were reported by Volkov et al. (5) and Verrill and Nichols (6) in experiments with droplets of similar size.

The data in Figures 4-2 and 4-3 show the sodium *retained* in droplets that had been pyrolyzed, but the fate of the sodium released from the droplets was not determined. Additional experiments were conducted in which both the char residue and the sodium volatilized were collected. Some of these measurements were made in pyrolysis and combustion experiments with the OSU laminar entrained-flow reactor. In these experiments, 100 μm particles of dry black liquor solids were pyrolyzed or burned for 0.4-0.6 s.

The amount of sodium collected as fume in these experiments is shown in Figure 4-4. The sodium collected was less than 5% of the sodium in the black liquor solids at the lower temperatures (700-900°C) and gas phase O_2 concentrations (0 and 4%). For furnace temperatures of 1000°C and 1100°C and for particles burned in air, the sodium recovered as fume was as high as 37% of the sodium in the black liquor solids. McKeough et al. (7) and Kymäläinen et al. (8) have also reported very low sodium fume generation at lower temperatures. The data in Figure 4-4, when plotted against the estimated particle temperature during char burning, fall reasonably well along a single curve (Figure 4-5). The particle temperatures during char burning were estimated as described in the Modeling section in Chapter 2.

The amount of sodium collected as fume in the experiments at 0% O_2 was much lower than the sodium lost during devolatilization from the single droplets in Figures 4-2 and 4-3. Verrill et al. (10) and Kauppinen et al. (11) suggested that the difference is due to fragmentation of the char particle, producing small, sodium containing char fragments that are an order of magnitude or more larger than fume particles.

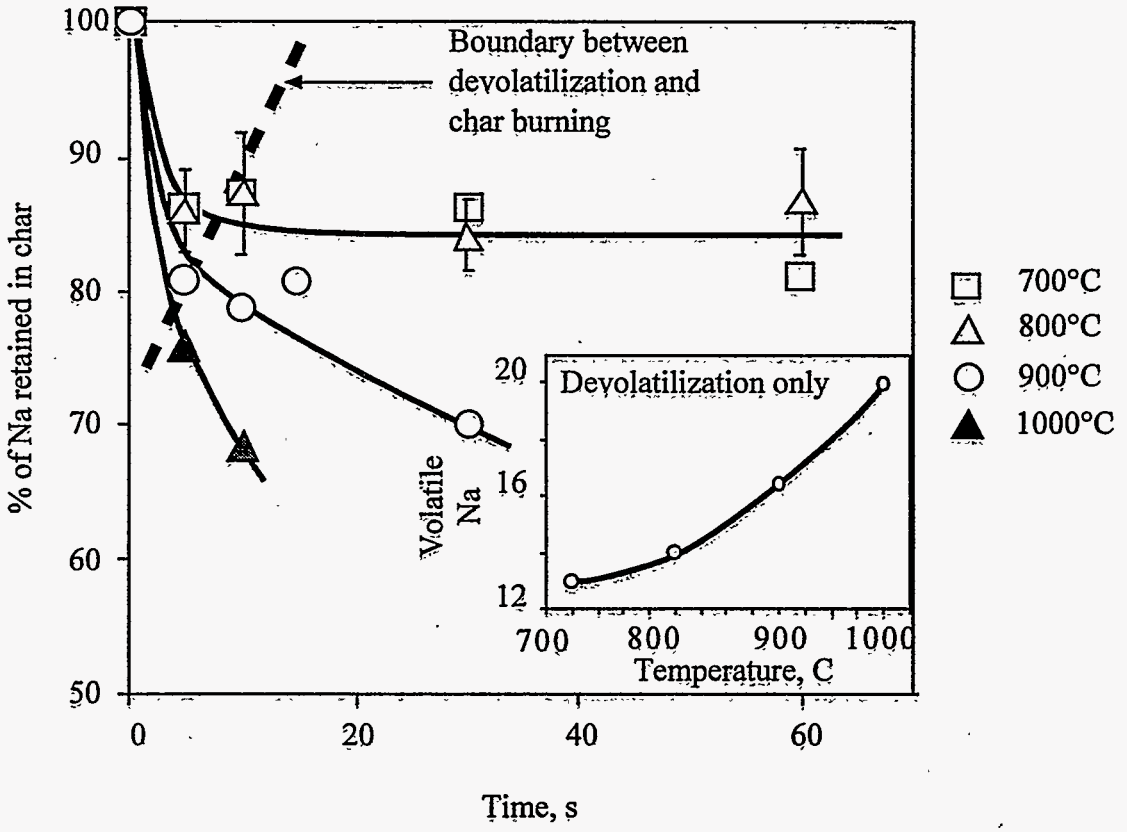

Figure 4-2. Sodium retained in the droplets versus time for 5-15 mg black liquor droplets heated for up to 60 seconds in a quiescent gas atmosphere, 5% CO, 95% N_2 at temperatures of 700-1000°C.

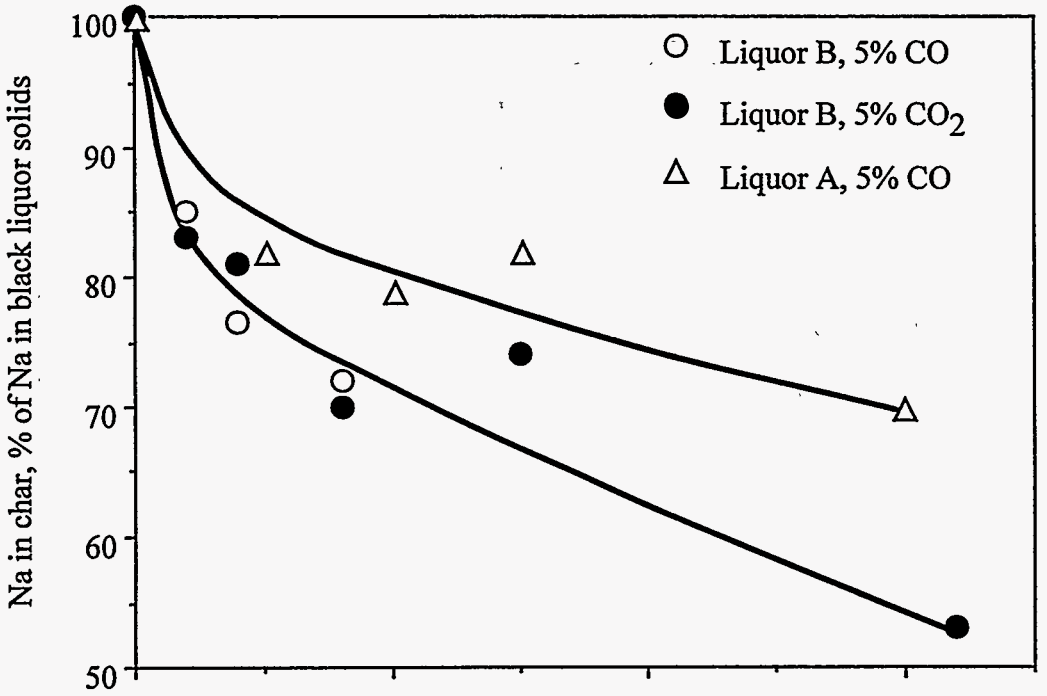

Figure 4-3. Sodium retained in the droplets versus time for single black liquor droplets heated for up to 30 seconds in a quiescent gas atmosphere containing 5% CO or 5% CO_2, 95% N_2 at 900°C.

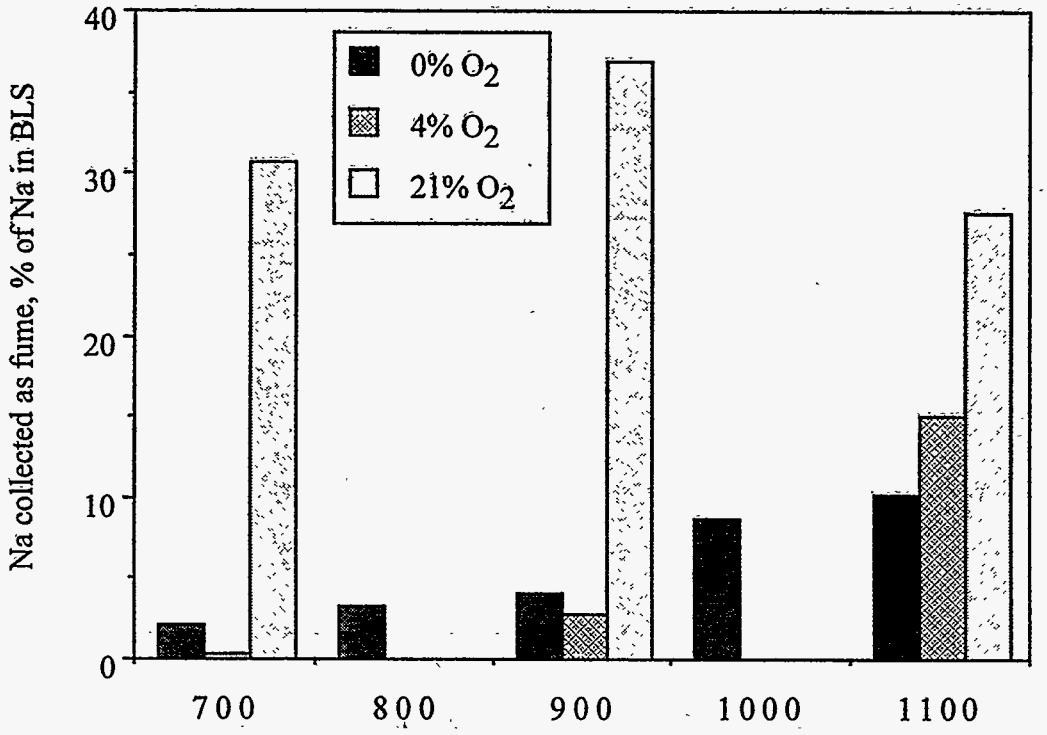

Figure 4-4. Sodium collected as fume during pyrolysis of 100 μm dry black liquor particles in N_2 in a laminar entrained-flow reactor, 0.4-0.6 s residence time.

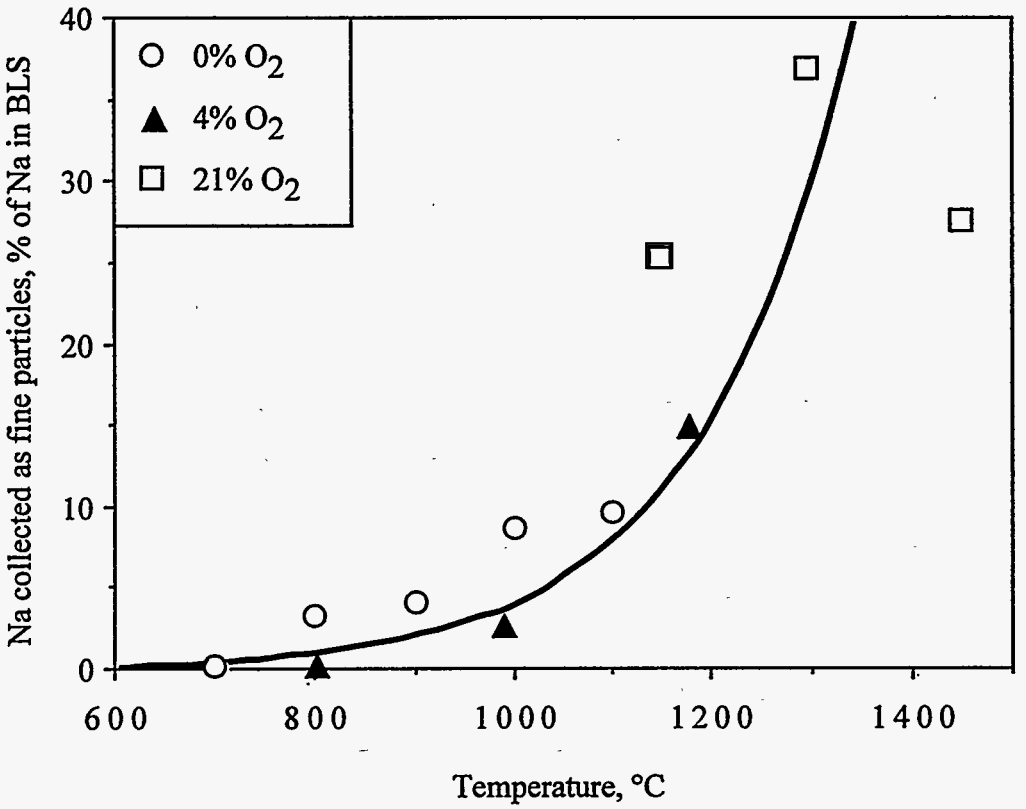

Figure 4-5. Sodium collected as fume versus particle temperature during pyrolysis of 100 μm dry black liquor particles in N_2 in a laminar entrained-flow reactor, 0.4-0.6 s residence time.

Additional data, in which the sodium volatilized was measured, was obtained by dropping black liquor char particles into a hot upflow reactor and collecting both the sodium fume and char residue produced (9). Table 4-1 contains the data obtained in these experiments for temperatures of 700°C and 800°C. The mean values for fume yield and the standard deviations at each condition are shown in Figure 4-6. In these experiments, the fume yield increased with increasing temperature and was greater when O_2 was present in the gas phase. The presence of CO_2 in the gas phase suppressed fume formation when compared to the results both in N_2 and in 2% O_2.

In these experiments, closure of the sodium material balance was reasonable, averaging between 84 and 94%. The last column in Table 4-1 shows how much fume was generated if all of the unaccounted sodium were fume. The qualitative conclusions regarding the effect of temperature would not be changed if all of the unaccounted sodium were fume, but the conclusion that CO_2 suppresses fume formation relative to that for particles heated in N_2 would not be valid.

Additional experiments were conducted at 1000°C. Only 20-30% of the sodium was retained in the char residue, suggesting that the rate of fume generation was much higher (Table 4-2). Closure of the sodium material balance was poorer in these runs, with about 40% of the sodium input accounted for. Fume particles were observed in gas leaks from the reactor in the 1000°C runs, and this probably accounted for the poor material balance closure.

Table 4-2. Sodium release data for char particles reacted for five minutes at 1000°C in a 2% O_2/98% N_2 gas mixture.

Gases	Temperature, °C	Run No.	Sodium, % of input		
			Char Residue	Fume	Total
2% O_2	1000	40	28.8	12.1	40.9
		41	19.1	20.2	39.3
		42	22.7	10.8	33.5
		Average	23.5	14.4	37.9
		St. Dev.	4.9	5.1	3.9

4.4 FUME PARTICLE CHARACTERISTICS

Fume particle differential mass size distributions measured at different conditions in the LEFR are shown in Figure 4-7. The size distributions are given as the mass size distribution relative to the total mass concentration as collected with the BLPI in the respective run. The mass size distributions for the combustion experiments (Figure 4-7) in air at 700°C, 900°C and 1100°C, peak at about 0.5 μm. The shape of the mass size distribution is very similar to those collected in actual recovery boilers (4). This suggests that the entrained-flow reactor is a valid device for measuring and characterizing fume particle formation during black liquor combustion.

Table 4-1. Sodium release data for char particles reacted for five minutes at 700°C or 800°C and the gas compositions indicated.

Gases	Temperature, °C	Run No.	Sodium, % of input			Na as fume plus unaccounted Na
			Char Residue	Fume	Total	
N_2	800	14	81.3	7.9	89.2	18.7
		16	96.5	1.8	98.4	3.5
		17	93.0	2.3	95.2	7.0
		18	79.5	13.4	92.9	20.5
		Average	87.6	6.3	93.9	12.4
		St. Dev	8.4	5.4	3.9	8.4
2% O_2	700	36	84.0	2.5	86.5	16.0
		37	82.5	1.9	84.4	17.6
		38	77.7	4.9	82.6	22.3
		Average	81.4	3.1	84.5	18.6
		St. Dev	3.3	1.6	2.0	3.3
2% O_2	800	19	77.3	6.0	83.2	22.7
		20	65.9	19.0	84.9	34.1
		21	66.2	14.2	80.4	33.8
		22	74.6	9.8	84.4	25.4
		Average	71.0	12.2	83.2	29.0
		St. Dev	5.8	5.6	2.0	5.8
2% O_2	800	25	82.1	1.6	83.7	18.0
20% CO_2		26	91.6	1.1	92.7	8.4
		27	84.5	1.6	86.1	15.6
		Average	86.0	1.5	87.5	14.0
		St. Dev.	5.0	0.3	4.7	5.0

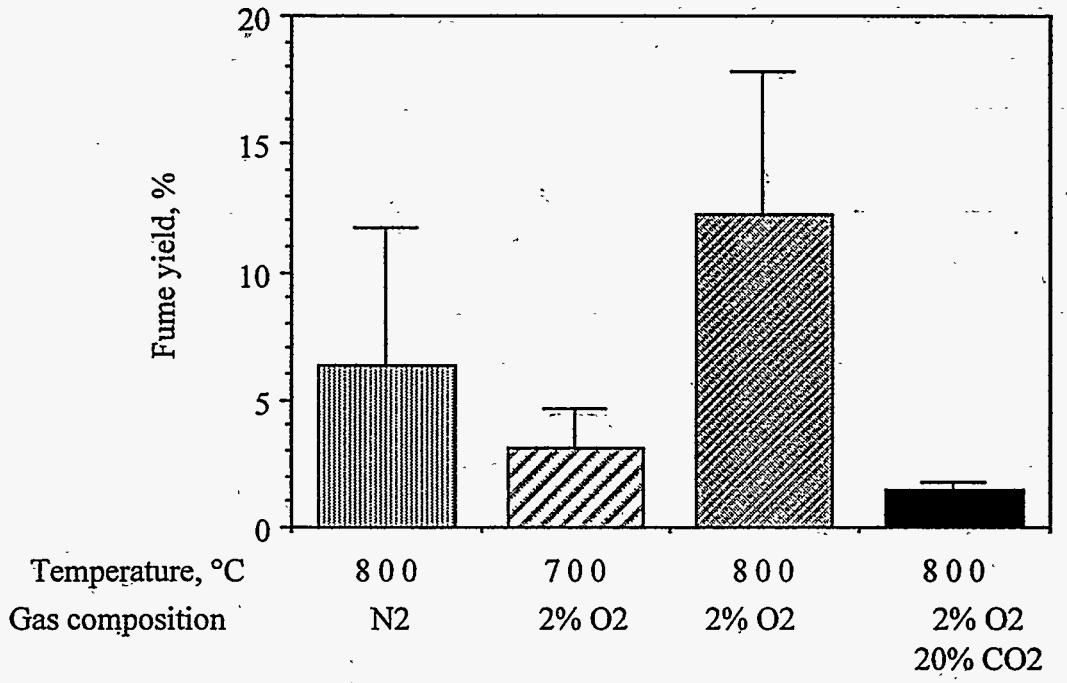

Figure 4-6. Summary of sodium release data for char particles reacted for five minutes at the temperatures and gas compositions indicated. The error bars indicate one standard deviation.

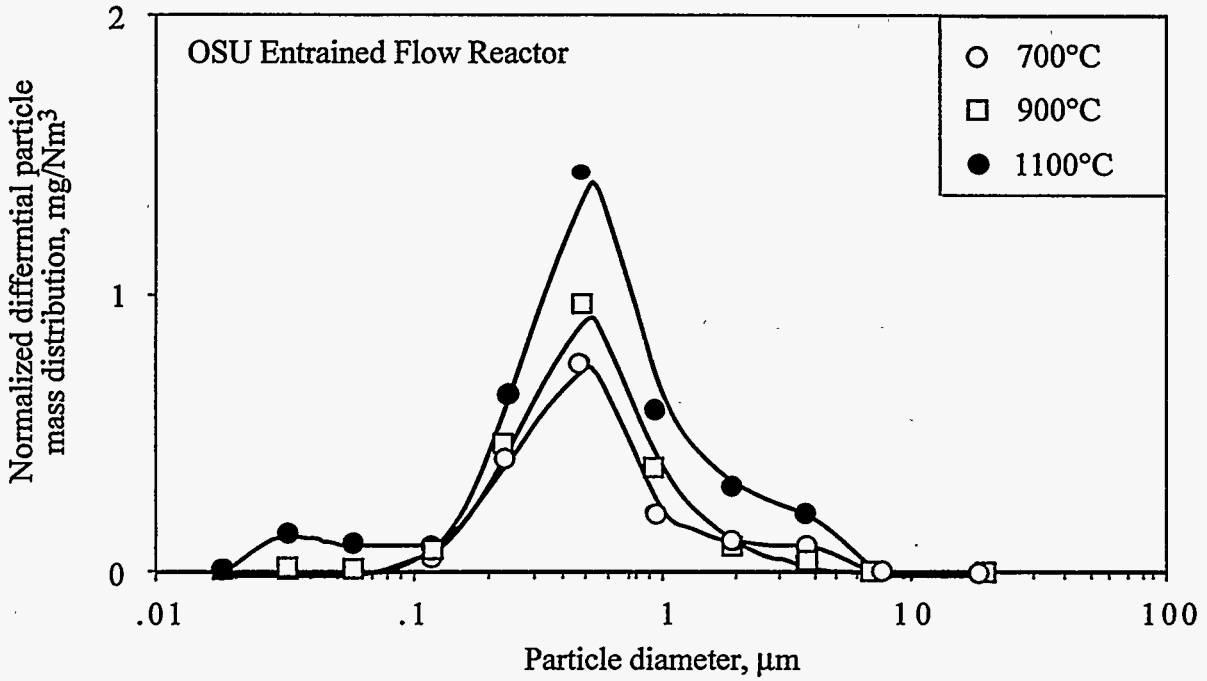

Figure 4-7. Normalized differential particle size distributions for fume particles measured in LEFR experiments with 100 µm dry black liquor particles burned in air.

The distributions of sodium, potassium, chloride, and sulfate in these fume particles are shown in Figure 4-8. These results show that the distributions of the four species are very similar at 700°C, with maxima at about 0,5 μm. At 900°C, small potassium and chloride peaks appear at about 0.03 μm, and at 1100°C are much larger. These peaks are the potassium and chloride present as vapor entering the collector which condense as fine aerosols during quenching.

4.4.1 Assessment of Sodium Release During Devolatilization

The experimental data on sodium release from pyrolyzing and burning black liquor particles falls into two categories. With single droplets of the size typically burned in recovery boilers, 10-30% of the Na in the black liquor was lost from the char residue. These results are based on the work of Volkov et al. (5) Verrill et al. (6), Frederick and Hupa (12), and this work. Fume particles were not collected or measured in any of these experiments.

With ~100 μm dry black liquor particles pyrolyzed or burned in laminar entrained-flow reactor and grid heater experiments, there was little or no Na loss at lower temperatures, i.e. 700°C and below. The experiments of McKeough et al. (7) showed clearly no Na loss. The experiments conducted in this project showed that less than 3% of the Na in black liquor solids was collected as sub-micron fume at 700°C in either N_2 or low oxygen content environments. Further, the inorganic fume collected at 700°C was mainly NaCl and KCl (9), suggesting that fume formation at these low temperatures may be mainly vaporization of these salts. The greater loss of Na from the larger droplets during devolatilization is most likely due to loss of black liquor or char fragments as the particles react as suggested by Verrill et al. (6,10); and Kauppinen et al., (11).

Kauppinen et al. (4), who measured the size distribution of fine particles from black liquor combustion in the gases from both recovery boilers and a laboratory entrained flow reactor, reported a bimodal distribution, with peaks in the range 0.1-1 μm and 1-30 μm. The smaller particles were clearly fume particles but the larger ones may have been formed by fragmentation of burning droplets or other mechanisms of breakup of burning black liquor droplets. Fragmentation during devolatilization has recently been reported in coal pyrolysis and combustion as well (13). At 700-800°C, reduction of Na_2CO_3 during devolatilization cannot proceed rapidly enough, based on the kinetic data reported by Li and van Heiningen (14), to account for 10-30% loss of sodium from a black liquor droplet during devolatilization.

We therefore suggest that there are three mechanisms of sodium loss from black liquor particles during ***devolatilization*** of black liquor:

1. vaporization of NaCl, forming sub-micron fume particles. This can occur at the lower temperatures at which many of the sodium release experiments were conducted.

2. Ejection or shedding of small liquor particles or char fragments from droplets during drying and devolatilization. These would form particles larger than the typical 0.1-1 μm fume particles

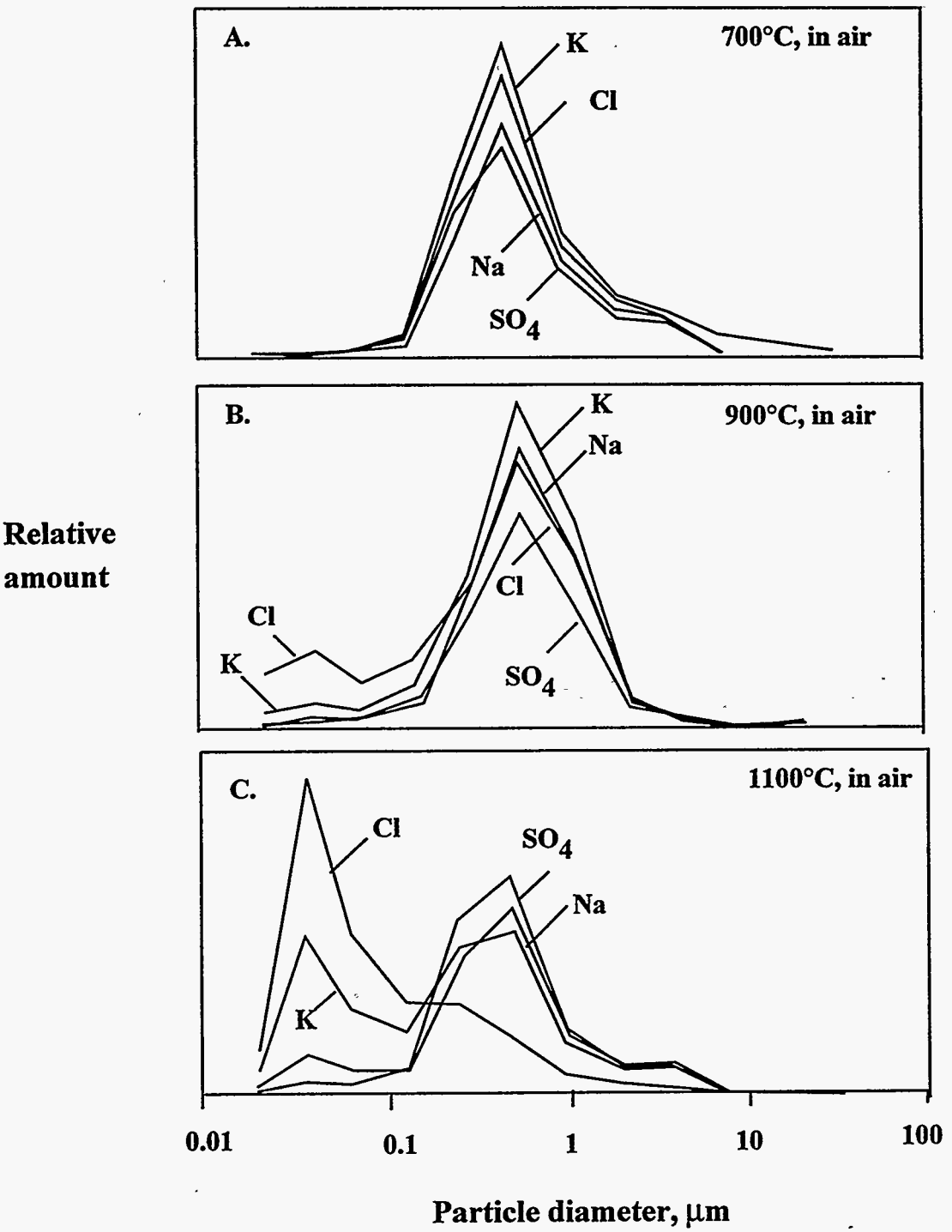

Figure 4-8. Differential size distribution of sodium, potassium, chloride, and sulfate in fume particles collected in LEFR experiments. Conditions were combustion of 100 μm particles in air at the temperatures indicated.

3. Reduction of Na_2CO_3 during devolatilization. This would occur to a significant extent only at higher furnace temperatures, where droplets are charred on the outside while still pyrolyzing on the inside, and where temperatures are high enough for Na_2CO_3 reduction to occur rapidly.

The relative importance of each of these depends upon the temperature of the gases very near the particle and the particle heating rate.

4.4.2 Na Release During Char Burning and Gasification

The data strongly supports Na_2CO_3 reduction as the source of Na fume during char burning. The work of Li and van Heiningen (14) showed that reduction of sodium carbonate in black liquor char can account for the loss of sodium from char. The experimental results for char reactions obtained in this study are consistent with that mechanism. Li and van Heiningen (14) indicated that Na volatilization from black liquor char could be suppressed completely in the presence of CO at 800°C and below. Data obtained in this project (Figures 4-6, 4-9) indicates that suppression occurs with either CO or CO_2 at 800°C and below but not at higher temperatures.

Reduction of Na_2CO_3 may also proceed according to reaction 4-1. However, the equilibrium sodium vapor partial pressure from the reduction of Na_2CO_3 with carbon is much greater than that obtained by reduction with Na_2S. Therefore Na_2CO_3 will be reduced by Na_2S only after the fixed carbon has been consumed.

$$Na_2CO_3 + 1/4\ Na_2S \ <=>\ 2\ Na + CO_2 + 1/4\ Na_2SO_4 \qquad (4\text{-}1)$$

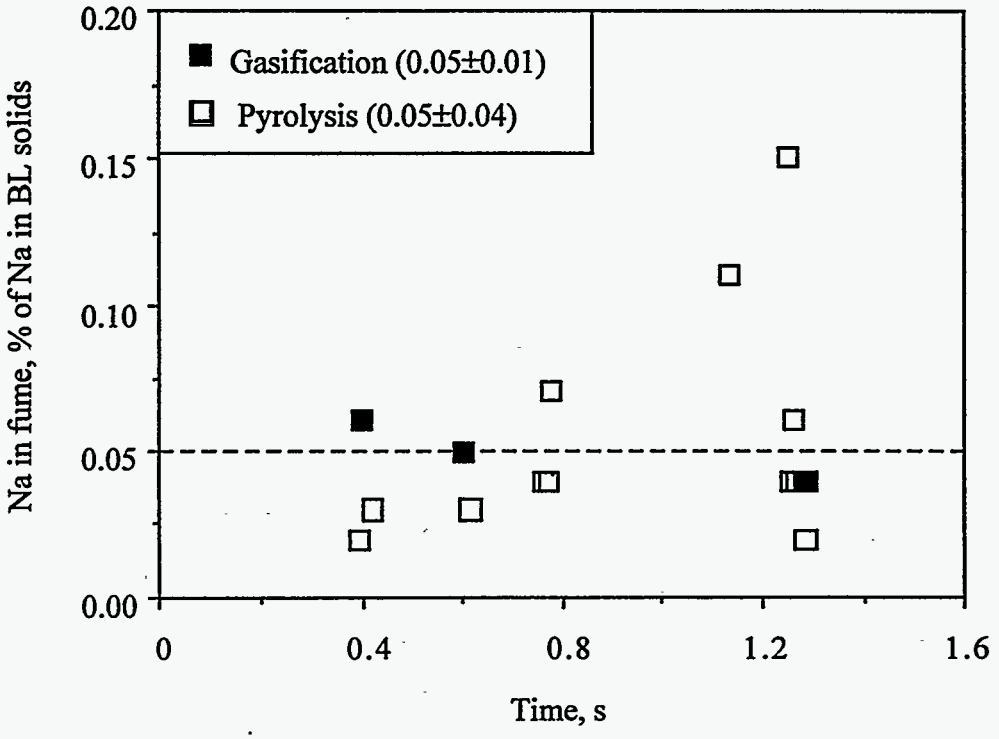

Figure 4-9. Sodium volatilized versus reaction time for 100 μm particles of a kraft black liquor pyrolyzed or gasified at 1000°C. Open symbols are for runs made in N_2; solid symbols are for runs made in 20% CO_2, 20% H_2O(v), 10% CO, 10% H_2, 40% N_2.

4.5 MODELING SODIUM VOLATILIZATION

Devolatilization

The model for sodium release during devolatilization is as follows:

1. no sodium is vaporized during devolatilization, and

2. sodium release from black liquor droplets does occur by fragmentation of the droplets.

The best way currently available to estimate the amount of sodium in these fragments is to use the data in the inset of Figure 4-3 as the total sodium lost from the droplets by fragmentation and by vaporization during char burning, and then subtracting the amount of sodium released by Na_2CO_3 reduction and NaCl vaporization after devolatilization and within the 10 seconds exposure of the droplets to the furnace temperature at each temperature. The results, for temperatures 700-1000°C, are shown in Table 4-3. Except for the point at 1000°C, these results suggest that the loss of sodium from the droplets during devolatilization as char fragments is 13-14% of the sodium initially in the droplets. The lower value at 1000°C may be because substantial sodium was volatilized from the charred outer droplet surface while devolatilization was still under way within the droplet at this highest experimental temperature.

Table 4-3. Estimation of sodium loss from black liquor droplets via Na_2CO_3 reduction versus via fragmentation.

Furnace temperature, °C	Na lost in 10 seconds at the indicated temperature, % of Na in BLS		
	Total	From Na_2CO_3 reduction	From fragmentation
700	13.0	0.0	13.0
800	14.6	0.5	14.1
900	16.4	3.4	13.0
1000	20.0	13.1	6.9

Char Burning

The rate of sodium vapor generation via Na_2CO_3 reduction during char burning is controlled by a combination of kinetic, pore diffusion, and gas-phase transport. The kinetic rate of Na_2CO_3 reduction in black liquor char reported by Li and van Heiningen (14) is described by Eqn. 4-2.

$$\frac{d[Na_2CO_3]}{dt} = 10^9 [Na_2CO_3] \exp\left(\frac{-244000}{RT}\right) \quad (4\text{-}2)$$

Pore diffusion and film mass transfer are accounted for by Eqns. 2-17 to 2-19 and 2-22 to 2-24 in Chapter 2.

Inhibition of reduction by CO or CO_2 is neglected at recovery furnace temperatures.

A model for vaporization of NaCl during char burning is described in the following section on chloride release.

4.6 ASSESSMENT OF NEEDS

To date, only limited data has been obtained on sodium volatilization in which the sodium balances were closed. Data in which a high degree of sodium balance closure needs to be obtained at the temperatures and gas compositions of interest in recovery boilers to test and validate the models for sodium volatilization.

The release of sodium from black liquor droplets as fragments of the droplets or resulting char particles needs to be confirmed experimentally.

The effect of carbonate/fixed carbon ratio in char on Na_2CO_3 reduction rate need to be determined.

A theoretical method for predicting the rate of diffusion of species generated within a char particle out of the particle needs to be developed.

4.7 REFERENCES

1. Borg, A., Teder, A., Warnqvist, B., *Tappi*, 57(1):126-129 (1974).

2. Pejryd, L., and Hupa, M., "Bed and furnace gas compositions in recovery boilers - advanced equilibrium calculations," *Proc. 1984 TAPPI Pulping Conf.*, San Fransisco, Nov., 1984.

3. Cameron, J. H. *Chem. Eng. Comm.*, 59: 243-257 (1988).

4. Kauppinen, E. I., Mikkanen, P., Jokiniemi, J.K., Iisa, K., Boonsongsup, L., Sinquefield, S. A. , Frederick, W. J. "Fume Particle Characteristics and Their Reactions With SO_2 at Kraft Recovery Boiler Conditions" Proc. 1993 TAPPI Engineering Conf., TAPPI Press, Atlanta, p. 369-376.

5. Volkov, A.D., Evseev, O.D., Ibatullina, R.I., Dravolina, E.I., Mezhvuz. Sb. Nauchn. Tr. Ser. Khim. Teknol. Tsellyul. no. 7, 72-5 (1980), Institute of Paper Chemistry translation to English.

6. Verrill, C.L., Nichols, K.M., "Inorganic aerosol formation during black liquor drop combustion." Presented at the 1993 AIChE Annual Meeting, St. Louis, November, 1993.

7. McKeough, P., Pyykönen, M., Arpiainen, V., Rapid pyrolysis of kraft black liquor, Part 2. Release of sodium. To be published in *Paperi ja Puu*, 1995.

8. Kymäläinen, M., Janka, K., Keskinen, J., Moisio, M., Backman, R., Hupa, M., Electrical low pressure impactor measurement of released fume particles in black liquor pyrolysis. To be published in *J. Pulp Paper Sci.*, 1995.

9. Frederick, W. J. Iisa, K. Wåg, K. J. Reis. V. V. Boonsongsup, L. Hupa, M. Forssén, M., 1995, Sodium and sulfur release and recapture during black liquor burning. Report to the U.S. Department of Energy, in press.

10. Verrill, C.L., Wessel, R.A., Sodium loss during black liquor drying and devolatilization: The application of laboratory data to understanding fume formation in recovery boilers. Paper 5.b.4, 1995 TAPPI-CPPA Intl. Chem. Recovery Conf., Toronto, April 24-27.

11. Kauppinen, E.I., Mikkanen, M.P., Valmari, T., Jokiniemi, J.K., Sinquefield, S.A., Frederick, W.J., Hupa, M., Backman, R., Forssén, M., Mckeough, P., Arpiainen, V., Pyykönen, M., Moisio, M., Keskinen, J., Mäkinen, M., "Sodium release during black liquor pyrolysis: Differences between the results from various laboratory-scale experiments. Paper 5.b.5, 1995 TAPPI-CPPA Intl. Chem. Recovery Conf., Toronto, April 24-27.

12. Frederick, W.J., Hupa, M., "Combustion Parameters for Black Liquor." Report to the U.S. Department of Energy, US DOE Report DOE/CE/40936-T1 (DE94007502), April, 1993.

13. Baxter, L.L., Mitchell, R.E., Fletcher, T.H., "Experimental determination of mineral matter release during coal devolatilization," Proc. Seventh Ann. Intl. Pittsburgh Coal Conference, p. 62-71 (Sept. 10-14, 1990).

14. Li, J. and van Heiningen, A.R.P., *Tappi Jl.*, 73(12):213-219 (1990).

CHAPTER 5. VOLATILIZATION OF POTASSIUM AND CHLORIDE DURING BLACK LIQUOR PYROLYSIS AND COMBUSTION

5.1 INTRODUCTION

Potassium and chloride are minor components in black liquor but they play a major role in the formation and hardening of deposits and in plugging of recovery boilers. These two elements are volatilized during combustion of black liquor. The dust captured by electrostatic precipitators is enriched in potassium and may or may not be enriched in chloride. Deposits in the superheater region of recovery boilers are often not enriched in these elements, while deposits in the colder regions are (1). The mechanisms involved in potassium and chloride volatilization have not previously been well understood.

In this chapter we present the results of an experimental investigation of potassium and chloride volatilization during pyrolysis and combustion of black liquor. We also present a model for predicting the rates of volatilization of K and Cl during combustion, compare the model predictions with the experimental data, and interpret them with respect to enrichment in recovery boilers.

5.2 EXPERIMENTAL

The pyrolysis and combustion experiments were conducted in the laboratory scale laminar entrained-flow reactor described in Chapter 2. For the experiments, we used dried particles of a southern pine kraft black liquor. The original liquor was dried in an oven, ground in a jar mill, and sieved to the desired 90-125 μm diameter. The composition of the liquor solids are shown in Table 5-1. All the experiments present in this work were performed under the conditions described in Table 5-2.

Table 5-1. Elemental composition of dried black liquor solids

Element	%
Carbon	34.90
Hydrogen	3.05
Oxygen *	35.21
Sodium	22.65
Sulfur	2.90
Potassium	0.62
Chloride	0.67

* Calculated by difference

Table 5-2. Conditions for the LEFR experiments

Experimental Conditions	
Kraft Black Liquor Solids	90-125 μm
Reactor Temperature	700-1100°C
Oxygen Content	0%, 4%, and 21% O_2
Residence Time	0.5 sec.
Feeding Rate	0.5 g of BLS/min.
Heating Rate	10^4 - 10^5 °C/sec.
Chemical Analysis	Ion Electrode and Capillary Electrophoresis

The concentration of sodium, potassium, and chloride in the fume samples were determined by ion-selective electrodes and capillary electrophoresis. The electrodes used for potassium and sodium analysis were manufactured by Corning, and the one used for chloride analysis by Orion. The capillary electrophoresis analysis were performed in a Dionex CES capillary electrophoresis system using a conventional fused-silica capillary.

Replicate LEFR runs were made at most of the experimental conditions. Typical data for the sodium, potassium, and chloride collected as fine particles on the filter at a wide range of furnace temperature and oxygen content are shown in Table 5-3. Both, the amounts of sodium, potassium, and chloride collected per mass of black liquor solids fed in these runs and the ratios of K/Na and Cl/Na in the fine particles collected were reasonably reproducible.

Table 5-3. Reproducibility of the Na, K, and Cl content of the fine particle samples collected in typical replicate experiments.

Run	Furnace Temperature, °C	O_2 content (%)	Elemental content of fine particles (% of element in black liquor solids)				
			Na	K	Cl	K/Na	Cl/Na
18	700	0	0.21	4.12	21.00	19.60	100.00
19	700	0	0.19	3.06	16.90	16.10	84.70
3	900	4	3.03	3.90	28.80	1.29	9.50
4	900	4	2.51	3.18	23.40	1.27	9.32
7	1100	21	29.70	40.30	95.40	1.36	3.21
8	1100	21	25.6	26.90	72.00	1.05	2.81

5.3 RESULTS AND DISCUSSION

5.3.1 Particle Characteristics

Figures 5-1 and 5-2 are scanning electron micrographs of typical char and fume respectively. Char is usually a large (>100 μm), spherical and porous particle. Fume particles, on the other hand, are very small (about 1 μm) and non-porous particles. The solid black liquor particles, when pyrolyzed, swelled to about 3-4 times their initial diameter. Studies on swelling characteristics of the original black liquor were also performed. This liquor behaved as an average liquor, swelling about 3 times its initial droplet diameter (maximum specific swelling volume of 35 cm^3/g).

5.3.2 Inorganic Fume Generation

The percentage of the black liquor solids input to the LEFR that was collected as fine particles on the post-cyclone filter is shown in Table 5-4, and the percentages of Na, K, and Cl inputs that were collected on the post-cyclone filter are shown in Figures 5-3 to 5-6. In low gas-phase oxygen concentrations, the total fume collected and the fraction of sodium recovered as fume increased rapidly with temperature in these experiments (Table 5-4). The data in these figures indicates that more inorganic fume was generated in the absence of oxygen than at 4% O_2. This apparent anomaly is the result of small char fragments being carried through the cyclone and collected on the fine particle filter during the runs made in nitrogen only (2). This hypothesis was supported by the very black appearance of the fume collected on the filter as compared with the much lighter colored fumes collected in experiments at 4 and 21% O_2. These char particles would contain sodium, potassium, and chloride, and would result in the apparently higher fractions of black liquor solids, Na, K, and Cl captured as fume under these conditions.

To estimate the amount of fixed carbon collected, the inorganic composition and the fixed carbon content of the filter catch were calculated based on the amount of solids collected on the post-cyclone filters and the analysis of sodium, potassium and chloride content of these solids. In these calculations, it was assumed that all the alkali metal (potassium and sodium) not in the form of chloride salt was in the form of either carbonate or sulfate, and total mass, species, and charge balances were forced to close. The results are included as Table 5-4. The results were that fixed carbon was present in the post-cyclone filter catch in only those runs made with 0% O-2 in the gas phase, and that the amount of fixed carbon collected decreased with increasing reactor temperature.

Figures 5-3 to 5-5 show the amounts of sodium, potassium, and chloride collected on the post-cyclone filter as percentages of the amounts of these elements in the black liquor solids fed to the LEFR. The data are at different temperature and oxygen content in the gas. These results show that both temperature and the oxygen content of the reaction gas can have a great effect on fuming.

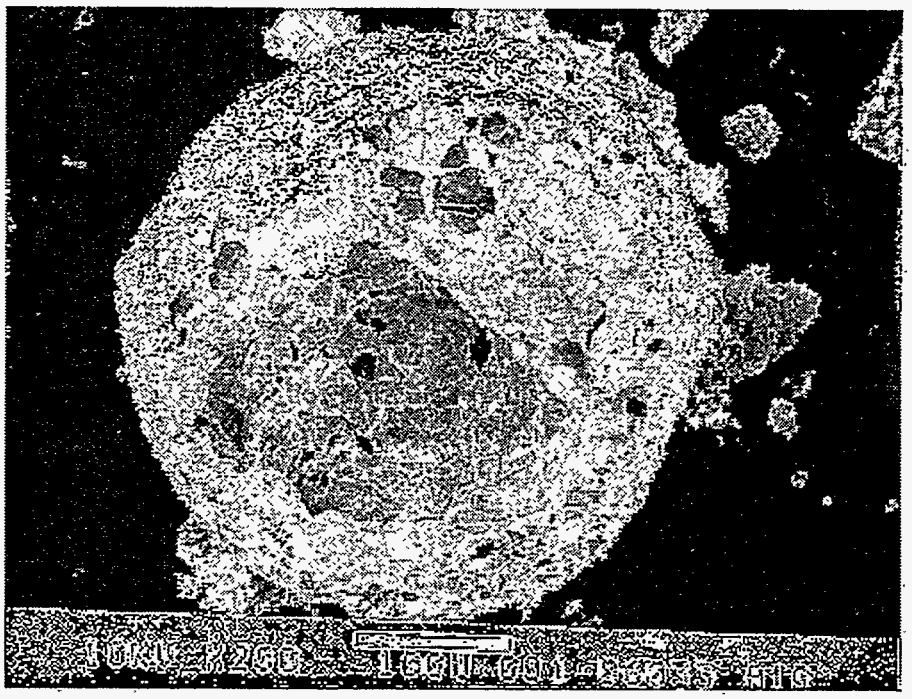

Figure 5-1. Typical SEM micrograph of black liquor char

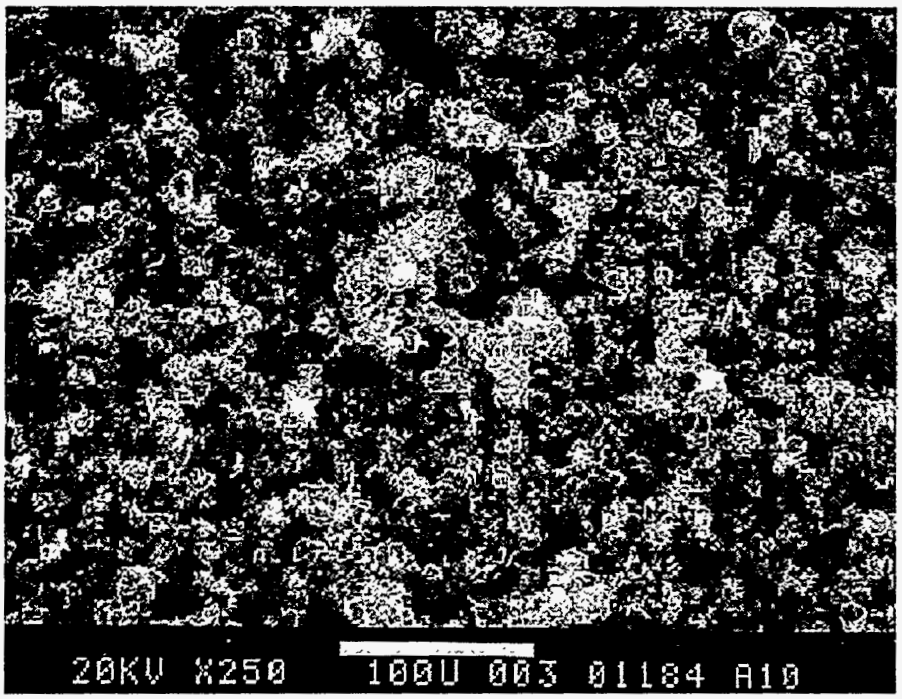

Figure 5-2. Typical SEM micrograph of black liquor fumes

Table 5-4. Composition of filter catch, weight %

T	O_2	Fume	Composition, mass %					
°C	%	% of BLS	Na	K	Cl	SO_4	CO_3	Fixed C
700	0	2.80	17.6	4.53	12.8	19.6	3.47	42.3
700	4	0.30	28.6	4.93	39.2	-	-	-
700	21	17.3	40.3	0.97	2.86	13.5	42.4	-
800	0	4.04	18.7	0.77	3.11	34.7	0.59	42.1
900	0	3.73	25.6	1.38	7.83	42.9	1.06	21.2
900	4	1.81	34.7	1.21	9.69	43.8	10.6	-
900	21	19.5	42.8	1.63	1.23	0	54.3	-
1000	0	8.26	23.9	0.88	4.97	43.1	0.68	26.5
1100	0	7.53	30.7	0.70	7.61	48.1	4.16	13.1
1100	4	9.01	37.5	1.09	4.31	29.1	28.0	-
1100	21	17.1	36.9	1.21	3.29	33.1	25.5	-

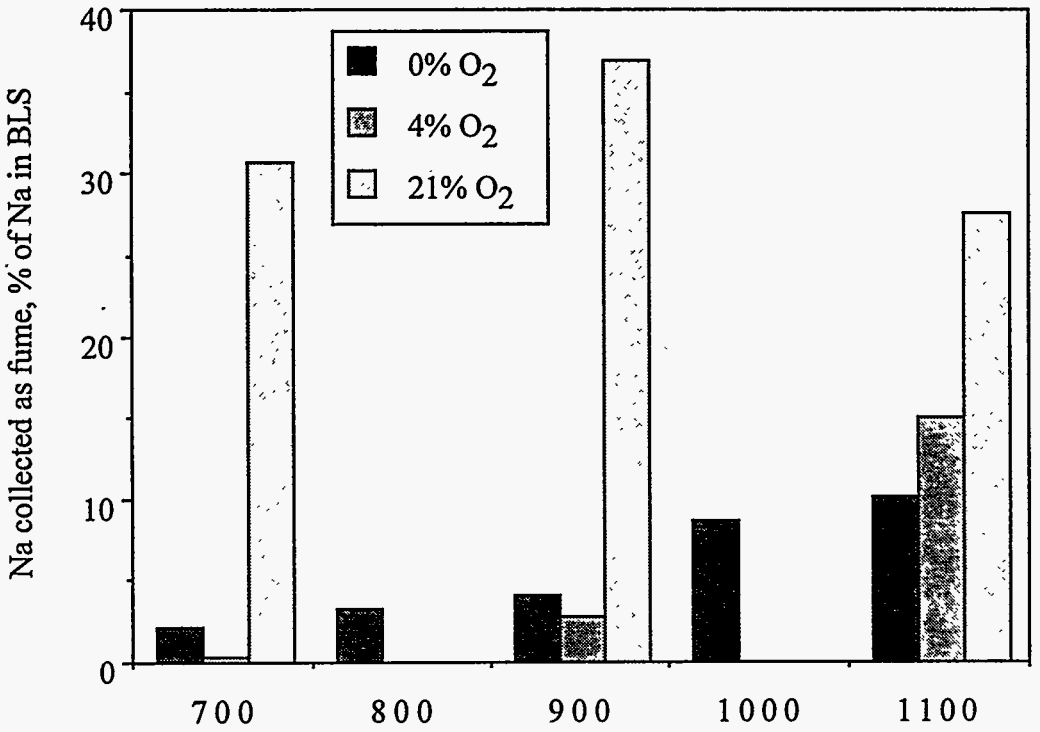

Figure 5-3. Sodium collected as fume during pyrolysis of 100 μm dry black liquor particles in N_2 in a laminar entrained-flow reactor, 0.4-0.6 s residence time.

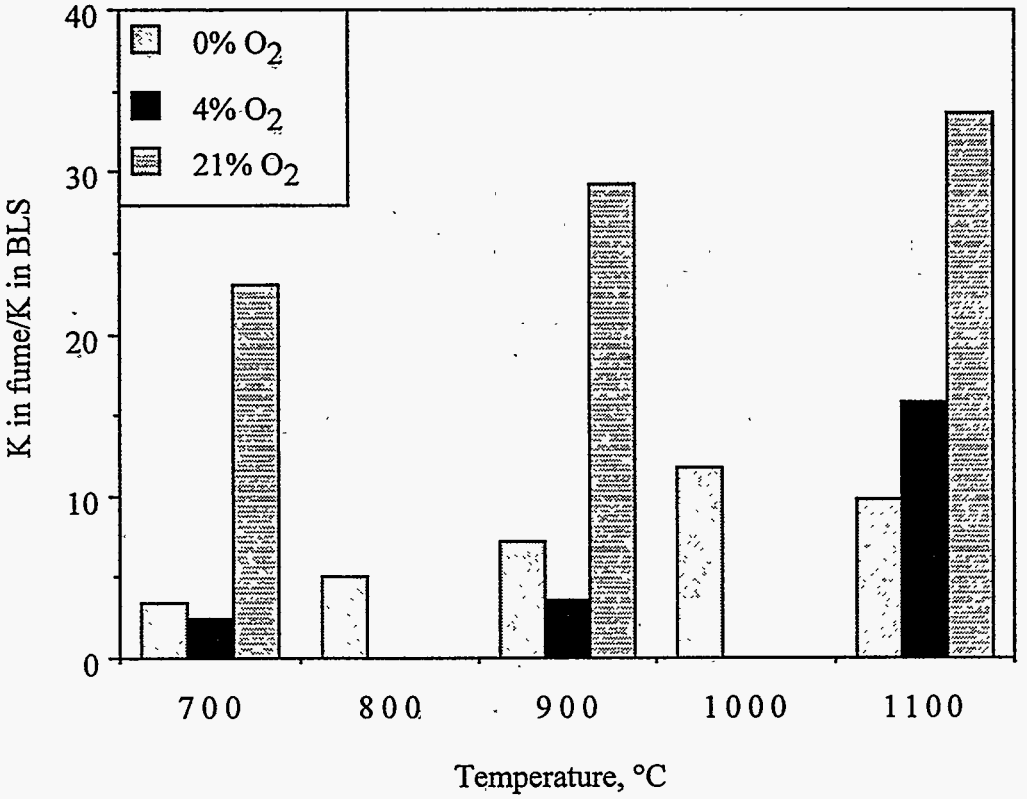

Figure 5-4. Potassium collected as fume during pyrolysis of 100 μm dry black liquor particles in N_2 in a laminar entrained-flow reactor, 0.4-0.6 s residence time.

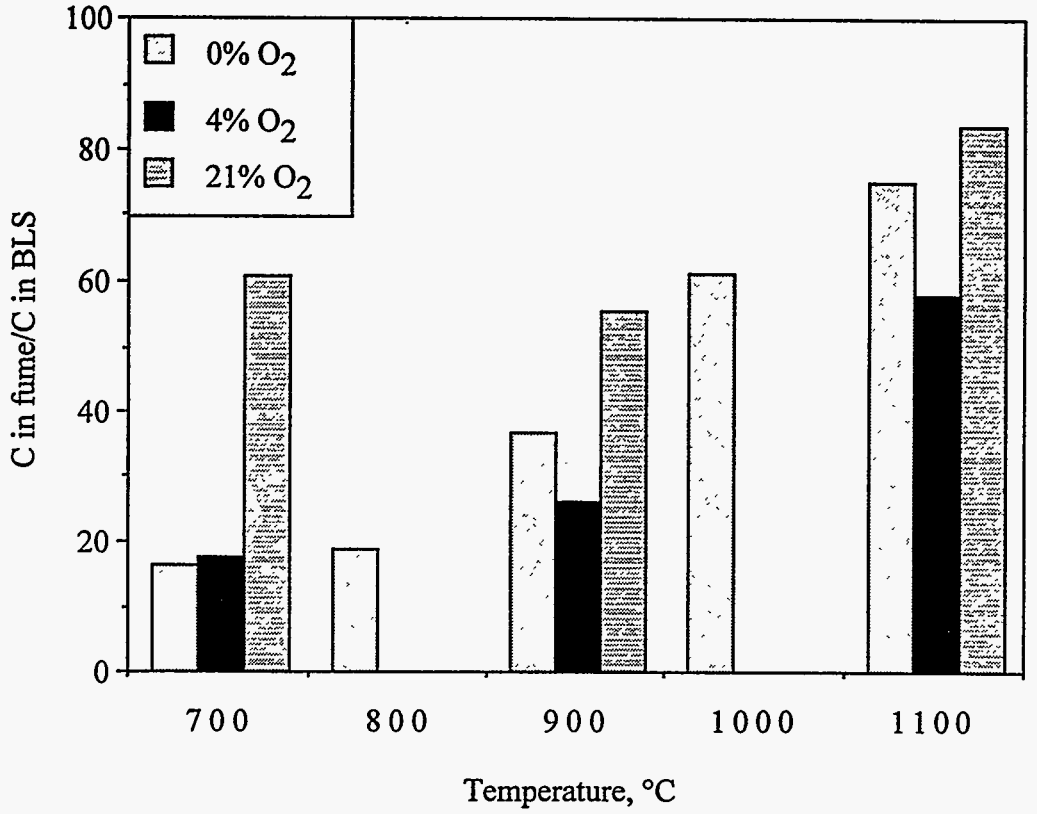

Figure 5-5. Potassium collected as fume during pyrolysis of 100 μm dry black liquor particles in N_2 in a laminar entrained-flow reactor, 0.4-0.6 s residence time.

5.3.3 Potassium and Chloride Enrichment

The potassium enrichment factor is defined as the ratio of the concentration of potassium to that of sodium in fume divided by the ratio of potassium to sodium in the black liquor, or

$$\text{Potassium Enrichment Factor} = \frac{\left[\frac{\text{K in Fume}}{\text{Na in Fume}}\right]}{\left[\frac{\text{K in BLS}}{\text{Na in BLS}}\right]} \tag{5-1}$$

An analogous definition is valid for the chloride enrichment factor,

$$\text{Chloride Enrichment Factor} = \frac{\left[\frac{\text{Cl in Fume}}{\text{Na in Fume}}\right]}{\left[\frac{\text{Cl in BLS}}{\text{Na in BLS}}\right]} \tag{5-2}$$

Using this definition, we calculated the potassium and chloride enrichment factors for several experimental conditions. For potassium, the greatest enrichment factor, over 15, was obtained at 700°C in nitrogen, as shown in Figure 5-6. At higher temperatures the enrichment factor was smallest. The general trend is that at a higher temperature, the enrichment decreases to the point that no potassium enrichment was obtained at 1100°C. Another interesting finding is that there was virtually no potassium enrichment in air at any temperature.

For chloride, Figure 5-7, a similar trend was found but even higher enrichment factors were obtained. An enrichment factor of about 80 in nitrogen at 700°C was achieved. Some enrichment was obtained in air, an enrichment factor of about 3, but it did not seem to be affected by the reactor temperature.

5.3.4 Proposed Mechanism of Potassium and Chloride Volatilization

Cameron (3) suggested that fuming processes involves salt vaporization and that sodium and potassium chloride vaporization are responsible for potassium and chloride enrichment observed in the fume. Cameron demonstrated this by comparing measured sodium chloride vaporization rates from molten salt pools with calculated values. The calculated rates were based on Raoult's Law (Equation 5-3) after assuming that the vaporization of sodium chloride is an equilibrium process, the smelt is an ideal system, and the gas stream is saturated with sodium chloride.

$$P_{NaCl}(T) = P^{*}_{NaCl}(T)\, X_{NaCl} \tag{5-3}$$

where: $P_{NaCl}(T)$ = equilibrium partial pressure of NaCl at temperature T
$P^{*}_{NaCl}(T)$ = vapor partial pressure of pure NaCl at temperature T
X_{NaCl} = mole fraction of NaCl in smelt

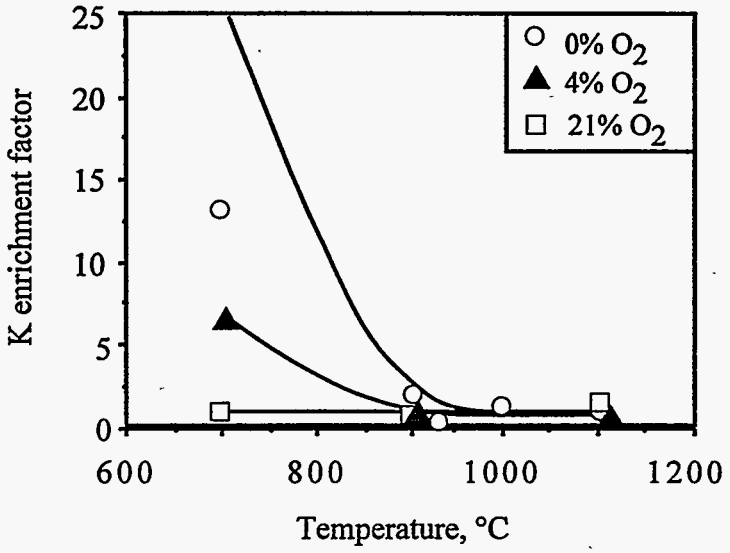

Figure 5-6. Potassium enrichment factors versus temperature at three different oxygen contents. The lines in the figure are calculated from the enrichment factor model.

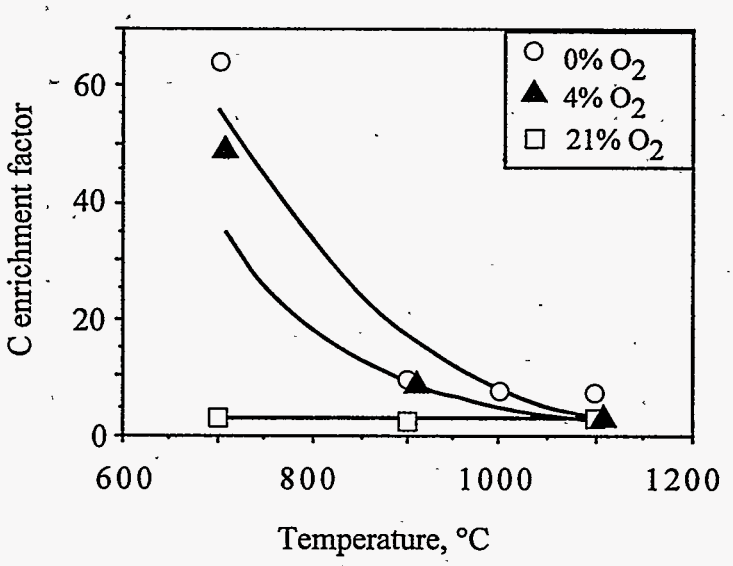

Figure 5-7. Chloride enrichment factors versus temperature at three different oxygen contents. The lines in the figure are calculated from the enrichment factor model.

Potassium volatilization could also occur by reduction of K_2CO_3, analogous to the process by which Na_2CO_3 is reduced (see Chapter 4). The reaction is:

$$K_2CO_3 + 2C \Leftrightarrow 3CO + 2K_{(v)} \tag{5-4}$$

A model was developed based on the above assumptions to predict the rates of volatilization of potassium and chloride and the theoretical potassium and chloride enrichment during black liquor combustion. The rates of NaCl and KCl vaporization were calculated by assuming that mass transfer across the gas film adjacent to the burning particles was the rate-limiting step and that the vapor pressures of NaCl and KCl in the bulk gas are negligible, so that

$$dCl/dt = dNaCl/dt + dKCl/dt = k_{g,NaCl} A_{ext} (P_{NaCl} + P_{KCl}) \tag{5-5}$$

The partial pressures of NaCl and KCl at the particle interface were assumed to be in equilibrium with an inorganic phase consisting of the Na^+, K^+, Cl^-, CO_3^{2-}, S^{2-},and SO_4^{2-} in the particle. In the results presented here, P_{NaCl} and P_{KCl} were calculated using the chemical equilibrium program HSC Chemistry.

The rate of potassium volatilization, dK/dt, was calculated as the sum of the rate of vaporization of KCl and the rate of potassium volatilization from reduction of K_2CO_3. Reduction of K_2CO_3 was treated as a reversible chemical reaction occurring within the particle, with carbonate reduction proceeding at a rate predicted by equation 4-2 multiplied by the ratio of K/Na in the particle. The overall rate of volatilization of potassium vapor formed by K_2CO_3 reduction was assumed to be limited by diffusion from the particle and transport across the gas boundary layer adjacent to the particle. The diffusion and transport processes were modeled according to equations 2-17 to 2-19 and 2-22 to 2-24 in Chapter 2.

The theoretical chloride enrichment factor is defined by the ratio of sodium chloride and potassium chloride vaporization rate and the rate of sodium released by the sodium carbonate reduction and NaCl volatilization.

$$\text{Chloride Enrichment Factor} = \frac{\int\left(\frac{dNaCl}{dt}\right)dt + \int\left(\frac{dKCl}{dt}\right)dt}{\int\left(\frac{dNa}{dt}\right)dt + \int\left(\frac{dNaCl}{dt}\right)dt} \quad \frac{[Na]_{BLS}}{[Cl]_{BLS}} \tag{5-6}$$

where:

$\int\left(\frac{dNaCl}{dt}\right)dt$ = chloride or sodium released by NaCl vaporization, mol

$\int\left(\frac{dKCl}{dt}\right)dt$ = chloride released by KCl vaporization, mol

$\int\left(\frac{dNa}{dt}\right)dt$ = sodium released by carbonate reduction mechanism, mol

$[Na]_{BLS}$ = concentration of sodium in black liquor solids, mol %

$[Cl]_{BLS}$ = concentration of chloride in black liquor solids, mol %

The integrations are performed over the time at which the particles were in the hot zone of the furnace. The rate of sodium volatilization is calculated as described in Chapter 4.

The theoretical potassium enrichment factor can be defined by the ratio of potassium released by potassium chloride volatilization and by potassium carbonate reduction to that of sodium released by sodium carbonate reduction and NaCl volatilization.

$$\text{Potassium Enrichment Factor} = \frac{\left[\int\left(\frac{dKCl}{dt}\right)dt + \int\left(\frac{dK}{dt}\right)dt\right]}{\left[\int\left(\frac{dNa}{dt}\right)dt + \int\left(\frac{dNaCl}{dt}\right)dt\right]} \frac{[Na]_{BLS}}{[K]_{BLS}} \qquad (5\text{-}7)$$

where:

$\int\left(\frac{dKCl}{dt}\right)dt$ = potassium released by KCl vaporization, mol

$\int\left(\frac{dK}{dt}\right)dt$ = potassium released by carbonate reduction mechanism, mol

$\int\left(\frac{dNa}{dt}\right)dt$ = sodium released by carbonate reduction mechanism, mol

$\int\left(\frac{dNaCl}{dt}\right)dt$ = chloride or sodium released by NaCl vaporization, mol

$[Na]_{BLS}$ = concentration of sodium in black liquor solids, % mol

$[K]_{BLS}$ = concentration of potassium in black liquor solids, % mol

The model accounts for the reaction kinetics as well as film mass transfer and diffusion out of the particles, but it does not account for the suppression of sodium carbonate reduction by CO and CO_2. These suppression effects were expected to be negligible in our experiments because of the dilution effect of the reaction gas. When the particles were pyrolyzed in N_2, the concentrations of CO an CO_2 resulting from the pyrolysis products were low, of the order of 1000 ppm or less. At temperatures of 900°C and above, suppression of carbonate reduction by CO an CO_2 is not expected to be important (see Chapter 4).

Tables 5-5 and 5-6 compare the theoretical and experimental enrichment factors for chloride and potassium, respectively. The results show that the theoretical enrichment factor agreed well with the experimental values.

Table 5-5. Comparison of experimental and theoretical enrichment factors for chloride.

		Experimental	Theoretical
700°C	0% O_2	80.7	35.3
	4% O_2	56.8	44.0
	21% O_2	2.8	1.5
900°C	0% O_2	10.0	17.1
	4% O_2	9.4	9.4
	21% O_2	1.5	0.8
1100°C	0% O_2	8.4	2.7
	4% O_2	3.9	1.3
	21% O_2	3.0	0.8

Conditions: 100 μm BLS particle, 0.5 sec

Table 5-6. Comparison of experimental and theoretical enrichment factors for potassium.

		Experimental	Theoretical
700°C	0% O_2	16.7	40.2
	4% O_2	7.9	11.0
	21% O_2	0.9	1.0
900°C	0% O_2	2.0	2.6
	4% O_2	1.3	1.4
	21% O_2	0.8	0.9
1100°C	0% O_2	0.8	1.1
	4% O_2	1.1	1.0
	21% O_2	1.2	1.0

Conditions: 100 μm BLS particle, 0.5 sec

The main reason for the high enrichment factors at 700°C in N_2 is the low sodium release rate via Na_2CO_3 reduction at 700°C. In Figure 5-3, we showed the sodium in fume as a percentage of the sodium initially in the black liquor solids versus temperature at several oxygen contents. As temperature increased, the rate of sodium released increased, by as much as 18 times from 700°C to 1100°C in N_2. The release of chloride, Figure 5-5, is increased only by a factor of about 3.5 at the same conditions. In Figure 5-3, it can be observed that the release of sodium fume in air is high even at lower temperatures. There are two effects that could be acting simultaneously to increase the amount of sodium being released by carbonate reduction. One is the oxygen-enhanced fuming mechanism (3) and the other is the temperature of the burning char particles.

It has been reported that a small particle achieves higher surface temperature when burning in air compared with those at 0 and 4% O_2 (4,5). Frederick et al. (4) measured, for larger particles (3-10 mm), the surface temperature during char burning at several O_2/N_2 mixtures in an 800°C furnace. They concluded that surface temperature for droplets burned in air increases by 300-400°C above the furnace temperature during char burning, but only by about 40°C at 4% O_2 content.

At the much higher particle temperatures achieved in air, Na_2CO_3 reduction proceeds rapidly and sodium release is high compared with that of particles burned in 4% O_2 or pyrolyzed in N_2. The enrichment factor is highly dependent on sodium carbonate reduction which increases sharply with temperature. This resulted in a large fraction (25-35%) of the sodium in the black liquor solids being volatilized at the higher furnace temperature and O_2 content conditions, and it explains why there was almost no enrichment in air at any temperature. Figure 5-8 shows the effect of particle surface temperature on the potassium and chloride enrichment factors.

The behavior of potassium, Figure 5-4, is a mix of the behavior of both chloride and sodium. It is released as potassium chloride by volatilization and also as potassium vapor by the carbonate reduction mechanism.

The data obtained in this work suggests that the increase in sodium, potassium, and chloride release with increasing oxygen content is in fact a temperature effect due to the higher particle temperatures at higher O_2 partial pressures. Also, the carbonate reduction mechanism is limited by reaction kinetics instead of equilibrium on which the oxidation-enhanced fuming mechanism is based. If the resistance to mass transfer diffusion from the particle were higher, the oxygen-enhance mechanism could play a more important role on the release of sodium under oxidizing conditions.

5.3.5 Effect of SO_2 Partial Pressure

A series of three LEFR runs were made at 1100°C in which 0, 10, and 100 ppm SO_2 was included in the gases. In these runs, the chloride content of both the fume and char collected decreased with increasing SO_2 partial pressure as shown in Table 5-7. This indicates that NaCl and KCl in both the char and fume are being converted to HCl and sulfates. Based on these results, lower chloride enrichment factors would be expected at higher SO_2 partial pressures in recovery boilers.

Table 5-7. Chloride content of fume and char and chloride enrichment factors from LEFR runs made at 1100°C and various SO_2 partial pressures.

SO_2, ppm	0	10	100
Cl in fume, mg/g fume	15.60	14.20	11.60
Cl in char, mg/g char	25.00	12.90	9.20
Cl enrichment factor	2.53	1.56	1.12

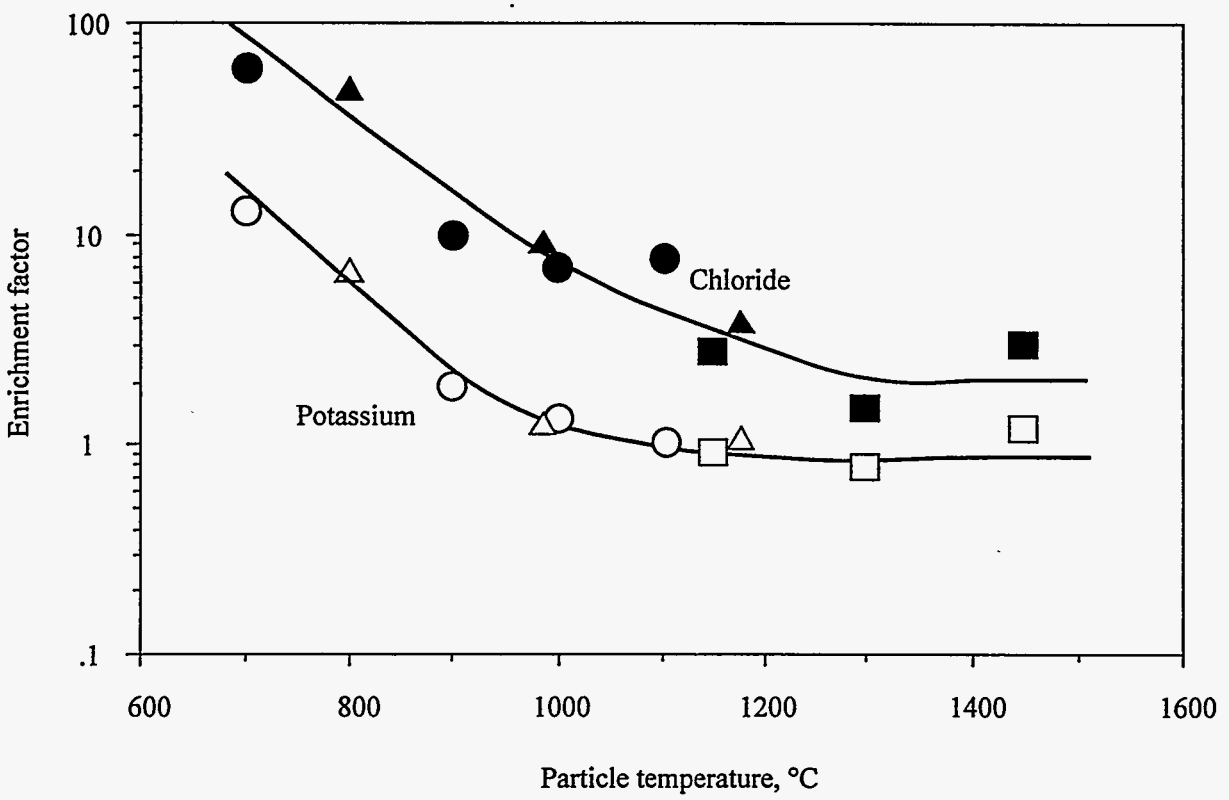

Figure 5-8. Effect of particle surface temperature on enrichment factors

5.4 ASSESSMENT OF NEEDS

As with the sodium data reported in Chapter 4, the material balance closure for potassium and chloride in the LEFR experiments is poor. Improved closure of the potassium and chloride material balances need to be accomplished to test and validate the models for potassium and chloride release.

Data on potassium and chloride release needs to be obtained at different residence times to test and validate the model.

The stability constant for the association of sodium ions with phenolic hydroxyl groups in lignin is lower than that for potassium ion. The effect of this difference on the formation of sodium and potassium carbonates, their subsequent reduction, and volatilization of Na(v) and K(v) needs to be established and incorporated into the model for potassium volatilization.

5.5 REFERENCES

1. Tran, H., Reeve, D. and Barnham, D., *Formation of Kraft Recovery Boiler Superheater Fireside Deposits,* Pulp Paper Canada 84(1):7-12 (1983).

2. Kauppinen, E.I., Mikkanen, M.P., Valmari, T., Jokiniemi, J.K., Sinquefield, S.A., Frederick, W.J., Hupa, M., Backman, R., Forssén, M., Mckeough, P., Arpiainen, V., Pyykönen, M., Moisio, M., Keskinen, J., Mäkinen, M., "Sodium release during black liquor pyrolysis: Differences between the results from various laboratory-scale experiments. Paper 5.b.5, 1995 TAPPI-CPPA Intl. Chem. Recovery Conf., Toronto, April 24-27

3. Cameron, J. H., *Vaporization from Alkali Carbonate Melts with Reference to the Kraft Recovery Furnace,* Pulp and Paper Sci. 14(4):76-81 (1988)

4. Frederick, W. J., Hupa, M., Stenberg, J. and Hernberg, R., *Optical Pyrometric Measurements of Surface Temperatures During Black Liquor Char Burning and Gasification,* In press

5. Hurt, R. and Mitchell, R., *On the Combustion Kinectics of Heterogeneous Char Particle Populations,* Twenty-Fourth Symposium (International) on Combustion, The Combustion Institute, 1992 pp. 1233-1241

CHAPTER 6. NITROGEN OXIDE FORMATION AND DESTRUCTION IN RECOVERY BOILERS

6.1 INTRODUCTION

The formation of NOx in combustion processes occurs by three independent mechanisms: thermal NOx, fuel NOx and prompt NOx. Thermal NOx involves the oxidation of nitrogen present in the combustion air by oxygen atoms. Prompt NOx involves the attack of a hydrocarbon free radical on N_2 in air and formation of HCN as an intermediate. Fuel NOx formation is due to the oxidation of nitrogen in the fuel.

During black liquor combustion in kraft recovery boilers, the fuel NOx mechanism has been found to be the leading NO formation pathway [1]. The formation of NO via this mechanism is dependent on several factors such as the type of black liquor, the nitrogen content, the type of furnace and the operating conditions.

The nitrogen contents of kraft black liquors range from 0.04 to 0.26 weight percent of dry black liquor solids, with an average of 0.11 wt. % [2]. Kraft black liquors have been found to contain heterocyclic nitrogen compounds [3], but an analysis of lignin, the main organic component of kraft black liquor, showed that the nitrogen was present almost exclusively as amino acids [4]. The nitrogen in the black liquor is of different form than in other fuels, and thus the mechanism of nitrogen devolatilization during black liquor combustion may be different from that in the combustion of other fuels.

Aho et al. [5,6] studied the release of nitrogen during the pyrolysis of black liquor using single droplets suspended in a tube furnace. Measurements with ten different black liquors indicated that 20-60 % of the nitrogen in the black liquor was released during pyrolysis. Approximately half of the nitrogen released was NH_3. Small amounts of NO (less than 5 % of the N released) were detected, and the rest was assumed to be N_2. No HCN was detected in the pyrolysis gases. The total release of NH_3 and NO during pyrolysis seemed to increase linearly with the nitrogen content of the black liquor. The amount of nitrogen released as NH_3 and NO during pyrolysis was found to be sufficient to explain typical NO emissions from recovery boilers.

As part of the recovery boiler modeling project, a study was undertaken to characterize the time evolution of nitrogen during black liquor pyrolysis. The study consists of three parts: study of black liquor pyrolysis in a laminar entrained flow reactor, study of NO destruction at recovery boiler conditions, and a simplified model explaining the results of the pyrolysis experiments.

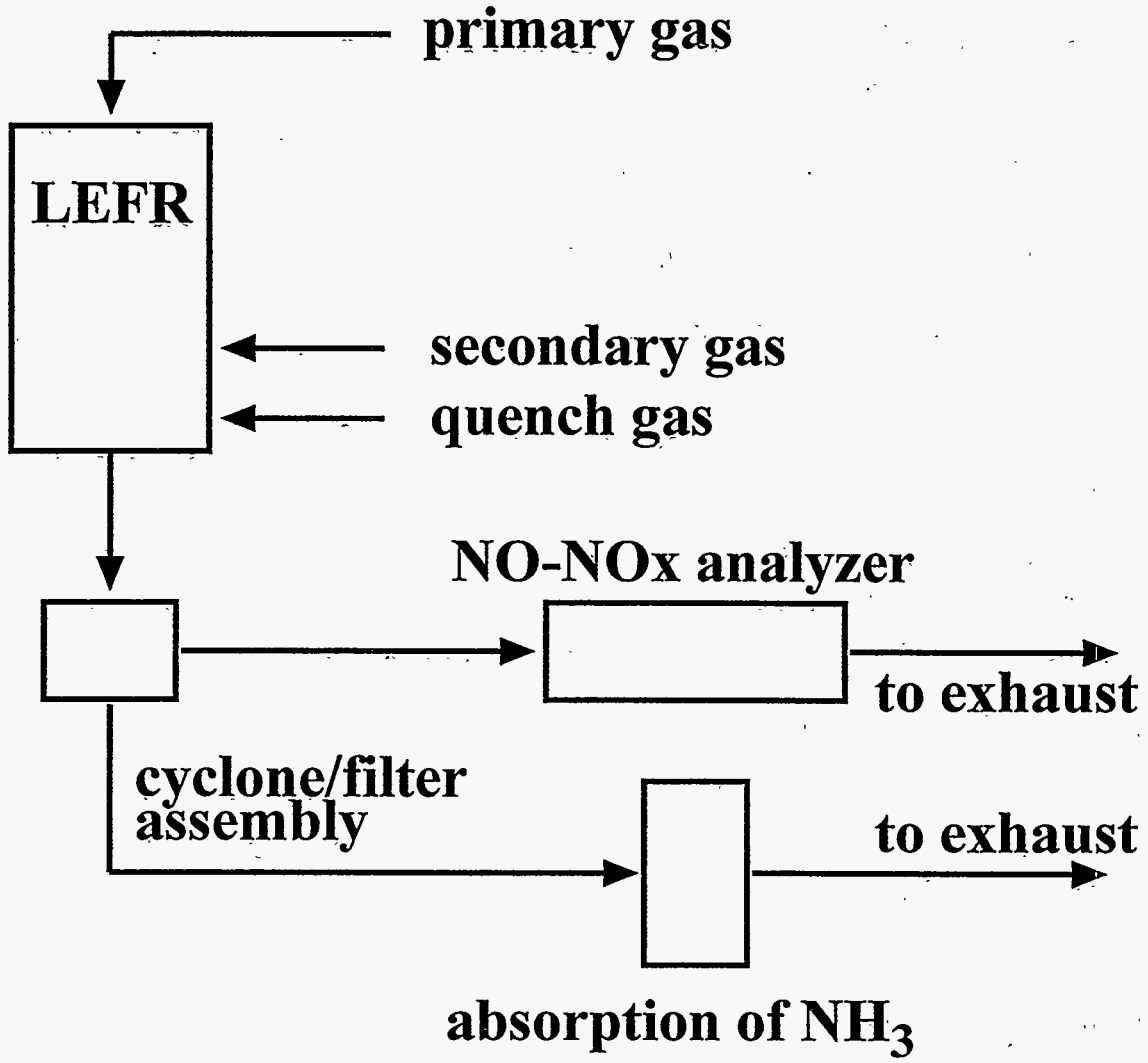

Figure 6-1. Experimental set-up for the black liquor pyrolysis experiments.

6.2 NITROGEN EVOLUTION DURING BLACK LIQUOR PYROLYSIS

6.2.1 Experimental

The experimental set-up used in this study is shown in Figure 6-1. It includes a laminar entrained flow reactor (LEFR), a cyclone/filter assembly, a chemiluminescence NO-NOx analyzer (NO-NOx meter), and an absorption bottle for NH_3 analysis.

The LEFR consists of two parts, the reactor and the collector. The reactor is a cylindrical ceramic tube made of mullite with an inside diameter of 70 cm. A three-zone tube furnace is used to heat up the reactor to a maximum temperature of 1150°C. Two gas flows, primary and secondary, enter the LEFR. The primary gas flow carries the black liquor particles through a water-cooled injector into the reactor. The secondary flow enters the LEFR through the bottom, is heated to the furnace temperature as it flows through the outer annulus of the reactor and enters the reactor through a flow straightener located at the top. The primary and secondary flows enter the reactor at equal gas velocities.

The gases and the particles exit the reactor through the collector. The collector can be moved inside the reactor to vary the reactor pathlength. The effective length of the reactor ranges from 10 to 75 cm. Equivalent particle residence times range from 0.3 to 2 seconds depending on the furnace temperature and the gas flow rates employed. The outer part of the collector consists of a layer of ceramic insulation and a two-pass shell for cooling water. The inner wall of the collector is porous to allow for the distribution of a quench gas. The major part of the quench gas enters through the tip of the collector to provide rapid cooling of the reactor effluent. The rest enters through the entire length of the collector to prevent particles from depositing on the collector walls.

The gas and particles from the LEFR flow into the cyclone/filter assembly in which course particles (char) and fine particles (fume) are collected. The cut size of the cyclone is 3 μm. From the filter the gas flows into the absorption bottle and the NO-NOx analyzer. A more detailed description of the LEFR is given by Sricharoenchaikul et al. [7].

A typical experiment lasted 5 minutes during which a total of 1.5-5 g of black liquor solids were fed. NO was measured continuously from the off-gases and the readings were recorded every 2 seconds by a data acquisition program. The NO readings were integrated to give the total amount of NO formed. The NH_3 in the absorption bottle was analyzed using an ion selective electrode. The total nitrogen content of the char particles were determined using the Kjeldahl method at the Oregon State University Plant Analysis Laboratory in the Department of Soil Science. The nitrogen content of the fume particles was measured in some experiments as well but the fume was found to contain no N.

This study involved one black liquor: a southern pine liquor obtained from a kraft pulp mill in Georgia. Black liquor solids (BLS) were obtained by drying the liquor in shallow pans and grinding the resulting dry solids to fine particle sizes. The particle size range used was 90-125 μm.

The elemental analysis of the BLS is presented in Table 6-1. The total nitrogen analysis of five samples of the BLS gave values of 0.126, 0.118, 0.105, 0.108 and 0.097 % by weight. The average nitrogen content of 0.11 wt. % was used in calculations. The other elements were analyzed by the Technology Center of Weyerhaueser Company.

Pyrolysis experiments were made at temperatures 600-1100°C and residence times 0.3-1.7 s. Each operating condition was run in duplicate or triplicate. The reproducibility of the total N measurement was not good and thus the total nitrogen analysis of each char sample was made in duplicates. Some of these duplicate N analyses differed by more than 0.01 wt. % on a black liquor solids basis.

Table 6-1. Analysis of the black liquor solids

Element	wt.% of BLS
carbon (C)	35.70
hydrogen (H)	3.05
nitrogen (N)	0.11
sodium (Na)	22.65
potassium (K)	0.62
sulfur (S)	2.85
chloride (Cl)	0.67
oxygen (O)*	34.35

* by difference

6.2.2 Results

Some of the black liquor pyrolysis experiments were made at furnace temperatures 600 - 1100°C and a constant residence time of 0.85 (±0.08) seconds. Figure 6-2 shows the amount of fuel N that was converted to NO. A maximum in NO formation was observed at 800°C. Depending on the temperature, near zero to 20 % of the fuel N was converted to NO. The NH_3 analysis showed that up to 6 % of the fuel N was NH_3 in the pyrolysis gases. However, some of the NH_3 may have adsorbed on the sample lines.

The average nitrogen content of the char for each of these experiments is shown in Figure 6-3. The weight of nitrogen retained in the char relative to the weight of the char seems to remain constant with temperature. The average nitrogen content for all the experiments was calculated to be 0.10 wt. %. The standard deviation was 0.01.

The char yields from these experiments are shown in Figure 6-4. The char yield is defined as the fraction of the black liquor feed that was collected in the cyclone. The amount of fuel N that remained in the char (char-N) after pyrolysis is plotted in Figure 6-5. The char-N ranged from 35 to 65 % of the fuel N depending on the furnace temperature. The amount of char-N decreased significantly as temperature was increased.

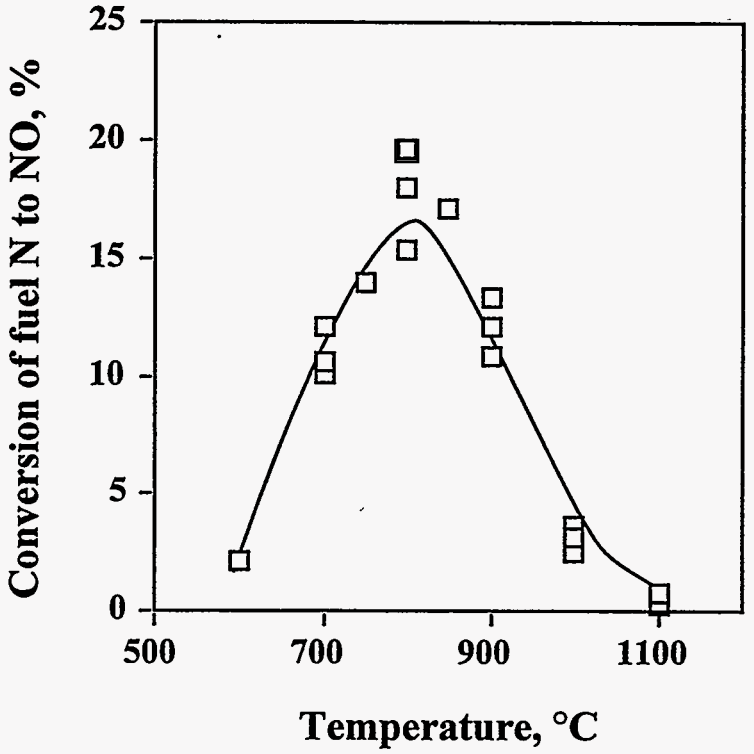

Figure 6-2. NO Formation as a function of temperature (residence time = 0.85 s).

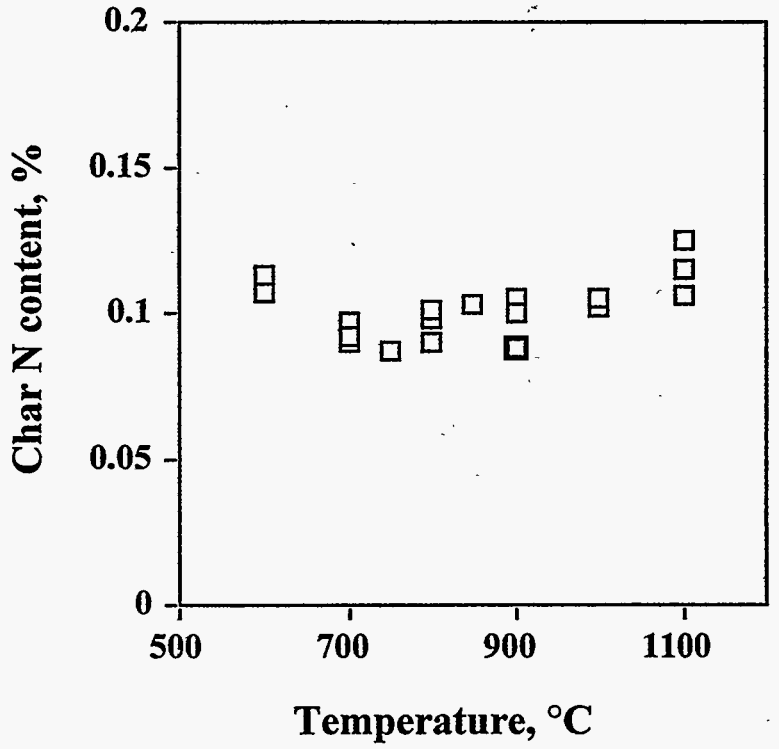

Figure 6-3. Char N content as a function of temperature (residence time = 0.85 s).

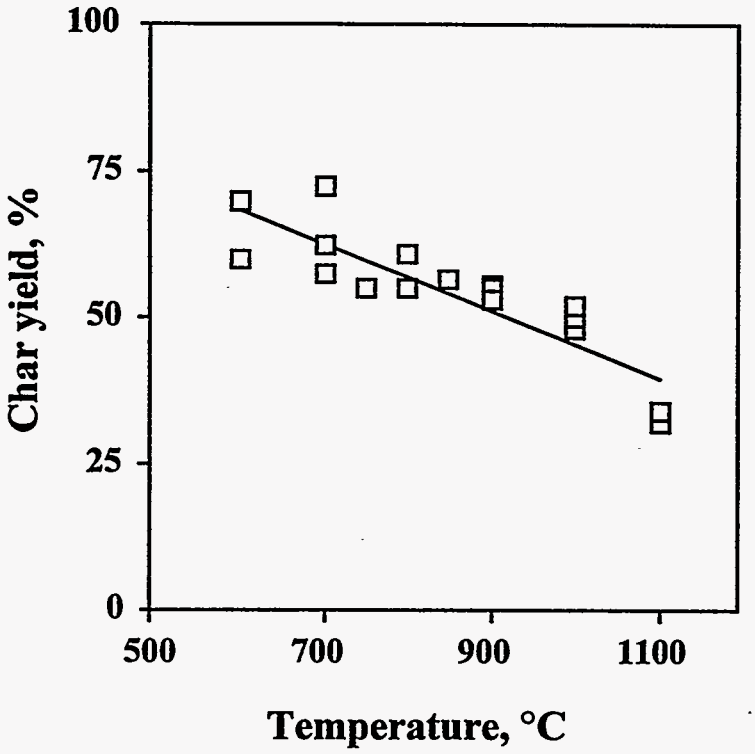

Figure 6-4. Char yield as a function of temperature (residence time = 0.85 s).

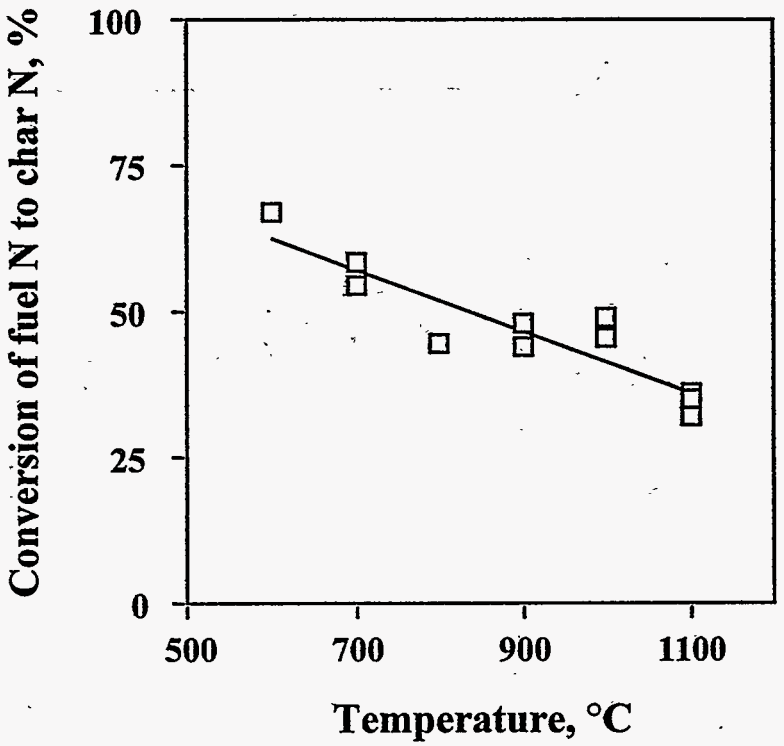

Figure 6-5. Char-N formation as a function of temperature (residence time = 0.85 s).

Experiments were also made at different residence times for furnace temperatures of 700°C, 800°C, and 900°C. Figure 6-6 shows the conversion of fuel N to NO as a function of residence time at the three furnace temperatures. Maxima in conversions to NO were observed at 0.4 seconds for 900°C and 0.8 seconds for 800°C. At 700°C, the NO concentration was still increasing at 1.7 seconds and no maximum was observed.

The char yields at 700, 800, and 900°C are shown in Figure 6-7. The char yield decreased with both increasing residence time and furnace temperature. There was a sharp decrease in the char yield during the first 0.5 seconds, after which the char yield decreased steadily. The fitted lines shown in the figure are results from a linear regression. The slopes of the three fitted were -2.9 ± 0.1 (g char)/(g BLS s).

The average nitrogen content of the char for each experiment at 900°C is plotted against the residence time in Figure 6-8. The relative weight of char-N to char seemed to be constant with residence time. The average nitrogen content was calculated to be 0.103 wt. % char-N and the standard deviation was 0.008. The amount of fuel N that remained in the char at 900°C is shown as a function of residence time in Figure 6-9. The fraction of fuel N as char-N decreased as residence time increased.

The Nitrogen Release Rate

The fraction of fuel N that remained in the char decreased with increasing temperature and residence time as observed from Figures 6.5 and 6.9. It was shown in Figure 6-5 that at 500°C, about 35 % of the fuel N volatilized in 0.85 seconds. At 1100 °C, about 65 % volatilized at the same residence time. Figure 6-9 illustrated the fraction of fuel N that remained in the char as a function of residence time at 900°C. The results indicated that that there was a rapid decrease in char-N at residence times less than 0.3 seconds. A major part of nitrogen was released at the short residence times. The amount of char-N further decreased gradually between 0.3 to 1 seconds.

The char yield decreased with increasing temperature and residence time as seen in Figures 6.4 and 6.7. Figure 6-4 showed that the rate of mass loss decrease was significantly affected by temperature. Figure 6-8 shows that significant amounts of volatile species were released below 0.3 seconds residence time, after which the amount of mass loss seemed to decrease gradually with residence time. The quick initial devolatilization agrees with the model developed by Frederick [8]. The model shows that the major part of devolatilization is complete at a residence time less than 0.1 second. As noted above the major part of N volatilization also occurred in this time frame.

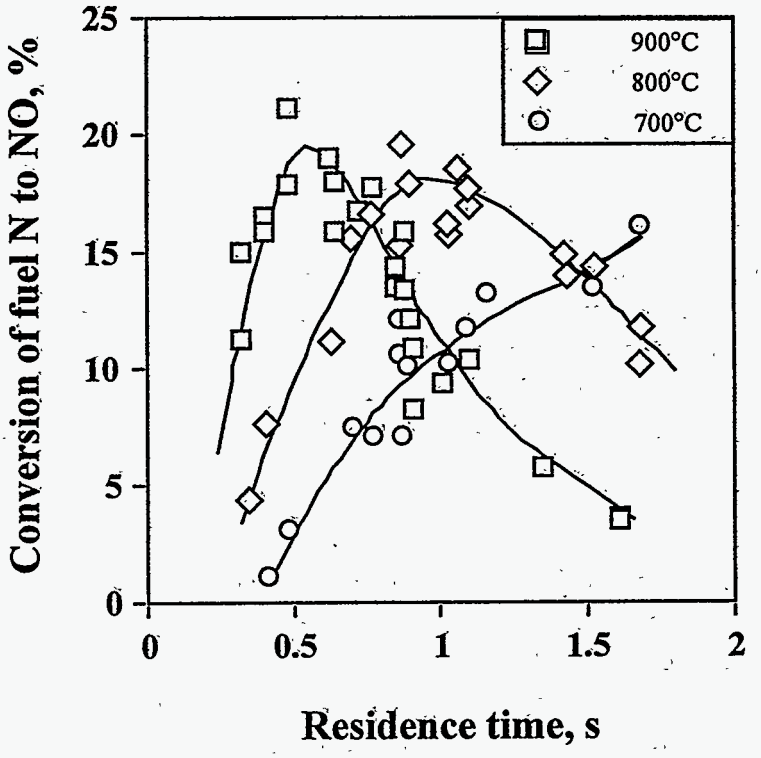

Figure 6-6. NO Formation as a function of residence time at 700°C, 800°C, and 900°C.

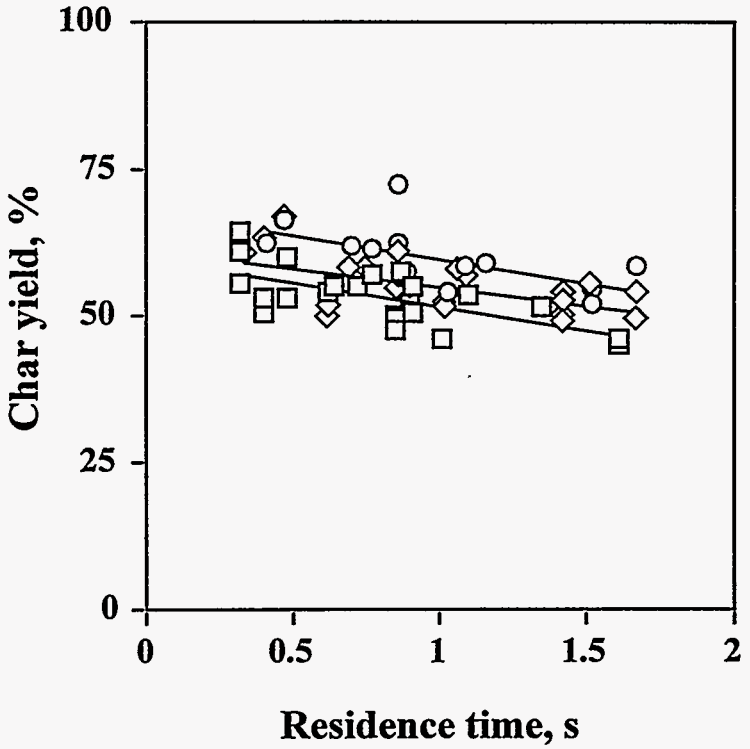

Figure 6-7. Char yield as a function of residence time at 700°C, 800°C, and 900°C.

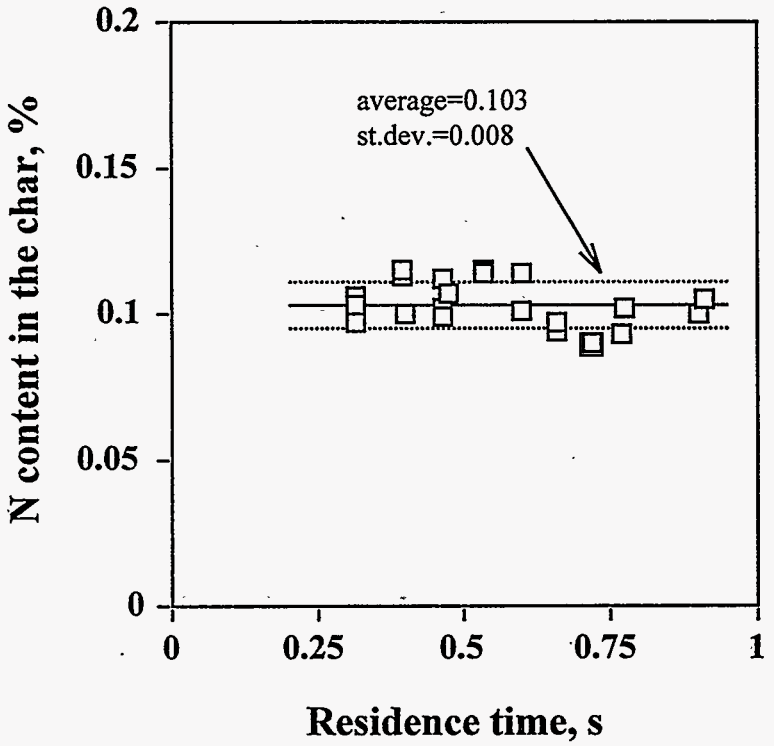

Figure 6-8. N content of char as a function of residence time at 900 °C.

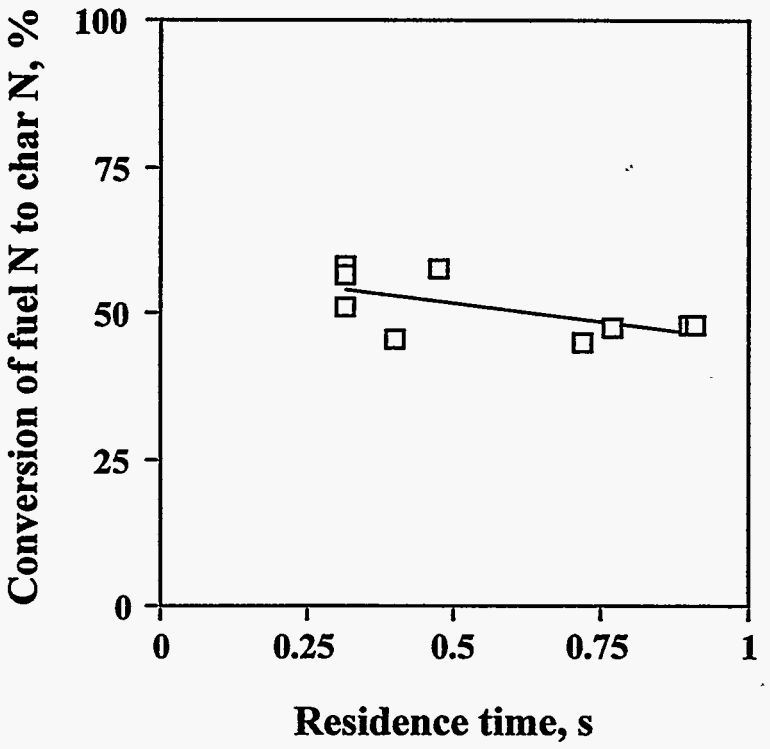

Figure 6-9. Char-N formation as a function of residence time at 900 °C.

The weight of char-N relative to the weight of char was shown in Figures 6.3 and 6.8. The fraction of nitrogen in the char was approximately constant at 0.10 wt. % in all the experiments. The original content of nitrogen in the black liquor was 0.11 wt. %. Measurements of the carbon content of char from the pyrolysis of the same liquor at the same temperature showed, however, that the carbon content decreased more significantly [9]. This implies that the carbon evolution rate was greater than the nitrogen evolution rate. This observation does not agree with the results of Nichols and Lien [1] who found that the nitrogen evolution rate was slightly greater than the carbon evolution rate. It is not known whether the difference is due to variations in the liquor properties or equipment (e.g. heating rate) in the two studies. The results in this study, however, agreed with the work of Wornat et al. [10] who found that, in biomass char, the nitrogen was retained preferentially to carbon during pyrolysis. They argued that the carbon in biomass chars is aliphatic and the bonds within the aliphatic material are, in general, easily broken. The nitrogen in biomass, however, is mainly present within heterocyclic ring structures and aromatic C-N bonds are harder to break.

Fuel NO Formation in Black Liquor Pyrolysis

Figure 6-2 illustrated the amount of fuel N that converted to NO. In the figure, the impact of increasing temperature to fuel NO formation during pyrolysis was apparent. The conversion of fuel N to NO initially increased with temperature. However, a maximum was reached and the NO destruction mechanisms dominated. At 0.85 seconds residence time, the maximum occurred at 800°C.

The formation of NO at 700, 800 and 900°C was illustrated in Figure 6-6. A maximum in NO formation was observed to occur at 0.8 and 0.4 seconds for 800 and 900°C, respectively. With these results, it can be assumed from Figure 6-2 that at 0.85 seconds, a considerable amount of NO was destroyed at 1000 and 1100°C. At these furnace temperatures, the NO formation and its maximum probably occurred earlier than at 900°C. At 700°C, no maximum occurred and the NO levels were still increasing at 1.7 seconds. The data suggested that the rate of NO destruction increased with increasing temperature.

In all the experiments, NH_3 was formed. A minimum range of near 0 to 7 % of fuel N was present as NH_3 in the off-gases from the pyrolysis experiments. Although the data were scattered, it was evident that NH_3 was present even when a major part of the NO was reduced.

A possible reaction pathway is that the volatile nitrogen formed NH_3, after which the NH_3 was oxidized to NO. As the residence time increased, the NO destruction mechanisms started to compete with the NO formation mechanisms. At higher residence times and higher temperatures, a significant part of NO probably reacted to form molecular nitrogen. The NO destruction mechanisms may have been due to homogeneous reactions of NO and other gas species or heterogeneous reactions of NO with char. It may also have been due to NO-fume reactions.

In the experiments presented, the maximum amount of NO formed was approximately 20 % at 800 and 900°C. About 20 % of the fuel N in the black liquor accounts for the typical levels of NOx emission in

recovery boilers [2]. With this, it can be concluded that it was possible to produce significant levels of NO during the pyrolysis stage.

This study can be compared to the work of Aho et al. [6,7]. The amounts of volatilized N in the two studies agree well (35-65 % vs. 20-60 %). However, the NO formation in this study was near zero to about 20%, whereas in the study of Aho et al. less than 5 %, usually 1-2 % was of the fuel N was NO. The residence time in the reactor of Aho et al. is not known. As the NO content varies significantly with residence time it is not possible to know which values in our experiments correspond to the measurements of Aho et al.

6.3. KINETICS OF NO REDUCTION BY BLACK LIQUOR CHAR

A number of studies of the kinetics of the NO-carbon reaction have been made. The carbon sources include graphite, activated carbon, coal char, coke, shale char, and soot from hydrocarbons [11,12,13,14,15]. A summary of these results is given by Teng [16]. The porous black liquor char has a very high sodium content and consists mainly of a mixture of carbon, Na_2CO_3, Na_2S, and Na_2SO_4. It has been reported that alkali metals catalyze the NO-carbon reaction in the order Cs>K>Na [17]. The CO_2 gasification rate of black liquor char has been reported to be about 20 times larger than that of coal char mixed with 10-20% Na_2CO_3 [18] and one order of magnitude larger than that of a high surface area activated carbon impregnated with 12% Na_2CO_3 [19]. This rather unusually high reactivity of the black liquor char is explained by the very fine dispersion of sodium throughout the carbon matrix as a result of formation of the char from a liquor precursor [19]. The study reported here was undertaken to characterize the reduction of NO by black liquor char by using a isothermal, fixed-bed flow reactor.

6.3.1 Experimental

A schematic diagram of the experimental apparatus is shown in Figure 6-10. The fixed bed reactor consisted of a quartz tube of 13 mm inner diameter x 1000 mm height. A bed of carbon source weighed to an accuracy of 1 mg was placed on quartz wool which was held by a fritted quartz glass fixed at the center of the reactor tube. A constant temperature was maintained within the bed by arranging the apparatus so that the reactor tube was centrally located in an electric furnace. The temperature was measured by a Chromel-Alumel thermocouple placed inside the reactor just above the bed. During the course of an experiment, reactants diluted in helium were continuously passed into the reactor. The outlet stream from the reactor was cooled down by flowing through a cooling tube. The product stream was analyzed for CO and CO_2 by nondispersive infrared analyzers, and for NO using a chemiluminescence analyzer. The instruments were connected in series and the responses were monitored by a multichannel chart recorder. More complete analysis of the product gases was obtained by Fourier Transform Infrared spectrometer (FTIR) for CO, CO_2, NO, and by gas chromatograph (GC) for N_2.

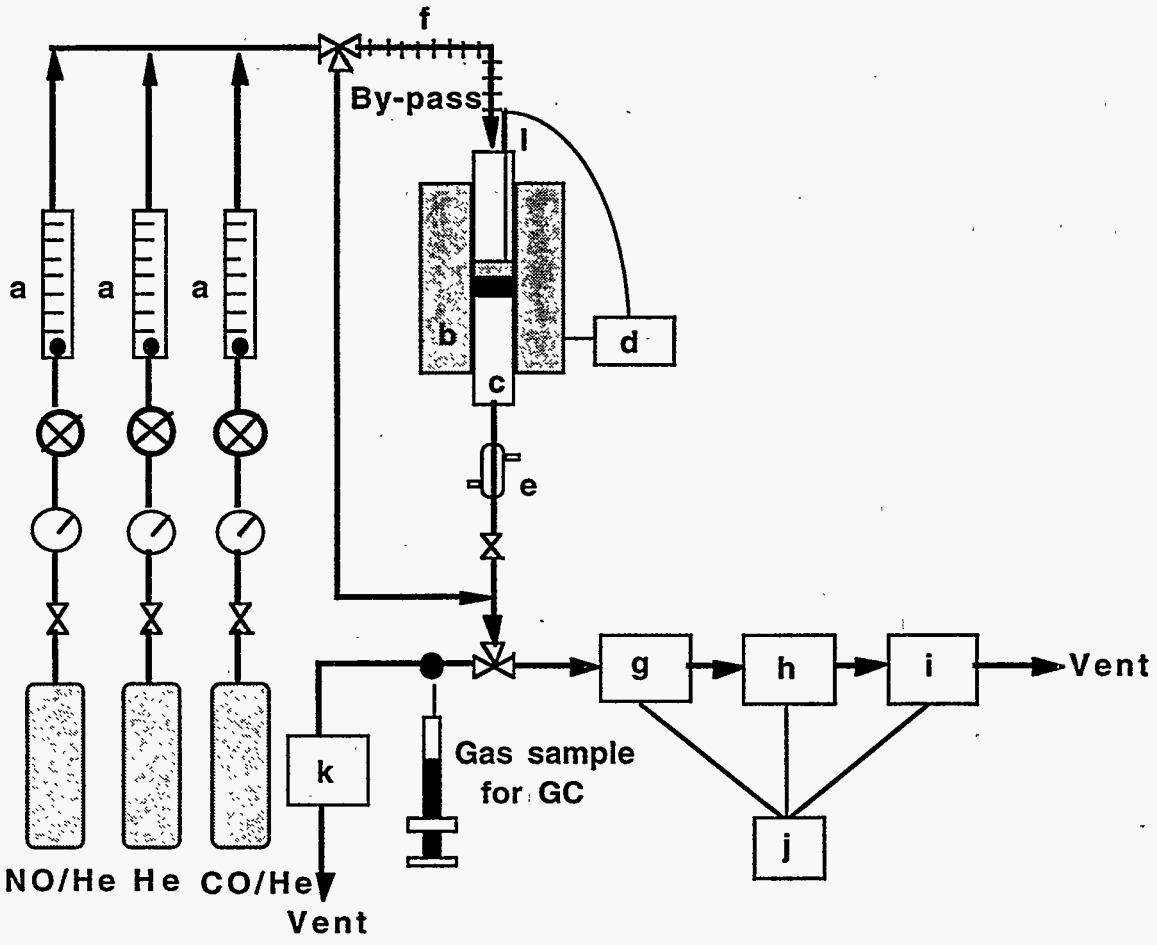

a : Flowmeter
b : Electric furnace
c : Reactor tube, 1.3 cm I.D.
d : Temperature controller
e : Cooling tube
f : Heating tape
g : CO nondispersive infrared analyzer
h : CO_2 nondispersive infrared analyzer
i : Chemiluminescence NO/NO_x gas analyzer
j : Multichannel chart recorder
k : Fourier transform infrared spectrometer
l : Thermocouple

Figure 6-10. Schematic diagram of the experimental apparatus.

In a kraft recovery furnace, the char bed provides a reducing atmosphere for the conversion of Na_2SO_4 to Na_2S. Thus, the char in a kraft recovery furnace that would react with NO, contains Na_2S, not Na_2SO_4. Prior to an experiment the black liquor char was heat treated in the experimental apparatus in order to reduce Na_2SO_4 to Na_2S. The reactor was heated electrically by a tube furnace to 700 °C. 5% CO in He was introduced when the temperature reached 500 °C. After holding the temperature at 700 °C for 40 minutes, the temperature was reduced to the required temperature. The preliminary experiments showed that sulfate reduction efficiency was 95% by using this thermal treatment conduction. When the temperature was stable, the flow of 5% CO was stopped and He was introduced into the reactor. After a flow of 5 minutes to allow complete removal of CO from the system, the reduction of NO was started by adding NO into reactor.

Two different carbonaceous solids were used in these experiments, black liquor char and activated carbon. The kraft black liquor char used for this study was produced by the pyrolysis of a liquor obtained from Champion International's Canton mill located in Canton, NC at a temperature of 950 °C in a black-liquor reactor at the Institute of Paper Science Technology (IPST) [20]. The char was then ground and sieved to the desired size range. The particle size of the char was in the range of 125-250 μ m. The internal surface area, pore volume, and pore size distribution of the black liquor char were measured by using the N_2 physical adsorption method (BET). The elemental and chemical analysis for black liquor char are given in Table 6-2.

The activated carbon used in this study was purchased from Fisher Scientific and it originally had 75 to 300 μm particle size. After passing through a sieve, the activated carbon was collected at the size range 125 to 250 μm. This activated carbon contains 5% ash but the composition of the ash is unknown. It has a surface area of 1150 m^2/g.

The physical properties of these two materials are listed in Table 6-3. The reduced char represents the char after the thermal treatment. The experimental conditions are listed in Table 6-4.

Table 6-2. Chemical and elemental analysis of the black liquor char

chemical analysis, wt%

material	$[SO_4^=]$	$[S^=]$	$[SO_3^=]$	$[S_2O_3^=]$	$[CO_3^=]$	$[K^+]$	$[Na^+]$	Fixed C
reduced char	1.42	8.78	0.99	0.14	33.5	2.1	38.8	7.6

elemental analysis, wt%

material	C	H	O	S	N	Na	K	Cl
reduced char	14.3	1.1	33.6	9.8	< 0.1	38.8	2.1	0.2

Table 6-3. Physical properties of the materials used

material	d_p, μm	ρ_b, g/cm^3	S_a, m^2/g	r_e, Å	V_p, cm^3/g
black liquor char	125-250	0.2	14.5	300	3.255
activated carbon	125-250	0.472	1150	-	-

Table 6-4. Experimental conditions

Reaction temperatures	450 ~ 650°C
Weight times (w/Vo)	0.6 ~ 12 kgs/m^3
Particle size	125 ~ 250 μm
NO concentration in He	
for measurement of reaction rate: 500 ~ 2050 ppm for NO/char reaction 2050 ppm for NO/activated carbon reaction 410 ppm for NO/CO/char reaction (40320 ppm CO)	
for measurement of reaction products: 2050 ppm for NO/char reaction 1640 ppm for NO/CO/char reaction (10080 ppm CO)	
for measurement of the effect of CO on NO reduction by char: 500 ppm (0~10000 ppm CO)	

6.3.2 Experimental Results and Discussions

6.3.2.1 Experimental Conditions

Blank test. In order to test the importance of any catalysis of the NO/CO reaction by the quartz wool, fritted quartz glass or the reactor walls, a selected run was made by passing a stream with a high concentration of NO and CO (NO=1640 ppm, CO=10080 ppm) over the bed at 700°C. The results showed no detectable NO or CO conversion.

Reproducibility. The reproducibility of the experiments was tested by repeating an experiment of NO reduction by black liquor char at same condition. The outlet concentrations of NO indicated excellent agreement between the two runs.

Uniform temperature in the bed. Because the bed was located centrally within the electric furnace, the bed was small (about 0.5-0.7 cm high), and the concentration used for these experiments was extremely low, 500 ppm, the temperature in the bed could be assumed uniform.

Plug flow. In order to assume that the flow within a fixed bed reactor is plug flow, it has been suggested in [21] that the bed height must be much greater than the diameter of the packed particles. In the present series of experiments the height of the fixed bed was about 30 times larger than the diameter of the packed particles. Therefore, gas flow through the inter particle spaces was assumed to be plug flow.

Investigation of carbon consumption during reaction. As the reaction proceeds, the reduction of NO by char or activated carbon will decrease as a result of the decreasing holdup of the carbon. To reduce this consideration, a low total NO concentration, less than 500 ppm, was employed in the kinetic experiments. To investigate the carbon consumption of black liquor char, two samples were sent to the Weyerhaeuser Company for analysis of total carbon and carbonate. The results showed that about 2% (from 7.52% to 7.36%) of the carbon present in the char was consumed by reacting with NO (531 ppm concentration) at the highest temperature studied for 15 minutes. Thus, the difference between the amounts of carbon present before and after the experiments was negligibly small. The holdup of carbon particles can be assumed constant during the time interval required for the experiment

6.3.2.2 Measurement of Reaction Rate

The outlet NO concentrations as a function of time for typical NO/char experiments at 550 °C are given in Figure 6-11. The initial concentration of NO is measured in the NO/He mixture which bypasses the reactor. When the mixture is passed through the bed the NO concentration suddenly decreases and then increases to the steady state level. The reactor was initially purged with He and the decrease in NO concentration is partly due to this. Adsorption of NO on the char may also contribute to the decrease. The following discussion deals with the kinetics of the reaction after steady state has been achieved.

The interpretation of the experimental data was based on the following relationship derived from mole balance of the fixed bed reactor, assuming first order reaction and steady state.

$$-\ln(1-X) = \eta k S_a \left(\frac{w}{V_o}\right) \qquad (1)$$

This equation gives the relationship between the conversion and the reaction rate constant for one-dimensional integral flow reactor.

First order reaction test. Confirmation for the first-order reaction assumption was obtained from the variation of the inlet NO concentration and flow rate at 550 °C. The results are shown in Figure 6-12. Data covering inlet NO concentrations from 500 to 2050 ppm and weight times (w/V_o) from 0.0055 to 0.011 gs/cm^3 are correlated by a single line which follows the functional relationship in equation (1). NO conversion is independent of the inlet NO concentration which is also typical for a first order reaction. This suggests that the NO/black liquor char reaction is first order with respect to NO. The first order dependence is in agreement with the results reported by other investigators [12,14,15,22] for NO reduction by other carbonaceous materials.

Investigation of transport processes resistance on the overall rate. To ensure that the measured rates were truly chemically controlled, the rate data obtained was tested for film mass transfer and pore diffusion limitations by both experiments and calculations. The experiments were performed by doubling both the gas flow rate and the packed length of the carbonaceous solids at the highest temperature studied and by using smaller particle size. The calculations were done by using the Mears'

criterion and the Weisz-Prater criterion [23]. The results in Table 6-5 showed that, in the film mass transfer limitation test, the steady state NO conversions at the highest temperature studied were independent of the gas flow rate at a fixed weight times (same w/V_o). Film mass transfer limitation is expected to be even less important at lower temperatures. For pore diffusion limitation test, the NO conversions were slightly lower with a smaller particle size. This indicates that the pore diffusion limitations are not important. The slightly lower NO conversion with the smaller particle size is probably due to channeling inside the bed. The molar volume of solid Na_2S is smaller than Na_2SO_4 and sintering may occur during the thermal treatment. These may contribute to the channeling effect.

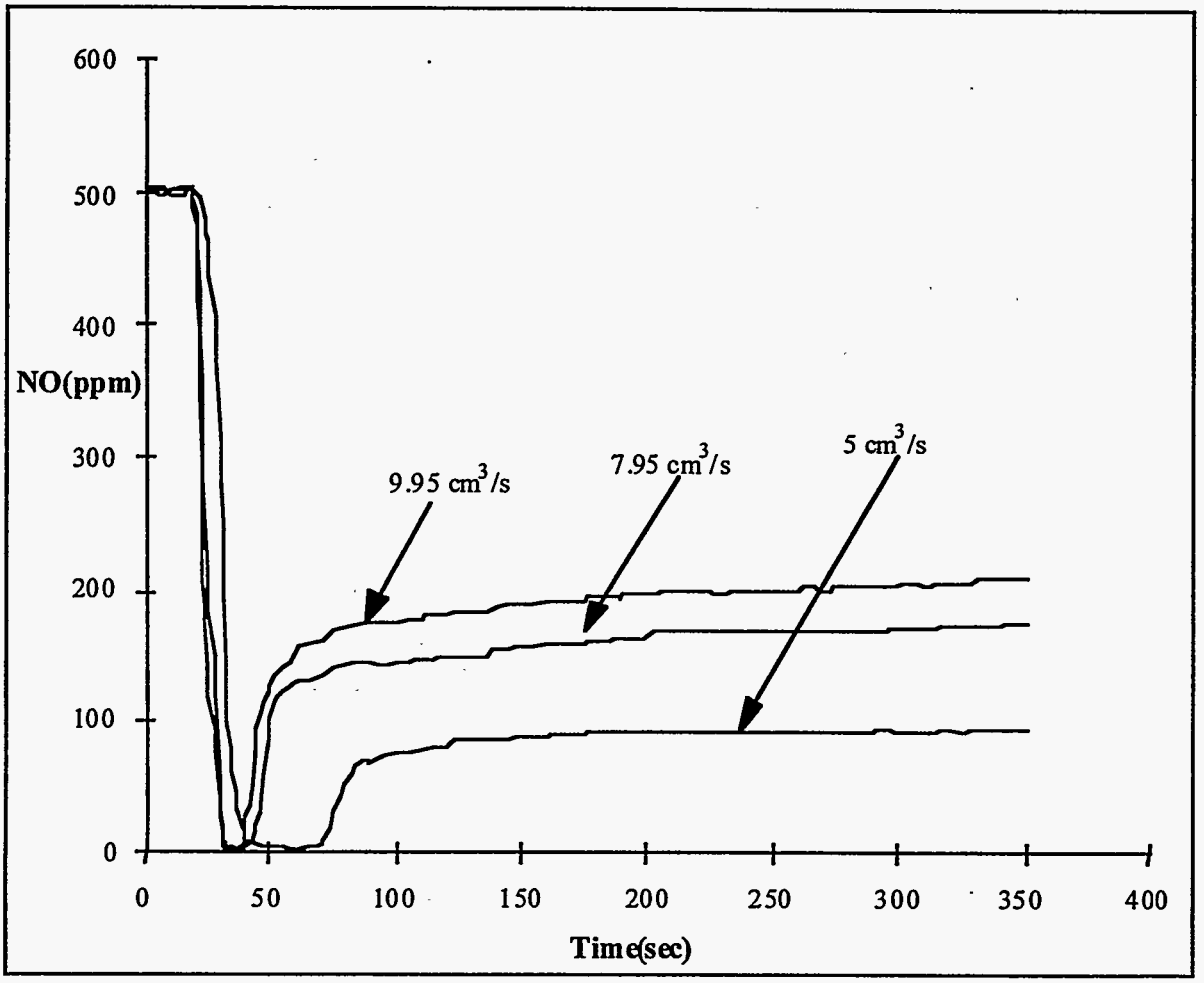

Figure 6-11. NO concentration profiles for NO/char reaction at 550 °C.

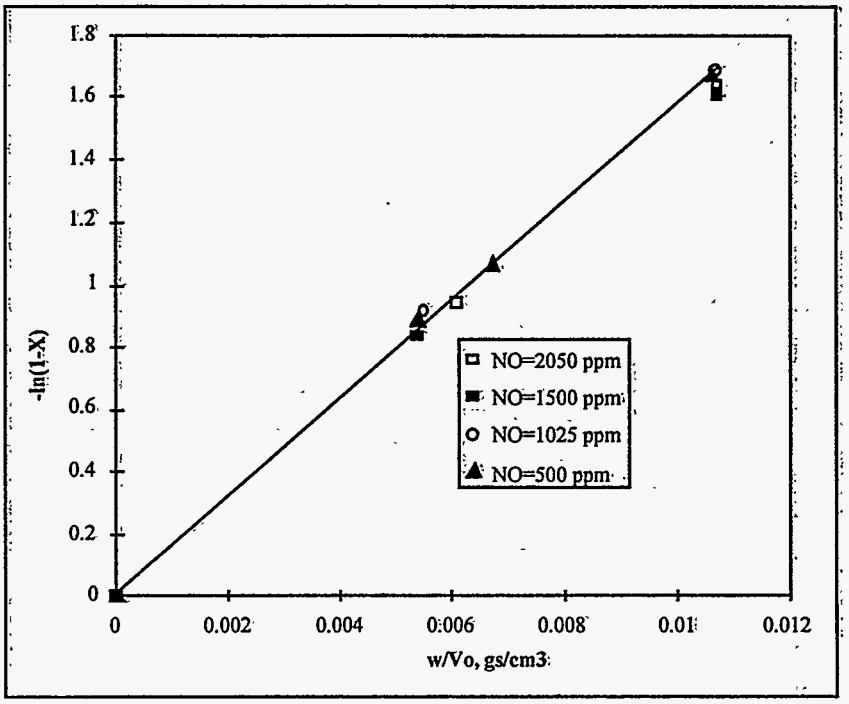

Figure 6-12. Test for a first-order reaction of NO reduction by char at 550 °C.

Table 6-5. Testing for film mass transfer and pore diffusion limitations
Film mass transfer limitation test at 650 °C, 125-250 μm

material	amount w, g	flow rate V_o, cm^3/s	NO ,ppm inlet	outlet	conv. X, %	Mears' criterion	Weisz-Prater criterion
black liquor char	0.05	4.0	500	68	86.4	$1.0x10^{-3}$	0.069
	0.1	7.9	500	70	86	$5.5x10^{-4}$	0.069
activated carbon	0.202	5.0	2050	1540	25.0	$1.8x10^{-4}$	0.014
	0.402	10	2050	1540	24.8	$1.0x10^{-4}$	0.014

Pore diffusion limitation test

material	temp. °C	particle size μm	amount g	flow rate cm^3/s	NO ,ppm inlet	outlet	conv. X, %
black liquor char	625	125-250	0.200	20	531	132	75.1
	625	< 63	0.200	20	531	147	72.3
activated carbon	650	125-250	0.202	5	2050	1540	25
	650	< 63	0.202	5	2050	1650	19.6

Note : The Mear's Criterion : $\frac{-r_{NO(obs)}\rho_p R}{k_c C_{NO}} < 0.15$, external diffusion can be neglected

The Weisz-Prater criterion : $\frac{-r_{NO(obs)}\rho_p R^2}{D_{NO,eff} C_{NO,s}} << 1$, pore diffusion can be neglected

The calculation of the Mears' criterion and the Weisz-Prater criterion also showed that neither film mass transfer nor pore diffusion were important factors in determining the overall reaction rates at these experimental conditions. Thus, the effectiveness factor can be eliminated from the equation (1), (η =1).

Calculation of the reaction rate constant k. The relationships between w/V_o and -ln(1-X) for black liquor char and activated carbon at different temperatures are shown in Figure 6-13 and Figure 6-14. It can be seen from these graphs that there was a linear relationship between w/V_o and -ln(1-X), within the range of these experiments. The fact, taken in conjunction with the fact that film resistance is also negligible, shows that the reaction of NO by black liquor char or activated carbon is a first order reaction with respect to NO concentration, over the entire temperature range studied.

The values of the reaction rate constant kS_a at various temperatures for the reduction of NO by black liquor char or activated carbon can then be determined from the slopes of the graphs in Figures 6.13 and 6.14. The internal surface area of the black liquor char, S_a, as measured by using BET method is 14.5 m^2/g. The surface area of the activated carbon is 1150 m^2/g.

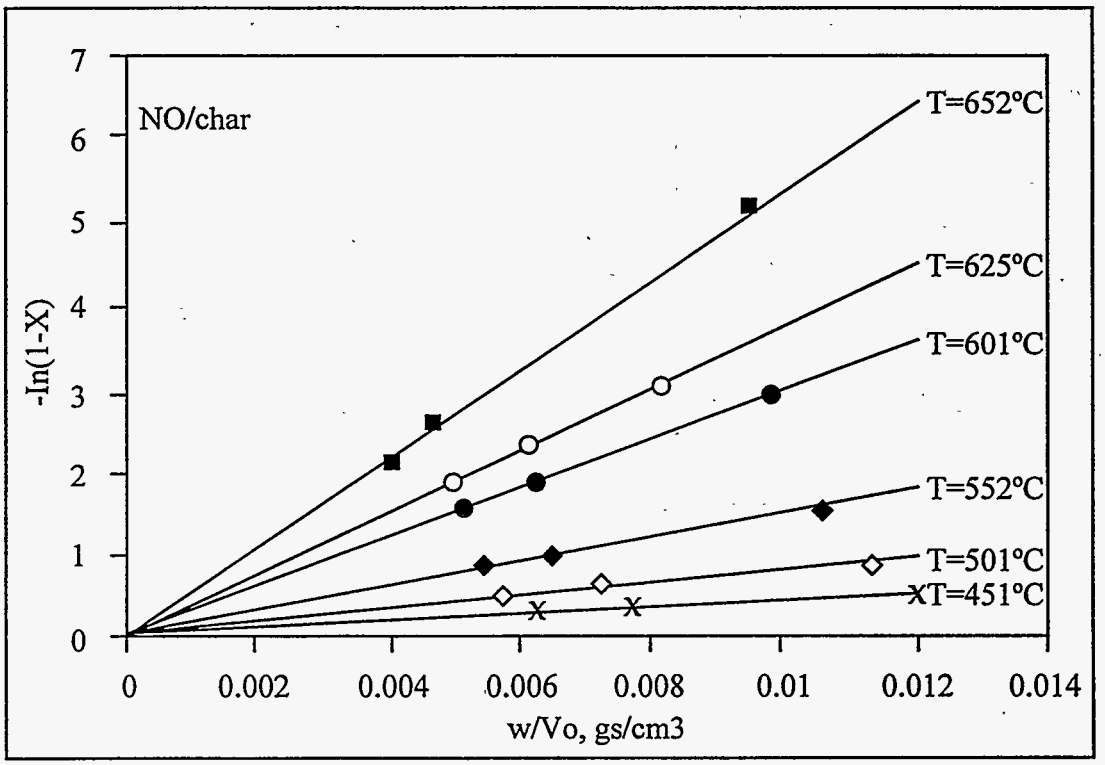

Figure 6-13. Integral analysis of the reaction data for NO/char reaction.

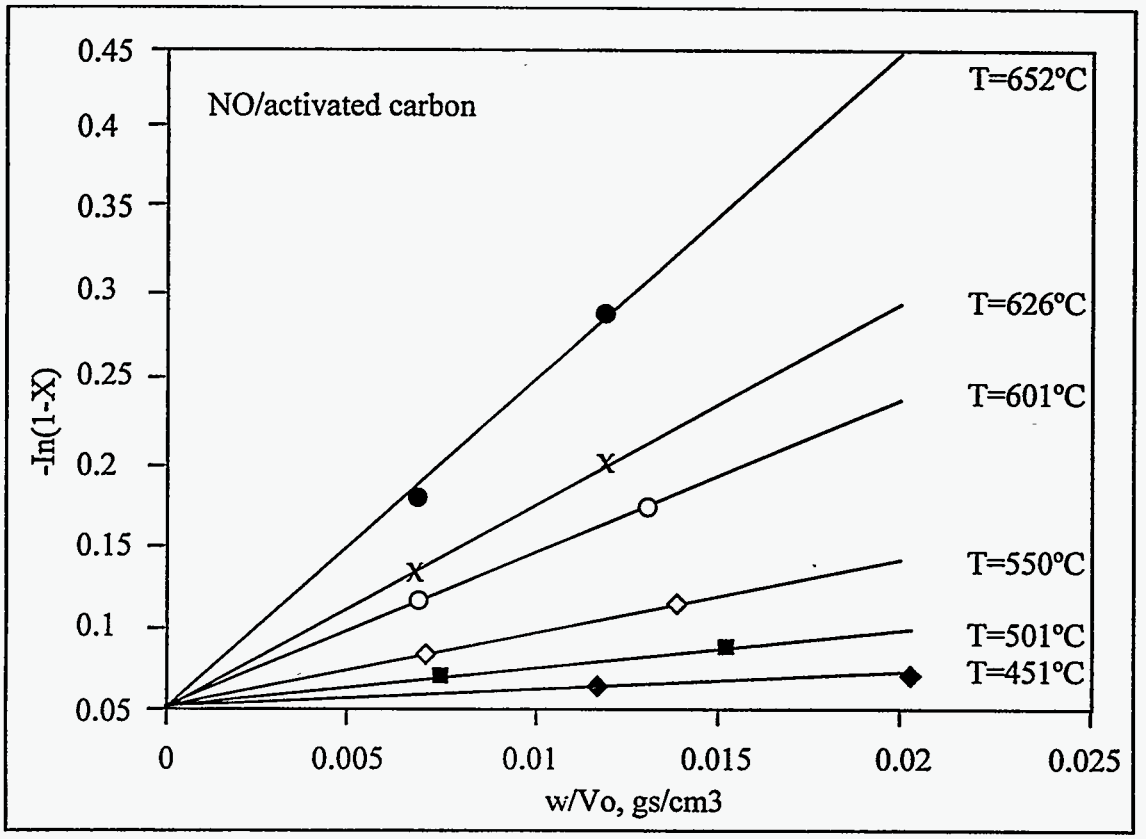

Figure 6-14. Integral analysis of the reaction data for NO/activated carbon reaction.

The reaction rates for both types of carbon are compared with those of Furusawa et al. [14] and Chan et al. [15] in Figure 6-15. The reaction rate constant k is based on the total surface area of the particle and provides a basis for comparing intrinsic reactivities of various carbonaceous solids. The rate of NO/char reaction is over three orders of magnitude faster than that of the other carbonaceous sources.

The activation energies for these different carbonaceous sources were approximately the same over this temperature range studied, from 450 °C to 650 °C. It is possible that the reaction mechanism is the same but that there are differences in catalyst sites i.e. different metals or different metal/carbon ratios. It has been reported that alkali metals catalyze the NO-carbon reaction [17]. Black liquor char has a very high Na/C ratio and shows a very high reactivity in the NO reduction reaction. This may be explained by very fine dispersion of sodium throughout the carbon matrix as a result of formation of the char from a liquor precursor [19].

6.3.3 Effect of CO on NO Reduction by Black Liquor Char

Figure 6-16 shows that the rate of NO reduction is increased with increasing CO concentration at a fixed NO concentration at 550 °C. This was also found for other chars by Chan [15] and Furusawa [24]. The NO concentration used was 500 ppm and the CO concentration varied from 0 to 10000 ppm.

In order to evaluate the relative importance of the CO/NO/char and NO/char reaction, selected experiments were performed by changing the gas flow rate and keeping the ratio of CO/NO at 100. The concentrations of NO and CO were 410 ppm and 40320 ppm, respectively. In this case, the concentration of CO in the bed can be treated as constant. By using equation (1), Figure 6-17 indicates that $-\ln(1-x)$ is linearly dependent on w/V_0. Thus the reaction in the presence of CO could also be analyzed as a first order reaction with respect to NO.

The rates of NO/CO/char reaction obtained, together with the previous results for NO/char and NO/activated carbon reactions are shown in Figure 6-18. A significantly enhanced rate of NO reduction was observed, which agrees with the findings of Chan [15] and Furusawa [24]. The rate of NO reduction by black liquor char was enhanced by CO by a factor of 2.5 with 40320 ppm CO. The activation energy is about the same in these three cases.

6.3.4 Measurement of Reaction Products

NO/char reaction. Figure 6-19 shows the results of on-line measurements of CO, CO_2 and NO by IR and chemiliminescence analyzers. It is seen that the reaction products approach steady state within 5 minutes. More complete analysis was obtained by FTIR and GC, and the results are shown in Table 6-6.

As Table 6-6 indicates, the major gaseous reaction products were N_2 and CO_2 in the entire temperature range studied, from 450 to 650 °C. Very little CO appeared in the product gases at this temperature range. The amount of CO increased with temperature and no CO detected at 450 °C. The CO/CO_2 ratio increased above 625 °C. This agrees with the measurements for coal char [11,14,15,16].

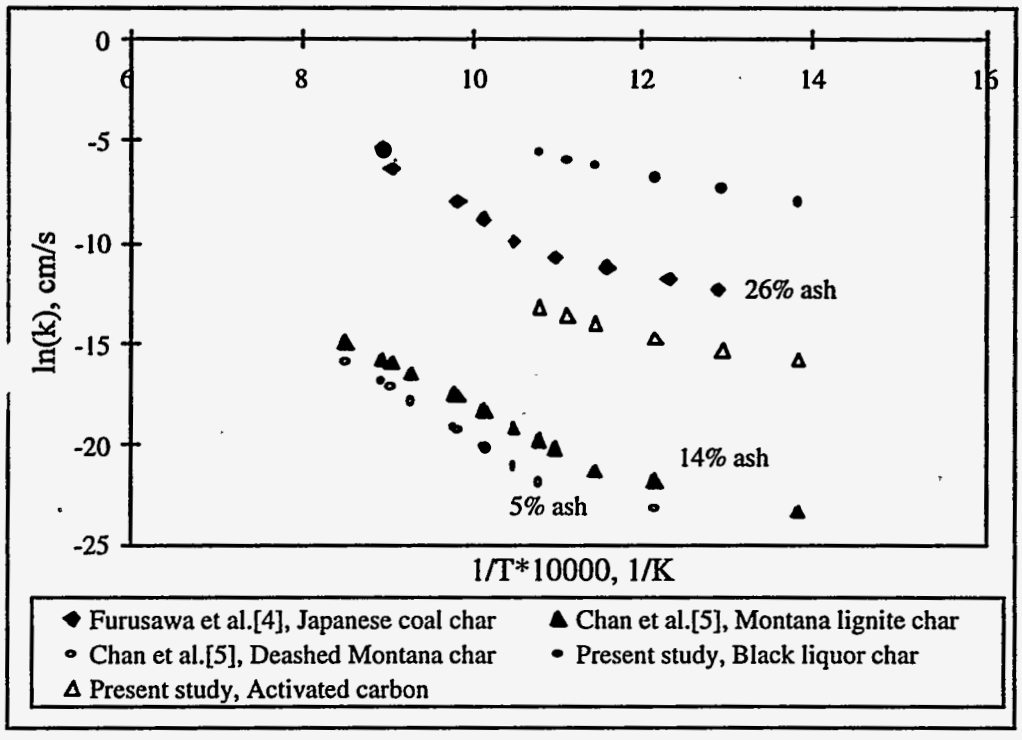

Figure 6-15. Comparison of NO reduction rate by various types of char.

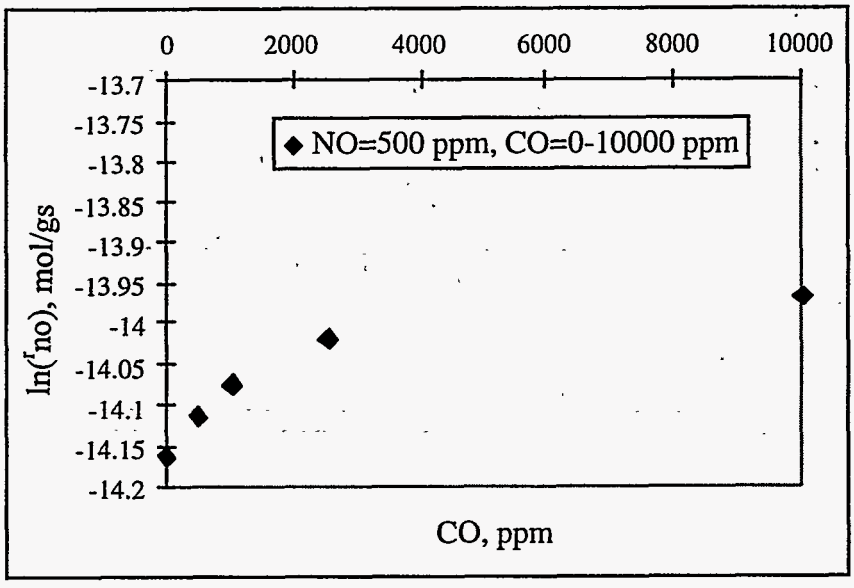

Figure 6-16. Effect of inlet CO concentration on the NO/char reaction at 550 °C.

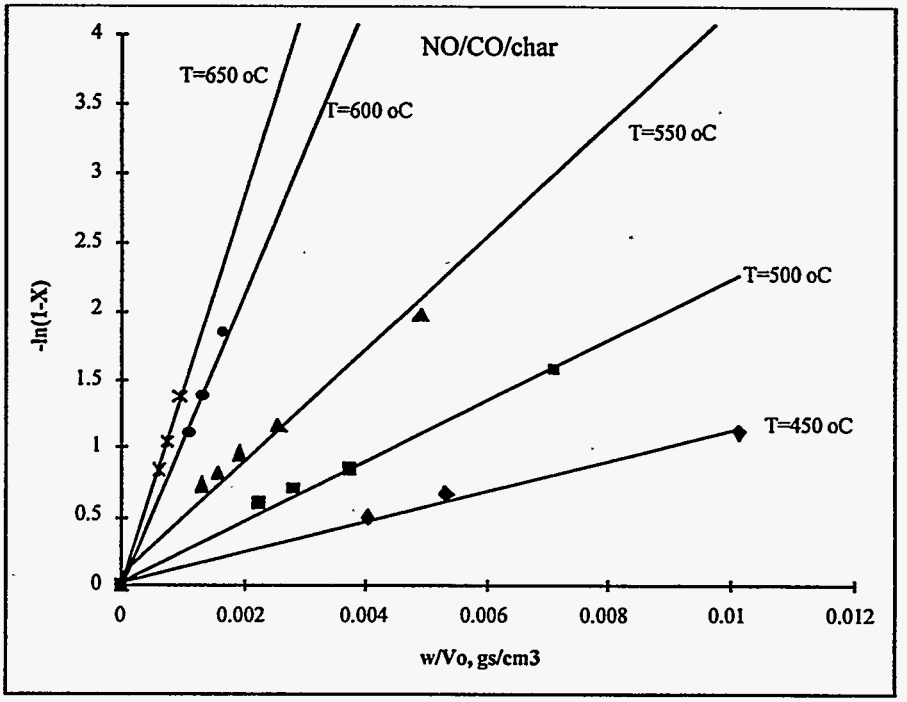

Figure 6-17. Integral analysis of the reaction data for NO/CO/char reaction. (NO=410 ppm, CO=40320 ppm)

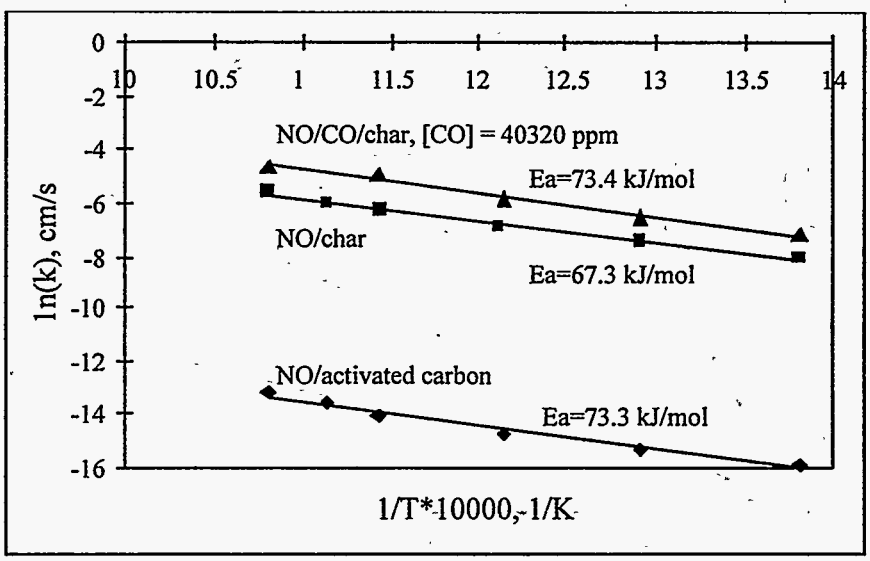

Figure 6-18. Comparison of the reaction rates of NO/char, NO/activated carbon, and NO/CO/char reactions.

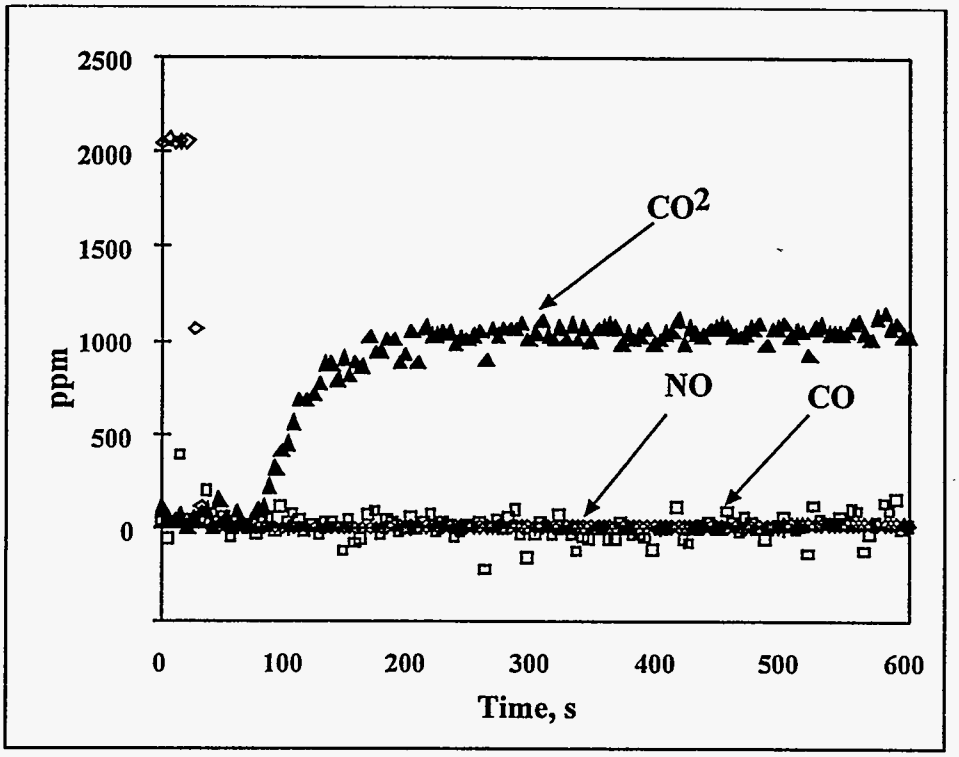

Figure 6-19. CO, CO_2, NO distribution from the NO/char reaction at 625 °C, continually analyzed for CO, CO_2 by IR analyzers, for NO by a chemiliminescence analyzer

Table 6-6 also shows the material balance closures for nitrogen and oxygen. The closures for both elements were excellent at temperature above 600 °C. The closures were not as good at lower temperatures and they were poorer for oxygen. It is possible that, at lower temperatures, the steady state was not reached when the gas sample was taken and the reactant NO combined with the carbon on the surface of the char to form an oxygen-carbon complex. This would explain the lower material balance closures.

Table 6-6. Observed reaction products for the NO/char reaction (0.3 g char and 5.72 cm^3/s gas flow), analyzed by FTIR for CO, CO_2, and NO and by GC for N_2.

Temp. , °C	C_{NOin}, , ppm	C_{NOout} , ppm	reaction CO	products CO_2	, ppm N_2	material N	balance (%) O
450	2050	862	0	95	322	73.6	51.4
500	2050	369	60	320	593	76.0	52.3
550	2050	146	62	570	802	85.4	65.9
600	2050	73	74	820	945	95.8	87.3
625	2050	16	71	958	996	98.0	97.8
650	2050	0	144	958	984	96.1	100.4

Note : (a) Oxygen balance is computed as ($CO+2*CO_2+NO_{out}$)/NO_{in}*100%
(b) Nitrogen balance is computed as ($NO_{out}+2*N_2$)/NO_{in}*100%

NO/CO/char reaction. To investigate the reaction products of the NO/CO/char reaction, two experiments were performed at CO/NO=6.1 (CO=10,080 ppm, NO=1640 ppm) at 500 °C and 600 °C. The results shown in Table 6-7 indicate that the amount of CO_2 formed by these experiments was about the same as the amounts of both CO and NO consumed. This indicates that the use of CO reduced the consumption of carbon to approximately zero and that the char provided a catalytic surface for NO reduction by CO.

Table 6-7. Observed reaction products for NO/CO/char reaction (NO=1640 ppm, CO=10080 ppm, 0.205g char, 10 cm^3/s gas flow).

Temp. °C	C_{NOin}-C_{NOout}, ppm	C_{COin}-C_{COout}, ppm	C_{CO2out}, ppm
500	890	1150	1050
600	1420	1480	1420

6.4 REDUCTION OF NO BY FUME

Experiments of NO reduction by Na_2CO_3 and Na_2SO_4 - the two main constituents in fume - were made in a fixed bed reactor at temperatures below the melting point. Gases containing NO in He were passed

Preliminary experiments showed that, in the absence of any added reducing compounds, there was no reduction of NO by either solid n the temperature range studied. When CO was added to the inlet gases there was, however, considerable reduction of NO over Na_2CO_3. There was no reduction of NO over Na_2SO_4 at 700°C or below and little at 750°C: less than 5 % reduction with 500 ppm NO, 5000 ppm CO with 2 g of Na_2SO_4 and a total gas flow of 760 ml/min (25°C). No reduction was observed in an empty reactor at any conditions.

The Na_2CO_3 used in the reduction study was prepared from reagent grade material by presintering it for 30 min at 780°C prior to the experiment. The aim of the pretreatment was to prevent the material from sintering in the NO reduction experiments. The presintered material was ground and sieved, and the fraction 90-125 µm was used in the experiments. The BET surface area of the material was measured to be 0.18 m^2/g. The NO reduction results are shown in Figure 6-20. The NO reduction ranged from 0-40 % at the conditions studied.

For a first order reaction in NO the reaction rate coefficient with 5000 ppm CO is:

$$k = 59\ 400\ m^3/sm^2\ e^{(-180\ kJ/mol/RT)} \qquad (3\text{-}2)$$

This reaction rate can be compared to the rate by black liquor char. At 650°C the reduction rate by black liquor char in the absence of CO was one to two orders of magnitude faster than that by Na_2CO_3 with 5000 ppm CO. The comparison is made on an equivalent surface area basis.

6.5 MODELING OF THE N VOLATILIZATION RESULTS

A simple model was developed to describe the nitrogen devolatilization behavior observed in the pyrolysis experiments. The model results were then compared to the NO reduction rates measured.

6.5.1 Model

The model consists of three stages: release of N from the black liquor, oxidation of the N released to NO, and reduction of NO. The model can be presented by the following three reactions:

$$N_{bls} \rightarrow N_{vol} \qquad (3\text{-}3)$$

$$N_{vol} \rightarrow NO \qquad (3\text{-}4)$$

$$NO \rightarrow N_{red}, \qquad (3\text{-}5)$$

where N_{bls} is the N in the black liquor solids, N_{vol} is the nitrogen released, and N_{red} is the reduced N compound.
The release of N was assumed to be instantaneous. The amount of N released was taken to be equal to the amount determined from the analysis of N remaining in the char at 0.85 s. All of the released N was assumed to be equally reactive in step 2, the oxidation to NO. Based on the results of Aho et al. [5,6] the released nitrogen compound is NH_3. The reduced N compound is most likely N_2.

The release of N was assumed to be instantaneous. The amount of N released was taken to be equal to the amount determined from the analysis of N remaining in the char at 0.85 s. All of the released N was assumed to be equally reactive in step 2, the oxidation to NO. Based on the results of Aho et al. [5,6] the released nitrogen compound is NH_3. The reduced N compound is most likely N_2.

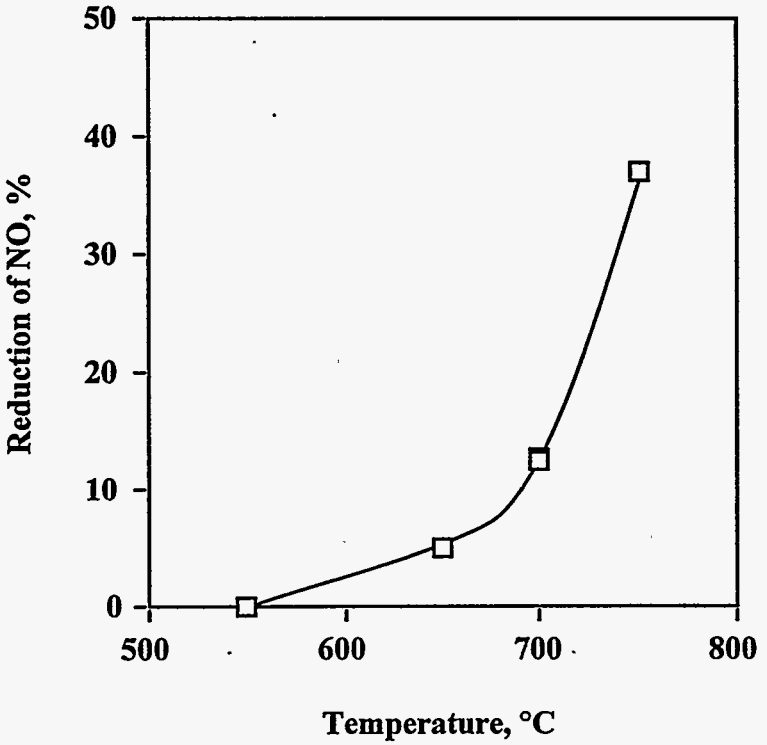

Figure 6-20. The reduction of NO by CO over Na_2CO_3 (3 g Na_2CO_3 of particle size 90-125 μm and surface area of 0.18 m^2/g, 912 ml/min (25°C) total gas flow with 460 ppm NO and 5000 ppm CO in He).

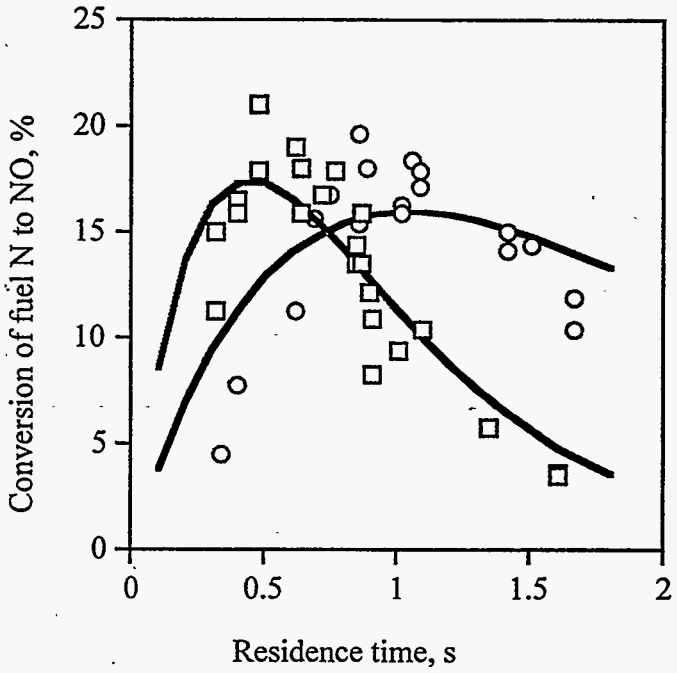

Figure 6-21. A comparison of the experimental values and the modeling results for the conversion of fuel N to NO.

The oxidation reaction was assumed to be irreversible and first order in the concentration of the released N compound N_{vol}. Similarly, the reduction rate was assumed to be irreversible and first order in NO. The reaction rate coefficients of the reactions are denoted as k_{ox} and k_{red} respectively. The effects of the other reactants, namely the oxidant for reaction step 2 and the reducer for step 3 are assumed to be constant for each temperature and are included in the coefficients k_{ox} and k_{red}.

The rates of the disappearance of the released NO compound and the rate of formation/disappearance of NO are thus:

$$d[Nvol]/dt = - k_{ox} [N_{vol}] \quad (3\text{-}6)$$

$$d[NO]/dt = k_{ox} [N_{vol}] - k_{red} [NO] \quad (3\text{-}7)$$

The concentrations of N_{vol} and NO are

$$[N_{vol}] = [N_{vol}]_o \, e^{-koxt} \quad (3\text{-}8)$$

and

$$[NO] = [N_{vol}]_o \frac{k_{ox}}{k_{ox}-k_{red}} (e^{-kredt} - e^{-koxt}) \quad (3\text{-}9)$$

where t is the residence time and $[N_{vol}]_o$ is the initial concentration of N_{vol}.

This model was applied to the measured values of NO in the pyrolysis experiments at different residence times at 800 and 900°C (Figure 6-6.) No fit was made at 700°C because there was no apparent reduction. The model was applied by minimizing the sum of squares of the error in the NO concentration using a Marquardt optimization routine. The parameters to be adjusted were k_{ox} and k_{red}. Instead of actual concentrations, the fraction of each N compound of the total N content in the black liquor was used for the terms $[N_{vol}]$ and [NO] in the calculations. The fits at the two temperatures are shown in *Figure 6-21*. The fits are reasonable taking into account the scatter in the original data. The fitted values of k_{ox}, k_{red} as well as the initial value of $[N_{vol}]$ determined from the experiments are shown in Table 6-8.

Table 6-8. The rate coefficients k_{ox} and k_{red} based on the optimization of the N release data by the model of equations 3-5, and the initial values of $[N_{vol}]$ as determined from the experiments.

Temperature, °C	800	900
$[N_{vol}]_o$, %	49.4	54.0
k_{ox}, 1/s	0.84	1.97
k_{red}, 1/s	1.09	2.56

6.5.2 Discussion of the Model Results

The model applied here is an extremely simplified one, and the real situation is much more complicated. The model does not distinguish between different volatile N compounds but assumes their reactivities to be equal. The model only takes into account one reaction leading to the formation of NO and one reaction for NO reduction. There are several different reactions by which NO can be formed or reduced as well as other reactions that account for the disappearance of N_{vol}. One of these reactions is a direct reduction of N_{vol} to N_{red}. One mechanism by which NO can be reduced is the reaction between NO and NH_3.

The dependence of the reactions on the reactants is not known either. As mentioned earlier the concentrations of the reducing or oxidative species were assumed to be constant.

The effects of some of these assumptions were briefly studied. The inclusion of a direct reaction leading from N_{vol} to N_{red} in the model changes the coefficient k_{ox} but does not affect k_{red}. Inclusion of a reaction N_{vol} + NO would decrease both k_{ox} and k_{red} but with measurements of only NO it is impossible to quantify this effect.

In the absence of other measurements except for NO concentration it was deemed unjustified to use a more complex model. The reduction rate coefficient k_{red} obtained with the model was compared to the measured rates of NO destruction by black liquor char and fume.

In the comparison, the fume reactivity was assumed to be the same as the reactivity of Na_2CO_3. The surface area of the fume particles was assumed to be equal to the external surface area of particles with a diameter of 0.1 μm which gives a value of 12 m^2/g. The 0.1 μm particle size is based on the measured diameter of the particles caught by the filter in the LEFR [28]. The concentration of CO was taken to be 700 ppm. This value is based on the measured values of 300-1000 ppm for the pyrolysis of the same black liquor in the same laminar entrained flow reactor at nearly identical conditions [29]. The rate of NO reduction by CO over Na_2CO_3 was assumed to be first order in CO. The rate coefficient of equation 3-1 was adjusted accordingly.

The NO reduction rate by black liquor char was taken to be represented by equation 1 in the temperature range 450-625°C. Above 625°C, the activation energy was assumed to be 245 kJ/mol. CO is known to enhance the reduction rate though the dependency of the rate on CO concentration is not known. It was assumed here that the rates of the reaction in the absence of CO and the reduction by CO are additive: $k = k_{noCO}\{1+[CO]/ppm\}$, where k_{noCO} is the rate coefficient in the absence of CO. Based on the reported effect with 400 ppm NO and 4000 ppm CO, the rate with 700 ppm CO was thus assumed to be 26 % higher than without any CO present. During the pyrolysis step, the black liquor is evolving, and thus its characteristics including composition and surface area change. The surface area was taken to be equal to that of the char used by Wu and Iisa [25]. No correction was made for the different carbon contents of the two chars.

The char yields measured for the 0.85 residence time were used in determining the amount of char. Based on typical experimental values [30] the fume yield was taken to be 1 % at both temperatures, and the gas flow (primary + secondary) was taken to be 13 l/min and the solids feed rate of 0.45 g/min .

Based on the assumptions and data above, coefficients of NO reduction corresponding to the k_{red} of the model were calculated for black liquor char and fume. The results are shown in Table 6-9.

Table 6-9. A comparison of the NO reduction coefficients from the model (k_{red}) and from the data for black liquor char and fume.

Temperature, °C	800	900
k_{red}, 1/s	1.09	2.56
k_{char}, 1/s	0.56	4.7
k_{fume}, 1/s	.000016	.000081

The reduction rates by the fume particles were about five orders of magnitude slower than the rates from the model. This clearly implies that the reduction by fume was negligible in these experiments. The rate by black liquor char, on the other hand, was of the same order of magnitude as that of the model: half of the model value at 800°C and twice the model value at 900°C. This strongly suggests that the reduction by char was important under these conditions. Taking into account the uncertainties in the estimates the correspondence is indeed very good.

6.6 Conclusions and Analysis

Black liquor pyrolysis experiments were made in a laminar entrained flow reactor. The results confirmed previous findings that significant amounts of N are released in compounds other than molecular nitrogen during black liquor pyrolysis. It was further shown that the majority of the nitrogen release occurred at very short residence times, of the order of 0.1 s or less. Considerable amounts of NO (up to 20 % of the N in the black liquor solids) were formed in the experiments. A significant fraction of the NO became subsequently reduced. The reduction rate increased as temperature was increased.

The NO reduction by black liquor char and activated carbon was investigated by using a fixed-bed, isothermal plug flow reactor at temperatures between 450 and 650 °C.

It was found that the NO/char and NO/activated carbon reactions were first order reaction with respect to NO concentration. The activation energies were about the same over the entire range of temperatures studied. However, the rate of the NO/char reaction was over 3 orders of magnitude higher than that of the NO/activated carbon.

In the presence of CO, CO enhanced the NO/char reaction rate and the enhancement of CO on the NO/char reaction increased with increasing CO concentration. CO also reduced carbon consumption to zero. This is a catalytic reduction of NO by CO over the char surface.

The gaseous reaction products that were formed at six different temperatures were analyzed in the case of NO/char reaction. It was found that the major reaction products were N_2 and CO_2. No CO was detected at 450 °C. The CO/CO_2 ratio increased above 625 °C.

A simple model was developed to describe the formation and destruction of NO that was observed in the pyrolysis experiments. The modeling results indicated that black liquor char was important in the reduction of NO whereas fume particles were not. The reduction of NO by black liquor char in recovery boilers may have significance in recovery boilers as well. It may be possible to abate NO emissions by improving the contact between black liquor char and NO at suitable temperatures.

6.7 Assessment and Needs

It has been established earlier that NOx in recovery boilers originates from fuel nitrogen and that NH_3 but not HCN is the key intermediate species in NOx formation (1,5,6,31). The release of nitrogen during devolatilization of black liquor, based on the work presented here and that of Aho et al. (5,6), has been characterized. Also, the kinetics of reduction of NO by char, by CO catalyzed by char, and by CO catalyzed by solid fume particles have been measured. These aspects of Nox formation and destruction are now well enough understood for the purpose of modeling NOx formation and destruction in recovery boilers.

Additional work needs to be completed in several areas of NOx formation and destruction. NH_3 evolution during pyrolysis has been measured at lower temperatures but not at the temperatures of interest in recovery boilers. Also the release of nitrogen species during char burning needs to be characterized. The kinetics of NH_3 decomposition or oxidation to NO with char and fume particles as catalysts need to be measured.
An overall model of NOx processes needs to be formulated. It should include these nitrogen species release processes and heterogeneous reaction kinetics as well as the well established global reaction kinetics for gas-phase NOx and NH_3 formation and destruction reactions.

6.8 Nomenclature

C_{COin} = inlet CO concentration, mol/cm^3
C_{COout} = outlet CO concentration, mol/cm^3
C_{CO2out} = outlet CO_2 concentration, mol/cm^3
C_{NO} = bulk concentration of NO, mol/cm^3
C_{NOin} = inlet NO concentration, mol/cm^3
C_{NOout} = outlet NO concentration, mol/cm^3

$C_{NO,s}$ = NO concentration at the external surface of particle, mol/cm^3
$D_{NO,eff}$ = effective diffusion coefficient, cm^2/s
Ea = activation energy, kJ/mol
k = reaction rate constant, cm/s
k_c = mass transfer coefficient, cm/s
R = particle radius, cm
r_e = pore radius, cm
$-r_{NO(obs)}$ = observed NO reaction rate, mol/gs
S_a = BET surface area per unit mass of catalyst, cm^2/g
V_o = volumetric flow rate, cm^3/s
V_p = pore volume, cm^3/g
w = weight of catalyst, g
X = the conversion of nitric oxide
r_b = bulk density of the catalyst bed, g/cm^3
r_p = particle density, g/cm^3
η = overall effectiveness factor

6.9 References

1. Nichols, K.M., and Lien, S.J., "Formation of Fuel NOx during Black-Liquor Combustion" *Tappi Journal*, Vol 76, No 3 p 185 (1993).
2. Nichols, K. M. , Thompson, L.M. , and Empie, H.J., "A Review of NOx Formation Mechanisms in Recovery Furnaces". *Tappi Journal* Vol 76 o 1 (1993).
3. Niemelä, K., "Low-Molecular Weight Organic Compounds in Birch Kraft Black Liquors." Ph.D. Dissertation, University of Helsinki (1990) referenced by [31].
4. Dill, I., Salnikow, J., and Kraepelin, G., " Hydroxyproline-Rich Protein Material in Wood and Lignin of Fagus Sylvatica". *Applied and Environmental Microbiology*. Vol 48, No 6,1259-1261 (1984) referenced by [31]
5. Aho, K. , Hupa, M. , and E. Vakkilainen, S., "Fuel Nitrogen Release During Black Liquor Pyrolysis, Part I: Laboratory Measurements at Different Conditions". *Tappi Journal* Vol 77 No 5 p. 121-127 (1994).
6. Aho, K. , Hupa, M. , and Nikkanen, S., "Fuel Nitrogen Release during Black Liquor Pyrolysis; Comparisons between Different Liquors." *Tappi Journal* Vol 77 p. 182-8 (1994).
7. Sricharoenchaikul, V., Reis, V. V., Carangal, A., Sinquefield, S. A., Iisa, K., Frederick, W. J., Experimental Measurements of the Pyrolysis Products from Black Liquor Using a Laminar Entrained-Flow Reactor, Paper 253c, AIChE 1994 Annual Meeting, San Francisco, Nov. 13-18 1994.
8. Frederick, W., "Combustion Processes in Black Liquor Recovery: Analysis and Interpretation of Combustion Rate Data and an Engineering Design Model", U.S. DOE Report DOE/CE/40637-T8 (DE90012712), (March 1990).
9. Sricharoenchaikul, V. and Frederick, W. J., unpublished research (1995)

10. Wornat, M., Hurt, R., Yang, N., and Headley, T., "Structural and Compositional Transformations of Biomass Chars During Combustion", Twenty-Fifth Symposium (International) on Combustion, The Combustion Institute, Pittsburgh, P.A., (1994).
11. Smith, R.N., Swinehart, J., and Lesnini, D., *J. Phys. Chem.*, Vol. 63, p.544, 1959.
12. Watts, H., *Transactions Faraday Society* , Vol. 54, p.93, 1951.
13. Lai, C.S., Peters, W.A., and Longwell, J.P., *Energy & Fuels*, Vol. 2, No. 4, p.586, 1988.
14. Chan, L.K., Sarofim, A.F., and Beer, J.M., *Combustion and Flame*, Vol. 52, p.37, 1983.
15. Furusawa, T., Kunii, D., Osuma, A., and Yamada, N., *International Chemical Engineering*, Vol. 20, No. 2, p.239, 1980.
16. Teng, H., Suuberg, E.M., and Calo, J.M., *Energy & Fuels*. Vol. 6, No. 4, p.398, 1992.
17. Kapteijn, F., Mierop, A.J.C., and Moulijn, J.A., *J. Chem. Soc., Chem. Commun.*, p.1085, 1984.
18. Li, J., and Van Heiningen, A.R.P., *The Canadian Journal of Chemical Engineering*, Vol. 67, August, p.693, 1989.
19. Li, J., and Van Heiningen, A.R.P., *Ind. Eng. Chem. Res.*, Vol. 30, No. 7, p.1594, 1991.
20. Lee, S.R., Ph.D. Thesis, Institute of Paper Science and Technology, Atlanta, Georgia, 1994.
21. Kubota, H. and Ikeda, N., *Kagaku Kagaku*, Vol. 27, p.373, 1963.
22. Song, Y.H., Beer, J.M., and Sarofim, A.F., *Combustion Science and Technology*, Vol. 25, p.23, 1981.
23. Fogler, H.S., "*Elements of Chemical Reaction Engineering*", 2nd ed., Prentice-Hall, New Jersey, p.607-634, p. 569-573, 1992.
24. Furusawa, T., Tsunoda, M., Tsujimura, M. and Adschiri, T., *Fuel*, Vol. 64, p. 1306, 1985.
25. Wu, S. L., Iisa, K. , Kinetics of NO Reduction by Black Liquor Char, submitted *to Ind. Eng. Chem. Res.* (1995).
26. Furusawa, T., Kunii, D., Osuma, A., and Yamada, N., "Rate of Reduction of Nitric Oxide by Char," *Int. Chem. Engr.* Vol 6, No 4, 239-244 (1980).
27. Teng, H., Suuberg, E. M., and Calo, J. M., "Studies on the Reduction of Nitric oxide by Carbon: the NO-Carbon Gasification Reaction," *Energy & Fuels*, Vol 6, No 4, p. 398-406 (1992).
28. Kauppinen, E. I., Mikkanen, P., Jokiniemi, J. K., Sinquefield, S. A., Frederick, W. J., and Mäkinen, M., "The Particle Size and Chemical Species Distribution of Aerosol Generated in Kraft Liquor Pyrolysis and Combustion", *AIChE Symp. Series, Vol* 90, No 302 46-54 (1994).
29. Sricharoenchaikul, V., Frederick, W. J., and Grace, T. M., "Thermal Conversion of Tars to Light Gases during Black Liquor Pyrolysis, 1995 Int. Chemical Recovery Conf., Toronto, Canada, April 24-27, 1995.
30. Carangal, A., Formation of NO during the Black Liquor Pyrolysis, M.Sc. Thesis, Oregon State University, Department of Chemical Engineering, Corvallis, OR, USA (1994).
31. Veverka P.J., Nichols, K., Horton, R., and Adams, T., "On the Form of Nitrogen in Wood and its Fate During Kraft Pulping". 1993 Environmental Conference Proceedings, Tappi Press, Atlanta, Georgia (1993).

APPENDIX 1. PUBLICATIONS AND REPORTS

Refereed Technical Journals

Frederick, W. J., Hupa, M., Stenberg, J., Hernberg, R., Optical Pyrometric Measurements of Surface Temperatures During Black Liquor Char Burning and Gasification. *Fuel,* v. 73, no. 12, p. 1889-1893 (1994).

Mikkanen, P., Kauppinen, E.I., Jokiniemi, J.K., Sinquefield, S.A., Frederick, W.J., Bimodal Fume Particle Size Distributions from Recovery Boiler and Laboratory Scale Black Liquor Combustion. *Tappi Jl.,* v77, no. 12,.p. 81-84 (1994)

Boonsongsup, L., Iisa, K., Frederick, W.J., SO_2 Capture and HCl Release at Kraft Recovery Boiler Conditions. AIChE Symp. Ser. v. 90, no. 302, p. 39-45 (1994)

Mikkanen, P., Kauppinen, E.I., Jokiniemi, J.K., Sinquefield, S.A., Frederick, W.J., Mäkinen, M., The Particle Size and Chemical Species Distributions of Aerosols Generated in Kraft Black Liquor Pyrolysis and Combustion. AIChE Symp. Ser. v. 90, no. 302, p. 46-54 (1994)

Hupa, M., Backman, R., Frederick. W.J. "Black liquor combustion properties" in *30 Years Recovery Boiler Cooperation in Finland*, Finnish Recovery Boiler Committee, Helsinki (1994).

Frederick, W. J., Hupa, M. The Effects of Temperature and Gas Composition on Swelling of Black Liquor Droplets During Devolatilization. *J. Pulp Paper Sci.* (October, 1994).

Frederick, W. J., Hupa M., Uusikartano, T. Volatiles And Char Carbon Yields During Black Liquor Pyrolysis. *Bioresource Technology* 48 (1994) 59-64.

Frederick, W.J., Wåg, K., Hupa, M., Rate and Mechanism of Black Liquor Char Gasification with CO_2 at Elevated Pressures. *Ind. Eng. Chem. Research*, 32(8):1747-1753 (1993).

Backman, R., Frederick, W.J., Hupa, M., "Basic Studies on Black-Liquor Pyrolysis and Char Gasification." Bioresource Technology, 46 (1993) 153-158.

Forssén, M., W.J. Frederick, M. Hupa, and P. Hyöty, "Sulfur release during pyrolysis from single black liquor droplets." AIChE 1991 Forest Products Symposium Proceedings, TAPPI Press, Atlanta, p. 11-22 (1992).

Frederick, W.J., M. Hupa, "The effect of swelling on droplet trajectories, carbon burn-out, and entrainment in black liquor combustion,." AIChE 1991 Forest Products Symposium Proceedings, TAPPI Press, Atlanta, p. 79-90 (1992).

Frederick, W.J., Noopila, T., and Hupa, M., "Combustion behavior of black liquor at high solids firing conditions," *Tappi Jl.*, 74(12):163-170, 1991.

Frederick, W.J., Hupa, M., "Evidence of sodium fuming during pyrolysis of black liquor," *Tappi Jl.*, 74(11):192-194, 1991.

Frederick, W.J., Noopila, T., and Hupa, M., "Swelling of spent pulping liquor droplets during combustion," *Jl. Pulp Paper Sci.*, 17(5):J164-J170 (1991).

Frederick, W.J., Backman, R., and Hupa, M., "Pressurized Gasification of Spent Pulping Liquors: Thermodynamic and Kinetic Constraints," *Proc. 1991 Int'l. Symp. on Energy and Environment*, August 25-28, Espoo, Finland, p. 190-196.

Frederick, W.J., and Hupa, M., "The combustion and swelling characteristics of black liquor droplets and their impact on entrainment in kraft recovery boilers," *Proc. 2nd European Conf. on Ind. Boilers and Furnaces*, Portugal, Vilamoura - Algarve, Portugal, April 2-5, 1991.

Frederick, W.J. and M. Hupa, "Gasification of Black Liquor Char with CO_2 at Elevated Pressures," *Tappi Jl.*, 74(7):177-184 (1991).

Symposium Proceedings and Non-refereed Journals

Iisa, K., Carangal, A., Scott, A., Pianpucktr, R., Tangpanyapinit, V. , Nitrogen Oxide Formation and Destruction in Recovery Boilers. Paper 7.b.4, 1995 TAPPI-CPPA Intl. Chem. Recovery Conf., Toronto, April 24-27.

Kauppinen, E.I., Mikkanen, M.P., Valmari, T., Jokiniemi, J.K., Sinquefield, S.A., Frederick, W.J., Hupa, M., Backman, R., Forssén, M., McKeough, P., Arpiainen, V., Pyykönen, M., Moisio, M., Keskinen, J., Mäkinen, M., "Sodium release during black liquor pyrolysis: Differences between the results from various laboratory-scale experiments. Paper 5.b.5, 1995 TAPPI-CPPA Intl. Chem. Recovery Conf., Toronto, April 24-27.

Kymäläinen, M., Janka, K., Frederick, W.J., Sricharoenchaikul, V., Jivakanun, N., Wåg, K.J., Littau, M., Sulphate reduction in an Entrained-Flow Black Liquor Gassifier. Paper 7.b.6, 1995 TAPPI-CPPA Intl. Chem. Recovery Conf., Toronto, April 24-27.

Sricharoenchaikul, V., Frederick, W.J., Grace, T,M., Thermal Conversion of Tar to Light Gases During Black Liquor Pyrolysis. Paper 3.b.2, 1995 TAPPI-CPPA Intl. Chem. Recovery Conf., Toronto, April 24-27.

Sricharoenchaikul, V., Frederick, W.J., Kymäläinen, M., Grace, T,M., Sulfur Species Transformations and Sulfate Reduction During Pyrolysis of Kraft Black Liquor. Paper 3.b.4, 1995 TAPPI-CPPA Intl. Chem. Recovery Conf., Toronto, April 24-27.

Vakkilainen , E.K., Frederick, W.J., Reis, V.V., Wåg, K.J., Potassium and Chloride Enrichment During Black Liquor Combustion. Laboratory and Mill Measurements and a Mechanistic Model. Paper 5.b.1, 1995 TAPPI-CPPA Intl. Chem. Recovery Conf., Toronto, April 24-27.

Wåg, K.J., Frederick, W.J., Sricharoenchaikul, V., Grace, T,M., Kymäläinen, M. Sulfate Reduction and Carbon Removal During Kraft Char Burning, Paper 7.b.5, 1995 TAPPI-CPPA Intl. Chem. Recovery Conf., Toronto, April 24-27.

Hupa, M., Frederick, W.J., "Combustion of black liquor droplets," *Proc. 1993 TAPPI Kraft Recovery Operations Short Course* ,TAPPI Press, Atlanta (1993), p. 185-194.

Kauppinen, E. I., Mikkanen, P., Jokiniemi, J.K., Iisa, K., Boonsongsup, L., Sinquefield, S. A. , Frederick, W. J. "Fume Particle Characteristics and Their Reactions With SO_2 at Kraft Recovery Boiler Conditions" Proc. 1993 TAPPI Engineering Conf., TAPPI Press, Atlanta, p. 369-376.

Sinquefield, S.A., Mikkanen, P., Frederick, W.J., Kauppinen, E.I., "A laminar entrained flow reactor for the study of aerosol formation and deposition during black liquor combustion and pyrolysis," in *Report Series in Aerosol Science*, no. 23 (1993), P. Mikkanen, K. Hämeri, and E.I. Kauppinen, Editors. Finnish Association for Aerosol Research, Espoo, Finland.

Hupa, M., Frederick, W.J., "Combustion of black liquor droplets," *Proc. 1991 TAPPI Kraft Recovery Operations Seminar*, TAPPI Press, Atlanta (1991), p. 191-200.

Frederick, W.J., Backman, R., and Hupa, M., "Pressurized Gasification of Spent Pulping Liquors: Thermodynamic and Kinetic Constraints," *Proc. 1992 TAPPI-CPPA Intl. Chemical Recovery Conf.,* TAPPI Press, Atlanta, p. 617-626.

Frederick, W.J., Forssén, M., Hupa, M., Hyöty, P., Sulfur And Sodium Volatilization During Black Liquor Pyrolysis Proc. 1992 TAPPI - CPPA International Chemical Recovery Conference, TAPPI Press, Atlanta, June 7-11, p. 599-608.

Skrifvars, B.-J., Frederick, W.J., Hupa, M. Chemical Reaction Sintering as a Cause for Lime Kiln Rings. Proc. 1992 TAPPI - CPPA International Chemical Recovery Conference, TAPPI Press, Atlanta, June 7-11, p. 161-167.

Whitty, K.J., Frederick, W.J., Hupa, M., Gasification of Black Liquor Char With H_2O at Elevated Pressures, *Proc. 1992 TAPPI-CPPA Intl. Chemical Recovery Conf.,* TAPPI Press, Atlanta, p. 627-639.

Frederick, W.J., Kulas, K.C., Clay, D.T., Hupa, M., Noopila, T., "Analysis of black liquor single droplet combustion data", *Proc. 1989 Int'l. Chem. Recovery Conference*, Ottawa, April 3-6, 1989, p. 81-88.

Technical Reports

Frederick, W.J., Hupa, M., "Combustion Parameters for Black Liquor." Report to the U.S. Department of Energy, US DOE Report DOE/CE/40936-T1 (DE94007502), April, 1993 and jointly as Combustion Chemistry Research Group Report 93-3, Åbo Akademi University, Turku, Finland, 1993.

Frederick, W.J., "Combustion processes in black liquor recovery: analysis and interpretation of combustion rate data and an engineering design model," Report No. 1, U.S. Department of Energy Report DOE/CE/406637-T8, March, 1990.

Frederick, W.J., Hupa, M., "Gasification of black liquor at elevated pressure. Part 2: Rate data with CO_2 and water vapor," *Combustion Chemistry Research Group Report 90-12,* Abo Akademi, Turku, Finland (1990).

Frederick, W.J., Hupa, M., "Single droplet burning behavior of pulping spent liquors," *Combustion Chemistry Research Group Report 90-2*, Abo Akademi, Turku, Finland (1990).

Frederick, W.J., Noopila, T., Hupa, M., "An analysis of swelling during the combustion of pulping liquor droplets," *Combustion Chemistry Research Group Report 89-12*, Abo Akademi, Turku, Finland (1989).

Frederick, W.J., Noopila, T., and Hupa, M., "Swelling of pulping liquor droplets during combustion," paper no. 157d, AIChE 1989 Annual Meeting, San Francisco, November 5-10, 1989. *Combustion Chemistry Research Group Report 89-14,* Abo Akademi, Turku, Finland (1989).

Frederick, W.J., Noopila, T., Hupa, M., "Modeling of black liquor droplet combustion," *Combustion Chemistry Research Group Report 89-15*, Abo Akademi, Turku, Finland (1989).

APPENDIX III

RADIATIVE HEAT TRANSFER PROPERTIES FOR BLACK LIQUOR COMBUSTION

Interim Project Summary Report

April 1, 1995 - October 31, 1995

By:

BABCOCK & WILCOX COMPANY

Richard A. Wessel
Ralph T. Bailey
Robert A. McIlroy

Date: October 31, 1995

Subcontract No. 1
Between
THE INSTITUTE OF PAPER SCIENCE AND TECHNOLOGY
AND
BABCOCK AND WILCOX

DOE DE-FG02-90CE40936
IPST Project No. 3605-2
B&W CRD No. 1328
B&W RDD No. 43383

NOTICE

This report was prepared by Subcontractor as an account of work sponsored by the United States Government. Neither the United States Government, nor the US Department of Energy, nor the Contractor, nor the Subcontractor, nor their subcontractors, nor any of their employees, makes any warranty, express or implied, or assumes any legal liability or responsibility for the accuracy, completeness, or usefulness of any information, apparatus, product, or process disclosed, or represents that its use would not infringe privately-owned rights.

TABLE OF CONTENTS

SUMMARY

The spectral emittance of kraft black liquor and intermediate condensed phase products of combustion were determined using two measurement techniques. Spectral emittance of black liquor, dried solids and char were measured at relatively low temperatures, 25°C, at which the amount of emitted energy is to small to be detected. The 67% solids black liquor was "painted" onto a substrate. The dried solids and char samples were pressed into pellets about 3 cm in diameter and 2 mm thick. These samples were illuminated by monochromatic light, and the reflected energy from the samples was measured. The spectral emittance was determined by comparing the reflected energy from the sample to that reflected from a standard surface of known emittance. Black liquor and black liquor solids have a high emittance at all wavelengths, with total emittance of 0.92 to 0.98 at 850°C (source temperature). The total emittance of the char was 0.86 at 850°C (source temperature).

High temperature emittance measurements of the char sample were attempted. However, it was difficult to heat the char above 650°C due to the low thermal conductivity of the sample. At this elevated temperature, the char wafer cupped, and the thermocouple junction detached from the surface of the char so that the surface temperature was underestimated and reliable data could not be obtained.

The smelt samples were heated to a high temperature, at which the amount of emitted spectral energy could be measured directly. The smelt samples were contained in a platinum dish, radiantly heated from the below, with a molten smelt thickness of 3 to 5 mm and maintained under a nitrogen purge containing 10% CO to suppress Na_2CO_3 decomposition. The spectral emittance was determined by comparing the emitted energy from the sample to that emitted by a blackbody at the same temperature. Spectral emittance was measured for oxidized and reduced synthetic smelt, and industrial smelt at temperatures of about 850°C. Measurements showed that the spectral emittances of the three types of smelt were quite similar at wavelengths greater than 3 microns. The emittance of the smelt samples are all quite high, with total emittance values ranging from 0.82 to 0.94. At visible wavelengths, less than 2 microns, the synthetic smelt samples were partially transparent and measurements were less reliable because they included radiation from the bottom of the dish.

The measurement phase of this project was completed and is the subject of this interim report. Spectral emittance results should be used to calculate total emissivity and absorptivity of black liquor, dried solids, char and smelt in the second phase of this project. General correlations for emissivity and absorptivity as a function of temperature should be developed for use in engineering models. Existing submodels for black liquor drop combustion should be used to evaluate the effect of radiative properties on predicted drop temperatures and heating rate. Global models of the recovery furnace should be used to evaluate the effect of radiative properties on furnace heat absorption and gas temperature exiting the furnace cavity.

1.0 INTRODUCTION

1.1 BACKGROUND

Radiation properties of black liquor, char and smelt are needed to calculate heat transfer in a kraft recovery boiler. Heat transfer in the lower furnace is dependent upon the emissivity and absorptivity of burning black liquor drops, char bed and deposits on the furnace walls. These properties can be determined from measurements of spectral emittance (or reflectance) over the infrared spectrum, at wavelengths from 0.8 to 10 μm. Radiation properties for combustion gases (H_2O, CO_2, CO and SO_2) and soot particles are also needed, but are readily available in the literature (Siegel and Howell, 1981; Edwards and Balakrishnan, 1973).

Properties of gas-entrained carryover and aerosol (fume) particles are needed for absorption and scattering of radiation in the upper furnace. Radiation properties of small particles, less than about 100 μm, are determined from measurements of the complex index of refraction and calculations based on Mie theory (Bohren and Huffman, 1983). Properties of particles, greater than 100 μm, can easily be determined from measurements of spectral emittance.

The radiative properties of black liquor cannot be found in the literature. Models have generally relied on estimates of these properties based on the properties of coal, char and ash (Wessel et al, 1993). Radiation properties are used to analyze and interpret black liquor combustion data to develop chemical kinetic relationships for combustion submodels (Frederick, 1990; Frederick and Hupa, 1993). Predicted drop heating rates and temperature, during drying and devolatilization stages of combustion, have a large effect on drop swelling and burning characteristics (Wessel and Verrill, 1995). Submodels for black liquor combustion and radiative heat transfer are used in global models for recovery boilers to predict boiler performance (Wessel et al, 1995; Nowak et al, 1995). Radiative properties are critical for predicting furnace heat absorption and the temperature of combustion gases exiting the furnace cavity. Local heat flux and temperature of furnace walls is sensitive to the emissivity of wall deposits.

1.2 PROJECT OBJECTIVE

The objective of this project is to develop a radiation model for black liquor combustion that is based on spectral emittance measurements of black liquor and intermediate condensed phase products of combustion at typical combustion temperatures. This objective will be accomplished in two phases:

1. Measure spectral emittance (or reflectance) of black liquor, dry solids, char and smelt.

2. Develop engineering correlations of total emissivity and absorptivity for use in black liquor combustion models.

Phase 1 was completed and is the subject of this interim report. Phase 2 is expected to begin in November 1995.

2.0 SPECTRAL EMITTANCE MEASUREMENTS

2.1 SAMPLE PREPARATION

Samples of black liquor, dry solids, char, industrial smelt and two synthetic smelts were prepared for emissivity measurements. A large sample of as-fired black liquor was obtained from a predominately softwood mill producing bleached kraft pulp. The black liquor sample was analyzed for gross heating value, solids content and elemental composition (Table 1). A sample of dry solids was prepared from the liquor sample by spreading the liquor in a shallow pan and drying for 16 hours (two 8 hour days) at 105°C under an air atmosphere. A sample of char was prepared by heating the liquor to 500°C in a muffle furnace. The furnace temperature was raised to the final temperature in several steps over a period of 3 hours.

Individual samples of solidified smelt were collected from each of the five smelt spouts in ingot molds. The solidified ingots were broken and material from the unoxidized center was analyzed for total sodium, potassium, sulfur, and chloride content, as well as sulfidity and degree of reduction (Table 2). Additional center material from the sample 53580 ingot was used as the industrial smelt sample. The synthetic mixtures were prepared from reagent grade compounds to represent a fully-reduced and fully-oxidized smelt. The ratios of sulfur to total alkali and potassium to sodium in the synthetic smelts were based on the average values from the industrial smelt analysis. The readily available reagent grade of Na_2S contained 9 waters of hydration. The material was dehydrated by heating to 105°C in an oven flushed with nitrogen. The dry product was then ground to a powder in a glove box flushed with nitrogen. The dry powders were then weighed and mixed together (Table 3). There was no attempt to premelt the mixtures since the emissivity measurement would melt the sample.

Table 1. Analysis of As-Fired Black Liquor

B&W sample No.		F-5871	
Basis (Oven dry)		As Received	Dry
Moisture	(%)	32.65	0.00
Solids	(%)	67.35	100.00
Total Sulfur	(%)	4.25	6.31
Gross Heating Value	(Btu/lb)	3810	5657
ELEMENTAL ANALYSIS			
Moisture	(%)	32.65	0.00
Carbon	(%C)	21.40	31.77
Hydrogen	(%H)	2.42	3.59
Nitrogen	(%N)	0.05	0.07
Sulfur	(%S)	4.25	6.31
Sodium	(%Na)	14.83	22.02
Potassium	(%K)	1.01	1.50
Chlorine	(%Cl)	0.55	0.82
Inerts	(%)	0.00	0.00
Oxygen (by diff.)	(%O)	22.84	33.92
Total	(%)	100.00	100.00

Table 2. Analysis of Smelt Samples

Composition as reported, % by weight							
Sample No.		53580	53581	53582	53583	53584	Average
Total S	(as SO_3)	29.9	29.7	30.4	30.9	30.1	30.2
Total Na	(as Na_2O)	58.0	56.1	61.0	59.4	58.1	58.5
Total K	(as K_2O)	3.2	3.1	3.2	3.2	3.0	3.1
Total Cl	(as Cl)	1.4	1.4	1.3	1.5	1.4	1.4
Calculated composition, % by weight							
Na_2CO_3		68.3	68.6	68.4	67.7	67.9	68.2
NaOH		0.0	0.0	0.2	0.8	0.0	0.2
NaCl		2.2	2.2	2.2	2.5	2.3	2.3
Na_2S		25.9	26.2	27.7	27.8	25.0	26.5
$Na_2S_2O_3$		1.7	1.8	1.5	1.4	1.7	1.6
Na_2SO_3		0.0	0.1	0.0	0.0	0.0	0.0
Na_2SO_4		2.4	3.3	2.1	2.2	5.3	3.1
NaHS		0.5	0.0	0.0	0.0	0.4	0.2
Total		101.0	102.2	102.1	102.4	102.6	102.1
Molar Ratios, %							
$S/(Na_2O+K_2O)$		38.550	39.595	37.343	38.871	38.779	38.610
K_2O/Na_2O		3.633	3.639	3.400	3.588	3.412	3.533

Table 3. Composition of Synthetic Smelt

Composition, % by weight	Oxidized	Reduced
Na_2CO_3	50.79	63.83
Na_2S	0.00	31.28
Na_2SO_4	45.31	0.00
K_2CO_3	3.89	4.89
Total	100.00	100.00
Molar Ratios, %		
$S/(Na_2O+K_2O)$	38.610	38.610
K_2O/Na_2O	3.533	3.533

2.2 EXPERIMENTAL APPARATUS

The spectral emittance of the different forms of black liquor were determined using two measurement techniques. The black liquor, dried solids and char were maintained at relatively low temperatures, 25°C, at which the amount of emitted energy is to small to be measured. These samples were illuminated by monochromatic light, and the reflected energy from the samples was measured. The spectral emittance was determined by comparing the reflected energy from the sample to that reflected from a standard surface of known emittance. The smelt samples were heated to a high temperature, 850°C, at which the amount of emitted spectral energy could be measured directly. The spectral emittance was determined by comparing the emitted energy from the sample to that emitted by a blackbody at the same temperature.

Spectral Reflectance Measurements

The Spectral Reflectance Facility consists of a blackbody radiation source, grating monochrometer, infrared integrating sphere and associated photo-detectors. The integrating sphere is 8 inches in diameter with the interior surface coated with gold to provide high reflectance over the measurement range of about 0.7 to 14 microns. Three penetrations are located around the equator of the sphere. Light enters one port and is focused onto the sample port, located on the opposite side of the sphere. Located at 90 degrees to these ports, is the third port in which a photo-detector is mounted. Light reflected from the sample at all angles is contained and reflected inside the sphere. The magnitude of the light energy, measured by the photo-detector, is a measure of the energy reflected by the sample.

Reflectance is determined by measuring the photo-detector signal from a gold-coated sample (reflectance, $\rho = 0.96$), from an open hole ($\rho = 0$), and from the sample of unknown reflectance. The spectral reflectances of the samples are between those of the gold-coated sample and the open hole, and the sample reflectance is determined by linear interpolation.

For measuring reflectance as a function of wavelength the integrating sphere was placed at the output of the monochrometer which together with the blackbody radiation source provided a repeatable source of wavelength separated light. This measurement provides the total hemispherical reflectance. The absorptance (emittance) is simply the difference between unity and reflectance.

An uncertainty analysis performed for the facility shows the uncertainty in spectral emittance at two standard deviations to be around 6 to 7 percent for wavelengths from 1 to 5 microns. For wavelengths greater than 6 microns, the uncertainty is about doubled. The increase above 6 microns is due to the increased electronic noise of the detector that is used in this wavelength range, and a greater sensitivity to detector temperature. This uncertainty analysis is based on measurements made with the facility in the emittance mode. However, the levels of uncertainty should be about the same, for room temperature reflectance measurements. The exception is increased uncertainty for data at wavelengths beyond 10 or 11 micrometers where the reflected energy is typically low.

Spectral Emittance Measurement Facility

Spectral and total emittance measurements for this project were performed at the Spectral Emittance Measurement Facility. The facility consists of a high-temperature furnace, optics, a grating monochromator, a series of photo detectors, and a personal computer-based data acquisition system. Figure 1 is a photograph of the facility, and Figure 2 provides a schematic of the facility. A description of the facility and measurement techniques is provided in Appendix A.

To determine the emittances, it is necessary to measure both the surface temperature and the spectral radiation from the heated samples. The furnace is designed to radiantly heat 2-inch square samples to temperatures in excess of 1100°C. For this test, a platinum crucible was mounted in a hole in a square plate, and the crucible was radiantly heated from the backside. The smelt material was then placed in the crucible and heated to melting.

A gold-plated mirror and a zinc selenide lens collect and focus the emitted radiant energy into the monochromator. The monochromator and gratings then disperse the radiant energy by wavelength and transmit it to the photo detectors. The photo-detector voltage signal, proportional to the incident energy, is measured using an A/D converter and input into the computer where it is saved. Measurements are also made on the blackbody calibration source so the emissive power of the sample at a given wavelength can be normalized to that of a theoretical blackbody at the same temperature. The resulting data are then analyzed according to the procedure outlined in Appendix A.

The level of uncertainty in the spectral emittance measurements is discussed here to qualify the data. A past uncertainty analysis that was performed for the facility identified the uncertainty in spectral emittance at two standard deviations to be around 6 to 7 percent for wavelengths from 1 to 5 microns. For wavelengths greater than 6 microns, the uncertainty was about doubled. The increase above 6 microns was due to the increased electronic noise of the detector that is used in this wavelength range, and a greater sensitivity to detector temperature. This uncertainty analysis was performed based on using thermocouples for determining the surface temperatures.

2.3 MEASUREMENT PROCEDURES

The spectral emittance of the black liquor, dried solids and char samples were determined from room temperature reflectance measurements. Samples were maintained in sealed containers in an inert atmosphere until testing. The liquid black liquor was "painted" onto a substrate. The char and dried solids samples were pressed into pellets about 3 cm in diameter and 2 mm thick. Spectral reflectance measurements were conducted at 25°C, in air.

Spectral emittance measurements were made for synthetic smelt and industrial smelt at temperatures of about 850°C (see Table 4). The smelt samples were heated to about 850°C to directly measure radiated energy and determine spectral emittance. The high-temperature tests were conducted under a nitrogen purge containing 10% CO to suppress Na_2CO_3 decomposition.

The platinum crucible was installed in the furnace and radiantly heated to a temperature of about 750°C. The CO/N_2 purge was started and about 5 grams of solid smelt was added to the crucible. The temperature of the crucible was then increased to melt the smelt sample and the Type S platinum/platinum-rhodium thermocouple was positioned just below the surface of the molten smelt. The 5 gram sample provided a molten smelt thickness of 3 to 5 mm in the crucible. The smelt temperature was then increased to about 850°C, and the spectral measurements were started.

High temperature emittance measurements of the char sample were also attempted. For this material, ground char was pressed into a wafer of about 30 mm diameter and 3 mm thickness. A Pt/Pt-Rh thermocouple was placed in a small groove in the surface of the wafer and lightly covered with powdered char. The wafer was placed on a thin stainless steel plate that was radiantly heated from the backside. As with the smelt samples, the char was contained in a CO/N_2 environment to prevent oxidation. Using this procedure, the char sample was heated to about 650°C. However, at this elevated temperature, the char wafer cupped, and the thermocouple junction detached from the surface of the char so that the surface temperature was underestimated and reliable data could not be obtained.

Table 4. Black Liquor Emittance Measurement Conditions

Sample Description	Measurement	Sample Temperature	Sample Environment
Black Liquor (67% Solids)	Reflectance	25 °C	Air
Dried Black Liquor Solids	Reflectance	25 °C	Air
Black Liquor Char	Reflectance	25 °C	Air
Industrial Smelt	Emittance	813 - 848 °C	10% CO in N_2
Synthetic Smelt (Oxidized)	Emittance	870 - 931 °C	10% CO in N_2
Synthetic Smelt (Reduced)	Emittance	872 °C	10% CO in N_2

3.0 EMITTANCE RESULTS

The spectral emittance of the black liquor, dried black liquor solids, and char are shown in Figures 3 through 5 respectively. High emittance was measured at nearly all wavelengths. The scatter in the individual data points about the smoothed curve is about 10%. This scatter is due to the weak signal associated with these measurements along with the detector noise. The data for the black liquor and dried solids in Figures 3 and 4 are nearly the same for wavelengths greater than 1.5 microns. The decrease in emittance indicated at wavelengths greater than 7 microns in Figures 3 and 4 may also be due to the weak signal and relatively large measurement uncertainty at these wavelengths.

The spectral emittance of the industrial smelt as a function wavelength is shown in Figures 6, 7 and 8 for three separate measurements of the same material, denoted as A, C and E. The emittance of the industrial smelt is near unity over the entire wavelength range measured in these tests. The three sets of data show similar inflections in the spectral emittance, in particular at a wavelength of about 4.5 micrometers.

At the shortest wavelength's, the measured emittance consistently exceeded a value of 1. This was likely caused by an underestimate of the surface temperature of the smelt, as radiant energy in the visible and near-infrared is very sensitive to temperature. For example, at a wavelength of 0.8 micron and a temperature of 850°C, a 5°C change in temperature causes a 10% change in radiant energy. For these samples, then, the spectral emittance at wavelengths below 1 to 2 microns is near 1. Visually, these molten samples appeared opaque, and the molten smelt surface contained several "black lines" that were likely carbon particles that congregated at the boundaries of convection bubbles in the molten smelt.

Figures 9 and 10 show the spectral emittance as a function of wavelength for a synthetic oxidized smelt, denoted as samples A and B. The two sets of data in these figures are quite repeatable, including the small inflections in spectral emittance at wavelengths above 4 microns. Although spectral data is provided down to a wavelength of about 1 micron, the data at the lowest wavelengths is suspect. This is because the molten sample was noticeably transparent at visible wavelengths. This implies that the source of the radiant energy measured at these short wavelength was the bottom of the platinum crucible rather than the molten surface of the smelt. Although the emittance of the platinum is probably quite low, the temperature of the platinum crucible can be significantly greater (i.e. 20 to 30°C) than the smelt surface. With the measurement procedure used in this test it is not possible to isolate radiation from the platinum from that of the smelt. For wavelengths of 3 microns and greater, the data for the synthetic oxidized smelt is very similar to the industrial smelt.

Figure 11 shows the spectral emittance of the synthetic reduced smelt. As with the other smelt samples, the spectral emittance of this sample at wavelengths above 3 microns is near 1 and shows similar spectral inflections with wavelength. Below 3 microns the spectral emittance averages about 0.7. As with the synthetic oxidized smelt, this sample was partially transparent at visible wavelengths, but somewhat less than so than the oxidized sample. The emittance data at short wavelengths is probably subject to similar types of errors.

The spectral emittance data shown in the preceding figures were numerically integrated over wavelength to determine the total emittance. To compare the different samples, this calculation was performed at a temperature of 850°C. The results are given in Table 5 which gives a description of the sample and the calculated total emittance. As shown, there is not a large difference in the total emittance of the samples at this temperature.

Table 5. Integrated Spectral Emittance Evaluated at a Temperature of 850°C

Sample Description	Integrated Spectral Emittance at 850°C
Black Liquor (67 % Solids)	0.977
Dried Black Liquor Solids	0.918
Black Liquor Char	0.859
Industrial Smelt Sample A	0.888
Industrial Smelt, Sample C	0.926
Industrial Smelt, Sample E	0.944
Synthetic Oxidized Smelt, Sample A	0.825
Synthetic Oxidized Smelt, Sample B	0.883
Synthetic Reduced Smelt, Sample A	0.851

4.0 CONCLUSIONS AND RECOMMENDATIONS

Spectral emittance measurements of black liquor, dried solids, char and smelt were successfully completed. Black liquor and black liquor solids have a high emittance at all wavelengths, with total emittance of 0.92 to 0.98 at 850°C (source temperature). The total emittance of the char was slightly lower, 0.86 at 850°C (source temperature). The emittance of the different smelt samples were similar, with total emittance values ranging from 0.82 to 0.94.

Reliable measurements for the high temperature emittance of the char sample could not be obtained. The char was difficult to heat above 650°C due to low thermal conductivity. Large temperature gradients caused the sample to deform in the platinum crucible and surface temperature was underestimated because the thermocouple junction detached from the surface of the char. Therefore, it was necessary to determine the spectral emittance of the char sample using room temperature reflectance measurements.

At visible wavelengths the synthetic smelt samples were at least partially transparent and this affected the measured emittances. For these samples the measured spectral emittances at wavelengths less than 2 microns are probably not reliable. Emittance measurements of transparent or semi-transparent samples can not be made with the existing measurement equipment and procedures.

The spectral emittance results in this report should be used to calculate total emissivity and absorptivity of black liquor, dried solids, char and smelt in the second phase of this project. General correlations for emissivity and absorptivity as a function of temperature should be developed for use in engineering models. Existing submodels for black liquor drop combustion should be used to evaluate the effect of radiative properties on predicted drop temperatures and heating rate. Global models of the recovery furnace should be used to evaluate the effect of radiative properties on furnace heat absorption and gas temperature exiting the furnace cavity.

5.0 REFERENCES

Bohren, C.F. and Huffman, D.R. *Absorption and Scattering of Light by Small Particles*, John Wiley and Sons, New York, (1983).

Edwards, D.K. and Balakrishnan, A., "Thermal Radiation from Combustion Gases," *International Journal of Heat and Mass Transfer,* Vol. 16, pp.25-40, (1973).

Frederick, W.J., "Combustion Processes in Black Liquor Recovery: Analysis and Interpretation of Combustion Rate Data and an Engineering Design Model, Report No. 1," *Department of Energy Report,* DOE/CE/40637-T8, (1990).

Frederick, W.J. and Hupa, M., "Combustion Properties of Kraft Black Liquors," Department of Energy Report, DOE Contract No. DE-FG02-90CE40936, (1993).

Nowak, P., Matys, P. Sabhapath, P. Abdullah, Z. And Salcudean, M., "Numerical Study of a Kraft Recovery Furnace," *1995 International Chemical Recovery Conference*, Toronto (1995).

Siegel, R. and Howell, J.R., *Thermal Radiation Heat Transfer*, 2nd Ed., McGraw Hill, New York, (1981).

Wessel, R.A., Parker, K.L., and Akan-Etuk, A., "Three-Dimensional Model of a Kraft Recovery Furnace," *1993 Tappi Engineering Conference,* Orlando, (1993).

Wessel, R.A., Parker, K.L., and Verrill, C.L., "Three-Dimensional Kraft Recovery Furnace Model; Implementation and Results of Improved Black Liquor Combustion Models," *1995 Tappi Engineering Conference*, Dallas (1995).

Wessel, R.A. and Verrill, C.L., "Sodium Loss During Black Liquor Drying and Devolatilization - Application of Modeling Results to Understanding Laboratory Data," *1995 International Chemical Recovery Conference*, Toronto (1995).

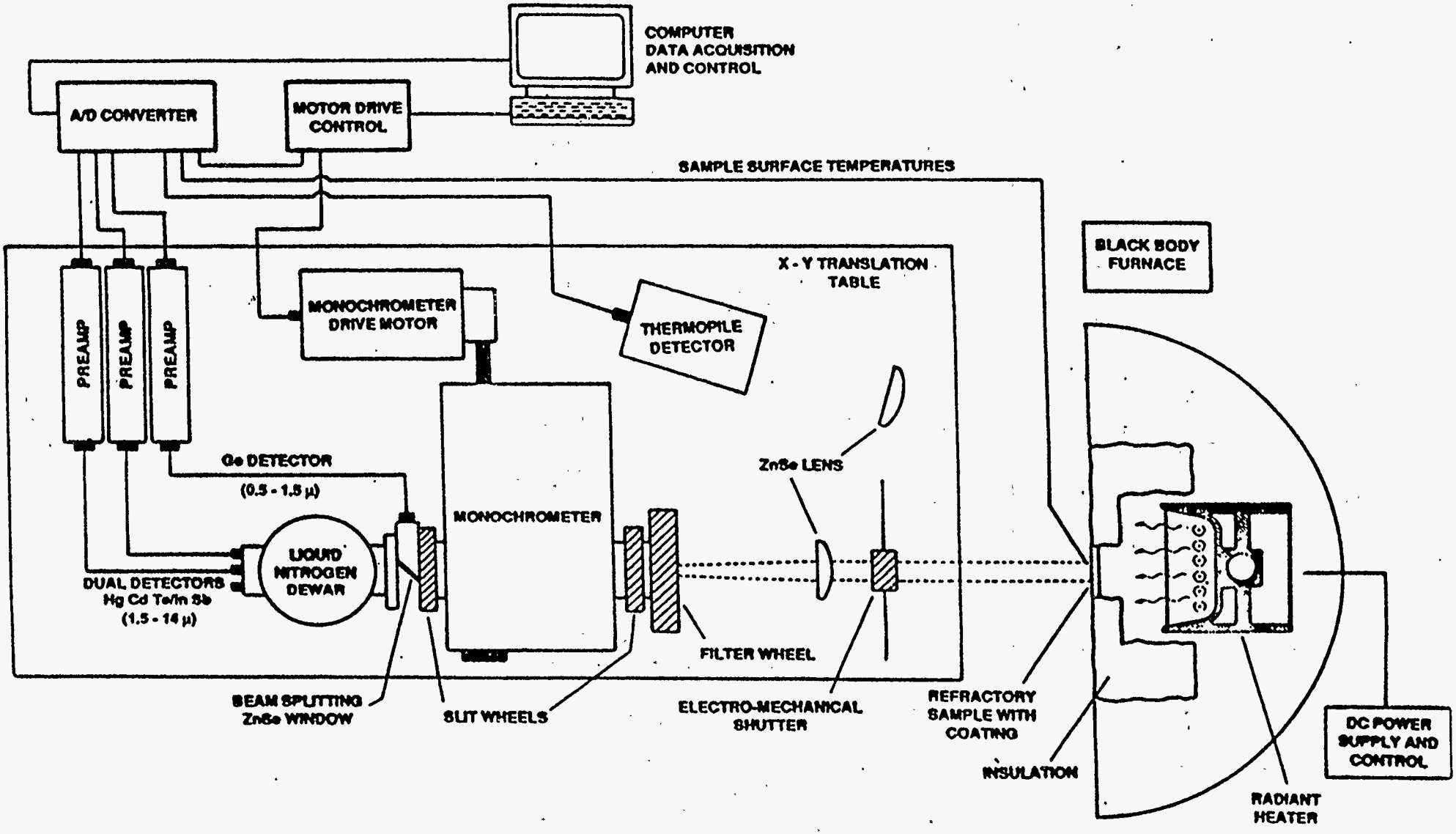

Figure 1. Schematic of High Temperature Spectral Emittance Measurement Facility.

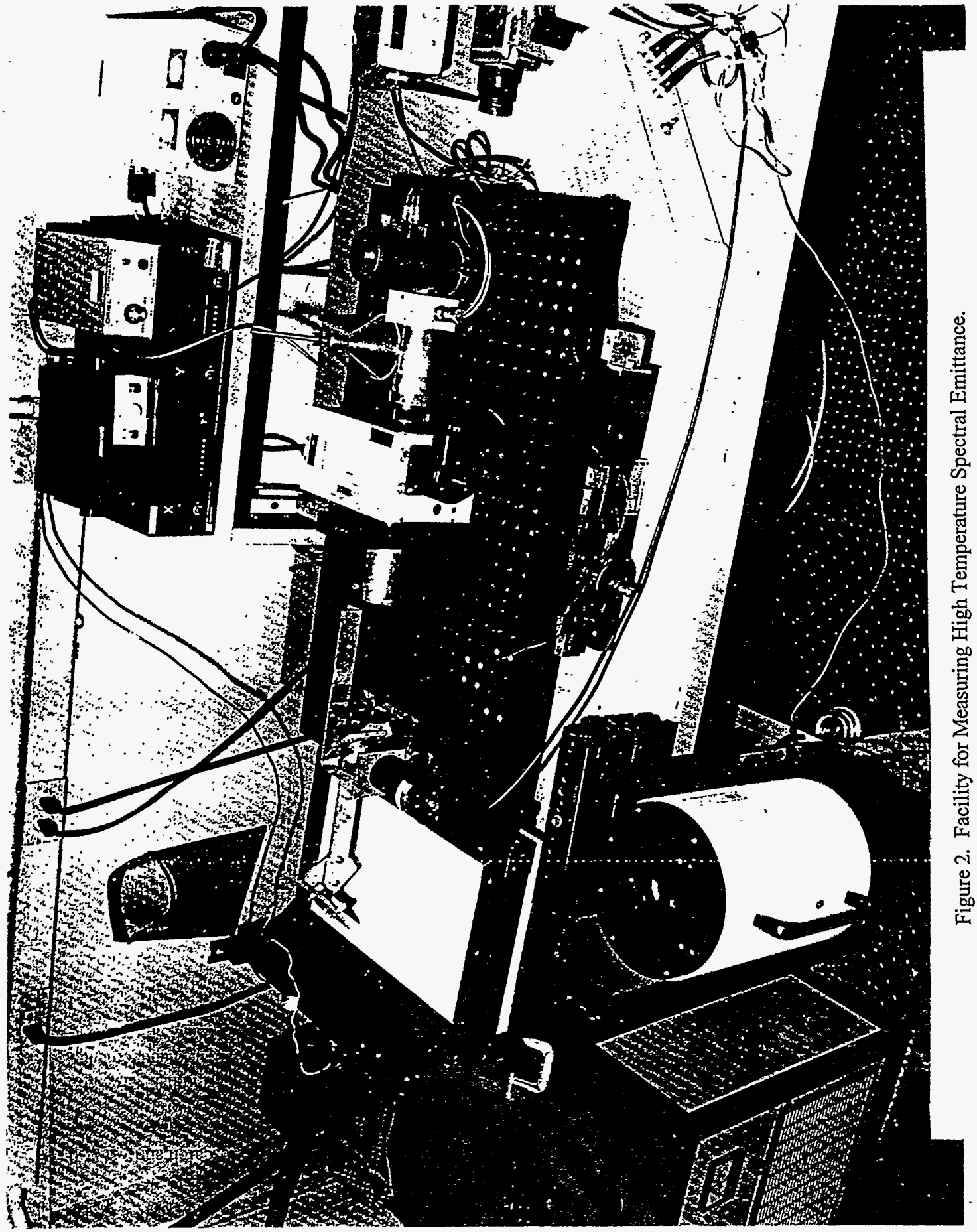

Figure 2. Facility for Measuring High Temperature Spectral Emittance.

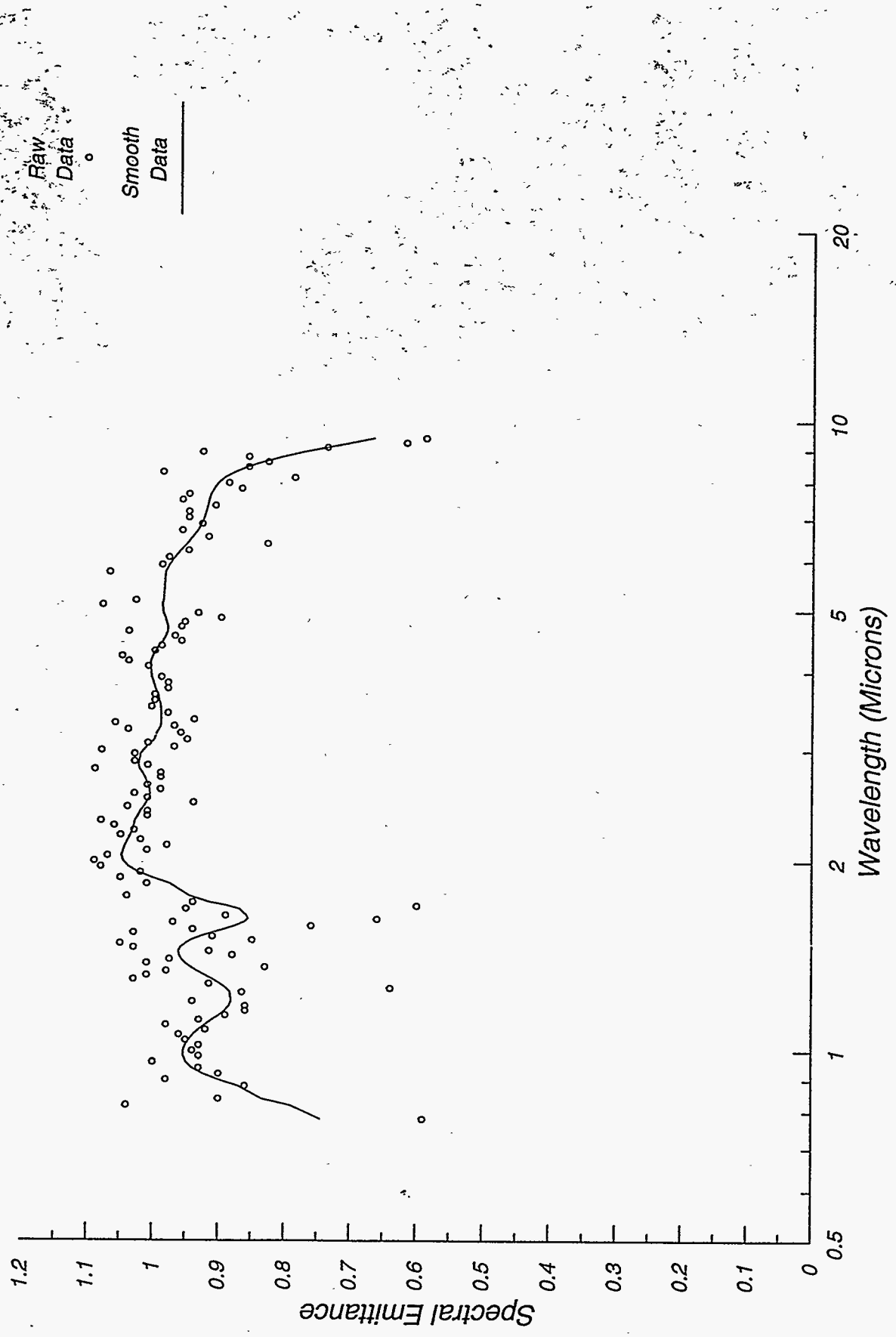

Figure 3. Spectral Emittance as a Function of Wavelength for Black Liquor (67% Solids).

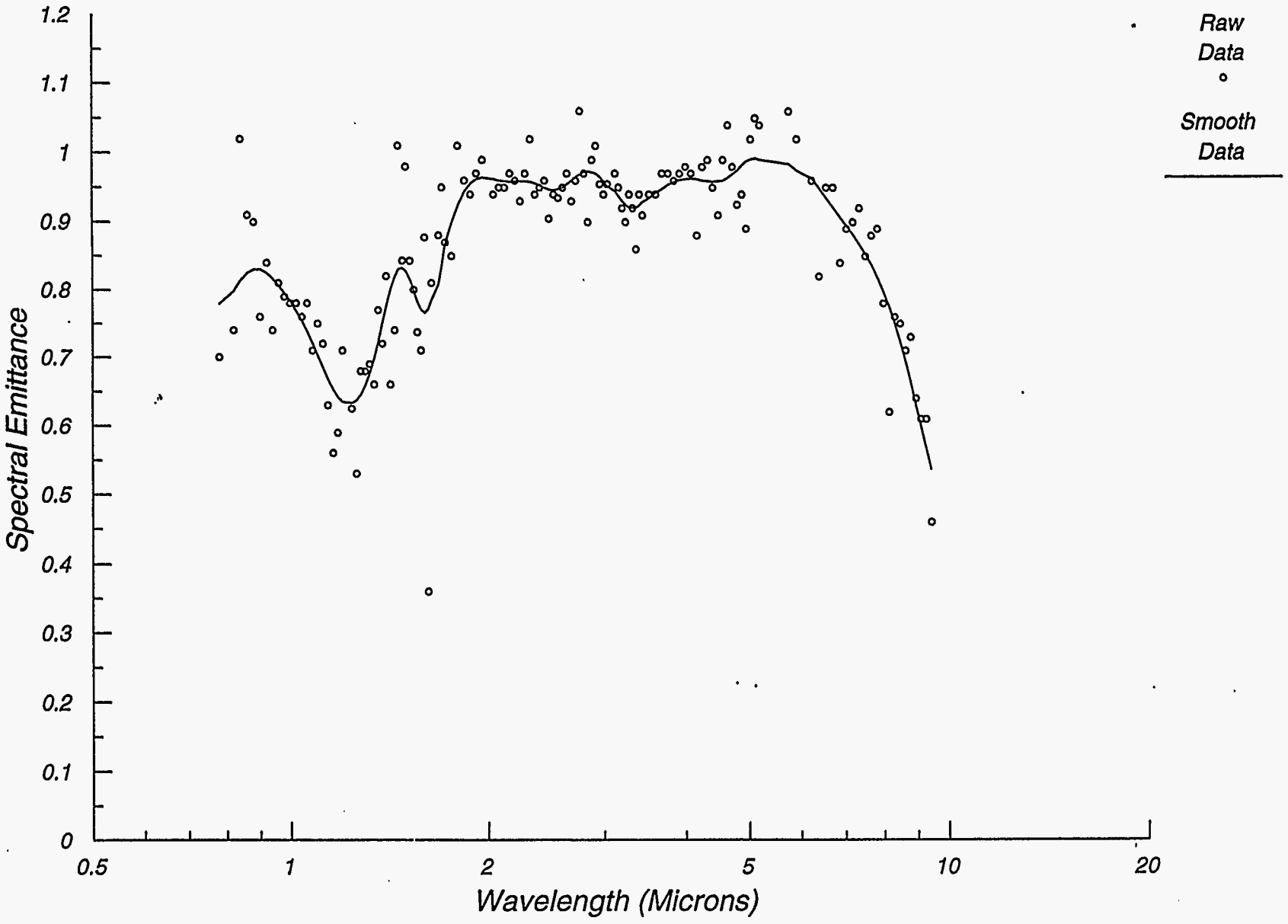

Figure 4. Spectral Emittance as a Function of Wavelength for Black Liquor Solids.

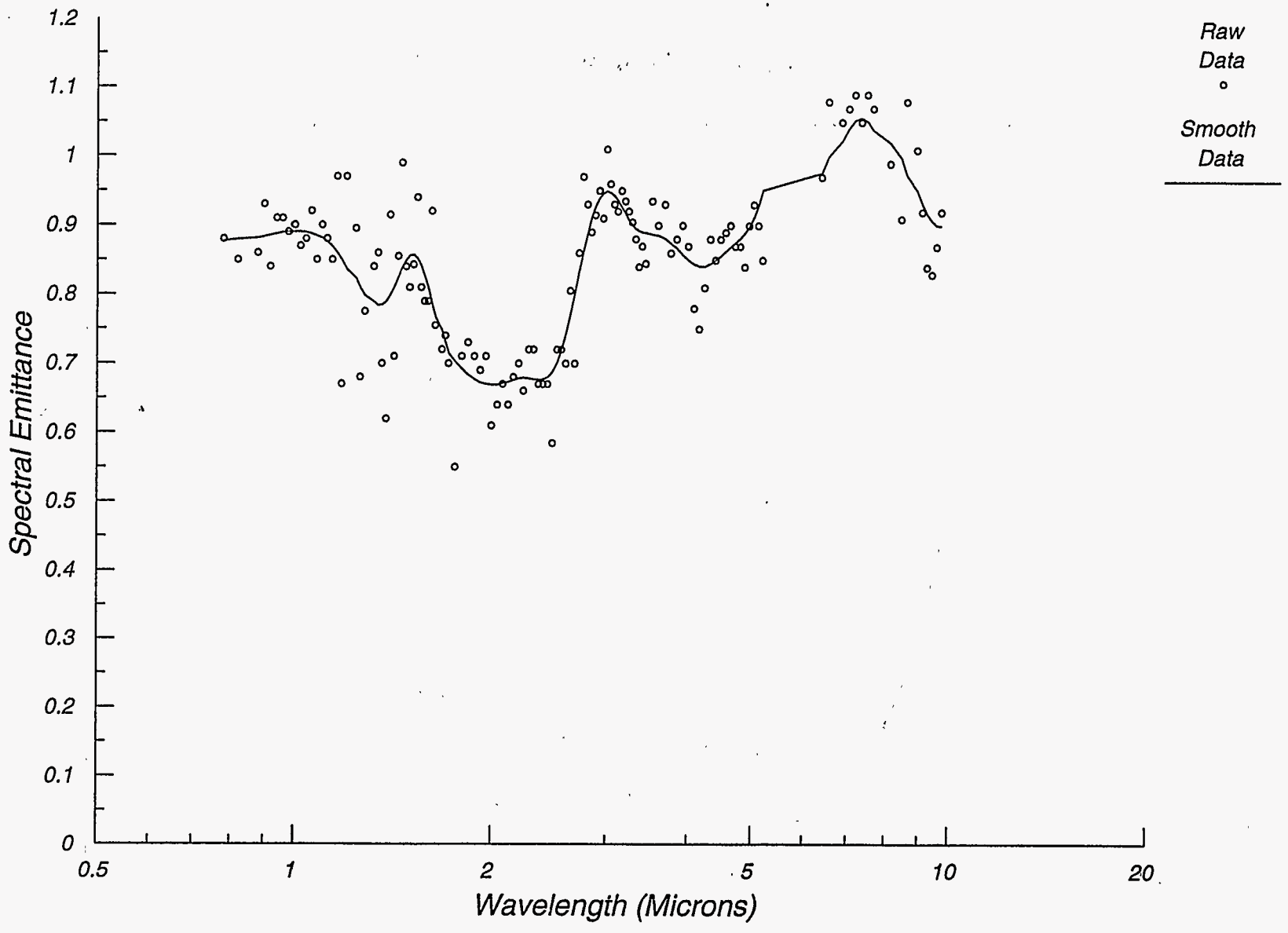

Figure 5. Spectral Emittance as a Function of Wavelength for Black Liquor Char.

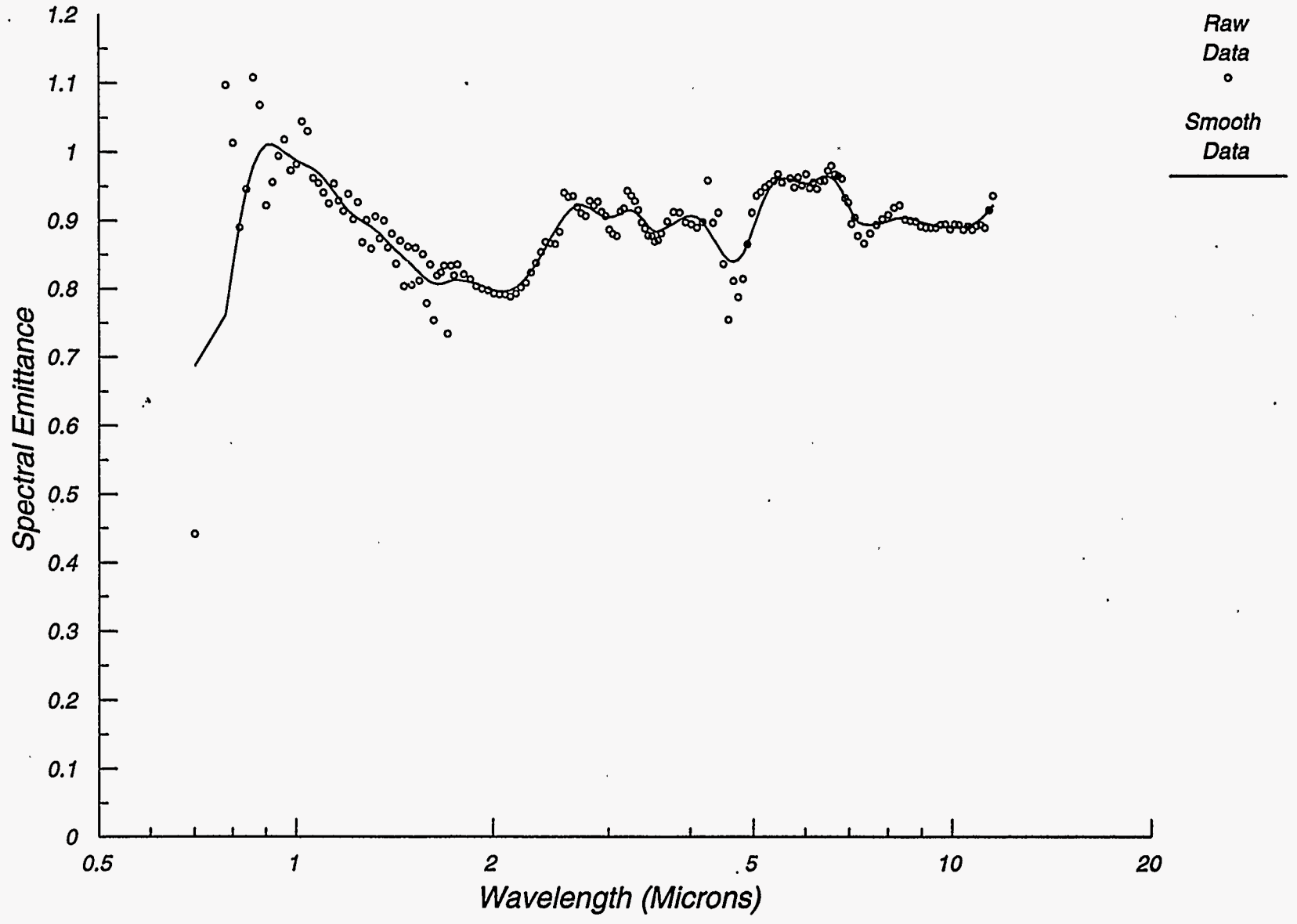

Figure 6. Spectral Emittance as a Function of Wavelength for Industrial Smelt Sample A.

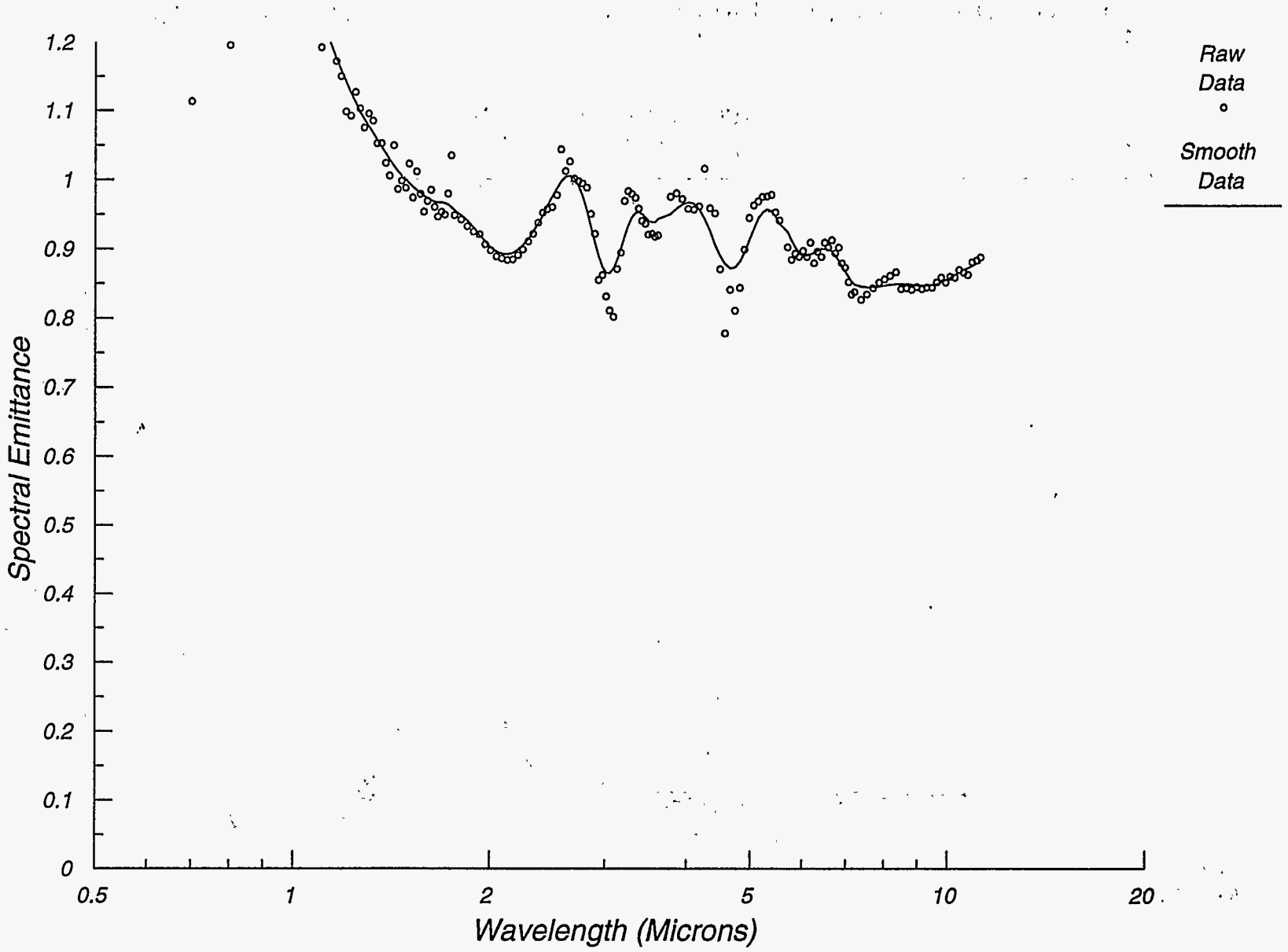

Figure 7. Spectral Emittance as a Function of Wavelength for Industrial Smelt Sample C.

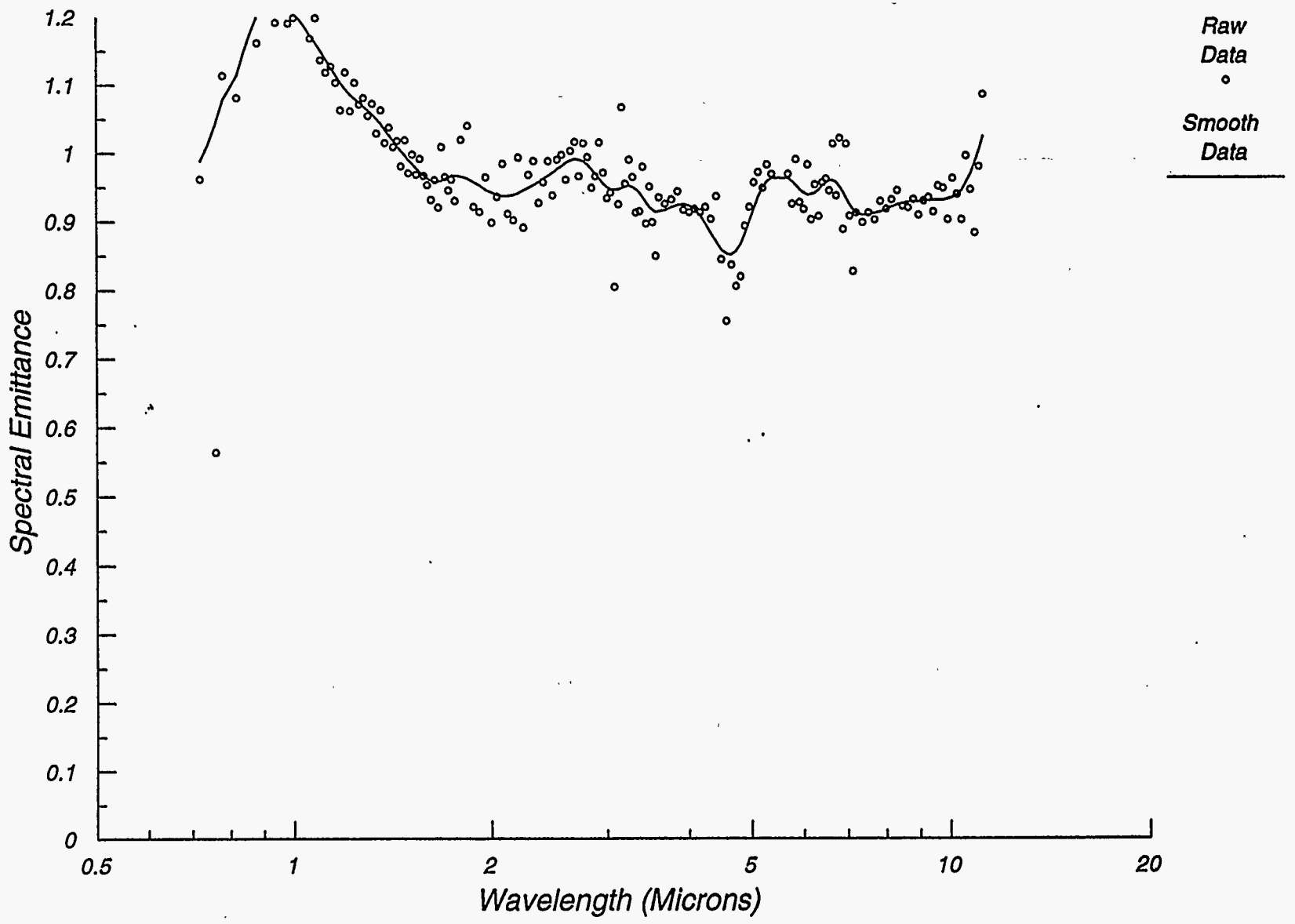

Figure 8. Spectral Emittance as a Function of Wavelength for Industrial Smelt Sample E.

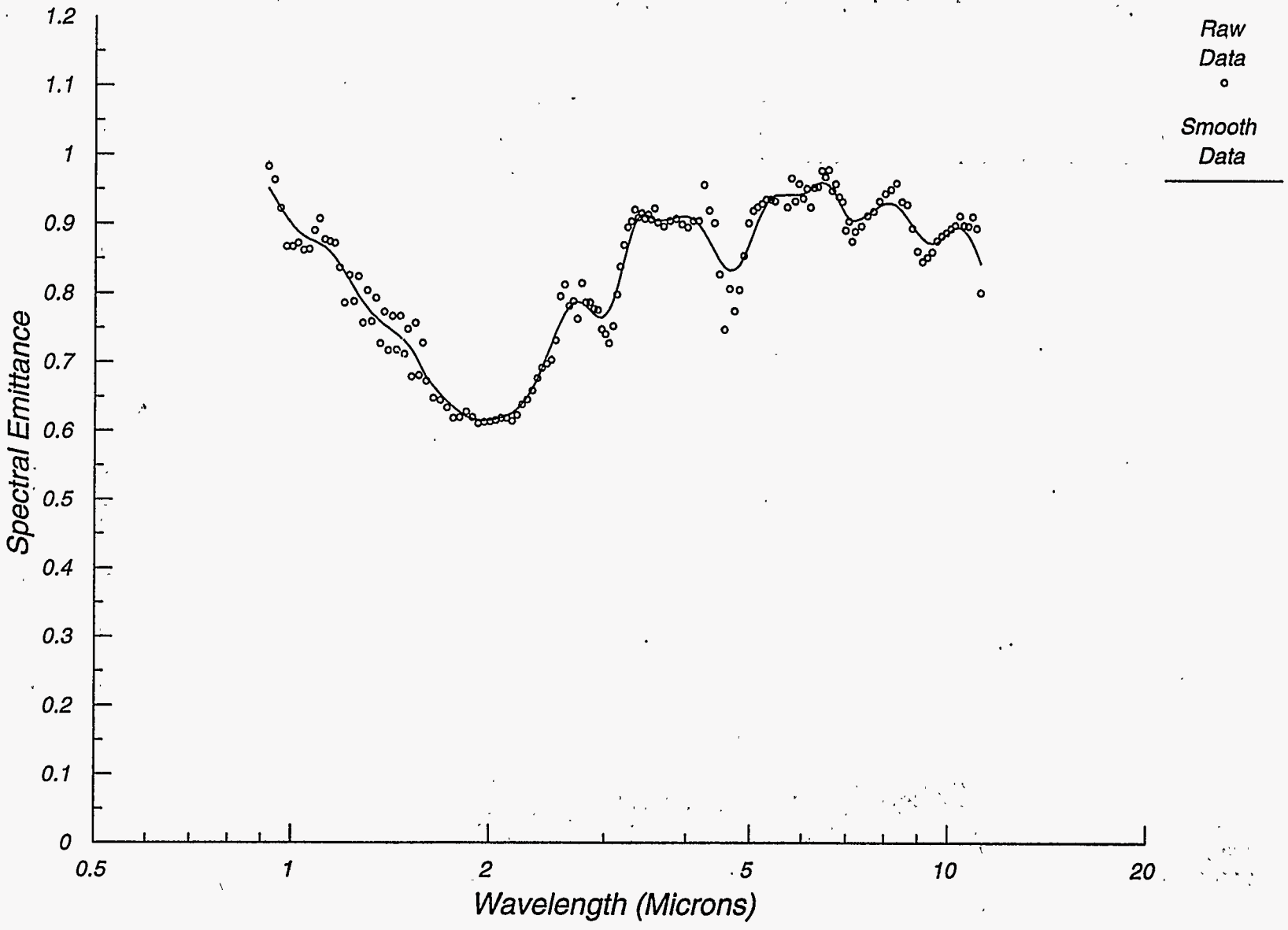

Figure 9. Spectral Emittance as a Function of Wavelength for Synthetic Oxidized Smelt Sample A.

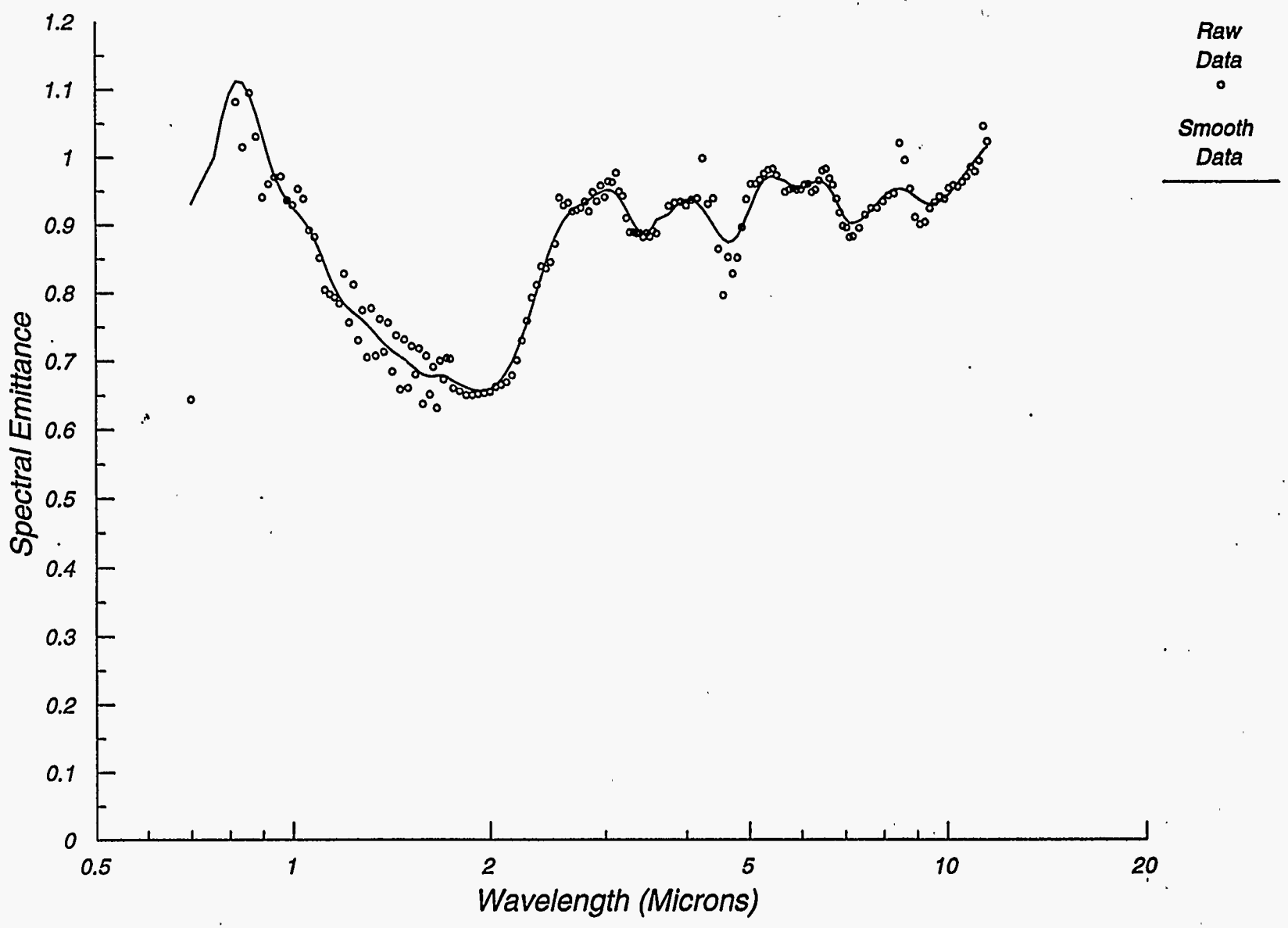

Figure 10. Spectral Emittance as a Function of Wavelength for Synthetic Oxidized Smelt Sample B.

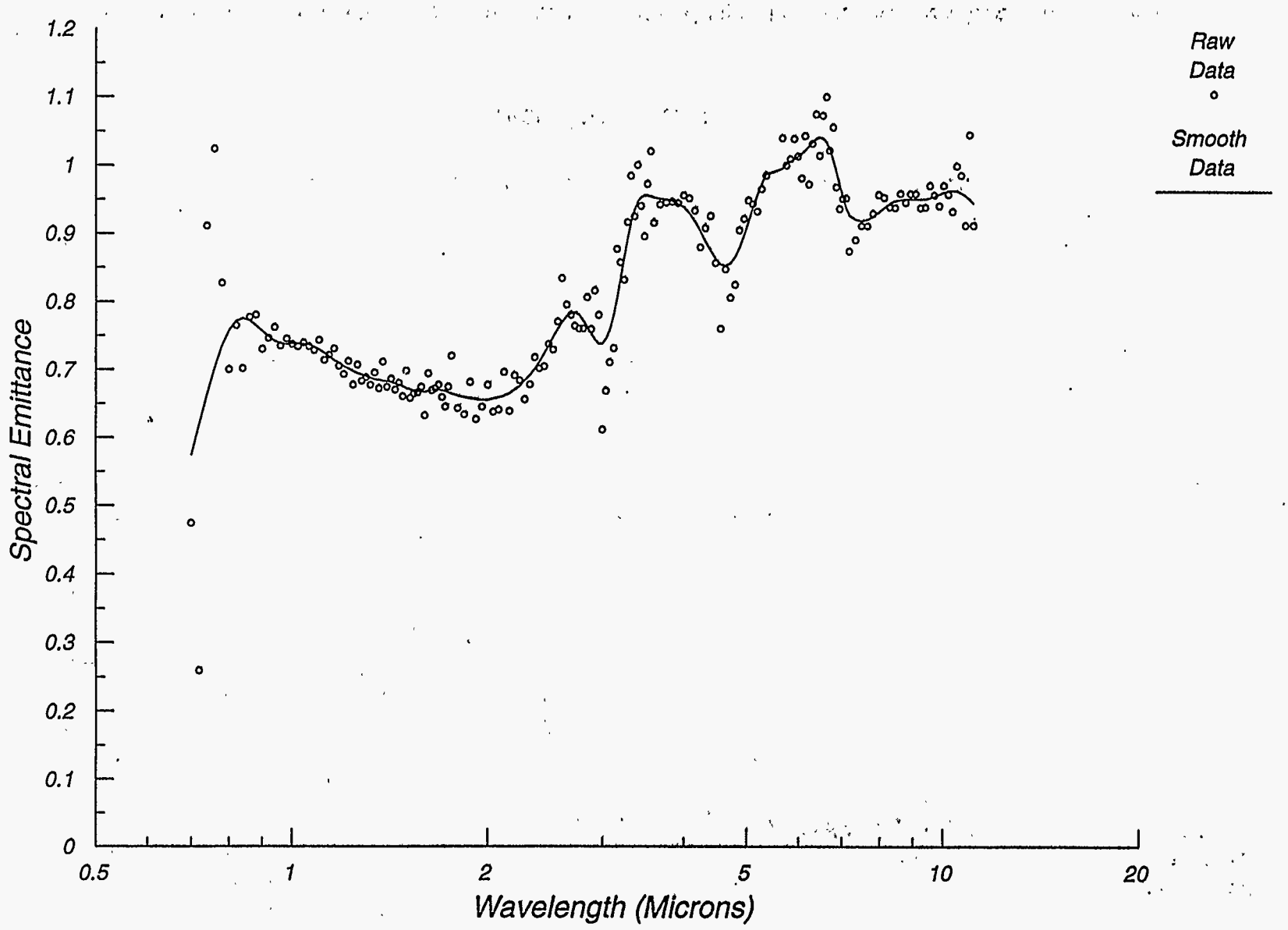

Figure 11. Spectral Emittance as a Function of Wavelength for Synthetic Reduced Smelt Sample B.

APPENDIX A

FACILITY AND TECHNIQUES

Spectral and total emittance measurements for this project were performed at the High Temperature Spectral Emittance Measurement Facility. The facility consists of a high temperature furnace, optics including a grating monochromator, a series of photodetectors, and a personal computer-based data acquisition system. Figure 1 is a photograph of the facility, and Figure 2 provides a schematic of the facility.

The method used at the Spectral Emittance Measurement Facility to determine the spectral emittance of a surface requires instrumentation to measure the temperature of the emitting surface and to measure the intensity of the emitted radiation by wavelength. Additionally, a radiation standard is required to provide a calibration source for the instrumentation.

The sample is heated from behind using the high-temperature furnace at the facility. The furnace is designed to heat 2-inch square samples. When necessary, a 2-inch square metal plate is used to support the sample. The sample is heated to the desired temperature as measured using thin gauge thermocouples and/or a hand-held pyrometer.

A gold-plated mirror and zinc selenide lens are used to collect and image energy radiated from the sample surface onto the input slit of the grating monochromator. The ruled grating in the monochromator diffracts incoming radiant energy into a spectral continuum, which is imaged at the output slit. Different wavelengths are passed through the slit by rotating the angle of the monochromator using a stepper motor drive. The selected wavelength was measured using a precision potentiometer located internal to the monochromator.

Each ruled grating for the monochromator spanned a wavelength range of about 3:1. Four different gratings were used to span the wavelength range from 0.6 to 14.4 microns, which also provides overlap between gratings.

To prevent measurement errors caused by second-order diffraction, order sorting filters (essentially high-pass filters) are set in front of the input slit of the monochromator. One of four filters is selected, depending on the wavelength of light measured.

Three photodetectors are used to measure light intensities from 0.6 to 14.4 microns. A room-temperature silicon/germanium detector sandwich spans the range from 0.6 to about 1.8 microns; a liquid nitrogen-cooled indium-antimonide/mercury-cadmium-telluride (InSb/HgCdTe) dual detector sandwich is used to measure light intensities from about 1.4 to 14.4 microns. AC coupling in the pre-amp circuits of the InSb/HgCdTe detectors requires modulation of the incident light energy. This was accomplished using a shutter operating at a frequency of about 40 Hz.

The thermopile detector that was used to measure total emittance directly has a spectrally neutral coating that is highly absorptive from 0.2 to greater than 50 microns. To protect the

sensing element, the detector is covered with a zinc selenide window that yields an effective wavelength range of about 0.6 microns to about 18 microns.

The method for experimentally measuring spectral emittance from high temperature surfaces is based on Planck's law for blackbody radiation:

$$W_B(\lambda,T)=\frac{C_1\lambda^{-5}}{e^{C_2/\lambda T}-1} \qquad [1]$$

where:

$W_B(\lambda,T)$ = monochromatic emissive power of a blackbody
λ = wavelength (microns)
T = absolute temperature (K)
C_1 = 3.74×10^4 (w-micron^4/cm^2)
C_2 = 1.44×10^4 (microns-K)

If T and λ are known, $W_B(\lambda,T)$ may be calculated and compared with the measured radiation from the sample. The emittance of the sample is generally a function of wavelength, temperature, angle, and possibly time. The surface normal spectral emittance at any temperature is:

$$\epsilon_\lambda=\frac{W_s(\lambda,T)}{W_B(\lambda,T)} \qquad [2]$$

where $W_s(\lambda,T)$ is the measured radiation from the deposit surface at a temperature (T), and wavelength (λ) and $W_B(\lambda,T)$ are defined in Equation 1. Thus, for a blackbody, $\epsilon_\lambda = 1$. To obtain the total emittance of the deposit, Equation 2 is integrated over all wavelengths:

$$\epsilon_{Total}=\frac{\int_0^\infty \epsilon_{(\lambda)} W_B(\lambda T)d\lambda}{\sigma T^4} \qquad [3]$$

In practice, ϵ_λ is measured over a limited wavelength range that represents most of the emitted energy. For temperatures between 700°-2200°F (371°-1204°C), more than 90 percent of the emitted radiation is within the wavelength range of 0.7 to 14.4 microns.

Data Acquisition and Reduction

Before testing, the optical instrumentation is calibrated using a blackbody radiation source. In this procedure, the blackbody source is set up as the sample, and data is recorded as in a normal test. This calibration data at each wavelength is then normalized using Planck's blackbody radiation equation evaluated at the temperature of the blackbody standard. Calibration constants, C_λ, are then determined as:

$$C_\lambda = \frac{V_{pd}}{W_B(\lambda T)} \qquad [4]$$

where V_{pd} is the measured photodetector voltage. Sets of calibration constants are determined this way for each of the photodetectors and for each of the monochromator gratings.

The total radiation pyrometer is calibrated similarly, where the thermopile voltage output generated by viewing a blackbody source is measured at several different temperatures. Since the thermopile is responsive to total radiation, the measured signal is normalized by the Stefan-Boltzman equation. Thus, the thermopile calibration constant is evaluated as:

$$C_t = \frac{V_t}{\sigma T^4} \qquad [5]$$

where V_t is the measured thermopile signal, σ is the Stefan-Boltzman constant, and T is the absolute temperature of the blackbody standard.

Test data are reduced using the calculated calibration constants and the measured surface temperature of the sample. The spectral emittances are calculated as:

$$\epsilon_\lambda = \frac{V_{pd}}{C_\lambda W_B(\lambda T)} \qquad [6]$$

The spectral emittance values are then screened and averaged at regions of overlap to arrive at a set of spectral emittances as a function of wavelength.

The total emittance is determined from the thermopile data as,

$$\epsilon_t = \frac{V_t}{(C_t \sigma T^4)} \qquad [7]$$

where C_t is the calibration constant for the thermopile and is determined as shown in Equation 5.

The total emittance is also calculated from the spectral data by integrating the spectral emittance over all measured wavelengths. Thus,

$$\epsilon_{Total} = \frac{\int_{\lambda 1}^{\lambda 2} \epsilon_{(\lambda)} W_B(\lambda T) d\lambda}{\int_{\lambda 1}^{\lambda 2} W_B(\lambda T) d\lambda} \qquad [8]$$

Equation 8 can be evaluated at the test temperature to calculate an integrated total emittance for direct comparison to that determined using Equation 7. Provided that the spectral emittance is relatively constant with temperature, Equation 8 also can be used to evaluate total emittance at different temperatures.

Data associated with the emittance measurement are acquired, reduced, and analyzed using computer programs. Program GRI6.V6 written in the BASIC language along with a machine language program, GRIASM, provided the data acquisition and reduction capabilities. Program EMITCALC.ASC, also written in BASIC, is used to analyze the reduced data and provide the formatted results. A third basic program, GRICCLC1.ASC, is used to analyze calibration data and calculate calibration constants.

APPENDIX B

TABULATED SPECTRAL EMITTANCE RESULTS

Table B.1 Tabulated Values of Emittance as a Function of Wavelength For Black Liquor (67% Solids).

Wavelength (microns)	Measured Emittance	Smoothed Emittance	Wavelength (microns)	Measured Emittance	Smoothed Emittance	Wavelength (microns)	Measured Emittance	Smoothed Emittance
0.78	0.59	0.745	1.7	0.6	0.888	3.68	1	0.995
0.82	1.04	0.79	1.72	0.94	0.915	3.76	0.98	0.999
0.84	0.9	0.833	1.76	1.04	0.945	3.84	0.98	1.002
0.88	0.86	0.87	1.84	1.01	0.975	3.92	0.99	1.005
0.9	0.98	0.901	1.88	1.05	1.002	4.08	1.01	1.007
0.92	0.9	0.924	1.92	1.02	1.024	4.16	1.04	1.006
0.94	0.93	0.94	1.96	1.08	1.038	4.24	1.05	1.003
0.96	1	0.949	2	1.09	1.046	4.32	1	0.999
0.98	0.93	0.953	2.04	1.07	1.048	4.4	0.99	0.994
1	0.94	0.953	2.08	1.01	1.046	4.48	0.96	0.988
1.02	0.93	0.95	2.12	0.98	1.043	4.56	0.97	0.984
1.04	0.95	0.945	2.16	1.02	1.039	4.64	1.04	0.981
1.06	0.96	0.938	2.2	1.05	1.035	4.72	0.96	0.981
1.08	0.92	0.93	2.24	1.03	1.032	4.8	0.955	0.983
1.1	0.98	0.92	2.28	1.06	1.03	4.88	0.9	0.985
1.12	0.93	0.91	2.32	1.08	1.028	4.96	0.935	0.988
1.14	0.89	0.899	2.36	1.01	1.024	5.12	1.08	0.989
1.16	0.86	0.89	2.4	1.01	1.02	5.2	1.03	0.988
1.18	0.86	0.884	2.44	1.04	1.015	5.76	1.07	0.985
1.2	0.94	0.881	2.48	0.94	1.011	5.92	0.99	0.979
1.24	0.865	0.883	2.52	1.01	1.007	6.08	0.98	0.971
1.26	0.64	0.889	2.56	1.03	1.006	6.24	0.95	0.962
1.28	0.915	0.898	2.6	0.99	1.007	6.4	0.83	0.952
1.3	1.03	0.909	2.64	1.01	1.009	6.56	0.92	0.944
1.32	1.01	0.921	2.72	0.99	1.014	6.72	0.96	0.936
1.34	0.98	0.933	2.76	0.99	1.018	6.88	0.93	0.931
1.36	0.83	0.943	2.8	1.09	1.022	7.04	0.95	0.927
1.38	1.01	0.951	2.84	1.01	1.024	7.2	0.95	0.924
1.4	0.975	0.957	2.88	1.03	1.023	7.36	0.91	0.922
1.42	0.88	0.96	2.96	1.03	1.021	7.52	0.96	0.92
1.44	0.915	0.961	3	1.08	1.016	7.68	0.95	0.917
1.46	1.03	0.958	3.04	0.97	1.011	7.84	0.87	0.912
1.48	1.05	0.951	3.08	1.01	1.005	8	0.89	0.906
1.5	0.85	0.941	3.12	0.95	1	8.16	0.79	0.896
1.52	0.91	0.927	3.2	0.96	0.996	8.32	0.99	0.881
1.54	1.03	0.91	3.24	1.04	0.993	8.48	0.86	0.862
1.56	0.94	0.892	3.28	0.97	0.991	8.64	0.83	0.837
1.58	0.76	0.875	3.32	1.06	0.99	8.8	0.86	0.808
1.6	0.97	0.862	3.36	0.94	0.99	8.96	0.93	0.775
1.62	0.66	0.856	3.44	0.98	0.99	9.12	0.74	0.739
1.64	0.89	0.858	3.52	1.005	0.991	9.28	0.62	0.703
1.68	0.95	0.869	3.6	1	0.993	9.44	0.59	0.669

Table B.2 Tabulated Values of Emittance as a Function of Wavelength For Black Liquor Dried Solids.

Wavelength (microns)	Measured Emittance	Smoothed Emittance	Wavelength (microns)	Measured Emittance	Smoothed Emittance	Wavelength (microns)	Measured Emittance	Smoothed Emittance
0.78	0.7	0.779	1.72	0.87	0.868	3.68	0.97	0.948
0.82	0.74	0.798	1.76	0.85	0.899	3.76	0.97	0.954
0.84	1.02	0.814	1.8	1.01	0.924	3.84	0.96	0.958
0.86	0.91	0.825	1.84	0.96	0.944	3.92	0.97	0.961
0.88	0.9	0.83	1.88	0.94	0.956	4	0.98	0.962
0.9	0.76	0.83	1.92	0.97	0.962	4.08	0.97	0.963
0.92	0.84	0.825	1.96	0.99	0.964	4.16	0.88	0.962
0.94	0.74	0.817	2.04	0.94	0.962	4.24	0.98	0.96
0.96	0.81	0.806	2.08	0.95	0.96	4.32	0.99	0.959
0.98	0.79	0.795	2.12	0.95	0.959	4.4	0.95	0.958
1	0.78	0.782	2.16	0.97	0.958	4.48	0.91	0.959
1.02	0.78	0.768	2.2	0.96	0.959	4.56	0.99	0.96
1.04	0.76	0.754	2.24	0.93	0.959	4.64	1.04	0.964
1.06	0.78	0.738	2.28	0.97	0.959	4.72	0.98	0.969
1.08	0.71	0.721	2.32	1.02	0.958	4.8	0.925	0.975
1.1	0.75	0.703	2.36	0.94	0.956	4.88	0.94	0.982
1.12	0.72	0.685	2.4	0.95	0.953	4.96	0.89	0.988
1.14	0.63	0.668	2.44	0.96	0.95	5.04	1.02	0.991
1.16	0.56	0.653	2.48	0.905	0.947	5.12	1.05	0.992
1.18	0.59	0.642	2.52	0.94	0.946	5.2	1.04	0.99
1.2	0.71	0.635	2.56	0.935	0.948	5.76	1.06	0.984
1.24	0.625	0.633	2.6	0.95	0.95	5.92	1.02	0.975
1.26	0.53	0.637	2.64	0.97	0.955	6.24	0.96	0.963
1.28	0.68	0.645	2.68	0.93	0.96	6.4	0.82	0.95
1.3	0.68	0.658	2.72	0.96	0.965	6.56	0.95	0.935
1.32	0.69	0.676	2.76	1.06	0.969	6.72	0.95	0.921
1.34	0.66	0.698	2.8	0.97	0.972	6.88	0.84	0.907
1.36	0.77	0.724	2.84	0.9	0.973	7.04	0.89	0.894
1.38	0.72	0.75	2.88	0.99	0.972	7.2	0.9	0.881
1.4	0.82	0.777	2.92	1.01	0.97	7.36	0.92	0.867
1.42	0.66	0.8	2.96	0.955	0.965	7.52	0.85	0.853
1.44	0.74	0.818	3	0.94	0.959	7.68	0.88	0.837
1.46	1.01	0.83	3.04	0.955	0.952	7.84	0.89	0.818
1.48	0.843	0.832	3.12	0.97	0.945	8	0.78	0.798
1.5	0.98	0.827	3.16	0.95	0.937	8.16	0.62	0.775
1.52	0.843	0.815	3.2	0.92	0.93	8.32	0.76	0.75
1.54	0.8	0.799	3.24	0.9	0.925	8.48	0.75	0.723
1.56	0.737	0.783	3.28	0.94	0.921	8.64	0.71	0.694
1.58	0.71	0.771	3.32	0.92	0.92	8.8	0.73	0.663
1.6	0.877	0.766	3.36	0.86	0.921	8.96	0.64	0.63
1.62	0.36	0.771	3.4	0.94	0.924	9.12	0.61	0.598
1.64	0.81	0.785	3.44	0.91	0.929	9.28	0.61	0.566
1.68	0.88	0.808	3.52	0.94	0.935	9.44	0.46	0.537
1.7	0.95	0.837	3.6	0.94	0.942			

Table B.3 Tabulated Values of Emittance as a Function of Wavelength For Black Liquor Char.

Wavelength (microns)	Measured Emittance	Smoothed Emittance	Wavelength (microns)	Measured Emittance	Smoothed Emittance	Wavelength (microns)	Measured Emittance	Smoothed Emittance
0.78	0.88	0.877	1.76	0.55	0.702	3.4	0.87	0.89
0.82	0.85	0.879	1.8	0.71	0.692	3.44	0.845	0.889
0.88	0.86	0.881	1.84	0.73	0.683	3.52	0.935	0.887
0.9	0.93	0.883	1.88	0.71	0.677	3.6	0.9	0.885
0.92	0.84	0.885	1.92	0.69	0.672	3.68	0.93	0.881
0.94	0.91	0.887	1.96	0.71	0.67	3.76	0.86	0.874
0.96	0.91	0.889	2	0.61	0.669	3.84	0.88	0.867
0.98	0.89	0.89	2.04	0.64	0.669	3.92	0.9	0.858
1	0.9	0.89	2.08	0.67	0.671	4	0.87	0.85
1.02	0.87	0.89	2.12	0.64	0.673	4.08	0.78	0.844
1.04	0.88	0.889	2.16	0.68	0.676	4.16	0.75	0.841
1.06	0.92	0.887	2.2	0.7	0.678	4.24	0.81	0.841
1.08	0.85	0.884	2.24	0.66	0.679	4.32	0.88	0.845
1.1	0.9	0.881	2.28	0.72	0.678	4.4	0.85	0.85
1.12	0.88	0.876	2.32	0.72	0.677	4.48	0.88	0.856
1.14	0.85	0.869	2.36	0.67	0.676	4.56	0.89	0.863
1.16	0.97	0.86	2.4	0.67	0.677	4.64	0.9	0.869
1.18	0.67	0.849	2.44	0.67	0.68	4.72	0.87	0.875
1.2	0.97	0.836	2.48	0.585	0.688	4.8	0.87	0.881
1.24	0.895	0.823	2.52	0.72	0.701	4.88	0.84	0.889
1.26	0.68	0.809	2.56	0.72	0.72	4.96	0.9	0.898
1.28	0.775	0.798	2.6	0.7	0.744	5.04	0.93	0.912
1.32	0.84	0.789	2.64	0.805	0.772	5.12	0.9	0.93
1.34	0.86	0.784	2.68	0.7	0.802	5.2	0.85	0.951
1.36	0.7	0.785	2.72	0.86	0.833	6.4	0.97	0.976
1.38	0.62	0.79	2.76	0.97	0.862	6.56	1.08	1
1.4	0.915	0.799	2.8	0.93	0.888	6.88	1.05	1.023
1.42	0.71	0.811	2.84	0.89	0.91	7.04	1.07	1.041
1.44	0.855	0.825	2.88	0.915	0.927	7.2	1.09	1.053
1.46	0.99	0.838	2.92	0.95	0.939	7.36	1.05	1.056
1.48	0.84	0.849	2.96	0.91	0.946	7.52	1.09	1.051
1.5	0.81	0.856	3	1.01	0.949	7.68	1.07	1.039
1.52	0.843	0.857	3.04	0.96	0.947	8.16	0.99	1.02
1.54	0.94	0.852	3.08	0.93	0.942	8.48	0.91	0.998
1.56	0.81	0.842	3.12	0.92	0.935	8.64	1.08	0.974
1.58	0.79	0.826	3.16	0.95	0.926	8.96	1.01	0.951
1.6	0.79	0.808	3.2	0.935	0.917	9.12	0.92	0.932
1.62	0.92	0.787	3.24	0.92	0.908	9.28	0.84	0.917
1.64	0.755	0.767	3.28	0.905	0.901	9.44	0.83	0.907
1.68	0.72	0.747	3.32	0.88	0.895	9.6	0.87	0.901
1.7	0.74	0.73	3.36	0.84	0.892	9.76	0.92	0.9
1.72	0.7	0.714						

Table B.4 Tabulated Values of Emittance as a Function of Wavelength for Synthetic Oxidized Smelt Sample A.

Wavelength (microns)	Measured Emittance	Smoothed Emittance	Wavelength (microns)	Measured Emittance	Smoothed Emittance	Wavelength (microns)	Measured Emittance	Smoothed Emittance
0.92	0.983	0.951	2.28	0.646	0.65	5.04	0.92	0.887
0.94	0.963	0.937	2.32	0.659	0.662	5.12	0.925	0.904
0.96	0.922	0.922	2.36	0.677	0.676	5.2	0.93	0.918
0.98	0.867	0.909	2.4	0.692	0.692	5.28	0.936	0.93
1	0.867	0.897	2.44	0.698	0.709	5.36	0.936	0.937
1.02	0.872	0.888	2.48	0.703	0.726	5.44	0.934	0.942
1.04	0.862	0.882	2.52	0.732	0.743	5.68	0.925	0.943
1.06	0.863	0.877	2.56	0.796	0.758	5.76	0.967	0.943
1.08	0.89	0.874	2.6	0.813	0.771	5.84	0.934	0.943
1.1	0.907	0.87	2.64	0.782	0.78	5.92	0.959	0.943
1.12	0.877	0.866	2.68	0.789	0.786	6	0.938	0.945
1.14	0.874	0.859	2.72	0.763	0.788	6.08	0.952	0.947
1.16	0.872	0.851	2.76	0.815	0.786	6.16	0.925	0.951
1.18	0.837	0.841	2.8	0.787	0.782	6.24	0.953	0.955
1.2	0.786	0.83	2.84	0.787	0.776	6.32	0.955	0.959
1.22	0.826	0.819	2.88	0.778	0.77	6.4	0.978	0.961
1.24	0.788	0.807	2.92	0.776	0.766	6.48	0.969	0.96
1.26	0.824	0.796	2.96	0.748	0.765	6.56	0.979	0.957
1.28	0.757	0.787	3	0.741	0.769	6.64	0.949	0.951
1.3	0.804	0.779	3.04	0.728	0.777	6.72	0.959	0.943
1.32	0.759	0.771	3.08	0.753	0.79	6.8	0.94	0.933
1.34	0.793	0.765	3.12	0.799	0.807	6.88	0.933	0.924
1.36	0.727	0.759	3.16	0.839	0.827	6.96	0.892	0.915
1.38	0.773	0.754	3.2	0.87	0.848	7.04	0.905	0.909
1.4	0.717	0.75	3.24	0.896	0.868	7.12	0.876	0.906
1.42	0.767	0.745	3.28	0.904	0.886	7.2	0.89	0.906
1.44	0.718	0.741	3.32	0.921	0.9	7.36	0.898	0.909
1.46	0.767	0.736	3.36	0.91	0.909	7.52	0.913	0.915
1.48	0.712	0.731	3.4	0.916	0.913	7.68	0.919	0.921
1.5	0.748	0.725	3.44	0.908	0.914	7.84	0.934	0.927
1.52	0.679	0.718	3.48	0.914	0.912	8	0.945	0.931
1.54	0.757	0.709	3.52	0.907	0.909	8.16	0.951	0.931
1.56	0.681	0.699	3.56	0.923	0.907	8.32	0.96	0.928
1.58	0.728	0.688	3.6	0.903	0.905	8.48	0.933	0.92
1.6	0.673	0.677	3.68	0.897	0.906	8.64	0.929	0.91
1.64	0.648	0.665	3.76	0.905	0.907	8.8	0.895	0.899
1.68	0.645	0.653	3.84	0.908	0.91	8.96	0.862	0.888
1.72	0.634	0.643	3.92	0.9	0.911	9.12	0.847	0.88
1.76	0.619	0.634	4	0.896	0.911	9.28	0.853	0.874
1.8	0.62	0.627	4.08	0.905	0.907	9.44	0.861	0.873
1.84	0.628	0.621	4.16	0.905	0.9	9.6	0.877	0.875
1.88	0.62	0.618	4.24	0.957	0.889	9.76	0.884	0.88
1.92	0.611	0.616	4.32	0.92	0.876	9.92	0.889	0.886
1.96	0.613	0.615	4.4	0.902	0.861	10.08	0.894	0.892
2	0.614	0.616	4.48	0.828	0.848	10.24	0.899	0.896
2.04	0.616	0.617	4.56	0.748	0.838	10.4	0.913	0.896
2.08	0.619	0.619	4.64	0.807	0.834	10.56	0.899	0.892
2.12	0.619	0.622	4.72	0.775	0.835	10.72	0.898	0.884
2.16	0.615	0.626	4.8	0.806	0.841	10.88	0.912	0.873
2.2	0.623	0.632	4.88	0.855	0.854	11.04	0.895	0.859
2.24	0.639	0.64	4.96	0.902	0.869	11.2	0.802	0.844

Table B.5 Tabulated Values of Emittance as a Function of Wavelength for Synthetic Oxidized Smelt Sample B.

Wavelength (microns)	Measured Emittance	Smoothed Emittance	Wavelength (microns)	Measured Emittance	Smoothed Emittance	Wavelength (microns)	Measured Emittance	Smoothed Emittance
0.7	0.644	0.931	1.96	0.654	0.657	4.88	0.898	0.898
0.76	1.35	1	2	0.656	0.66	4.96	0.939	0.914
0.78	1.42	1.056	2.04	0.663	0.665	5.04	0.962	0.93
0.8	1.364	1.094	2.08	0.666	0.673	5.12	0.962	0.946
0.82	1.082	1.112	2.12	0.67	0.685	5.2	0.968	0.959
0.84	1.015	1.11	2.16	0.68	0.699	5.28	0.977	0.968
0.86	1.095	1.092	2.2	0.702	0.716	5.36	0.983	0.972
0.88	1.031	1.064	2.24	0.731	0.736	5.44	0.984	0.973
0.9	0.941	1.031	2.28	0.76	0.758	5.52	0.975	0.97
0.92	0.961	0.999	2.32	0.794	0.78	5.68	0.95	0.966
0.94	0.971	0.972	2.36	0.813	0.804	5.76	0.953	0.961
0.96	0.972	0.951	2.4	0.84	0.826	5.84	0.955	0.958
0.98	0.937	0.936	2.44	0.837	0.848	5.92	0.953	0.955
1	0.93	0.926	2.48	0.846	0.867	6	0.954	0.955
1.02	0.953	0.917	2.52	0.873	0.883	6.08	0.961	0.957
1.04	0.939	0.907	2.56	0.941	0.897	6.16	0.962	0.96
1.06	0.893	0.895	2.6	0.93	0.908	6.24	0.95	0.963
1.08	0.883	0.879	2.64	0.933	0.916	6.32	0.953	0.965
1.1	0.852	0.861	2.68	0.921	0.922	6.4	0.967	0.966
1.12	0.805	0.842	2.72	0.923	0.927	6.48	0.982	0.965
1.14	0.799	0.823	2.76	0.926	0.931	6.56	0.984	0.962
1.16	0.794	0.807	2.8	0.935	0.934	6.64	0.97	0.955
1.18	0.785	0.794	2.84	0.921	0.938	6.72	0.961	0.947
1.2	0.829	0.784	2.88	0.949	0.942	6.8	0.94	0.936
1.22	0.757	0.777	2.92	0.936	0.946	6.88	0.92	0.926
1.24	0.813	0.771	2.96	0.959	0.949	6.96	0.9	0.916
1.26	0.731	0.766	3	0.942	0.952	7.04	0.898	0.909
1.28	0.775	0.76	3.04	0.965	0.952	7.12	0.884	0.904
1.3	0.706	0.754	3.08	0.964	0.951	7.2	0.885	0.904
1.32	0.778	0.747	3.12	0.978	0.947	7.36	0.897	0.907
1.34	0.708	0.74	3.16	0.95	0.94	7.52	0.917	0.914
1.36	0.762	0.732	3.2	0.944	0.932	7.68	0.926	0.923
1.38	0.714	0.726	3.24	0.911	0.923	7.84	0.927	0.933
1.4	0.757	0.72	3.28	0.89	0.913	8	0.936	0.942
1.42	0.685	0.715	3.32	0.89	0.904	8.16	0.945	0.949
1.44	0.738	0.711	3.36	0.889	0.896	8.32	0.948	0.953
1.46	0.659	0.707	3.4	0.889	0.89	8.48	1.022	0.955
1.48	0.732	0.703	3.44	0.883	0.888	8.64	0.997	0.953
1.5	0.661	0.698	3.48	0.889	0.888	8.8	0.955	0.949
1.52	0.722	0.693	3.52	0.884	0.892	8.96	0.913	0.943
1.54	0.681	0.689	3.56	0.892	0.899	9.12	0.903	0.938
1.56	0.719	0.684	3.6	0.889	0.908	9.28	0.906	0.934
1.58	0.638	0.681	3.76	0.929	0.917	9.44	0.926	0.932
1.6	0.708	0.679	3.84	0.934	0.927	9.6	0.935	0.933
1.62	0.652	0.678	3.92	0.935	0.934	9.76	0.943	0.936
1.64	0.692	0.678	4	0.93	0.938	9.92	0.94	0.941
1.66	0.632	0.679	4.08	0.938	0.938	10.08	0.956	0.947
1.68	0.701	0.679	4.16	0.94	0.933	10.24	0.96	0.955
1.7	0.674	0.679	4.24	1	0.925	10.4	0.958	0.963
1.72	0.705	0.677	4.32	0.932	0.913	10.56	0.965	0.971
1.74	0.704	0.674	4.4	0.94	0.9	10.72	0.973	0.98
1.76	0.661	0.671	4.48	0.866	0.889	10.88	0.987	0.988
1.8	0.657	0.666	4.56	0.798	0.88	11.04	0.981	0.997
1.84	0.651	0.662	4.64	0.854	0.876	11.2	0.997	1.004

Table B.6 Tabulated Values of Emittance as a Function of Wavelength for Synthetic Reduced Smelt Sample A.

Wavelength (microns)	Measured Emittance	Smoothed Emittance	Wavelength (microns)	Measured Emittance	Smoothed Emittance	Wavelength (microns)	Measured Emittance	Smoothed Emittance
0.7	0.474	0.574	1.88	0.681	0.657	4.64	0.849	0.854
0.72	0.259	0.618	1.92	0.627	0.656	4.72	0.807	0.857
0.74	0.911	0.662	1.96	0.645	0.655	4.8	0.826	0.867
0.76	1.024	0.702	2	0.677	0.655	4.88	0.906	0.881
0.78	0.827	0.735	2.04	0.638	0.657	4.96	0.923	0.899
0.8	0.7	0.758	2.08	0.641	0.659	5.04	0.95	0.92
0.82	0.765	0.771	2.12	0.696	0.661	5.12	0.945	0.94
0.84	0.701	0.775	2.16	0.639	0.665	5.2	0.934	0.959
0.86	0.777	0.772	2.2	0.691	0.67	5.28	0.967	0.975
0.88	0.78	0.764	2.24	0.684	0.676	5.36	0.987	0.988
0.9	0.73	0.756	2.28	0.656	0.684	5.68	1.042	0.997
0.92	0.746	0.748	2.32	0.678	0.692	5.76	1.002	1.004
0.94	0.762	0.742	2.36	0.718	0.701	5.84	1.011	1.008
0.96	0.735	0.738	2.4	0.702	0.712	5.92	1.041	1.011
0.98	0.745	0.737	2.44	0.705	0.724	6	1.015	1.015
1	0.737	0.738	2.48	0.738	0.736	6.08	0.983	1.019
1.02	0.734	0.738	2.52	0.73	0.749	6.16	1.045	1.024
1.04	0.739	0.738	2.56	0.771	0.761	6.24	0.974	1.03
1.06	0.734	0.736	2.6	0.835	0.771	6.32	1.034	1.036
1.08	0.728	0.733	2.64	0.796	0.779	6.4	1.077	1.041
1.1	0.743	0.729	2.68	0.781	0.783	6.48	1.016	1.043
1.12	0.714	0.724	2.72	0.765	0.784	6.56	1.075	1.042
1.14	0.721	0.719	2.76	0.761	0.781	6.64	1.102	1.036
1.16	0.731	0.713	2.8	0.761	0.773	6.72	1.024	1.025
1.18	0.705	0.709	2.84	0.807	0.764	6.8	1.058	1.01
1.2	0.693	0.704	2.88	0.76	0.754	6.88	0.97	0.992
1.22	0.712	0.701	2.92	0.817	0.745	6.96	0.938	0.973
1.24	0.677	0.697	2.96	0.781	0.739	7.04	0.953	0.955
1.26	0.707	0.694	3	0.612	0.739	7.12	0.954	0.94
1.28	0.683	0.692	3.04	0.669	0.746	7.2	0.876	0.928
1.3	0.688	0.689	3.08	0.711	0.76	7.36	0.892	0.922
1.32	0.677	0.687	3.12	0.732	0.781	7.52	0.913	0.92
1.34	0.695	0.685	3.16	0.878	0.807	7.68	0.913	0.922
1.36	0.672	0.684	3.2	0.859	0.836	7.84	0.931	0.927
1.38	0.711	0.683	3.24	0.833	0.866	8	0.959	0.933
1.4	0.674	0.682	3.28	0.918	0.894	8.16	0.955	0.94
1.42	0.686	0.681	3.32	0.986	0.917	8.32	0.941	0.946
1.44	0.67	0.679	3.36	0.926	0.935	8.48	0.94	0.95
1.46	0.68	0.677	3.4	1.002	0.948	8.64	0.961	0.952
1.48	0.66	0.675	3.44	0.942	0.954	8.8	0.948	0.953
1.5	0.698	0.672	3.48	0.897	0.957	8.96	0.961	0.953
1.52	0.658	0.67	3.52	0.974	0.957	9.12	0.961	0.953
1.54	0.664	0.668	3.56	1.022	0.956	9.28	0.94	0.953
1.56	0.666	0.667	3.6	0.917	0.954	9.44	0.941	0.953
1.58	0.674	0.667	3.68	0.944	0.952	9.6	0.973	0.955
1.6	0.632	0.667	3.76	0.947	0.951	9.76	0.959	0.957
1.62	0.694	0.668	3.84	0.948	0.949	9.92	0.943	0.96
1.64	0.669	0.669	3.92	0.946	0.945	10.08	0.973	0.963
1.66	0.672	0.67	4	0.957	0.94	10.24	0.96	0.965
1.68	0.677	0.67	4.08	0.953	0.931	10.4	0.935	0.965
1.7	0.659	0.669	4.16	0.935	0.919	10.56	1.002	0.965
1.72	0.645	0.668	4.24	0.881	0.905	10.72	0.988	0.962
1.74	0.674	0.666	4.32	0.909	0.89	10.88	0.914	0.958
1.76	0.72	0.664	4.4	0.927	0.876	11.04	1.048	0.953
1.8	0.643	0.661	4.48	0.858	0.864	11.2	0.914	0.947
1.84	0.634	0.659	4.56	0.761	0.856			

Table B.7 Tabulated Values of Emittance as a Function of Wavelength for Industrial Smelt Sample A.

Wavelength (microns)	Measured Emittance	Smoothed Emittance	Wavelength (microns)	Measured Emittance	Smoothed Emittance	Wavelength (microns)	Measured Emittance	Smoothed Emittance
0.7	0.442	0.687	2	0.793	0.798	4.88	0.866	0.866
0.78	1.097	0.762	2.04	0.792	0.796	4.96	0.912	0.884
0.8	1.013	0.833	2.08	0.792	0.796	5.04	0.937	0.903
0.82	0.89	0.895	2.12	0.789	0.798	5.12	0.942	0.921
0.84	0.946	0.944	2.16	0.793	0.802	5.2	0.949	0.936
0.86	1.108	0.979	2.2	0.802	0.808	5.28	0.953	0.948
0.88	1.068	1	2.24	0.809	0.816	5.36	0.958	0.956
0.9	0.922	1.01	2.28	0.824	0.826	5.44	0.968	0.961
0.92	0.956	1.01	2.32	0.838	0.837	5.52	0.956	0.962
0.94	0.994	1.006	2.36	0.854	0.849	5.68	0.962	0.961
0.96	1.018	0.999	2.4	0.869	0.861	5.76	0.949	0.958
0.98	0.973	0.993	2.44	0.867	0.874	5.84	0.963	0.956
1	0.982	0.987	2.48	0.866	0.886	5.92	0.952	0.955
1.02	1.044	0.983	2.52	0.884	0.896	6	0.968	0.954
1.04	1.03	0.979	2.56	0.941	0.906	6.08	0.948	0.955
1.06	0.962	0.975	2.6	0.935	0.913	6.16	0.956	0.957
1.08	0.955	0.969	2.64	0.936	0.919	6.24	0.947	0.96
1.1	0.941	0.961	2.68	0.92	0.922	6.32	0.958	0.963
1.12	0.925	0.952	2.72	0.911	0.923	6.4	0.959	0.965
1.14	0.954	0.942	2.76	0.907	0.921	6.48	0.973	0.965
1.16	0.929	0.932	2.8	0.929	0.919	6.56	0.98	0.963
1.18	0.914	0.922	2.84	0.922	0.915	6.64	0.968	0.959
1.2	0.939	0.914	2.88	0.928	0.911	6.72	0.965	0.952
1.22	0.902	0.908	2.92	0.913	0.908	6.8	0.962	0.944
1.24	0.927	0.903	2.96	0.907	0.906	6.88	0.933	0.933
1.26	0.868	0.899	3	0.887	0.905	6.96	0.927	0.923
1.28	0.901	0.895	3.04	0.881	0.906	7.04	0.896	0.913
1.3	0.859	0.891	3.08	0.878	0.908	7.12	0.905	0.904
1.32	0.906	0.886	3.12	0.914	0.91	7.2	0.878	0.898
1.34	0.874	0.881	3.16	0.918	0.913	7.36	0.867	0.895
1.36	0.9	0.875	3.2	0.944	0.915	7.52	0.882	0.894
1.38	0.861	0.868	3.24	0.937	0.915	7.68	0.894	0.895
1.4	0.881	0.862	3.28	0.929	0.913	7.84	0.903	0.897
1.42	0.837	0.856	3.32	0.916	0.909	8	0.909	0.9
1.44	0.871	0.851	3.36	0.898	0.904	8.16	0.919	0.903
1.46	0.804	0.845	3.4	0.889	0.898	8.32	0.923	0.904
1.48	0.862	0.84	3.44	0.879	0.892	8.48	0.902	0.904
1.5	0.806	0.835	3.48	0.878	0.887	8.64	0.9	0.903
1.52	0.86	0.829	3.52	0.87	0.884	8.8	0.899	0.901
1.54	0.812	0.824	3.56	0.872	0.884	8.96	0.892	0.898
1.56	0.851	0.818	3.6	0.882	0.886	9.12	0.89	0.896
1.58	0.779	0.814	3.68	0.899	0.891	9.28	0.89	0.894
1.6	0.836	0.81	3.76	0.913	0.896	9.44	0.89	0.892
1.62	0.754	0.808	3.84	0.912	0.902	9.6	0.894	0.891
1.64	0.82	0.807	3.92	0.898	0.906	9.76	0.895	0.891
1.66	0.824	0.807	4	0.895	0.907	9.92	0.888	0.89
1.68	0.834	0.808	4.08	0.89	0.905	10.08	0.895	0.89
1.7	0.734	0.81	4.16	0.898	0.898	10.24	0.894	0.891
1.72	0.834	0.812	4.24	0.959	0.887	10.4	0.887	0.891
1.74	0.82	0.813	4.32	0.897	0.875	10.56	0.892	0.892
1.76	0.836	0.813	4.4	0.912	0.862	10.72	0.887	0.895
1.8	0.821	0.812	4.48	0.837	0.85	10.88	0.893	0.898
1.84	0.814	0.81	4.56	0.755	0.842	11.04	0.894	0.903
1.88	0.804	0.807	4.64	0.812	0.84	11.2	0.89	0.909
1.92	0.8	0.804	4.72	0.788	0.843	11.36	0.916	0.916
1.96	0.798	0.8	4.8	0.815	0.852	11.52	0.937	0.923

Table B.8 Tabulated Values of Emittance as a Function of Wavelength for Industrial Smelt Sample C.

Wavelength (microns)	Measured Emittance	Smoothed Emittance	Wavelength (microns)	Measured Emittance	Smoothed Emittance	Wavelength (microns)	Measured Emittance	Smoothed Emittance
0.7	1.114	1.214	1.96	0.908	0.912	4.8	0.845	0.883
0.74	1.486	1.243	2	0.899	0.903	4.88	0.901	0.897
0.8	1.196	1.269	2.04	0.89	0.897	4.96	0.947	0.914
0.82	1.268	1.292	2.08	0.887	0.894	5.04	0.965	0.931
0.84	1.409	1.31	2.12	0.885	0.893	5.12	0.971	0.946
0.86	1.327	1.32	2.16	0.886	0.895	5.2	0.977	0.955
0.88	1.356	1.324	2.2	0.892	0.9	5.28	0.978	0.959
0.9	1.302	1.323	2.24	0.9	0.907	5.36	0.98	0.956
0.92	1.317	1.317	2.28	0.912	0.915	5.44	0.955	0.949
0.94	1.32	1.308	2.32	0.923	0.926	5.52	0.943	0.938
0.96	1.299	1.298	2.36	0.939	0.938	5.68	0.904	0.926
0.98	1.263	1.289	2.4	0.954	0.95	5.76	0.886	0.914
1	1.259	1.28	2.44	0.959	0.964	5.84	0.895	0.904
1.02	1.287	1.272	2.48	0.962	0.977	5.92	0.89	0.897
1.04	1.262	1.263	2.52	0.979	0.989	6	0.899	0.893
1.06	1.287	1.254	2.56	1.045	0.999	6.08	0.89	0.892
1.08	1.258	1.242	2.6	1.014	1.006	6.16	0.911	0.894
1.1	1.193	1.229	2.64	1.028	1.007	6.24	0.881	0.896
1.12	1.222	1.213	2.68	1.003	1.003	6.32	0.898	0.899
1.14	1.255	1.196	2.72	0.999	0.993	6.4	0.89	0.902
1.16	1.173	1.177	2.76	0.996	0.977	6.48	0.911	0.902
1.18	1.151	1.159	2.8	0.99	0.957	6.56	0.904	0.901
1.2	1.099	1.142	2.84	0.952	0.934	6.64	0.915	0.898
1.22	1.093	1.126	2.88	0.923	0.911	6.72	0.896	0.893
1.24	1.128	1.112	2.92	0.856	0.89	6.8	0.904	0.885
1.26	1.104	1.099	2.96	0.863	0.875	6.88	0.881	0.877
1.28	1.076	1.088	3	0.832	0.866	6.96	0.875	0.869
1.3	1.096	1.078	3.04	0.812	0.866	7.04	0.854	0.861
1.32	1.086	1.068	3.08	0.803	0.873	7.12	0.836	0.855
1.34	1.053	1.058	3.12	0.872	0.886	7.2	0.839	0.85
1.36	1.053	1.048	3.16	0.896	0.902	7.36	0.828	0.847
1.38	1.025	1.039	3.2	0.971	0.92	7.52	0.836	0.846
1.4	1.007	1.029	3.24	0.985	0.935	7.68	0.845	0.846
1.42	1.05	1.021	3.28	0.981	0.947	7.84	0.853	0.847
1.44	0.987	1.013	3.32	0.976	0.953	8	0.858	0.849
1.46	0.999	1.007	3.36	0.96	0.955	8.16	0.863	0.85
1.48	0.989	1.001	3.4	0.942	0.952	8.32	0.868	0.851
1.5	1.024	0.995	3.44	0.938	0.947	8.48	0.844	0.851
1.52	0.975	0.99	3.48	0.922	0.942	8.64	0.845	0.851
1.54	1.013	0.986	3.52	0.923	0.94	8.8	0.843	0.85
1.56	0.98	0.981	3.56	0.919	0.94	8.96	0.847	0.849
1.58	0.955	0.977	3.6	0.921	0.945	9.12	0.844	0.849
1.6	0.97	0.974	3.76	0.977	0.952	9.28	0.846	0.849
1.62	0.986	0.971	3.84	0.982	0.96	9.44	0.846	0.85
1.64	0.962	0.969	3.92	0.974	0.966	9.6	0.854	0.851
1.66	0.948	0.968	4	0.96	0.969	9.76	0.861	0.854
1.68	0.955	0.968	4.08	0.959	0.967	9.92	0.854	0.857
1.7	0.951	0.967	4.16	0.963	0.959	10.08	0.862	0.861
1.72	0.981	0.965	4.24	1.018	0.945	10.24	0.861	0.865
1.74	1.036	0.962	4.32	0.961	0.927	10.4	0.872	0.868
1.76	0.95	0.957	4.4	0.953	0.908	10.56	0.868	0.872
1.8	0.944	0.95	4.48	0.872	0.891	10.72	0.865	0.875
1.84	0.934	0.942	4.56	0.779	0.879	10.88	0.883	0.878
1.88	0.926	0.932	4.64	0.842	0.873	11.04	0.886	0.881
1.92	0.922	0.921	4.72	0.812	0.875	11.2	0.89	0.883

Table B.9 Tabulated Values of Emittance as a Function of Wavelength for Industrial Smelt Sample E.

Wavelength (microns)	Measured Emittance	Smoothed Emittance	Wavelength (microns)	Measured Emittance	Smoothed Emittance	Wavelength (microns)	Measured Emittance	Smoothed Emittance
0.72	0.962	0.988	1.92	0.915	0.953	4.64	0.838	0.853
0.74	1.209	1.012	1.96	0.965	0.947	4.72	0.807	0.858
0.76	0.564	1.043	2	0.899	0.943	4.8	0.821	0.869
0.78	1.114	1.078	2.04	0.937	0.939	4.88	0.895	0.884
0.82	1.081	1.114	2.08	0.985	0.938	4.96	0.922	0.902
0.84	1.439	1.148	2.12	0.912	0.938	5.04	0.958	0.921
0.86	1.245	1.178	2.16	0.903	0.939	5.12	0.973	0.938
0.88	1.162	1.202	2.2	0.994	0.942	5.2	0.95	0.951
0.9	1.263	1.218	2.24	0.892	0.946	5.28	0.984	0.96
0.92	1.201	1.226	2.28	0.969	0.95	5.36	0.97	0.964
0.94	1.192	1.228	2.32	0.989	0.954	5.68	0.97	0.964
0.96	1.25	1.224	2.36	0.928	0.958	5.76	0.927	0.96
0.98	1.191	1.217	2.4	0.958	0.963	5.84	0.992	0.954
1	1.199	1.207	2.44	0.989	0.967	5.92	0.929	0.948
1.02	1.222	1.196	2.48	0.939	0.972	6	0.919	0.943
1.04	1.21	1.185	2.52	0.991	0.977	6.08	0.984	0.94
1.06	1.169	1.173	2.56	0.998	0.982	6.16	0.904	0.941
1.08	1.199	1.162	2.6	0.962	0.987	6.24	0.955	0.943
1.1	1.137	1.15	2.64	1.004	0.99	6.32	0.909	0.948
1.12	1.119	1.138	2.68	1.017	0.992	6.4	0.958	0.954
1.14	1.128	1.126	2.72	0.967	0.991	6.48	0.963	0.958
1.16	1.104	1.114	2.76	1.015	0.989	6.56	0.946	0.961
1.18	1.063	1.103	2.8	0.995	0.984	6.64	1.015	0.961
1.2	1.119	1.094	2.84	0.95	0.977	6.72	0.939	0.958
1.22	1.062	1.086	2.88	0.967	0.97	6.8	1.023	0.952
1.24	1.104	1.08	2.92	1.016	0.963	6.88	0.89	0.944
1.26	1.072	1.074	2.96	0.972	0.956	6.96	1.015	0.935
1.28	1.081	1.069	3	0.935	0.951	7.04	0.91	0.926
1.3	1.055	1.063	3.04	0.943	0.948	7.12	0.829	0.919
1.32	1.073	1.057	3.08	0.806	0.947	7.2	0.914	0.913
1.34	1.029	1.05	3.12	0.926	0.948	7.36	0.9	0.911
1.36	1.063	1.043	3.16	1.068	0.95	7.52	0.914	0.911
1.38	1.015	1.034	3.2	0.956	0.952	7.68	0.904	0.913
1.4	1.038	1.026	3.24	0.991	0.953	7.84	0.931	0.916
1.42	1.009	1.018	3.28	0.966	0.951	8	0.92	0.919
1.44	1.018	1.01	3.32	0.914	0.948	8.16	0.933	0.923
1.46	0.981	1.003	3.36	0.916	0.943	8.32	0.947	0.926
1.48	1.019	0.997	3.4	0.981	0.936	8.48	0.924	0.928
1.5	0.971	0.99	3.44	0.898	0.929	8.64	0.922	0.93
1.52	0.998	0.984	3.48	0.952	0.922	8.8	0.934	0.931
1.54	0.969	0.978	3.52	0.9	0.918	8.96	0.911	0.931
1.56	0.992	0.972	3.56	0.851	0.915	9.12	0.932	0.932
1.58	0.967	0.967	3.6	0.936	0.916	9.28	0.937	0.932
1.6	0.954	0.963	3.68	0.927	0.918	9.44	0.916	0.933
1.62	0.932	0.96	3.76	0.933	0.922	9.6	0.954	0.933
1.64	0.961	0.958	3.84	0.945	0.925	9.76	0.951	0.933
1.66	0.921	0.959	3.92	0.918	0.926	9.92	0.905	0.935
1.68	1.009	0.96	4	0.915	0.924	10.08	0.965	0.937
1.7	0.965	0.963	4.08	0.919	0.919	10.24	0.942	0.941
1.72	0.946	0.965	4.16	0.915	0.91	10.4	0.905	0.948
1.74	0.962	0.967	4.24	0.922	0.898	10.56	0.998	0.959
1.76	0.931	0.967	4.32	0.905	0.884	10.72	0.949	0.972
1.8	1.02	0.966	4.4	0.938	0.871	10.88	0.886	0.989
1.84	1.041	0.963	4.48	0.846	0.86	11.04	0.983	1.007
1.88	0.922	0.958	4.56	0.756	0.854	11.2	1.088	1.027

☆U.S. GOVERNMENT PRINTING OFFICE: 1997 - 549-208/20012